IN-07
CR 768

NASA Contractor Report 202319

Impact of Periodic Unsteadiness on Performance and Heat Load in Axial Flow Turbomachines

Om P. Sharma and Gary M. Stetson
Pratt & Whitney
East Hartford, Connecticut

William A. Daniels
United Technologies Research Center
East Hartford, Connecticut

Edward M. Greitzer
Massachusetts Institute of Technology
Cambridge, Massachusetts

Michael F. Blair and Robert P. Dring
United Technologies Research Center
East Hartford, Connecticut

January 1997

Prepared for
Lewis Research Center
Under Contract NAS3–25804

National Aeronautics and
Space Administration

FOREWORD

This program is a research project, funded by the National Aeronautics and Space Administration-Lewis Research Center (NASA-LeRC), to investigate the impact of periodic unsteadiness on performance and heat load in axial flow turbomachines. The overall project is under the direction of Mr. James W. Gauntner, the program manager for NASA-LeRC, and Dr. John J. Adamczyk, the technical monitor for NASA-LeRC. The program was conducted at Pratt & Whitney (P&W) under the direction of Dr. O.P. Sharma, the program manager, and Mr. Gary M. Stetson, the principal investigator.

Intentionally Left Blank

SYMBOLS/NOMENCLATURE

C_{ps}	Static pressure coefficient $(P_{ti} - P_s)/q2$ or $(P_{ti} - P_s)/0.5\rho Um^2$
C_{pt}	Total pressure coefficient $(P_{ti} - P_t)/0.5\rho Um^2$
C_{ptr}	Relative total pressure coefficient $(P_{ti} - P_{tr})/0.5\rho Um^2$
Cr	Velocity in radial direction
Ct	Velocity in tangential direction
Cx	Velocity in axial direction
r	Radius from center line
x	Axial distance
y	Tangential distance (Normal to X in Cartesian system)
α	Yaw angle ($\tan \alpha = Cx/Ct$)
ϕ	Phi angle ($\tan \phi = Cr/Cx$)
θ	Tangential angular displacement
θ/s	Momentum thickness divided by suction surface length of airfoil
Fr	Radial body force
Ft	Tangential body force
Fx	Axial body force

Cx'Cx'	Axial Velocity Normal Stress	Random, Temporal or Spatial, Depending on Averaging Noted by Superscripts
Ct'Ct'	Tangential Velocity Normal Stress	
Cr'Cr'	Radial Velocity Normal Stress	
Cx'Ct'	Axial-Tangential Velocity Shear Stress	
Cx'Cr'	Axial-Radial Velocity Shear Stress	
Ct'Cr'	Tangential-Radial Velocity Shear Stress	

87894.cdr

τ_{tr}	Tangential-radial shear stress
τ_{tx}	Tangential-axial shear stress
τ_{xr}	Axial-radial shear stress

SYMBOLS/NOMENCLATURE(CONTINUED)

H	Heat transfer coefficient
ρ	Density
v	Viscosity
P_s	Static pressure
P_t	Total pressure
P_{ti}	Rig inlet total pressure
P_{tr}	Relative total pressure
q2	Row exit dynamic head
s	Suction surface length from leading edge of airfoil
S	Airfoil height (span)
s_{max}	Suction surface length of airfoil
Um	Rotational speed at the mean radius of the rotor
μt	Turbulent viscosity
εm	Eddy viscosity
μa	Apparent viscosity
S	Entropy $\equiv LN[P/P_i \times (\rho_i/\rho)^{\gamma}]$
$Q_2 =$	$V_{x2} + V_{t2} + V_{r2}$
$T_s =$	$V_x V_t + V_x V_r + V_t V_r$

V_{x2} (turbulent) $= \overline{Cx'Cx'}/\overline{Cx}^2$

V_{x2} (temporal) $= \overline{\overline{Cx'Cx'}}/\overline{Cx}^2$

V_{x2} (spatial) $= \overline{\overline{\overline{Cx'Cx'}}}/\overline{Cx}^2$

V_{t2} (turbulent) $= \overline{Ct'Ct'}/\overline{Cx}^2$

V_{t2} (temporal) $= \overline{\overline{Ct'Ct'}}/\overline{Cx}^2$

V_{t2} (spatial) $= \overline{\overline{\overline{Ct'Ct'}}}/\overline{Cx}^2$

V_{r2} (turbulent) $= \overline{Cr'Cr'}/\overline{Cx}^2$

V_{r2} (temporal) $= \overline{\overline{Cr'Cr'}}/\overline{Cx}^2$

V_{r2} (spatial) $= \overline{\overline{\overline{Cr'Cr'}}}/\overline{Cx}^2$

V_xV_t (turbulent) $= \overline{Cx'Ct'}/\overline{Cx}^2$

V_xV_t (temporal) $= \overline{\overline{Cx'Ct'}}/\overline{Cx}^2$

V_xV_t (spatial) $= \overline{\overline{\overline{Cx'Ct'}}}/\overline{Cx}^2$

V_xV_r (turbulent) $= \overline{Cx'Cr'}/\overline{Cx}^2$

V_xV_r (temporal) $= \overline{\overline{Cx'Cr'}}/\overline{Cx}^2$

V_xV_r (spatial) $= \overline{\overline{\overline{Cx'Cr'}}}/\overline{Cx}^2$

V_tV_r (turbulent) $= \overline{Ct'Cr'}/\overline{Cx}^2$

V_tV_r (temporal) $= \overline{\overline{Ct'Cr'}}/\overline{Cx}^2$

V_tV_r (spatial) $= \overline{\overline{\overline{Ct'Cr'}}}/\overline{Cx}^2$

St =	Stanton Number = $h/\rho_e V_e C_p$
h =	Heat transfer coefficient
ρ_e =	Airfoil exit plane — density
v_E =	Airfoil exit plane — velocity
C_p =	Specific heat ratio
γ =	Specific heat ratio

Superscripts

$\overline{(\ )}$	Time-average random
$\overline{\overline{(\ )}}$	Time-average temporal
$\overline{\overline{\overline{(\ )}}}$	Time-average spatial
$(\ )'$	Instantaneous

SYMBOLS/NOMENCLATURE(CONTINUED)

Derivatives

$\frac{\partial(\ )}{\partial x}$	First Partial Derivative with 'x' (in Cartesian and cylindrical coordinate system)
$\frac{\partial(\ )}{\partial r}$	First Partial Derivative with 'r' (in cylindrical coordinate system)
$\frac{\partial(\ )}{\partial y}$	First Partial Derivative with 'y' (in Cartesian coordinate system)
$\frac{\partial^2(\ )}{\partial x^2}$	Second Partial Derivative with 'x'
$\frac{\partial^2(\ )}{\partial r^2}$	Second Partial Derivative with 'r'

The nomenclature used in Appendix C, *Large-Scale Rotating Rig 1-1/2 Stage Rig Baseline Data,* is listed in Table i. For accessibility, this listing of nomenclature is also provided in Appendix C.

Table i. Nomenclature for Appendix C

Nomenclature	*Definition*
CP	Pressure coefficient $(P_0 - P)/Q_{UM}$
CPTABSM	Mass-averaged absolute total poressure coefficient $(P_0 - PTABS)/Q_{UM}$
CPSA	Area-averaged static pressure coefficient = $(P_0 - PSA)/Q_{UM}$
CPTRELM	Mass-averaged relative total pressure coefficient = $(P_0 - PTREL)/Q_{UM}$
CPROTM	Mass-averaged rotary total pressure coefficient = $(P_0 - PTROT)/Q_{UM}$
CTANM	Mass-averaged absolute tangential velocity ratio = $CTANM/U_m$
CTANA	Area-averaged absolute tangential velocity ratio = $CTANA/U_m$
CTOT	Total absolute velocity
CTOTM	Mass-averaged absolute total velocity ratio = $CTOT/U_m$
CTOTA	Area-averaged absolute total velocity ratio = $CTOT/U_m$
CRA	Area-averaged radial velocity ratio = CR/U_m
CXA	Area-averaged axial velocity ratio = CX/U_m
C_x	Rig inlet average midspan axial flow velocity, ft/sec
C_x/U_m	Rig flow coefficient
P	Static pressure, psia
P_0	Rig inlet total pressure, psia
PCSPAN	Percent of airfoil span = (R - Rhub)/(Rtip-Rhub)* 100
PHIABSA	Area-averaged absolute pitch angle, deg
PHIRELA	Area-averaged relative pitch angle, deg
PTREL	Relative total pressure = $(PTREL = P+Q_{local})$
PTROT	Rotary total pressure = $(PTROT=PREL-Q_{UM})$
Q_{local}	$1/2\ \rho_0 CTOT^2$
Q_{UM}	Dynamic pressure = $1/2\rho_0 Um^2$, psia
S	Airfoil span, inches

Table i. Nomenclature for Appendix C (Continued)

Nomenclature	*Definition*
STA1	Station 1 - 1V exit plane
STA2	Station 2 - 1B exit plane
STA3	Station 3 - 2V exit plane
TNCTMCXA	Area averaged absolute yaw angle = $\tan^{-1}$(CTANM/CXA)
TNWTMCXA	Area averaged relative yaw angle = $\tan^{-1}$(WTANM/CXA)
U_m	Rotor midspan wheel speed, ft/sec
WTANA	Area-averaged relative tangential velocity ratio = WTANA/ U_m
WTANM	Mass-averaged relative tangential velocity ratio = WTANM/ U_m
WTOTA	Area-averaged relative total velocity ratio = WTOTA/ U_m
WTOTM	Mass-averaged relative total velocity ratio = WTOTM/ U_m
YAWABSA	Area-averaged absolute yaw angle, deg
YAWRELA	Area-averaged relative yaw angle, deg
X	Airfoil axial location from leading edge, inches
X_1	Axial distance from leading edge of rotor to trailing edge of first stator, inches
X_2	Axial distance from trailing edge of rotor to leading edge of second stator, inches
ρ_0	Rig inlet density, slugs/ft^3
r	Radius, inches

CONTENTS

This Page Is Intentionally Left Blank

FIGURES

TABLES

This Page Is Intentionally Left Blank

1. SUMMARY

Flows in advanced axial flow turbines are highly unsteady and three-dimensional (3-D) due to the relative movement of adjacent airfoil rows, large turnings, and low-aspect ratios. The effect of the unsteadiness is not well understood; therefore, unsteadiness is not explicitly accounted for in the aerodynamic design process, except through empirical correlations. The main goal of the present investigation was to quantify the impact of periodic unsteadiness on the loss and heat load generation mechanisms in an axial flow turbine environment. Five tasks were identified to complete this investigation, which was performed in the following three phases:

- *Phase I* — Consisted of analyzing unsteady data, previously acquired in a 1 1/2-stage, large-scale, axial flow turbine, to determine essential features of periodic unsteady flows and associated terms (*deterministic stresses*) that needed to be accounted for in the multistage flow prediction systems.
- *Phase II* — Consisted of performing supporting analyses using computational fluid dynamics (CFD) codes to determine: (1) limitations of their flow prediction capabilities and *new* modeling requirements, and (2) the appropriate experimental program needed to assess the impact of periodic unsteadiness on the time-averaged flows in a 1 1/2-stage turbine rig.
- *Phase III* — Consisted of experimental quantification of the effect of periodic unsteadiness on the losses and heat loads in the turbine rig environment.

Results from this investigation indicated that the magnitude of the terms representing periodic unsteadiness (deterministic stresses) were as large or larger than those representing the random unsteadiness (turbulence) at the inlet to every airfoil row, except the first airfoil row in a multistage turbine. The experimental data acquired during this program also showed that the aerodynamic performance of an airfoil row was affected by spacing between adjacent airfoil rows, indicating the importance of deterministic stresses on the loss generation. A demonstration of the impact of deterministic stress terms was depicted through numerical experiments, which were conducted to investigate the phenomenon of combustor-generated hot streak migration through turbine rotors. This effect can be modeled through deterministic stress-like terms in continuity and energy equations.

This Page Is Intentionally Left Blank

2. INTRODUCTION

The unsteady effects from rotor-stator interaction in multirow turbomachines have been qualitatively known for many years. However, robust, readily applicable methods to quantify the phenomena of interest were not developed until recently. A principal driver for these methods has been the trend to lower aspect ratio and increase Mach numbers, two design tendencies of modern aircraft engines. This trend, coupled with increases in computer power, has led to the development of computational procedures for examining basic issues concerning rotor-stator flow interactions.

A rigorous conceptual framework for addressing these effects has been proposed and applied by Adamczyk [1]. In this approach, unsteady terms associated with blade periodicity were separated from unsteady effects not linked to blade passing. The effect of the former on the time mean flowfield was characterized by *deterministic stresses*, which appeared as time averages of the quadratic products of the periodic fluctuations. Important concerns dealt with the magnitudes and distributions of these *deterministic stresses*, and, even more relevantly, their effect on the overall flowfield, compared to non-blade periodic unsteady phenomena (e.g., turbulence or vortex shedding).

Pratt & Whitney (P&W) was interested in unsteady flow as it related to impacting the eventual product, the turbomachinery in an aircraft gas turbine engine, or other similar device. Understanding unsteady flow, i.e., sorting out the many different phenomena, was a necessary part of the process, but not the complete process. To affect the design process in a substantial manner, it was crucial to have the capability to implement this understanding into improved design procedures. These procedures needed to specify how the design of blades and vanes should be changed. Therefore, P&W sought ways of *translating* the increased understanding into the design process, through procedures that contained sounder, more physically-based flow descriptions and rational ways to assess, account for, and design for time mean effects of flow unsteadiness. Modeling procedures of this type were useful because current unsteady flow computations are too time consuming to be used as part of routine design procedure.

Experimental information was presented concerning time mean effects of unsteady flow in an axial turbine on losses and heat transfer. This included the influence of axial spacing between rows, and changes in performance due to the clocking (indexing) of one row of stators relative to another. Comparisons between steady-state computations and the time-averaged unsteady analyses were also shown to demonstrate that unsteady flow had a clear and significant time mean effect. Finally, P&W described instances in which the use of insight about unsteady flow had an impact on the design of actual engine hardware.

This Page Is Intentionally Left Blank

3. BACKGROUND

The technical content of this program has undergone considerable evolution since its initiation. These evolutionary changes have provided insight into the basis for strategies that address unsteady flow phenomena. A critical factor in this evolution has been the rapidity with which three-dimensional (3-D) unsteady flow computational procedures have become reliable enough for numerical experiments. At the start of the program (1990), Pratt & Whitney (P&W) anticipated that the most effective approach would be to use available detailed experimental data on the *deterministic* and random (turbulent) stresses. This was true, although the data set was not complete enough to permit the resolution of all stress terms in the equations of motion. During the execution of the program, however, this situation changed as the capability to capture unsteady flow phenomena through computations increased. The current position is that it is more useful to compute the *deterministic stress* terms (i.e., to use the results of the unsteady flow calculations as data) in developing approaches to implement the time-averaged effect of unsteady flows. When this is performed in a consistent manner, the time-averaged effect is well represented. The experimental data thus play a smaller role in the development of the models than what was initially envisioned. As an example, early emphasis was on examining approaches to developing models that allowed closure of the system of equations that contained *deterministic stresses.* (The *nondeterministic stress* terms, which would arise from turbulence, still need to be modeled.) This is presently of less concern, and the approach would be to compute these terms.

A further factor that shaped the evolution concerns P&W's assessment of the importance of unsteady flow effects, including *deterministic stresses,* on overall figures of merit for turbomachinery performance, such as efficiency and heat load. Time-averaged manifestations of unsteady flow have nonlinear effects, i.e., involving quadratic or higher products of the perturbations from the time mean flow. If these perturbations have a magnitude of the order of ten percent of the mean, which is a reasonably large unsteadiness, the nonlinearity would be expected to be of the order of one percent. In the past, therefore, many unsteady effects have been too small to have a significant impact. The two design trends mentioned in Section 2, however, have resulted in increased levels of unsteady perturbations and substantially larger time-averaged values. For example, this was observed in turbine performance that was measured in engine tests. In addition, increased attention is now being given to efficiency changes on the order of one percent, so this level has assumed greater significance.

For these reasons, there is a desire to incorporate information concerning these flow effects into the design process, so that hardware could be affected. As a result, the research has also examined the development of the methodology by which the design process could be effectively conducted. The results have been extremely encouraging, and (under internal P&W support) the technology has been applied to compressors as well as turbines. This was not explicitly envisioned in the initial formulation. Specific applications that relate to this project are described in detail below; the unsteady flow concepts associated with the present program have provided a springboard to new designs.

Two other aspects connected with specific items initially singled out to be addressed were also contributors to the change in emphasis. The first aspect was the realization of the strong effect of inlet boundary conditions on the angle profile at the exit of a blade row. This was found initially using a heuristic approach, and was then verified computationally. The implication was that the discrepancy between computations and experiment, as far as second stator exit flow angle, could be directly traced to improper modeling of the second stator inlet profile.

The second aspect was the detailed scrutiny of previous heat transfer data. These data showed a heat transfer rate on the suction surface that could not be explained using current predictive measures. These data appeared to indicate there were phenomena occurring that were not captured by the state-of-the-art models. The goal was thus to investigate what these might be and how they might be modeled. Repeats of the experiments with new test hardware, however, indicated that: (1) previous data were in error, and (2) the behavior on the suction side of the second vane was in accordance with predictions. Therefore, this point was not addressed.

After addressing the above two items, efforts were directed toward conducting numerical and physical experiments in flow situations, where time mean effects of periodic unsteadiness had yielded results that could not be

explained on the basis of conventional steady flow techniques. In addition to providing insight into physical mechanisms governing the levels of heat loads and losses in turbine airfoil rows in a multistage environment, the experiments were expected to provide guidance in the design of next generation of turbomachines. The main activities were divided into analytical experiments, physical experiments, and design of actual turbine hardware.

- *Numerical Experiments* — These experiments were directed toward simulating the migration of burner generated hot streaks in two model turbines. Unsteady, multistage Euler- and Reynolds-averaged Navier-Stokes (RANS) codes were used to conduct the numerical simulations.

- *Physical Experiments* — These experiments quantified the effect of the inlet *deterministic stresses* on the airfoil row loss and heat transfer. These tests were conducted by altering the physical spacing between adjacent airfoil rows.

  These experiments also investigated the impact of indexing (clocking) of the second stator airfoil relative to a first airfoil on the performance and heat transfer coefficient of the second stator.

- *Designs of Actual Turbine Hardware* — Designs were based on the experiments discussed above during the course of the contract (using internal P&W funding).

The remainder of this report is organized to discuss the detailed work conducted as part of this contract or supporting evidence provided by P&W-funded programs.

Analysis of the unsteady flow data, previously acquired by P&W from experiments conducted in the United Technologies Research Laboratory (UTRC) large-scale rotating rig (LSRR), is discussed in Section 4. The relative magnitude of terms, which represent the periodic (deterministic) and random (turbulence) unsteadiness, are compared in Section 4. This comparison demonstrates the need to model the effects of periodic unsteadiness in multistage turbines.

Results obtained from numerical experiments conducted by using multistage 3-D steady and unsteady, Euler and RANS codes, are discussed in Section 5. The importance of accurate specification of boundary conditions on the prediction of flow features for an airfoil row is highlighted. Discussions on the appropriateness of steady and unsteady Euler codes, together with a strategy to account for the adverse effects of combustor generated hot streaks on the turbine performance and heat load characteristics, are provided in Section 5.

Results obtained from the initial phase of the experimental program conducted in the UTRC LSRR are discussed in Section 6. The detailed aerodynamic and heat transfer data acquired in the rig, and the comparisons with simulations from recently developed, multistage, 3-D RANS codes are also discussed.

Results from the physical experiments conducted in this program are discussed in Section 7, including the impact of stator-to-stator clocking on performance and heat load characteristics of downstream stators. Also discussed in Section 7 are the results obtained from altering the spacing between adjacent airfoil rows. This can be used to quantify the impact of periodic unsteadiness (*deterministic stresses)* on the performance of an airfoil row in a multirow environment.

The impact of the work, which was conducted during the present contract, on the evolution of design processes and the actual engine hardware, is discussed in Section 8. The specific items addressed are the impact on turbine performance and heat loads, and compressor efficiency and stall margin. Conclusions and recommendations for future work are provided in Section 9. References cited throughout Sections 1 through 9 are listed in Section 10. Appendix A discusses the three approaches used to investigate whether deterministic stresses influence the performance of the second stator in the LSRR configuration. Appendix B describes the facility at United Technologies Research Center that was used for the LSRR. A comprehensive data set is summarized in Appendix C. A synopsis of the proposed program is provided in Appendix D.

4. EVALUATION OF UNSTEADY DATA

This section summarizes the evaluation of the high-response data acquired prior to this contract in the United Technologies Research Center (UTRC) large-scale rotating rig (LSRR). The facility is a large-scale, low-speed rig that allows detailed measurement of the aerodynamic flowfield. The objective of the evaluation was to ascertain the relative magnitudes of the random and periodic unsteady flowfield components, and their relation to steady computational fluid dynamics (CFD) analysis tools. This section provides a brief background of Pratt & Whitney's (P&W's) experience in turbine unsteady flows, and is followed by a discussion of the measured results and summary.

4.1 BACKGROUND OF UNITED TECHNOLOGIES CORPORATION EXPERIENCE

United Technologies Corporation (UTC), specifically P&W and UTRC, has been acquiring unsteady aerodynamic data for many years. These data include unsteady measurements in cascades, high- and low-pressure turbine (HPT and LPT) rigs, and in the actual engine environment. United Technologies Corporation has: (1) determined boundary layer transition using surface hot films, (2) measured unsteady total and static pressures using close-coupled, high-response transducers and infinite tube probes (ITP), and (3) measured unsteady flowfields using three-element hot wires, high-response five-hole probes, and/or laser doppler velocimetry (LDV). The data, however, have never been analyzed in a manner consistent with the *average-passage* equations described by Adamczyk [1]. Data (previously acquired in the UTRC LSRR) were processed consistent with these equations to assist in determining the importance of additional terms, identified by Adamczyk, relative to turbulence (random unsteady flow).

4.1.1 Previous Experiments

From 1977-1978, the LSRR (Figure 1) at UTRC was used to acquire unsteady flowfield data in a low-aspect ratio, 1 1/2-stage turbine rig (Sharma et al., 1984 [2]). Computer resources (at that time) limited the amount of data that could be processed. As computer resources became more available, visualization of unsteady flow measurements became possible, and the data were analyzed to study the time dependence of the rotor flowfield.

The UTRC LSRR rig has 22 first stators, 28 rotor blades, and 28 second stators. Two, 180 degree, annular segments, exist at any given *snapshot* in time (rotor position), comprised of 11 first stators, 14 rotor blades, and 14 second stators, where the flow patterns are repeated in each annular segment. Each rotor blade of a given annular segment will have a different position, relative to a nearby first stator. Therefore, if the rotor flowfield is influenced by the first stator airfoil row, each rotor blade passage of this annular segment will have different flow characteristics.

To determine if there were an unsteady effect of the first stator on the rotor in the LSRR, a total pressure contour at the rotor exit (for four rotor passages) was created for one *snapshot* in time. To assist with orientation, the location of the data plane is graphically depicted in Figure 2 for an unsteady three-dimensional (3-D) numerical calculation. The experimental results of the unsteady relative pressures show that (Figure 3) at an instant in time, four rotor passages have differences from 0 to 80 percent span. These distortions coincide with rotor/stator passing frequency, and therefore, the rotor flowfield is being affected by the upstream stator. To better understand the influence of this unsteady flow phenomena, a detailed evaluation of the unsteady data previously acquired in the UTRC LSRR was undertaken as a part of the present investigation.

4.1.2 Description of Flow Stresses

The governing equations, pertinent to this evaluation, are the time and spatially-averaged incompressible radial, tangential, and axial momentum equations (Equations 1, 2, and 3) per Adamczyk [1]. In addition to the Reynolds stresses typically associated with random unsteady flow features, there are additional terms in the momentum equations. These terms appear as axial, tangential, or radial gradients of the following parameters: $Cx'Cx'$, $Ct'Ct'$, $Cr'Cr'$, $Cx'Cr'$ $Cx'Ct'$, and $Ct'Cr'$. These terms can be identified, as outlined by Adamczyk [1], as normal and shear stresses.

Radial Momentum

$$Cr\frac{\partial Cr}{\partial r} - \frac{Ct^2}{r} + Cx\frac{\partial Cr}{\partial x} = \frac{Fr}{\rho} - \frac{1}{\rho}\frac{\partial Ps}{\partial r} + \nu\left(\frac{\partial^2 Cr}{\partial r^2} + \frac{1}{r}\frac{\partial}{\partial}\frac{Cr}{r} - \frac{Cr}{r^2} + \frac{\partial^2 Cr}{\partial x^2}\right)$$

$$[\text{Random (Turbulent)}] - \frac{\partial\overline{(Cr'Cr')}}{\partial r} - \frac{\overline{(Cr'Cr')}}{r} - \frac{\partial\overline{(Cr'Cx')}}{\partial x} + \frac{\overline{(Ct'Ct')}}{r}$$

$$[\text{Temporal}] - \frac{\partial\overline{\overline{(Cr'Cr')}}}{\partial r} - \frac{\overline{\overline{(Cr'Cr')}}}{r} - \frac{\partial\overline{\overline{(Cr'Cx')}}}{\partial x} + \frac{\overline{\overline{(Ct'Ct')}}}{r}$$

$$[\text{Spatial}] - \frac{\partial\overline{\overline{\overline{(Cr'Cr')}}}}{\partial r} - \frac{\overline{\overline{\overline{(Cr'Cr')}}}}{r} - \frac{\partial\overline{\overline{\overline{(Cr'Cx')}}}}{\partial x} + \frac{\overline{\overline{\overline{(Ct'Ct')}}}}{r} \qquad \text{[Equation 1]}$$

Tangential Momentum

$$Cr\frac{\partial Ct}{\partial r} + \frac{CrCt}{r} + Cx\frac{\partial Ct}{\partial x} = \frac{Ft}{\rho} + \nu\left(\frac{\partial^2 Ct}{\partial r^2} + \frac{1}{r}\frac{\partial}{\partial}\frac{Ct}{r} - \frac{Ct}{r^2} + \frac{\partial^2 Ct}{\partial x^2}\right)$$

$$[\text{Random (Turbulent)}] - \frac{\partial\overline{(Ct'Cr')}}{\partial r} - \frac{2\overline{(Ct'Cr')}}{r} - \frac{\partial\overline{(Ct'Cx')}}{\partial x}$$

$$[\text{Temporal}] - \frac{\partial\overline{\overline{(Ct'Cr')}}}{\partial r} - \frac{2\overline{\overline{(Ct'Cr')}}}{r} - \frac{\partial\overline{\overline{(Ct'Cx')}}}{\partial x}$$

$$[\text{Spatial}] - \frac{\partial\overline{\overline{\overline{(Ct'Cr')}}}}{\partial r} - \frac{2\overline{\overline{\overline{(Ct'Cr')}}}}{r} - \frac{\partial\overline{\overline{\overline{(Ct'Cx')}}}}{\partial x} \qquad \text{[Equation 2]}$$

Axial Momentum

$$Cr\frac{\partial Cx}{\partial r} + Cx\frac{\partial Cx}{\partial x} = \frac{Fx}{\rho} - \frac{1}{\rho}\frac{\partial Ps}{\partial x} + \nu\left(\frac{\partial^2 Cx}{\partial r^2} + \frac{1}{r}\frac{\partial Cx}{\partial r} + \frac{\partial^2 Cx}{\partial x^2}\right)$$

$$[\text{Random (Turbulent)}] - \frac{\partial\overline{(Cx'Cr')}}{\partial r} - \frac{\overline{(Cx'Cr')}}{r} - \frac{\partial\overline{(Cx'Cx')}}{\partial x}$$

$$[\text{Temporal}] - \frac{\partial\overline{\overline{(Cx'Cr')}}}{\partial r} - \frac{\overline{\overline{(Cx'Cr')}}}{r} - \frac{\partial\overline{\overline{(Cx'Cx')}}}{\partial x}$$

$$[\text{Spatial}] - \frac{\partial\overline{\overline{\overline{(Cx'Cr')}}}}{\partial r} - \frac{\overline{\overline{\overline{(Cx'Cr')}}}}{r} - \frac{\partial\overline{\overline{\overline{(Cx'Cx')}}}}{\partial x} \qquad \text{[Equation 3]}$$

where:

Cx′Cx′ } Ct′Ct′ } Cr′Cr′ }	Normal Stresses
Cx′Cr′ } Cx′Ct′ } Ct′Cr′ }	Shear Stresses

defined as:

Cx′Cx′ = Axial Intensity
Cr′Cr′ = Radial Intensity
Ct′Ct′ = Tangential Intensity
Cx′Ct′ = Axial-Tangential Shear Stress
Cx′Cr′ = Axial-Radial Shear Stress
Ct′Cr′ = Tangential-Radial Shear Stress.

The detailed evaluation of the unsteady data focuses on the assessment of these additional stresses (spatial, temporal) with respect to their relative importance to turbulence in the UTRC LSRR.

4.2 ANALYSIS OF UNSTEADY DATA

Random and periodic flow behavior are depicted in Figure 4. This figure schematically represents a velocity distribution (or time history) over one period (i.e., rotor blade passing). The implication is that a velocity distribution aft of an airfoil row is composed of mean, periodic (rotor passing frequency), and random components.

To assess the relative importance of the random and periodic unsteadiness on performance, a first step is to compare the relative magnitudes of the random unsteadiness (turbulence) with the periodic unsteadiness (temporal and spatial) from the unsteady data measured in the LSRR facility. The data will be presented as: (1) gap-averaged stresses (random and periodic) versus span, and (2) contour plots for the first stator exit (rotor inlet) (Station 1), rotor exit (second stator inlet) (Station 2), and the second stator exit (Station 3) measurement planes.

The random stresses are referred to as turbulent stresses, while the spatial and temporal stresses are called deterministic stresses. To assist in understanding what these stresses are and how they are determined, Figure 5 depicts velocity and associated stresses as they might appear downstream of an airfoil trailing edge (TE). Donaldson [3] derives and presents the equations and processing technique used to analyze the actual unsteady data. As described by Donaldson, numerous time records of data were obtained at each probe position (i.e., each circumferential and radial coordinate). These were ensemble averaged to obtain mean velocity components and components of stresses due to unsteady flow. The analytical procedure involved calculations of specific variances of instantaneous and time-averaged velocity components relative to mean quantities. Although the analysis is based on statistical algorithms, a conceptual description is provided below.

The random stresses, at each geometrical position, are determined by processing the instantaneous correlation (CxCx, CtCt, CrCr, CxCt, CxCr, CtCr), averaging over time, subtracting off the square of the time-averaged, and filtering out periodic fluctuations associated with wheel speed/airfoil passing frequency. Temporal stresses (periodic), at each spatial position, are determined in the same manner as the random, except the random fluctuations are filtered out. The spatial stresses are not associated with time, and only appear when the equations are spatially averaged. These stress terms are determined by obtaining the time-averaged velocities at each spatial position (radially and circumferentially), averaging over the circumference at one radial position, subtracting off the square of the circumference-averaged (i.e., $\overline{Cx'Cx'}circ-avg = \overline{Cx^2}circ-avg - \overline{CxCx}\ circ-local$) [Equation 4]. This analysis was applied to the measured data to obtain the stresses associated with the unsteady flow in the UTRC LSRR, namely, the random (i.e., turbulent), temporal, and spatial stresses.

Understanding the frame dependency of the deterministic stress is necessary to understand the measured results and discussed in the following sections. A spatial stress in the absolute frame contributes to the component of temporal stress in the relative frame, while a spatial stress in the relative frame contributes to the component of temporal stress in the absolute frame. Therefore, spatial and temporal unsteadiness components are locked to a given airfoil row. For example, if the first stator exit flowfield were not influenced by the passing of the rotor, the first stator exit flowfield would only have random and spatial components of stress, and the first stator exit (absolute frame) spatial stress would be equivalent to the rotor inlet temporal stress. If the rotor does influence the first stator exit flowfield, then the stator exit would have an additional temporal (i.e., periodic) stress induced by the rotor. Therefore, the spatial and temporal stresses have reference frame dependencies, while the random (i.e., turbulent) stresses are independent of reference frame.

To assess the possible impact of periodic unsteadiness on aerodynamic loss and heat transfer from the UTRC LSRR data, it will be assumed that there is an analogy between turbulence and deterministic stress, as described below.

The first analogy is assuming the magnitude of deterministic stress has a similar influence on boundary layer transition as free stream turbulence (disturbance). Free stream turbulence, as summarized by Hinze [4], begins to affect the transition of the boundary layer at magnitudes of 0.2 percent. For a free stream turbulence intensity of 0.5 percent, the transition Reynolds number (REX) is approximately 1×10^6; for a 3 percent free stream turbulence, the transition Reynolds number is approximately 1×10^5. Assuming a similar impact as free stream turbulence, a measurable effect on airfoil performance is expected for inlet deterministic stress of 3 percent or larger.

The second analogy is comparing the turbulent stress terms with the deterministic stress terms as they appear in the momentum equations described in Section 4.1.2. This comparison will not provide the importance of turbulent stresses or deterministic stresses; it will only provide the relative importance. If turbulence and deterministic

stresses show the same magnitudes and gradients as they appear in the equations, then they have the same relative importance in closure of the equations. Since the axial gradients are not available, the radial gradients of deterministic stress will be compared to the turbulent stresses along with absolute magnitudes.

The final analogy assumes that there is an apparent viscosity associated with deterministic stress, which is similar to the turbulent viscosity developed using Boussinesq's hypothesis. For example, for a similar two-dimensional (2-D) incompressible boundary layer, the time-averaged momentum equation takes on the following form:

$$\overline{Cx}\frac{\partial \overline{Cx}}{\partial x} + \overline{Ct}\frac{\partial \overline{Cx}}{\partial y} + \frac{1}{\rho}\frac{\partial \overline{Ps}}{\partial x} = \frac{\partial}{\partial y}\left(\nu\frac{\partial \overline{Cx}}{\partial y} - \overline{Cx'Ct'}\right) \qquad \text{[Equation 5]}$$

Since flow deformation is associated with surface stress, and Cx′Ct′ is an additional stress on the fluid, an assumption is made that Cx′Ct′ is proportional to flow deformation, as noted in Equation 6:

$$\overline{Cx'Ct'} \propto \frac{\partial \overline{Cx}}{\partial y} \qquad \text{[Equation 6]}$$

The proportionality constant is called the eddy diffusivity for momentum (εm), or the equation below:

$$\overline{Cx'Ct'} = -\varepsilon m\frac{\partial \overline{Cx}}{\partial y} \qquad \text{[Equation 7]}$$

The turbulent dynamic viscosity is then defined as: ($\mu t = \rho \varepsilon m$), and after substitution and rearranging, it is defined as the following equation:

$$\mu t = -\frac{\rho}{\partial \overline{Cx}/\partial y}\overline{Cx'Ct'} \qquad \text{[Equation 8]}$$

Substituting these assumptions into the 2-D incompressible boundary layer equations and rearranging, the resulting equation becomes the following:

$$\overline{Cx}\frac{\partial \overline{Cx}}{\partial x} + \overline{Ct}\frac{\partial \overline{Cx}}{\partial y} + \frac{1}{\rho}\frac{\partial \overline{Ps}}{\partial x} = \frac{\partial}{\partial y}\left[\nu\left(1 + \frac{\mu t}{\rho \nu}\right)\frac{\partial \overline{Cx}}{\partial y}\right] \qquad \text{[Equation 9]}$$

This equation shows that the impact of viscosity in the flowfield is enhanced by the ratio of turbulent to molecular viscosity.

By assuming deterministic stress is analogous to turbulent stress, an *apparent* viscosity can be calculated from the LSRR data and compared to the turbulent viscosity. The discussion of the evaluation of the unsteady data focuses on the data acquired at the first stator exit/rotor inlet (Station 1), the rotor exit/second stator inlet (Station 2), and the second stator exit (Station 3).

4.2.1 Station 1 — Absolute Frame (First Stator Exit)

The first stator exit flowfield (Figure 6, reproduced from Joslyn, et al. [5]) showed a full span, narrow width defect in total pressure that represented the stator wake. Secondary flow vortices, situated at approximately 15 and 70 percent spans, were also interpreted from the contours, and the more typical pitch average loss versus span. These data suggested there will be absolute frame spatial stresses with large radial gradients that will appear as temporal stresses in the relative frame.

The spanwise distributions of measured stresses at Station 1 were provided in Figures 7 and 8. The temporal stresses were approximately 0.0, with no radial gradient, indicating that the rotor had little influence on the stator exit flowfield. These results, in general, indicated that the magnitudes of spatial stresses (the disturbances the rotor will sense) in this plane were larger than the turbulent stresses. These magnitudes were compared to typical turbulence (Q_2), as shown in Figure 7, where the deterministic stress level was twice as large as the turbulent level. The time-averaged terms that appeared in the momentum equations as magnitudes (V_{r2}, V_{t2}, V_xV_r, V_tV_r) showed that the deterministic stresses were the same level as the turbulent stress. The radial gradient terms that appeared in the momentum equations (V_{r2}, V_tV_r, V_xV_r), shown in Figures 7 and 8, indicated that turbulent stress gradients were almost nonexistent, relative to deterministic stress gradients. The locations of the highest levels of the deterministic stresses and radial gradients coincided with the secondary flow vortices located between 5 and 25, and 55 and 85 percent span. The correlation of the locations of the highest deterministic stresses, and the locations of the secondary flow vortices, were significant when comparing the experimental and computed CFD results in Section 5.

4.2.2 Station 1 — Relative Frame (Rotor Inlet)

The results described above indicated that the rotor had minimal influence on the first stator exit flowfield, as shown by the first stator exit temporal stress. Therefore, the rotor relative frame inlet temporal stresses (Figures 9 and 10) were essentially the same as the first stator exit spatial stresses. The data indicated that components of the deterministic stresses (temporal in the relative frame) and their radial gradients, in general, may be important in any closure models where turbulence is a factor.

4.2.3 Station 2 — Relative Frame (Rotor Exit)

The total pressure contours and secondary flow vectors of the rotor exit flowfield, as shown in Figure 11 (Joslyn, et al.[5]), depicted a strong secondary flow, as indicated by the time-averaged relative rotary total pressure contour and velocity vector plots. At the rotor exit, as derived for the relative frame, the total turbulence (Figure 12) showed that the average turbulence was approximately 20 percent ($Q_2 = 0.2$), as compared to the spatial stress of approximately 10 percent ($Q_2 = 0.1$). As previously discussed, if deterministic stress was analogous to turbulence, then the level could easily influence transition of the airfoil boundary layer.

Additionally, the magnitudes of the normal turbulent stress, in the equations of motion, were larger than the deterministic values (V_{r2}, V_{t2}), while the turbulence shear was about the same level as deterministic shear (V_tV_r, V_xV_r), as shown in Figures 12 and 13. The radial (spanwise) gradient terms that appeared in the equations of motion (V_{r2}, V_tV_r, V_xV_r) indicate, by inspection, that the deterministic (spatial) terms were the same level as the turbulent terms.

From both a magnitude and radial gradient perspective, the deterministic stresses were as important as the turbulent stress at the rotor exit plane in obtaining closure of the equations. Finally, the relative frame stress data presented in Figures 12 and 13 indicated that the deterministic stresses were largest at approximately 30 and 65 percent span, and coincided with the secondary flow vortices indicated by Joslyn, et al. [5].

Contour plots of the data used to obtain the spanwise distributions (Figure 12) of the random and temporal intensities (V_{x2}, V_{t2}, V_{r2}) are presented in Figure 14. To assist with interpretation of the flowfield, the relative pressure contour plot is also shown. The temporal stress contours for all components are shown in Figures 15 and 16. These contour plots show that high turbulence levels are present, as expected, in the wake regions, and that the deterministic temporal stresses are concentrated in the secondary vortex flow regions. Therefore, the turbulent

stresses are predominately associated with the wakes, whereas the temporal stresses are predominately due to the periodic behavior of the secondary flow, which are believed to be associated with the first stator/rotor interaction.

4.2.4 Station 2 — Absolute Frame (Second Stator Inlet)

The large secondary flow in the rotor (i.e., rotor spatial stresses) implied the temporal stress at the second stator inlet, in the absolute frame, will be large (Figures 17 and 18). Since the turbulent stresses were frame independent, the high turbulent stresses (discussed in the rotor exit relative frame data) will be the same for the second stator inlet absolute frame. The potential influence of the stresses on the flowfield and/or boundary layer was the same as discussed in Section 4.2.3, except that the spatial stresses at the rotor exit are now the temporal stresses at the second stator inlet because of the change of the reference frame. The spatial stress (second stator to second stator distortion) at the second stator inlet is a combination of the second stator induced distortions, and the first stator distortions that propagate through the rotor. The first stator distortions, for instance, would be the wake distortions of the first stator being present at the inlet to second stator. Relative to the other components of stress, the second stator inlet spatial stresses are quite small, and would imply that these stresses are not as important as the temporal and turbulent stresses in obtaining closure in the flow modeling of the governing equations.

4.2.5 Station 3 — Absolute Frame (Second Stator Exit)

Based on cascade data and time-averaged rotor data, the second stator exit is expected to have large secondary flows. However, as shown in Figure 19, the time-averaged exit loss contours and secondary flow vector distribution indicated only weak hub and tip vortices at 15 and 80 percent span. Two snapshots of total pressure contours aft of the second stator exit (Figure 20) indicated a rotor blade vortex for some relative rotor positions, but not others. Although not shown in Figures 19 and 20, flow animation of the second stator exit indicated the typical secondary flow structure was never observed aft of a rotor, as would be expected in a typical stationary cascade with this turning. This lack of typical secondary flow (flow typical in cascade or as shown in rotor) suggests that the inlet conditions generated by the rotor are impacting the second stator exit flowfield.

The spanwise distributions of stress at the second stator exit are different from the second stator inlet measurement plane (rotor exit). In general, the relative magnitudes of the temporal stresses decreased in level from the inlet of the second stator to the exit, while the relative magnitudes of the spatial stresses increased. The spatial stress magnitude is approximately 10 percent (Q_2 approximately 0.10), and turbulent stress is 14 percent (Q_2 approximately 0.14), as shown in Figure 21. Potentially, the stress could impact the transition of the downstream airfoil boundary layer. Figures 21 and 22 show the magnitude terms, which appear in the governing equations (V_{r2}, V_{t2}, V_xV_r, V_tV_r), have approximately the same magnitude of turbulent and spatial stress terms for V_tV_r and V_{t2}. The V_{r2} term is 0.04 higher for turbulence relative to spatial, and V_xV_r term is 0.0075 higher for spatial relative to turbulence. The radial (spanwise) gradients of the terms that appear in the governing equations (V_{t2}, V_tV_r, V_xV_r), shown in Figures 21 and 22, indicated that spatial stress gradients are the same order of magnitude as turbulent stress gradients.

Figure 23 shows the average turbulent and temporal stresses plotted versus the axial distance from the LSRR first to second stator exit. The figure shows that the average temporal stress in the rotor frame is relatively unchanged from the inlet to exit, while the temporal stress decayed by a factor of 5 from inlet to exit of the second stator. The average turbulence intensity (Figure 23) increased by a factor of 10 through the rotor and subsequently decayed by 25 percent through the second stator. From a modeling perspective, the ratio of turbulent stress production-to-decay is greater in the rotor airfoil row than in the second stator row (where the average turbulent intensity decreases) and must be taken into account if and when these terms are required for closure.

4.3 APPLICATION OF UNSTEADY ANALYSIS TO DEVELOPMENT OF DETERMINISTIC STRESS MODEL

The importance of the deterministic stresses and how they relate to steady CFD analysis tools is addressed in this section. Turbulent viscosity concepts are commonly used for computational modeling closure. One way that the deterministic stress information presented above may be used is to alter the apparent viscosity in the governing equations. A simple model is derived for comparison with the estimated turbulent viscosity.

A key step in the modeling of these observed effects is resolving the relationship between the deterministic stresses and the properties of the mean average-passage flow. If an analogy is drawn between the turbulent mixing, and mixing induced by the periodic unsteadiness, a simple model can be developed. Using the Boussinesq's hypothesis (shear stress is eddy viscosity times a velocity gradient), the magnitude of an apparent viscosity can be determined as follows:

Apparent Viscosity = (Deterministic shear stress)/(time-averaged mean flow stress)

The apparent and turbulent viscosities are defined in Equations 10 through 14:

$$\text{Turbulent Viscosity} = \frac{\mu t}{\rho} = \sqrt{\frac{(\overline{Cx'Cr'})^2 + (\overline{Cx'Ct'})^2 + (\overline{Ct'Cr'})^2}{\bar{\tau}xt^2 + \bar{\tau}xr^2 + \bar{\tau}tr^2}} \qquad \text{[Equation 10]}$$

$$\text{Apparent Viscosity} = \frac{\mu a}{\rho} = \sqrt{\frac{\overline{Cx'Cr'}^2 + \overline{Cx'Ct'}^2 + \overline{Ct'Cr'}^2}{\bar{\tau}xt^2 + \bar{\tau}xr^2 + \bar{\tau}tr^2}} \qquad \text{[Equation 11]}$$

where:

$$\bar{\tau}xt = \left(\frac{1}{r}\frac{\partial \overline{Cx}}{\partial \theta} + \frac{\partial \overline{Ct}}{\partial x}\right) \qquad \text{[Equation 12]}$$

$$\bar{\tau}xr = \left(\frac{\partial \overline{Cx}}{\partial r} + \frac{\partial \overline{Cr}}{\partial x}\right) \qquad \text{[Equation 13]}$$

$$\bar{\tau}tr = \left(\frac{\partial \overline{Ct}}{\partial r} + \frac{1}{r}\frac{\partial \overline{Cr}}{\partial \theta} - \frac{\overline{Ct}}{r}\right) \qquad \text{[Equation 14]}$$

The spanwise distributions of apparent viscosity (i.e., derived from the measurements of the deterministic stresses) and the estimated turbulent viscosities for the first stator, rotor, and second stator exit planes are shown in Figure 24. These apparent and turbulent viscosities, normalized by the molecular viscosity at ambient conditions, show that for all downstream airfoil rows, the apparent viscosity is larger than the turbulent viscosity.

4.4 SUMMARY OF ANALYSIS AND EVALUATION OF LARGE-SCALE ROTATING RIG UNSTEADY DATA

The unsteady data, previously acquired in the UTRC LSRR rig, have been analyzed to assess the magnitudes of the turbulent and deterministic stresses. The stresses were calculated from the measured data, and presented as annular contours and spanwise gap-averaged distributions. An apparent viscosity model, simulating the deterministic stresses using gradients of the time-mean flow, was developed. Evaluation of the unsteady data yielded the following conclusions:

- The magnitudes of spanwise deterministic stresses range between 0 and 0.25, and, in general, are larger in magnitude than the turbulent stresses.
- The radial gradients of the deterministic stresses, as they appear in the equations of motion are, in general, larger than the gradients of turbulent stresses.
- The turbulent stresses are predominately associated with the airfoil wake region, whereas the deterministic stresses are predominately associated with flow distortions coinciding with secondary (pressure-driven) flow structures.
- The average turbulence intensity increases by a factor of 10 through the rotor and subsequently decays by 25 percent through the second stator.
- The average temporal stress and intensity in the rotor frame is relatively unchanged from the inlet to exit.
- The average temporal stress in the absolute frame decays by a factor of 5 through the second stator.
- The secondary flows at the exit of the rotor and second stator are different, although the geometries and mean flow angles of the two blade rows are almost identical. This indicates that the inlet flow to the second stator significantly affects the secondary flow in the second stator.
- The apparent viscosity calculated from the deterministic stresses is larger than turbulent viscosity and is anticipated to impact turbulence modeling in steady CFD codes.

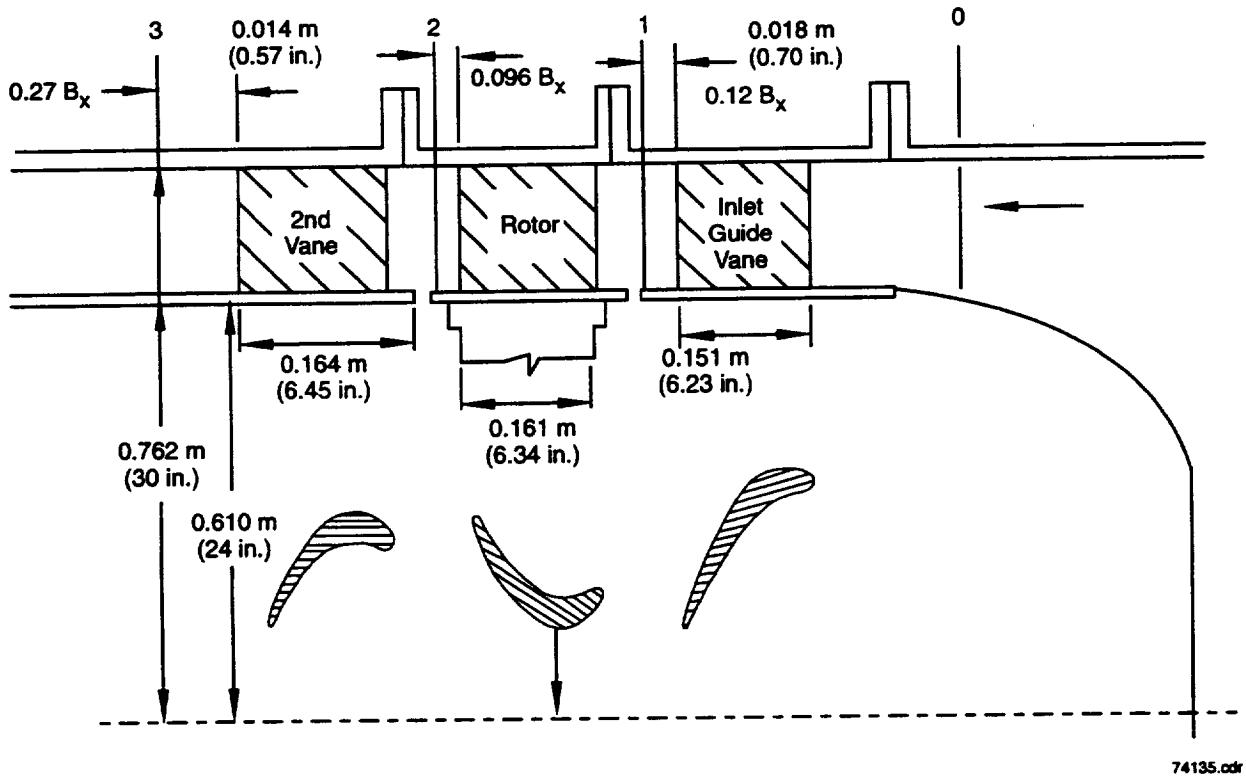

Figure 1. Schematic of UTRC Large-Scale Rotating Rig

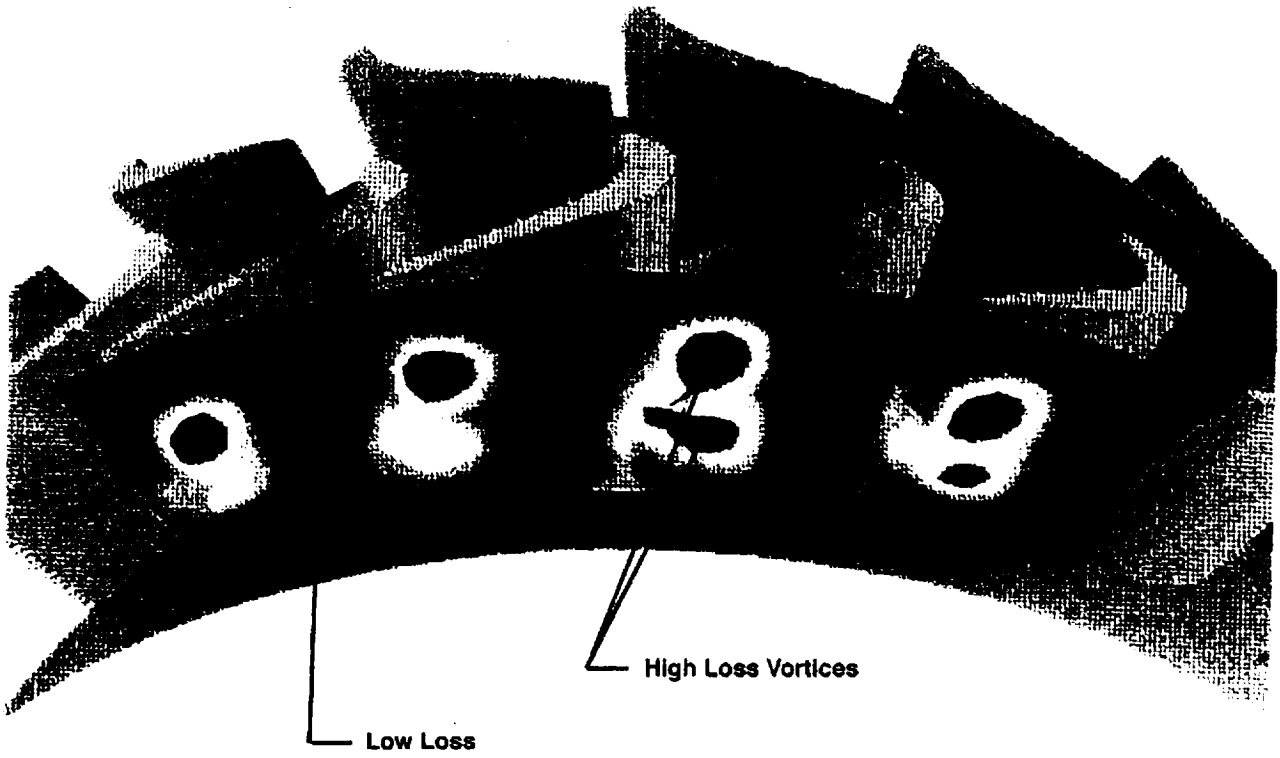

Figure 2. Numerical Unsteady Euler Simulations of Large-Scale Rotating Rig Rotor Flowfield at Four Relative Positions of First-Stage Stator; This Figure Assists Reader With Orientation of Experimental Data (Shown in Figure 3)

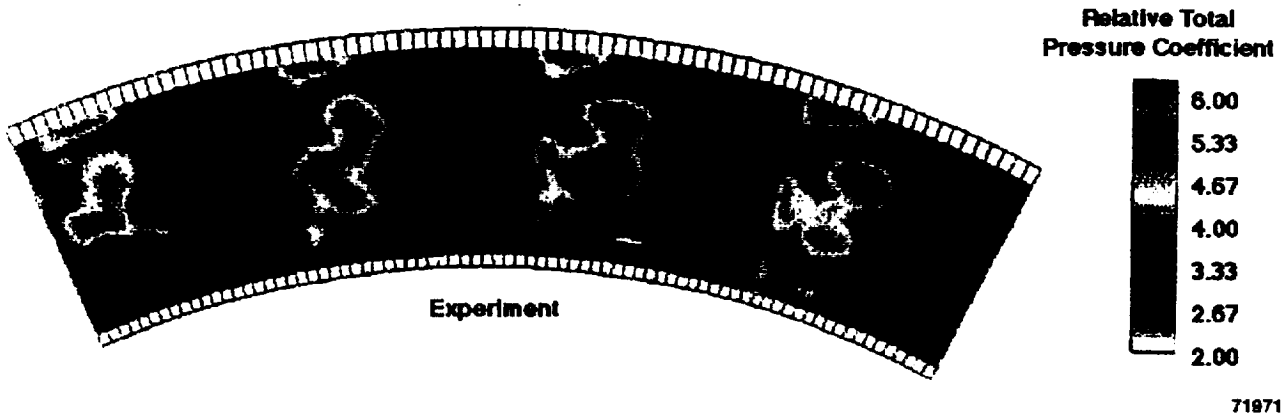

Figure 3. Experimental Values of Relative Total Pressure Loss at Exit of Rotor Show That Rotor Flowfield Is Influenced by Upstream Stator

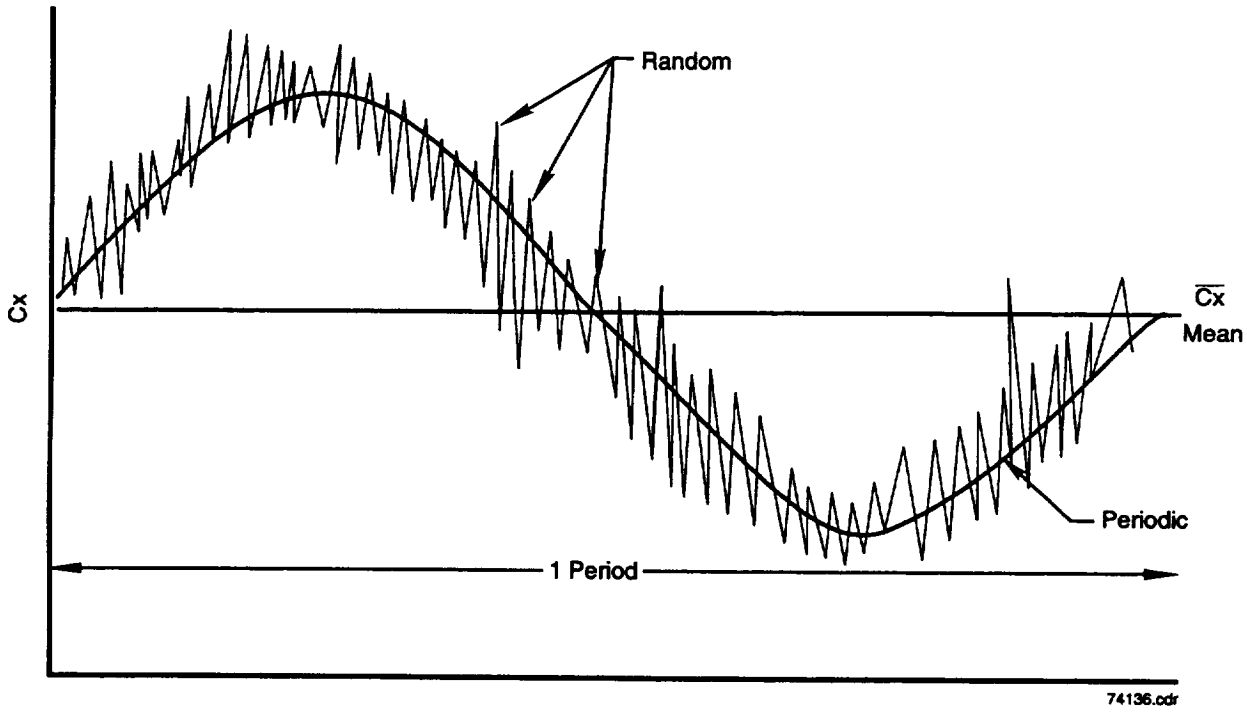

Figure 4. Schematic of Random Velocities as They May Occur Over One Period Shows Flow Can Be Separated into Mean, Periodic, and Random Components (in Airfoil Reference Frame of Interest)

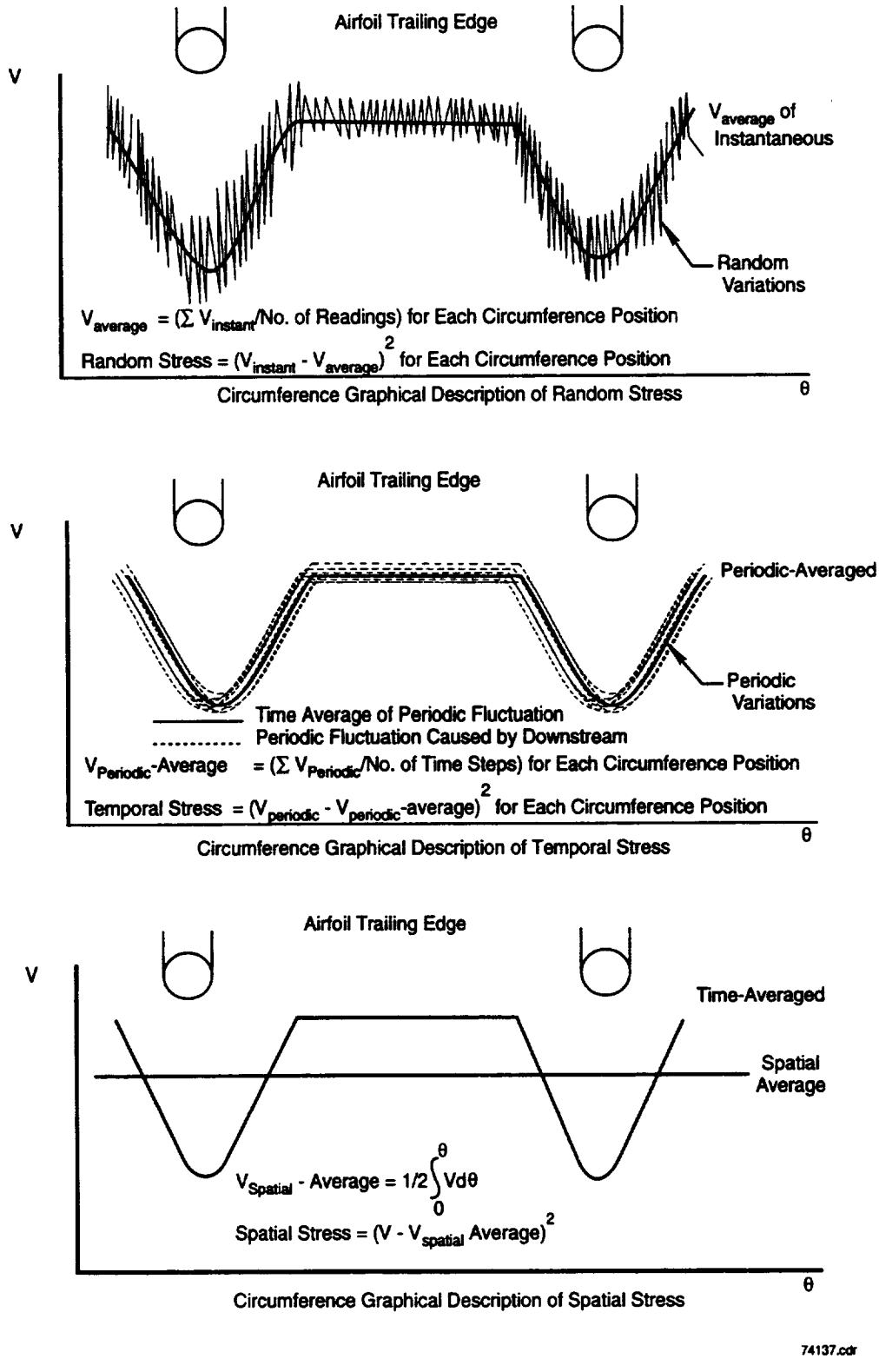

Figure 5. Schematics of Random (Turbulence), Temporal, and Spatial Stresses

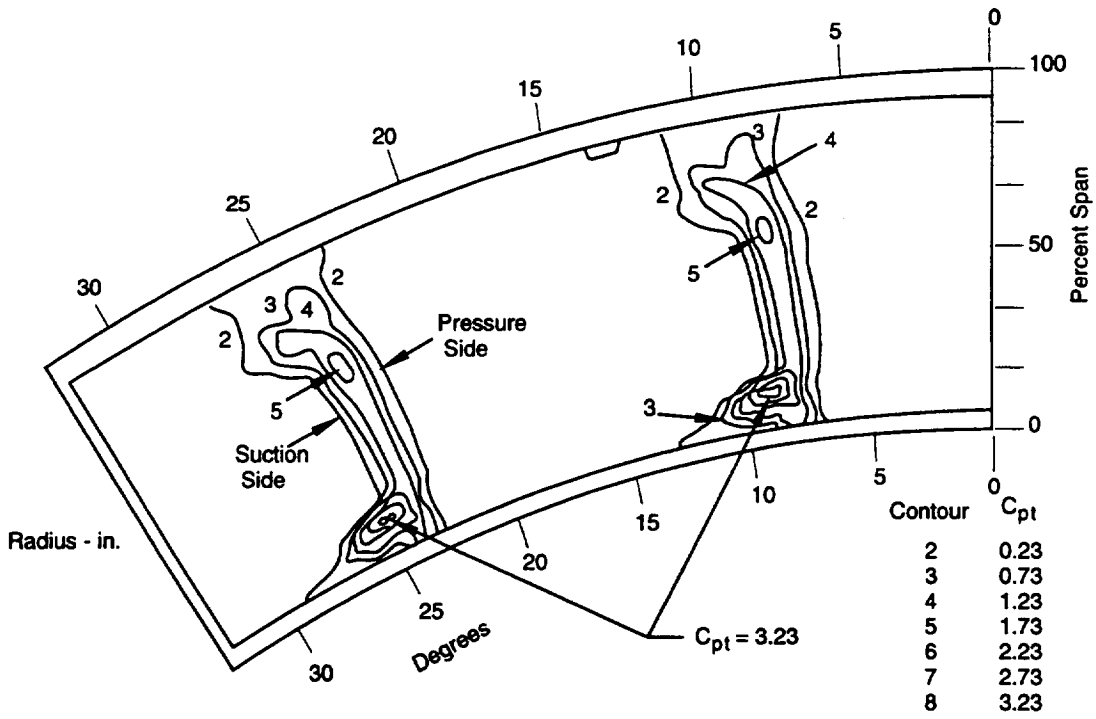

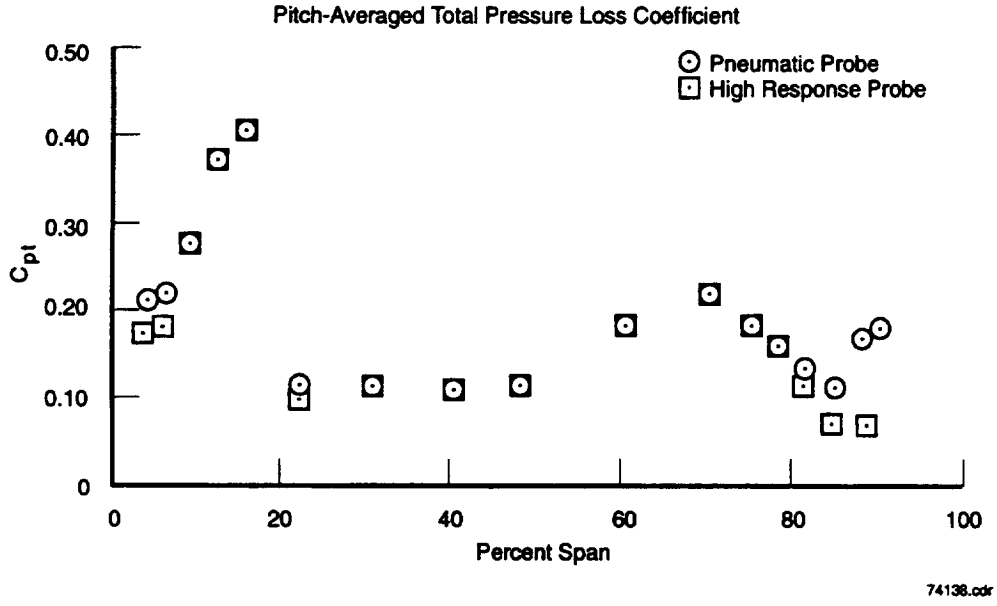

Figure 6. First Stator Total Pressure Contours and Pitch-Average Loss Versus Span Suggest There Will Be Spatial Stress With Radial Gradients That Will Appear as Temporal Stress in Relative Frame of Rotor

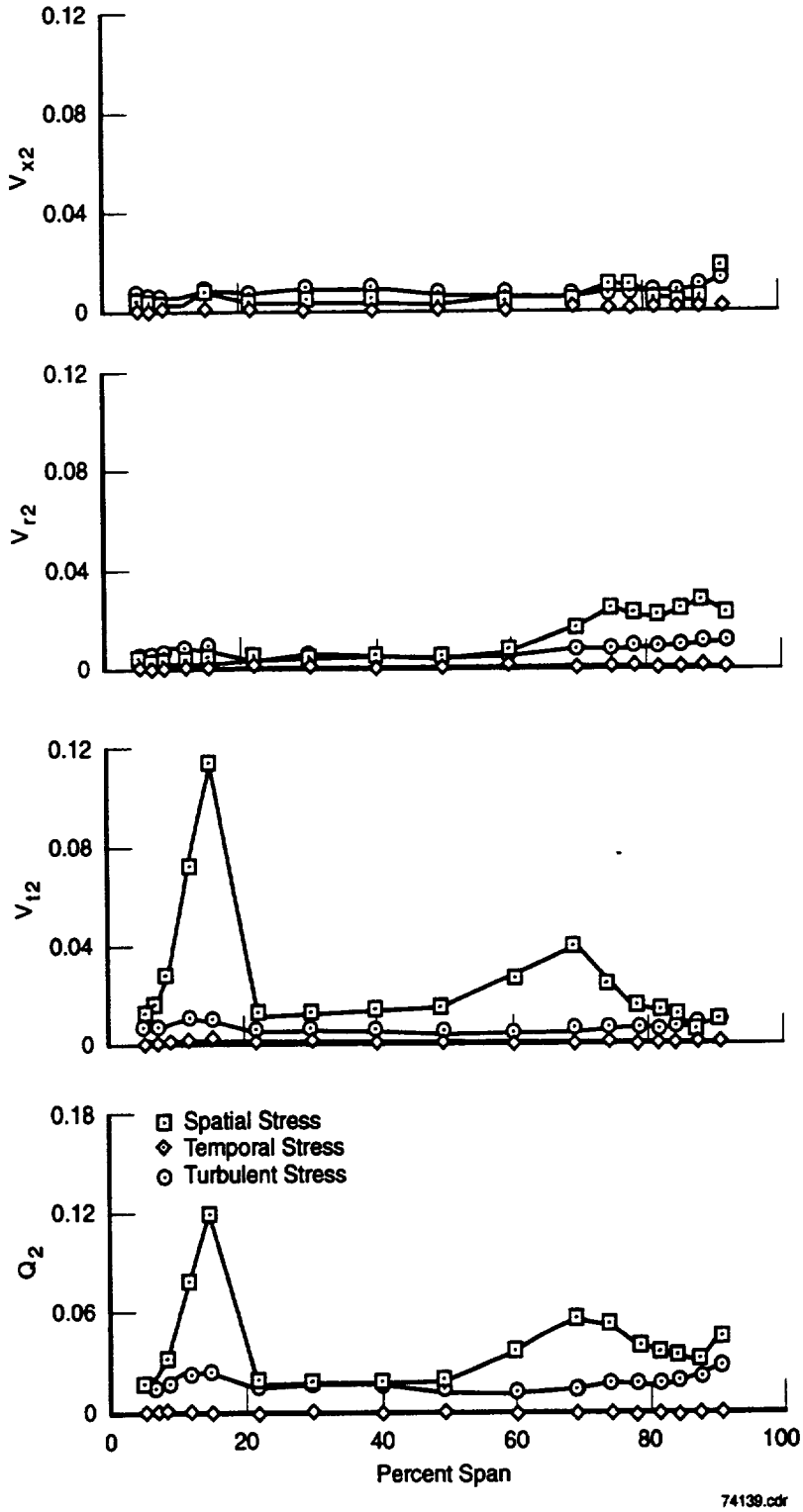

Figure 7. Temporal Stresses Are Approximately Zero, Indicating That Rotor Has Almost No Influence on First Stator Flowfield (Spatial Stresses Show, in General, That Magnitude and Radial Gradients [Through Inspection] Are Larger Than Turbulent Stresses)

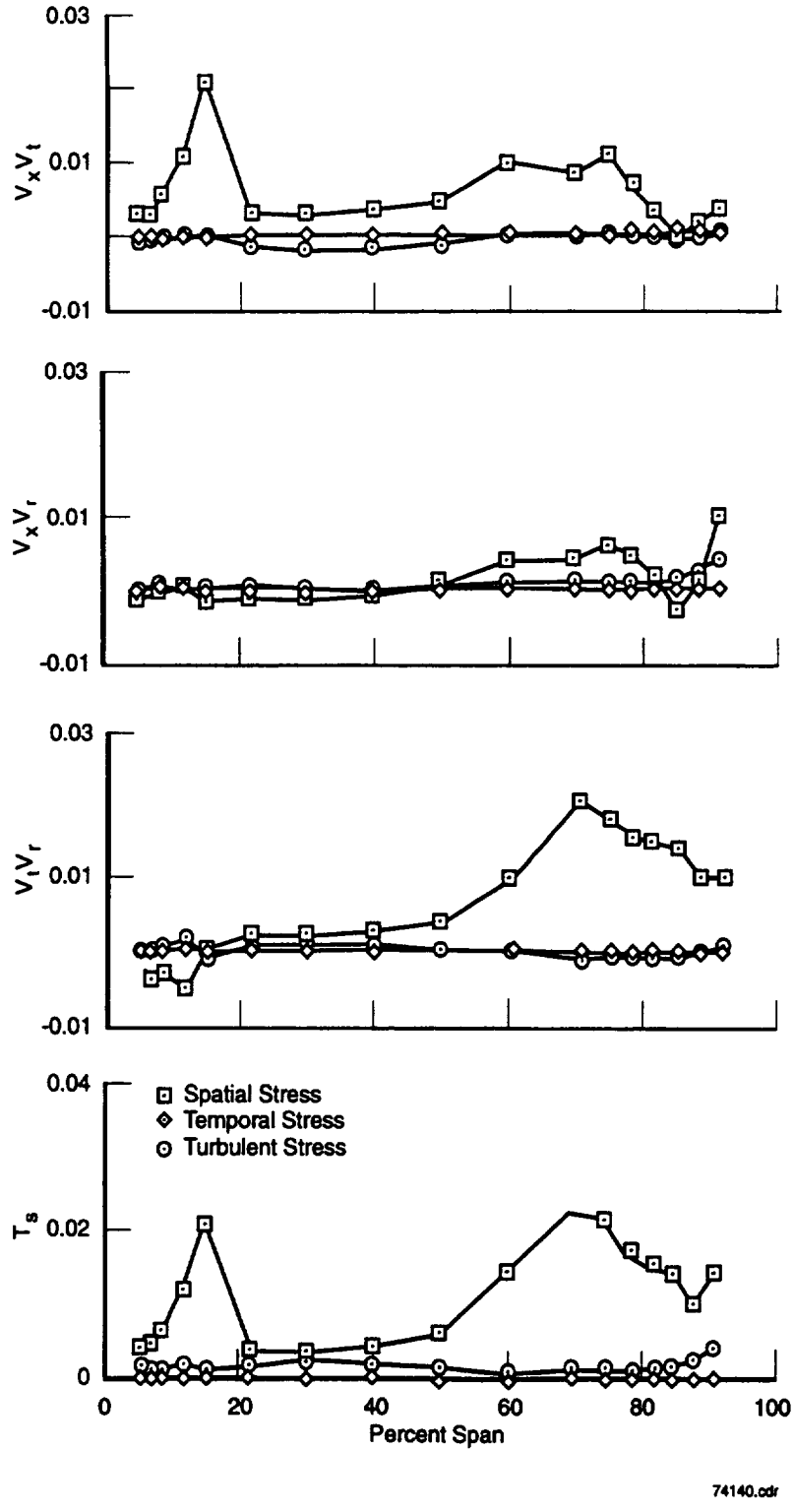

Figure 8. Temporal Stresses Are Approximately Zero, Indicating That Rotor Has Almost No Influence on First Stator Flowfield (Spatial Stresses Show, in General, That Magnitude and Radial Gradients [Through Inspection] Are Larger Than Turbulent Stresses)

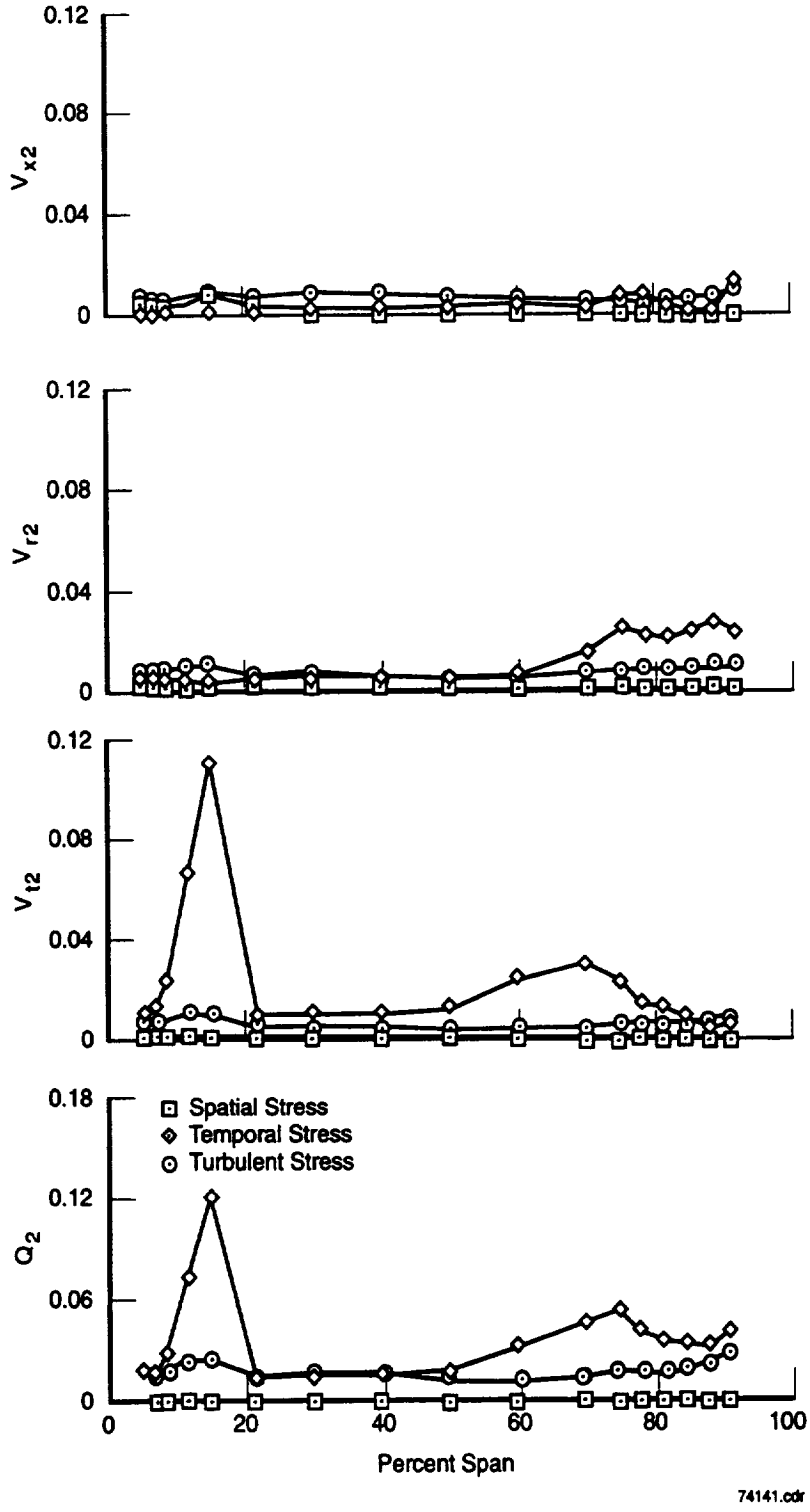

Figure 9. These Data Indicate That Inlet Normal Temporal Stresses and Their Radial Gradients (Through Inspection), in General, May Be More Important in a Closure Model Where Turbulence Is a Factor

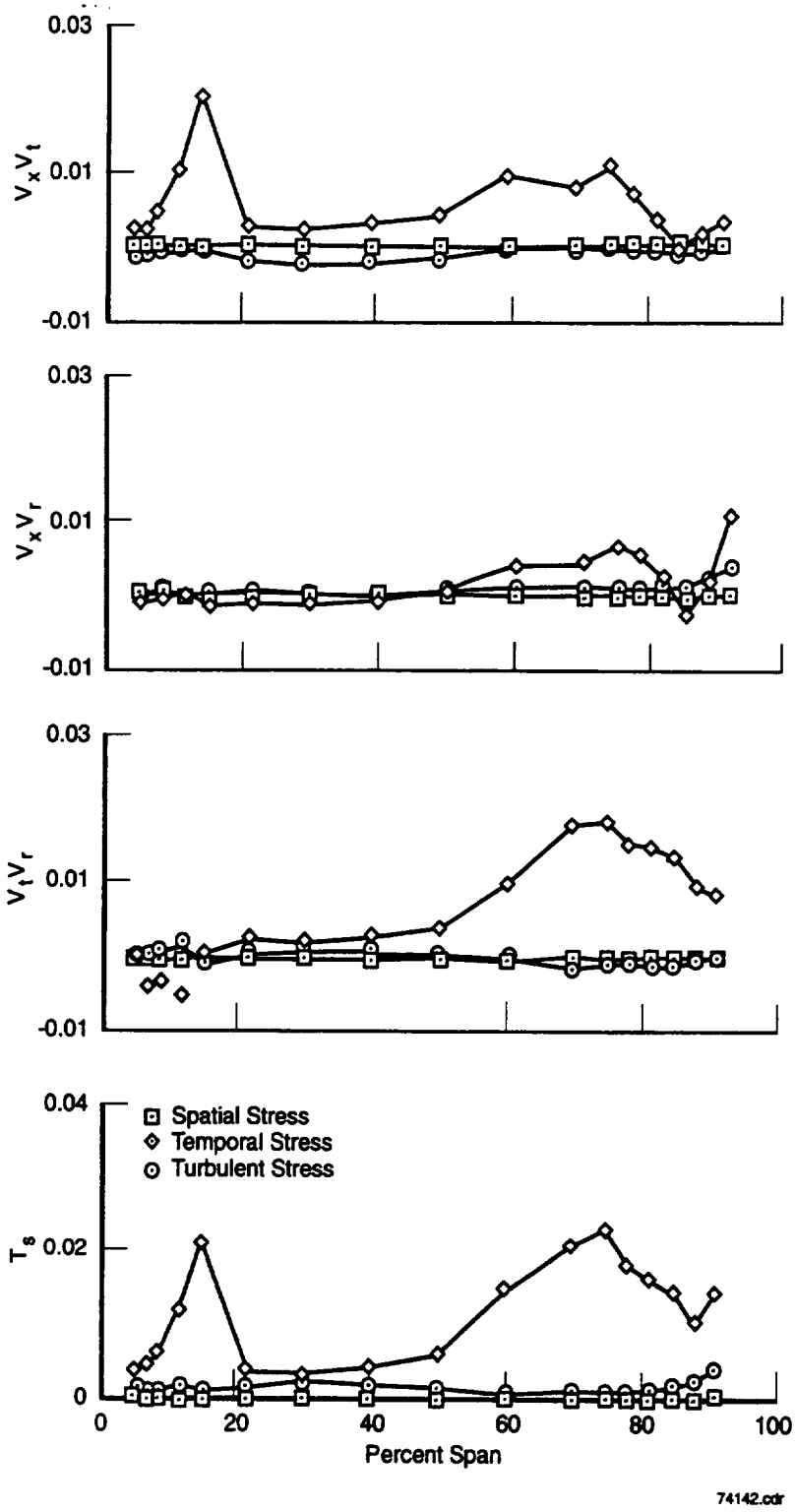

Figure 10. These Data Indicate That Inlet Shear Temporal Stresses and Their Radial Gradients (Through Inspection), in General, May Be More Important in a Closure Model Where Turbulence Is a Factor

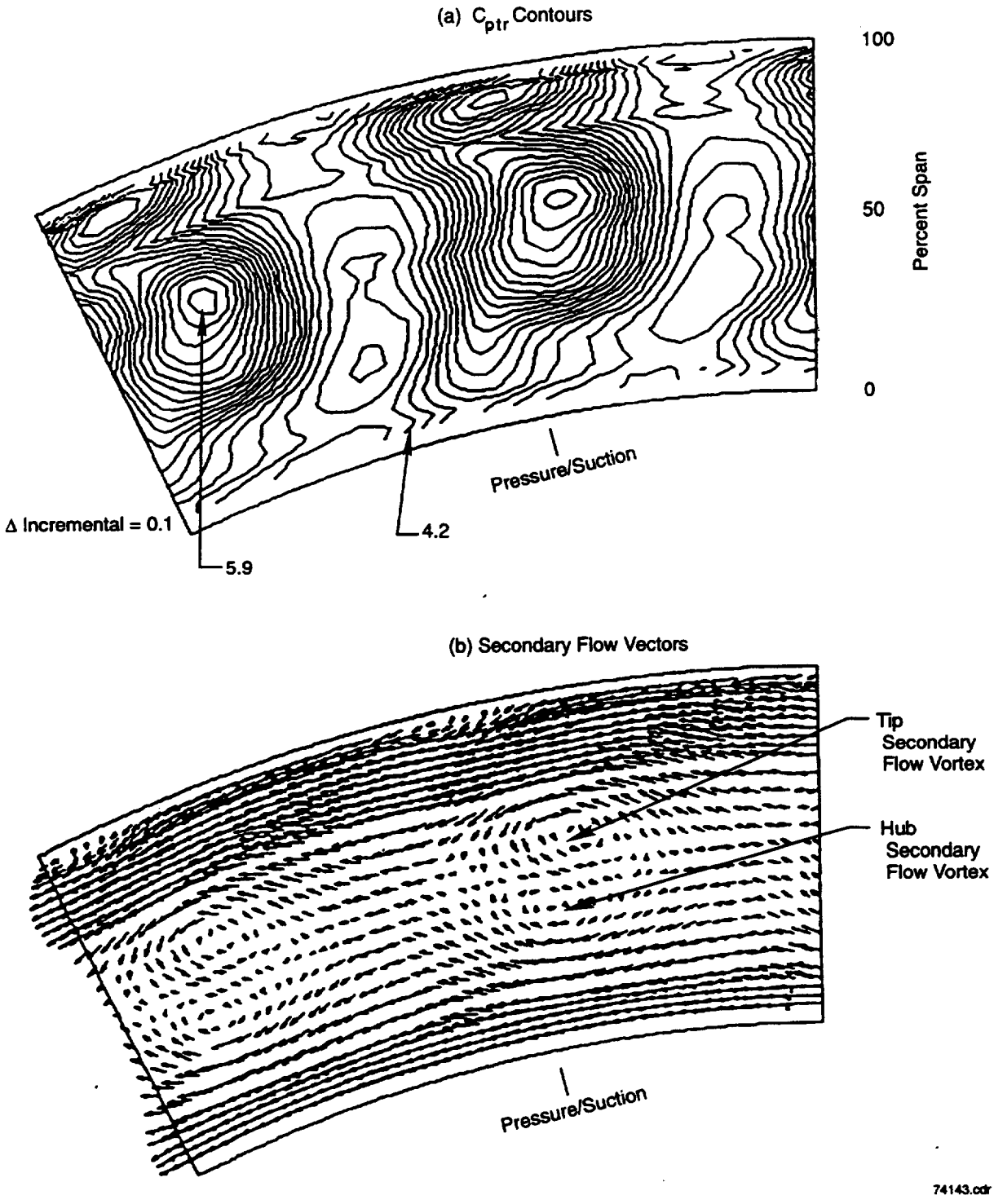

Figure 11. Rotor Relative Exit Pressure Contours and Vector Plots Indicate Large Secondary Flows

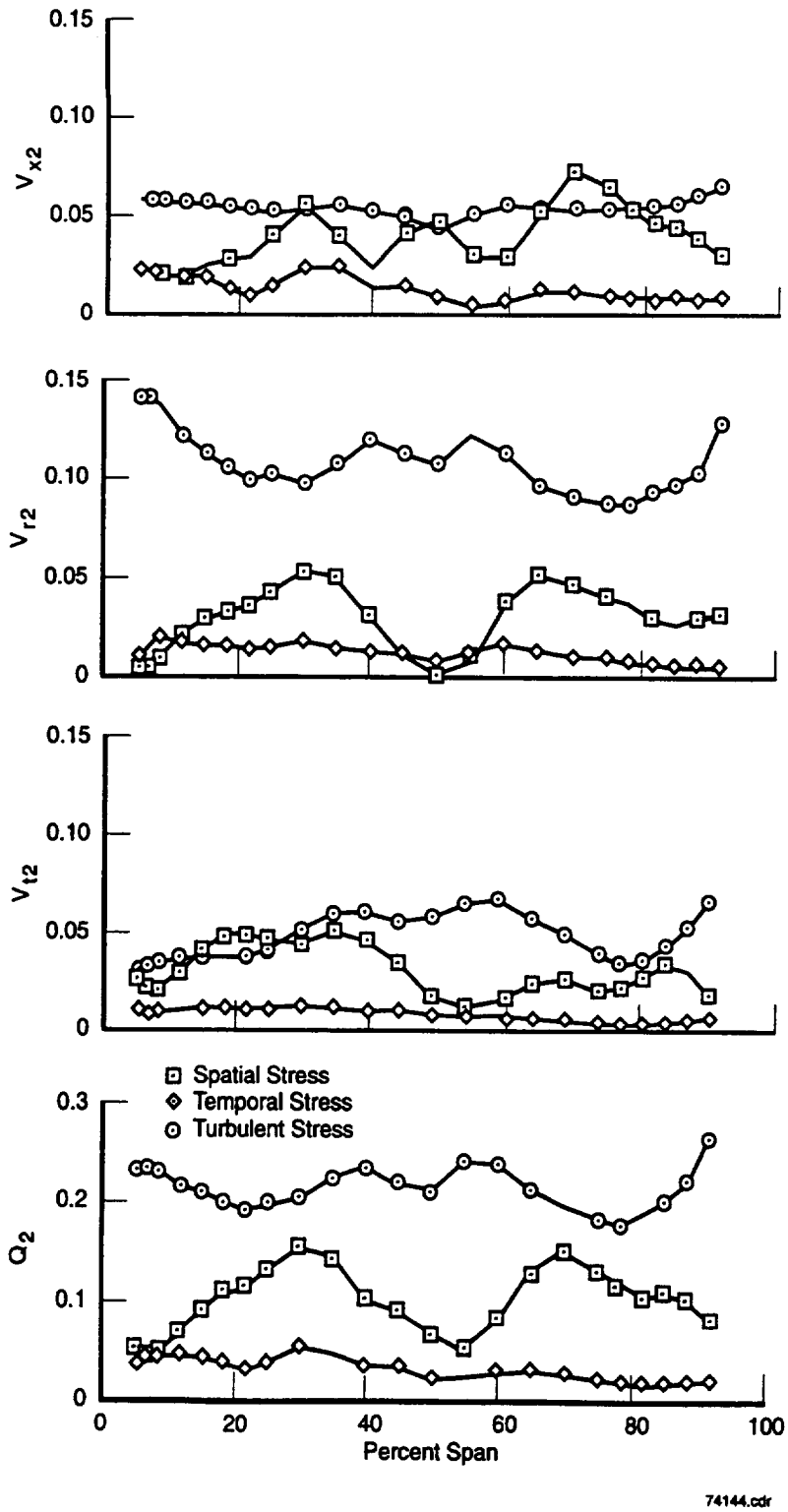

Figure 12. Magnitude of Normal Turbulent Stress, in Equations of Motion, Is Larger Than Deterministic Values (V_{r2}, V_{t2}). Radial Gradients That Appear in Equations of Motion (V_{r2}) Indicate, by Inspection, That Spatial Terms Are Same Level as Turbulent Terms

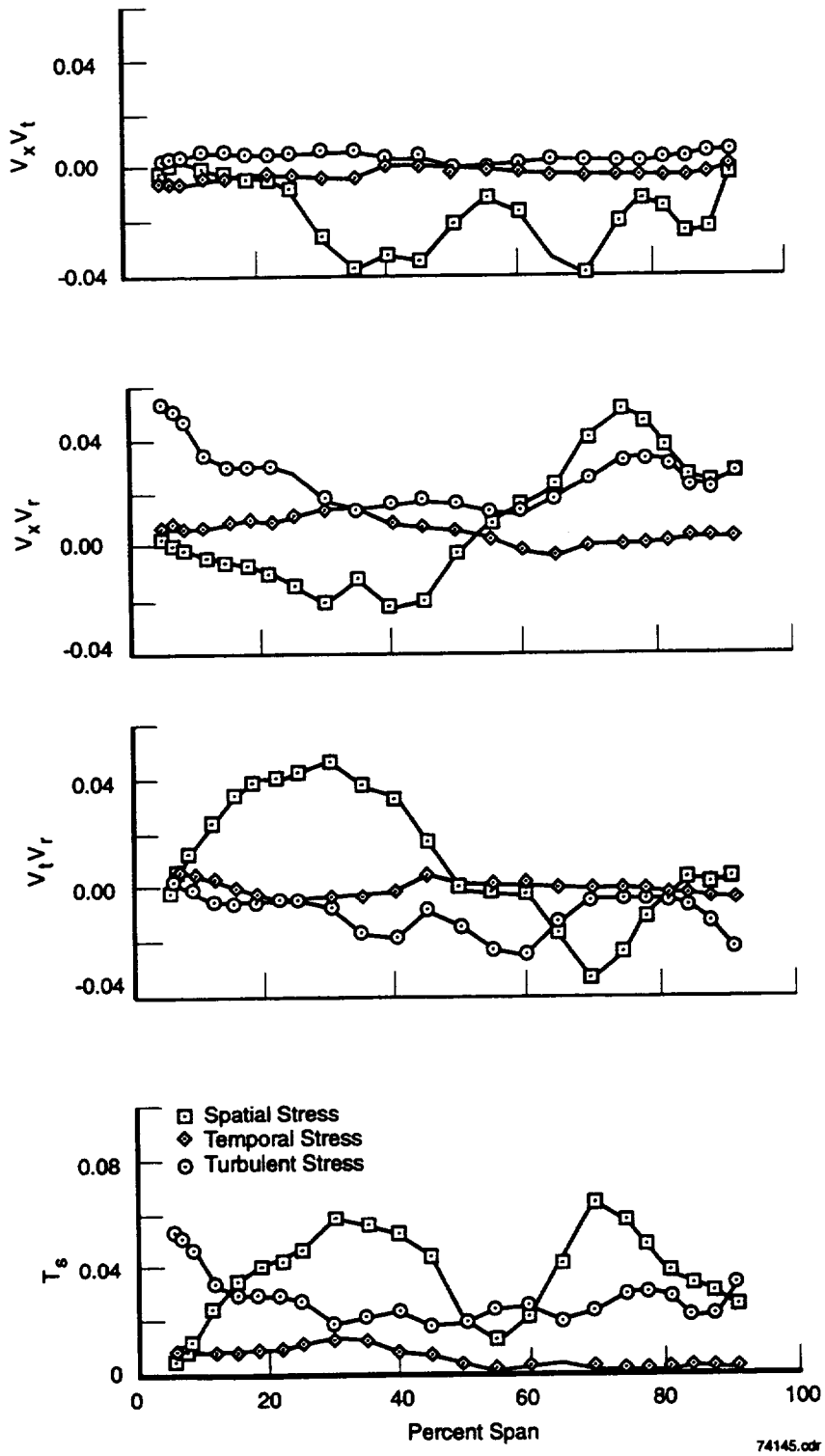

Figure 13. Magnitude of Turbulent Shear Stress That Appears, in Equations of Motion, Is About Same Level as Deterministic Shear Stress (VtVr, VxVr). Radial Gradient Terms (VtVr, VxVr) Indicate, by Inspection, That Spatial Deterministic Stresses Are Larger Than Turbulent Terms

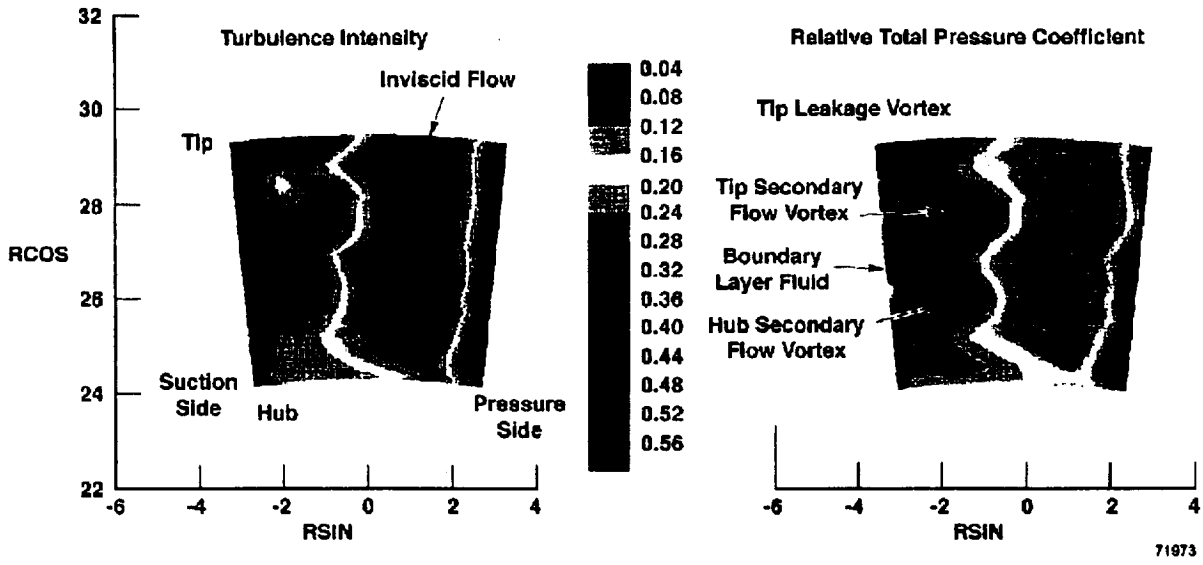

Figure 14. Contour Plots of Time-Averaged Total Turbulence Intensity and Relative Total Pressure Coefficients at Exit of LSRR Rotor. These Plots Identify Features of Flowfield That Are Most Familiar to Turbine Community. This Figure Will Assist the Reader in Interpreting Information Shown in Other Contours Where Stresses That Induced Periodic Unsteadiness Are Plotted.

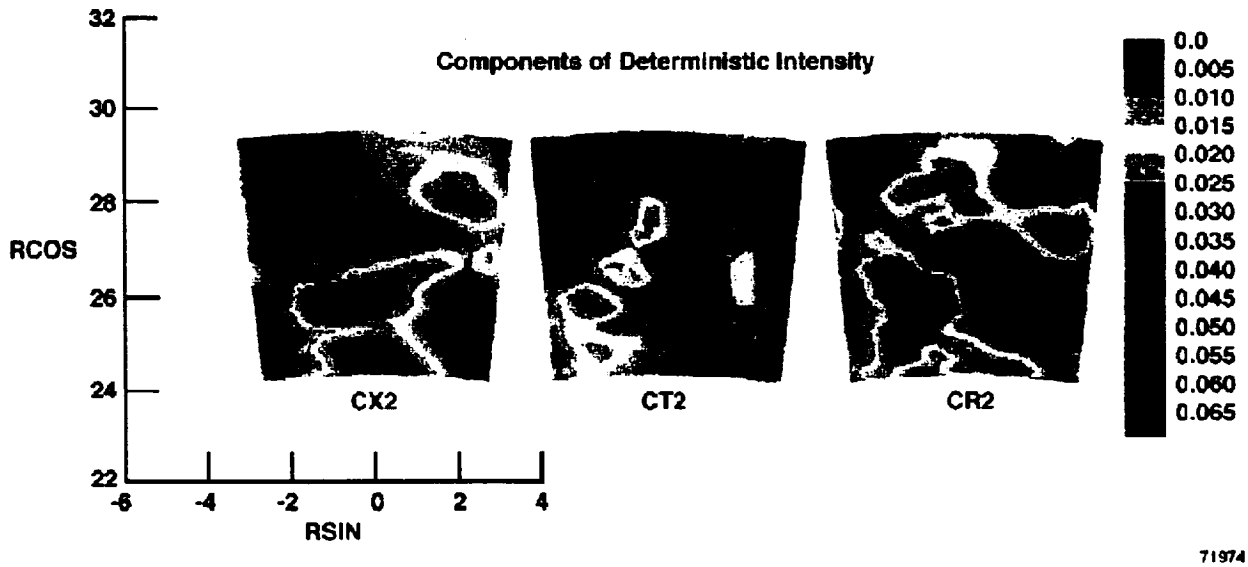

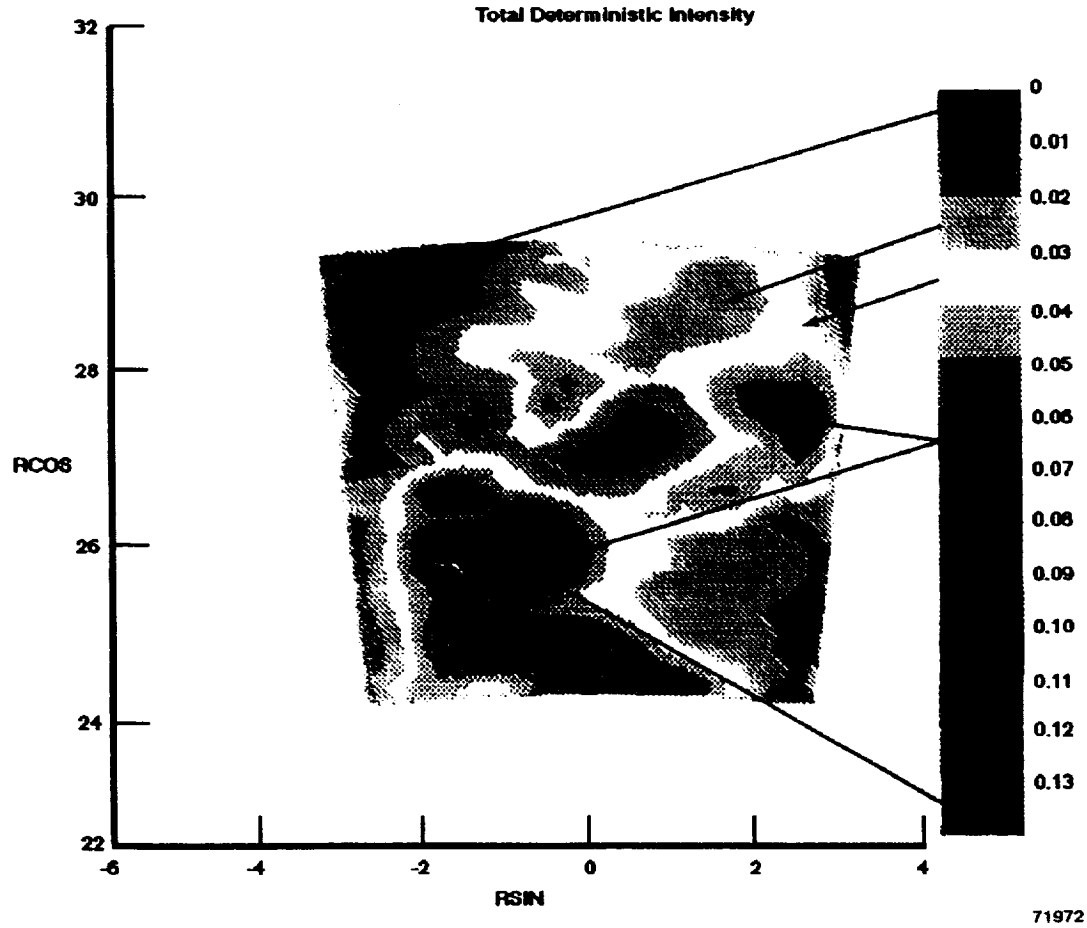

Figure 15. Contour Plots for Total and Three Components of Deterministic Temporal Intensity Downstream of Rotor for UTRC LSRR. Largest Levels of Intensity Are Measured in Region Where Flow Is Dominated by Hub Secondary Flow Vortex. High Levels of Intensity Are Also Shown Observed Near Pressure Side of Rotor Airfoil Where Flow Is Primarily Inviscid

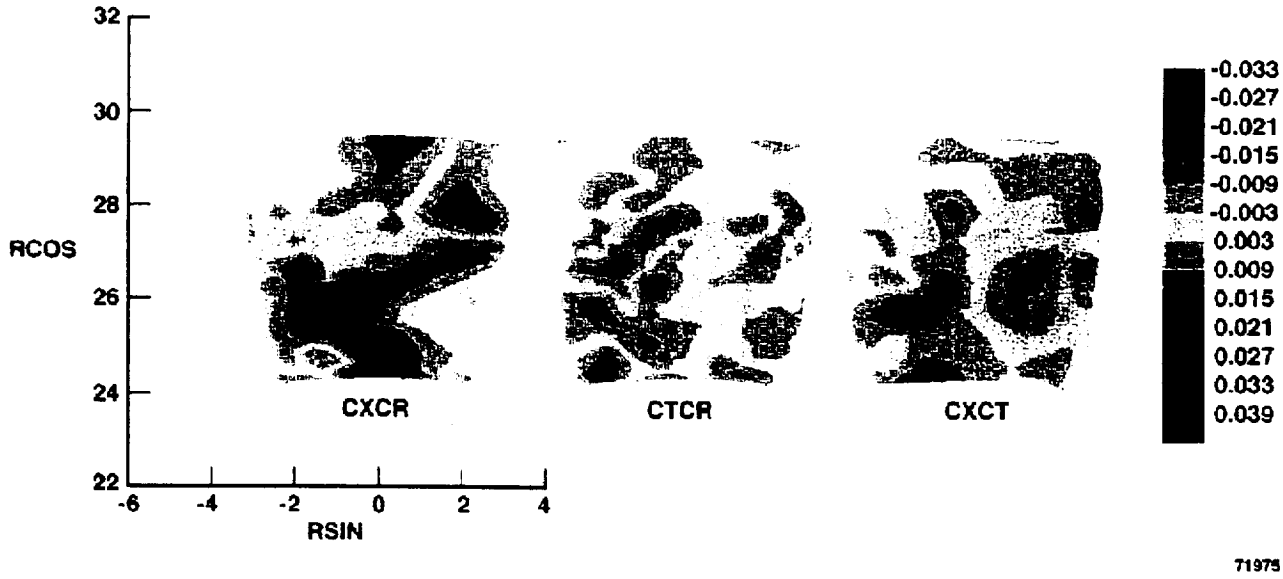

Figure 16. Contour Plots for Three Components of DeterministicTemporal Stress Downstream of Rotor for UTRC LSRR

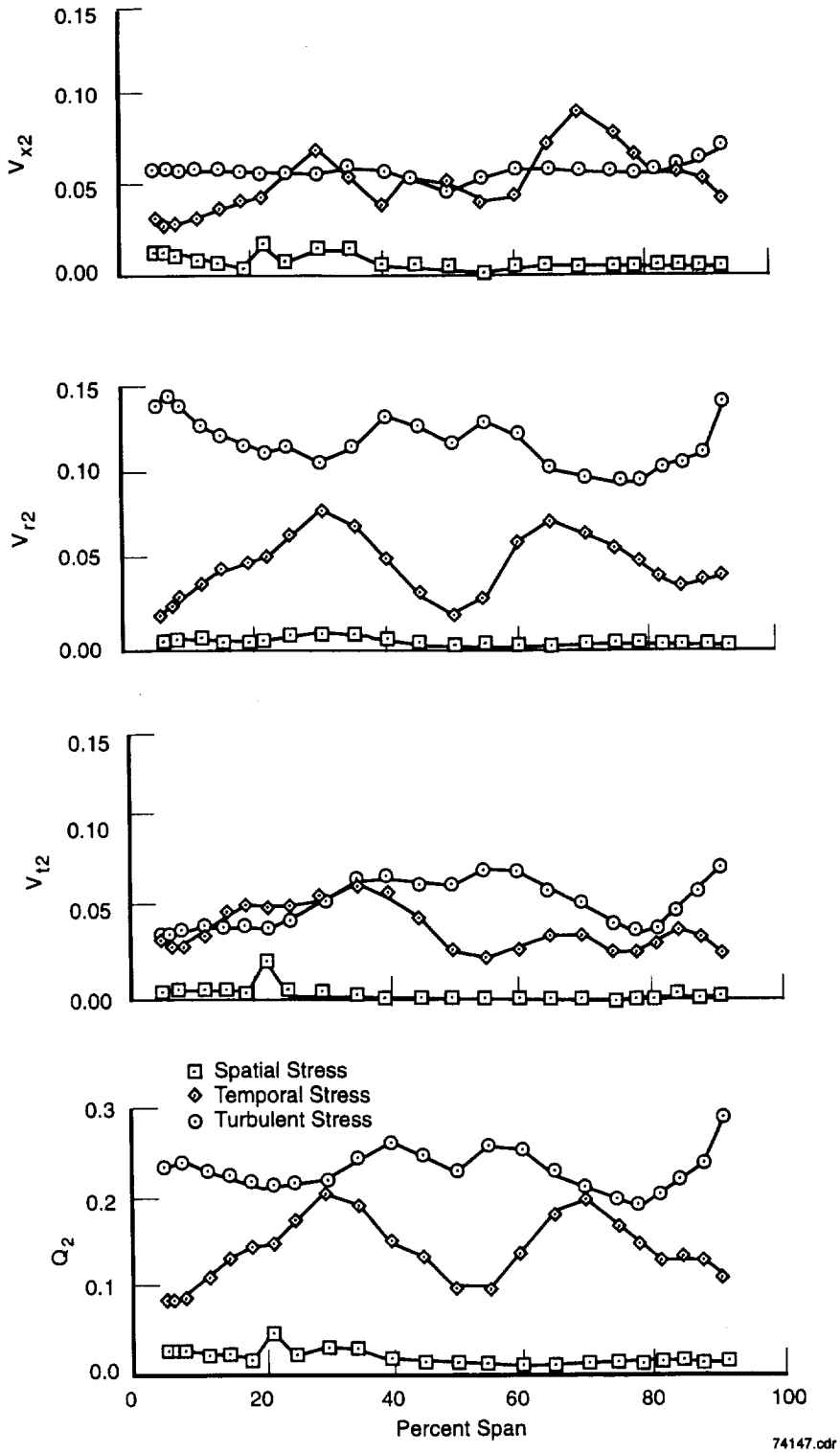

Figure 17. Magnitude of Normal Turbulent Stress, in Equations of Motion, Is Larger Than Deterministic Temporal Stress (V_{r2}, V_{t2}). Radial Gradients That Appear in Equations (V_{r2}) Indicate, by Inspection, That Temporal Terms Are Same Level as Turbulent Terms

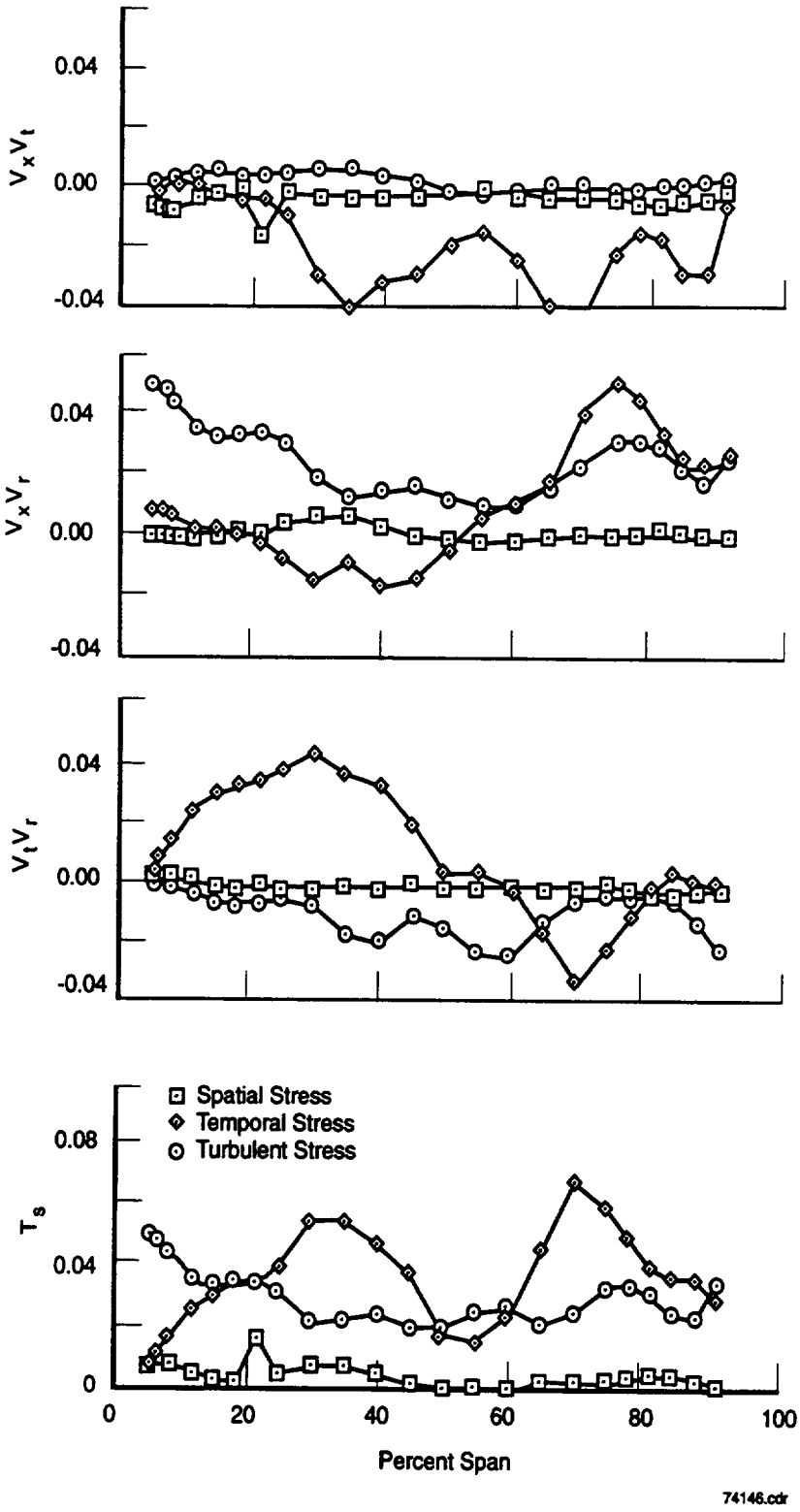

Figure 18. Magnitude of Turbulent Shear Stresses That Appear, in Equations of Motion, Are About Same Level as Deterministic Shear Stress (Vt, Vr) Radial Gradient Terms (Vt, Vr) Indicate, by Inspection, That Temporal Deterministic Stresses Are Larger Than Turbulent Terms

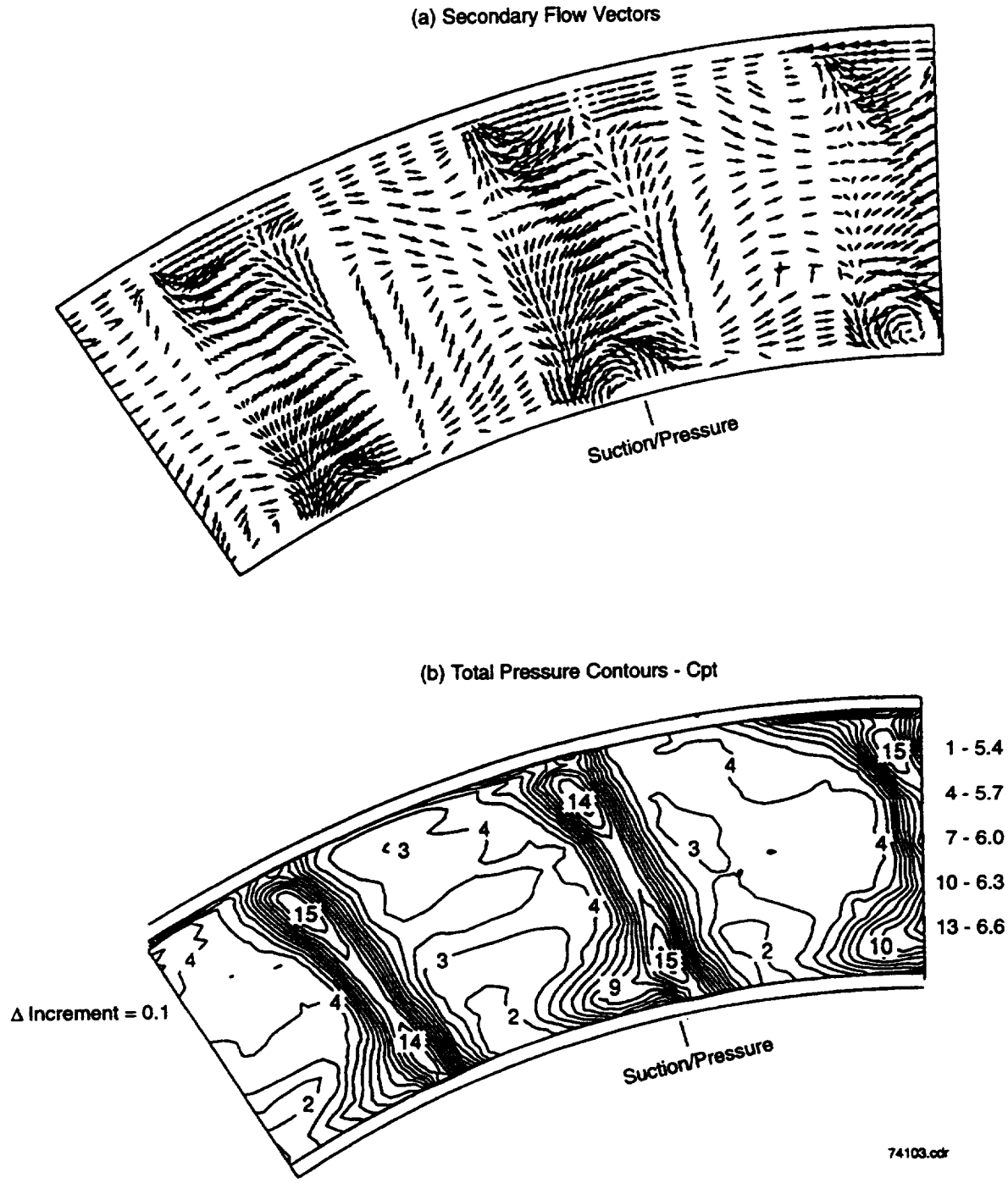

Figure 19. Second Stator Exit Loss Contour and Vector Plot Indicate Unexpected Secondary Flow Patterns (Second Stator Geometry Is Almost Identical to Rotor, and Flowfield Was Expected To Be Similar to Rotor)

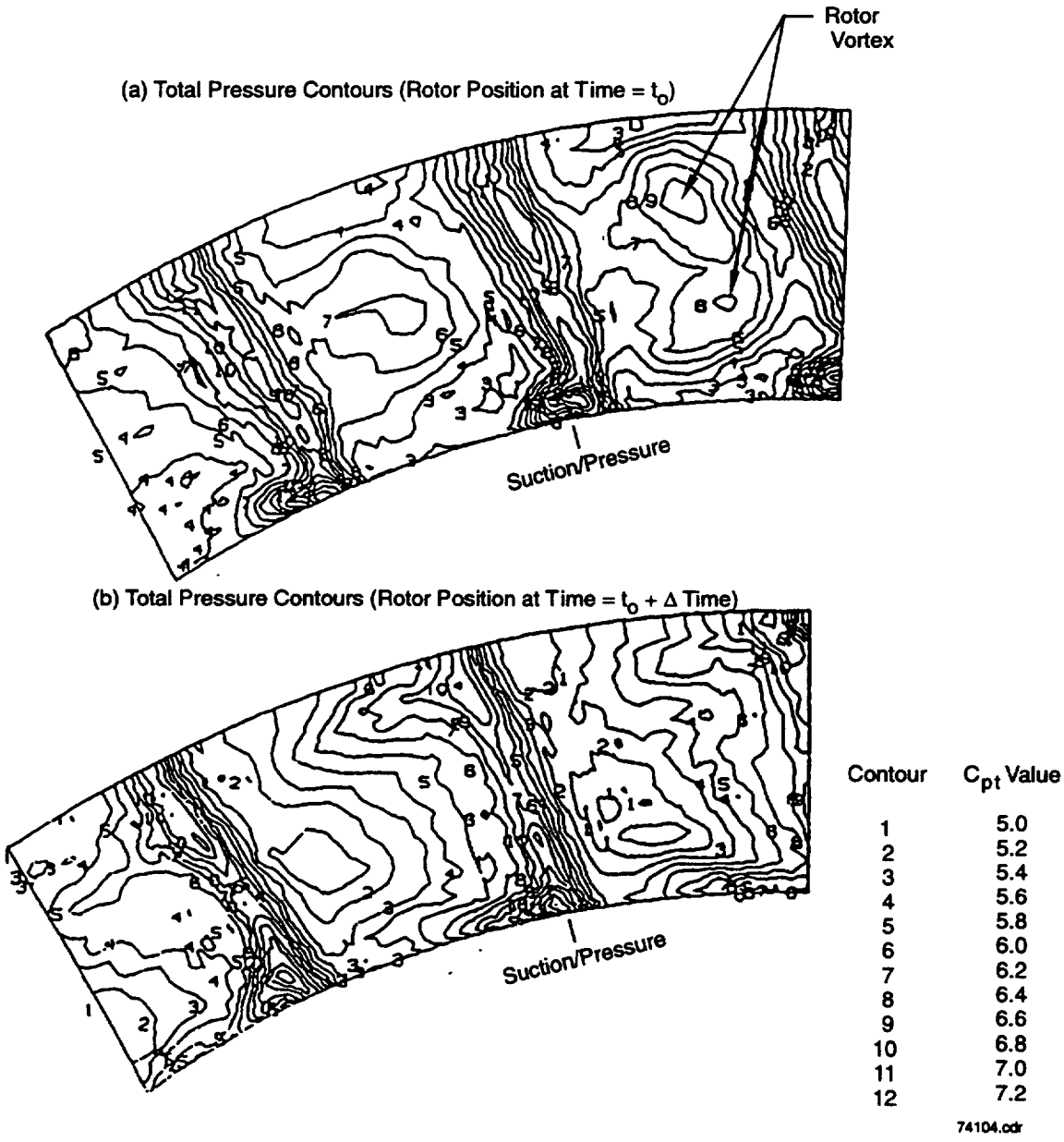

Figure 20. From Animation of Second Stator Exit Flowfield (Not Shown) as Function of Time (Rotor Position); (a) and (b) Represent Two Time Steps With Extremes of Rotor Present. This Figure Shows Rotor Vortex Present (a) and Not Present (b), Indicating That Second Stator Exit Is Not as Similar to Rotor (Typical) as Might Be Expected

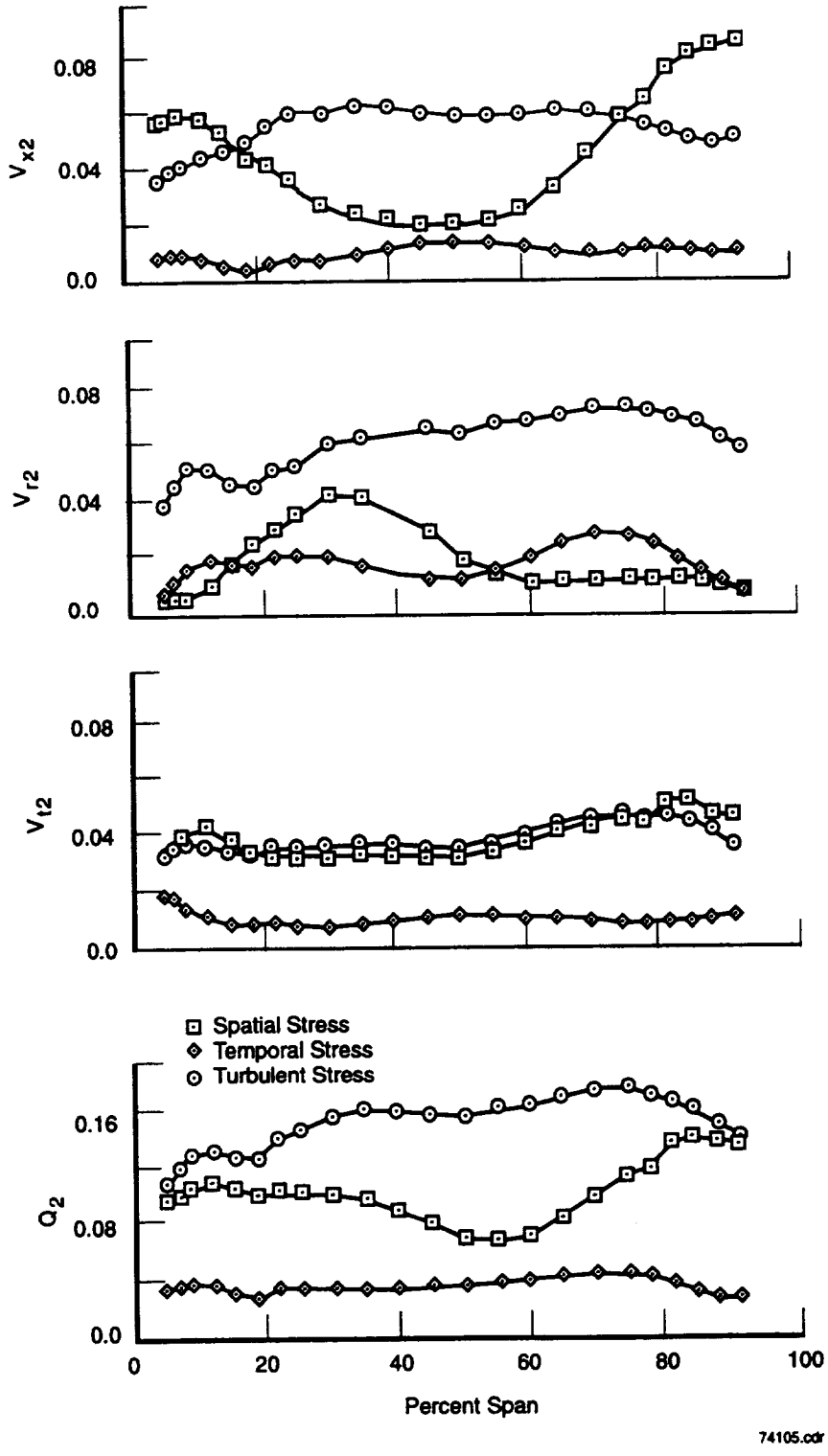

Figure 21. Second Stator Exit Turbulent Stresses Are Approximately 4 Percent Higher Than Spatial Stresses; High Level of Both Components Could Potentially Impact Transition

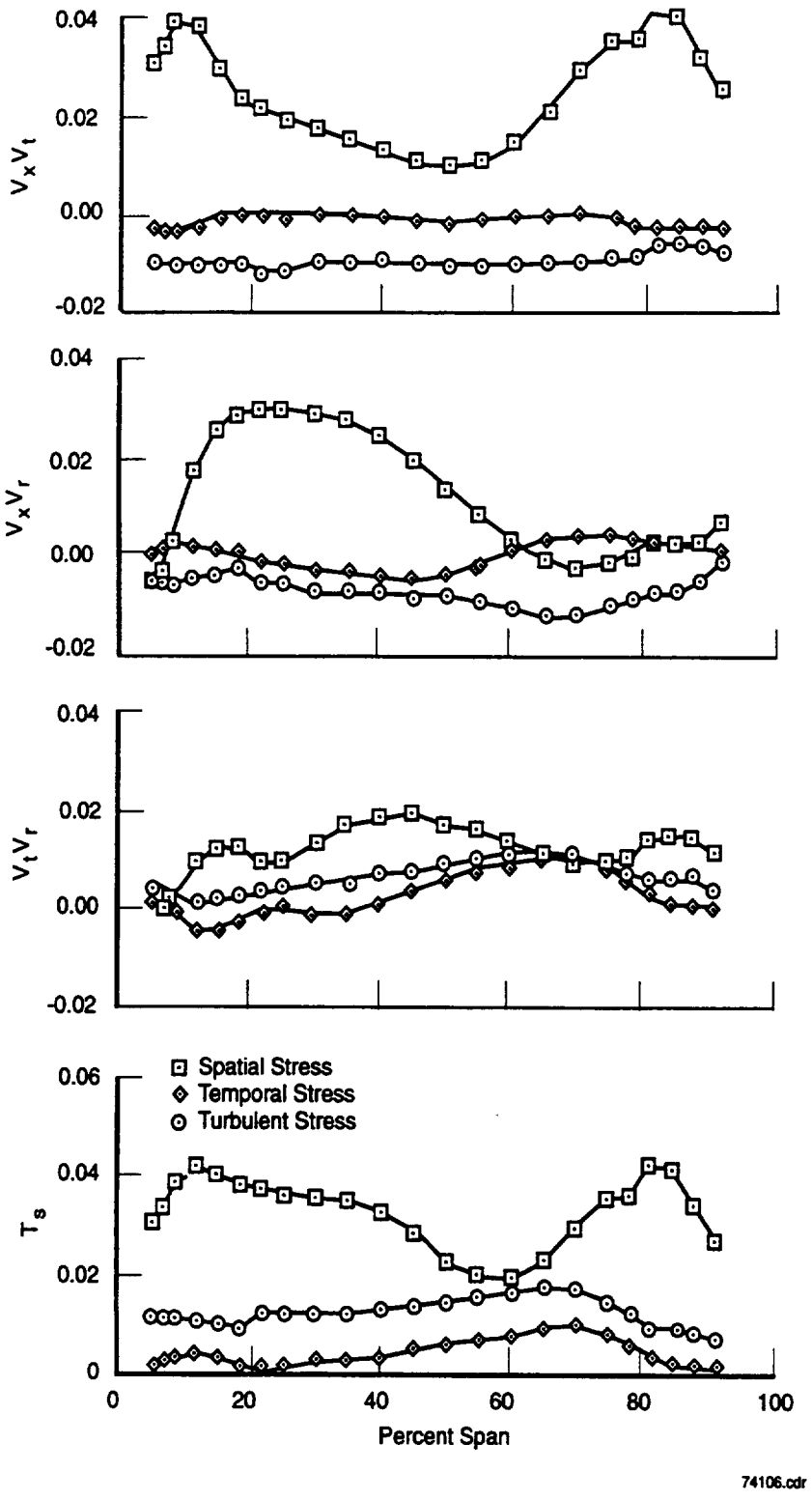

Figure 22. Second Stator Exit Shear Stress Indicates That Spatial Stresses Are Larger Than Turbulent Stresses

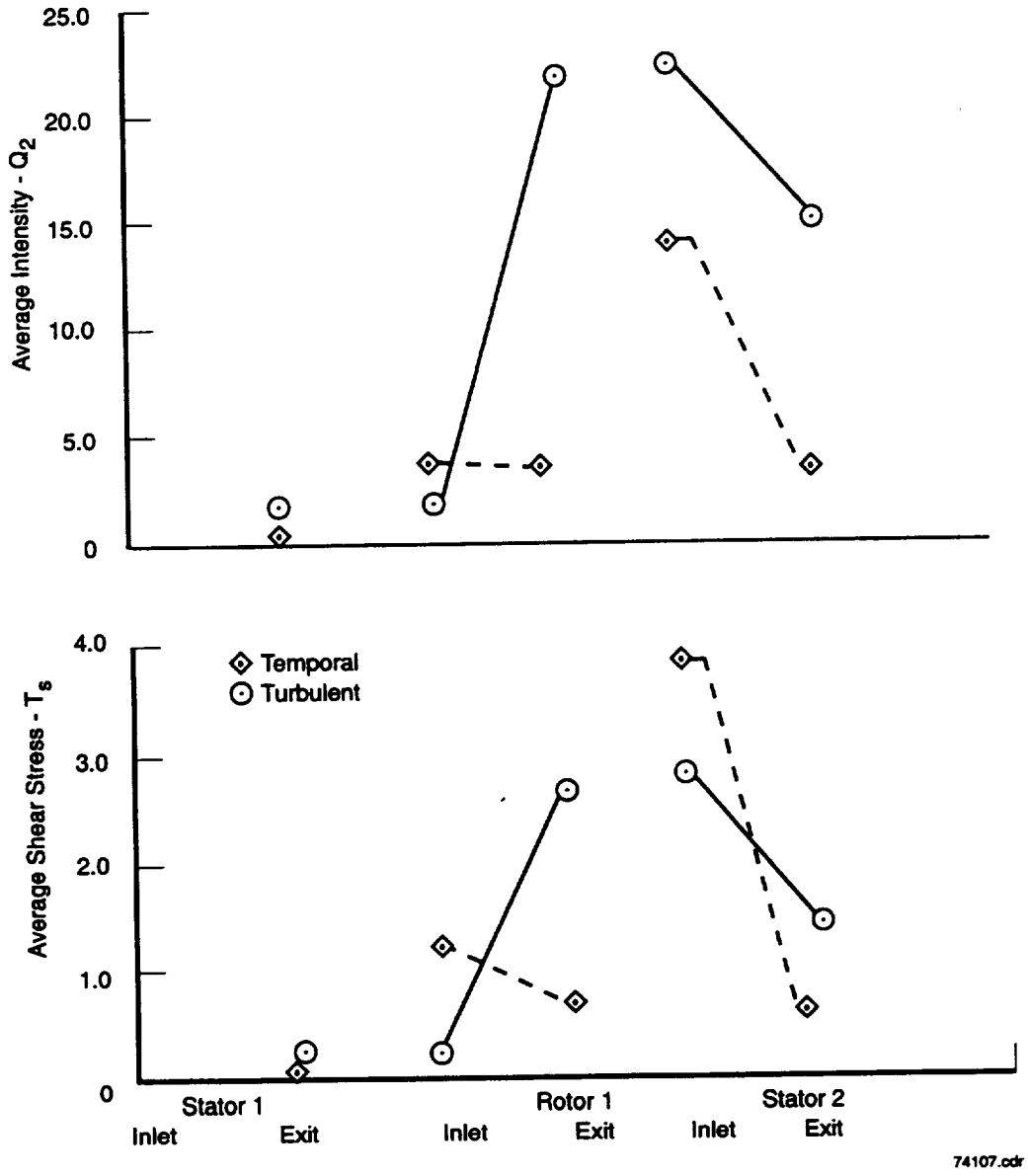

Figure 23. Average Temporal and Turbulent Stresses as They Are Present at Each Location Between Airfoil Rows; This Feature Indicates That Temporal Stresses Are Almost Constant from Rotor Inlet to Exit, But Rapidly Decay Through Second Stator

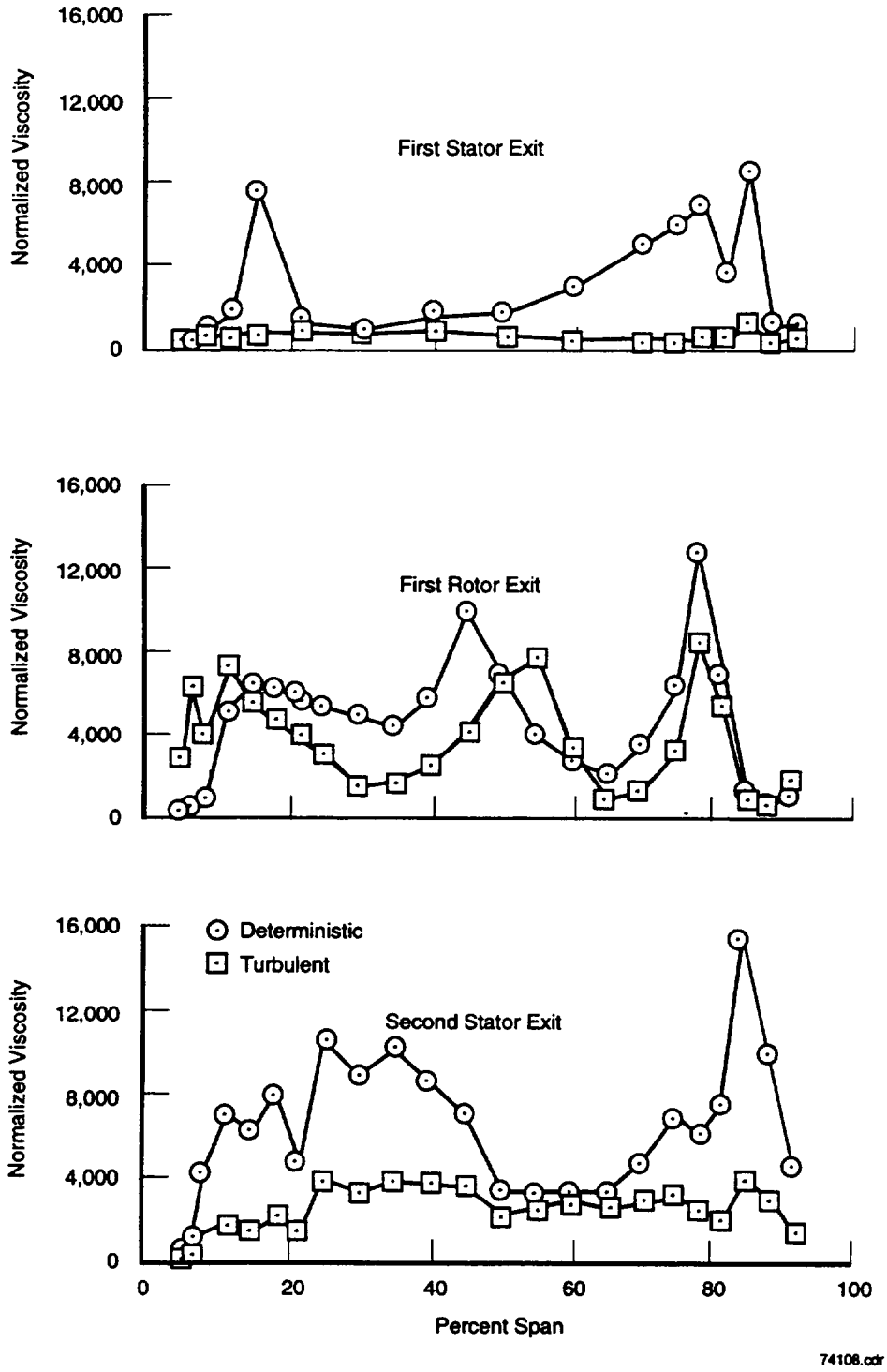

Figure 24. Comparison Between Turbulent Viscosity and Deterministic Viscosity Shows That for Every Airfoil Row, Deterministic Viscosity Is Larger Than Turbulent Viscosity

This Page Is Intentionally Left Blank

5. NUMERICAL EXPERIMENTS

Results of numerical simulations, conducted for the United Technologies Research Center (UTRC) large-scale rotating rig (LSRR) by using steady and unsteady versions of a three-dimensional (3-D), multistage Euler code developed by Ni [6], are discussed in this section. The main goal of these simulations was to identify unsteady phenomena with effects, if any, that needed to be incorporated into multistage codes to enhance the predictive capabilities.

5.1 THREE-DIMENSIONAL STEADY MULTISTAGE EULER SIMULATIONS

The first set of numerical simulations was conducted by using the steady version of Ni's 3-D, multistage Euler code. A wall shear force model, similar to the one developed by Denton [7], is used in the code to simulate the effect of viscous stresses. Tip clearance flows were not included. In this code, 3-D flow is calculated through one representative airfoil passage for each airfoil row. The flow properties are conserved (momentum, continuity, and energy) at an interface plane in the circumferential direction (Figure 25) before information is exchanged between adjacent airfoil rows during each solution iteration. The technique used to transfer flowfield information across the interface boundary between airfoil rows is classified as *average-plane* or *mixing-plane*. This steady code permits simulation of flow through multistage turbines with minimal computer memory requirements and is used extensively in the turbine design process.

5.1.1 Full-Scale Turbine Flow Simulation

Numerical results from the steady Ni code are compared to the experimental data measured in a full-scale, two-stage turbine rig, as shown in Figure 26 (a and b). Reasonable agreement between the experimental data and numerical results indicates that the code can be used to conduct the numerical studies for a subsonic two-stage turbine rig configuration.

5.1.2 Large-Scale Rotating Rig Flow Simulations

Calculations were performed for the 1 1/2-stage turbine configuration of the LSRR. The airfoil loadings are compared with time-averaged measured data in Figures 27, 28, and 29 for the first stator, rotor, and second stator, respectively. The good agreement between the calculated and measured loadings indicates that airfoil loadings are not appreciably affected by unsteadiness for this configuration, and steady computational fluid dynamics (CFD) codes can be used to estimate airfoil pressure distributions for airfoil rows operating at subsonic flow conditions.

Spanwise distributions of exit gas angles for the three airfoil rows are compared with calculations in Figure 30. The agreement between the data and calculation is reasonable for the first stator. However, the yaw angles at the rotor exit, with large secondary flow, show disagreement between the calculations and data, especially in the endwall regions. The second stator results show substantial disagreement, across the whole span, between the data and calculations. This second stator calculated profile appears to be inverted, relative to the data.

The calculated and measured loss profiles, for the first stator and rotor, are also compared and shown in Figure 30. The figure shows that the wall shear force model in the code provides a reasonable estimate for two-dimensional (2-D) type losses, as in the midspan of the first stator, but is not adequate for the endwall regions. This argument is also bolstered by the rotor loss profiles, which show disagreement between the measured and computed losses in the midspan region, where the cross-passage vortices are located. Comparisons of losses in the second stator are not shown because the experimental data were not acquired over an integral number of first and second stator airfoils, and therefore, do not provide representative loss levels.

5.2 THREE-DIMENSIONAL, UNSTEADY, MULTISTAGE, EULER SIMULATIONS

Numerical simulations were conducted by using the unsteady version of Ni's 3-D multistage Euler code, again with no tip clearance. The grid and wall shear force model for the unsteady version was the same one that was used in the steady version of the code. The main objective was to quantify the impact of unsteadiness and circumferential variations on airfoil surface static pressure distributions and exit flow angle profiles.

5.2.1 Geometry Selection for LSRR

Unsteady simulations of multistage turbomachines, with different numbers of airfoils in each row, require special gridding to retain airfoil-to-airfoil distortions as they convect through succeeding airfoil rows. The LSRR turbine rig contains 22 first stators, 28 rotors, and 28 second stators. Computationally, this would require simulation through an integral number of airfoil passages (11, 14, and 14 in the first stator, rotor, and second stator, respectively) to preserve periodicity in the circumferential direction. Since computer hardware was not available to conduct such a large numerical simulation, it was conducted using a 3, 4, 4 airfoil count for the first stator, rotor, and second stator, respectively. The 3, 4, 4 *reduced-set* airfoil count is an approximation to the LSRR geometry (it corresponds to a complete turbine airfoil count of 21, 28, 28). The first stator was scaled to hold the pitch-to-chord ratio, Zwieffel load coefficient, and exit gas angle. Since the aerodynamics are almost identical to the original configuration, the importance of unsteadiness can be highlighted with this simulation.

5.2.2 Unsteady Flow Simulation for LSRR

The results from the unsteady simulation, shown in Figure 31, indicate that the time-averaged loadings for all airfoil rows are the same as calculated by the steady multistage code, except in the rotor tip region. The agreement between the steady and unsteady airfoil loadings indicates that airfoil loadings are unaffected by unsteadiness, and can be predicted by steady codes incorporating an average-plane (or a mixing-plane) approach.

The spanwise distributions of exit gas angles for all airfoil rows from the unsteady simulation are compared to those obtained from the steady multistage in Figure 32. Computed exit gas angle profiles for the first stator show little impact of unsteadiness. The rotor shows some spanwise redistribution, and the second stator angle shows a flattening when unsteadiness is accounted for. This result indicates that the mixing plane technique accumulates through the turbines.

5.2.3 Comparisons with LSRR Data for Deterministic Stresses

Computed spatial *deterministic stresses* from numerical data for the steady multistage flow simulation were compared to the experimental data at the exit of the first stator and rotor. Results from the unsteady code were similar to those from the steady code. These comparisons (Figures 33 through 36) show that the magnitudes of V_{x2}, V_xV_t, and V_xV_r were poorly estimated for both the rotor and stator. All components of stresses calculated for the first stator did not compare well with the data, whereas reasonable predictions were obtained for V_{r2}, V_{t2} and V_tV_r profiles at the rotor exit. This indicates that the distortions in axial velocity, generally associated with loss, are not being calculated, most likely associated with the limitations in the *viscous modeling* in the code. However, the large-scale flow features (associated with secondary flow) in the rotor were reasonably well captured in the code, as would be represented by the spatial stresses (V_{r2}, V_{t2}, and V_tV_r).

The time-averaged average-passage flowfield (yaw angles and entropy) downstream of each airfoil row, computed by using the unsteady code, was compared to results obtained by using the steady code in Figures 37 through 39. These contour plots show that steady and unsteady results were similar for the first stator and rotor. However, differences in the contour plots were observed for the flow downstream of the second stator. This difference is due to the existence of larger circumferential variations in flow properties at the inlet to the second stator, in the unsteady results, compared with the steady flow simulations.

Time-averaged flow, for a periodic segment, at the inlet and exit of the second stator, is shown in Figure 40. This figure shows that the inlet angle is periodic with the downstream airfoil count (four repeating contour features), while the entropy is periodic with the upstream vane count (three repeating contour features). This results in a different flowfield for each airfoil passage for the second stator. These contours show that the exit flow angles vary up to 22 degrees, and entropy varies by 50 percent in the tip, from one second stator passage to another, over one periodic flowfield (four downstream stators to three upstream stators). For a two-stage turbine, where there is a rotor behind the second stator, the rotor will periodically pass through an angle variation of an additional 12 degrees (Figure 39 versus 40). Although this steady/unsteady analysis does not quantify the impact on loss for a truly periodic boundary versus a representative passage, it will become clear that the periodic boundary is

extremely important for combustor-induced hot streaks. This aperiodic variation in flow and temperature, at the exit of the first stator, will be shown to affect the performance and heat load characteristics for both the rotor and second stator. Both aspects of the flowfield are discussed in Section 5.4.

As previously shown, the magnitude of spatial deterministic stress, in general, is not reproduced by the Euler code. This is associated with the limitations of viscous modeling. The unsteady analysis, however, should indicate trends of the deterministic stresses not significantly influenced by viscous effects. The experimental data, discussed in Section 4 (Figure 23), indicated that the magnitude of temporal stress and intensity is approximately the same at the inlet and exit of the rotor, and decayed across the second stator. Review of the numerical data, obtained from the unsteady flow simulation, indicates a similar trend. Figure 41 shows the total intensity and shear for four grid lines through the rotor passage, as follows:

- 1st grid line: suction surface
- 2nd grid line: pressure surface
- 3rd grid line: 8 percent of the rotor pitch circumferentially offset from the pressure surface
- 4th grid line: 8 percent of the rotor pitch circumferentially offset from the suction surface.

Figure 41 shows that the temporal stress level either remains about constant through the passage, or enhances before decaying back to approximately the inlet levels. For the rotor, the inlet and exit levels are approximately the same and are consistent with measured data (shown in Figure 23).

The numerical results for the second stator are shown in Figure 42 for four grid lines through the stator passage as follows:

- 1st grid line: suction surface
- 2nd grid line: pressure surface
- 3rd grid line: 8 percent of the stator pitch circumferentially offset from the pressure surface
- 4th grid line: 8 percent of the stator pitch circumferentially offset from the suction surface.

This result shows, in general, that the temporal stress decays significantly from the inlet to exit of the second stator, which is the same trend observed in the data in Figure 23.

This results suggests that the temporal stress distribution may be an inviscid effect and that unsteady Euler codes possibly can be used to generate distributions of deterministic stresses, which can be used in steady multi-stage Reynold-Averaged Navier-Stokes (RANS) codes to simulate the effects of unsteady flow.

In an average-passage (steady) analysis, the deterministic stresses are created through circumferential averaging. The downstream propagation and/or segregation of the stress is currently undefined for a steady solution. The results from unsteady analysis indicate that even without the absolute magnitudes of the deterministic stress captured by the code, the temporal stress shows higher levels in specific regions of the rotor and second stator passage. Figures 43 and 44 show that these pockets of highest stress occur on or near the pressure surface of both the rotor and second stator. For the rotor, this pocket appears as a streak along the pressure side from approximately 20 to 110 percent axial chord. The highest stresses in the rotor are three times the level of the inlet stress and imply that the unsteadiness is either enhanced through the rotor, or there is unsteady radial movement of flow. From a modeling perspective, these figures also show the ratio of shear stress to intensity (Ts/Q = structural coefficient). This parameter suggests that the shear stress terms are approximately 1/2 of the intensity and could possibly be modeled with one transport equation similar to a transport equation for *turbulent kinetic energy.*

Results from the unsteady analysis for the second stator showed that the highest temporal stress appeared in the airfoil passage, near the pressure side, at approximately 30 percent axial chord. The level of this stress pocket is different from the rotor stress since it has approximately the same magnitude as the inlet stress (displayed along the inlet boundary condition). From a modeling perspective, the intensity stress was 30-40 percent larger than the

unsteady shear stress, and suggested that the shear stress terms could possibly be modeled with one transport equation similar to a transport equation for *turbulent kinetic energy.*

Based on the steady and unsteady 3-D analysis, these simulations did not predict the second stator exit gas angle profile, as anticipated, and did not capture all the magnitudes of the spatial deterministic stress. It did show that an average-passage approach suppresses pertinent flowfield information, and modeling these stresses through an airfoil row using a steady CFD code will require segregation modeling (transport equation) when, or if, the stress influences performance. This analysis also suggests that the measured angle profile at the second stator exit is a result of something other than has been modeled in the current simulation.

5.3 THREE-DIMENSIONAL STEADY EULER AND RANS SIMULATION FOR AIRFOIL ROW ASSESSMENT OF EFFECT OF BOUNDARY CONDITIONS

Since the exit gas angle downstream of the second stator could not be accurately simulated by using either the steady or unsteady versions of the multistage Euler code, an additional numerical study was performed to assess the impact of inlet boundary conditions on the stator exit flowfield. This study was conducted by using the steady version of Ni's code and a 3-D RANS code developed by Rhie [8].

The studies performed with the Euler code included varying inlet yaw angle, removing *surface viscous modeling* effects, and modifying the inlet total pressure profile. The Euler analysis consisted of a steady row calculation of the second stator, with axial plane boundaries consistent with the previous 1 1/2-stage simulation. The inlet boundary conditions consist of spanwise distributions of total pressure (P_t), total temperature (T_t), radial gas angle (ϕ), and yaw angle (α). The exit condition consists of static pressure at midspan with the spanwise gradient determined by simple radial equilibrium ($\frac{1}{\rho}\frac{\partial Ps}{\partial r} = Ct^2/R$). The base case is a row calculation performed with the inlet and exit boundary conditions from the 3-D steady 1 1/2-stage simulation. Figure 45 shows the result of the row boundary condition study.

The base case (squares in Figure 45) shows that there is a calculated dropoff in both yaw angle and total pressure at 0 and 100 percent span from the steady 1 1/2-stage simulation. The boundary condition results in a reduced axial velocity, at the inlet, near 0 and 100 percent span. At the exit, as previously discussed, the yaw angle drops near the endwalls (0 and 100 percent span) and rises up toward midspan where the angle is almost constant at 22 degrees from 20 to 80 percent span. Removal of the total pressure profile, by maintaining the average (igloo symbol in Figure 45), shows that the inlet velocity distribution changed slightly from the base, but the exit yaw angle profile has been inverted. This angle profile is high near the endwalls and drops toward midspan, changing the endwall angles 10 to 15 degrees, and the midspan by 5 degrees. Maintaining the flat pressure profile and removing the angle profile (holding average yaw) result in an angle profile similar in shape to the base (1/4 arc symbol in Figure 45). This flat inlet angle results in an exit angle change on the endwalls of 8 to 13 degrees and at midspan of 4 degrees. The inlet axial velocity no longer drops near the endwall and is almost constant at 80 ft/sec. The final configuration examined is the case where the inlet pressure and angle profiles are a constant, and the surface shear model is removed from the analysis (triangle symbols in Figure 45). The analytical result shows that the inlet axial velocity increased about 1 ft/sec, but the spanwise profile remained the same (as with shear). The exit angle responded in a near linear fashion from 0 to 100 percent span, as anticipated based on P&W's experience. The viscous shear model changed the endwall angles by 3 to 5 degrees, and the midspan angle by 1 degree. This analysis indicated that the inlet boundary condition influenced the exit angle profile distribution the same order of magnitude as the mismatch previously discussed, and is important if exit gas angles are to be calculated.

Since the inlet boundary conditions have shown to influence the exit gas angle, a RANS and Euler (with shear) analysis was performed using the time-averaged measured data required in the 1 1/2-stage rig. This simulation incorporated a flat temperature profile, measured pressure profile, measured yaw and phi angles, and downstream measured static pressure.

As previously shown from the Euler results, the airfoil loading was relatively insensitive to the ability to capture the unsteadiness or viscous terms. However, the loading is an indicator of the overall flow, flow distribution, and trailing edge (TE) modeling of any analysis and is shown for the RANS analysis in Figure 46. The loading showed reasonable agreement, and therefore, the overall potential flowfield is satisfactorily captured. The resultant exit gas angle from the RANS code showed good agreement with the data, except for some discrepancy in the tip. This miss in the tip may be associated with obtaining a true periodic second vane segment, as this was where the unsteady analysis showed the most discrepancy between periodic and representative passage. Euler analysis with the measured boundary conditions, into the second vane, showed much better agreement than previously shown from the multistage Euler analysis in Figure 30.

The result of the 3-D steady analysis performed on the second stator indicated the need for the RANS code to be used in the multistage simulations to ensure more reliable flowfield predictions.

5.4 TWO-DIMENSIONAL UNSTEADY EULER AND RANS SIMULATIONS FOR TURBINES WITH INCOMING HOT STREAKS

Numerical simulations were conducted in three model turbines operating with incoming hot streaks by using 2-D versions of Ni's unsteady, multistage Euler and RANS codes. The main objectives for conducting these simulations were to demonstrate that:

- There is a need to simulate flow through more than one *representative passage* in each airfoil row in a multistage environment to ensure accurate predictions of time-averaged flow properties.
- The *deterministic stresses/fluxes* for simulating flow through high-pressure turbines (HPTs) are important.
- The adverse effect of hot streaks in turbines can be managed.

5.4.1 Flow Simulations Through 1 1/2-Stage Turbine

Simulations were performed for the mean section of the UTRC LSRR turbine by using one hot streak, three first stator, four rotor blade, and four second stator airfoil passages. The 2-D version of Ni's unsteady, multistage Euler code, with the wall shear force model, was used to conduct the numerical simulations. Results from this simulation at an instant in time are provided in Figure 47. This figure shows the distributions of temperature through the flowfield with a hot streak entering between two first stator airfoils, and convecting through the rotor into the second stator.

The time-averaged total temperature distribution from the simulation (Figure 48) shows segregation of hot and cold flow in the rotor passage. The rotor airfoil pressure side operates at a higher temperature than the suction side. In addition, one of the four second stator airfoil passages operates in a higher temperature environment than the other passages. It is apparent from this figure that unsteady computations are needed to properly describe the temperature field in the turbine with an incoming hot streak.

This configuration can be represented with an *average-period* approach to compute flow through multistage machines. Simulation of flow, through the above configuration, using the conventional approach, where a single *representative passage* is used to compute the flow through each airfoil row, will yield incorrect results for the temperature distribution in the three second stator passages. A steady flow simulation through this turbine, by using either the conventional *representative passage* or the *average period* approach, will yield incorrect temperature distributions for the rotor, unless the temperature segregation phenomena can be accounted for. One approach to simulate this effect is described below.

5.4.2 Model for Deterministic Stress/Flux Terms

Three numerical simulations were conducted to develop a model for *deterministic stress/flux* terms, which can be used in turbine design/analysis. The mean section of the UTRC LSRR turbine stage, with an incoming hot streak and with the same number of airfoils in the rotor and first stator, was used as the model turbine for the simu-

lations. The 2-D steady and unsteady versions of Ni's Euler codes with the wall shear force modeling, discussed above, were used to conduct the simulations.

The first simulation was conducted by using the steady version of the code with interface averaging prior to calculating the rotor flowfield. Calculated temperature distributions from this simulation, shown in Figure 49(a), illustrate that the temperature field for the rotor from this simulation is uniform, and there is no effect induced by the incoming streaks. Based on the steady and unsteady result, there is a need to develop models that will predict elevated levels of temperatures on the rotor airfoil pressure sides in turbine stages operating with incoming hot streaks.

The second simulation was conducted by using the unsteady version of the code. This simulation was used to establish the magnitudes of the time-averaged flow properties for the stator and the rotor airfoil passages as well as the *deterministic stress/flux* quantities. The time-averaged temperature field obtained from this simulation is shown in Figure 49(b). This figure illustrates the migration of hot streak through the stator passage, its distribution over the rotor inlet, and the appearance of hot gas near the airfoil pressure side. The increased levels of temperatures shown near the airfoil pressure side are in agreement with experimental data of Butler et al. [9].

The third simulation was conducted by using the steady version of the code, but with appropriate gradients of *deterministic stress/flux* terms as sources in the transport equations for mass, momentum, and energy. These source terms were computed from the unsteady simulations discussed above. The computed temperature field from this simulation is compared to those obtained from the unsteady flow simulation in Figure 50. Almost identical results, predicted by the two simulations, indicated that the unsteady flow effects induced by the turbine inlet hot streak can be simulated through *deterministic stress/flux* distributions. This result may not be surprising, but to P&W's knowledge, has not been previously demonstrated. The values of *deterministic stress/flux* were calculated from the unsteady flow simulation, which was also used to establish the temperature field representing the basis of comparison. The agreement between the two calculations in this figure demonstrated that steady flow simulations, with stresses included, can be used to get as accurate estimates of the temperature field as unsteady flow simulations.

This idea can be implemented by establishing the magnitudes of *deterministic stress/flux* terms in rotor passages from unsteady Euler flow simulations for the turbine with incoming hot streaks. These calculated *deterministic stress/flux* terms can be included in steady multistage RANS codes to obtain realistic estimates of hot streaks in a viscous flow environment, assuming that the viscous flows have relatively small effects on the temperature migration in the rotor passages.

5.4.3 Hot Streak Management in Turbines

Results of numerical simulations discussed in the above two subsections demonstrate that a turbine rotor performing in the presence of nonuniform inlet temperature is likely to have a higher temperature on the rotor airfoil pressure side than on the suction side. Experience in the industry is consistent with these results, since maximum thermal distress is invariably found on the airfoil pressure side. Extensive efforts have been undertaken over a period of decades to explain this higher than expected heat load on the airfoil pressure sides. Numerical simulations were conducted in the present program to establish whether a procedure could be identified to manage the adverse effect of hot streaks in turbines. The simulations were conducted for the mean section of a model turbine stage, representing a state-of-the-art design for commercial aircraft engines. The airfoil rows in this turbine were designed to operate at subsonic flow conditions. Both rows were designed to have the same airfoil count to facilitate numerical simulations.

Three sets of computations were conducted for the turbine by using the unsteady, multistage version of Ni's RANS code, with the following:

- Uniform temperature at the first stator inlet to represent an *Idealized Design*, which is consistent with the assumptions used in the current design processes.
- Hot streak in the mid-passage of the first stator to represent a *Conventional Design*, a configuration likely to be optimized from a *Steady Flow Design* approach
- A hot streak aligned to the first stator to represent a *Managed Hot Streak Design*, which is developed by using an approach that acknowledges the presence of unsteady flows in turbines.

All three simulations were conducted for identical operating conditions, as indicated in Table 1. Time-averaged temperature fields obtained from these simulations are shown in Figure 51. The highest levels of rotor airfoil surface temperatures are predicted for the configuration represented by the *Conventional Design*, whereas the *Idealized Design* shows the lowest rotor surface temperatures. Moderate values of rotor airfoil temperatures on the pressure side are predicted for the *Managed Hot Streak Design*. Instantaneous contours of the total temperatures through the rotor for the *Conventional* and the *Managed Hot Streak Design* configurations are shown in Figures 52 and 53, respectively. Four contour plots in each of these figures illustrate the migration of hot streak through the turbine rotor and its accumulation on the airfoil pressure side. Aligning of the hot streak with the first stator may initially appear as an incorrect strategy since it yields higher temperatures on the first stators. The first stators for the HPTs are, however, designed for almost stoichiometric temperatures. Cooling air in the stator does not have as much of a detrimental effect on turbine performance as the cooling air in the rotor. Aligning the hot streak to the first stator reduces the temperature and velocity of the hotter gas, and yields less distortion at the inlet to the rotor than the configuration with hot streak in the mid-passage of the first stator.

Time-averaged specific work of the rotor was not affected by the hot streak, as suggested by the time-averaged rotor surface static pressure distribution for the three simulations (shown in Figure 54). Since the static pressures are not impacted, incorporating the steady pressure field solution into a time-averaged code may eliminate the need for a deterministic stress transport equation, and should be investigated in future efforts.

Time-averaged airfoil surface static temperatures for the three rotor configurations are shown in Figure 55. Highest surface temperatures are predicted for the configuration with the hot streak through the middle of the first stator. The *Managed Hot Streak* configuration shows low temperatures on both sides of the airfoil, indicating that an improved understanding of the flow phenomena can be used to accommodate the adverse effects of hot streaks in the rotor passage.

Performance estimates (Table 1) were obtained from the numerical simulations for the three configurations. Best overall efficiency was found for the *Idealized Design* with a uniform inlet temperature. The *Conventional Design* configuration, with the hot streak through the middle of the first stator airfoils, had almost 0.8 percent lower efficiency than the *Idealized Design*. The *Managed Hot Streak Design* was performed at 0.4 percent higher efficiency than the *Conventional Design*, and lower than the *Idealized Design* by the same amount.

In summary, understanding of flow phenomena, deduced from the numerical experiments conducted in this program, has shown the potential to improve performance and reduce head load in a realistic turbine environment. In addition, these simulations have identified limitations in the current design process, where the assumption of uniform inlet temperature to the turbine first stator can lead up to a 0.8 percent overestimation of the turbine efficiency, and an underestimation of the rotor pressure side temperature on the order of about 3.3 percent of the rotor inlet temperature. This underestimation of the temperature, or the heat load on the airfoil pressure side, can reduce the life of the rotor airfoil by a factor of four.

5.5 SUMMARY

Results from the numerical experiments are summarized below:

- Time-averaged measured pressure distributions on airfoil surfaces agree well with all versions of the codes used in the present exercise. Designs of turbines have historically been conducted by using *Design Criteria,* based on airfoil pressure distributions. Although more complex analyses (RANS, unsteady) are not needed to estimate the airfoil surface static pressure distributions, there is a need to develop *Next Generation of Design Criteria,* since the efficiency and heat loads on airfoils have been strongly affected by flow unsteadiness.
- The shear force model used in Ni's multistage Euler code has been shown to be inadequate to simulate secondary flows in multistage turbines. Based on computational results, a RANS code is needed to provide reliable simulations of angle profiles for multistage turbines.
- Accurate inlet and exit boundary conditions are needed to obtain realistic predictions of flow angles through an airfoil row. A RANS code is needed to ensure accurate estimates of boundary conditions for an airfoil row in a multistage environment.
- Simulations of flow through one representative periodic segment (not one representative airfoil passage) are needed to ensure that the circumferential flow distortions, generated by the upstream airfoil row (or fuel nozzle) in the same frame of reference as the current airfoil, are properly accounted for.
- From the computations, *Deterministic Stresses* have a relatively small effect on the airfoil loadings and the profiles of mean flow angles and velocity in flow situations with no gradients in temperatures. The experiments discussed in Section 7 show more quantitatively the effects of *Deterministic Stress* on performance.
- Deterministic stress/flux terms generated in turbines with hot streaks have a significant effect on the efficiency and heat loads in turbine rotors. A procedure has been proposed to compute the distributions of these stress/flux terms by using unsteady Euler codes and distributions in steady, multistage RANS codes.
- This numerical effort has identified that efficiency and rotor temperature can be impacted through *Hot Streak Management.* Computations imply that proper placement of incoming hot streaks may improve the efficiency of a single-stage turbine by up to 0.4 percent and reduce the temperature/heat load on the airfoil pressure side by 3.3 percent, yielding a potential improvement in airfoil life by a factor of four, or reduce cooling requirements in the rotor by 10 percent.

Table 1. Operating Conditions for Model Turbine Used in Hot-Streak Management Numerical Experiment

	Idealized Design	*Managed Hot-Streak Design*	*Conventional Design*
Inlet Temperature (°F)	800.00	800.07	800.14
Inlet Pressure (psi)	10.00	10.00	10.00
Flow Parameter	57.67	57.50	57.64
Adiabatic Efficiency	93.65	93.26	92.89
Pressure Ratio	1.9273	1.9310	1.9284
Temperature Ratio	1.1906	1.1903	1.1889

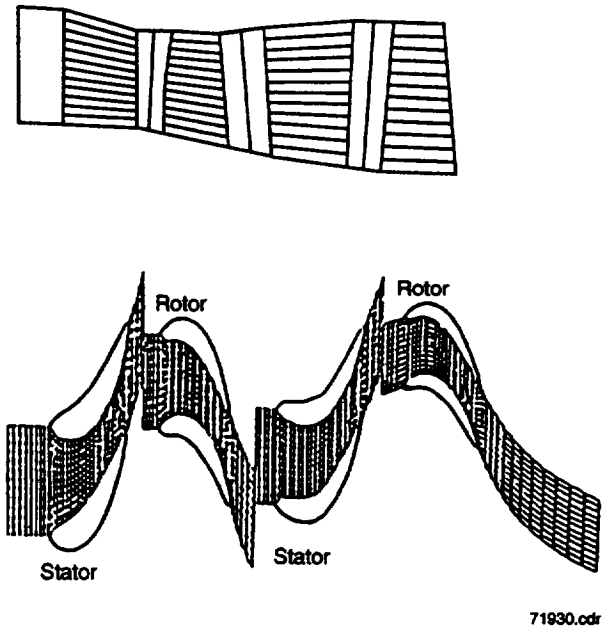

Figure 25. Schematics of Two-Stage Turbine Showing Strategy Used in Computing 3-D Flows by Using Multistage Euler Code; Flow Downstream of Each Airfoil Is Averaged, and Calculations Are Conducted in Their Frame of Reference

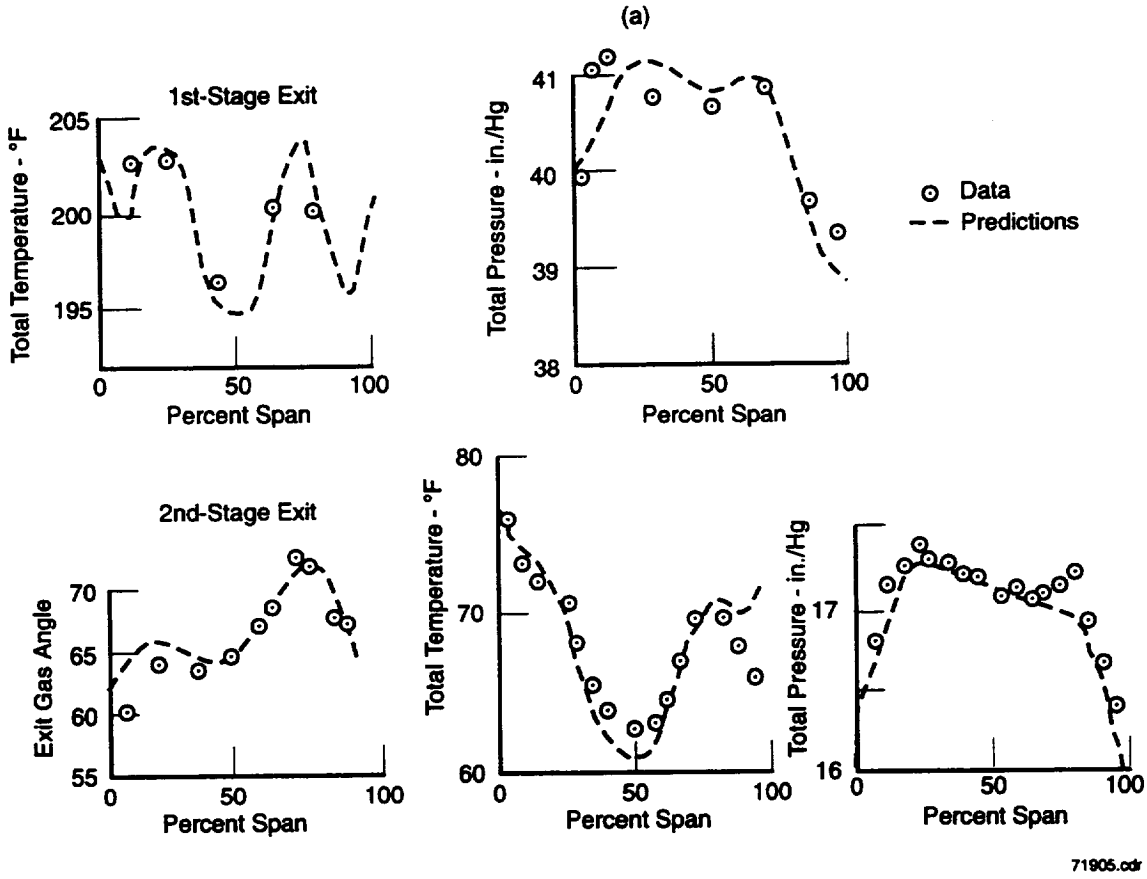

(a) Provides Good Estimates of Interstage and Turbine Exit Flow Conditions

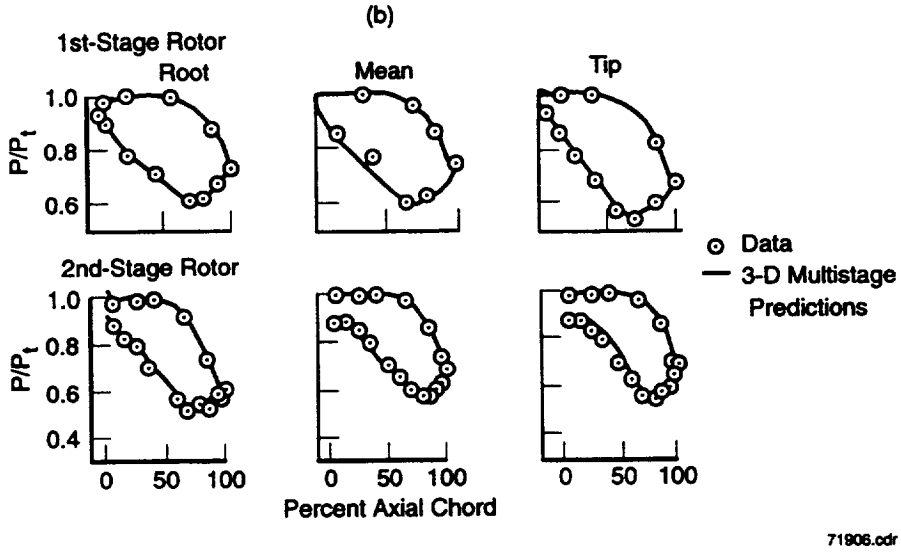

(b) Provides Good Estimates of Airfoil Loadings

Figure 26. 3-D Multistage Euler With Wall Shear Model

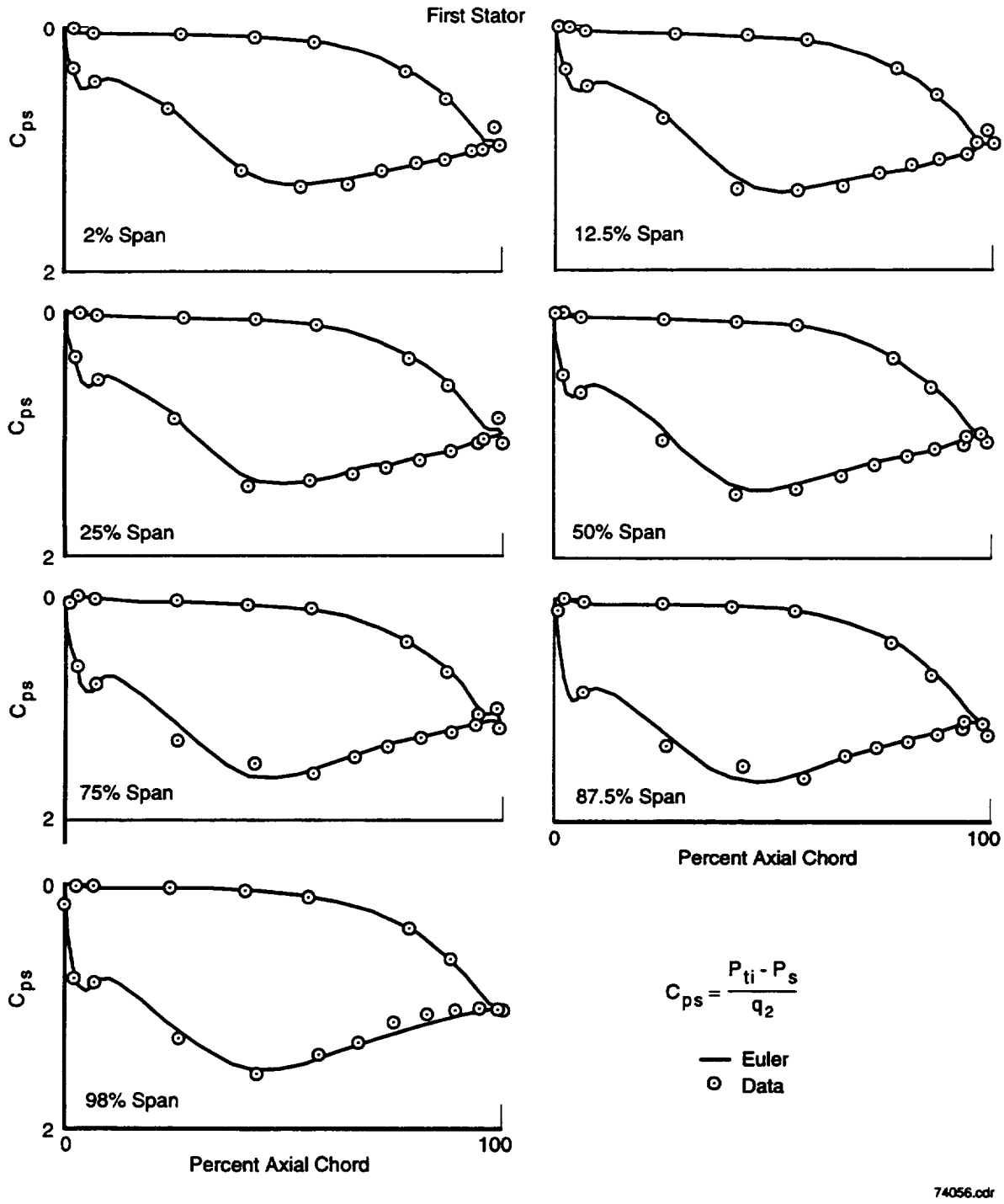

Figure 27. Steady Multistage Euler (With Shear and Mixing Plane) Shows Good Agreement With LSRR Measured First Stator Loadings

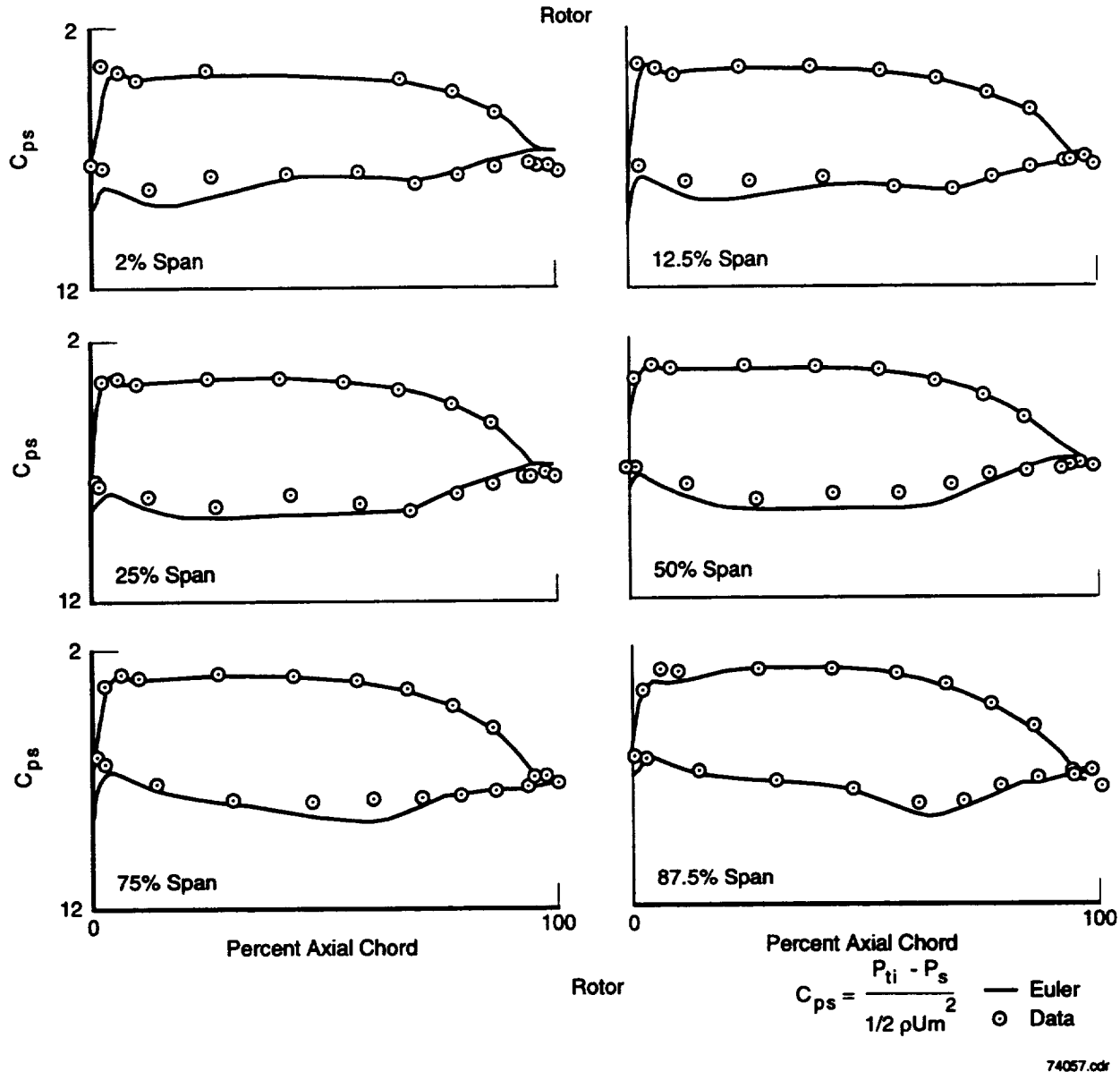

Figure 28. Steady Multistage Euler (With Shear and Mixing Plane) Shows Good Agreement With LSRR Measured Rotor Loadings

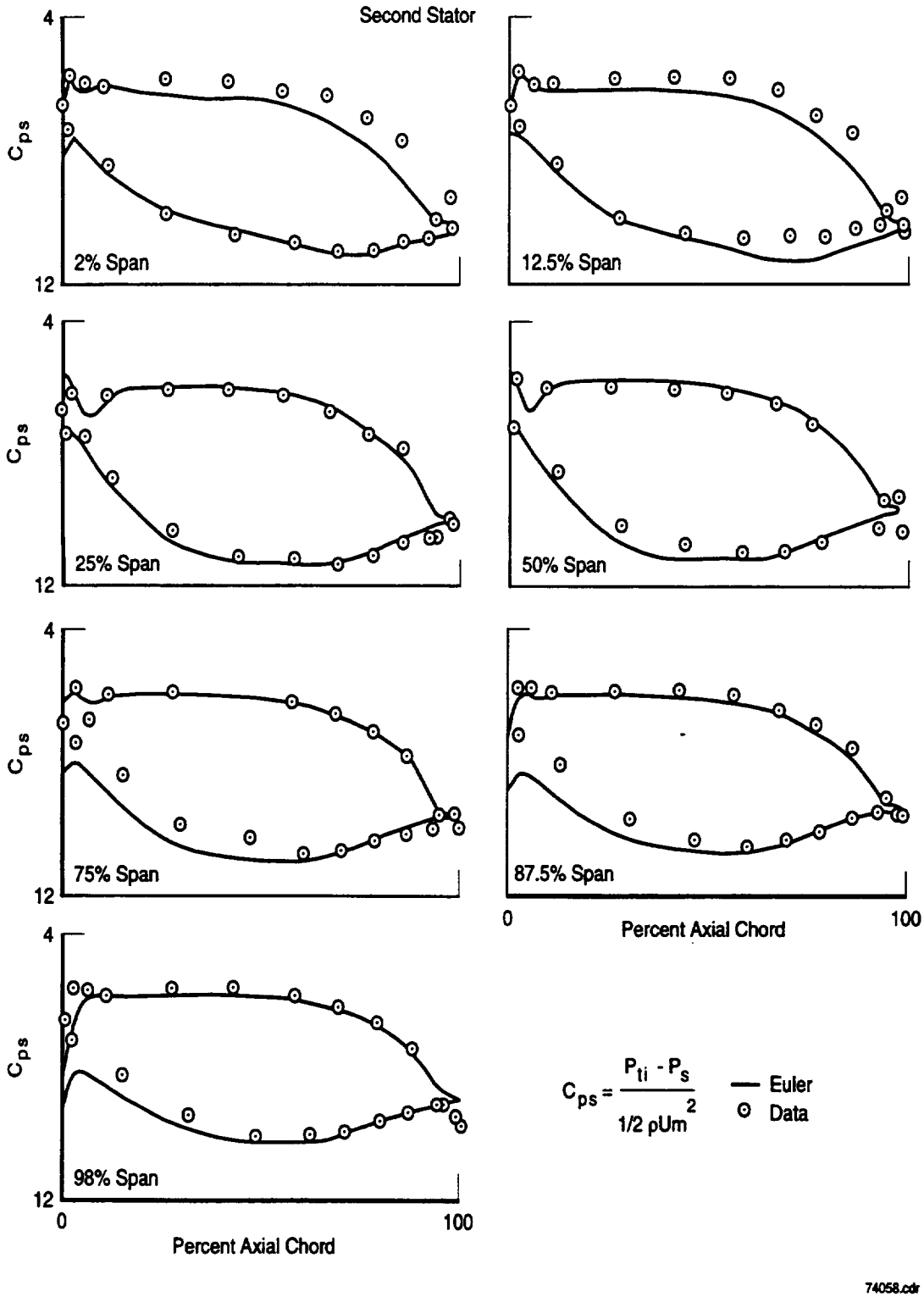

Figure 29. Steady Multistage Euler (With Shear and Mixing Plane) Shows Good Agreement With LSRR Measured Second Stator Loadings

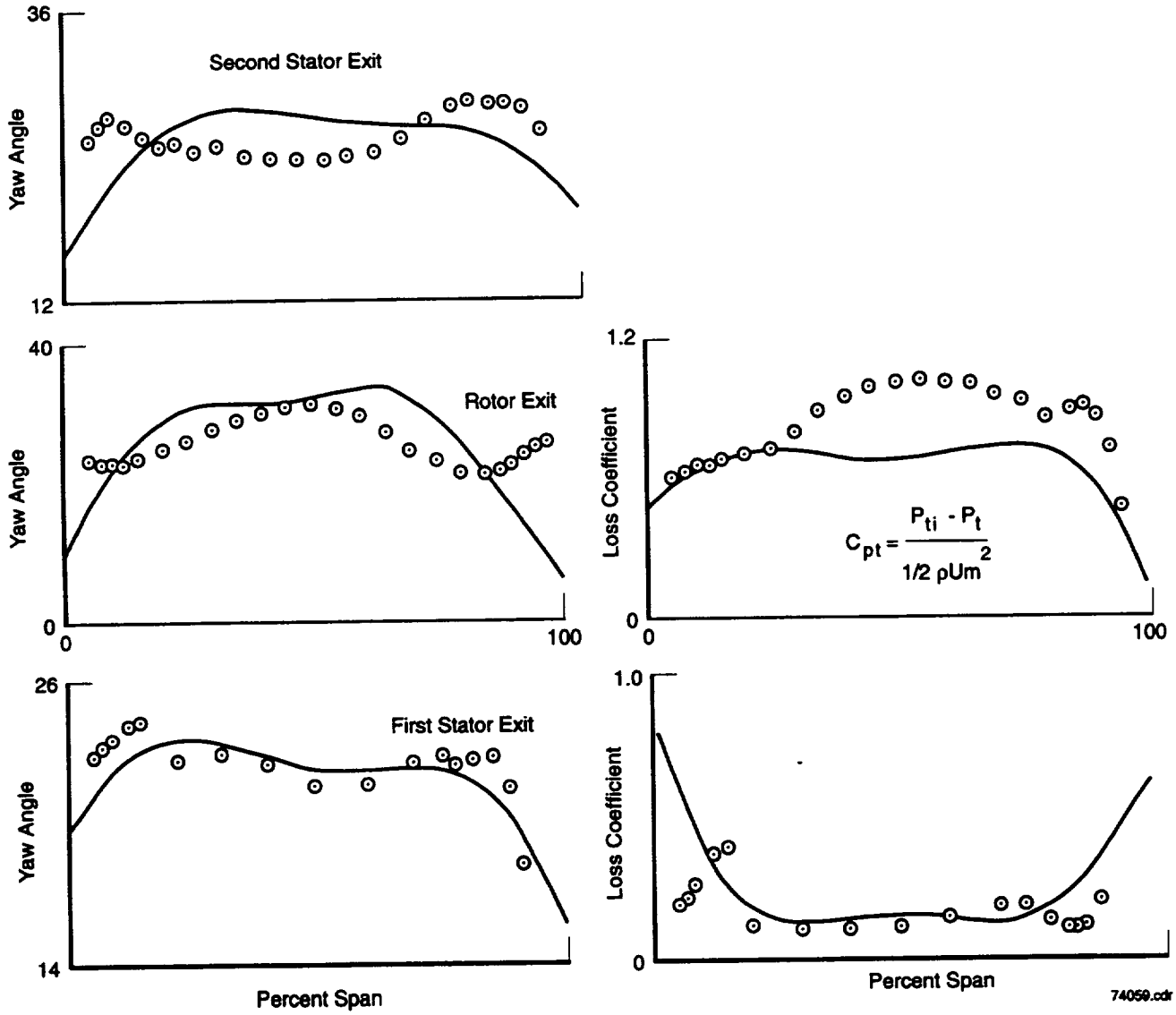

Figure 30. Results from Steady Euler Analysis (With Shear and Mixing Plane) Shows Ability To Match Exit Gas Angle and Loss Deteriorates from First Airfoil Row (First Stator) Through Last Airfoil Row (Second Stator)

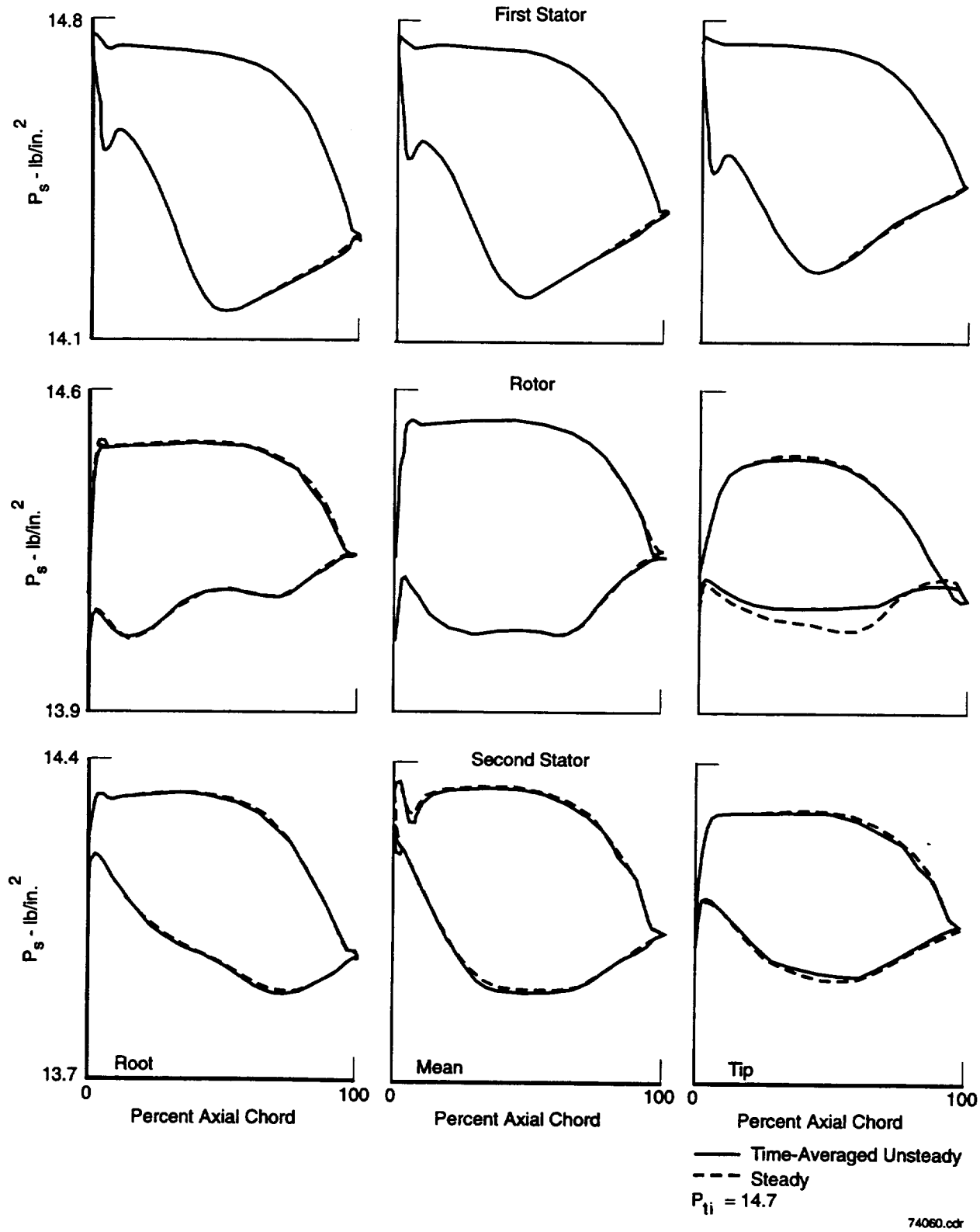

Figure 31. Time-Averaged Airfoil Loadings Obtained by Using Unsteady Euler Code Show Good Agreement With Those Obtained from Steady Code for UTRC LSRR

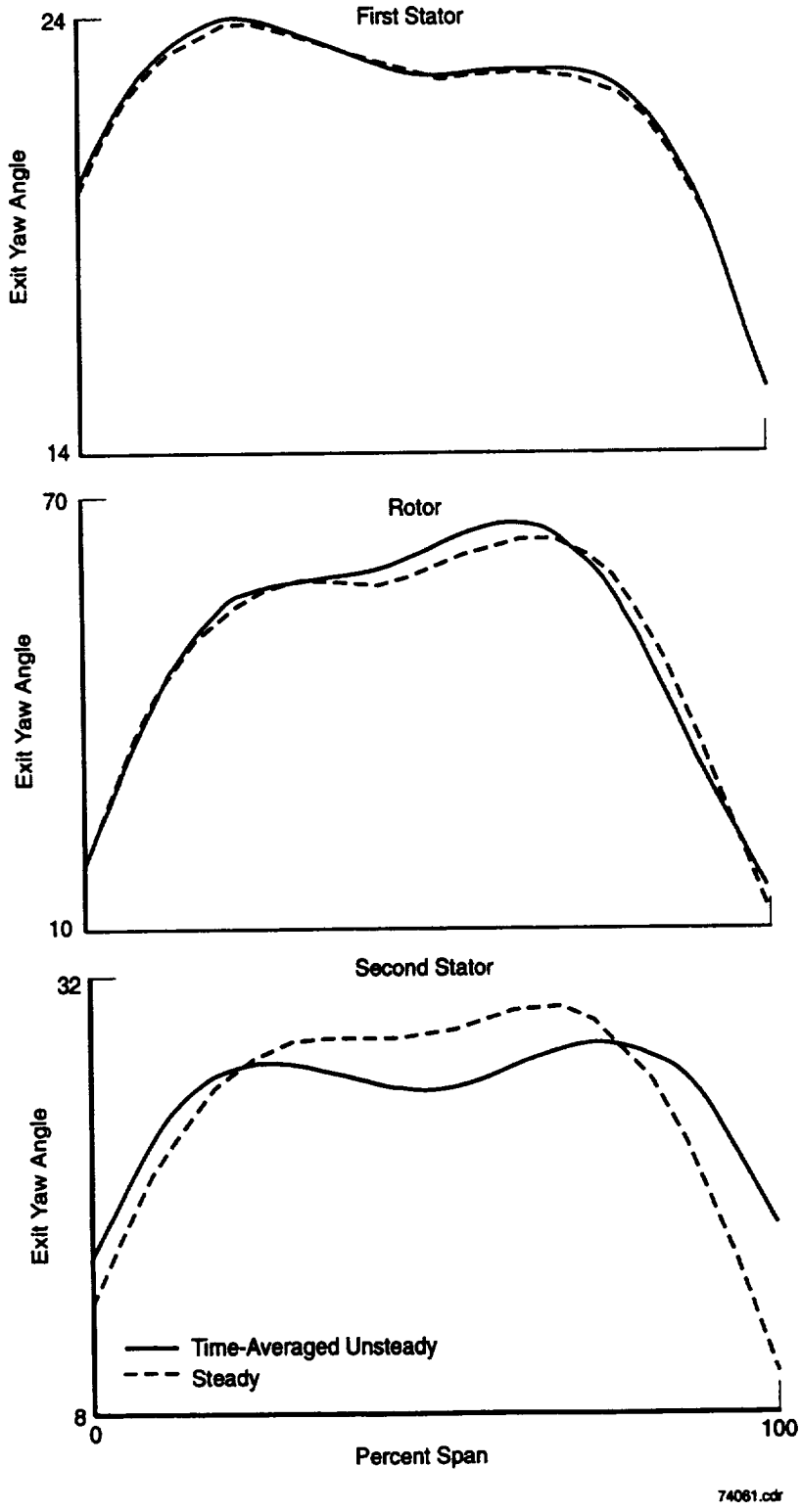

Figure 32. Steady and Unsteady Calculations Performed for LSRR Show That Mixing Plane Approach Accumulates Differences in Yaw Angle Through Turbine

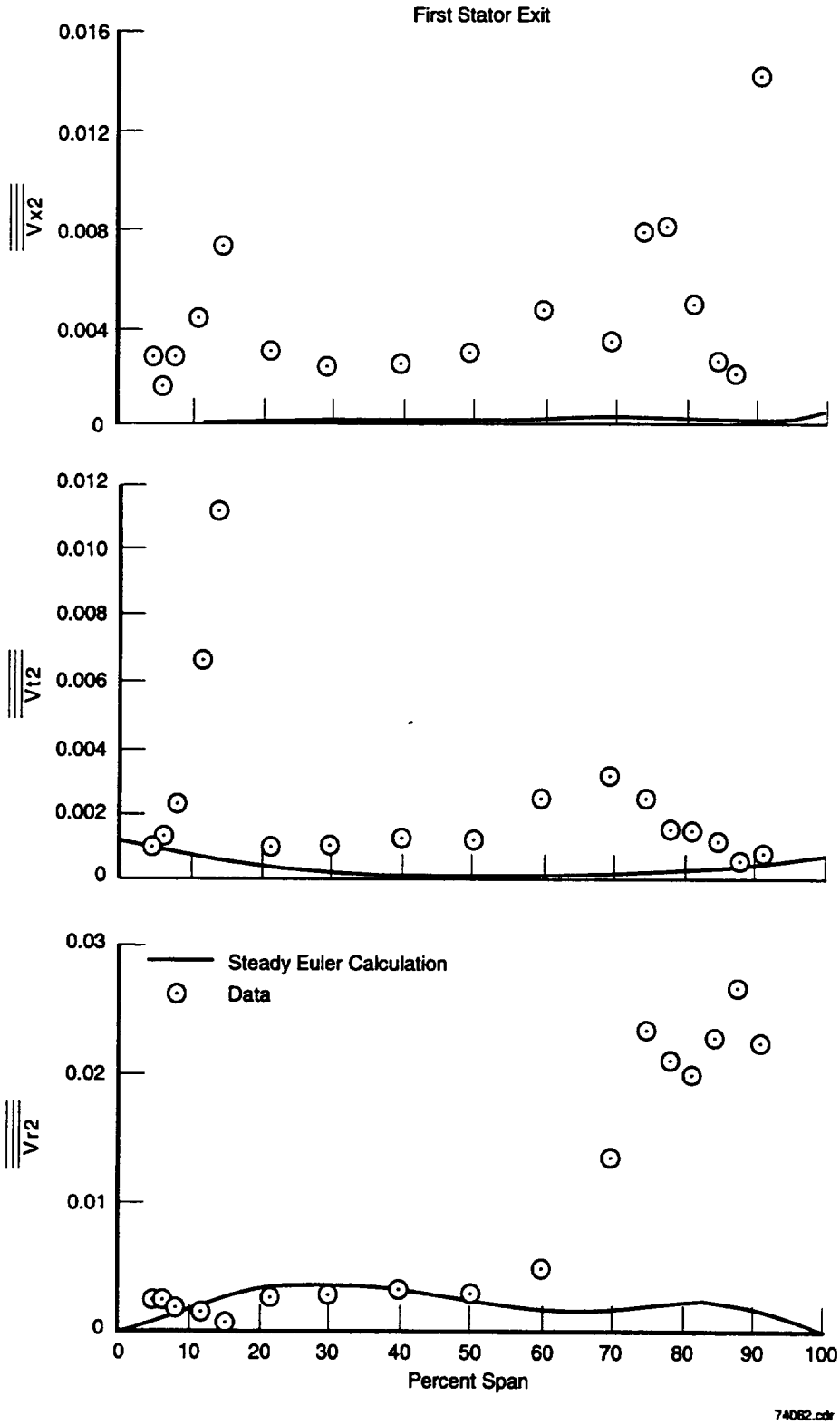

Figure 33. Spatial Stresses at First Stator Exit Show That Steady Euler (With Shear) Does Not Predict Measured Flow Distortion

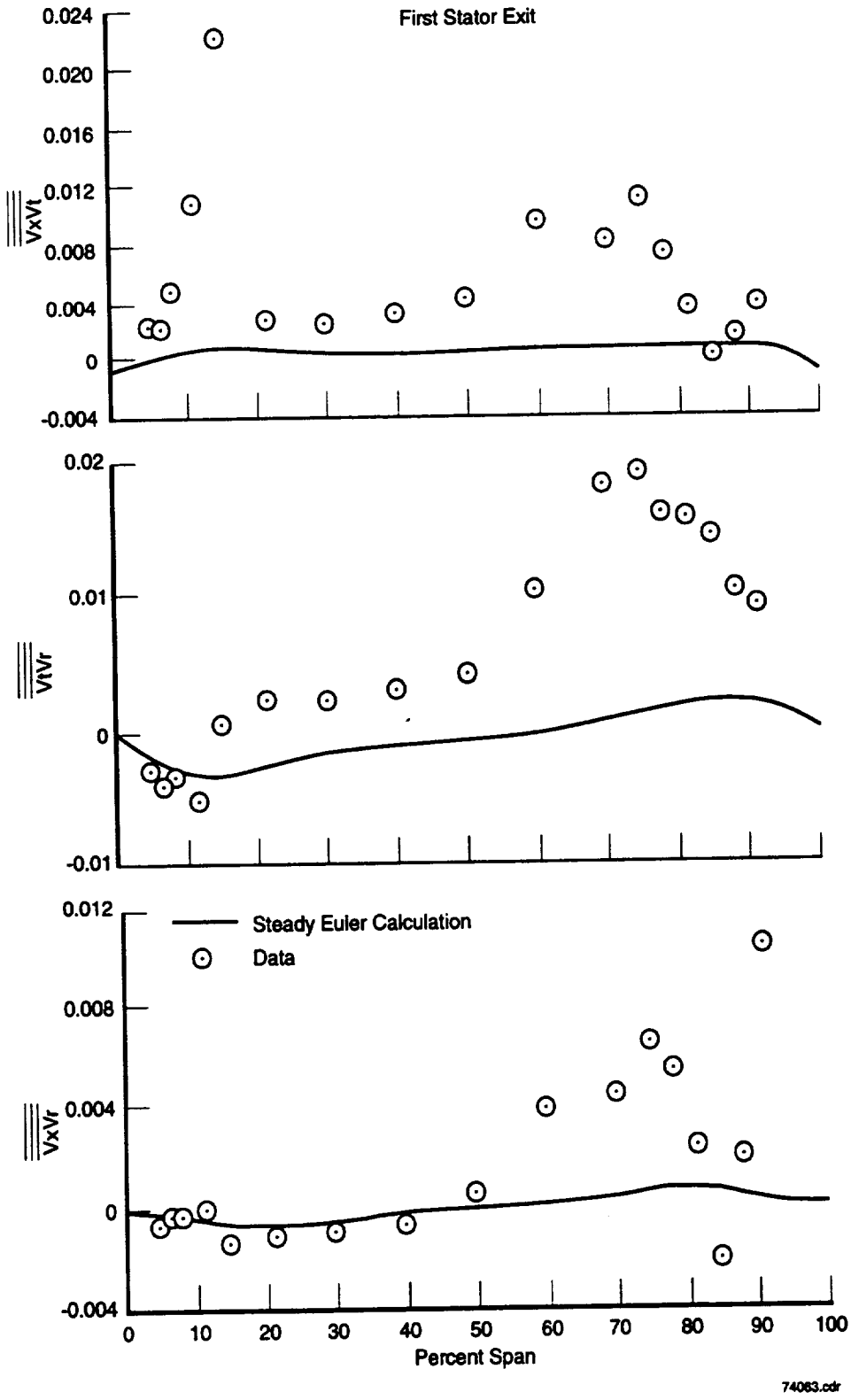

Figure 34. Spatial Stresses at First Stator Exit Show That Steady Euler (With Shear) Does Not Predict Measured Flow Distortion

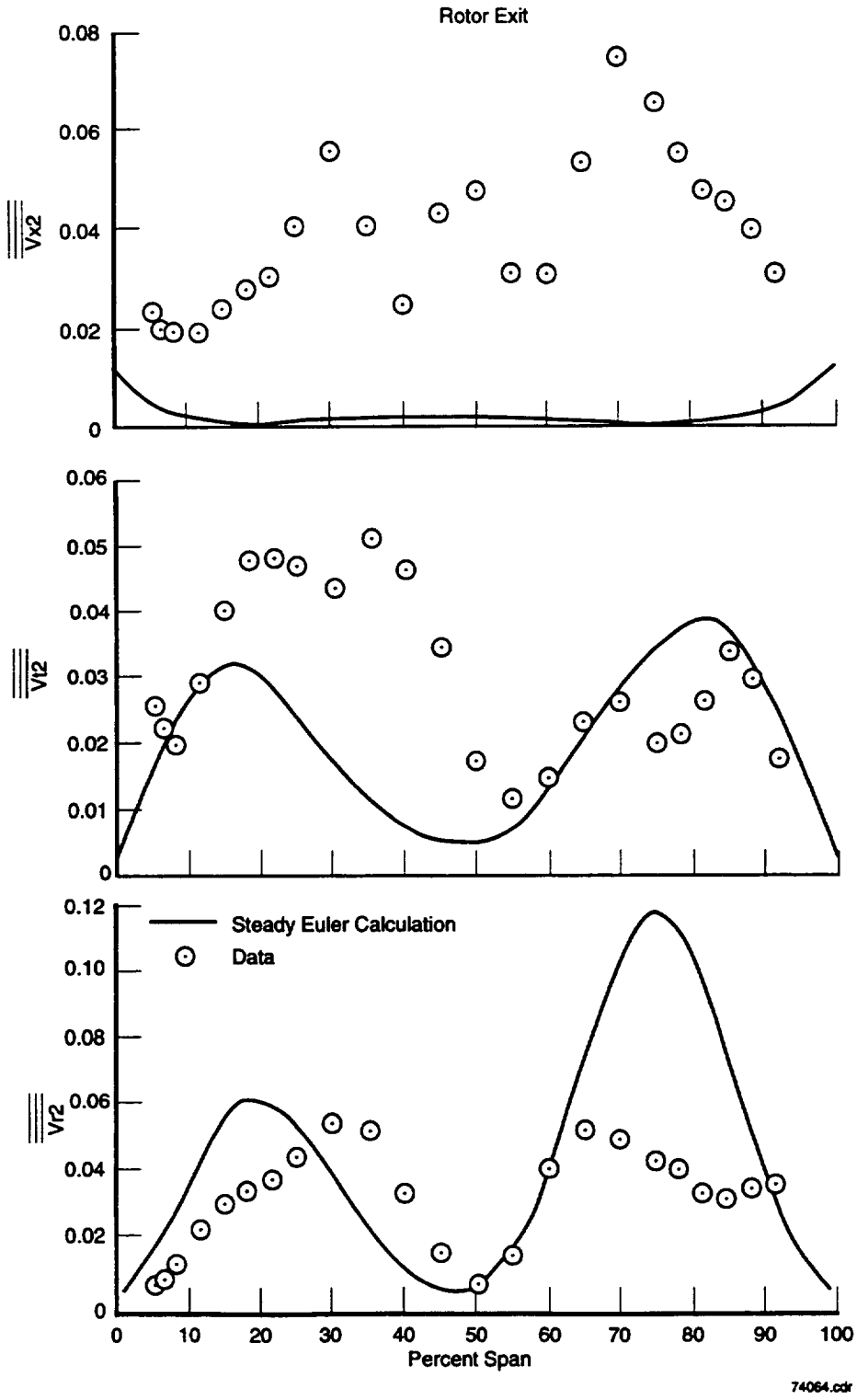

Figure 35. Spatial Stresses at Rotor Exit Show That Steady Euler (With Shear) Captures Secondary Flow Vortex (V_{t2}, V_{r2}), But Not Associated Blockage (V_{x2})

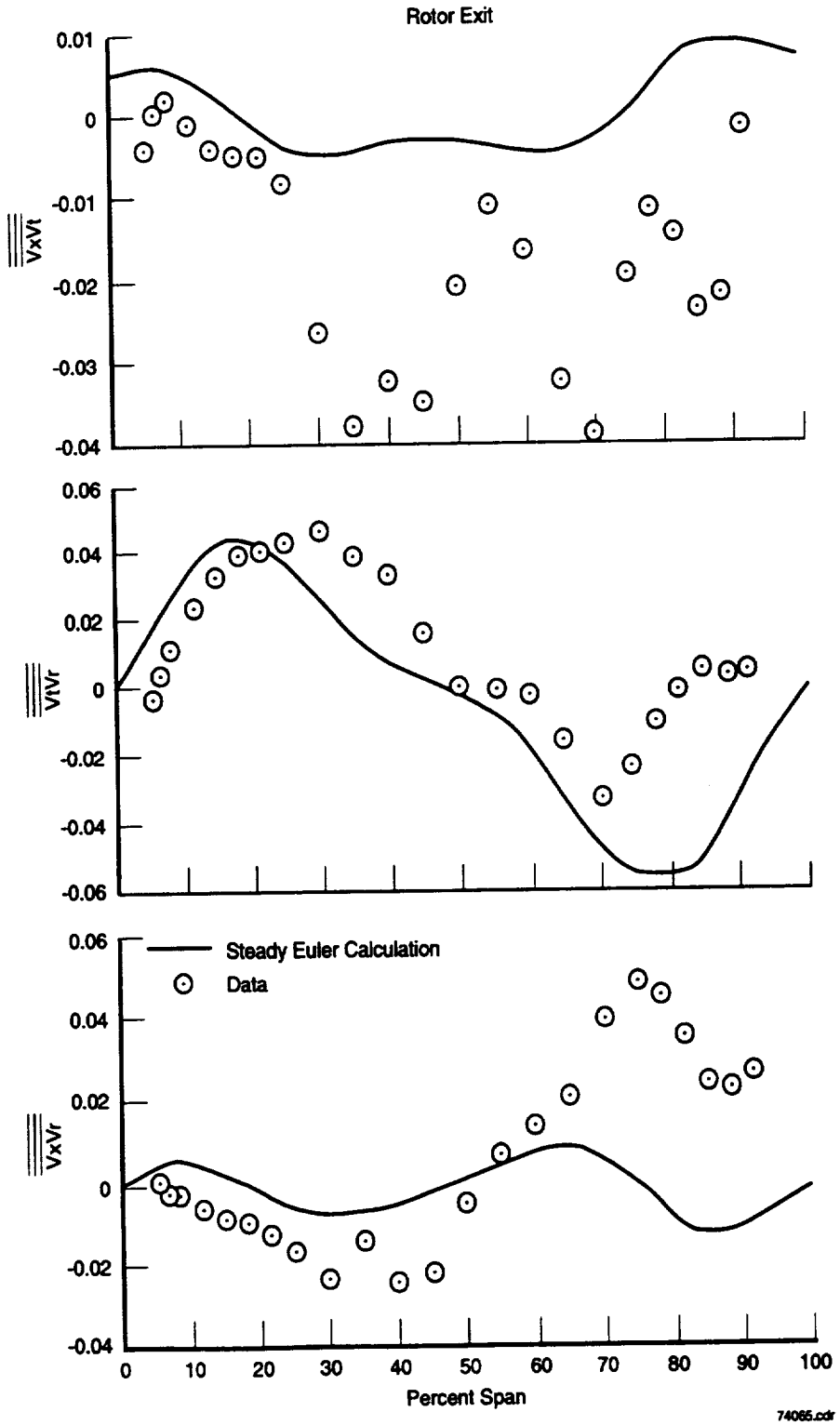

Figure 36. Spatial Stresses at Rotor Exit Again Show That Steady Euler (With Shear) Captures Vortex Structure (V_tV_r), Associated Blockage Is Not Well Captured (V_xV_t, V_xV_r)

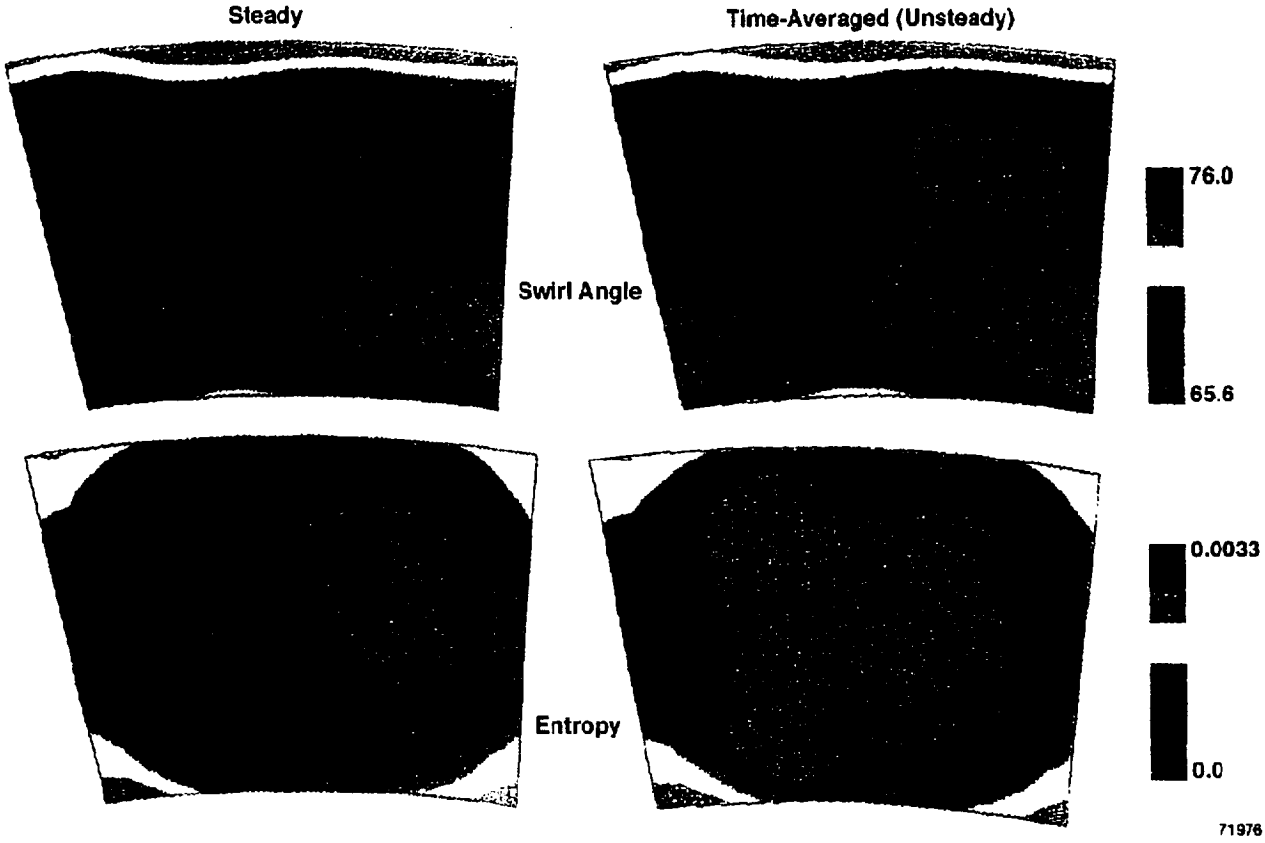

Figure 37. Large-Scale Rotating Rig First Stator Exit Flowfield Calculated To Be Almost Identical by Using Steady and Unsteady Multistage Euler Code; Some Effects in Gas Angle Can Be Observed

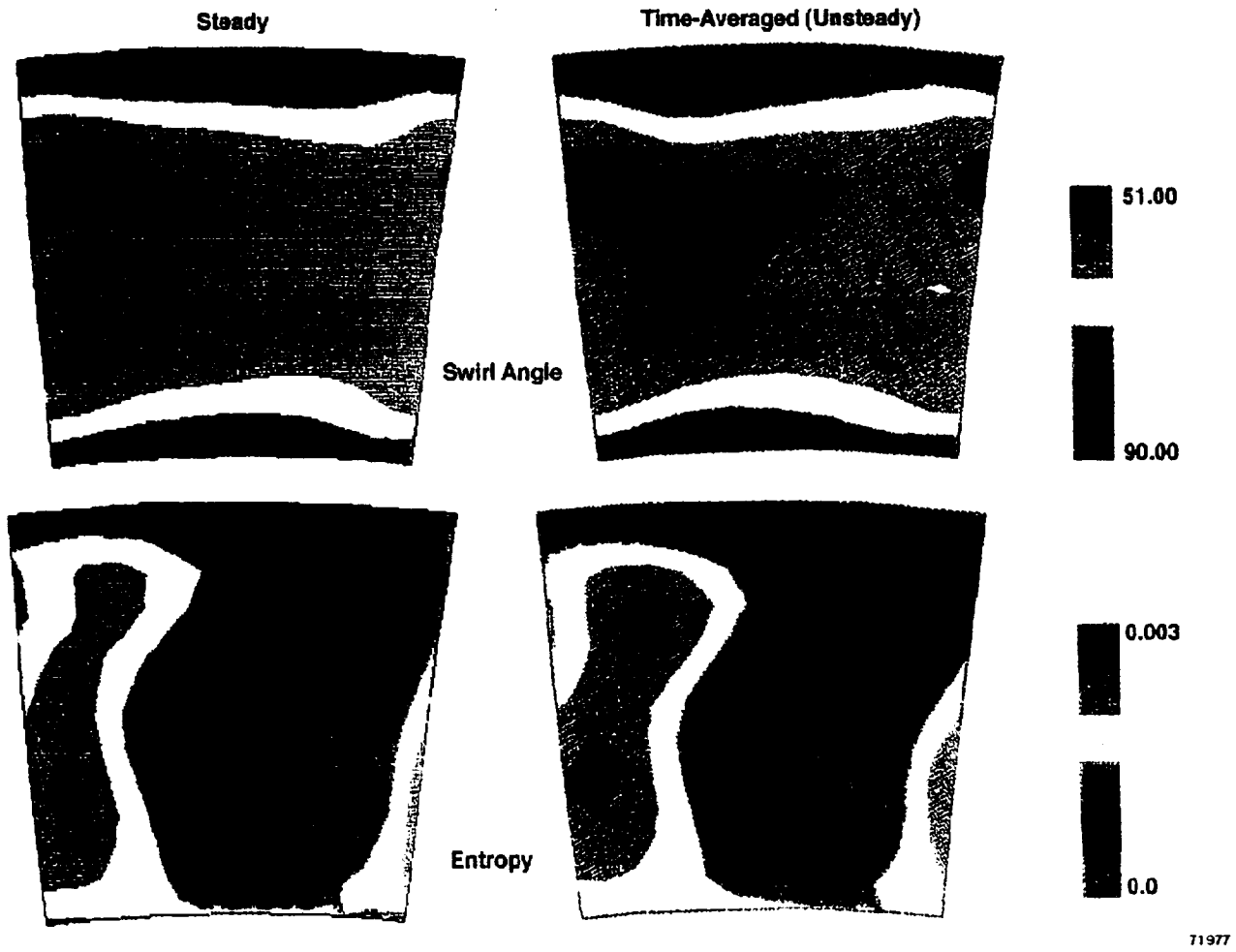

Figure 38. Large-Scale Rotating Rig Rotor Exit Flowfield Calculated To Be Fairly Similar by Steady and Unsteady Multistage Euler Code; Some Effects of Unsteadiness Evident in Entropy and Angle Contours

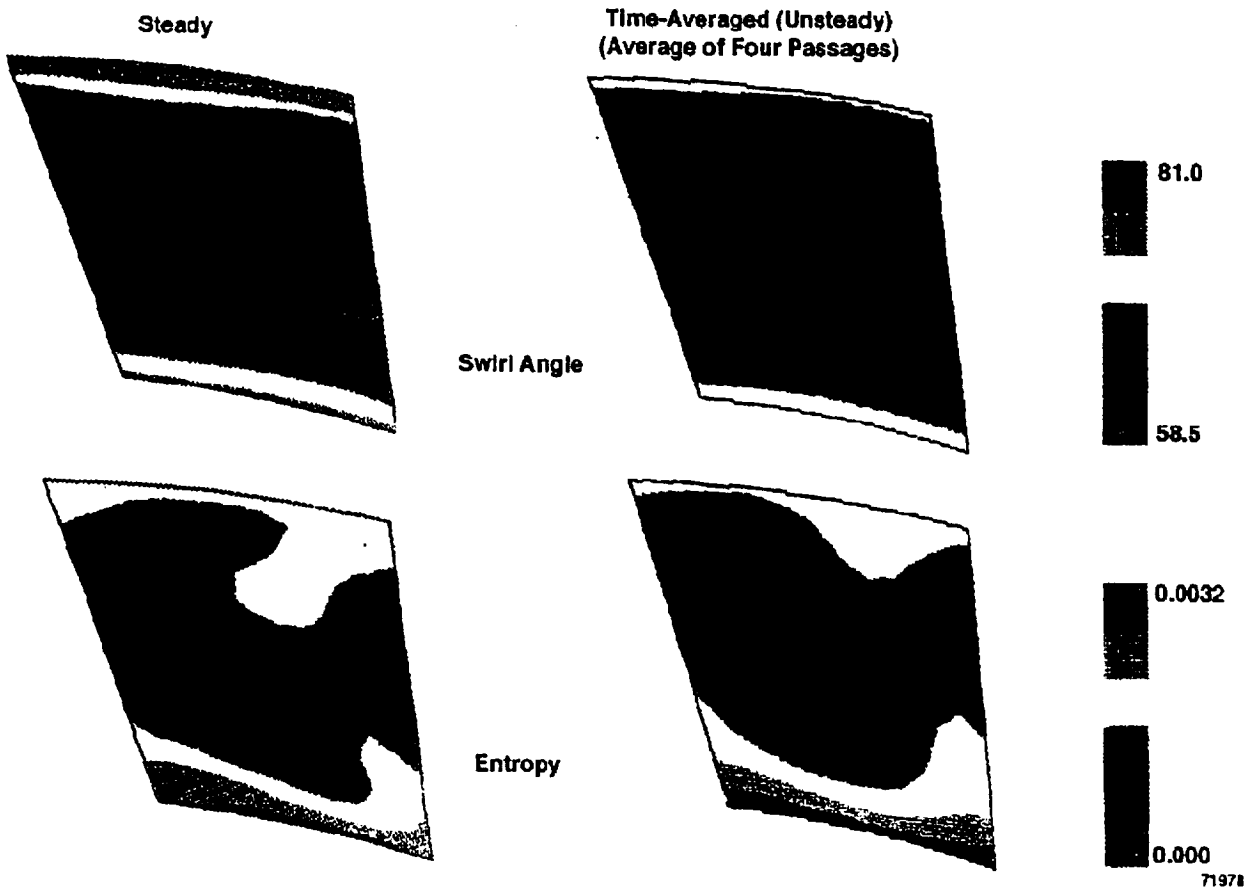

Figure 39. Large-Scale Rotating Rig Second Stator Exit Flowfield Calculated To Be Fairly Different by Steady and Unsteady Multistage Euler Codes

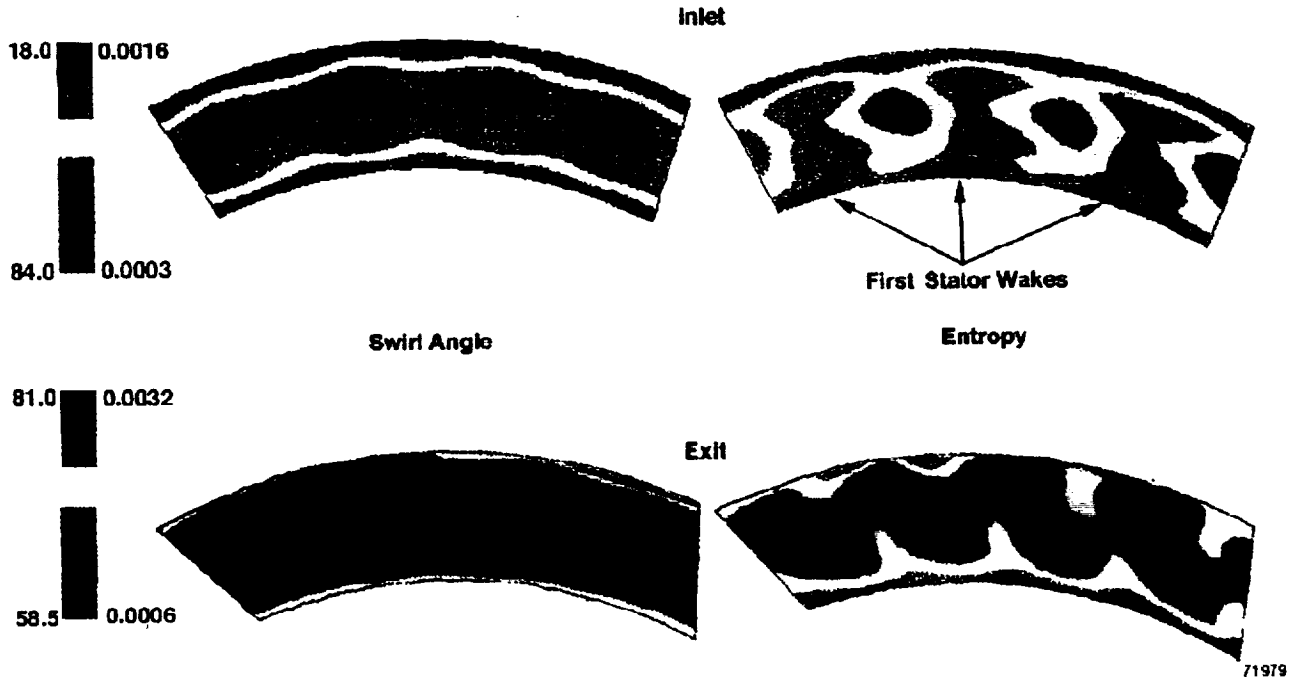

Figure 40. Unsteady Multistage Euler Shows Simulation for UTRC LSRR; First Stator Signature Can Be Identified Through Entropy Contours at Stator Inlet

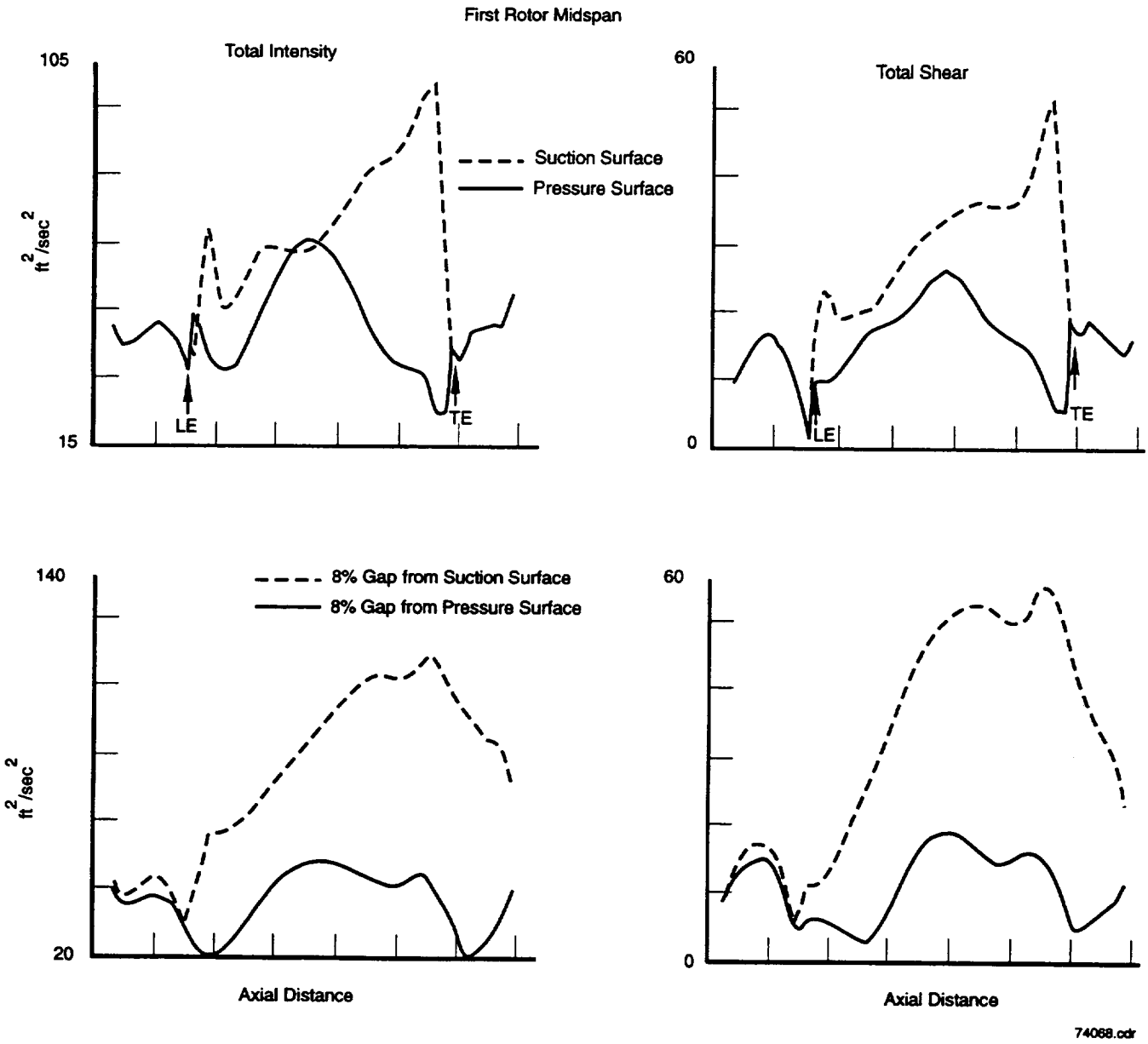

Figure 41. 3-D Unsteady Euler Simulations Show That Level of Stress Through Rotor Blade Intensifies and Then Decays at Exit of Passage; This Result Shows Same Trend as Data, Where Measured Inlet and Exit Stress and Intensity Are Approximately Same at Rotor Inlet as at Rotor Exit

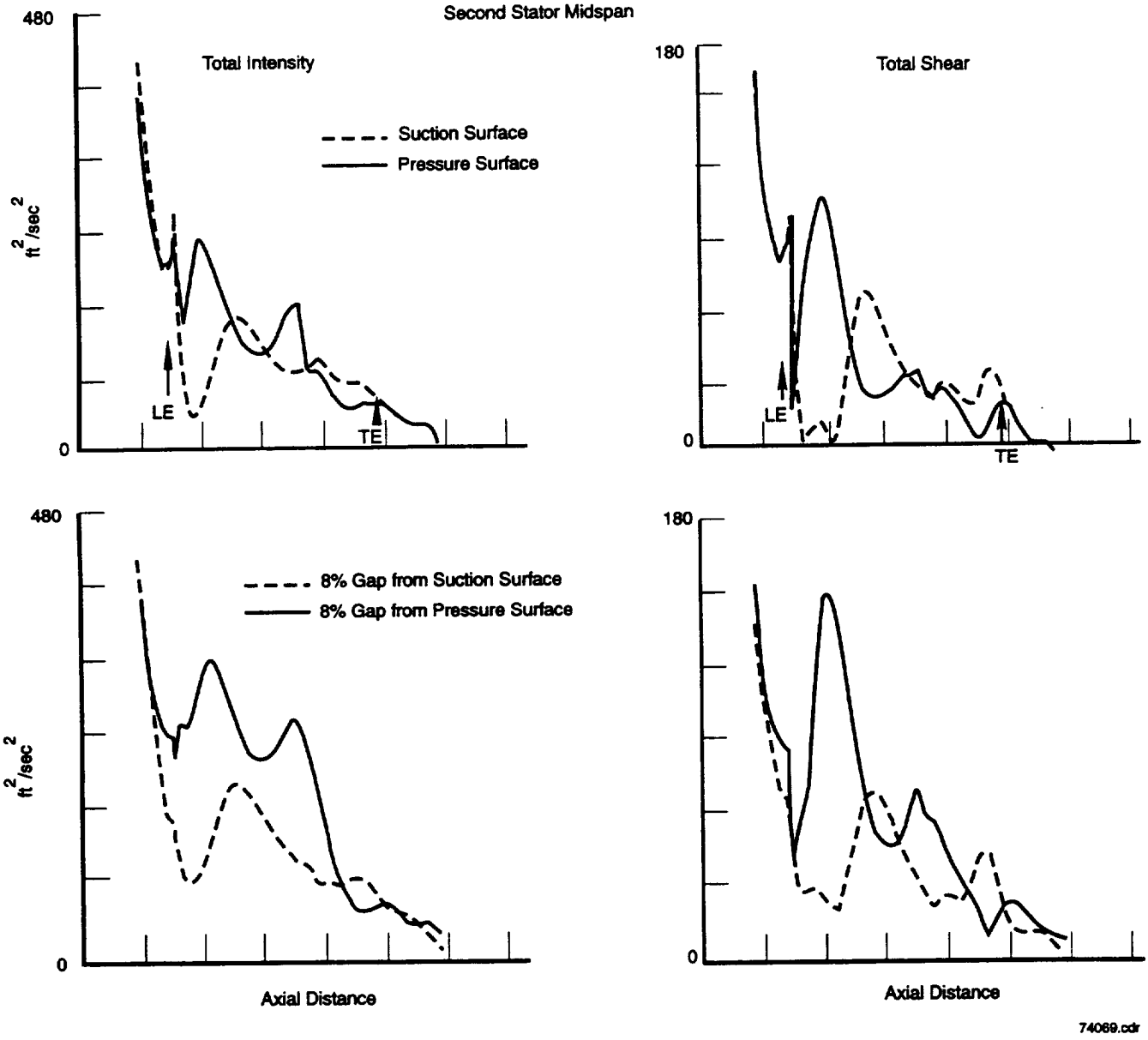

Figure 42. 3-D Unsteady Euler Simulations Show That Flow Enters Second Stator With High Stress and Decays Quickly Through Passage; As Shown Previously, Data Show Similar Trend Where Measured Inlet and Exit Stress and Intensity Show Large Change from Inlet of Second Stator Compared to Exit

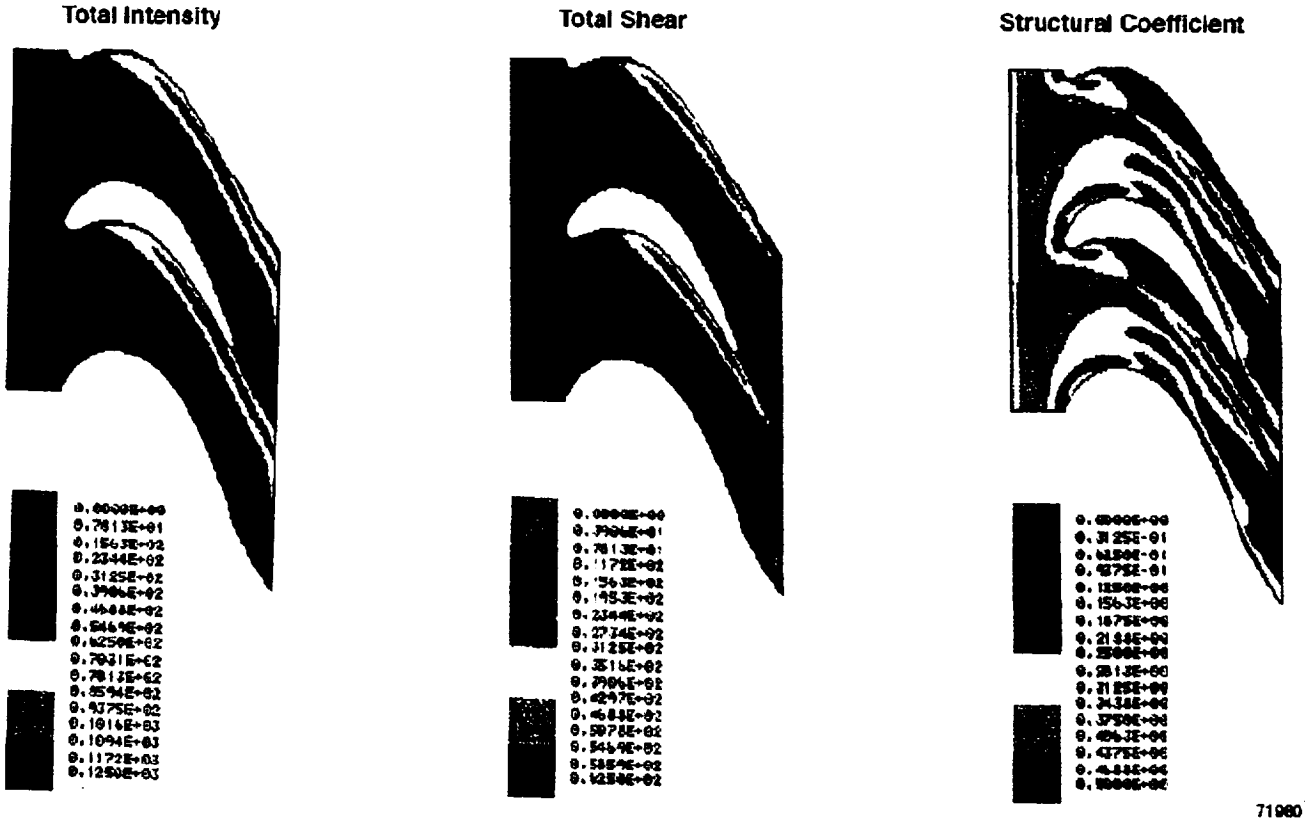

Figure 43. 3-D Unsteady Euler Simulation of LSRR Rotor Shows that Total Intensity and Total Shear Reasonably Correlate as Shown by Structural Coefficient

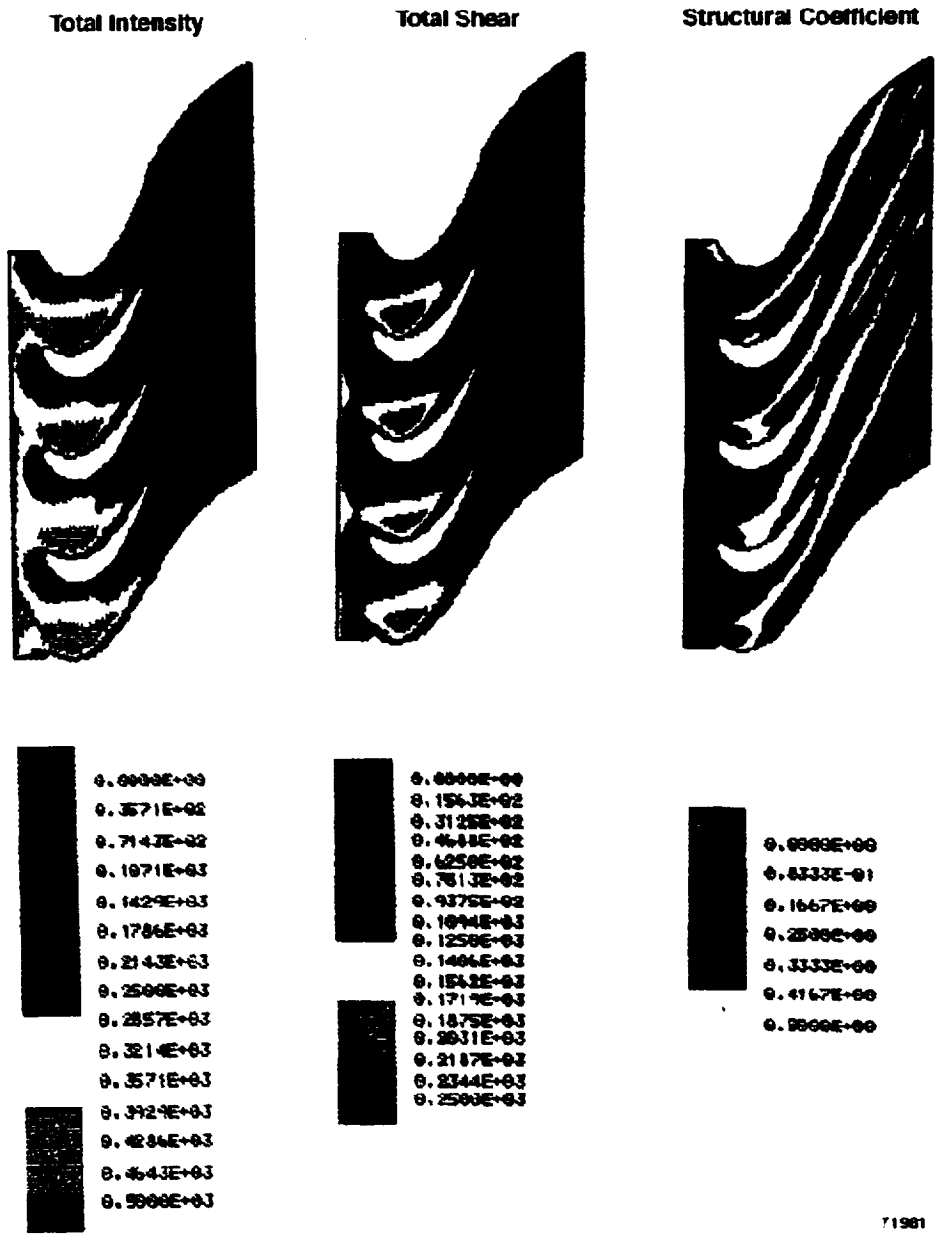

Figure 44. 3-D Unsteady Analysis of LSRR Stator Shows That Intensity and Shear Reasonably Correlate as Shown by Structural Coefficient

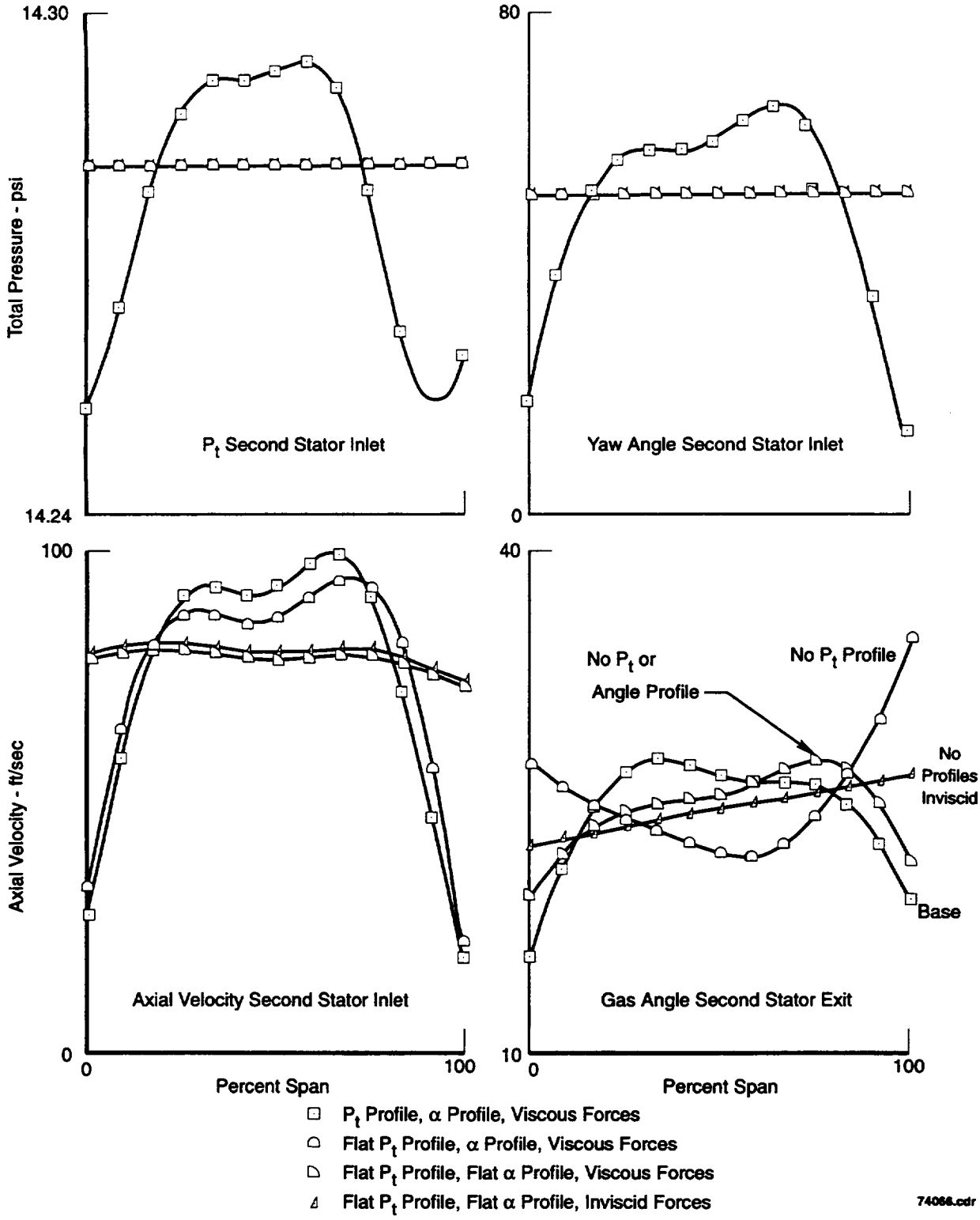

Figure 45. Second Stator Boundary Condition Studies Using Euler Code With Shear Indicates That Inlet Total Pressure Significantly Impacts Exit Angle Profile; Yaw Angle and Wall Shear Also Influence Profile to Lesser Extent

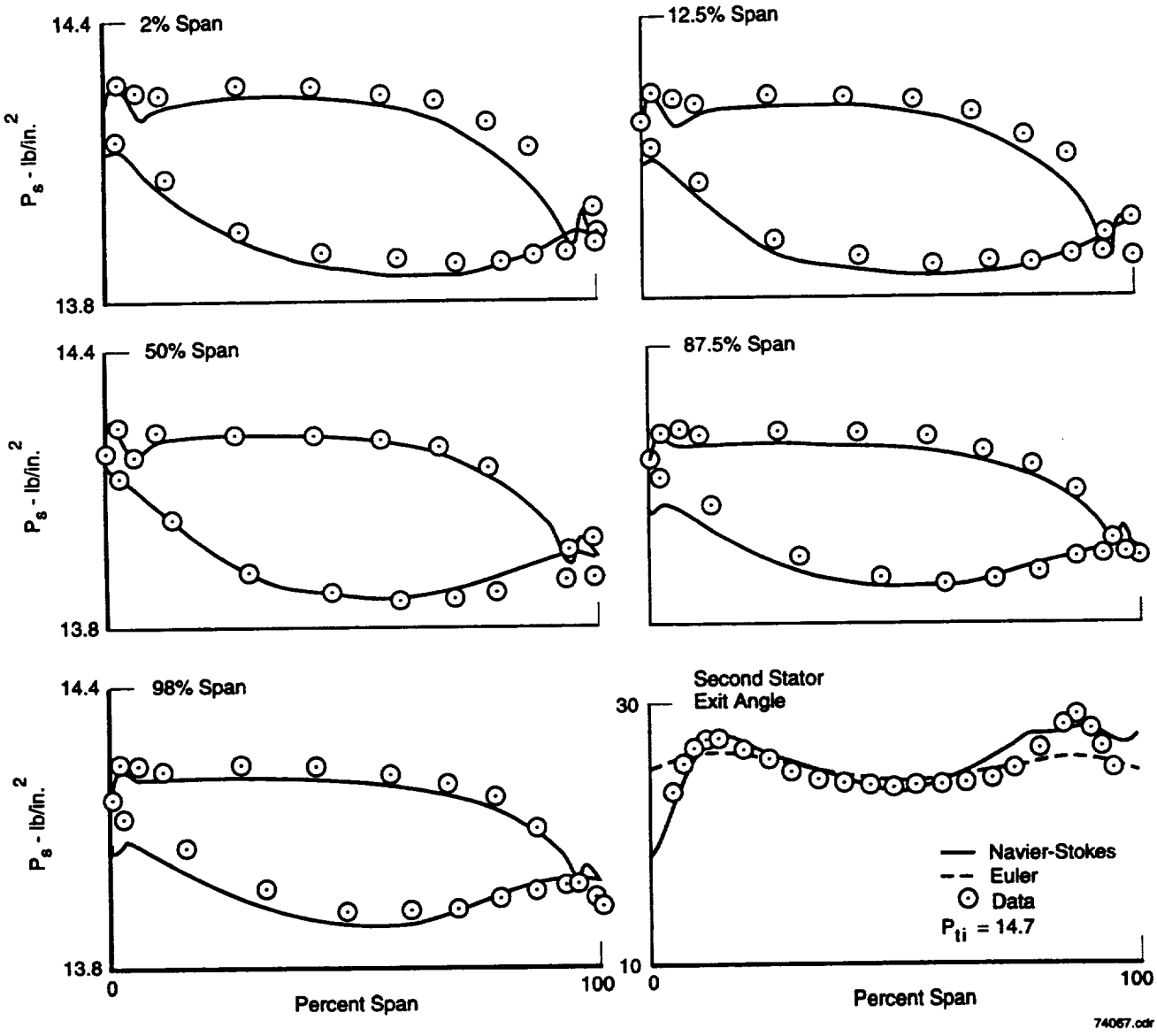

Figure 46. Rhie's RANS Code Provides Good Estimate of Second Stator Airfoil Surface Static Pressure and Angle (Simulation Conducted With Measured Boundary Conditions)

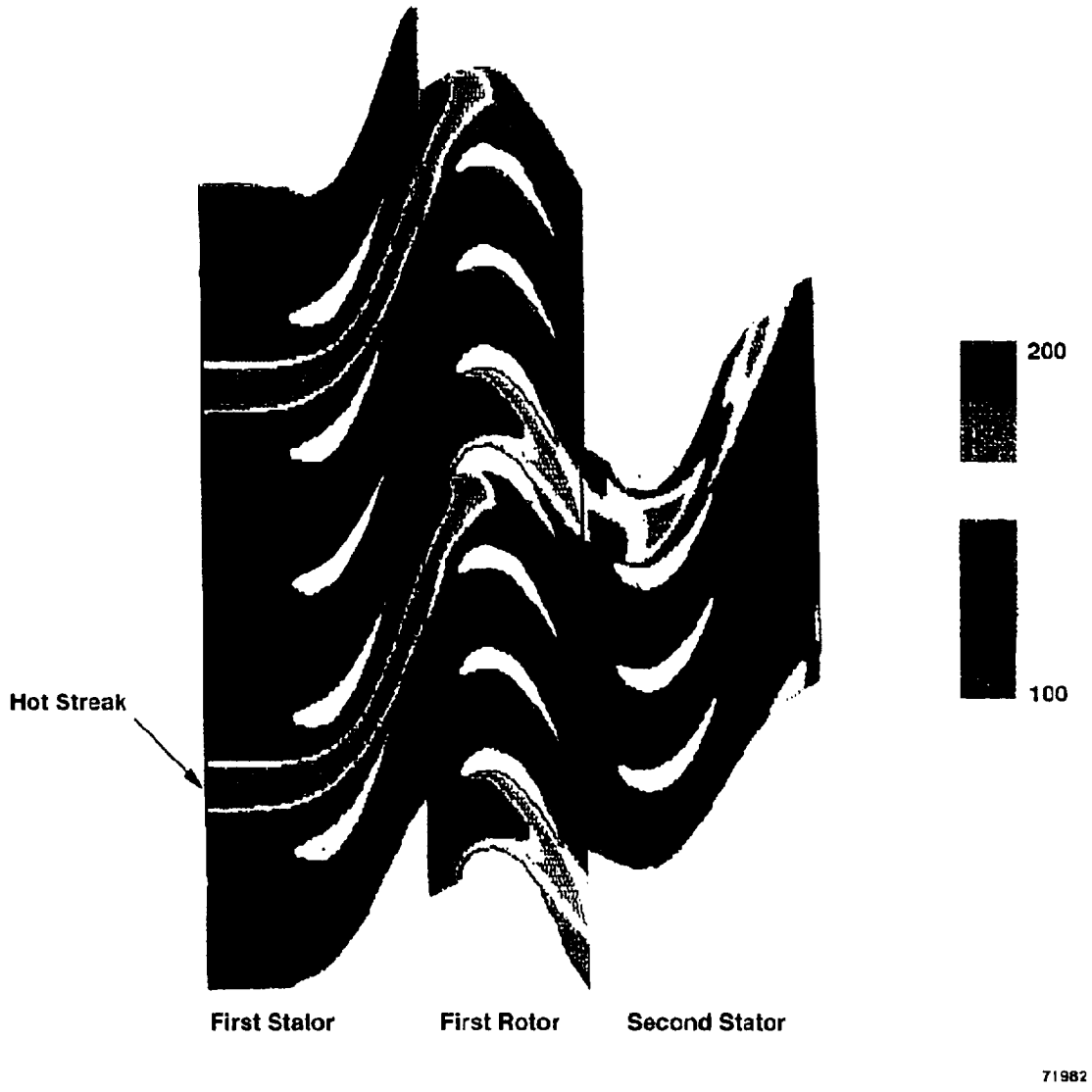

Figure 47. 2-D Instantaneous Flow of Hot Streak Simulated by P&W Unsteady Euler Code Identifies Regions of Temperature Disturbances; Understanding of This Simulation Will Assist in Average-Passage Model Development

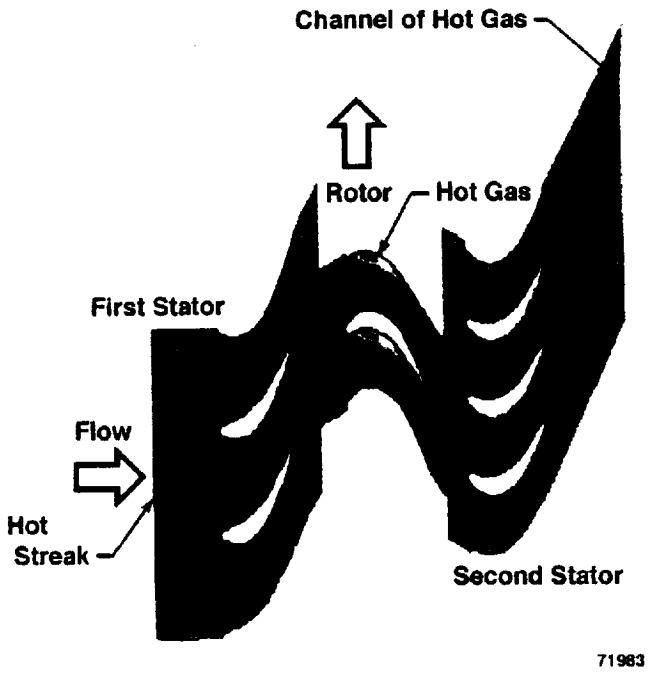

Figure 48. Time-Averaged Temperature Calculated by Using Ni's Unsteady Euler Code Shows High Levels of Temperatures on Rotor Pressure Side and High Temperature in One of Four Second Stator Passages

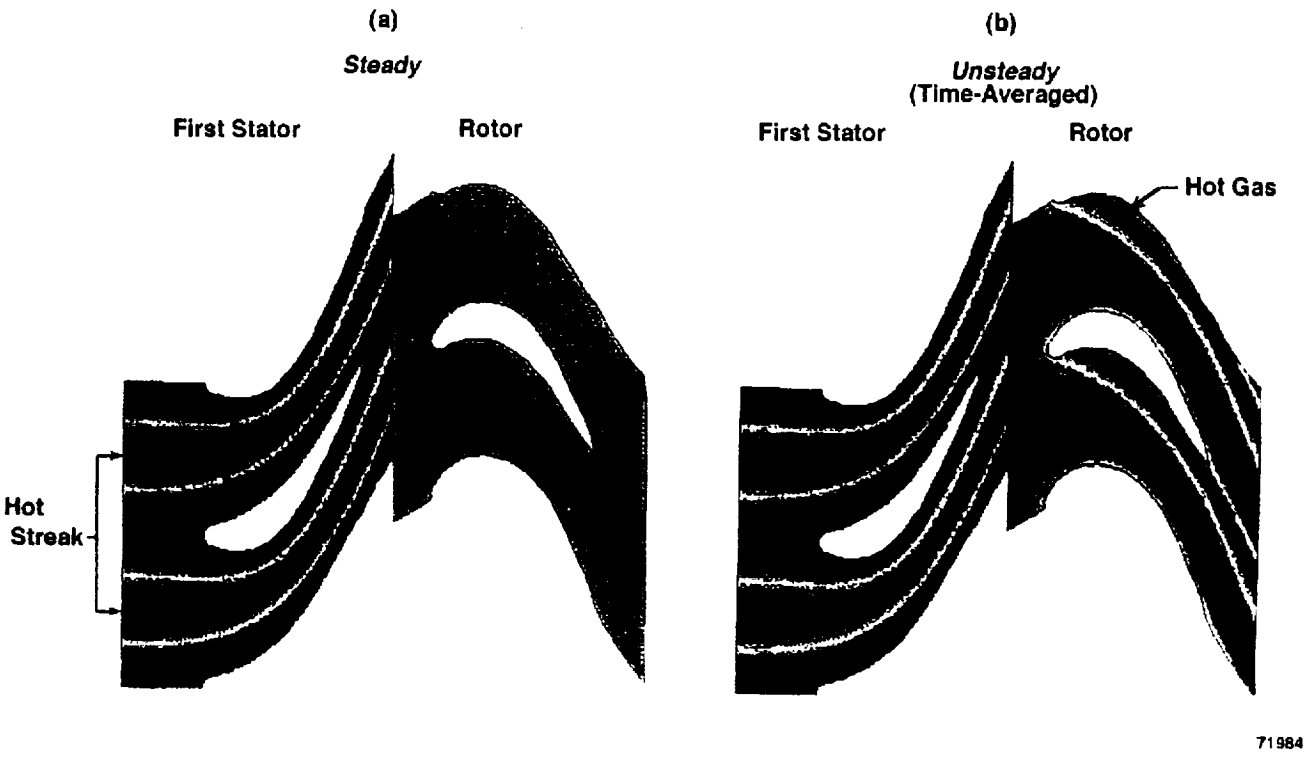

Figure 49. Numerical Simulation for Mean Section of UTRC LSRR Turbine Stage With Incoming Hot Streak by Using Steady and Unsteady Versions of Ni's Euler Codes. Time-Averaged Results from Unsteady Simulation Show High Temperatures on Rotor Airfoil Pressure Side, Which Is in Agreement With Experimental Data. Steady Flow Simulation Shows Constant Temperature in Rotor Passage, Indicating Need To Account for Effects of Periodic Unsteadiness

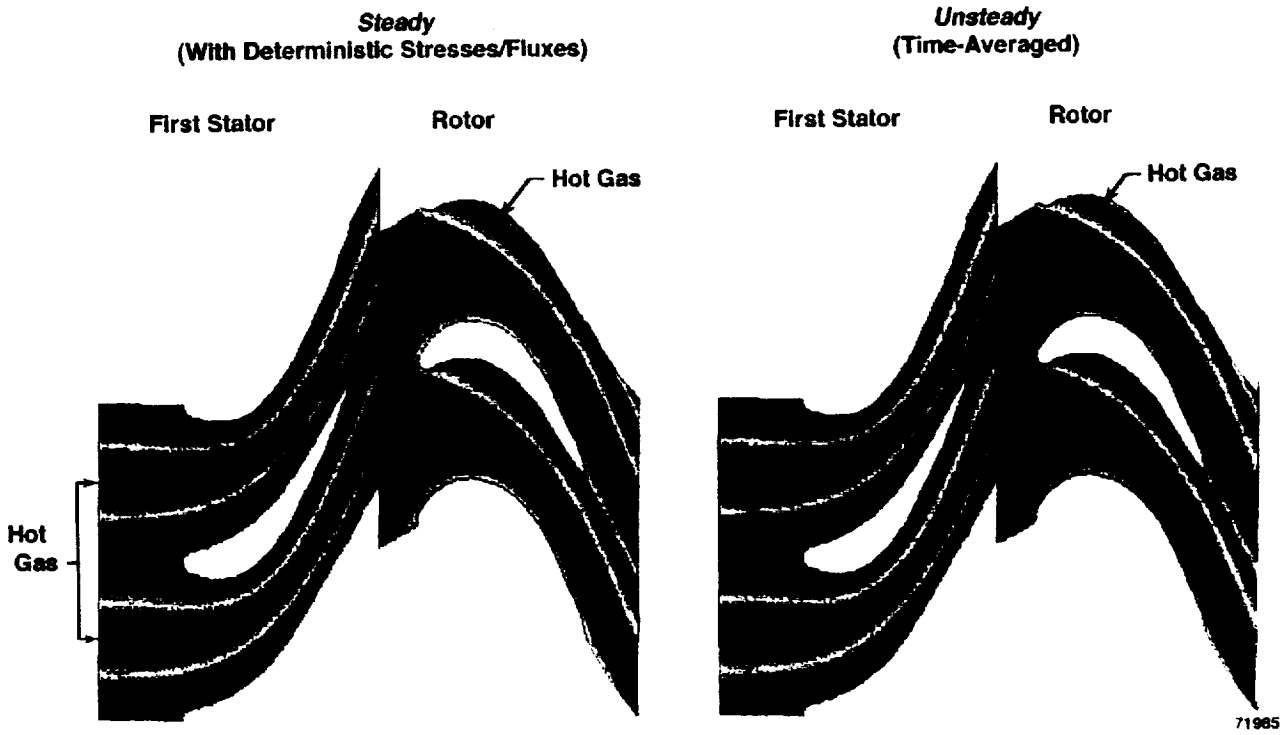

Figure 50. Numerical Simulation for Mean Section of UTRC LSRR by Using Unsteady and Steady Versions of Ni's Euler Codes. Steady Flow Simulations Conducted by Using Deterministic Stress Flux Terms Show Similar Patterns as Obtained from Time-Averaged Results from Unsteady Code

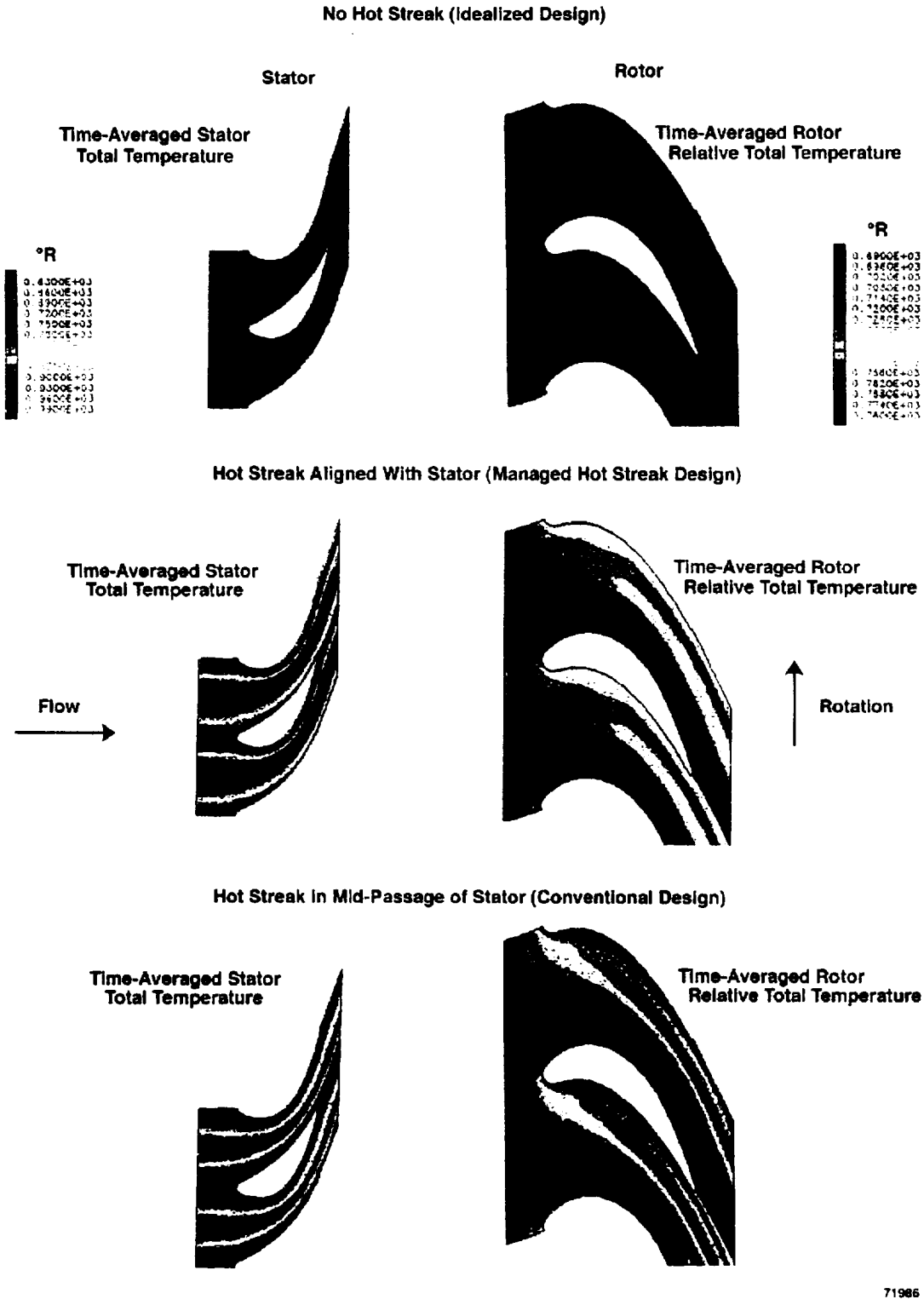

Figure 51. Time-Averaged Temperature Distribution for Model Turbine Stage by Using Ni's Unsteady RANS Code. Impact of Stator Inlet Hot Streak on Rotor Airfoil Pressure Side Can Be Minimized by Aligning Hot Streak to Turbine Stator

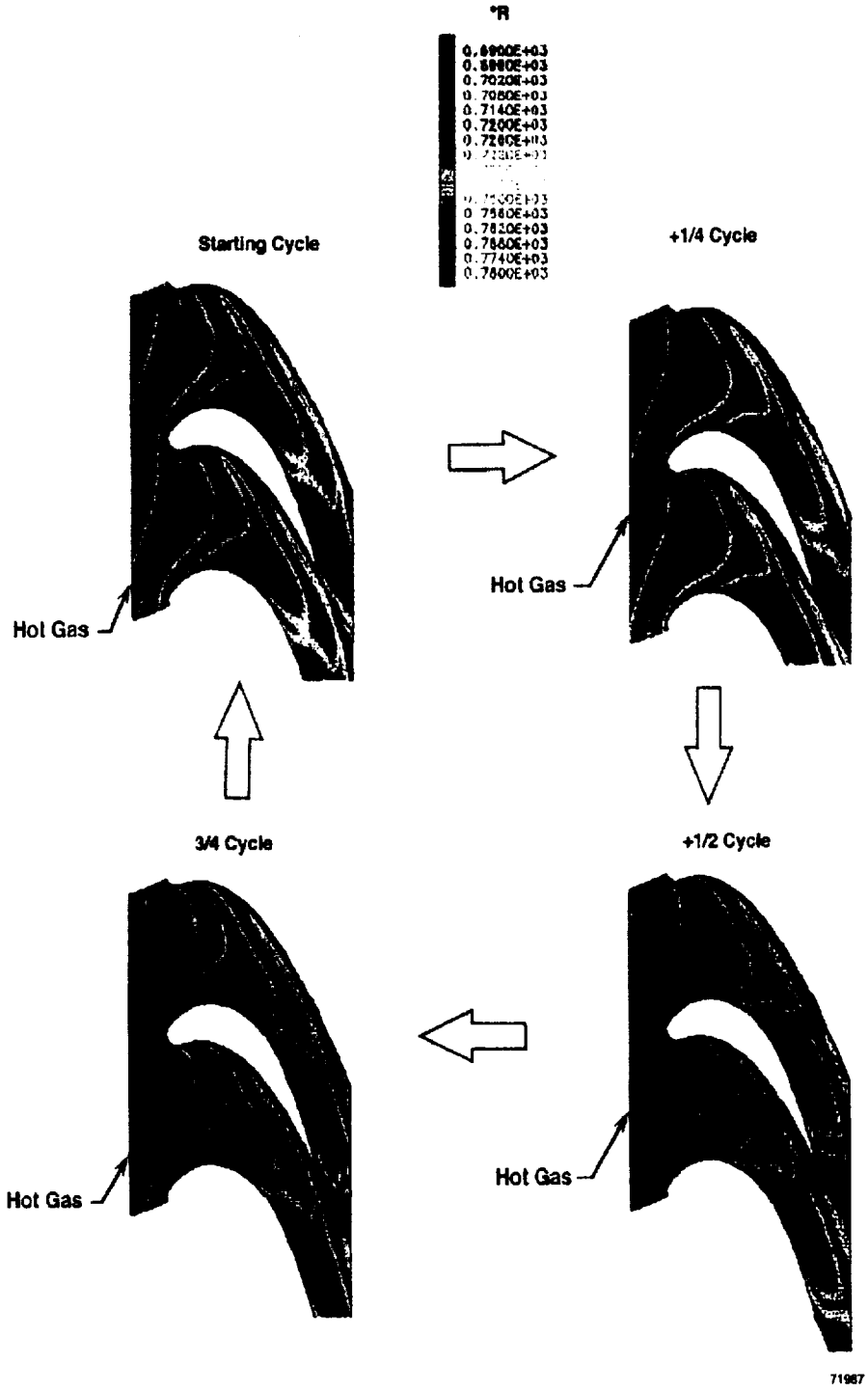

Figure 52. Four Instantaneous Results of Rotor, from 2-D Unsteady RANS Code, With Inlet Temperature Profile in Middle of Stator Representing Conventional Design

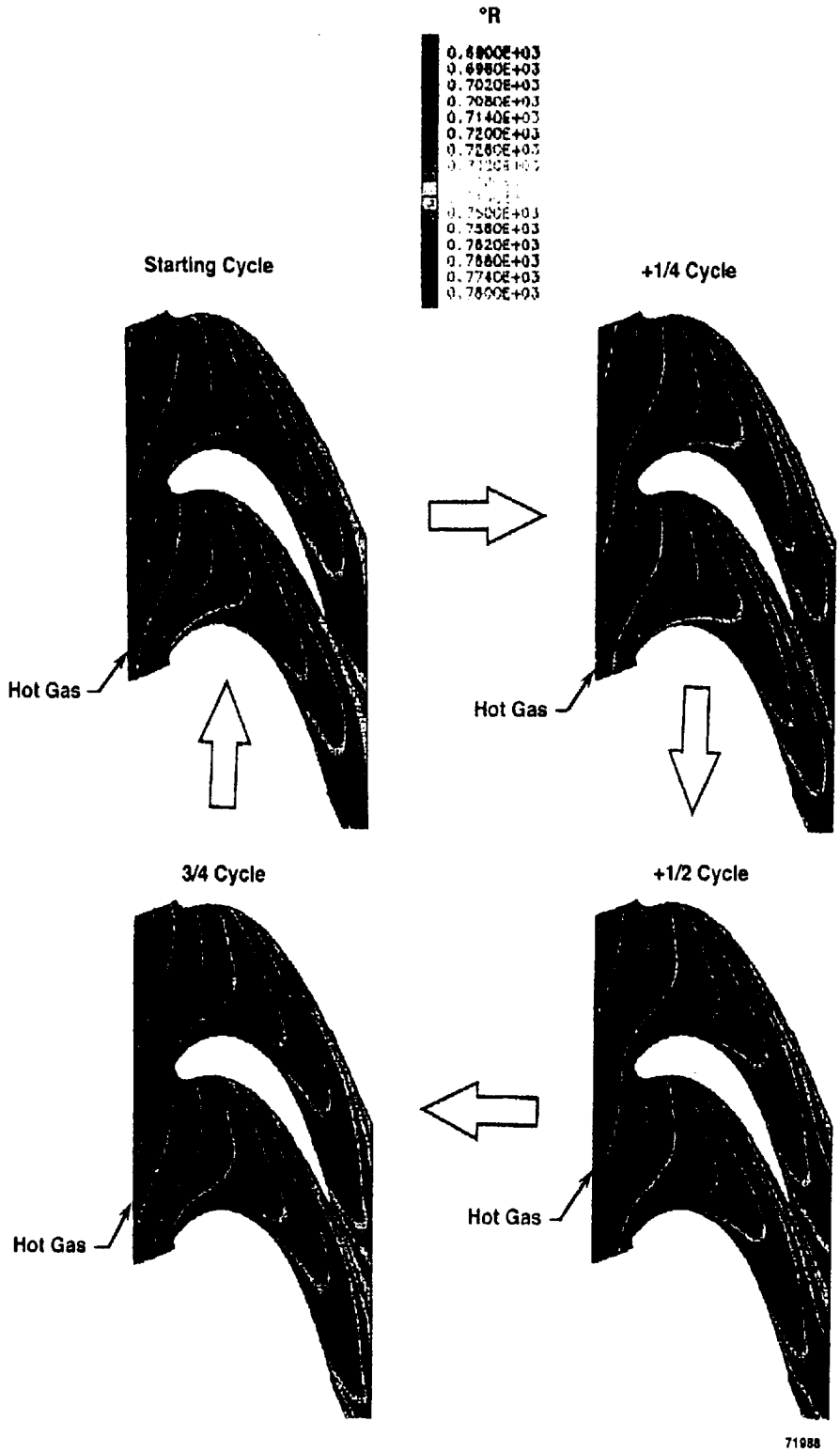

Figure 53. Four Instantaneous Results of Rotor, from 2-D Unsteady RANS Code, With Inlet Temperature Profile Aligned With Stator To Represent Managed Hot Streak Design

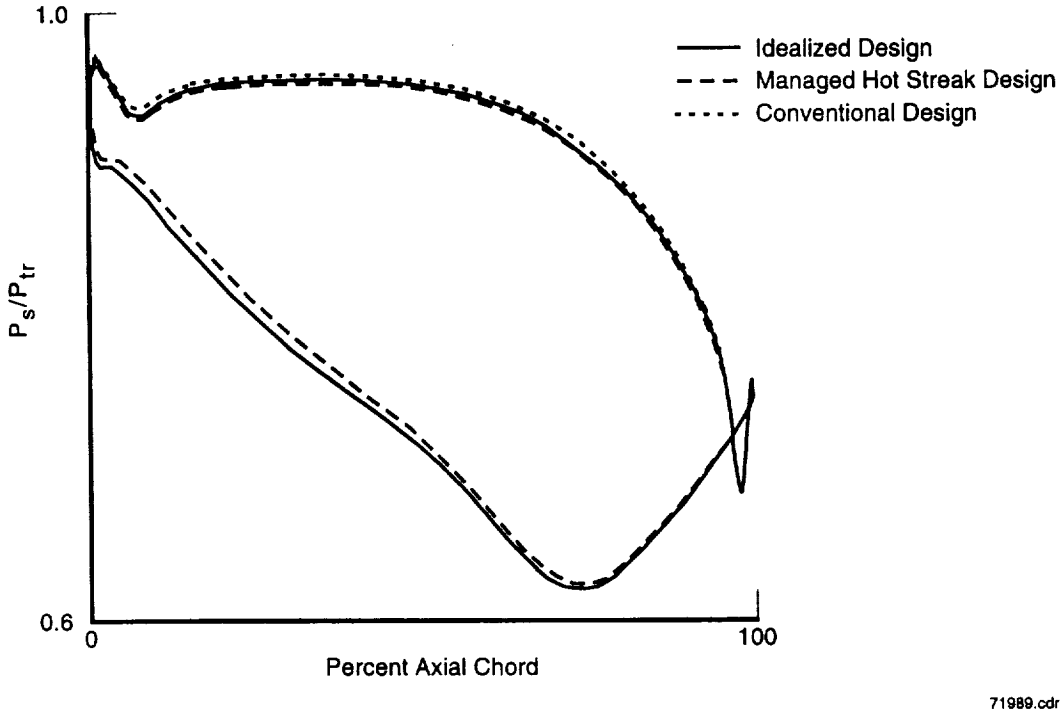

Figure 54. Unsteady RANS Code Predicts Same Time-Averaged Pressure Distribution on Rotor Surface for Turbine Configurations With Different Stator Inlet Temperature Alignment; This Indicates That Rotor Work Is Not Impacted by Hot Streak

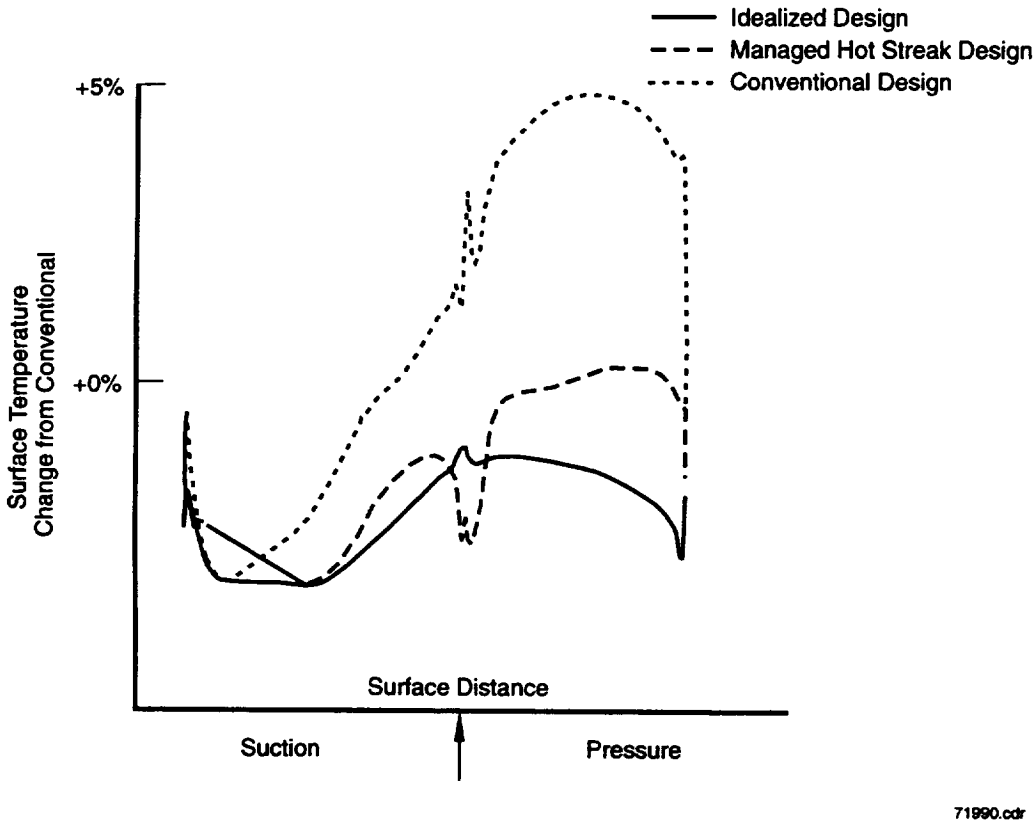

Figure 55. Unsteady RANS Code Predicts, on Average, 4 Percent Lower Adiabatic Wall Temperature on Rotor Pressure Side for Managed Hot Streak Configuration Relative to Conventional

This Page Is Intentionally Left Blank

6. BACKGROUND OF EXPERIMENTAL PROGRAM SELECTION

The objective of the experimental program was to determine the effect of deterministic stresses on aerodynamic performance and heat load. Since the largest deterministic stresses measured were at the rotor exit, the experimental program focused on the interaction of the rotor and second stator. This section describes the design of the experimental program, the newly acquired benchmark data, data analysis, and the selection of the experimental program.

6.1 BASIC RIG CONFIGURATION

The original large-scale rotating rig (LSRR) configuration contained airfoil counts and a data acquisition process that was not periodic for the second stator aerodynamic information (22 first stator, 28 rotor, and 28 second stator airfoils) data acquired over two first stator pitches. In a multistage turbomachine, periodicity occurs when the ideal flowfield repeats over a circumferential segment of the annulus. For the original LSRR configuration, this occurs in a 180-degree annular sector comprised of 11 first stator, 14 rotor, and 14 second stator airfoils. Because the available traverse capability only extended over two first stator pitches, modifications to the rig were necessary to ensure periodic data.

The following approaches were explored to achieve measurements over a periodic boundary:

- Modify the existing rig to enable traverse data acquisition over 180 degrees
- Circumferentially index the first stator, relative to the second stator, in increments that capture all airfoil-to-airfoil interactions, thus requiring no traverse system modifications
- Modify the first and/or second stator airfoil count to reduce the extent of the periodic segment from 180 degrees to a segment consistent with the existing traverse system.

After reviewing each of the three options, it was determined that changing the first stator count to 28 was most viable and cost effective. Changing the first stator count required no changes to the traverse system and/or data reduction software, and two periodic segments (i.e., two first/second stator pitches) can be traversed for averaging. Also, computational fluid dynamics (CFD) simulations become more efficient (requiring analysis of only one first stator, one rotor, and one second stator airfoil passage).

6.2 EXPERIMENTAL CONFIGURATIONS

The collaborative effort between the National Aeronautics and Space Administration-Lewis Research Center (NASA-LeRC), United Technologies Research Center (UTRC), Pratt & Whitney (P&W), and Massachusetts Institute of Technology (MIT) resulted in numerous discussions about the data, calculations, and various supporting experimental programs. Three potential experimental configurations were considered and investigated in detail, while the new baseline data (loadings, angles, pressures, and velocity) from the LSRR with the 28-28-28 airfoil count were being acquired. Since the expectation was that all data would repeat the original experiment (heat load, angles, etc.), hardware was to be designed and fabricated to be installed upon completion of the data acquisition.

From previous data and analysis (Sections 4 and 5), the *non-typical* heat transfer measured on the second stator (Dring et al., [10]) was hypothesized to be associated with the secondary flow from the rotor. Three experimental approaches, therefore, had been initially formulated on controlling the flow into and/or passing through the second stator. Each option was analyzed with the new airfoil count of 28-28-28. The first approach was to design a second stator to minimize the effect of the rotor secondary flow. The second approach was to redesign a rotor to change the vorticity and deterministic stress entering the second stator. The third approach was to let the flowfield mix and decay to reduce incoming stresses. A brief description of the methodologies is discussed below (more details are available in Appendix A).

6.2.1 Experimental Program Selection

Experimental Approach 1 — A second stator was designed to achieve a uniform spanwise exit angle distribution given the inlet vorticity from the rotor. This was achieved by an interactive design process, combining CFD with airfoil recontouring. The final design resulted in highly three-dimensional (3-D) stacking of the airfoil sections.

Experimental Approach 2 — The rotor was redesigned to produce uniform spanwise exit angle distribution to minimize the inlet spanwise vorticity to the second stator. Computational fluid dynamics tools were used to achieve this result by recontouring the airfoil surface and incorporating a 3-D stacking. This airfoil was fabricated, under UTRC funding, to ensure that the overall program schedule would be minimally affected. However, due to the concern that the gap-average vorticity changed, but the deterministic stress was estimated to remain approximately the same, it was decided that this option should be tested with a configuration that minimized the midspan deterministic stress. This was accomplished by designing *secondary flow fences* that contained the secondary flow vortices close to the endwall. A large-scale/low-speed wind tunnel with smoke visualization was used to ensure that the fence configuration achieved all the requirements. These fences were also fabricated, along with a new set of base rotor blades (under UTRC funding), to ensure the program schedule would be minimally affected.

Experimental Approach 3 — The third option was to allow the flow distortion to decay by introducing various axial spacings between the rotor and second stator. Although there was capability in the existing rig to accommodate this test, the spacing was fixed between the first and second stator, creating the spacing between the rotor and first stator to also vary. Therefore, the rig needed to be modified to maintain first stator to rotor axial gapping, while the second stator to rotor axial gap was varied. Computational fluid dynamics computations implied (discussed in Section 5), that as the axial spacing changed, the first stator wake would impinge differently on the second stator. The first stators, therefore, must be indexed circumferentially (*clocked*), relative to the second stators, to achieve a proper average result for axial spacing.

6.3 CONFIGURATION CHANGES

As previously mentioned, the first stator airfoil count was modified to give periodic boundary conditions by adding six first stators to the rig at equal circumferential spacing. The stagger angles were re-set to achieve the *original* velocity triangles. In addition to the airfoil count change, the second stator suction side heat transfer model was rebuilt due to visible deterioration of the original model.

6.4 RESULTS

6.4.1 Aerodynamic Data (New Baseline)

To verify that proper flow was achieved in the rig, airfoil surface static pressures, airfoil exit angles and pressures, and endwall static pressures were acquired. This section briefly discusses the data, as compared to previously acquired data, for the original configuration. A complete description of the remaining data is provided in Appendix C. Because the major changes in the rig were associated with the first stator, most of the discussion is focused on the first stator experimental results.

Figure 56 shows that the average total pressure versus span behind the first stator is in good agreement with data acquired for the original 22 first stator airfoil count, except in the tip region. After an investigation of the possible causes of differences at the tip, it was determined that the original data most likely had seal leaks while traversing the probe, creating non-representative flow in the tip region. As Figure 57 shows, the difference in loss appears across the complete circumference in the tip area. Leakage was determined to be the most likely cause, since the same characteristic was observed for the existing first stator (28 count), when the probe was intentionally not sealed in the traversing slot.

Within the accuracy of the five hole probe, the new stator airfoil count and stagger angle achieved the design flow angle intent, as shown in Figure 58. To confirm the gas angle measurement, the spanwise static pressures at

the exit to the first stator were reviewed. From analysis of the original configuration, simple radial equilibrium $\frac{1}{\rho}\frac{\partial P}{\partial R} = Ct^2/R$, the measured pressure gradient, and density ($\frac{1}{\rho}\partial P/\partial R$) were found to be within 2 percent of being equivalent to Ct^2/R. By using simple radial equilibrium, the calculated axial velocity, and the spanwise static pressures (shown in Figure 59), the average exit gas angle was determined to be within 0.3 degrees of the original design, and the angle measurements were confirmed to be valid and consistent with the original design.

The first stator surface static pressures are shown in Figure 60. The pressure distributions reflect the unloading as a result of the increased airfoil count. These surface static pressures were integrated as a function of axial chord to obtain the tangential loading. As shown in Figure 61, the measured loading is approximately at the level anticipated for the airfoil count change from 22 to 28 (lift per airfoil expected to reduce by 1.0-22/28 ≅ 21.5 percent). Overall, the aerodynamic data obtained for the first stator show that the design intent flowfield was obtained.

The rotor exit aerodynamics were measured in the same manner as the stators, except the probe rotated with the rotor rpm. The data measured at the rotor exit plane (Figures 62 and 63) show that the relative flow angle, total pressure, and rotary pressure have the same spanwise distribution. The rotor spatial stresses (Figure 64) also show spanwise distribution similar to previous data, indicating the same flowfield aft of the rotor with 28 first vanes, compared to 22 first vanes, was achieved. Finally, the spanwise rotor loadings showed good agreement with previously acquired data within 2 percent repeatability of pressure, as demonstrated by the 50 percent span surface static pressure distribution in Figure 65. Overall, the measured rotor results with 28 first stators demonstrate that the rotor flowfield has been reasonably repeated relative to previously acquired data.

The second stator flowfield is difficult to compare to previously acquired data because of the non-periodic flow conditions in the original rig. However, the data show that exit gas angle (Figure 66) displays the same spanwise characteristics originally observed. The typical ±1.5 degree repeatability is not accomplished in this case and is believed to be associated with non-periodically averaged data previously acquired. The second stator indicates unloading relative to the original configuration, as shown by the midspan surface static pressures in Figure 67, but is not believed to significantly alter the measured heat transfer trends. Overall, the results from the baseline aerodynamic testing indicate that the changes to the rig were not expected to alter the heat transfer data trends previously observed.

6.4.2 Second Stator Heat Transfer Data

From the aerodynamic data acquired in the rig, it was expected that the heat transfer data on the second stator suction side, at midspan, would display the same characteristics as previously observed. However, as shown in Figure 68, lower heat transfer was measured in the aft portion of the suction side. These data suggest that the difference may be attributed to a transition phenomena. To investigate what may have caused the transition change (i.e., incidence, first stator/second stator interaction, airfoil smoothness, and turbulence), various conditions were examined (Table 2) to evaluate the influence of various operating conditions.

This matrix of diagnostic testing was assembled to operate the rig at many conditions to acquire the sensitivity of the heat load for these conditions. This ensures the ability to capture any sudden *unexpected* changes in the heat load. The Cx/U impacts the incidence, and axial spacing addresses airfoil interaction; clocking addresses first to second stator influences. Trip wires were used to promote premature boundary layer transition, and first stator airfoil count change was used to reproduce the original configuration. As shown in Figure 69, Cx/U and/or clocking variation did not achieve the level of suction side heat transfer level or the slope in the aft-portion of the airfoil. Figures 70 and 71 also show that axial spacing and incorporating trip wires on the airfoil, at 3.5 inches from the leading edge, did not repeat the heat load.

Because of concern over the possibility of some phenomena associated with the airfoil count, the original configuration was reassembled and retested, as shown in Figure 72. The *original configuration* heat transfer data did not repeat. Extensive diagnostics were thus performed on the existing model. These diagnostics confirmed the validity of the existing heat transfer, concluding that the model used for the previous testing was not representative.

6.5 ANALYSIS OF EXPERIMENTAL RESULTS

6.5.1 Multistage Analysis of Aerodynamics

As reviewed in Section 5, the second stator *steady* inlet boundary conditions dominated the second stator exit gas angle distribution. Multistage steady RANS and Euler codes (with a mixing plane between blade rows, across which mass and momentum are conserved) were used to analyze the new rig configuration to re-examine the predictability of the CFD analysis. At the first stator exit, the measured spanwise yaw angle static pressure coefficient and total pressure coefficient were compared with the RANS and Euler (with shear) results in Figure 73. Near the inner diameter, the RANS results show angles that peak around 10 percent span, which is more in agreement with the data than the Euler, which peaks around 25 percent. From midspan to 100 percent span, neither code displays the increase in angle at 70 percent span. The spanwise static pressure coefficient distribution shows that the data fall between the simulations, and both codes agree to the same extent. The spanwise distribution of measured total pressure coefficient is shown to have a low value at 5 percent span, increase up to 13 percent span, and falls to a flat region at 25 percent span. The simulations show that the Euler does not capture this feature, whereas the Navier-Stokes simulation reproduces the trend. Both codes show a flat profile, through the midspan region, with the Euler level in better alignment with the data relative to the RANS code. This level difference is most likely associated with the fully turbulent boundary layer assumed in the Navier-Stokes, and a shear force factor representative of transitional flow in the Euler. In the region near the shroud, the Navier-Stokes reproduces the spanwise data trend better than the Euler.

A similar trend, as shown for the first stator, was observed at the rotor exit (Figure 74). The RANS shows trends that are in better agreement with the data, as compared to the Euler. The measured angles show an increase near the endwall regions, which is partially captured with the RANS code. The Euler results indicate a decrease in angle. The spanwise static pressure coefficient is calculated to have approximately the same trend, for both CFD calculations, as the data, except near the inner portion of the flowpath, which neither code captures. The absolute level from these results shows that the RANS code is slightly closer to the data relative to the Euler results. The calculated blade loss profile shows that the Navier-Stokes result agrees better with the measured spanwise distribution from 4 to 80 percent span, as compared to the Euler. In the tip region neither code agrees with the data, and is likely associated with the lack of a tip clearance in the simulation.

The results from the multistage steady simulation of the second stator are shown in Figure 75. This figure shows exit yaw angle and loss versus span. Since the downstream static pressure profile is a specified boundary condition for the simulation, it is not shown. The yaw angle trend versus span shows that the Navier-Stokes captures the second stator measured profile much better than the multistage Euler. The loss profile shows that between 20 and 50 percent span, both calculations have approximately the same level and trend, and they are similar to the data. Between 50 and 90 percent span, the level and trends of the Navier-Stokes capture the measured loss better than the Euler. From 90 to 95 percent span, the data show a loss rate increase consistent with the RANS, while the Euler loss remains relatively flat. In the inner portion of the flowfield, the Euler solution is more in agreement with the data relative to the Navier-Stokes.

Overall, using a steady analysis with a mixing plane, shows that the steady RANS typically captures flow features (static pressure, angle, and loss) better than the steady *viscous* Euler. The exit flow angle distribution from the second stator was shown to be highly dependent on the inlet boundary conditions, as shown in Section 5. The ability of the RANS code to capture the second stator exit angle trend suggests that in a low-speed, multistage turbine, viscous modeling dominates the flow angles.

6.5.2 Heat Transfer Analysis of Second Stator

The computed loadings on the second stator were used with a STAN-5 boundary layer calculation to obtain the two-dimensional (2-D) heat transfer distributions for the airfoil at 50 percent span. As shown compared to the data in Figure 76, the measured heat transfer levels and trends are captured using STAN-5. This implies that the large secondary flow and associated large deterministic temporal stress entering the second stator do not significantly

influence the heat load. The aerodynamic and heat transfer analysis shows that the data are reasonably simulated without accounting for deterministic stresses.

6.6 EXPERIMENTAL PROGRAM SELECTION

The original experimental approach assumed that the unexplained second stator heat load and exit gas angle distribution, previously measured, were due to the deterministic stresses induced by the rotor secondary flow. These experimental and numerical investigations, conducted as part of this program, showed that the second stator exit angle profile was strongly influenced by the steady inlet boundary conditions. Additionally, the unexplained heat load distribution previously obtained was due to erroneous experimental measurements. At this point, the only experimental indication that stresses may influence the performance is the change of heat load (with axial spacing) observed during diagnostic testing.

Experimental data acquired as part of this program, and part of another program, showed that the second stator deterministic stress would change by approximately 50 percent by varying the axial gap between the rotor and second stator by ≈ 55 percent (from x_2/B_x [~ 0.36 to 0.81]). By evaluating the second stator performance at various axial spacings, the effect of the deterministic stress could be reviewed. Therefore, Experimental Approach 3 (Section 6.2.2) was chosen to evaluate the impact of deterministic stress on second stator performance.

Table 2. New Baseline Second Stator Heat Transfer Data Acquisition Matrix

First Stator Count	*Cx/U*	*Axial Gap* x_2/B_x	*Indexing Position*	*Trip Wire*
28	0.76	0.75	1,2,3,4,5	None
28	0.78	0.75	1,2,3,4,5	None
28	0.96	0.75	1,2,3,4,5	None
28	1.15	0.75	1	None
28	0.78, 0.96, 1.1	0.53	1	None
28	0.78, 1.1	0.53	1	0.010 in. height at 3.5 in.
28	0.78, 1.1	0.53	1	0.018 in. height at 3.5 in.
22	0.68, 0.78, 0.96	0.53	1	0.018 in. height at 3.5 in.
22	0.78	0.53	1,2,3,4,5	None

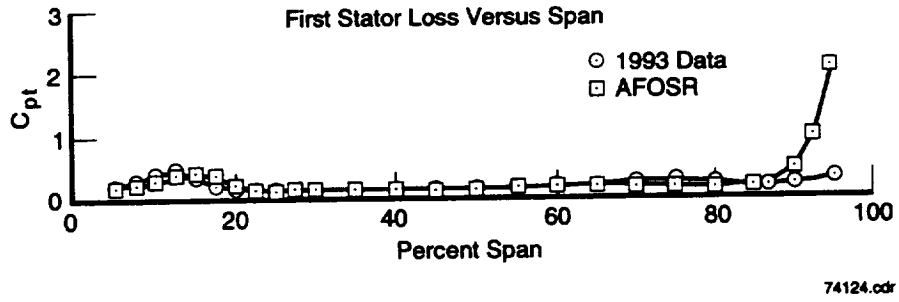

Figure 56. First Stator Measured Loss Versus Span Shows Higher Loss in Tip Region With 22 Compared to 28 Stators

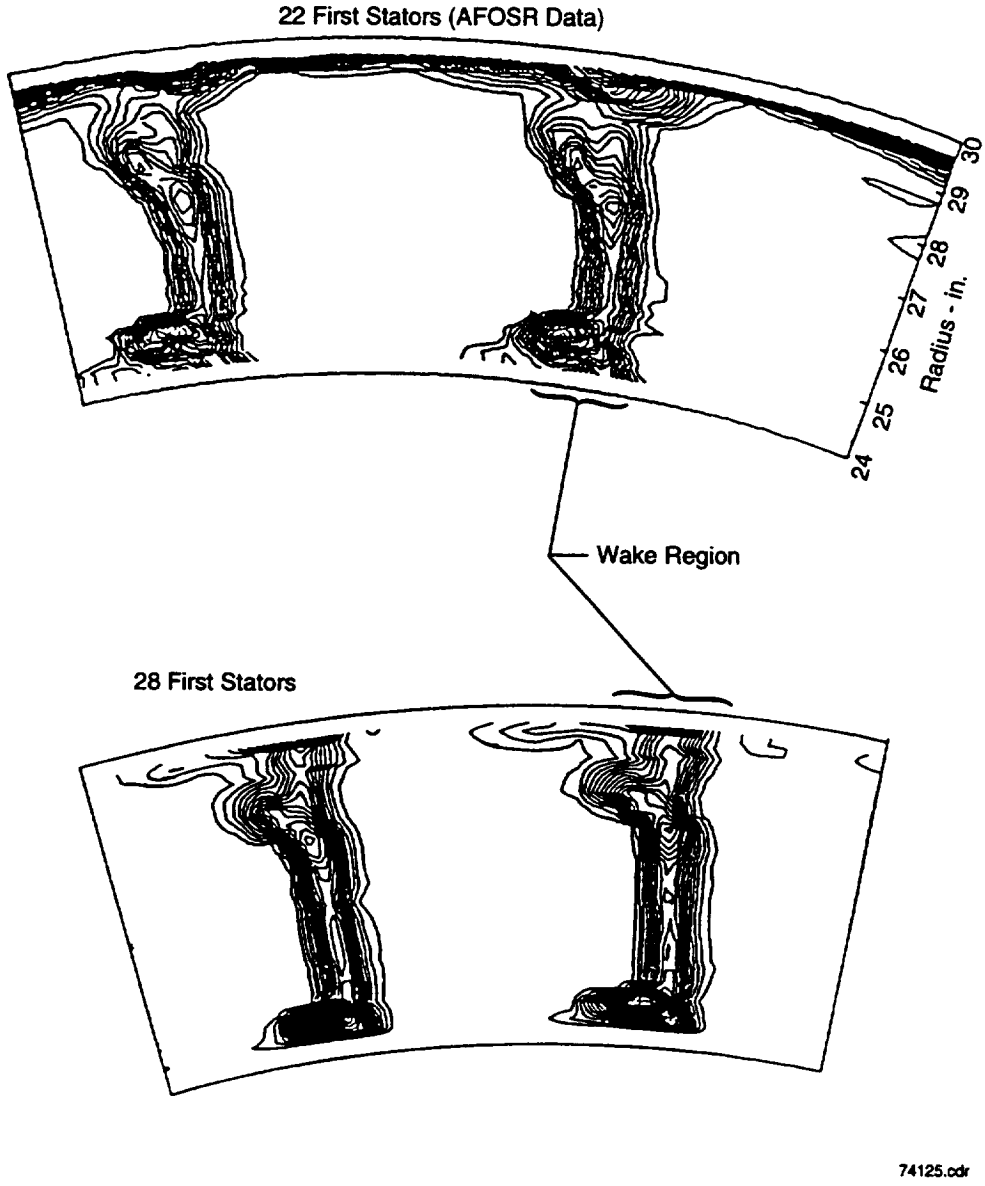

Figure 57. First Stator Measured Loss Contours Show That There Is High Concentration of Loss in Tip Region With 22 Compared to 28 Stators; This Loss Occurs in Regions Outside Wakes and Is Believed To Be Associated With Leakage in Traverse Seal

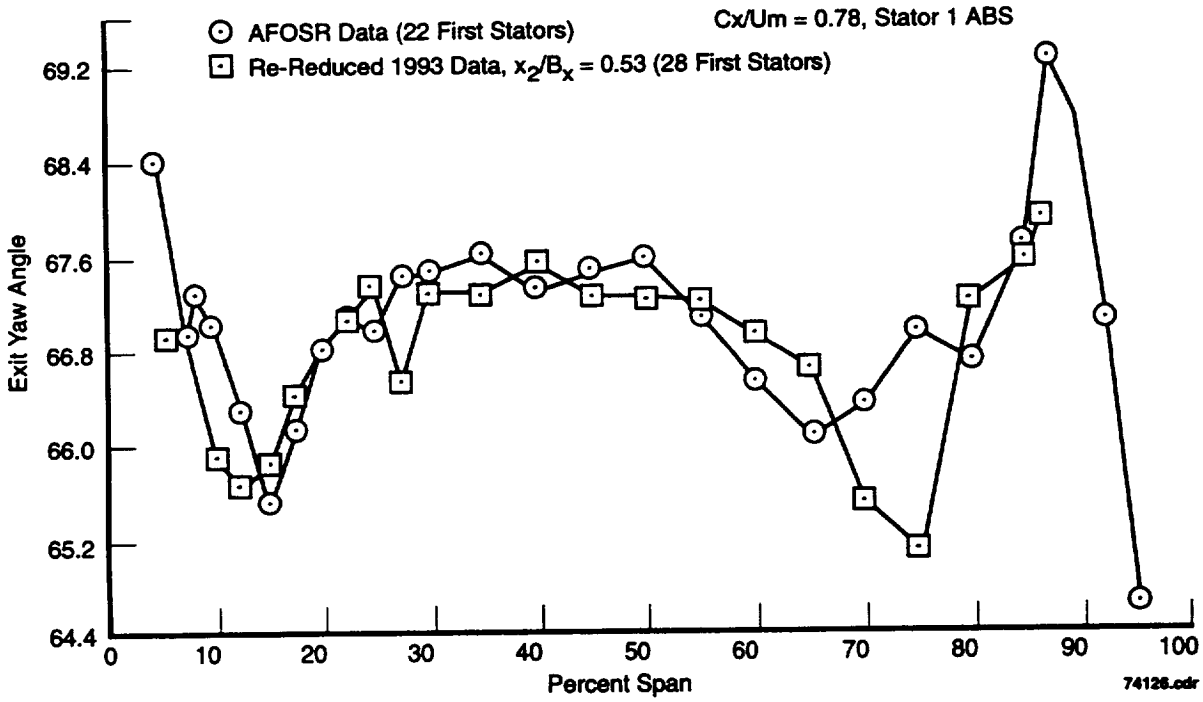

Figure 58. Measured Angles at Exit to First Stator Show That New Airfoil Count and Stagger Angle Are Within Measurement Accuracy, Achieving Design Intent

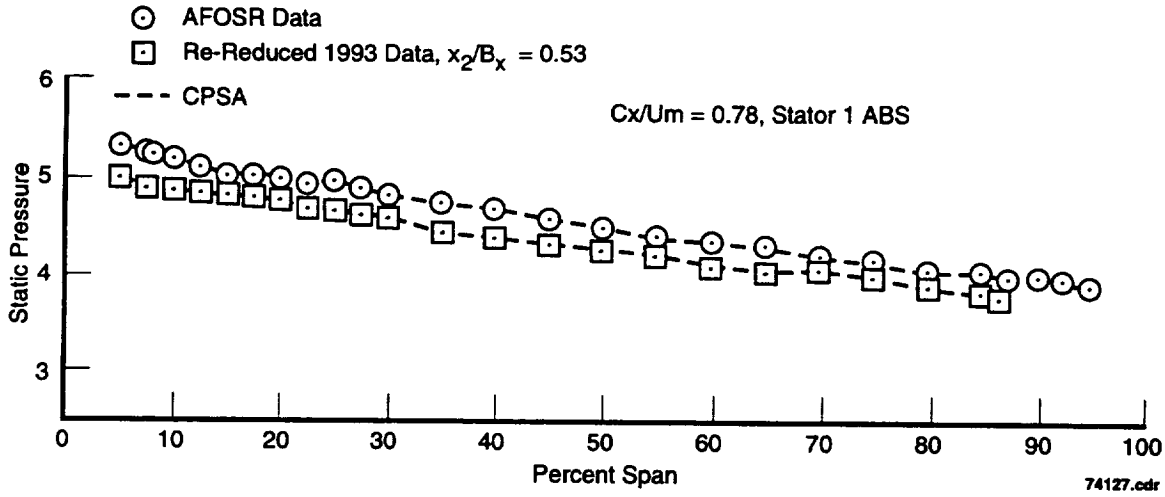

Figure 59. Through Simple Radial Equilibrium ($\frac{1}{\rho}\frac{\partial P}{\partial R} = Ct^2/R$), Static Pressure Gradient Confirms Exit Gas Angle Is Within 0.3 Degrees of Design Intent

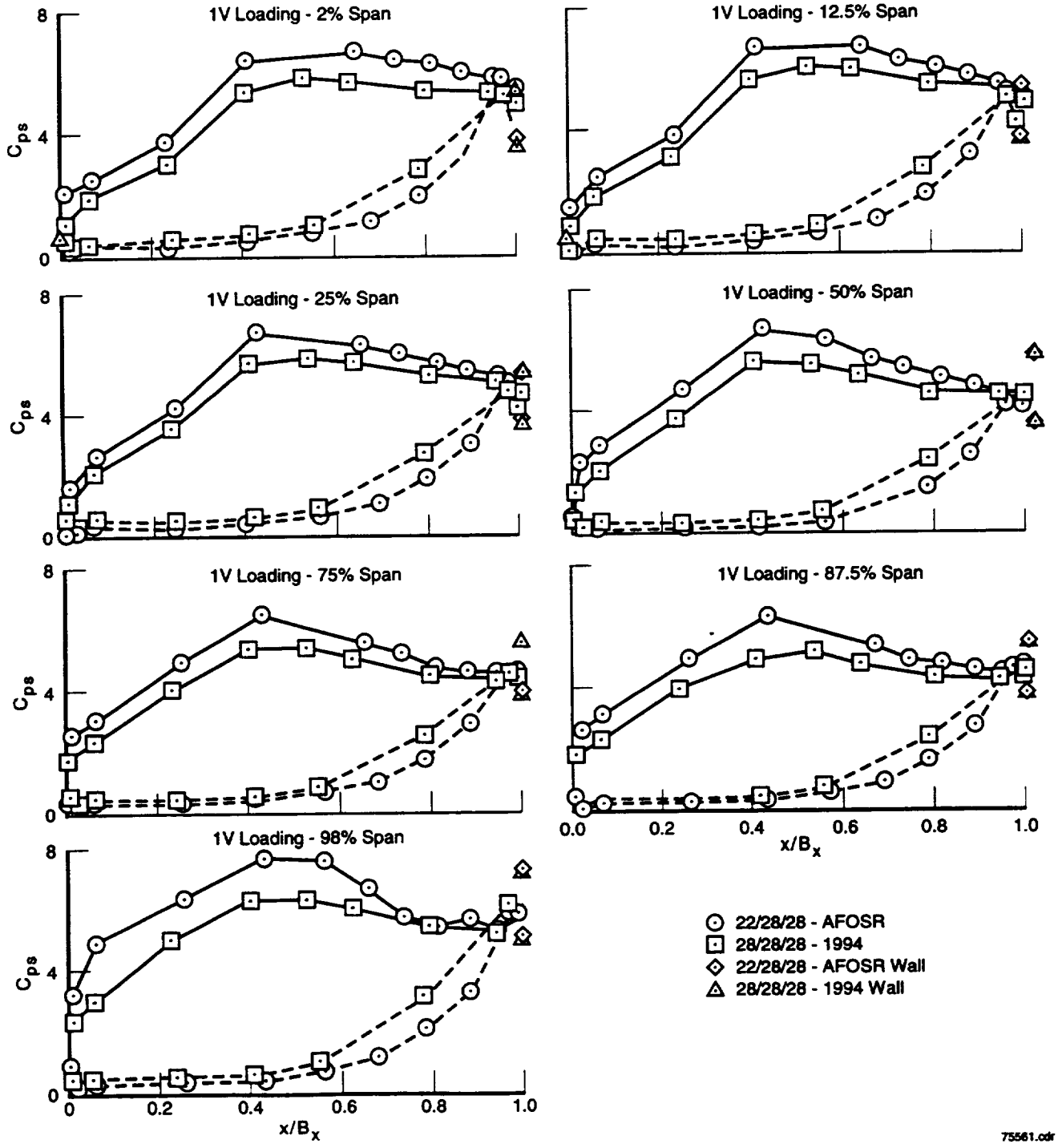

Figure 60. First Stator Surface Static Pressures Indicate Unloading Due to First Stator Airfoil Count Modification

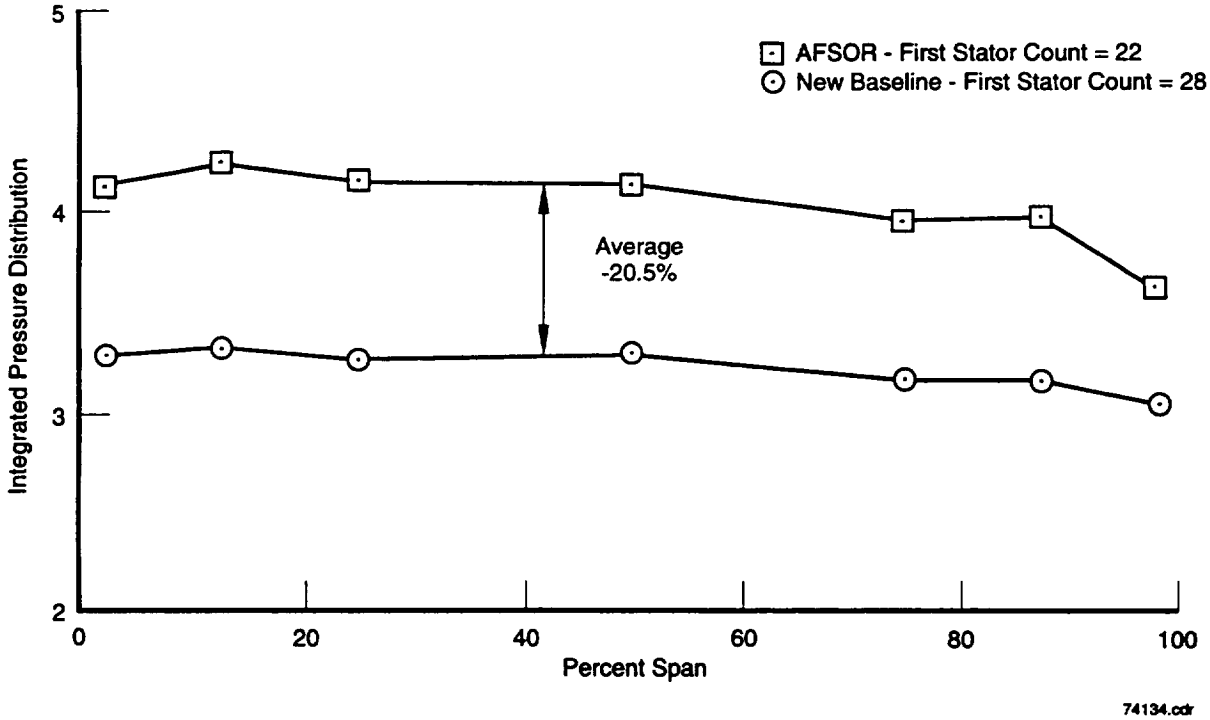

Figure 61. Integrated First Stator Loadings Indicate That Loading per Airfoil Has Reduced Approximately by Foil Count Change (22 to 28)

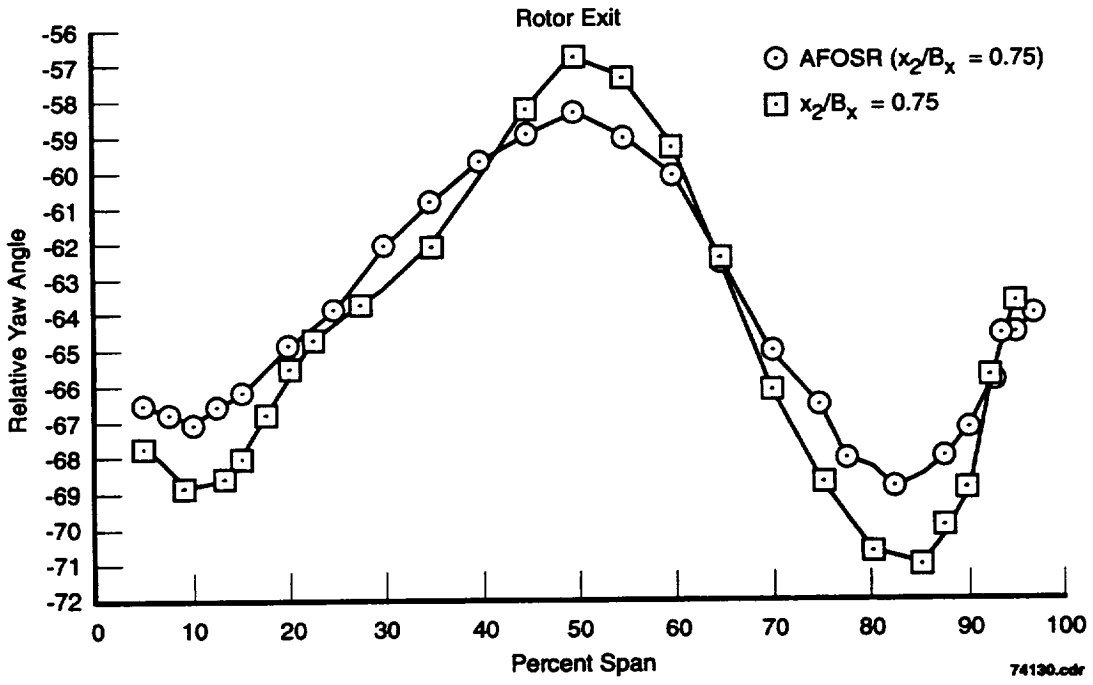

Figure 62. Relative Yaw Angle at Rotor Exit Shows Repeatability, With Measurement Accuracy, to Previously Acquired Data

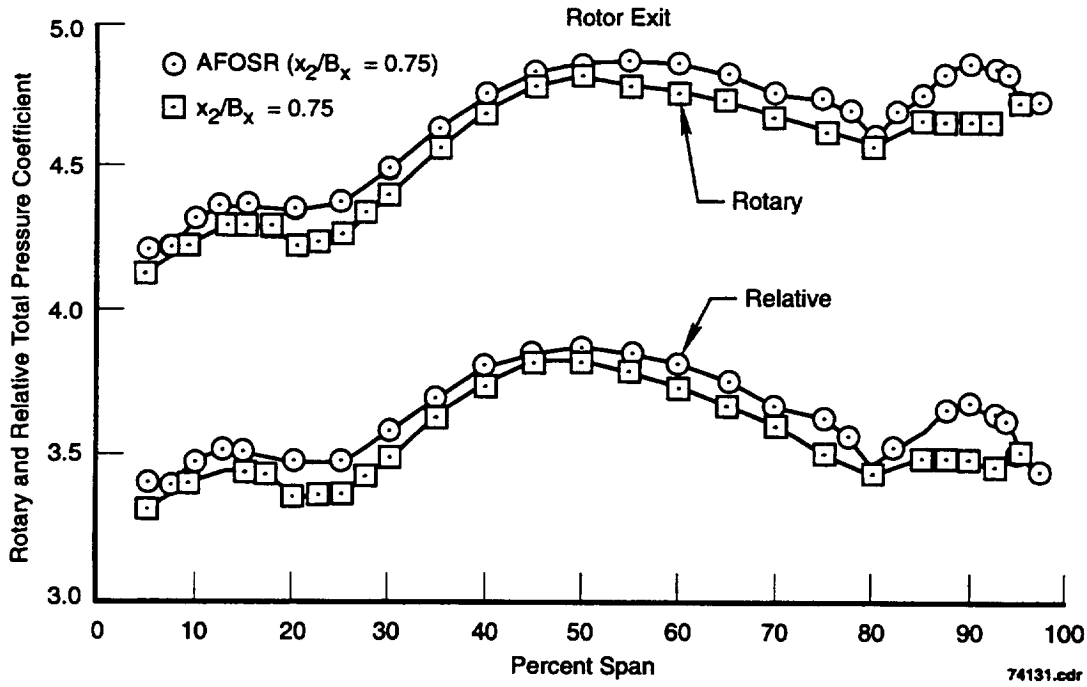

Figure 63. Relative Total Pressure and Rotary Total Pressure Coefficients at Exit to Rotor Show Reasonable Agreement With Previous Data With 22 First Stators

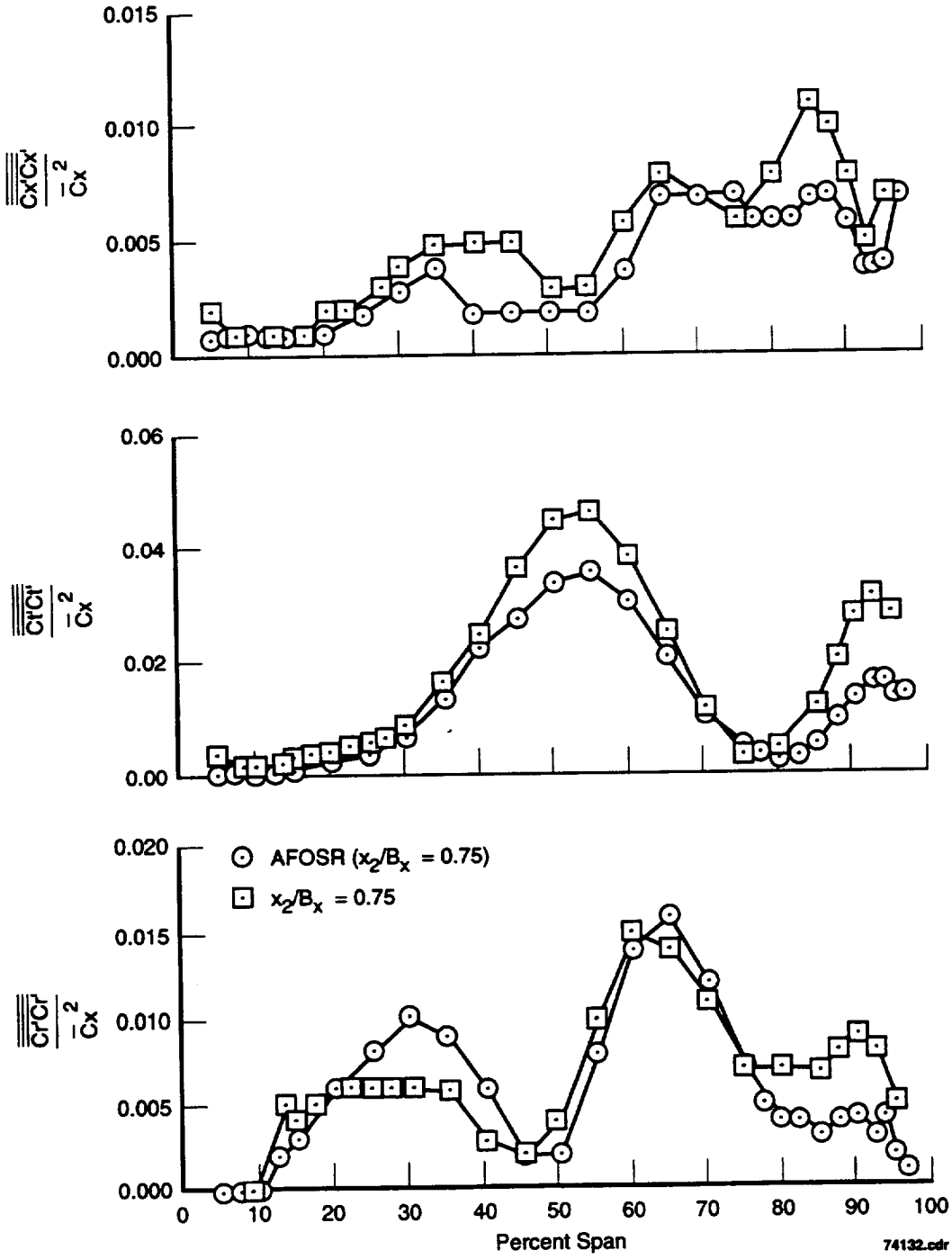

Figure 64. Rotor Exit Spatial Stress Shows That Flowfield Distortion Is Repeated With New First Stator Airfoil Count

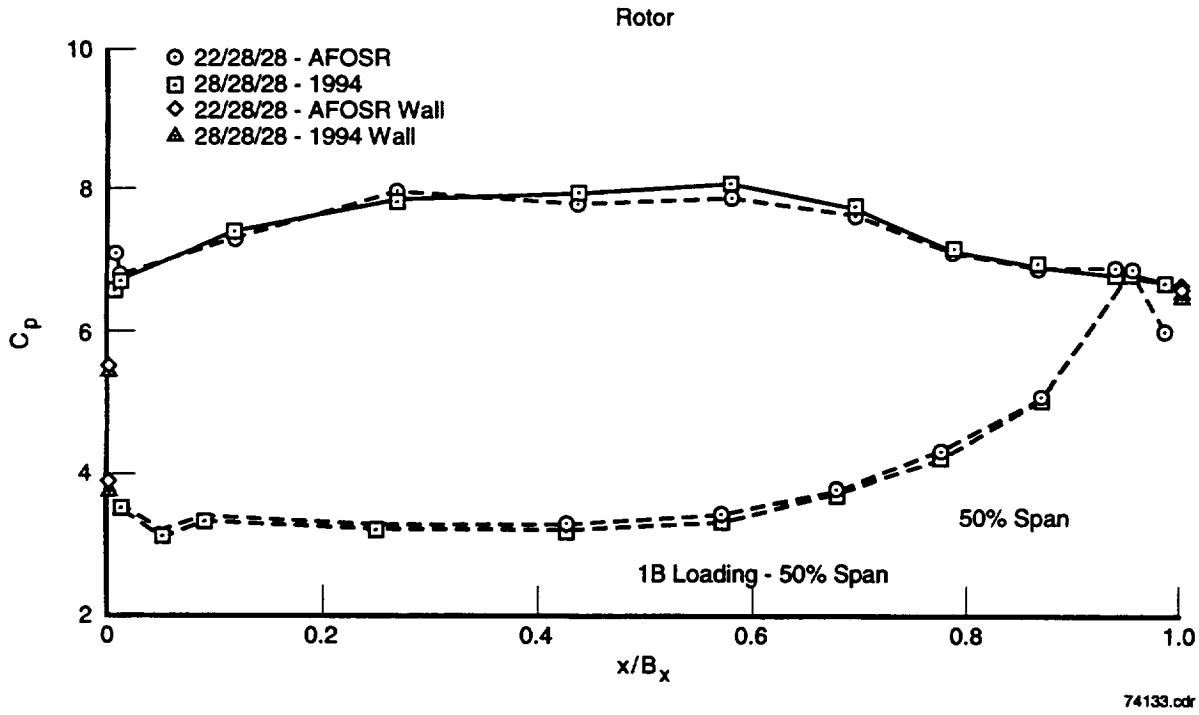

Figure 65. Rotor Surface Static Pressure Coefficients Indicate That First Stator Airfoil Count Change (22 to 28) Does Not Significantly Alter Inlet Gas Angle or Average Loading

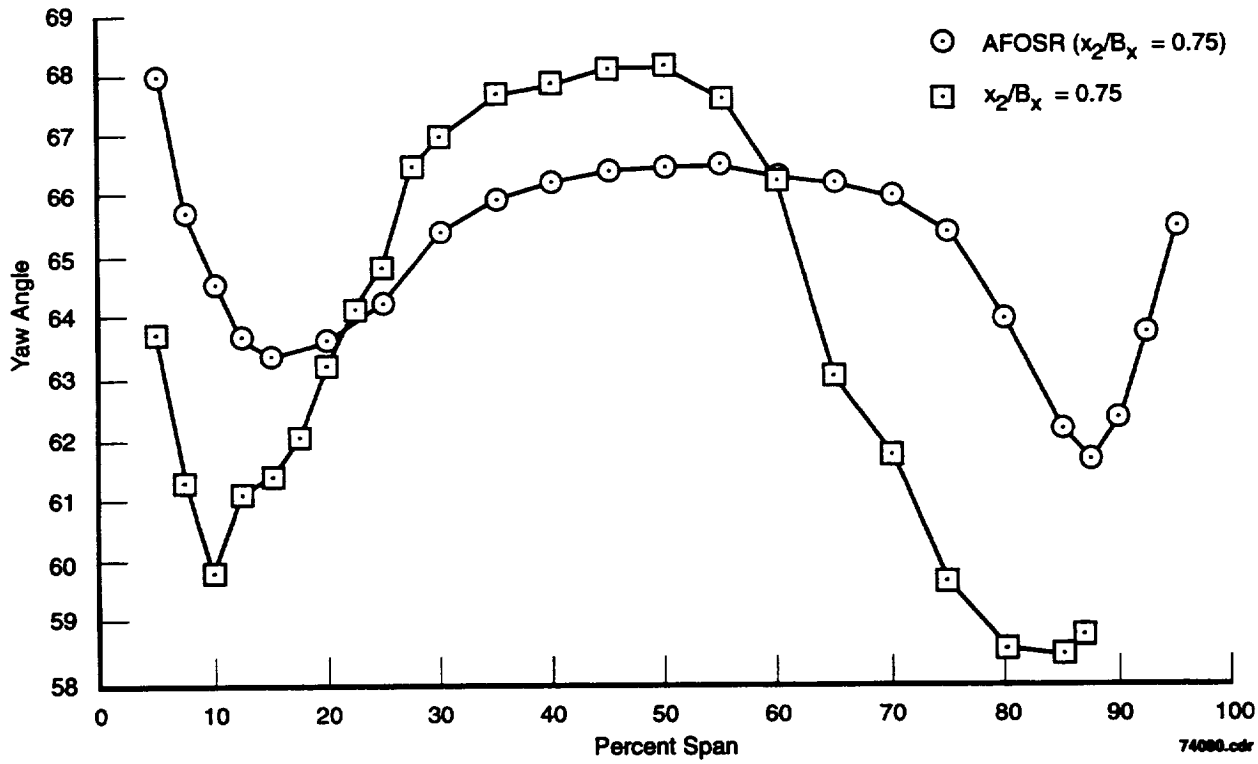

Figure 66. Second Stator Exit Yaw Angle Shows Same Spanwise Characteristic Previously Observed, the Lack of Exact Repeatability Is Associated With the True Periodic Condition Measured With the New Data

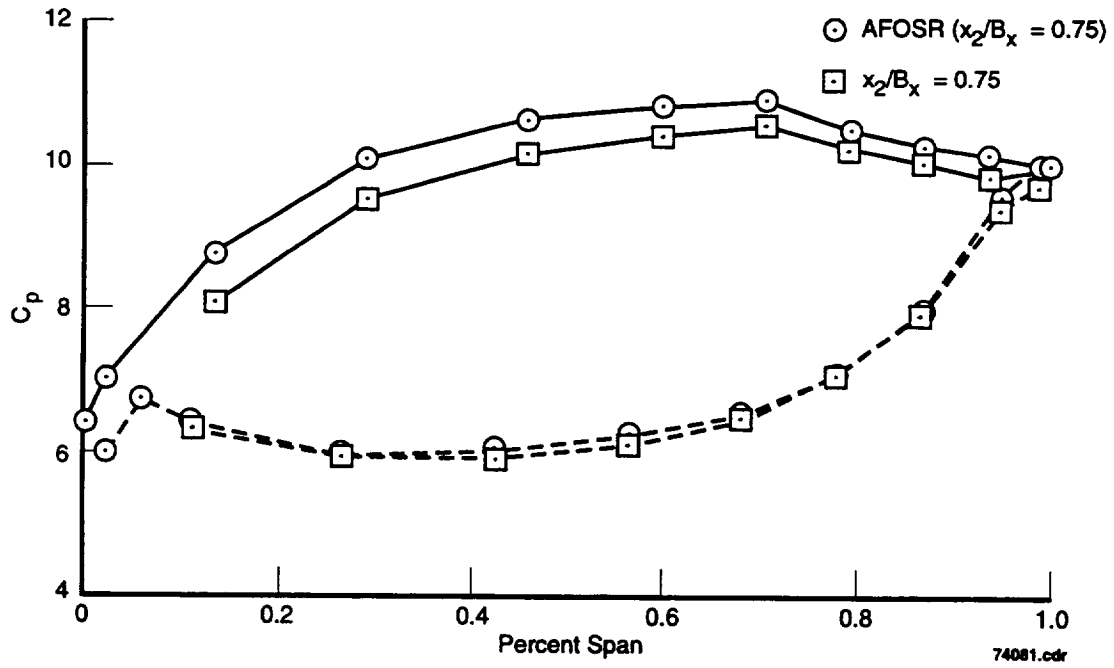

Figure 67. Second Stator Midspan Loading Shows Unloading Relative to Previously Acquired Data

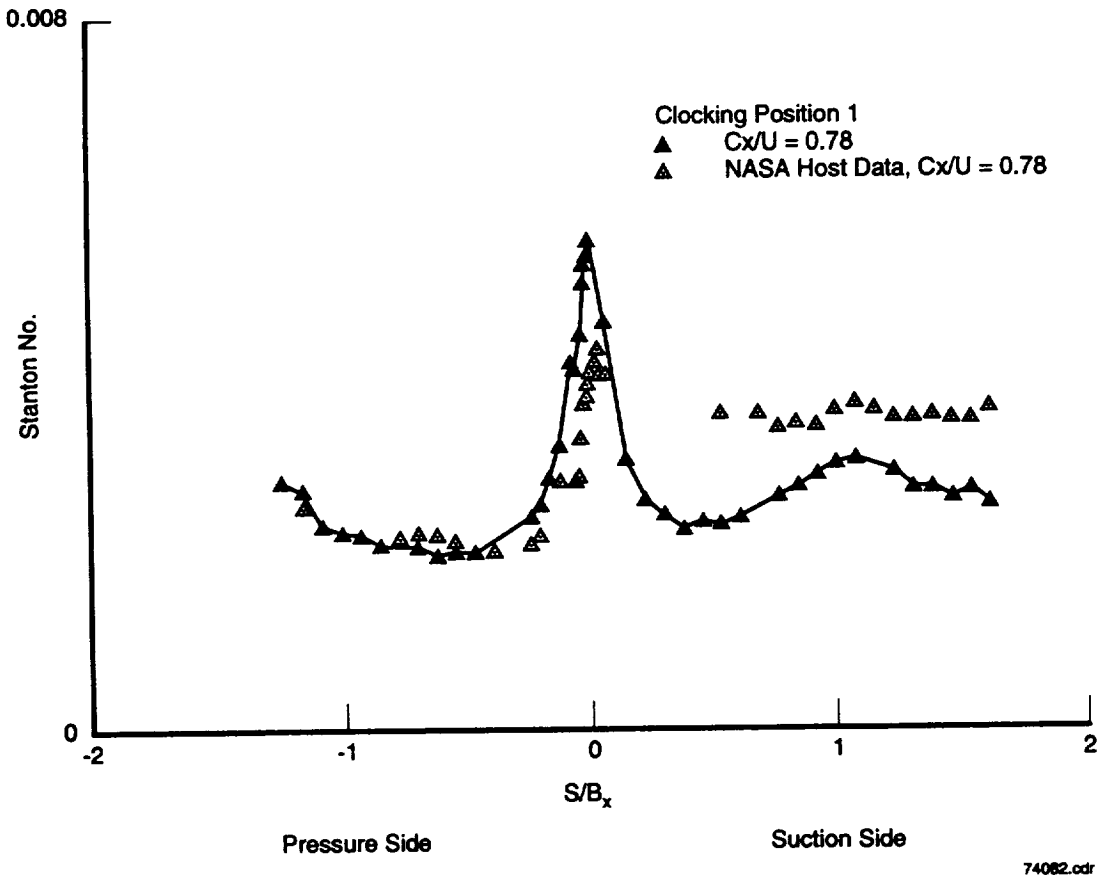

Figure 68. Heat Transfer Data for Second Stator for New Rig Configuration Does Not Reproduce Original Data (NASA Host Data)

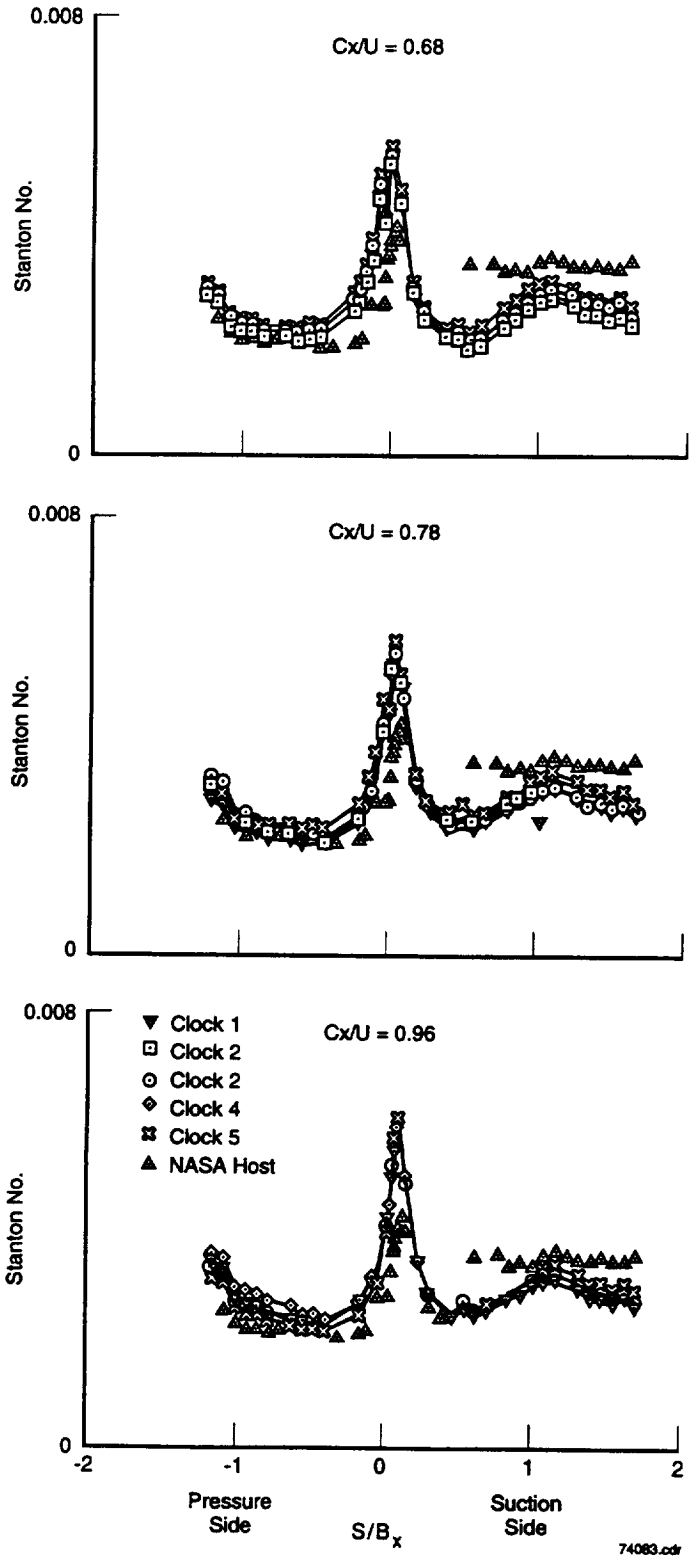

Figure 69. Original Second Stator Heat Transfer Data (NASA Host) Did Not Repeat for New Configuration for Any Flow Coefficients (Cx/U) or Indexing Positions Tested

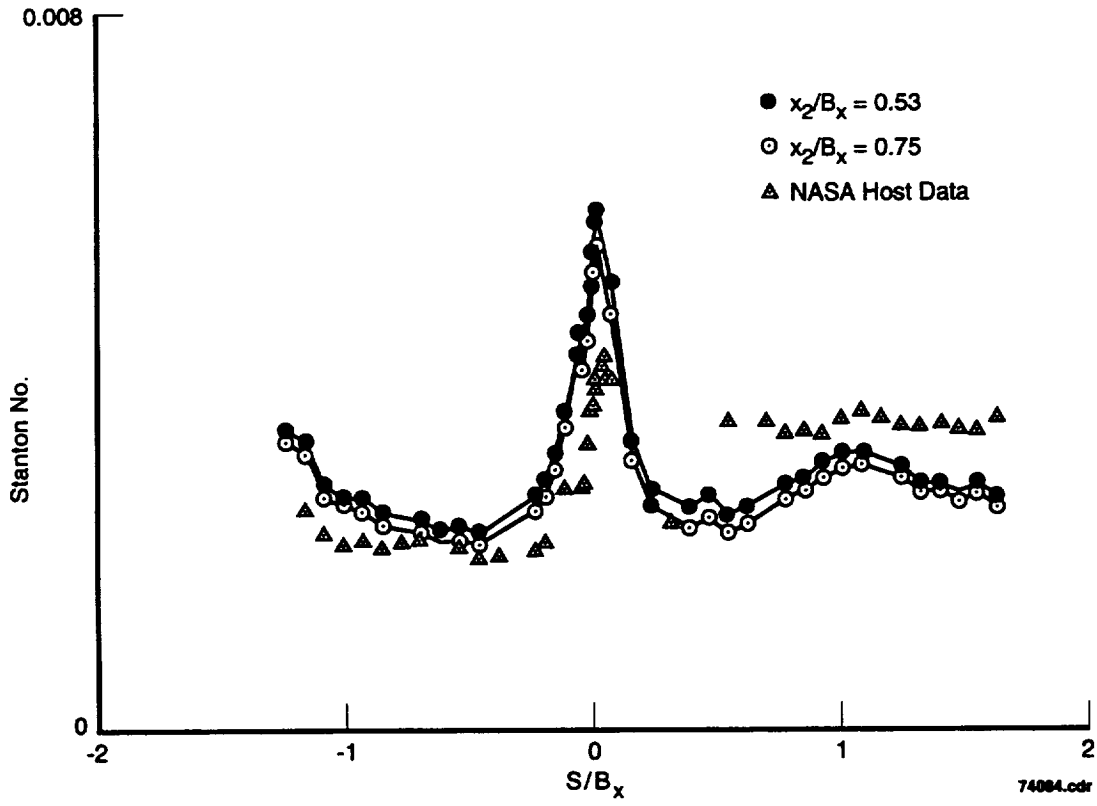

Figure 70. Original Second Stator Heat Transfer Data (NASA Host) Did Not Repeat for Modifying Axial Gap Between Second Stator and Rotor; For This Gapping Configuration, Axial Gap Between Rotor and First Stator Also Changed

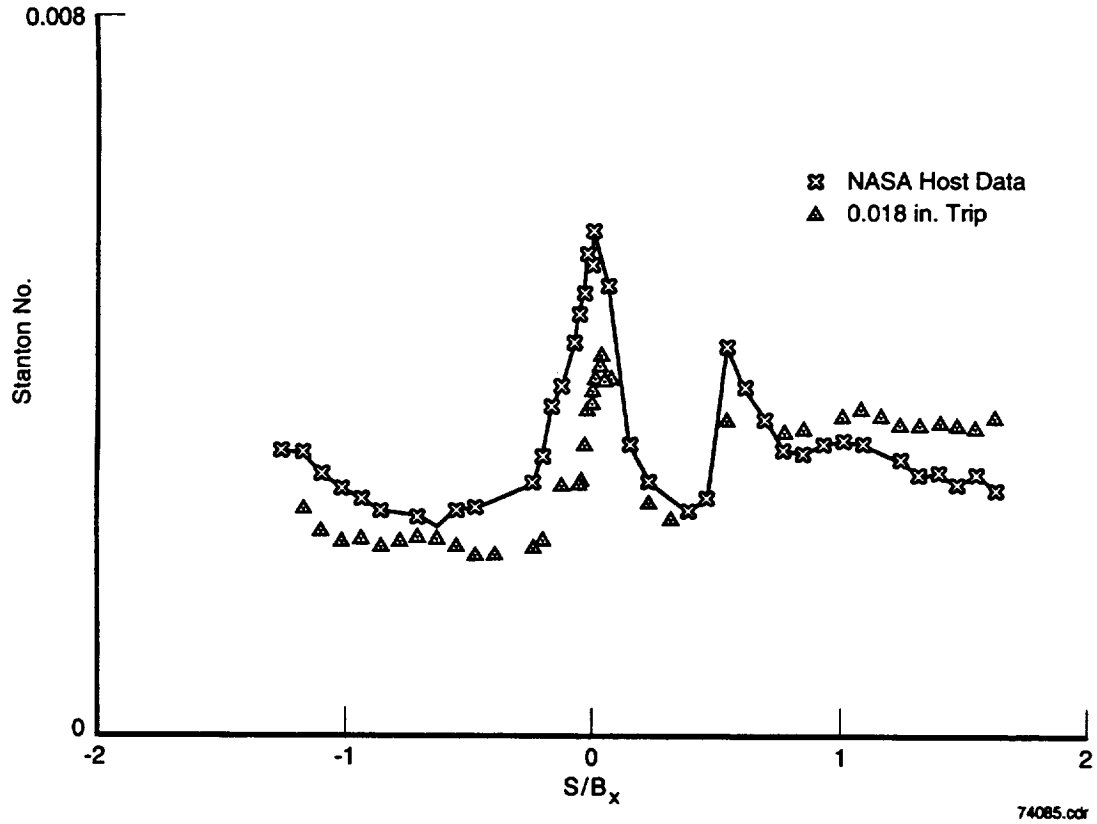

Figure 71. Second Stator Heat Transfer Data for New Configuration at Closest Position Between Second Stator and Rotor, With 0.018-Inch Trip Wire, Does Not Reproduce Original Data (NASA Host)

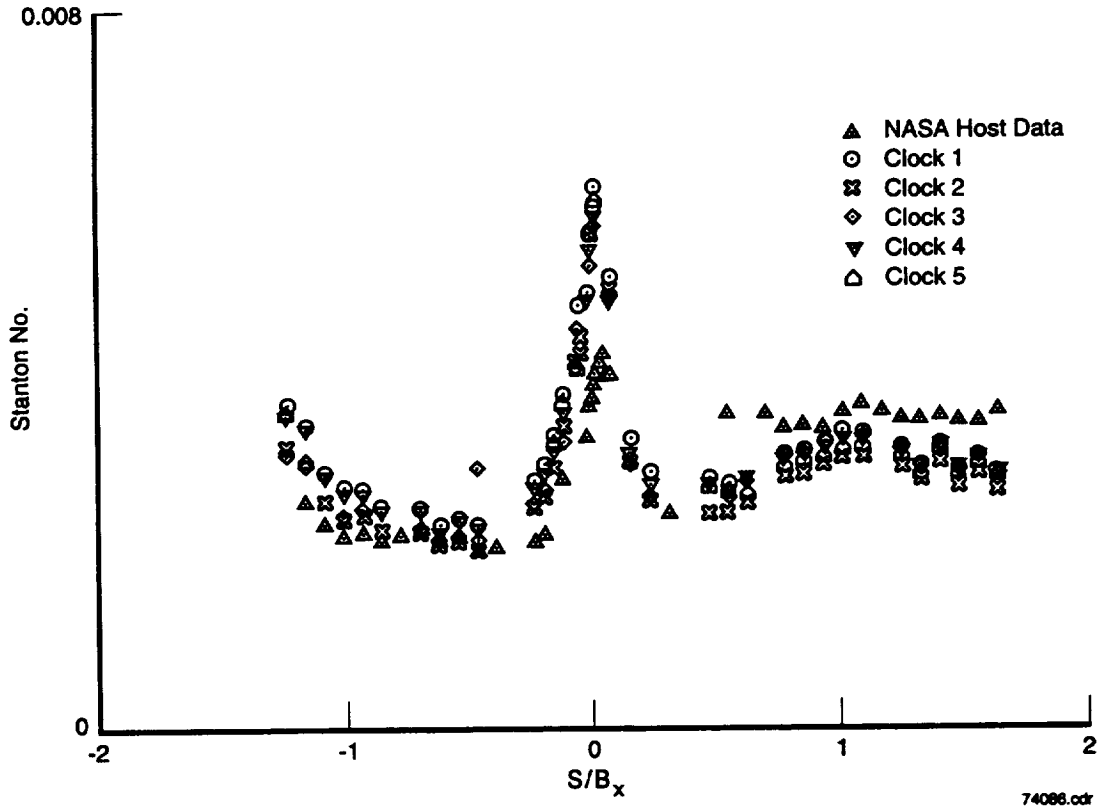

Figure 72. Second Stator Heat Transfer Data, With Original First Stator Count of 22, Does Not Reproduce Original Data (NASA Host) for Any Indexing Position

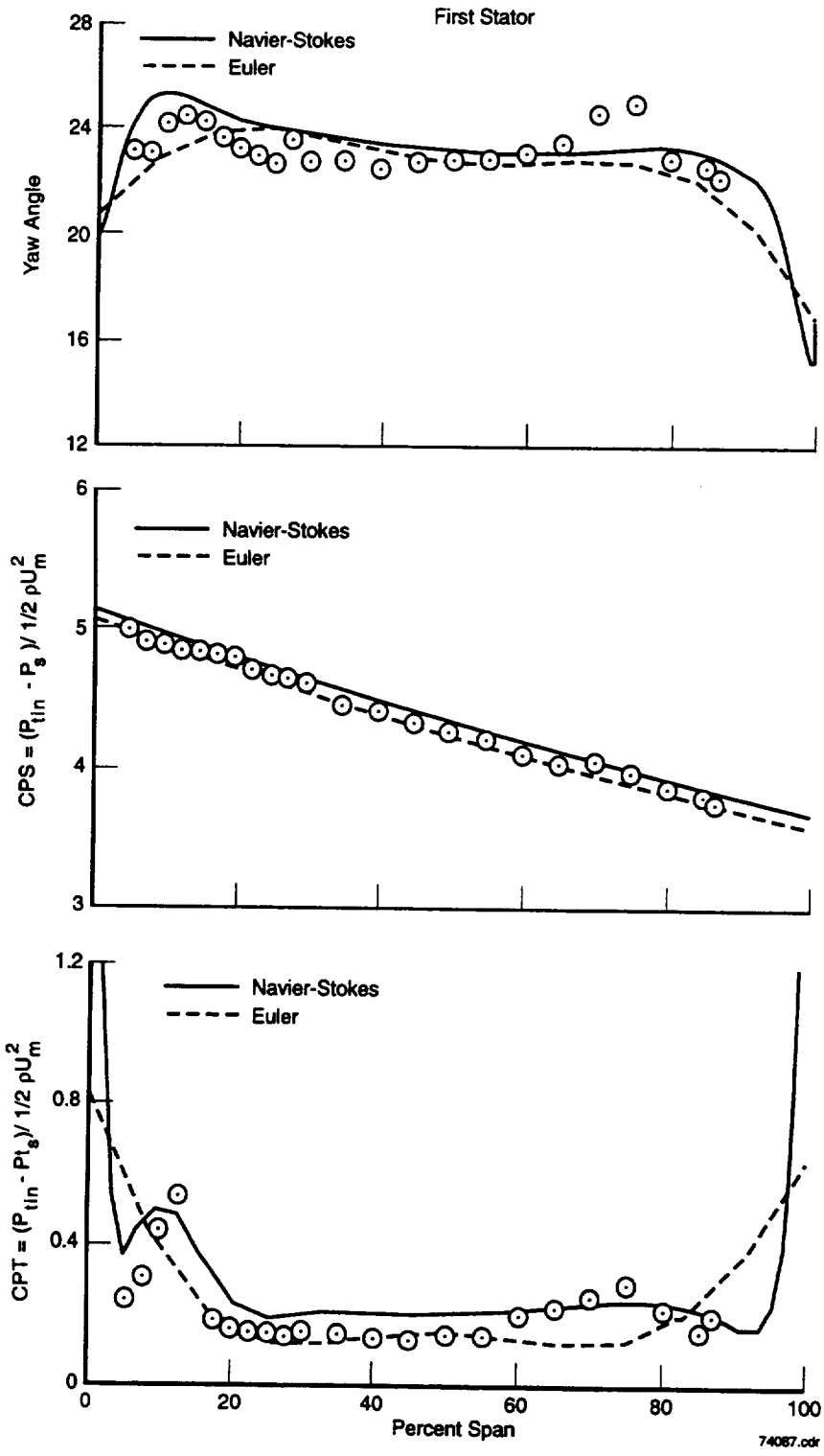

Figure 73. Steady Navier-Stokes Simulation Shows Much Better Agreement With Data Trends Compared to Viscous Euler

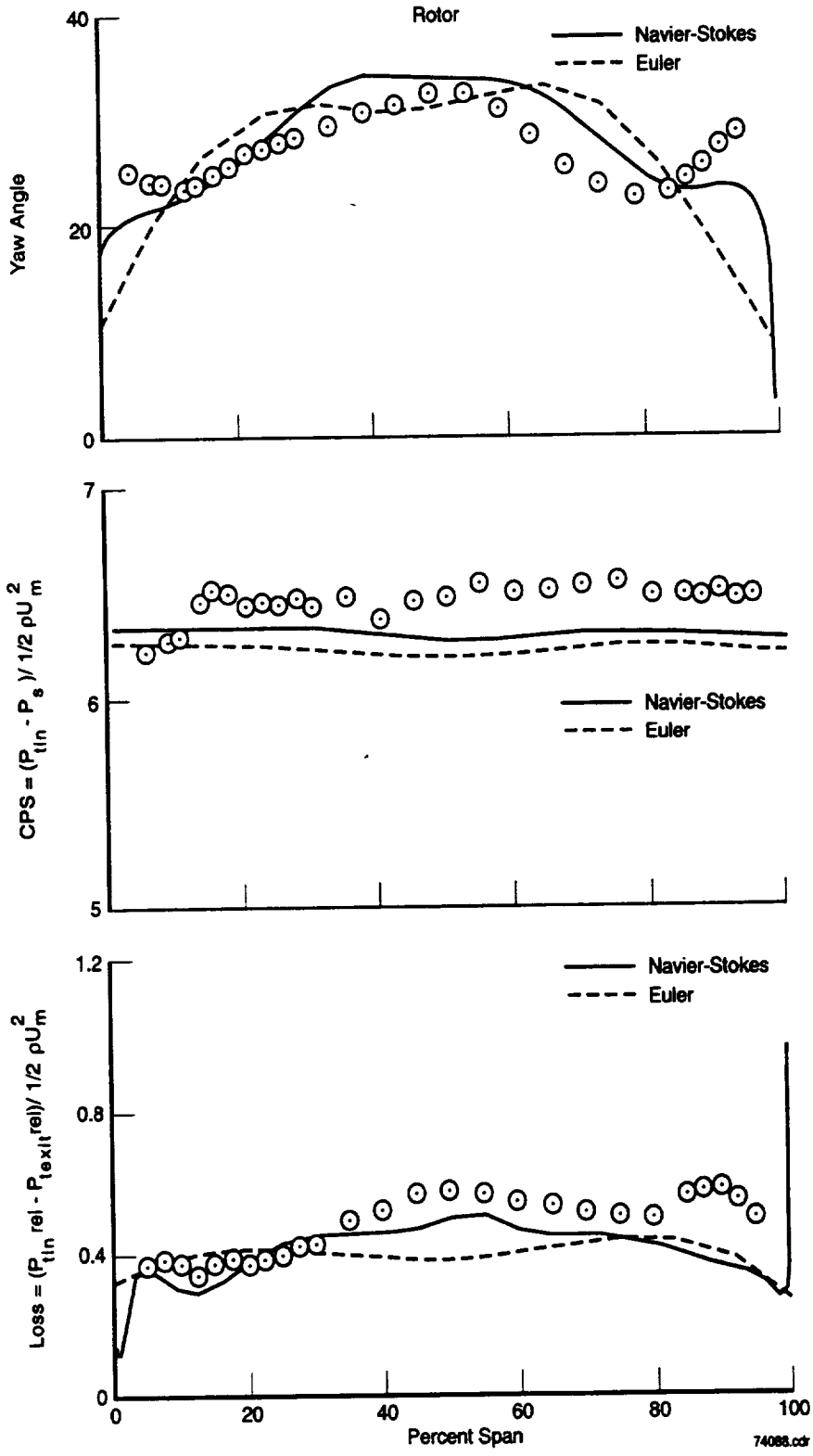

Figure 74. Steady Navier-Stokes Simulation Shows Much Better Agreement With Data Trends Compared to Viscous Euler

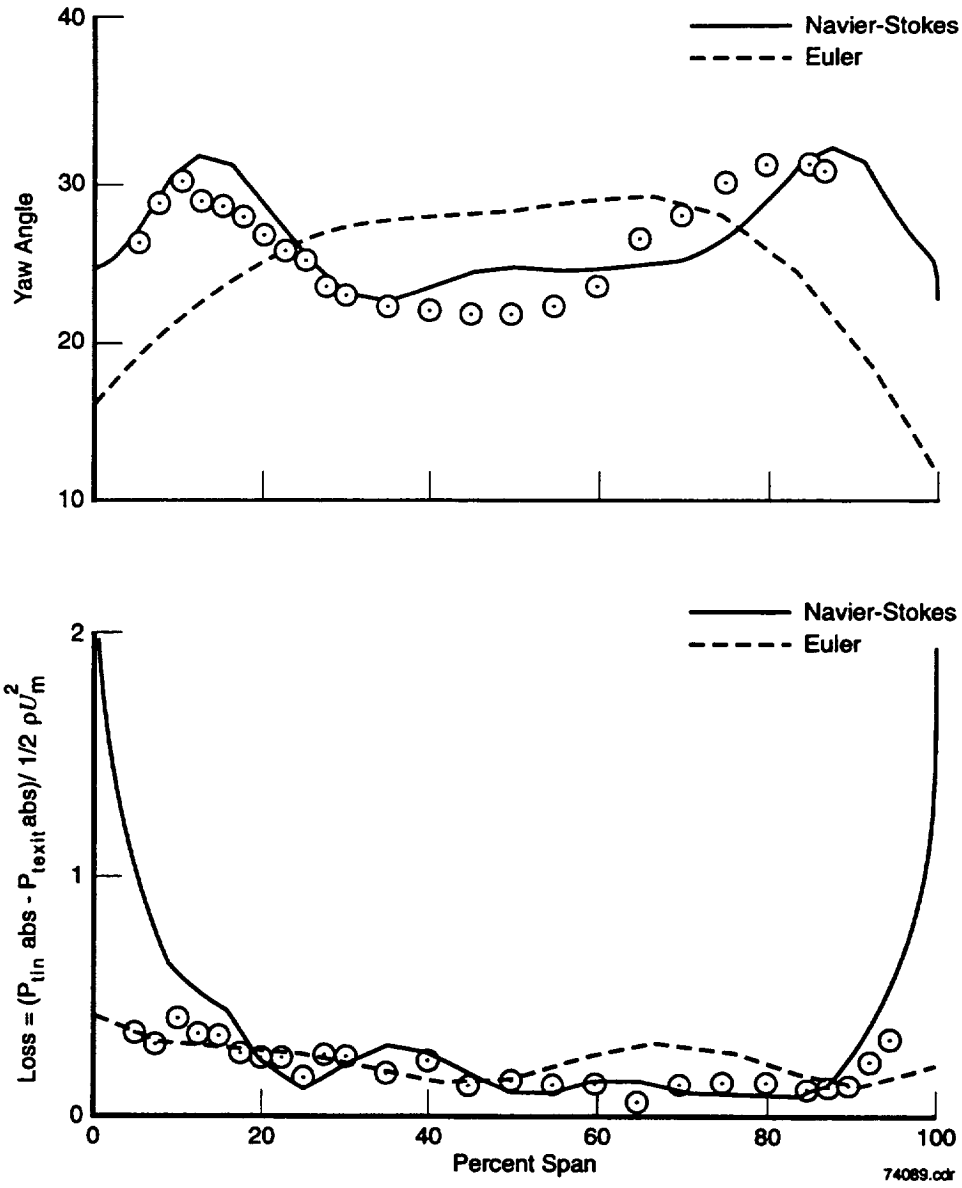

Figure 75. Steady Navier-Stokes Simulation Shows Much Better Agreement With Second Stator Data TrendsCompared to Viscous Euler

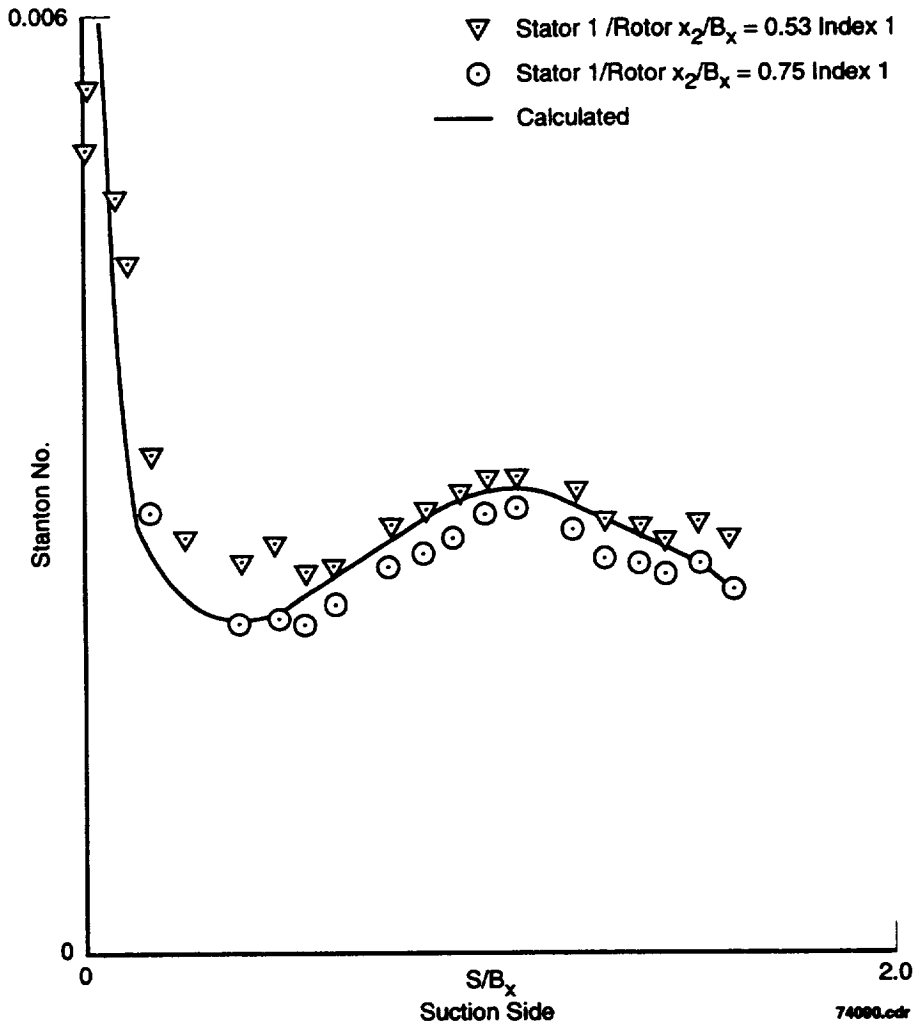

Figure 76. Second Stator Predictions Agree Well With Measured Data for Two Axial Spacings Between Rotor and Second Stator at One Indexing Position; For This Experiment, Spacing Between First Stator and Rotor Also Changed

7. EXPERIMENTAL ASSESSMENT

This section discusses the experimental results, from the turbine configuration described in Section 6, as part of (or in collaboration with) the present contract, where the main objective is to define the effects of second stator incoming deterministic stress level on the aerodynamic performance and heat load characteristics of the second stator. This was determined by acquiring heat load and loss at midspan of the second stator for three axial spacings between the rotor and second stator over five first stator-to-second stator clocking positions at each of the axial spacings.

The deterministic stress characteristics and measurements obtained are discussed in Section 7.1. Experimental results acquired to assess the clocking effect are discussed in Section 7.2. Results obtained for different axial spacing are discussed in Section 7.3, followed by a summary in Section 7.4.

7.1 EXPERIMENTAL PARAMETERS

The experimental configuration was designed to change the spacing between the rotor and downstream stator, as shown schematically in Figure 77. Three different spacings between the rotor and second stator were investigated. The values of spacing (i.e., axial distance between the rotor trailing edge [TE] and second stator leading edge [LE] normalized by axial chord of the rotor at midspan) were 0.39, 0.55, and 0.71. Axial spacing between the first stator and rotor was maintained at a fixed value to ensure that the rotor first stator interaction was not affected. From previous and new baseline data (Section 6), it was determined that the magnitude of the deterministic intensity could be changed by over 60 percent (Figure 78) by altering the axial gap between the rotor and second stator by approximately 55 percent. Since this data acquisition occurred prior to the setup of this configuration, the axial gaps in Figure 78 were not identical to the axial spacing performed in this experiment. The deterministic intensity stresses, therefore, were determined by interpolation of this information to the present experimental configurations. The data used to assess the second stator performance consisted of midspan total pressure measurements, at the inlet and exit of the second stator, and the distribution of heat transfer coefficients along the airfoil surfaces at the midspan. The pressure data were acquired over two airfoil pitches using a single-element kiel head probe. Measurements were obtained for midspan airfoil surface static pressures (first stator, rotor, second stator).

A limited amount of unsteady surface static pressure data was also acquired using flush-mounted Kulite pressure probes at the midspan of the second stator. These data were acquired, at one axial position (Gap/B_x-rotor = 0.75) and five clocking positions, as part of the experimental documentation described in Section 6.

The operating conditions for all measurements (total pressure, heat transfer, surface static pressure) were at the design flow coefficient of 0.78 to maintain the design incidence angle at the second stator mean section.

The data were acquired for three spacings between the rotor and second stator. At each axial spacing, the first stator was indexed (clocked) relative to the second stator at five distinct positions extending over one airfoil pitch (detailed positions described in Appendix B). The first and fifth indexing (clocking) positions were exactly one airfoil pitch apart, and the intermediate indexing increments were 25 percent of one airfoil pitch. These data, at different clocking positions, were acquired to ensure that performance and heat load characteristics represented an accurate average at each axial spacing.

7.2 STATOR CLOCKING EFFECTS

Clocking of alternate stator airfoil rows have altered the midspan efficiency of a turbine stage by 0.8 percent, as discussed by Huber, et al. [11] and Sharma, et al. [12]. The location of the first vane wake impingement on the second vane is dependent on axial gap. Therefore, clocking must be performed to separate clocking from gapping effects. The effects of clocking on performance and heat transfer in the second stator are discussed in this section.

7.2.1 Steady Airfoil Loadings

Time-averaged surface static pressure data acquired with pneumatic instrumentation, at the midspan of the second stator, are shown in Figure 79 for all five clocking positions. The data are for a normalized axial spacing between the rotor and second stator of 0.39. The data show that airfoil loadings (integrated pressures) are affected by less than ±1.5 percent by the clocking between the first and second stator, and therefore, only expected to influence the boundary layer by approximately the same amount.

7.2.2 Unsteady Airfoil Loadings

As part of the new baseline data acquired (Section 6), unsteady airfoil surface data were acquired for a limited set of test conditions at the midspan of the second stator. (The axial gap tested was not part of the axial gap testing, i.e., axial gap/B_x-rotor = 0.75.) These data were reduced into time-averaged, periodic, and random components. The measured data for the time-averaged values of the surface static pressure agreed within 2 percent of those measured with the pneumatic instrumentation and are not shown.

The RMS values of periodic and random parts of the wall surface static pressure on the airfoil suction side are shown in Figure 80, for five clocking positions, at a value of normalized axial spacing of 0.75. The random unsteady pressure fluctuations (Figure 80[a]) show similar levels for all clocking positions, except for the 75 percent clockwise position. The periodic unsteady pressures (Figure 80[b]) show the largest levels in periodic unsteadiness for the clocking position of 75 percent and lowest levels for the 25 percent position.

7.2.3 Airfoil Midspan Heat Transfer Coefficient

Measured distributions of heat transfer coefficients at the midspan of the second stator are shown in Figure 81 for five different clocking positions. The experimental data, acquired at the normalized axial spacings of 0.39 and 0.55, are shown in Figures 81(a) and 81(b), respectively. Both sets of data show similar characteristics. The heat transfer coefficients on the airfoil suction side are affected more (about 10 percent) than those on the pressure side (about 5 percent). The physical mechanisms associated with these changes are not yet understood, but do not appear to be associated with transition since the general shape along the surface was not influenced (generally associated with transition).

7.2.4 Aerodynamic Performance

Aerodynamic performance data, representing the midspan loss of the second stator, were obtained for the three axial spacings and five clocking positions. The variation of the midspan loss, at each axial spacing, is plotted as a function of the clocking position in Figure 82(a). Data are shown for the three spacings. All the data show similar behavior and indicate that loss is affected by roughly 10 percent due to stator clocking. To put this in perspective, the 10 percent change in the second stator loss causes a ±0.25 percent change in the efficiency of a typical two-stage turbine.

As previously mentioned, unsteady pressures were acquired, for five clocking positions, during the baseline testing described in Section 6. The axial gap between the rotor and second stator was different than the axial spacing performed for the effect on loss and heat transfer. This axial gap resulted in the upstream wakes impinging on the second stator at a different circumferential position. Therefore, a circumferential adjustment was made to ensure consistent aerodynamic wake positioning (wake impingement location). Once this adjustment was made, a comparison of the airfoil unsteadiness to loss and heat load was made. By integrating in time and along the airfoil surface, the unsteady surface pressures and heat load, the surface unsteadiness can be compared to overall performance. Figure 82(b) shows that average heat transfer and loss qualitatively correspond to the surface unsteadiness measured on the suction side of the airfoil at midspan.

7.3 PERIODIC UNSTEADINESS EFFECTS

The effect of inlet periodic unsteadiness was examined by changing axial spacing between the second stator and upstream rotor. This change allows the flow distortion to decay and reduce the periodic unsteadiness. This change also alters the turbulence level entering the second stator. However, based on the level of midspan turbu-

lence (Figure 17) and the expected rate of decay discussed in References [4], [13], and [14], it is not expected to change the loss by more than approximately 2 percent.

7.3.1 Airfoil Loadings

Measured time-averaged airfoil surface static pressures at the midspan of the second stator are plotted in Figure 83. The data represent all three axial spacings. Data at each axial spacing represent an average of the clocking positions between the first and second stators. An increase in midspan loading is observed with the increase in axial spacing between the rotor and second stator. This increase in loading is directionally proportional to the change in tangential momentum, and therefore, implies a redistribution of spanwise flow and/or turning.

7.3.2 Airfoil Midspan Heat Transfer Coefficients

Heat transfer coefficient distributions along the midspan of the second stator are shown in Figure 84 for two values of axial spacing between the rotor and second stator (the heat transfer model overheated and failed at the largest axial gap). The data for each axial spacing represent an average of the data acquired by clocking the first stator relative to the second stator. The data show that the average heat transfer coefficient (Stanton number) only showed ≈1 percent variation as the axial gap was changed.

7.3.3 Airfoil Midspan Performance

Midspan loss data for the second stator are plotted as a function of axial spacing between the rotor and second stator in Figure 85. Each data point in this figure represents an average of loss values obtained from clocking. The magnitude of midspan losses is reduced by almost 15 percent as the axial spacing between the rotor and second stator increases from 0.39 to 0.71. As previously mentioned in Section 7.3.1, the airfoil loading increased as the axial spacing increased. From two-dimensional (2-D) boundary layer theory, maintaining transition location, it is expected that the loss would increase by approximately 10 percent for the increased loading. Rematching the airfoil to achieve the design intent loading, an additional 10 percent reduction of loss would be expected at the 0.71 axial spacing relative to 0.39.

The loss is plotted as a function of the *deterministic intensity* at the second stator inlet in Figure 86 (the values of deterministic intensity were obtained from the interpolation of the data plotted in Figure 78). The measured loss levels can be representative as varying linearly with the deterministic stress magnitude. The extrapolated values of loss at zero inlet deterministic intensity are close to the midspan loss estimated from a 2-D boundary layer code and a wake mixing model. Figure 86 shows the changes in midspan loss due to periodic unsteadiness (quantified as the level of deterministic intensity at stator inlet).

7.3.4 Impact of Airfoil Spacing on Performance-Comparison With Additional Data

Experimental data discussed in Section 7.3.3 were compared to additional data available from another program in the large-scale rotating rig (LSRR). Rotor loss data were acquired in these tests using United Technologies Corporation (UTC) Independent Research and Development (IR&D) funds.

Total pressure loss data were obtained, in the IR&D-funded programs, for the rotor by altering axial spacing between the rotor and upstream stator. The losses were determined by traversing the flowfield at the inlet and exit of the rotor in the relative frame by using kiel head total pressure probes. These tests were conducted for high and low flow coefficient operating conditions. The first stator was restaggered to maintain the design intent rotor loading and incidence at each flow coefficient. For each first stator stagger and flow coefficient, the rotor was positioned at two distinct locations downstream of the first stator.

Normalized overall losses for the rotor, along with the data discussed in Section 7.3.3, are plotted in Figure 87 as a function of normalized axial spacing between the current and upstream airfoil row. The data, both for the rotor and second stator, follow similar behavior. Each set of data indicates a reduction in loss as the axial spacing between the two airfoil rows of interest is increased.

7.4 SUMMARY OF EXPERIMENTAL PROGRAM

The data presented in this section provide a quantifiable demonstration of the effect periodic unsteadiness (deterministic stress) has on airfoil performance. The physical mechanism through which these losses are generated has not yet been identified. However, these results indicate there is a need to account for the effects of periodic unsteadiness to achieve accurate estimates of time-averaged performance for airfoil rows in a multi-row environment.

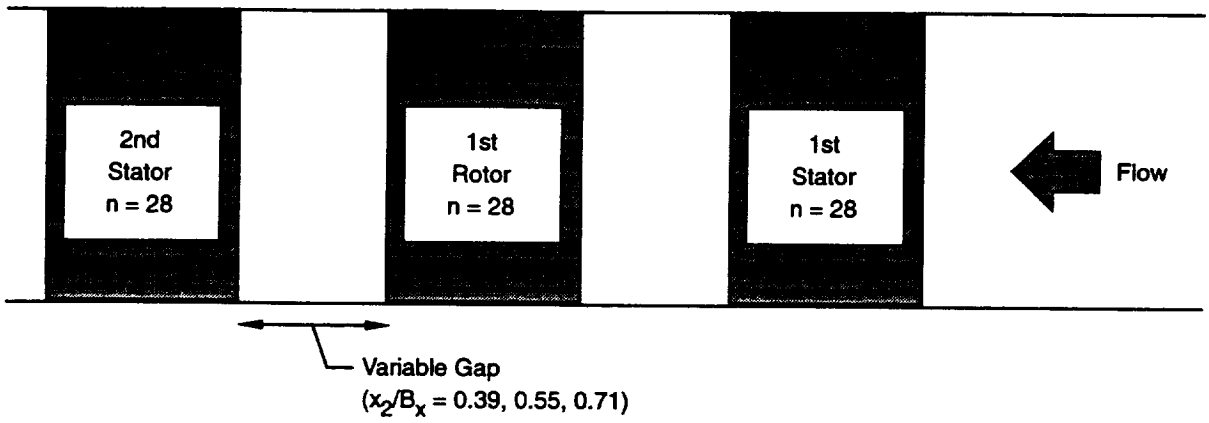

Figure 77. Schematic of Large-Scale Rotating Rig Experimental Configuration

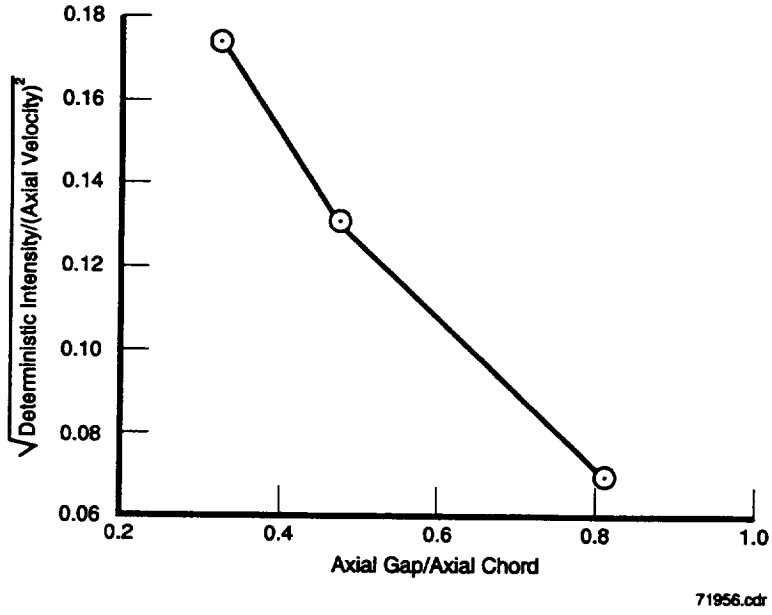

Figure 78. Magnitude of Deterministic Intensity at Various Axial Positions Downstream of Rotor

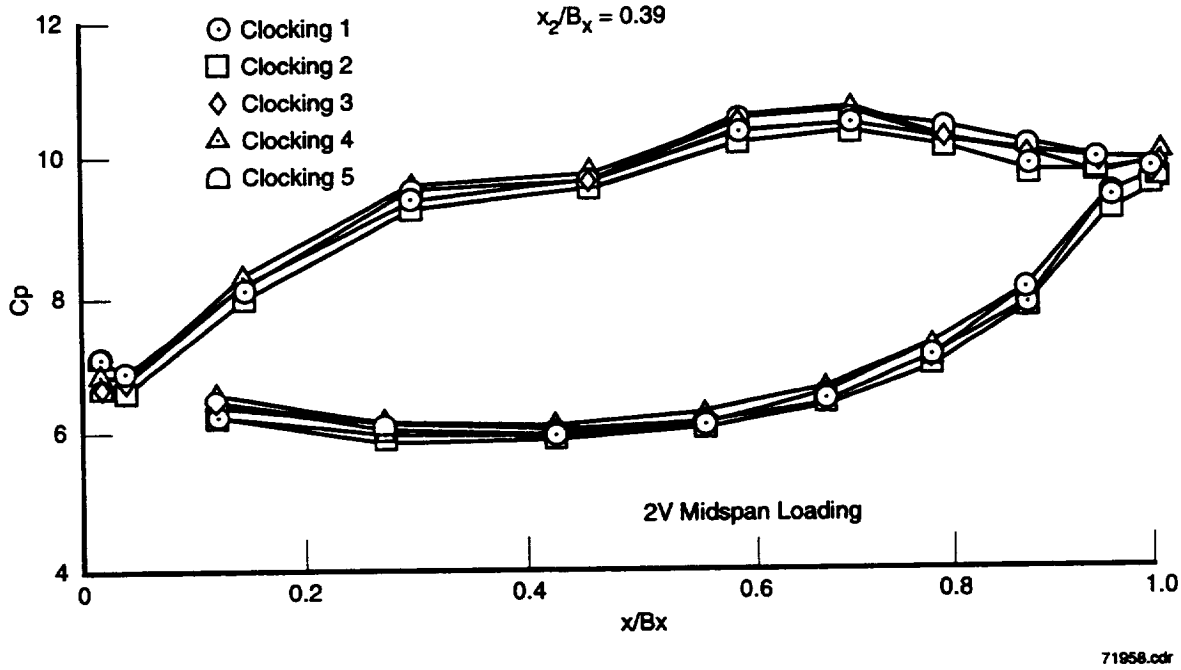

Figure 79. Airfoil Surface Static Pressure Distribution on Second Stator Not Significantly Affected by Clocking Between Stators; Integrated Tangential Lift on Stator Within ±1.5 Percent; Integrated Airfoil Surface Static Pressures Are Not Significantly Affected by Clocking Between Stators (Tangential Lift Is Within ±1.5 Percent)

(a) Random Suction Surface Pressure Fluctuations, on Second Stator, Show Maximum Influence at 75 Percent Clocking Position

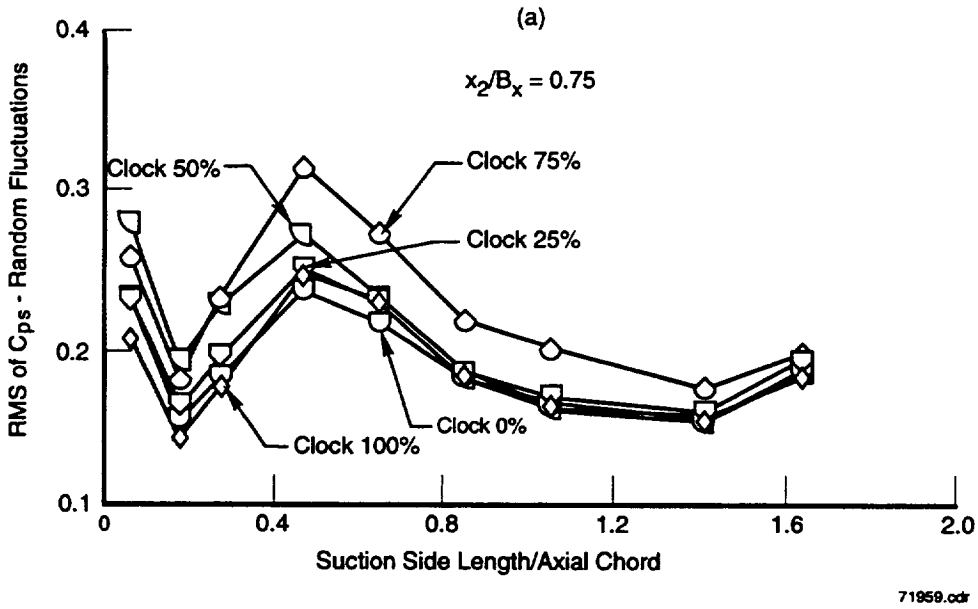

(b) Periodic Suction Surface Pressure Fluctuations, on Second Stator, Show Larger Magnitude for 75 Percent and Least Amount at 25 Percent Clocking Position

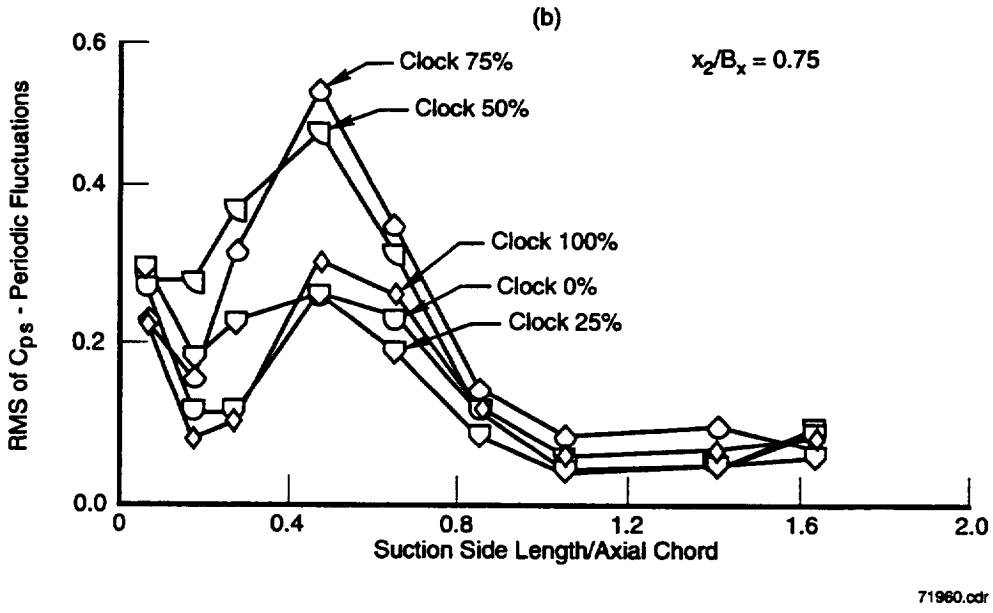

Figure 80. Wall Surface Static Pressure Fluctuations on Second Stator

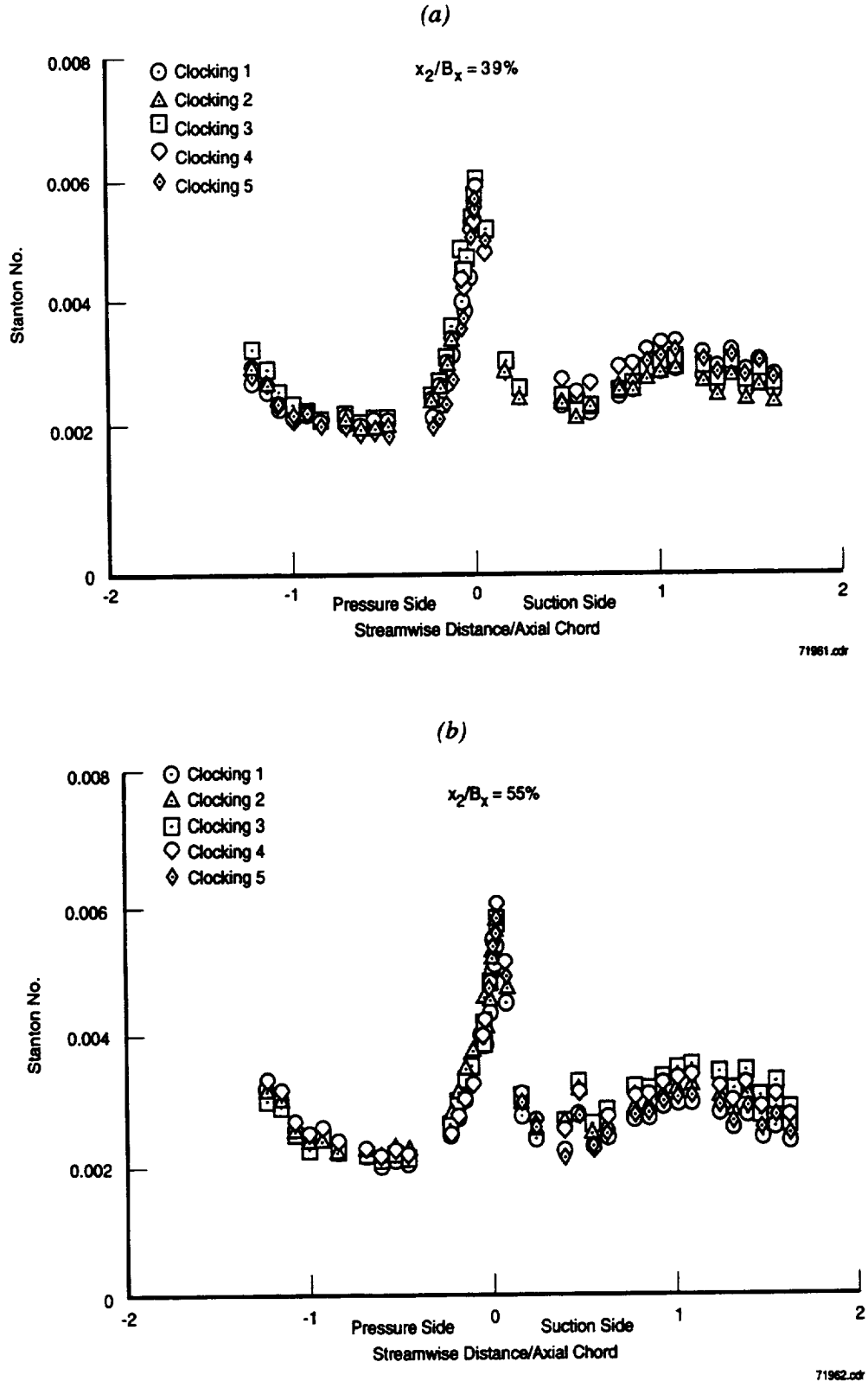

Figure 81. Heat Load on Second Stator Affected by Clocking (Between First and Second Stator)

(a) Strongly Influenced by Clocking Between First and Second Stator

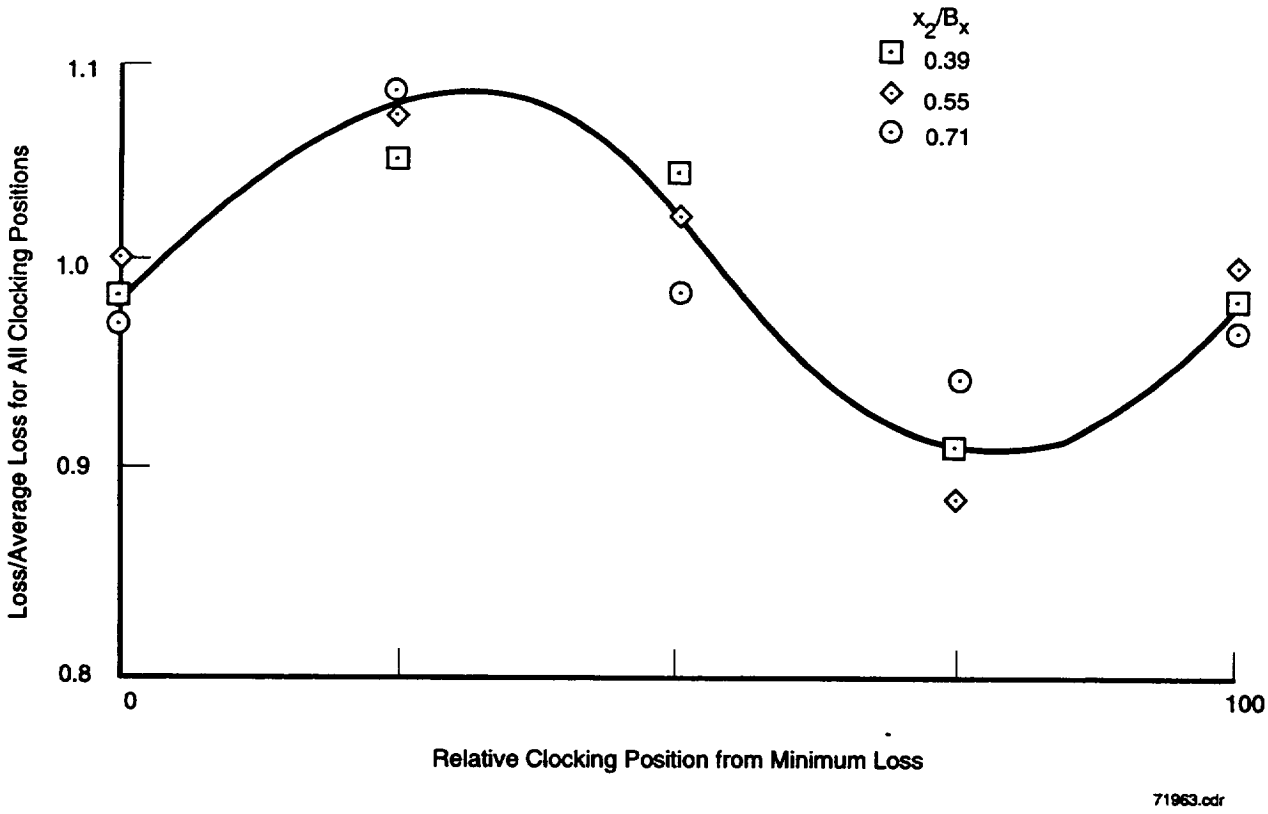

Figure 82. Midspan Performance of Second Stator

(b) Second Stator Midspan Loss and Heat Transfer Coefficient Correlates With Surface Unsteady Pressures

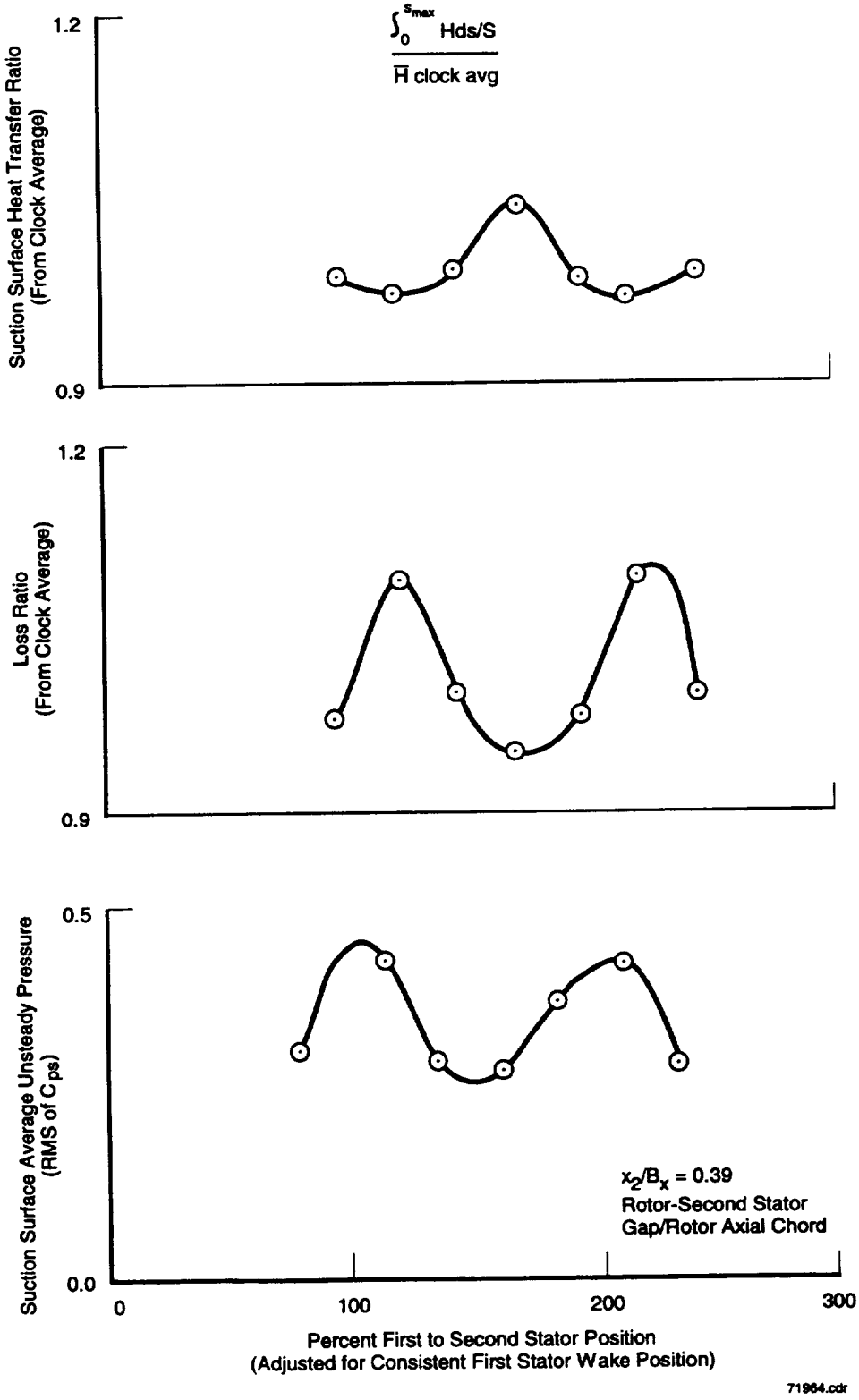

Figure 82 (Continued). Midspan Performance of Second Stator

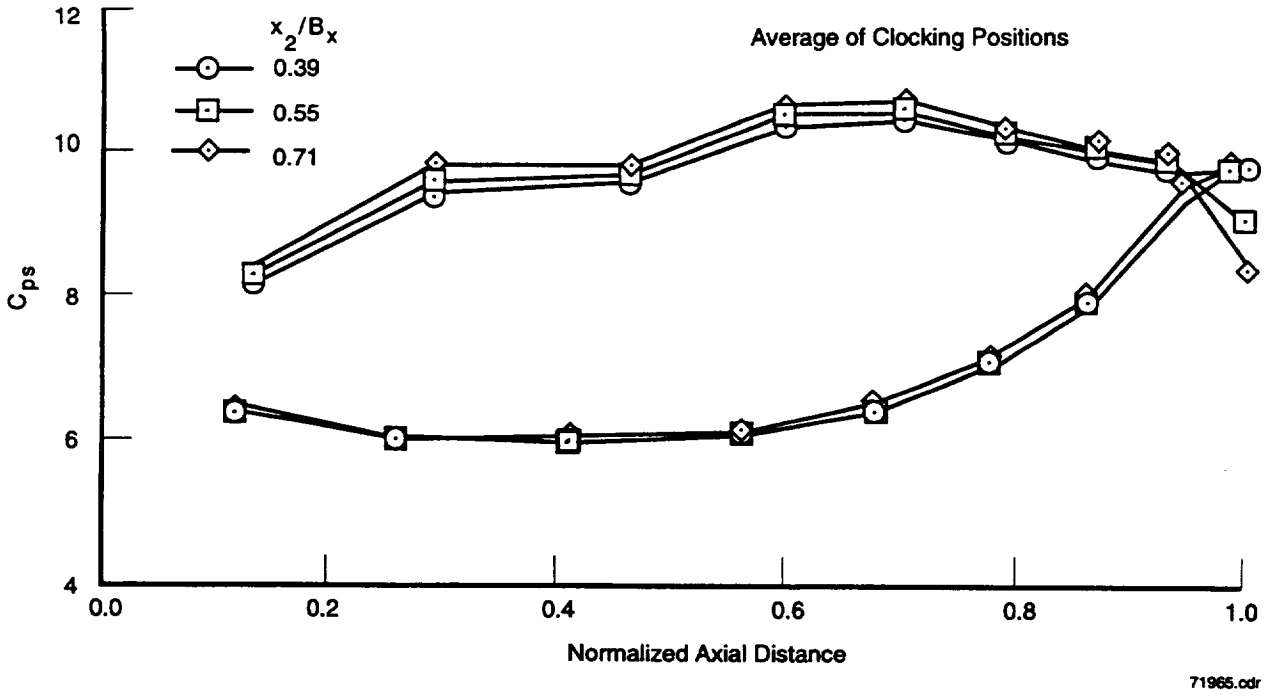

Figure 83. Loading on Second Stator Affected by Axial Spacing Between Stator and Upstream Rotor

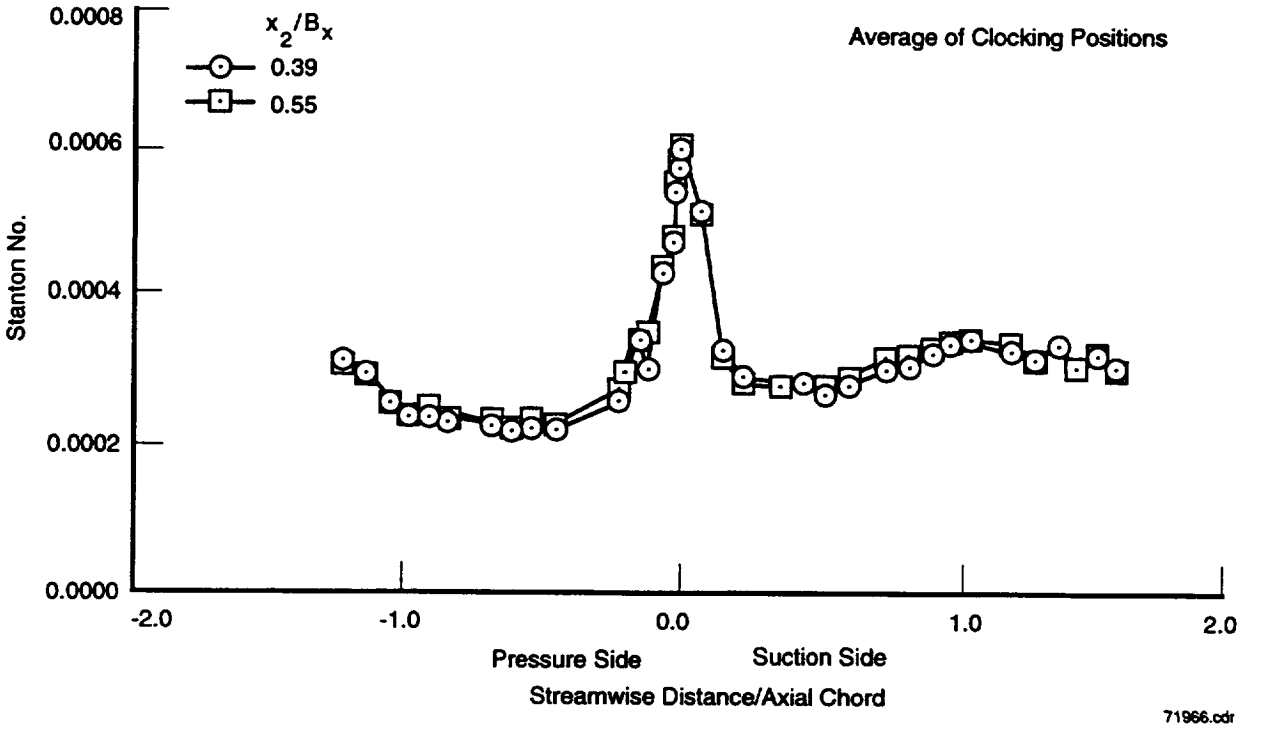

Figure 84. Heat Load on Second Stator Not Affected by Axial Spacing Between Stator and Upstream Rotor

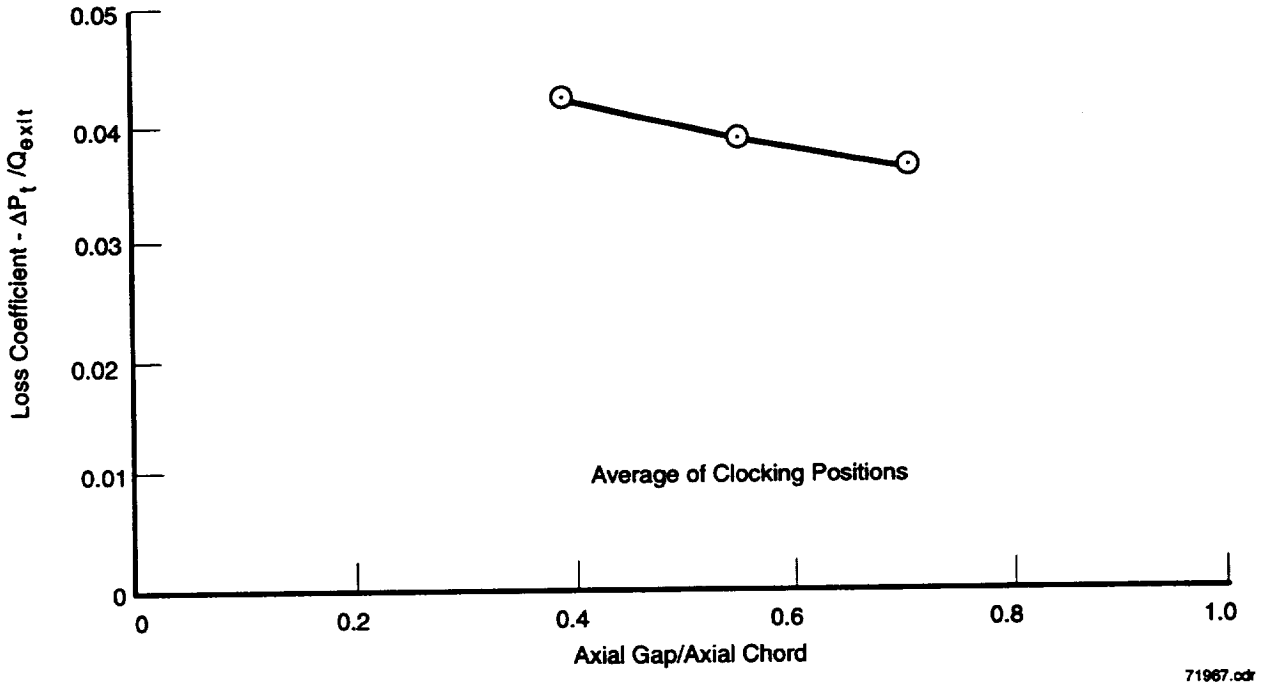

Figure 85. Second Stator Midspan Loss Shows Sensitivity to Axial Spacing Between Stator and Upstream Rotor

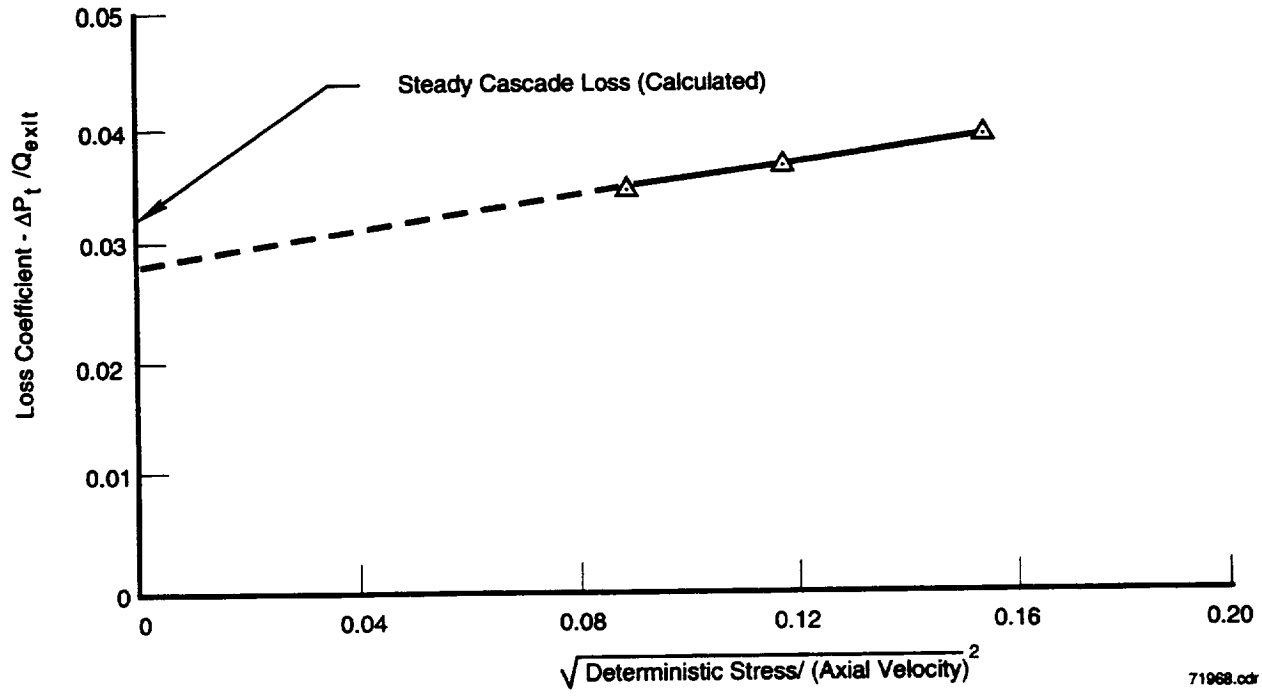

Figure 86. Loss for Second Stator Changes Linearly With Level of Deterministic Stress at Stator Inlet

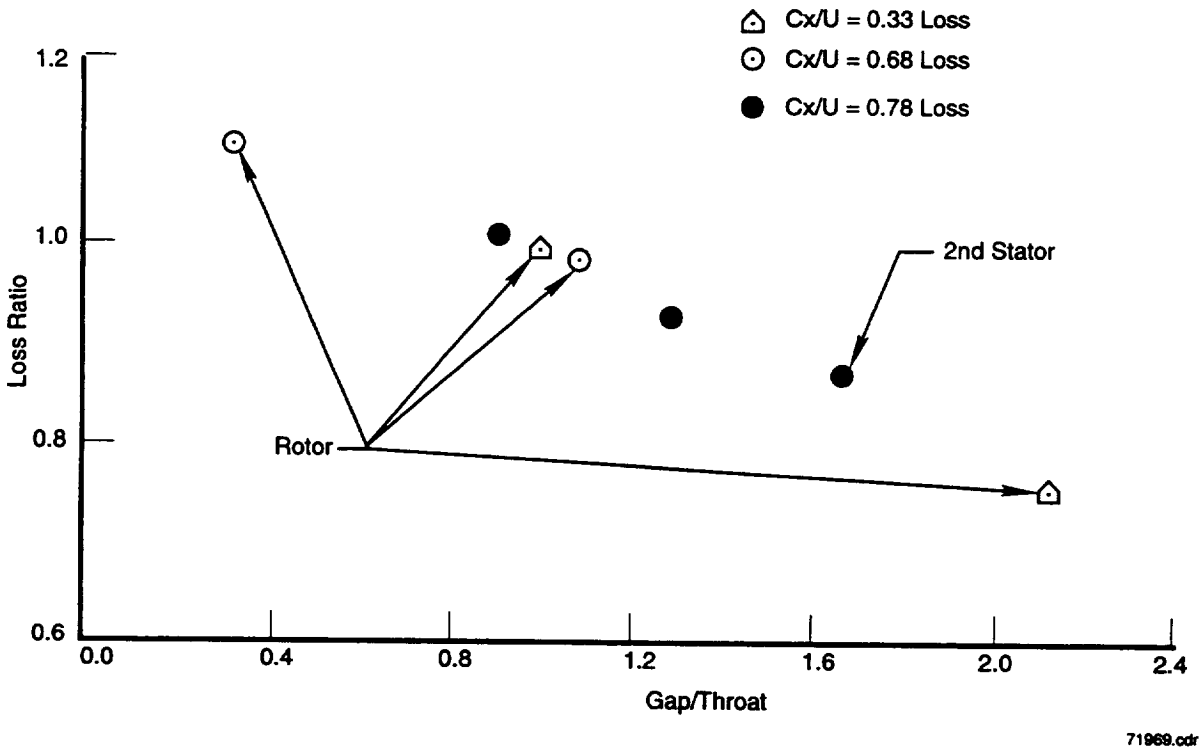

Figure 87. Normalized Loss for Rotor and Second Stator Indicates That Performance of Airfoil Is Strongly Affected by Its Distance from Upstream Airfoil

This Page Is Intentionally Left Blank

8. IMPACT ON DESIGN PROCEDURES AND ENGINE HARDWARE

This section provides an overview of the turbine aerodynamic design and analysis process, shortcomings of the process, advancements in understanding of flow physics, and how this understanding has been successfully used in the design of both a high-pressure turbine (HPT) and a high-pressure compressor (HPC) for a commercial engine aircraft application.

8.1 OVERVIEW OF TURBINE AERODYNAMIC ANALYSIS AND DEVELOPMENT

The evolution of the turbine design systems during the execution of this program is depicted in Figure 88(a). The tools used in the 1980s consisted of meanline and streamline flow solvers used to optimize the flowpath shapes and radial flow distributions. Two-dimensional (2-D) blade-to-blade flow prediction methods (potential and Euler flow solvers), combined with boundary layer codes, were used to optimize airfoil shapes for loss and heat load levels. Effects of periodic unsteadiness were accounted for in these codes (Sharma, et al. [12]) by assuming that the main impact of unsteadiness was to alter the nature of boundary layers (laminar-turbulent) on airfoil surfaces. (Airfoil pressure distributions were assumed to be unaffected by the periodic unsteadiness.)

The optimized 2-D airfoil sections were stacked in the radial direction to comply with structural requirements. Upon completion of the airfoil stacking, three-dimensional (3-D) multistage steady flow solvers (such as Ni's Euler code with *wall shear force* models) were used to analyze the configuration. The assessment of the design was based on a *figure of merit* (FOM) developed from extensive rig and engine testing. This FOM includes the following parameters:

- Pressure gradients along the airfoil surface and endwall
- Incidence angles
- Surface Mach number levels
- Surface Reynolds numbers
- Flow differences between streamline analysis and 3-D Euler analysis
- Curvature along the airfoil surface.

An additional FOM also included 2-D boundary layer calculations along airfoil surface slices along flow lines. This procedure yielded candidate turbine designs; the most promising designs were experimentally evaluated in rigs. Turbines designed through this process provided good performance, but typically required modifications to reflect less than optimal cooling designs because of the poor estimation of the airfoil heat load.

Experimental programs, conducted to investigate the impact of combustor-generated hot streak migration in turbine rotors (Sharma et al. [15]), clearly showed higher than average temperatures on the rotor airfoil pressure sides. Unsteady Euler codes were then added to analysis tools used in the turbine design process in the early 1990s, as indicated in Figure 88(b), defining the levels of adiabatic wall temperatures on rotor airfoil surfaces. These codes were used to conduct numerical experiments to enhance understanding of these flows and to develop FOM for managing hot streaks in turbines. An example is discussed in Section 5.4 — *Two-Dimensional Unsteady Euler and RANS Simulations for Turbines With Incoming Hot Streaks.*

Numerical experiments were conducted by Rangwala et al. [16] using an unsteady RANS code. These experiments showed (Figure 89) that time-averaged pressure distribution on the nozzle guide vane of a highly-loaded single-stage turbine was affected by the axial gap between the vane and downstream rotor. This result indicated that the airfoil surface static pressure distributions, predicted by a steady code, would most likely yield errors when applied in a supersonic flowfield. Since loading was used as an important ingredient for the FOM, unsteady codes (RANS and Euler) became an integral part of the design process for both defining loadings and determining the adiabatic wall temperatures.

Unsteady flow simulations were conducted for various HPTs from production engines. Ni's 3-D multistage unsteady Euler code indicated that poor performing turbines exhibited two to ten times the unsteady pressure fluctuations along airfoil surfaces, compared with better performing turbines, as indicated in Figure 90. Instantaneous and time-averaged pressure distributions from one of these turbines is shown in Figure 91. This time-averaged pressure distribution, along the airfoil surface, met the design intent and was considered a *good* pressure distribution. A visual comparison showed that the instantaneous pressure distribution did not display the same shape along the suction surface and, based on the understanding of *steady* flow (correlations and/or 2-D boundary layer theory), the instantaneous performance would be poor. This result indicated a need to quantify the impact of unsteady pressures on the loss generation.

Experiments were conducted in the United Technologies Research Center (UTRC) large-scale rotating rig (LSRR) to investigate the impact of axial spacing between the rotor and upstream stator on the performance of the rotor. Unsteady flow calculations (Euler) were conducted for these experimental configurations. Both numerical and experimental results are shown in Figure 92. The figure shows a reduction in total pressure loss for the rotor as the axial spacing between the rotor and the upstream stator was increased. A reduction in the amplitude of unsteady pressure was also predicted as the axial spacing between the rotor and stator was increased. This numerical and experimental evidence suggested that a reduction in the unsteady static pressure amplitude on the rotor had a beneficial impact on the performance.

An additional potential performance improvement concept was identified, while interrogating unsteady flow data from the UTRC LSRR (discussed in Section 4). A circumferential measurement of the unsteady flow entering the second stator, in the absolute frame, showed that the unsteadiness was not axisymmetric. This circumferential variation in unsteadiness is graphically shown in Figure 93 through the apparent viscosity (Equation 11). Based on this figure, it was hypothesized that the performance of the downstream stator was likely to be affected, depending on the circumferential position. Since the first stator was believed to be the cause of this circumferential variation, the concept of clocking (indexing) of the two stator rows was established.

Physical experiments were conducted for a rocket turbine at National Aeronautics and Space Administration-Marshall Space Flight Center (NASA-MSFC) to investigate the effect of clocking on the two-stage turbine performance. Results from this investigation (Sharma et al. [12], Huber et al. [11]), plotted in Figure 94, indicate that the midspan performance of the turbine changes by 0.4 percent by clocking the two stator airfoils. Results from numerical simulations conducted for this configuration by using Ni's unsteady 2-D RANS code are also shown in this figure. The variation in performance, predicted by the RANS code, was lower than measured, but displayed similar characteristics to the measured data. In addition, levels of unsteady airfoil surface static pressures for the second stator indicated that higher efficiency (lower loss) occurred when there were lower levels of unsteady pressures. Results indicated a reduction in unsteadiness on the airfoil surfaces was likely to have a beneficial effect on the performance of the turbine (Figures 90 through 94).

8.2 UNSTEADY AERODYNAMIC ENGINE APPLICATION

The HPT used in large commercial aircraft engines was redesigned by using *managed hot-streak* and *wake-management* (clocking and axial spacing) concepts discussed above. The flowpath cross-sections are shown in Figure 95. The turbine was designed to minimize the envelope of unsteady pressures on airfoil surfaces, clock the first to second rotor, and align the hot streak with the first stator. The change in the efficiency measured from this redesign exercise, shown in Figure 96, demonstrated that the concepts developed during the execution of this program have yielded at least 1.5-percent improvement in the efficiency of the HPT. The first rotor airfoil pressure side has been measured to be at least 80°F cooler, relative to the baseline design for the same rotor inlet temperature. The observed reduction in rotor pressure side metal temperature was approximately what was expected, based on results from the unsteady Euler code and applying the expected effect of cooling flow. The cooler rotor airfoil pressure surface temperature can either be traded for improved performance with the same life, or substantial improvement in life with the same performance.

Multistage RANS codes, with *mixing-plane* approach by using the strategy to simulate flow through one representative airfoil passage in each airfoil row, were used to predict the flowfield of turbines. Significant gains in performance have been realized since the introduction of these codes.

8.3 HIGH-PRESSURE COMPRESSOR APPLICATION

Multistage RANS codes have also been used to enhance the performance and stability of an HPC. Loss generation mechanisms in compressor airfoil rows were typically dominated by flow separation in the endwall regions (viscous boundary layer and/or tip clearance induced separation). These separation regions were normally on the order of the pitch of the airfoil, which can be fairly well captured by the state-of-the-art turbulence models and grid structures. Flow in endwall regions in compressors separated much earlier than on the airfoil surfaces (i.e., midspan region). Therefore, inaccuracy in resolving airfoil boundary layers (laminar – transitional – turbulent) never limited the performance predictive capabilities of the codes. A review of the development work for an HPC was outlined by Coons [17] and LeJambre et al. [18], and indicated that the application of multistage RANS codes has lead to the improvement in performance and stability of an 11-stage HPC.

Flow through an existing 11-stage HPC was analyzed by using a 3-D, steady multistage RANS code with *mixing plane* boundary conditions. Flow simulations showed large regions of separated flows in the endwall regions, as shown in Figure 97. Stator airfoils were *bowed,* and shapes of endwalls on rotor roots were contoured to eliminate predicted separations in endwall regions at the design point (Figure 98 [a] and [b]). The HPC (shown in Figure 99 was tested and found to yield up to 2 percent improvement in the efficiency. Stall margin was lower than the goal, but it was in good agreement with experience, as indicated in Figure 100. Analysis of the experimental data from the rig indicated a deficit of flow in the tip region of the HPC Build 1, which may have been responsible for stall margin (Figure 101).

Numerical simulations were conducted for the HPC by using Rhie's [19] steady, 3-D multistage RANS code. Modifications to the code were necessary to account for the effects induced by adjacent airfoil rows (in terms of body forces and deterministic stresses), using simplified versions of terms developed by Adamczyk [1]. Effects due to rotor tip clearances were also modeled in the Rhie code. Results from these simulations (Figure 101) indicated flow separation in the outer regions of the stators. Two subsequent builds of the HPC were tested by implementing stator root cutbacks to redistribute flow toward the tip for the middle and the rear of the HPC. Measured results from the rig tests (Figure 102) demonstrated improvement in the stall margin of the machine, while maintaining the performance measured in the first build of the rig. This effort has demonstrated that 3-D steady multistage RANS codes, with simple models to account for the effects induced by adjacent airfoil rows, can be used to enhance the performance and stability of HPC.

8.4 SUMMARY

The examples discussed in this section indicate that enhancement in the design procedures for both turbines and compressors over the last five years (the duration of the contract) have resulted in hardware changes. A reduction of almost 2.25 percent has been realized in specific fuel consumption for engines used in commercial aircraft. Although these enhancements were not developed directly under this contract, the technical efforts and improved understanding developed through this contract have played an important role in these demonstrated successes. In addition, new areas of opportunities have been identified to further improve the performance, stability, and durability of machines.

(a) Turbine Design System - Late 1980s

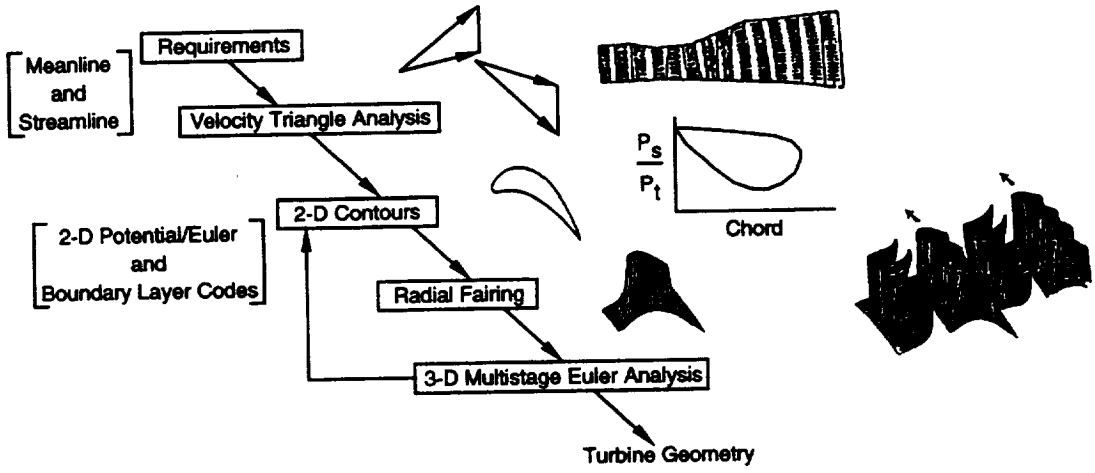

(b) Turbine Design System - Current Status

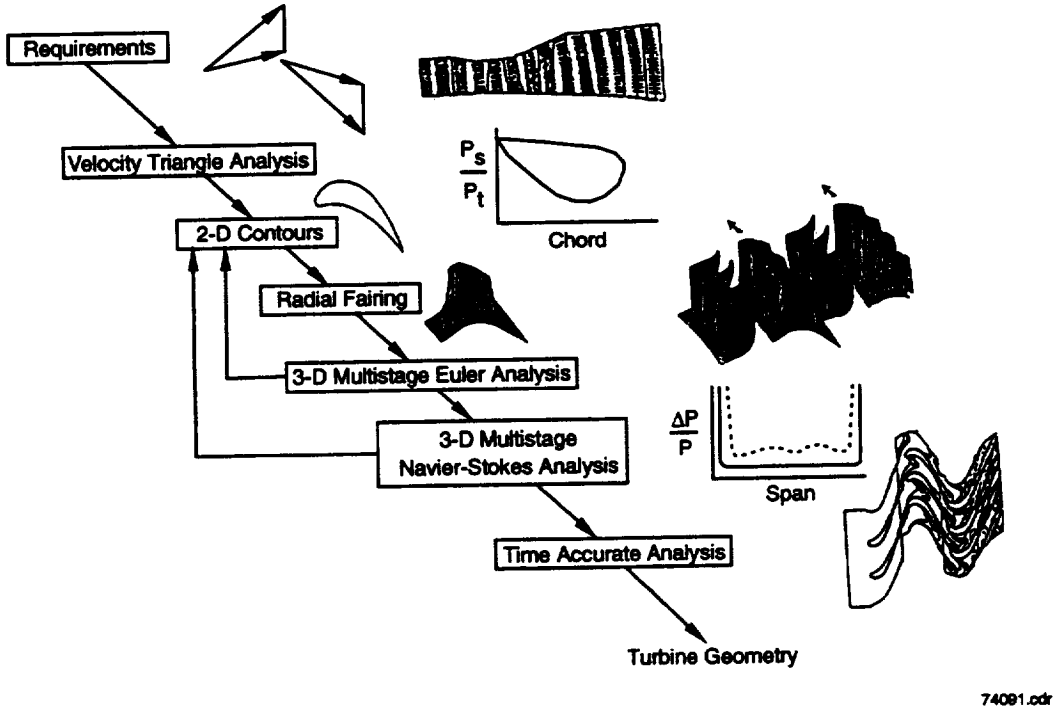

Figure 88. Turbine Aerodynamic Design Process Evolution

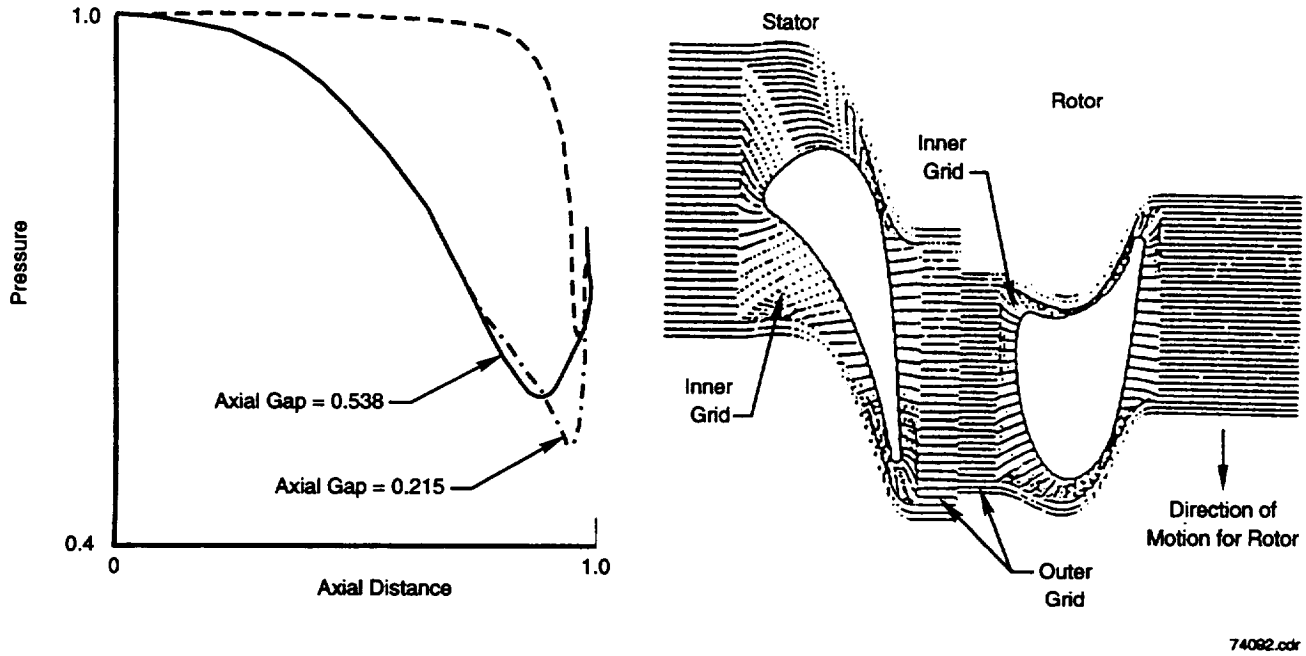

Figure 89. Time-Averaged Static Pressures on Upstream Stator Are Affected by Axial Gaps Between Stator and Rotor Airfoils

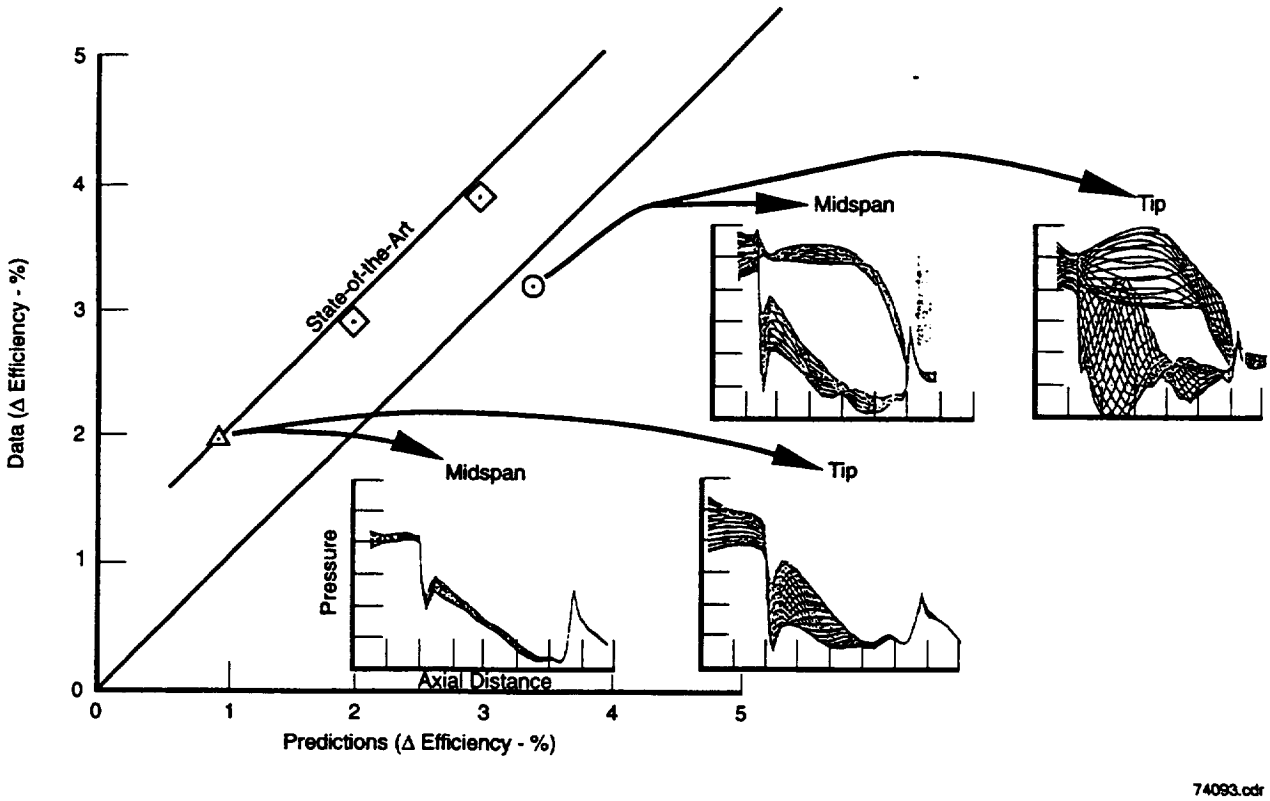

Figure 90. Turbine With Poorer Performance Calculated To Have Higher Levels of Unsteadiness of Airfoil Pressures; Results Obtained by Using Ni's 3-D Multistage Unsteady Euler Code With Surface Shear

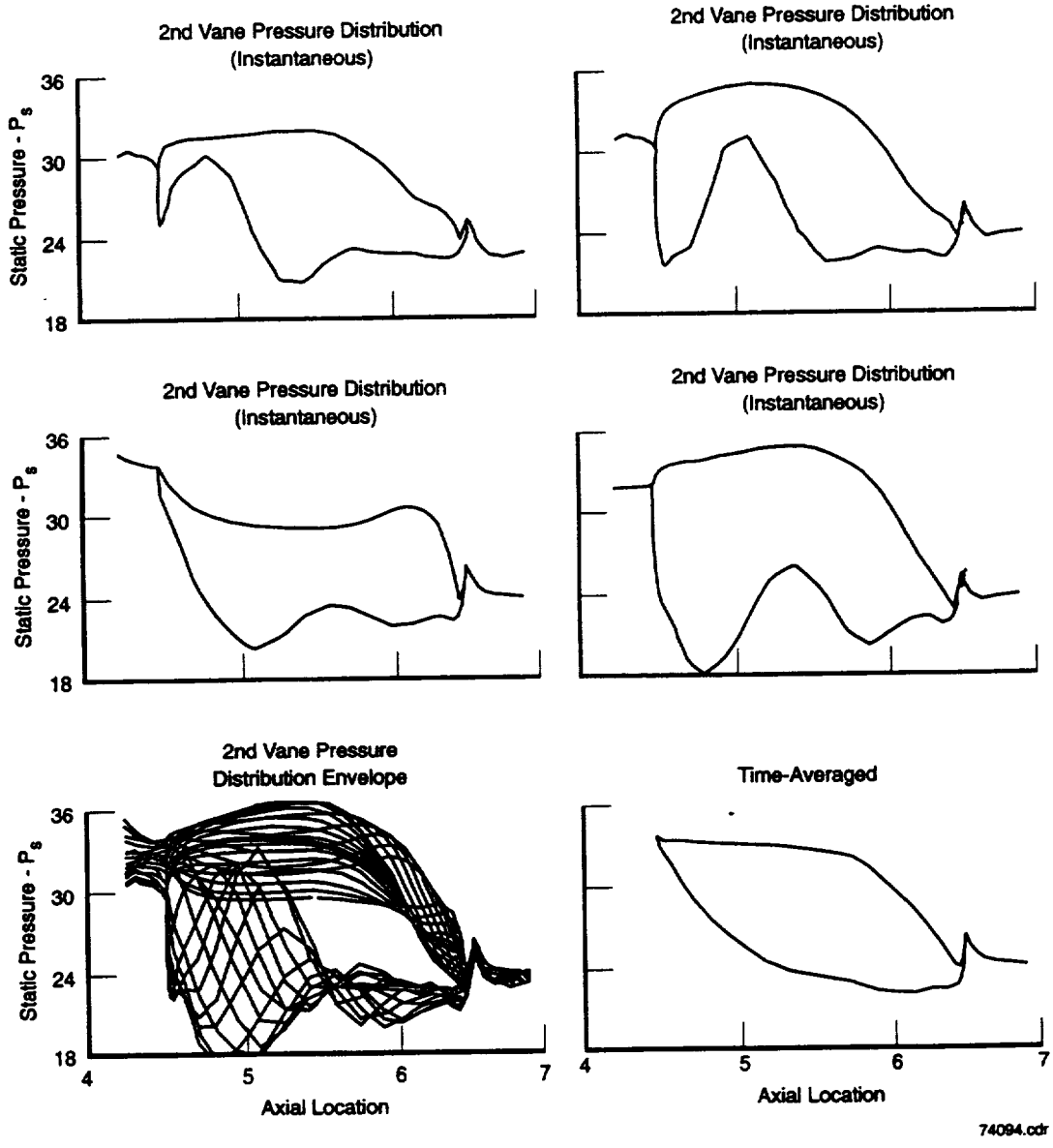

Figure 91. Predicted Unsteady Pressures on Second Stator of Two-Stage HPT Show Good Time-Averaged Pressure Distribution Shapes

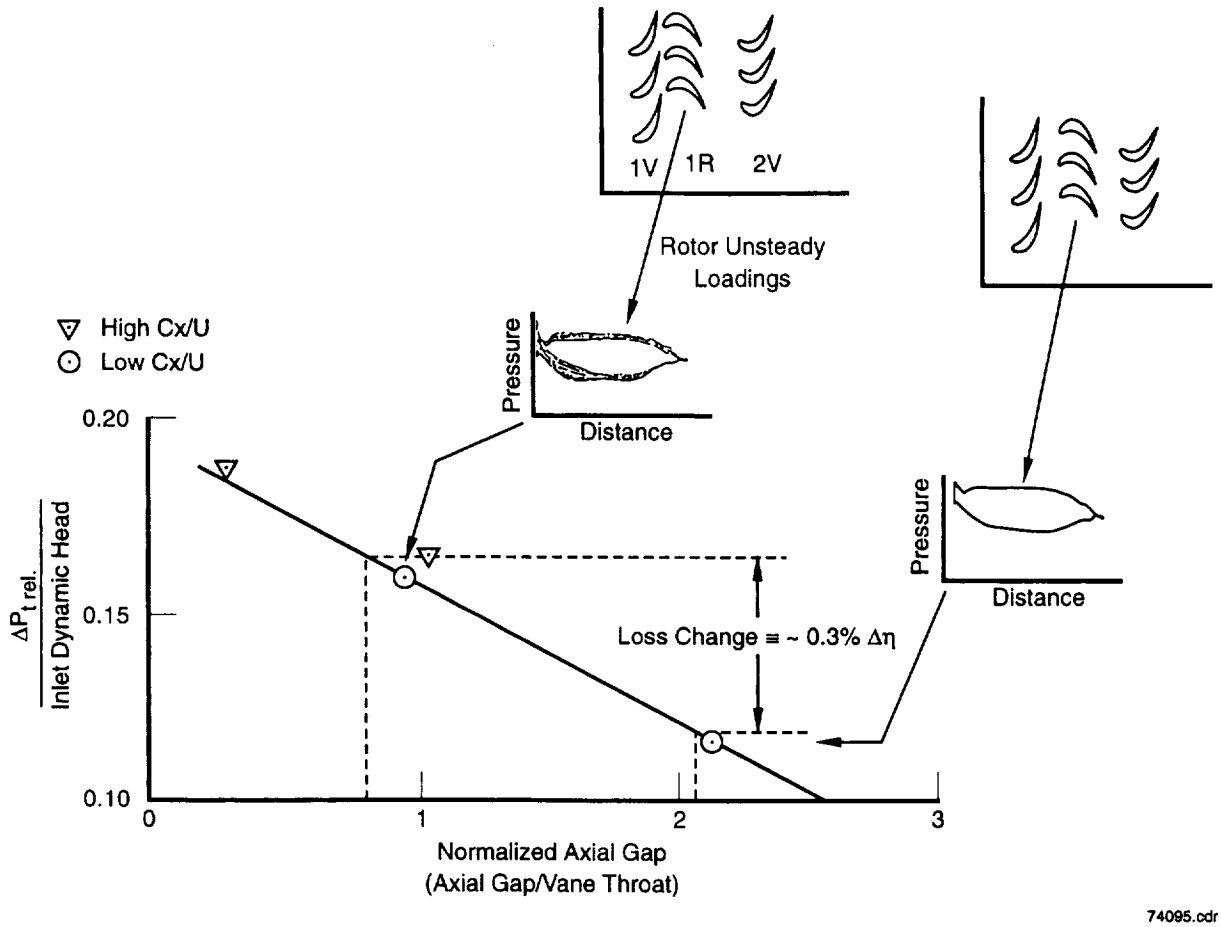

Figure 92. Rotor Loss in LSRR Affected by Spacing Between Rotor and First Stator

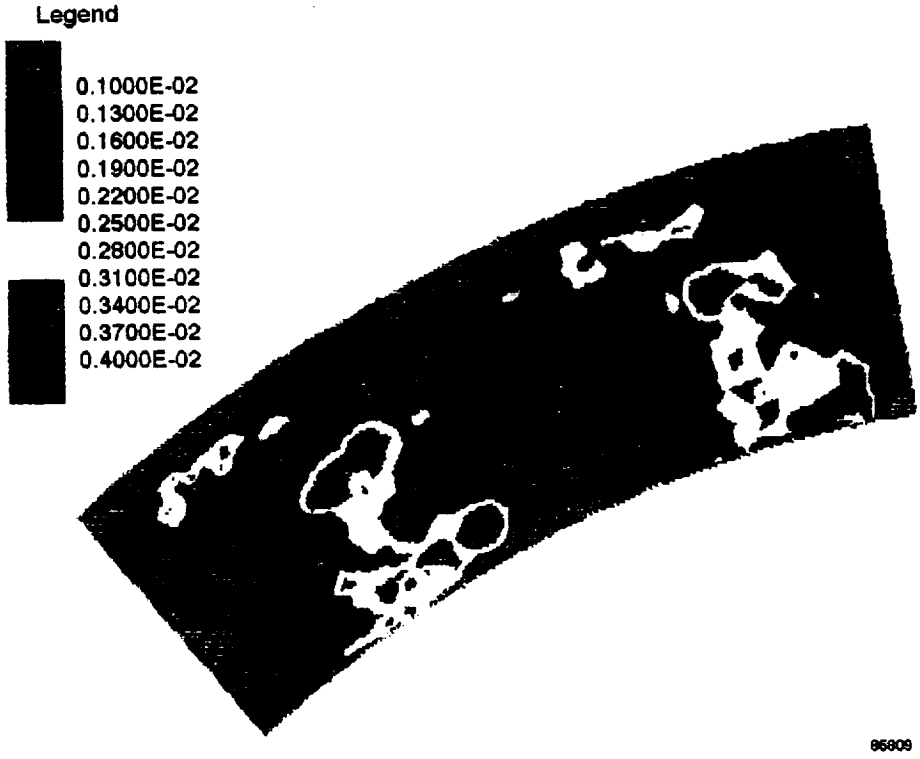

Figure 93. Apparent Viscosity Contours, Downstream of Rotor in Absolute Frame, Indicate Presence of Upstream Stator Wake; It Was Hypothesized That There May Be a Performance Benefit Achievable Through Clocking the Upstream Stator Relative to Second Stator

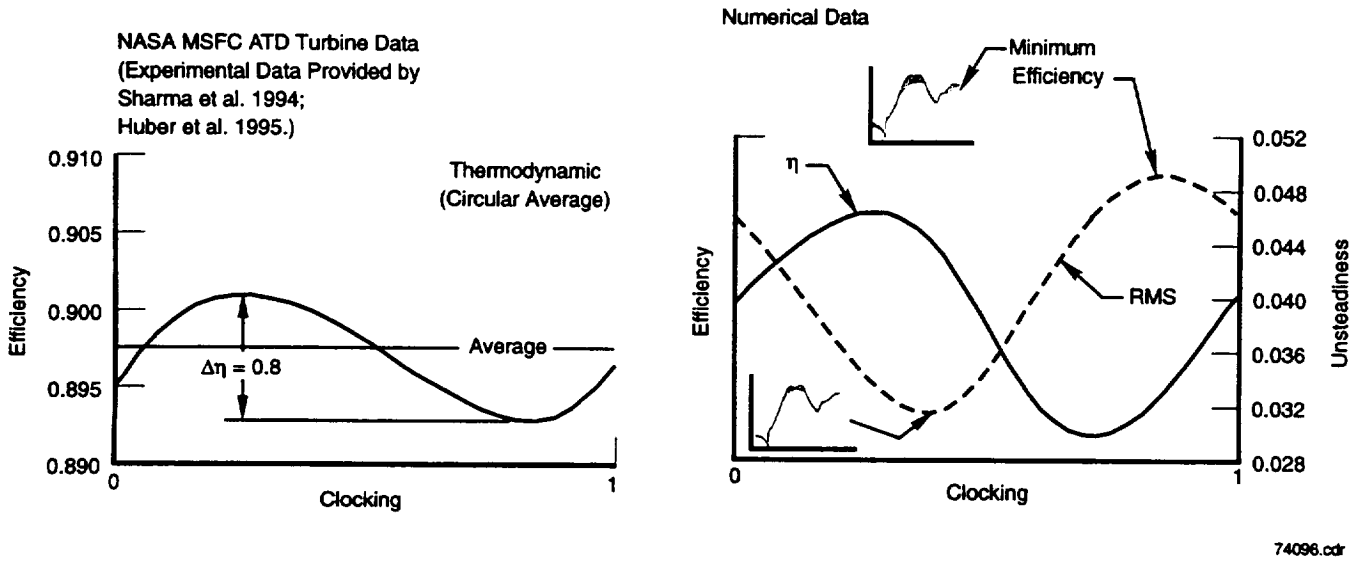

Figure 94. Numerical Simulations Provide Qualitative Impact of Stator Clocking (i.e., The Lower the Average Airfoil Surface Pressure Fluctuations, the Better the Efficiency)

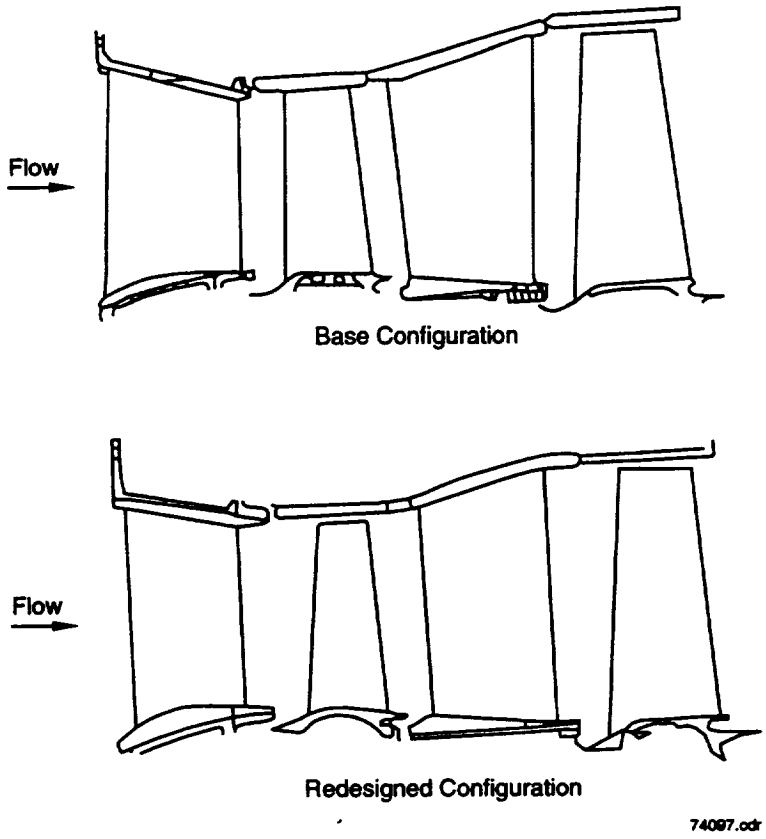

Figure 95. Elevations of Base and Redesigned HPTs

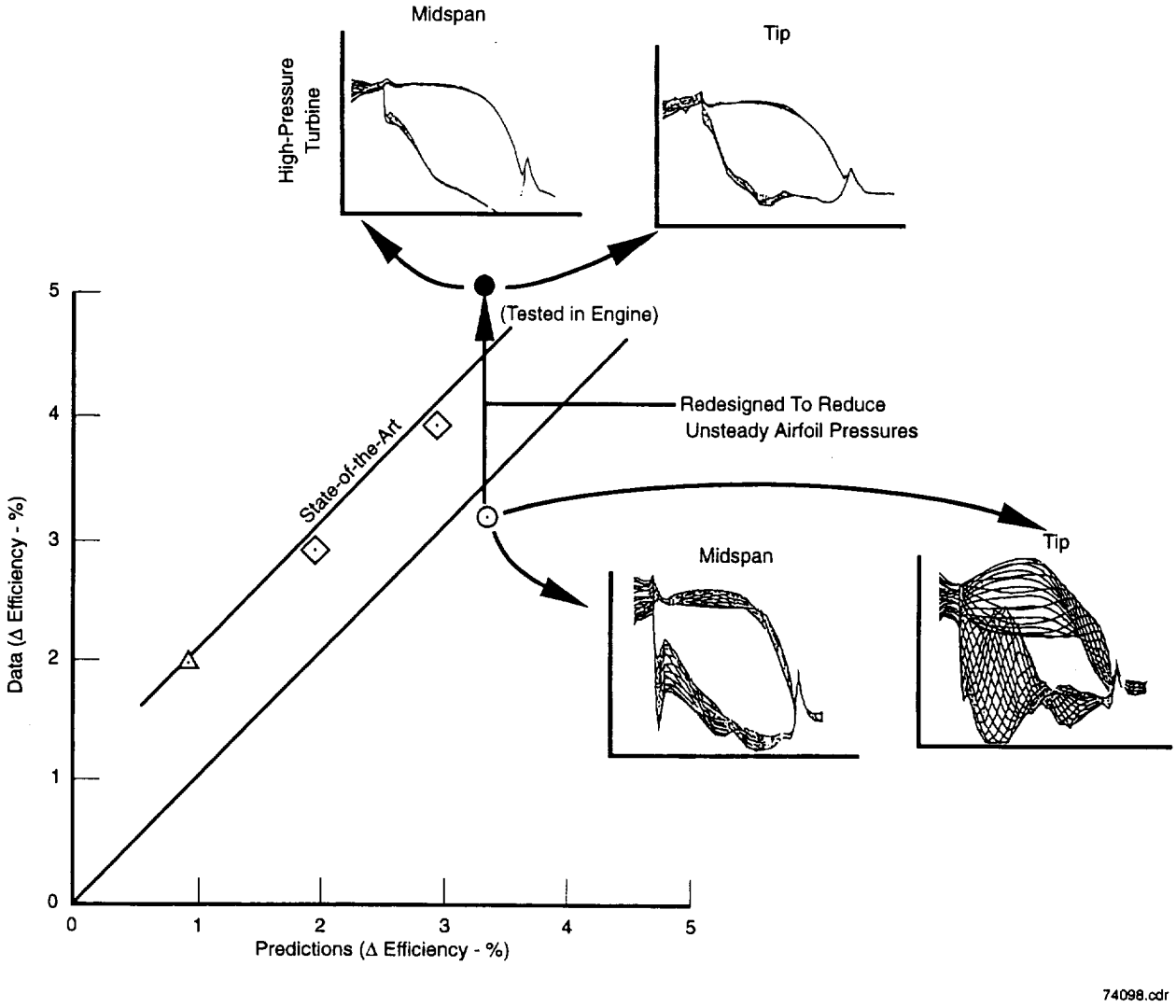

Figure 96. HPT Redesigned To Minimize Unsteadiness on Airfoils With Resulting Efficiency Improvement

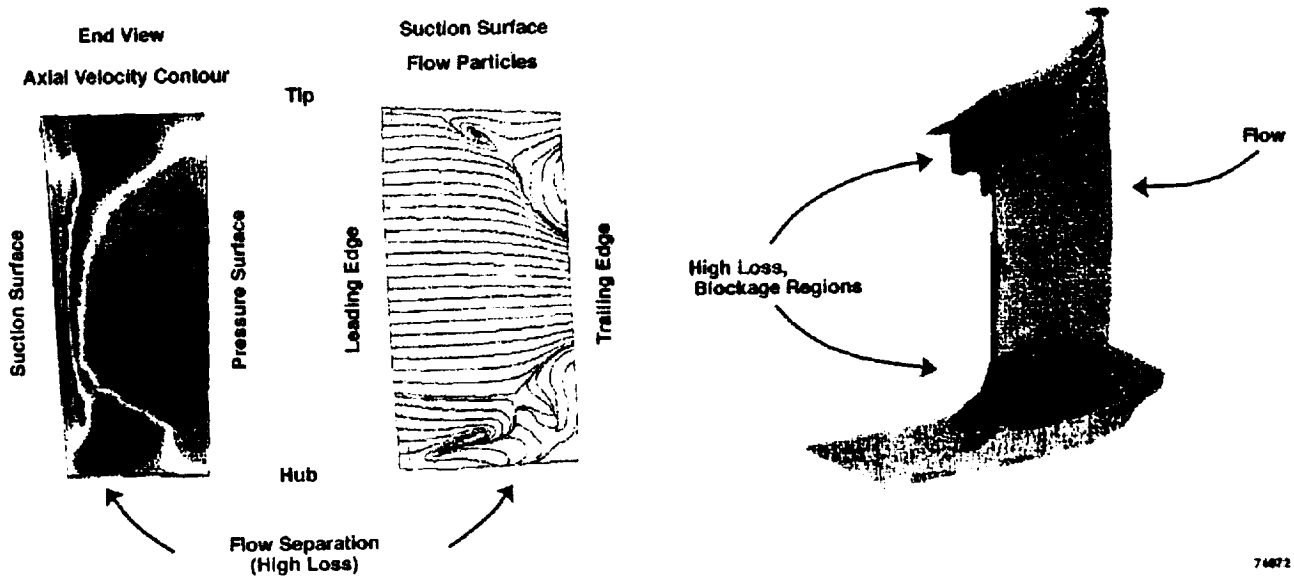

Figure 97. Numerical Stimulations Predict Large Regions of Separation for Baseline Compressor Stators in Endwall Regions

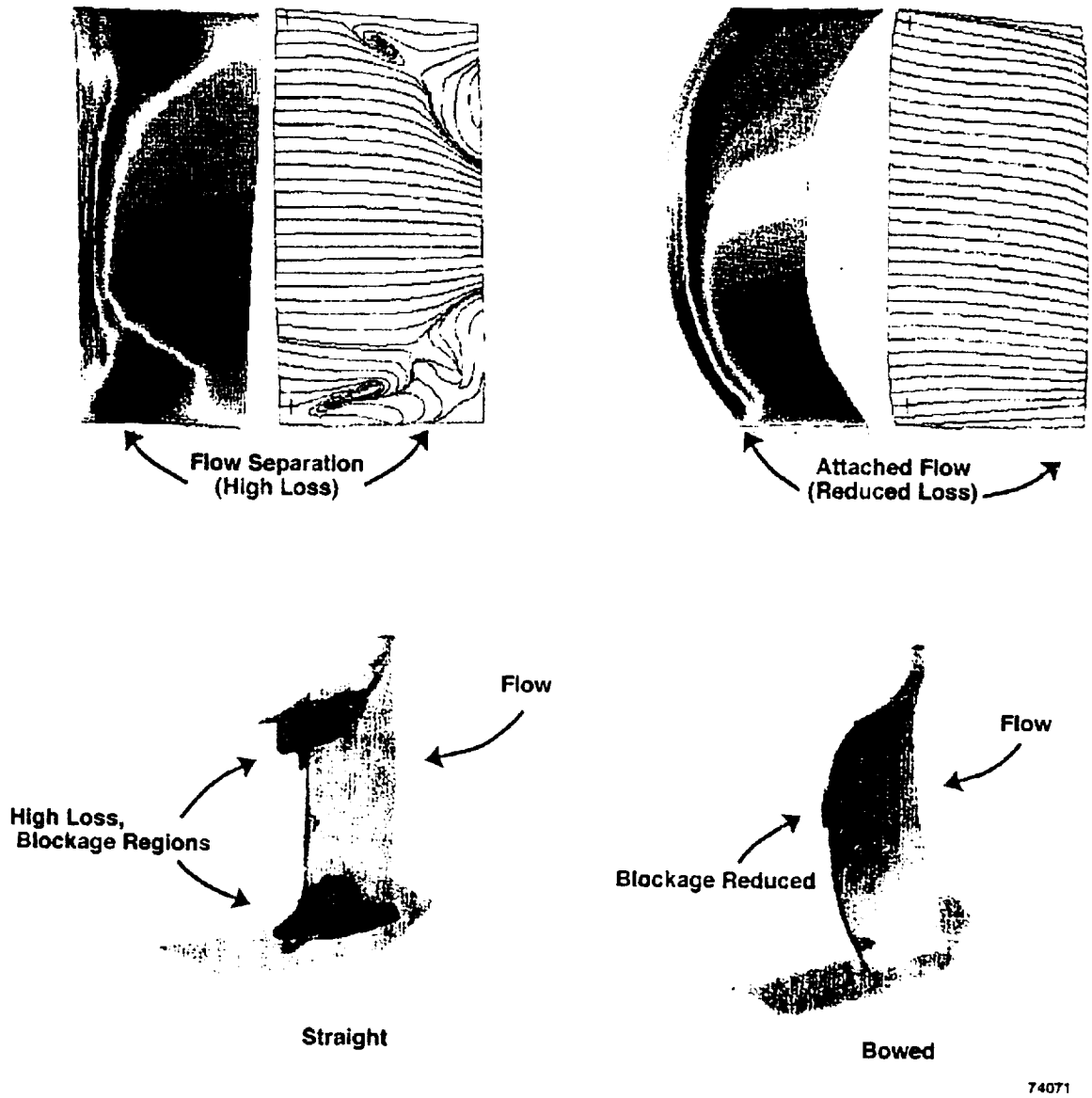

Figure 98. 3-D Multistage RANS Code (Rhie et al. [1995]) Used To Minimize Losses in Endwall Regions

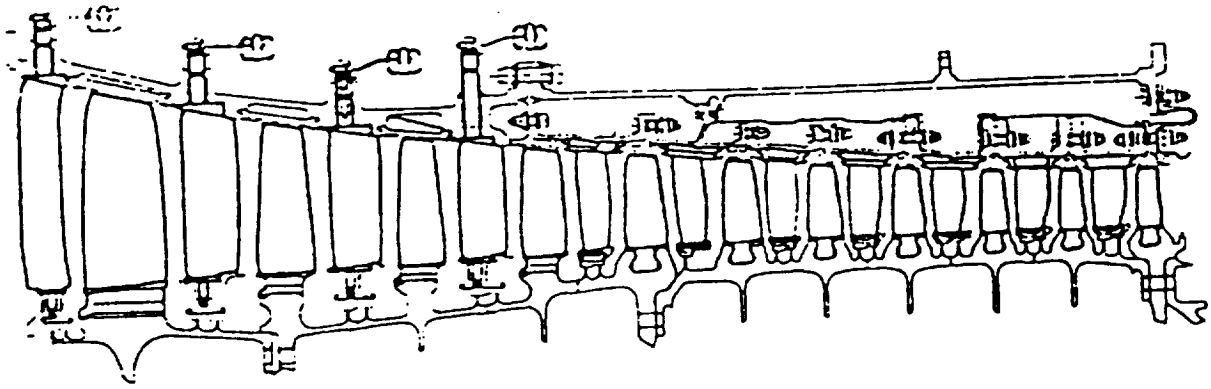

Designed Point Comparisons

	Baseline Compressor	Redesigned Compressor
Inlet Corrected Flow	120 lb/sec	120 lb/sec
Pressure Ratio	10:1	10:1
Solidity		
• Rotors	1.095	1.201
• Stators	1.208	1.348
Axial Mach Number		
• Inlet	0.54	0.54
• Exit	0.23	0.23
Mean Wheel Speed	950 ft/sec	950 ft/sec

74099.cdr

Figure 99. Cross-Section of Baseline and Redesigned Compressor (LeJambre, et al. [1995])

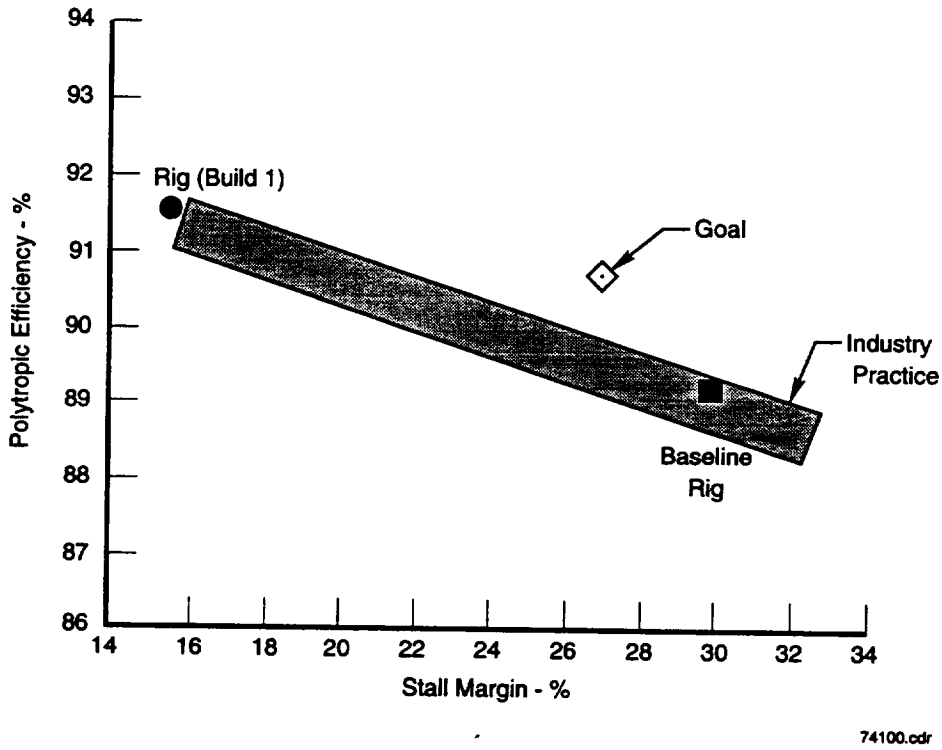

Figure 100. HPC Rig Build 1 Performance and Stall Margin Consistent With Practice

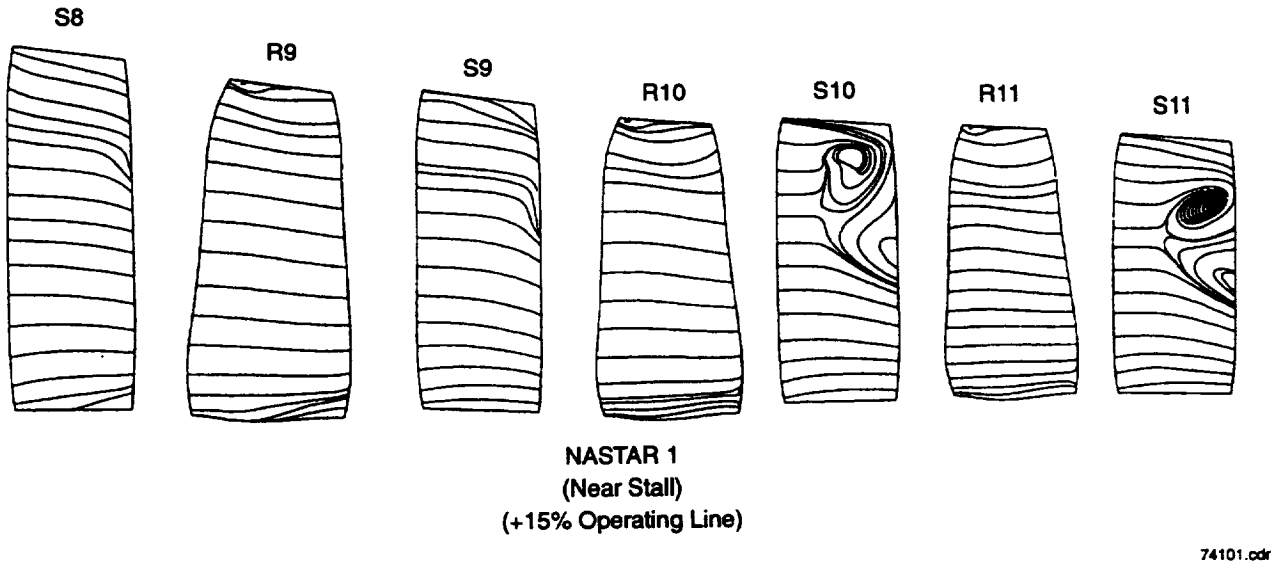

Figure 101. Flow Simulations Conducted by Using Multistage RANS Code (Rhie et al., [1995]) Identified Flow Separations in Tip Regions

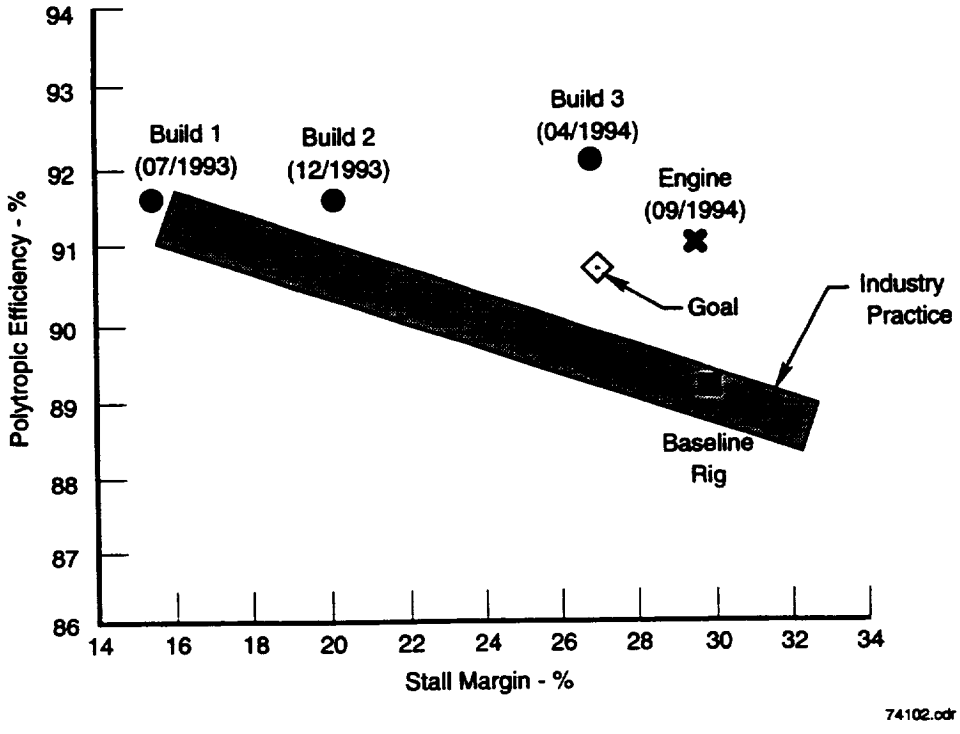

Figure 102. HPC Goals Achieved as Demonstrated in Rig and Engine Testing in Record Time Using Multistage RANS Code and New Development Process

9. CONCLUSIONS AND RECOMMENDATIONS FOR FUTURE WORK

Although real flows in turbomachinery are highly unsteady, due to relative movements of adjacent airfoil rows and circumferential gradients in total pressure and total temperatures, steady flow predictions methods are historically used in the design optimization processes. The effects of unsteadiness are implicitly accounted for in the design process through *empirical correlations* and *experience factors*. The inability to properly account for the flow physics in these correlations and factors invariably leads to non-optimal designs, requiring extensive development times and costs. The objective of the present investigation was to develop analysis procedures that accounted for these unsteady flow effects explicitly in the design process through *deterministic stress/flux terms*, shown by Adamczyk [1], in the equations of motion.

This investigation consisted of analyzing unsteady flow data available from previous work at Pratt & Whitney (P&W), execution of numerical experiments to assess affects of boundary conditions and unsteady flow management concepts, and execution of physical experiments to quantify impact of clocking and spacing (*deterministic stress*) on performance and heat load of airfoil rows in a multistage environment. The following conclusions can be derived from the studies conducted as a part of, and in collaboration with, the present program.

Performance and heat load characteristics of an airfoil row are affected by its relative circumferential position (clocking) to the upstream airfoil row. A ±10 percent change in loss equivalent to a ±0.25 percent change in efficiency of a typical two-stage turbine can be expected as a result of this clocking effect. The change in loss due to clocking can be correlated to the level of unsteadiness on the airfoil surface (the larger the unsteadiness, the higher the loss). A reduction of unsteadiness on the airfoil surface invariably results in improved performance. Performance of an airfoil row is affected by the magnitude of periodic unsteadiness (*deterministic stress*) at inlet to that airfoil row. An increase in inlet deterministic stress results in increased loss for the airfoil row, and therefore, should be accounted for in a design process. Adverse effects of combustor generated hot streaks on the turbine performance and the rotor heat load can be minimized by aligning the hottest regions of the combustor to the nozzle guide vane. To ensure realistic prediction of flow through multistage turbomachines, flow through one *representative period* (not one representative passage) needs to be simulated. To model the impact of unsteadiness, a procedure is proposed to compute *deterministic stresses/fluxes* from a coarse grid unsteady Euler simulation and incorporate these terms into a steady multistage RANS simulation. This will account for the effects of large-scale flow features, such as hot streaks, and potential effects on the flow evolution through turbines. RANS steady multistage codes are superior to *viscous* multistage steady Euler codes in predicting inlet boundary conditions to the next airfoil row, exit flow distortions (secondary flow), and exit gas angle distributions.

In summary, a need to account for the effects of periodic unsteadiness was demonstrated for a turbine second stator through improved performance (loss) and reduced heat load. Two percent improvement in the compressor efficiency was achieved through the incorporation of body forces and stress terms in a steady multistage RANS code. Modeling of the effects of body forces from adjacent row airfoils also resulted in improved calculation of the pressure rise through compressor rotors.

The studies conducted as a part of, and/or in collaboration with, the present program contributed to increased understanding of the effects of unsteadiness and have resulted in performance improvements in turbomachines.

This Page Is Intentionally Left Blank

10. REFERENCES

1. Adamczyk, J.J., *Model Equation for Simulating Flows in Multistage Turbomachinery,* ASME Paper No. 85-GT-226, 1985.

2. Sharma, O.P.; Butler, T.L.; Joslyn, H.D.; and Dring, R.P., *Three-Dimensional Unsteady Flow in an Axial Flow Turbine,* Journal of Propulsion and Power, Volume 1, No. 1, January-February 1985.

3. Donaldson, S.N., *Comparison Deterministic and Turbulent Stresses in a 1 1/2-Stage Low-Speed Research Turbine,* Master's Thesis, University of Connecticut, 1993.

4. Hinze, J.O., *Turbulence — An Introduction to Its Mechanism and Theory,* McGraw-Hill, New York, 1959.

5. Joslyn, H.D., and Dring, R.P., *Three-Dimensional Flow and Temperature Profile Attenuation in Axial Flow Turbine,* United Technologies Research Center, Report No. R89-957334-1, 15 March 1989.

6. Ni, R.H., and Bogoian, J.C., *Prediction of 3-D Multistage Turbine Flow Field Using a Multiple-Grid Euler Solvers,* AIAA Paper No. 89-0203, 1989.

7. Denton, J.D., *The Use of a Distributed Body Force To Simulate Viscous Flow in 3-D Flow Calculations,* ASME Paper No. 86-GT-144, 1986.

8. Rhi, C.M., *A Pressure Based Navier-Stokes Solver Using the Multi-Grid Method,* AIAA Paper No. 86-0207, 1986.

9. Butler, T.L.; Sharma, O.P.; Joslyn, H.D.; and Dring, R.P., *Redistribution of an Inlet Temperature Distortion in an Axial Flow Turbine Stage,* Journal of Propulsion and Power, Vol. 5, pp. 64-71, 1989.

10. Dring, R.P.; Blair, M.F.; and Joslyn, H.D., *The Effects of Inlet Turbulence and Rotor Stator Interactions on the Aerodynamics and Heat Transfer of a Large-Scale Rotating Turbine Model,* NASA CR-179468, May 1986.

11. Huber, F.W.; Johnson, P.D.; Sharma, O.P.; Staubach, J.B.; and Gaddis, S.W., *Performance Improvement Through Indexing of Turbine Airfoils - Part 1 - Experimental Investigation,* ASME Paper No. 95-GT-27, 1995.

12. Sharma, O.P.; Ni, R.H.; and Tanrikut, S., *Unsteady Flows in Turbines - Impact on Design Procedures,* AGARD-LS-195, 1994.

13. Ravindranath, A., and Lakshminarayana, B., *Structure and Decay Characteristics of Turbulence in Near and Far Wake of a Moderately Loaded Compressor Rotor Blade,* ASME 80-GT-95.

14. Schlichting, H., *Boundary-Layer Theory,* McGraw-Hill, Seventh Edition, New York, reissue, 1987.

15. Sharma, O.P.; Renaud, E.; Butler, T.L.; Milsaps, K.; Dring, R.P.; and Joslyn, H.D., *Rotor-Stator Interaction in Multistage Axial-Turbines,* AIAA Paper No. 88-3013, 1988.

16. Rangwalla, A.A.; Madavan, N.K.; and Johnson, P.D., *Application of Unsteady Navier-Stokes Solver to Transonic Turbine Design,* AIAA Paper No. 2468, 1991.

17. Coons, L., *Large Commercial Engine Turbomachinery Design Using a Fully Viscous Navier-Stokes Code,* Proceedings of the Colloquium on Turbomachinery Turbo and Power Machinery Research Center, Seoul National University, Seoul, Korea, pp. 83-114, 1994.

18. Lejambre, C.R., Zacharias, R.M., Biederman, B.P., Gleixner, A.J., and Yetka, C.J., *Development and Application of a Multistage Navier-Stokes Solver, Part II: Application to a High Pressure Compressor Design*, ASME No. 95-GT-343, 1995.

19. Rhie, C.M.; Gleixner, A.J.; Spear, D.A.; Fischberg, C.J.; and Zacharias, R.M., *Development and Application of a Multistage Navier-Stokes Solver, Part I: Multistage Modeling Using Bodyforces and Deterministic Stresses*, ASME No. 95-GT-342, 1995.

20. (Reference for Appendix C) Joslyn, D. and Dring, R.P., *Three-Dimensional Flow in an Axial Turbine: Part 1 - Aerodynamic Mechanisms*, J. of Turbomachinery, Vol. 114, 1992, pp. 61-70.

APPENDIX A — DISCUSSION OF EXPERIMENTAL DESIGN APPROACH

Three approaches were used to investigate whether deterministic stresses influence the performance of the second stator in the large-scale rotating rig (LSRR) configuration. These concepts were developed in parallel with the acquisition of the new baseline data (28 first stators).

A.1 APPROACH 1

In the first approach, the second stator was redesigned to minimize the heat load and aerodynamic loss.

Analysis indicated that the inlet vorticity from the rotor may be critical in determining the second stator performance. The design philosophy was, therefore, to create a uniform second stator exit gas angle distribution to minimize the gap-average spanwise vorticity. To achieve this distribution, three-dimensional (3-D) Euler and Navier-Stokes codes were used to analyze the flowfield from airfoil geometry designed using the Pratt & Whitney (P&W) airfoil design system. The 3-D analysis incorporated measured inlet boundary conditions from the original 1 1/2-stage configuration (22 first stators) and the average exit static pressure previously measured.

Multiple airfoil cross-sections were explored in conjunction with various spanwise stacking of the cross-sections; the final configuration is shown in Figure 103. The resulting exit angles, loadings, and profile losses from the Euler (with boundary layer analysis) and Navier-Stokes are shown in Figures 104 through 106. A stereolithography model was fabricated and examined for the possible incorporation of heat transfer instrumentation on the airfoil surface.

A.2 APPROACH 2

The second approach consisted of designing a rotor to reduce the gap-average spanwise vorticity entering the second stator. This was accomplished using the same design procedure, as described for the second stator redesign (Approach 1); the resulting rotor was a highly 3-D shape, as shown in Figure 107. The resulting angle distribution showed that a uniform spanwise angle was approximately achieved, and therefore, a reduction of gap-average vorticity (Figure 108). The loading of this design, and the resulting losses from boundary layer analysis, are shown in Figures 109 and 110. The concern with this approach was that the rotor secondary flow structure would still exist, and therefore, high deterministic stresses would be present at the inlet to second stator. Since no known design concept has been able to eliminate the secondary flow structure (high vortical motion) and associated stresses, a design was pursued to contain the structures very close to the endwall. Since P&W has had past success with constant span fences to control the spanwise movement of secondary flow, this was the approach used to reduce the stress in the midspan region. Since there is no known available fence design system, fences were designed and developed in a large-scale/low-speed wind tunnel using the root cross-section of the rotor. On the third design attempt, the vortex structure was contained near the endwall in both the passage and downstream, and therefore, achieving the design objective. Actual size fences were then designed for easy installation on the root and tip of the rotor. A sketch of the fences is shown in Figure 111.

A.3 APPROACH 3

This approach addressed the issue of flow interaction, by determining the performance of the second stator with the same gas triangles, but with decayed wakes and secondary flow, and different levels of stress. This was accomplished by placing the rotor of the base rig to its rear most position (closest to the second stator) and then fabricating inner and outer annular spacer rings to create two additional axial spacings between the rotor and second stator. A schematic is shown in Figure 112. Because of the anticipated success of this configuration, this is the option chosen for the experimental program.

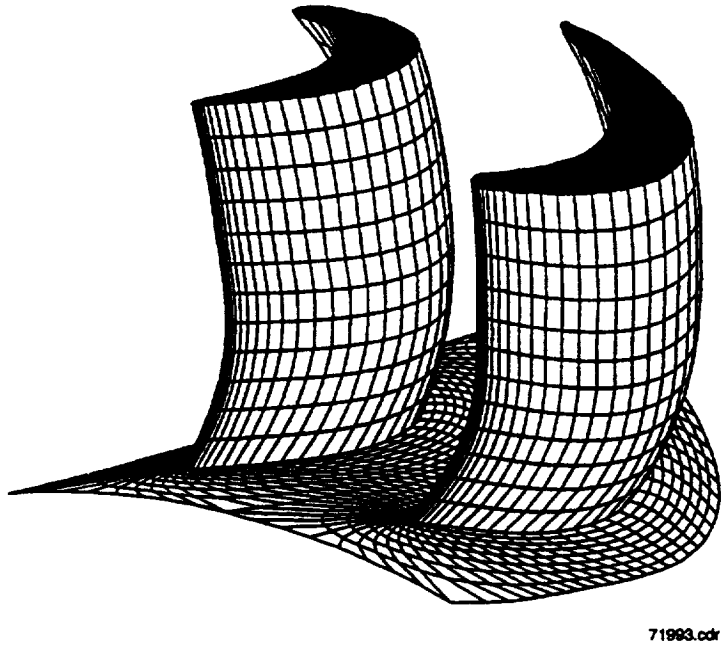

Figure 103. Second Stator Redesign Combines Stacking and Revortexing To Achieve Desired Flow Conditions

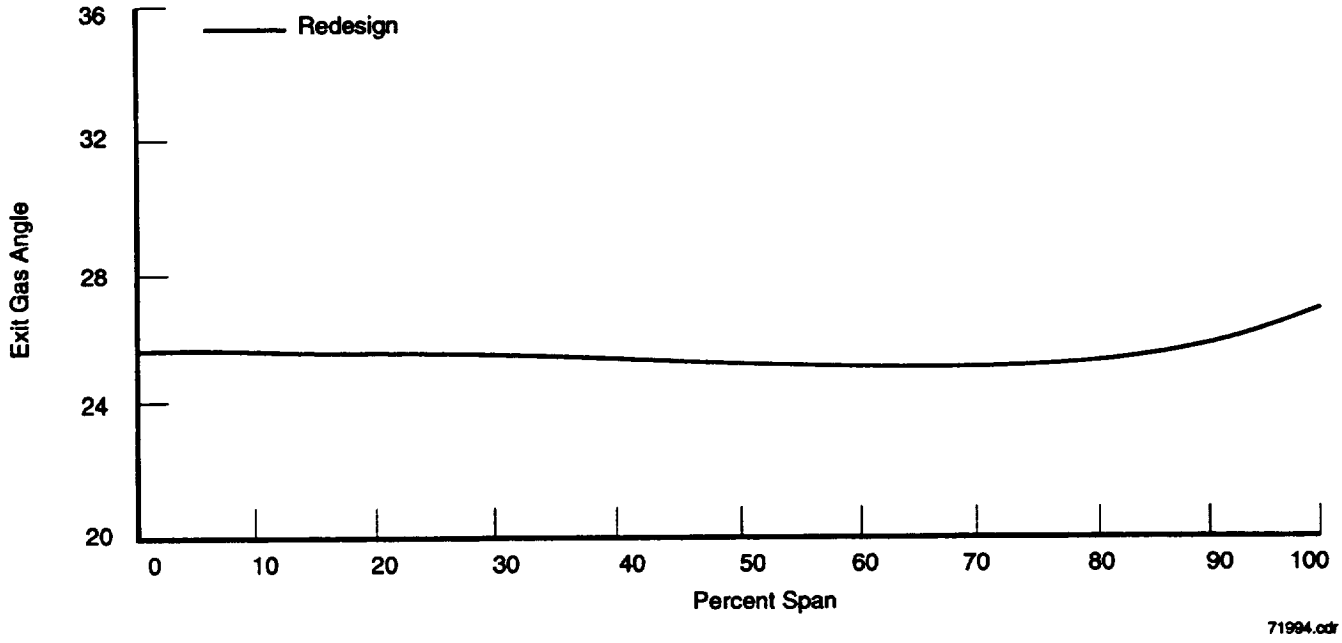

Figure 104. Second Stator Analysis Shows That Spanwise Exit Gas Angles Are Achieved for Redesign

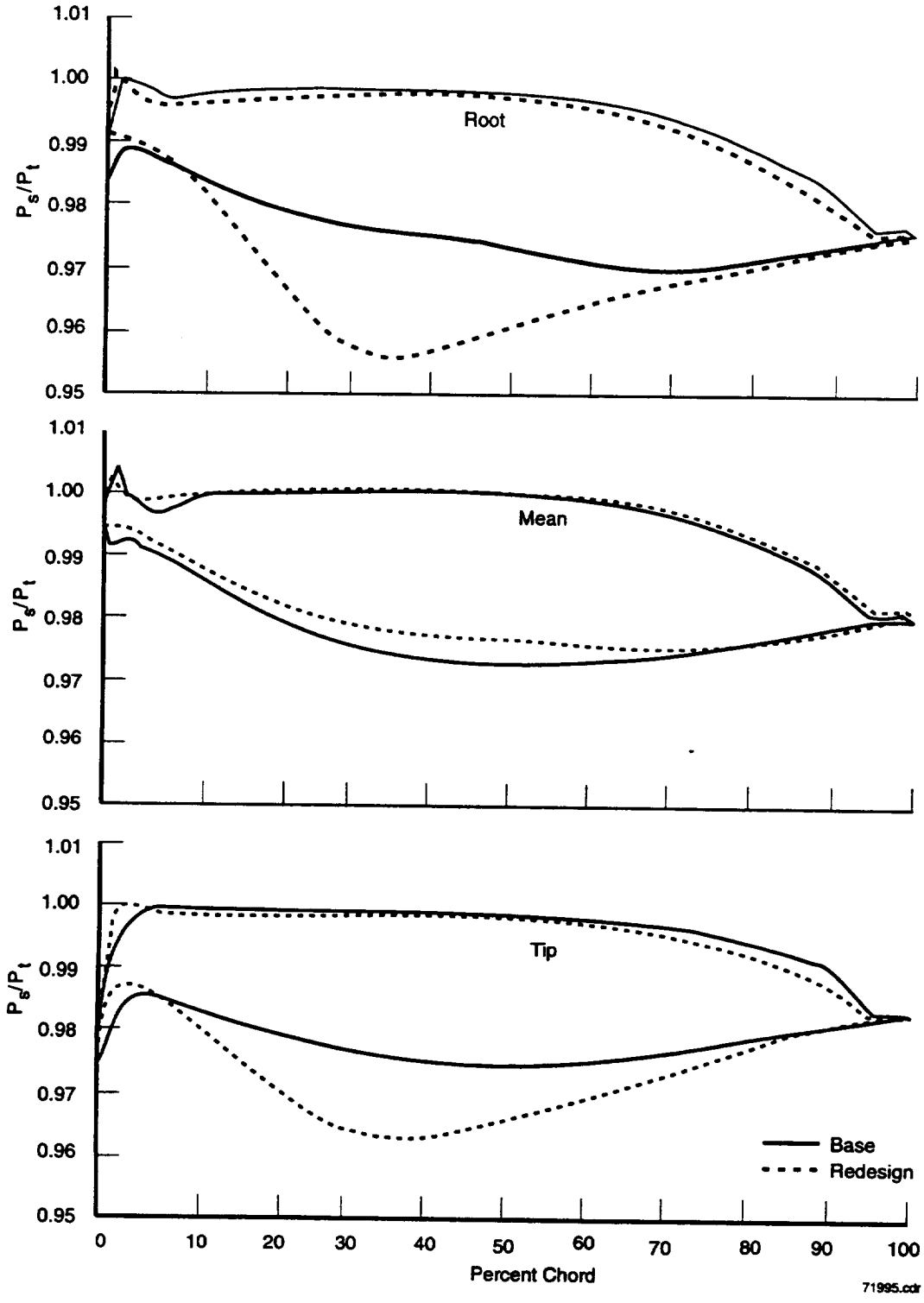

Figure 105. Comparison of Second Stator Loadings Between Base and Redesign Shows Endwalls More Loaded Than Baseline

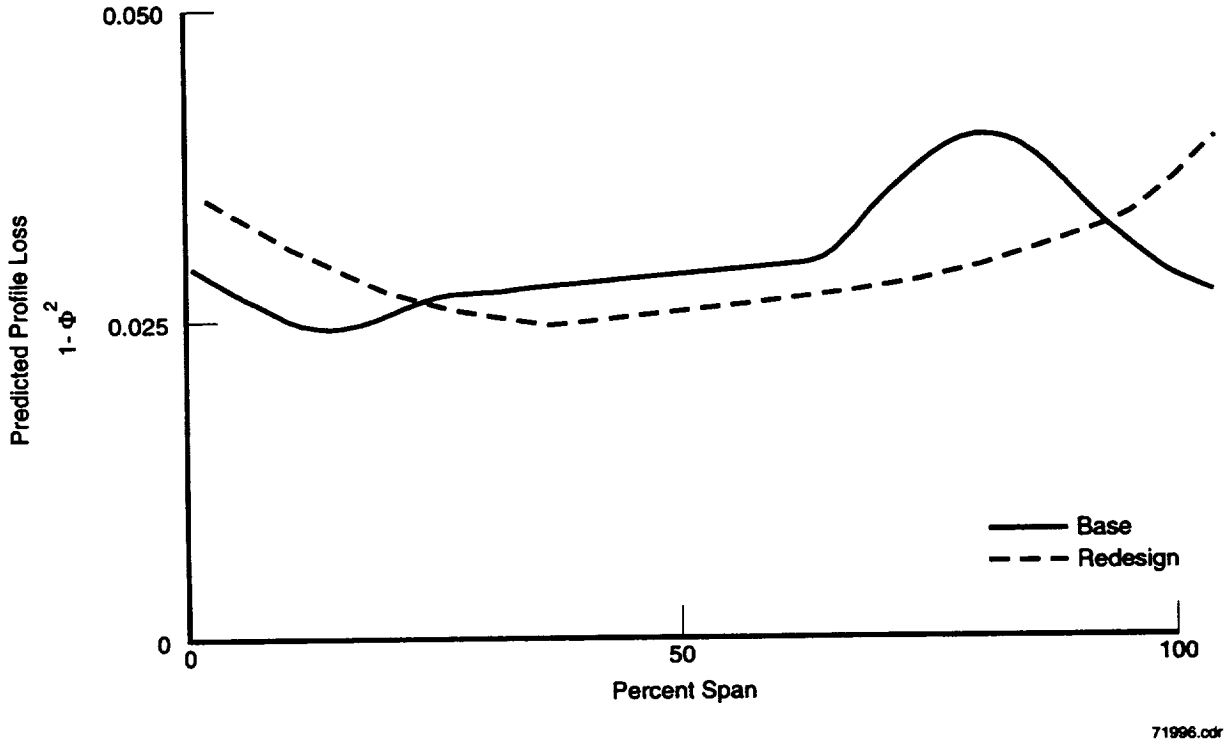

Figure 106. Redesigned Second Stator Shows Higher Losses Confined to the Endwalls

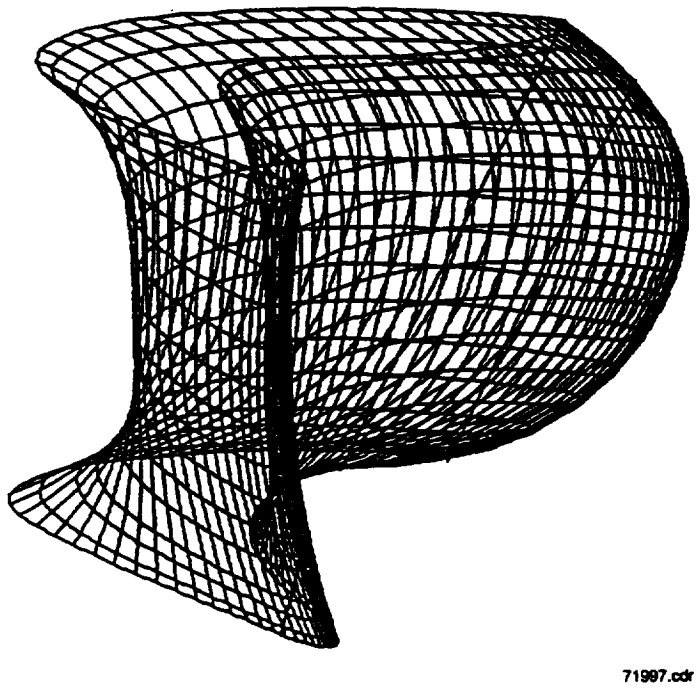

Figure 107. Redesigned First Blade Uses 3-D Stacking - Bowed

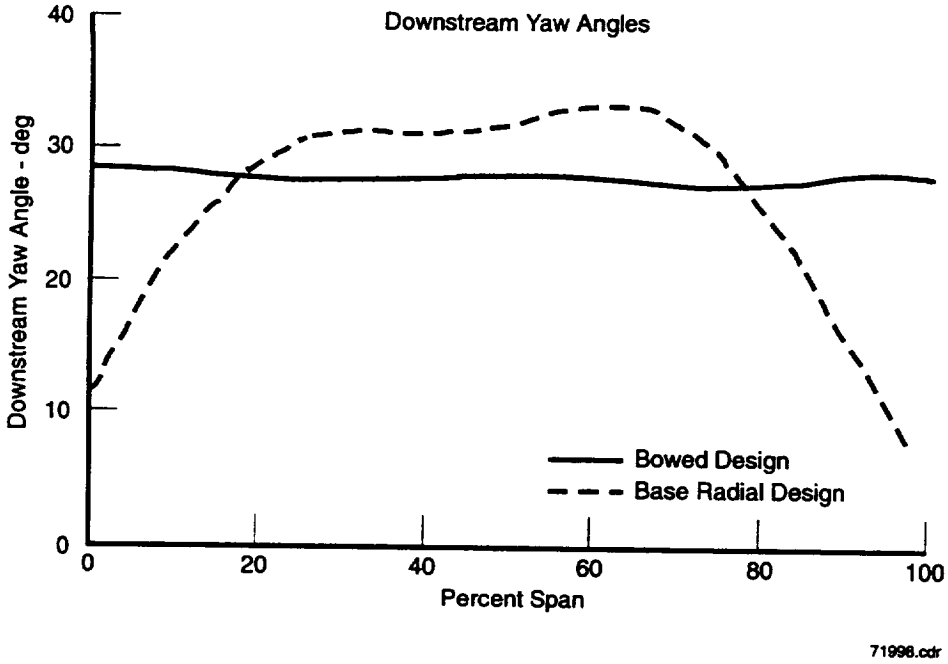

Figure 108. Bowed Airfoil Gives Flat Gap-Averaged Air Angle Profile

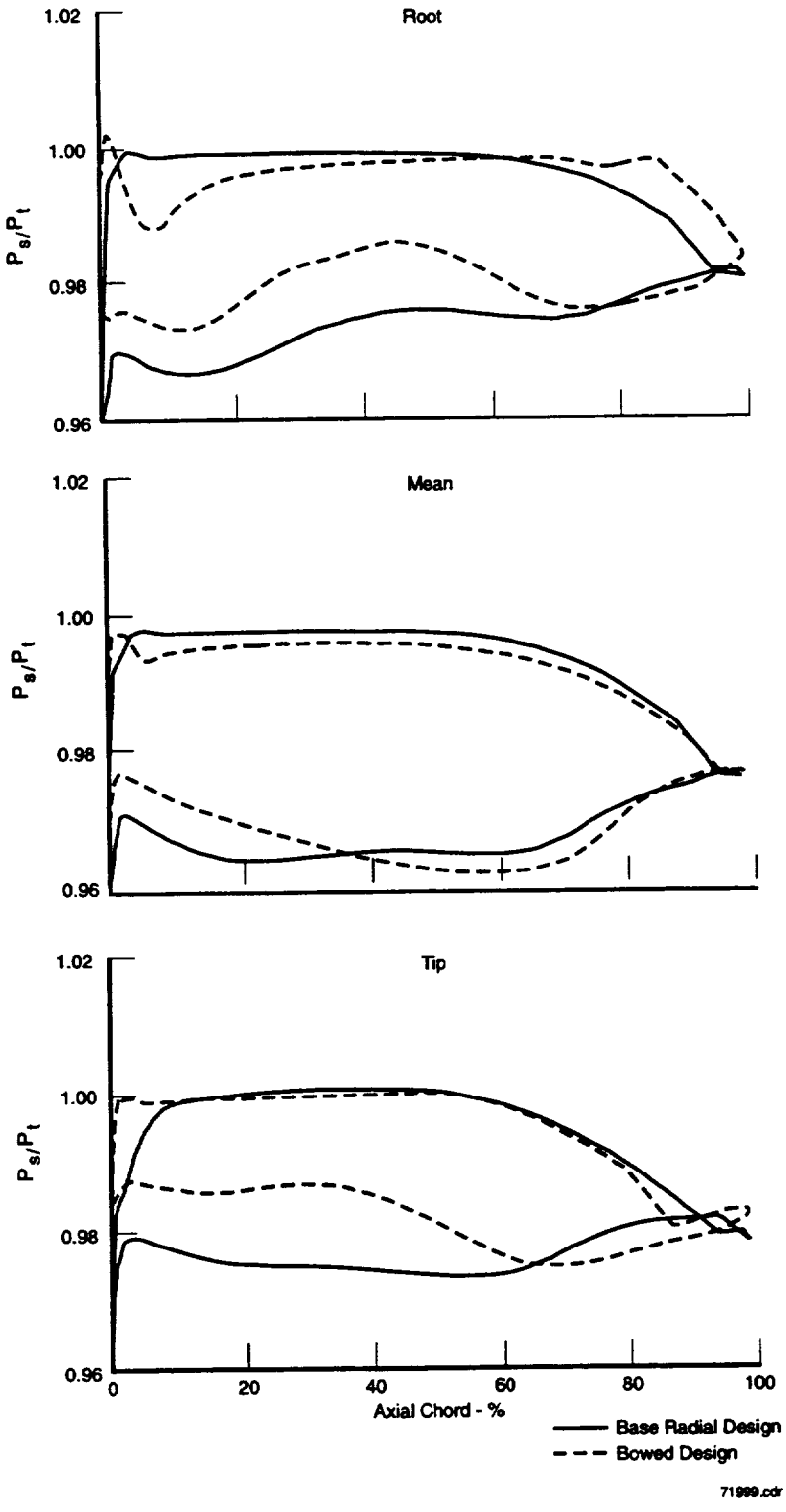

Figure 109. Bowed Airfoil Unloads Endwalls

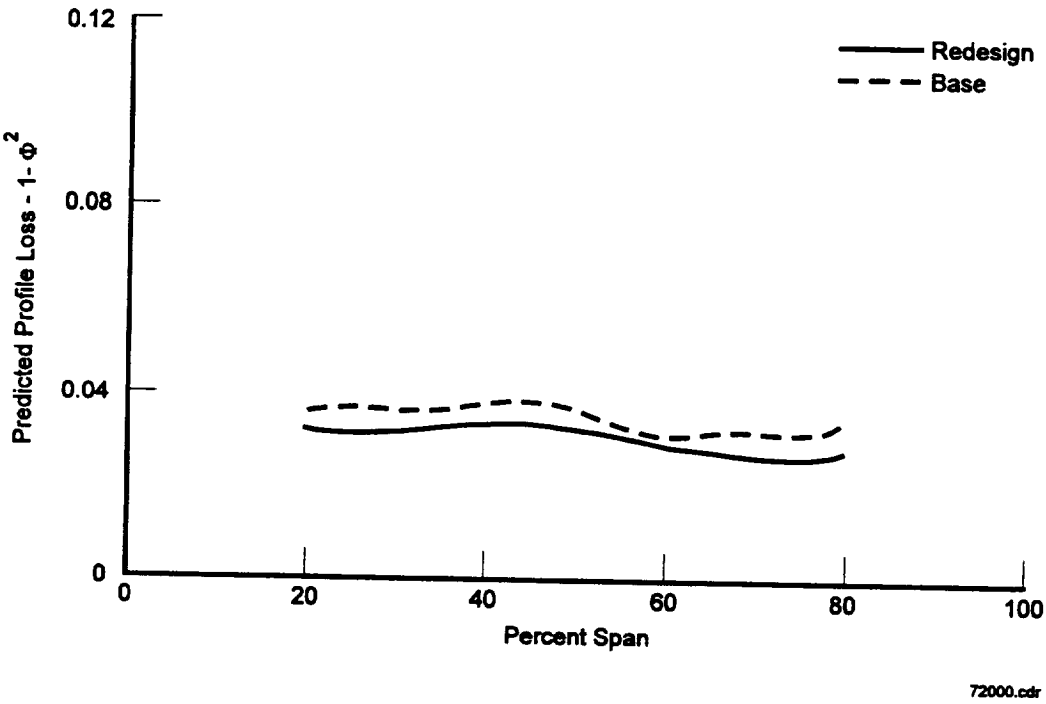

Figure 110. Profile Loss in Core Region Shows Redesign Has Slightly Lower Loss as Compared to Base Distribution

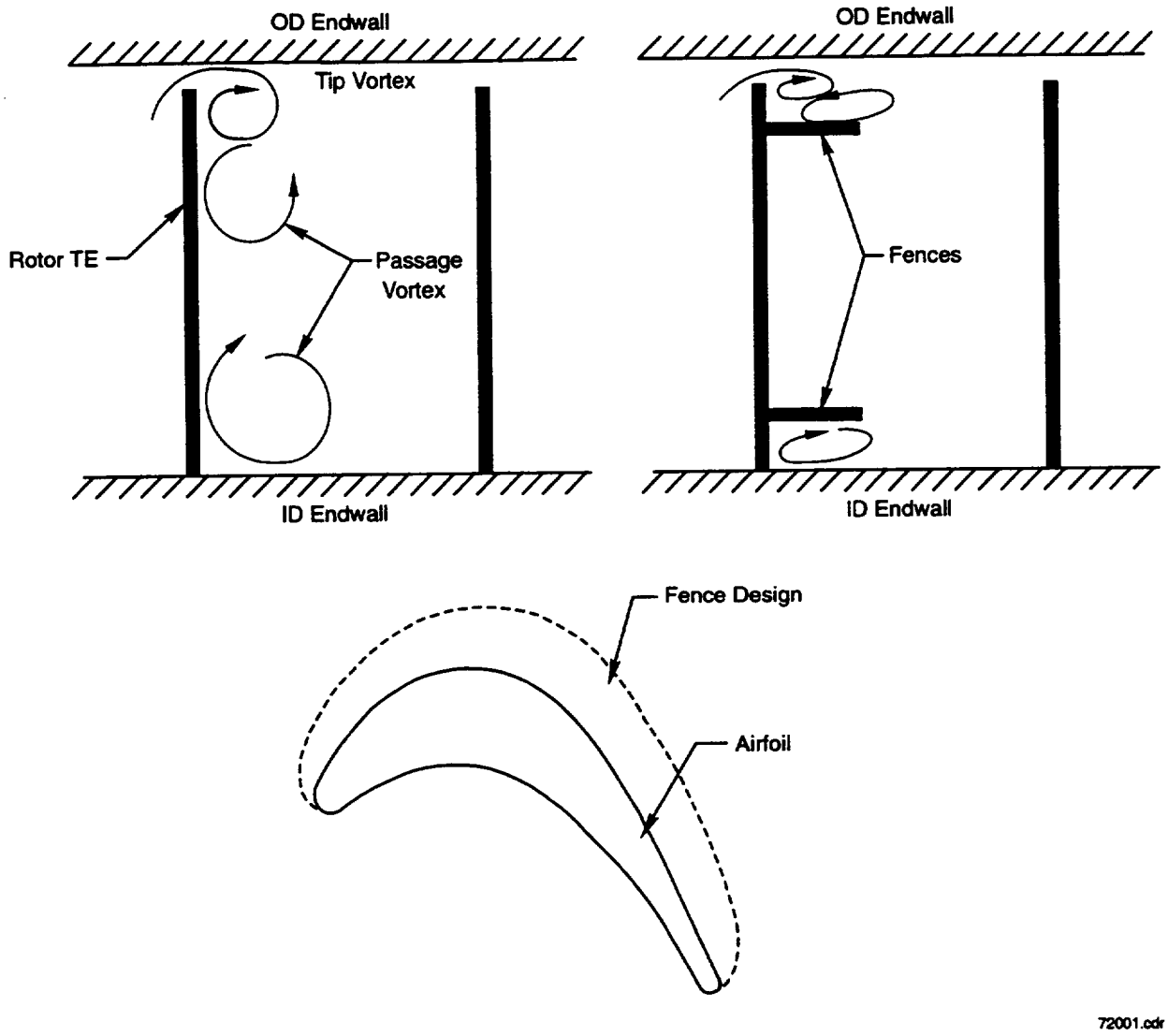

Figure 111. Schematic of Rotor Fence Design — Trailing Edge and Top Views

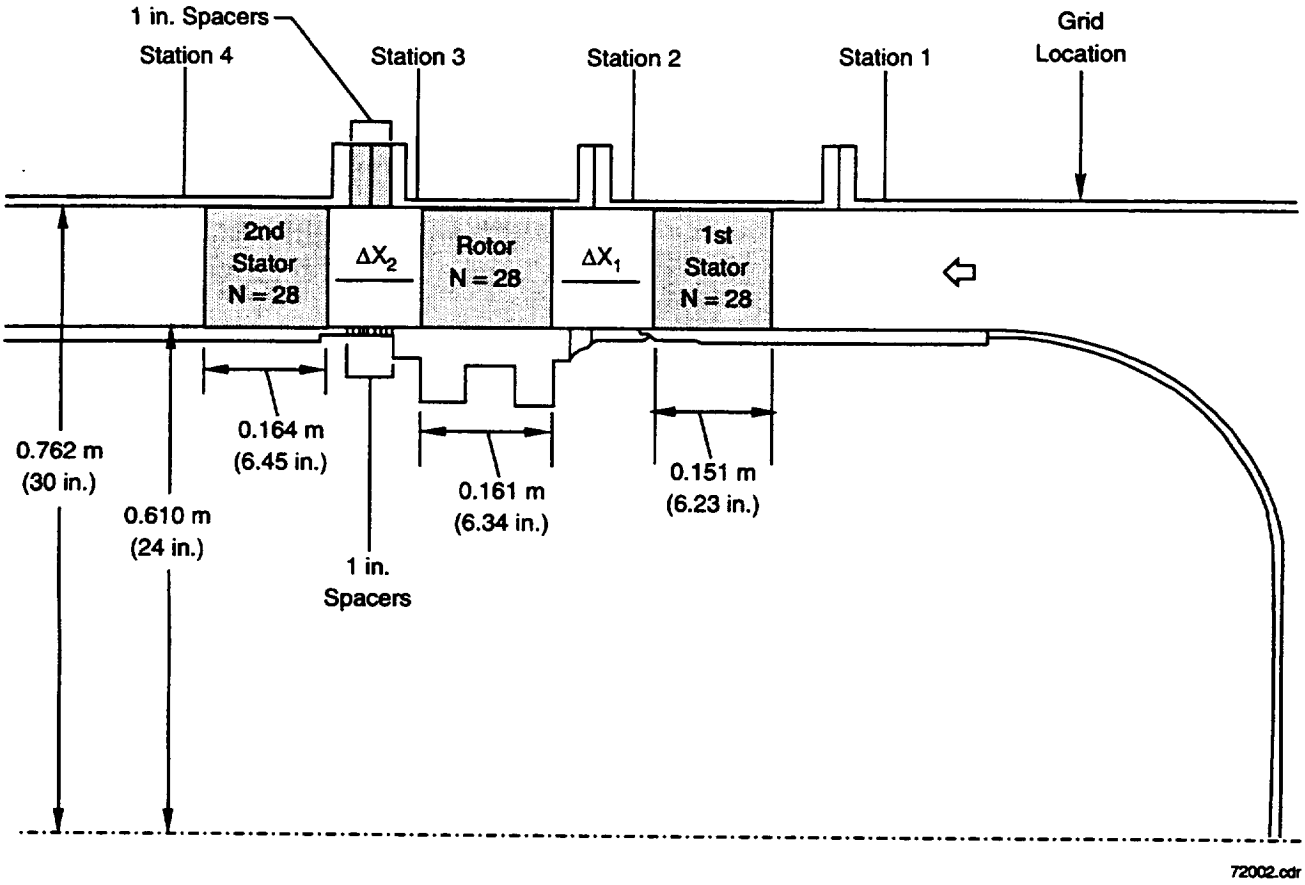

Figure 112. United Technologies Research Center Large-Scale Rotating Rig Cross-Section

APPENDIX B — DESCRIPTION OF LARGE SCALE ROTATING RIG 1-1/2 STAGE TURBINE RIG FACILITY

B.1 DESCRIPTION OF TEST FACILITY

The large-scale rotating rig (LSRR) facility at United Technologies Research Center (UTRC) is of the open circuit type. Flow enters the rig through a 12-foot diameter inlet at ambient conditions. A 6-inch thick section of honeycomb is mounted at the inlet face to reduce any entrance cross-flow effects. The inlet smoothly contracts the cross-section to a 5-foot diameter. The flow passes through three sets of fine mesh screens to reduce the turbulence level. Downstream of the test section, the flow passes through an annular diffuser into a centrifugal blower and is discharged into the atmosphere. A vortex valve at the blower inlet (downstream of the turbine rig) controls the flow through the rig. The rig is shown schematically in Figure 113.

The initial portion of the experimental program consisted of acquiring new baseline data for the rig with 28 first stators. Up to this point, the rig had been operating with 22 first stators, 28 rotors, and 28 second stators. The baseline data consisted of airfoil spanwise pressure distributions on all three rows of airfoils, second stator midspan heat transfer data, and full plane traverse data at the exit of each airfoil row. The rig geometry at which these data were acquired is shown in Figure 114. The full span traverse data were acquired with a non-nulling 5-hole probe (oval type head) in the absolute frame behind each stator row and in the relative frame behind the rotor.

Setting the rig operating conditions consisted of iterating the inlet flow to 75 ft/sec by using the inlet total pressure, inlet static pressure, and inlet density. The rig speed was set by adjusting the load until the shaft encoder recorded a speed of 410 rpm. These rig operating conditions resulted in the flow coefficient and Reynolds numbers shown in Table 3. The airfoil coordinates are summarized in Tables 4, 5, and 6 for the first stator, Tables 7, 8, and 9 for the rotor, and Tables 10, 11, and 12 for the second stator.

All data were acquired and stored electronically on tape. Computer programs processed the data in an on-line or off-line mode, depending on the data being processed.

The key portion of the experimental program was to acquire loss data on the second stator at three axial spacings between the rotor and second stator for five first stator/second stator circumferential indexing positions at each axial spacing. To accomplish this portion of the program, spacers were added to the hub and case of the rig to change the axial spacing between the second stator leading edge (LE) and the rotor trailing edge (TE). This change in axial spacing was accomplished to ensure axial spacing between the first stator TE and the rotor LE remained constant. The axial spacing values at which data were acquired is shown in Figure 114. To accomplish the first stator/second stator indexing, the first stator ring was modified with five equally-spaced circumferential mounting holes to mount the first stator ring to the rig. These holes were spaced such that mounting the first stator ring at each location indexed the first stators with respect to the second stators by 25 percent of a stator pitch. Therefore, when the first stator ring was indexed from Holes 1 through 5, the stators were indexed by exactly one stator pitch. The relative circumferential positions of the first to second stator are shown in Figure 115.

The loss data were acquired at the second stator inlet and exit plane at the second stator midspan. These data were acquired with a kiel probe, which was traversed over two stator pitches. A comprehensive data set is summarized in Appendix C.

Table 3. Aerodynamic and Geometric Parameters for Large-Scale Rotating Rig

Parameter		*First Stator*	*Rotor*	*Second Stator*
Shaft Speed	410 rpm			
Through Flow Velocity (C_x)	75.0 ft/sec			
Inlet Total Pressure	Ambient, 1.0 atm			
Inlet Total Temperature	Ambient, 530.0 °R			
Flow Coefficient (C_x/Um)	0.78			
Axial Chord (in.)		6.23	6.34	6.45
Number of Airfoils		28	28	28
Aspect Ratio (S/B_x)		0.964	0.946	0.930
Tip Clearance/ (B_x)			0.01	
Midspan Inlet Metal Angle (deg) from Tangential		90.0	42.0	46.0
Midspan Exit Metal Angle (deg) from Tangential		21.0	26.0	25.0
Exit Velocity Absolute Frame (ft/sec)		210.0	112.0	165.0
Exit Reynolds Number per in.		1.09×10^5	1.04×10^5	0.86×10^5

Legend for Tables 4 through 12:

RAD	Section Radius
ROTD	Rotation of the coordinates about the stacking line + value (trailing edge mean camber angle more axial) - value (trailing edge mean camber angle more tangential)
YOFF	Staking line location on the airfoil (Rθ = YPRES or YSUC – YOFF) The coordinates must be shifted to achieve a correct radial line
X	X coordinate
YPRES	Lower coordinate Rθ
YSUC	Upper coordinate Rθ
RTE	Airfoil trailing edge circle radius
TEMA	Airfoil trailing edge mean camber angle from tangential
TEWA	Airfoil trailing edge wedge angle

RAD	YOFF	ROTD	RTE	TEMA	TEWA
24.000	4.530	2.550	0.10988	23.510	6.840

Table 4. First Stator Coordinates (Constant Radius, Section 1)

X	*YPRES*	*YSUC*
0.0	5.952954	5.952954
0.059320	5.731017	6.174897
0.118640	5.650505	6.255410
0.177960	5.597065	6.308854
0.237280	5.559505	6.346412
0.296600	5.533540	6.372378
0.355920	5.515660	6.390074
0.415240	5.498162	6.406327
0.474560	5.480083	6.421952
0.533880	5.461425	6.436905
0.593200	5.442157	6.451178
0.741500	5.391428	6.483678
0.889800	5.336922	6.511263
1.038099	5.278517	6.533433
1.186399	5.216124	6.549635
1.334700	5.149617	6.559224
1.483000	5.078863	6.561522
1.631299	5.003724	6.555774
1.779599	4.924031	6.541155
1.927899	4.839602	6.516750
2.076200	4.750246	6.481636
2.224500	4.655717	6.434777
2.372800	4.555770	6.375116
2.521100	4.450059	6.301601
2.669399	4.338339	6.213168
2.817699	4.220198	6.108792
2.966000	4.095206	5.987559
3.114300	3.962868	5.848683
3.262600	3.822608	5.691515
3.410899	3.673766	5.515681
3.559199	3.515574	5.320966
3.707500	3.347166	5.107466
3.855800	3.167598	4.875420
4.004100	2.975931	4.625218
4.152400	2.771418	4.357356
4.300700	2.553686	4.072423
4.448999	2.323049	3.771061
4.597300	2.080339	3.453983
4.745600	1.826675	3.121941
4.893900	1.563282	2.775686
5.042200	1.291080	2.416018
5.190499	1.011100	2.043701
5.338799	0.724229	1.659515
5.398120	0.607620	1.502681
5.457439	0.490098	1.344112
5.516760	0.371566	1.183858
5.576079	0.252162	1.021960
5.635400	0.131831	0.858465
5.694719	0.010645	0.693411
5.754040	-0.086249	0.526846
5.813360	-0.109530	0.358808
5.872680	-0.097556	0.189341
5.932000	-0.000000	-0.000000

RAD	YOFF	ROTD	RTE	TEMA	TEWA
27.000	4.990	2.55	0.10988	22.420	6.84

Table 5. First Stator Coordinates (Constant Radius, Section 2)

X	*YPRES*	*YSUC*
0.0	6.807672	6.807672
0.059320	6.585734	7.029614
0.118640	6.505220	7.110127
0.177960	6.451777	7.163571
0.237280	6.414219	7.201129
0.296600	6.388252	7.227096
0.355920	6.370353	7.244769
0.415240	6.352731	7.260880
0.474560	6.334418	7.276229
0.533880	6.315411	7.290779
0.593200	6.295690	7.304498
0.741500	6.243258	7.334962
0.889800	6.186240	7.359463
1.038099	6.124480	7.377408
1.186399	6.057821	7.388117
1.334700	5.986043	7.390843
1.483000	5.908972	7.384750
1.631299	5.826344	7.369001
1.779599	5.737885	7.342593
1.927899	5.643272	7.304532
2.076200	5.542140	7.253724
2.224500	5.434062	7.189085
2.372800	5.318542	7.109488
2.521100	5.195001	7.013876
2.669399	5.062754	6.901218
2.817699	4.920987	6.770595
2.966000	4.768749	6.621239
3.114300	4.604922	6.452586
3.262600	4.428277	6.264286
3.410899	4.237734	6.056254
3.559199	4.032559	5.828587
3.707500	3.812809	5.581624
3.855800	3.579494	5.315832
4.004100	3.333980	5.031751
4.152400	3.077984	4.730038
4.300700	2.812677	4.411396
4.448999	2.539376	4.076603
4.597300	2.258724	3.726468
4.745600	1.971685	3.361802
4.893900	1.678823	2.983438
5.042200	1.380585	2.592209
5.190499	1.077408	2.188899
5.338799	0.769558	1.774302
5.398120	0.645175	1.605473
5.457439	0.520144	1.435001
5.516760	0.394509	1.262932
5.576079	0.268196	1.089313
5.635400	0.141204	0.914186
5.694719	0.013623	0.737597
5.754040	-0.086249	0.559584
5.813360	-0.109530	0.380189
5.872680	-0.097556	0.199450
5.932000	-0.000000	-0.000000

RAD	YOFF	ROTD	RTE	TEMA	TEWA
30.000	5.450	2.55	0.10988	21.210	6.84

Table 6. First Stator Coordinates (Constant Radius, Section 3)

X	*YPRES*	*YSUC*
0.0	7.608827	7.608827
0.059320	7.386889	7.830770
0.118640	7.306376	7.911283
0.177960	7.252933	7.964726
0.237280	7.215374	8.002285
0.296600	7.189407	8.028251
0.355920	7.171492	8.045890
0.415240	7.153745	8.061640
0.474560	7.135189	8.076213
0.533880	7.115813	8.089700
0.593200	7.095606	8.102010
0.741500	7.041376	8.127399
0.889800	6.981698	8.144959
1.038099	6.916318	8.154146
1.186399	6.845032	8.154509
1.334700	6.767533	8.145548
1.483000	6.683485	8.126675
1.631299	6.592488	8.097393
1.779599	6.494081	8.057024
1.927899	6.387715	8.004932
2.076200	6.272738	7.940394
2.224500	6.148359	7.862688
2.372800	6.013621	7.770950
2.521100	5.867317	7.664369
2.669399	5.708129	7.541998
2.817699	5.534410	7.402905
2.966000	5.344632	7.246008
3.114300	5.137786	7.070239
3.262600	4.914193	6.874393
3.410899	4.675468	6.657235
3.559199	4.423703	6.417642
3.707500	4.160830	6.154808
3.855800	3.888413	5.868458
4.004100	3.607717	5.558789
4.152400	3.319713	5.226550
4.300700	3.025181	4.872856
4.448999	2.724557	4.499182
4.597300	2.418539	4.107169
4.745600	2.107473	3.698550
4.893900	1.791744	3.275075
5.042200	1.471648	2.838350
5.190499	1.147367	2.389950
5.338799	0.819287	1.931245
5.398120	0.686965	1.745163
5.457439	0.554071	1.557703
5.516760	0.420742	1.368945
5.576079	0.286726	1.178940
5.635400	0.152112	0.987766
5.694719	0.017003	0.795470
5.754040	-0.086249	0.602115
5.813360	-0.109530	0.407757
5.872680	-0.097556	0.212433
5.932000	-0.000000	-0.000000

RAD	YOFF	ROTD	RTE	TEMA	TEWA
24.000	3.1171	0.00	0.1900	25.980	5.324

Table 7. Rotor Coordinates (Constant Radius, Section 1)

X	*YPRES*	*YSUC*
0.0	2.843099	2.843099
0.063410	2.642578	3.058255
0.126820	2.574073	3.189213
0.190230	2.532454	3.310042
0.253640	2.507565	3.422071
0.317050	2.495788	3.526332
0.380460	2.495789	3.623659
0.443870	2.507565	3.714722
0.507280	2.532454	3.800081
0.570690	2.572521	3.880201
0.634100	2.614538	3.955475
0.792625	2.708907	4.124577
0.951150	2.789188	4.269553
1.109674	2.856535	4.393410
1.268199	2.911833	4.498372
1.426724	2.955770	4.586142
1.585250	2.988893	4.658020
1.743774	3.011625	4.715034
1.902300	3.024307	4.757972
2.060824	3.027205	4.787455
2.219350	3.020523	4.803946
2.377874	3.004428	4.807789
2.536399	2.979041	4.799217
2.694924	2.944449	4.778348
2.853449	2.900708	4.745224
3.011974	2.847843	4.699767
3.170500	2.785847	4.641819
3.329024	2.714681	4.571112
3.487550	2.634271	4.487248
3.646074	2.544517	4.389718
3.804600	2.445262	4.277844
3.963124	2.336329	4.150743
4.121649	2.217483	4.007302
4.280174	2.088434	3.846083
4.438699	1.948846	3.665222
4.597224	1.798315	3.462717
4.755750	1.636407	3.237349
4.914274	1.462449	2.988995
5.072800	1.275860	2.718733
5.231324	1.075852	2.428502
5.389850	0.861515	2.120841
5.548374	0.631757	1.798331
5.706899	0.385278	1.463487
5.770309	0.281658	1.326585
5.833719	0.174951	1.188185
5.897129	0.065176	1.048406
5.960539	-0.047920	0.907344
6.023949	-0.141274	0.765113
6.087359	-0.179025	0.621788
6.150769	-0.190000	0.477461
6.214179	-0.179187	0.332199
6.277589	-0.141685	0.186081
6.341000	-0.000000	-0.000000

RAD	YOFF	ROTD	RTE	TEMA	TEWA
27.000	3.6171	0.00	0.190	25.980	5.324

Table 8. Rotor Coordinates (Constant Radius, Section 2)

X	*YPRES*	*YSUC*
0.0	3.916514	3.916514
0.063410	3.715993	4.124468
0.126820	3.647488	4.240133
0.190230	3.605869	4.345597
0.253640	3.580979	4.442324
0.317050	3.569202	4.531429
0.380460	3.569203	4.613784
0.443870	3.580979	4.690091
0.507280	3.605869	4.760917
0.570690	3.643682	4.826735
0.634100	3.680748	4.887945
0.792625	3.762573	5.022881
0.951150	3.830230	5.135066
1.109674	3.884964	5.227402
1.268199	3.927680	5.302007
1.426724	3.959025	5.360468
1.585250	3.979447	5.404005
1.743774	3.989225	5.433540
1.902300	3.988501	5.449780
2.060824	3.977271	5.453254
2.219350	3.955420	5.444344
2.377874	3.922703	5.423305
2.536399	3.878751	5.390265
2.694924	3.823067	5.345256
2.853449	3.755038	5.288191
3.011974	3.674091	5.218878
3.170500	3.579574	5.136995
3.329024	3.471066	5.042087
3.487550	3.348359	4.933536
3.646074	3.211631	4.810525
3.804600	3.061360	4.671988
3.963124	2.898102	4.516526
4.121649	2.722503	4.342320
4.280174	2.535254	4.146918
4.438699	2.336952	3.928189
4.597224	2.128133	3.685281
4.755750	1.909256	3.419081
4.914274	1.680757	3.131847
5.072800	1.442969	2.826617
5.231324	1.196291	2.506544
5.389850	0.940778	2.174561
5.548374	0.676829	1.833075
5.706899	0.404603	1.484083
5.770309	0.293375	1.342753
5.833719	0.180962	1.200542
5.897129	0.067250	1.057544
5.960539	-0.047761	0.913809
6.023949	-0.141274	0.769413
6.087359	-0.179025	0.624418
6.150769	-0.190000	0.478855
6.214179	-0.179187	0.332767
6.277589	-0.141685	0.186204
6.341000	-0.000000	-0.000000

RAD	YOFF	ROTD	RTE	TEMA	TEWA
30.000	4.1171	0.000	0.190	25.980	5.324

Table 9. Rotor Coordinates (Constant Radius, Section 3)

X	*YPRES*	*YSUC*
0.0	4.989928	4.989928
0.063410	4.789409	5.191723
0.126820	4.720902	5.289268
0.190230	4.679284	5.378238
0.253640	4.654395	5.459727
0.317050	4.642617	5.534590
0.380460	4.642617	5.603510
0.443870	4.654395	5.667048
0.507280	4.679284	5.725664
0.570690	4.711117	5.779745
0.634100	4.740527	5.829617
0.792625	4.804027	5.937627
0.951150	4.854175	6.024423
1.109674	4.891876	6.092466
1.268199	4.917761	6.143572
1.426724	4.932235	6.179105
1.585250	4.935519	6.200087
1.743774	4.927660	6.207289
1.902300	4.908542	6.201283
2.060824	4.877872	6.182473
2.219350	4.835148	6.151113
2.377874	4.779667	6.107325
2.536399	4.710367	6.051112
2.694924	4.625827	5.982346
2.853449	4.524091	5.900775
3.011974	4.402612	5.805990
3.170500	4.259274	5.697424
3.329024	4.093709	5.574307
3.487550	3.908832	5.435608
3.646074	3.708482	5.279967
3.804600	3.495772	5.105564
3.963124	3.272803	4.909987
4.121649	3.041380	4.690133
4.280174	2.802365	4.444331
4.438699	2.556817	4.173303
4.597224	2.305195	3.880044
4.755750	2.048160	3.568663
4.914274	1.786127	3.243157
5.072800	1.519417	2.906872
5.231324	1.248415	2.562467
5.389850	0.973304	2.211964
5.548374	0.694339	1.856716
5.706899	0.411773	1.497858
5.770309	0.297712	1.353492
5.833719	0.183149	1.208697
5.897129	0.067939	1.063536
5.960539	-0.047643	0.918034
6.023949	-0.141274	0.772206
6.087359	-0.179025	0.626092
6.150769	-0.190000	0.479718
6.214179	-0.179187	0.333102
6.277589	-0.141685	0.186250
6.341000	-0.000000	-0.000000

RAD	YOFF	ROTD	RTE	TEMA	TEWA
24.000	3.680	0.000	0.190	25.00	6.500

Table 10. Second Stator Coordinates (Constant Radius, Sections 1)

X	*YPRES*	*YSUC*
0.00000	3.69263	3.68263
0.06452	3.48015	3.89472
0.12904	3.41120	4.01869
0.19356	3.36955	4.13494
0.25808	3.34493	4.24410
0.32260	3.33372	4.34672
0.38712	3.33462	4.44324
0.45164	3.34773	4.53408
0.51616	3.37461	4.61958
0.58068	3.41583	4.70006
0.64520	3.45739	4.77578
0.80650	3.55269	4.94580
0.96780	3.63560	5.09069
1.12910	3.70599	5.21287
1.29040	3.76376	5.31424
1.45170	3.80880	5.39634
1.61300	3.84106	5.46037
1.77430	3.86048	5.50735
1.93560	3.86704	5.53806
2.09690	3.86072	5.55317
2.25820	3.84153	5.55319
2.41950	3.80950	5.53852
2.58080	3.76468	5.50948
2.74210	3.70714	5.46629
2.90340	3.63698	5.40908
3.06470	3.55430	5.33790
3.22600	3.45921	5.25273
3.38730	3.35168	5.15348
3.54860	3.23245	5.03995
3.70990	3.10111	4.91189
3.87120	2.95802	4.76892
4.03250	2.80339	4.61058
4.19380	2.63745	4.43628
4.35510	2.46037	4.24527
4.51640	2.27244	4.03662
4.67770	2.07384	3.80928
4.83900	1.86483	3.56222
5.00030	1.64569	3.29479
5.16160	1.41663	3.00662
5.32290	1.17789	2.69784
5.48420	0.92975	2.36890
5.64550	0.67246	2.02068
5.80690	0.40629	1.65431
5.87132	0.29738	1.50296
5.93084	0.18710	1.34900
6.00036	0.07548	1.19252
6.06488	-0.03748	1.03361
6.12940	-0.13603	0.87238
6.19392	-0.17738	0.70890
6.25844	-0.18997	0.54327
6.32296	-0.17996	0.37560
6.38748	-0.14267	0.20595
6.45200	0.00000	0.00000

RAD	YOFF	ROTD	RTE	TEMA	TEWA
27.000	3.680	0.00	0.190	25.000	6.500

Table 11. Second Stator Coordinates (Constant Radius, Section 2)

X	*YPRES*	*YSUC*
0.00000	4.10291	4.10291
0.06452	3.89750	4.30650
0.12904	3.82830	4.40610
0.19356	3.78700	4.50013
0.25808	3.76200	4.58895
0.32260	3.75100	4.67285
0.38712	3.75200	4.75210
0.45164	3.77650	4.82695
0.51616	3.79454	4.89760
0.58068	3.83206	4.96425
0.64520	3.86762	5.02707
0.80650	3.94796	5.16834
0.96780	4.01599	5.28865
1.12910	4.07162	5.38963
1.29040	4.11482	5.47259
1.45170	4.14552	5.53859
1.61300	4.16371	5.58849
1.77430	4.16934	5.62296
1.93560	4.16244	5.64258
2.09690	4.14298	5.64778
2.25820	4.11101	5.63888
2.41950	4.06655	5.61615
2.58080	4.00965	5.57973
2.74210	3.94037	5.52972
2.90340	3.85879	5.46611
3.06470	3.76498	5.38882
3.22600	3.65906	5.29771
3.38730	3.54111	5.19255
3.54860	3.41127	5.07300
3.70990	3.26967	4.93863
3.87120	3.11644	4.78891
4.03250	2.95172	4.62316
4.19380	2.77568	4.44053
4.35510	2.58849	4.24001
4.51640	2.39030	4.02052
4.67770	2.18130	3.78134
4.83900	1.96166	3.52218
5.00030	1.73160	3.24330
5.16160	1.49128	2.94535
5.32290	1.24090	2.62941
5.48420	0.98064	2.29682
5.64550	0.71074	1.94914
5.80680	0.43141	1.58790
5.87132	0.31707	1.43996
5.93584	0.20126	1.29018
6.00036	0.08400	1.13867
6.06488	-0.03471	0.98552
6.12940	-0.13607	0.83080
6.19392	-0.17738	0.67459
6.25844	-0.18997	0.51699
6.32296	-0.18008	0.35805
6.38748	-0.14267	0.19786
6.45200	0.00000	0.00000

RAD	YOFF	ROTD	RTE	TEMA	TEWA
30.000	3.680	0.00	0.190	24.990	4.090

Table 12. Second Stator Coordinates (Constant Radius, Section 3)

X	*YPRES*	*YSUC*
0.00000	4.53429	4.53429
0.06452	4.33178	4.73679
0.12904	4.26282	4.81836
0.19356	4.22116	4.89463
0.25808	4.19652	4.96641
0.32260	4.18530	5.03396
0.38712	4.18619	5.09751
0.45164	4.19929	5.15728
0.51616	4.22602	5.21343
0.58068	4.25762	5.26613
0.64520	4.28729	5.31552
0.80650	4.35297	5.42538
0.96780	4.40647	5.51708
1.12910	4.44777	5.59199
1.29040	4.47688	5.65117
1.45170	4.49364	5.69551
1.61300	4.49819	5.72567
1.77430	4.49045	5.74219
1.93560	4.47047	5.74550
2.09690	4.43822	5.73590
2.25820	4.39375	5.71360
2.41950	4.33706	5.67874
2.58080	4.26823	5.63135
2.74210	4.18728	5.57140
2.90340	4.09426	5.49876
3.06470	3.98924	5.41323
3.22600	3.87229	5.31449
3.38730	3.74348	5.20215
3.54860	3.60289	5.07566
3.70990	3.45062	4.93435
3.87120	3.28675	4.77738
4.03250	3.11139	4.60366
4.19380	2.92465	4.41196
4.35510	2.72666	4.20188
4.51640	2.51749	3.97077
4.67770	2.29731	3.72077
4.83900	2.06620	3.45177
5.00030	1.82436	3.16495
5.16160	1.57187	2.86176
5.32290	1.30689	2.54389
5.48420	1.03553	2.21304
5.64550	0.75199	1.87091
5.80680	0.45841	1.51902
5.87132	0.33818	1.37585
5.93584	0.21639	1.23140
6.00036	0.09302	1.08577
6.06488	-0.03190	0.93902
6.12940	-0.13607	0.79122
6.19392	-0.17738	0.64244
6.25844	-0.18996	0.49272
6.32296	-0.17995	0.34214
6.38748	-0.14267	0.19073
6.45200	0.00000	0.00000

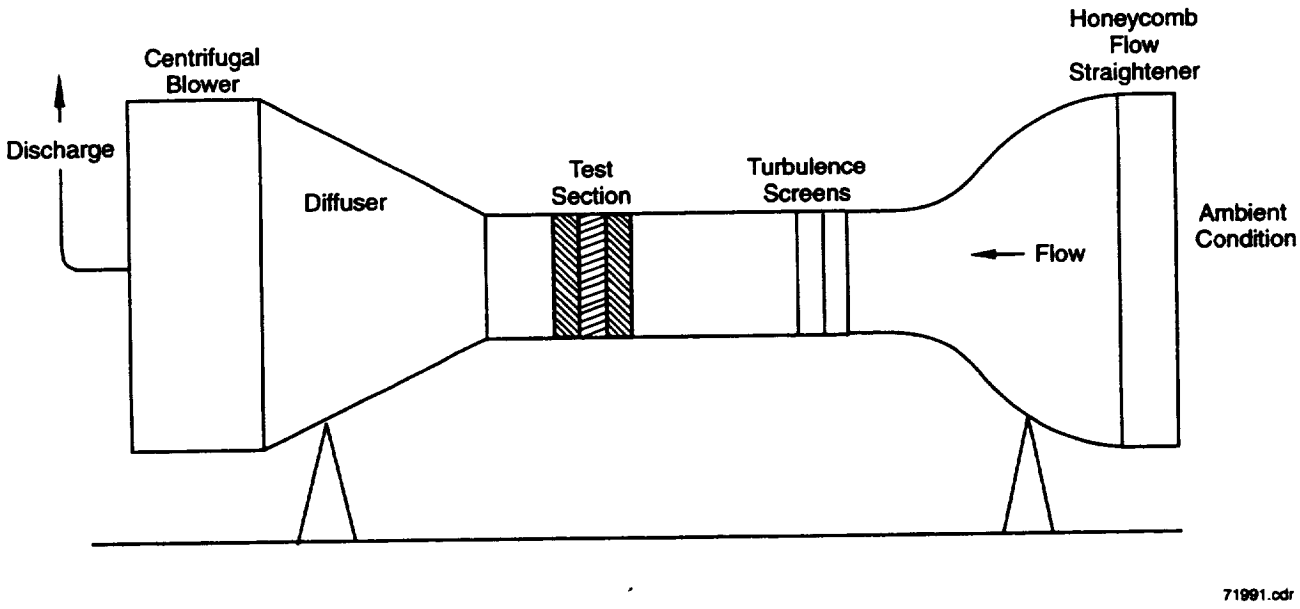

Figure 113. Schematic of United Technologies Research Center Test Facility

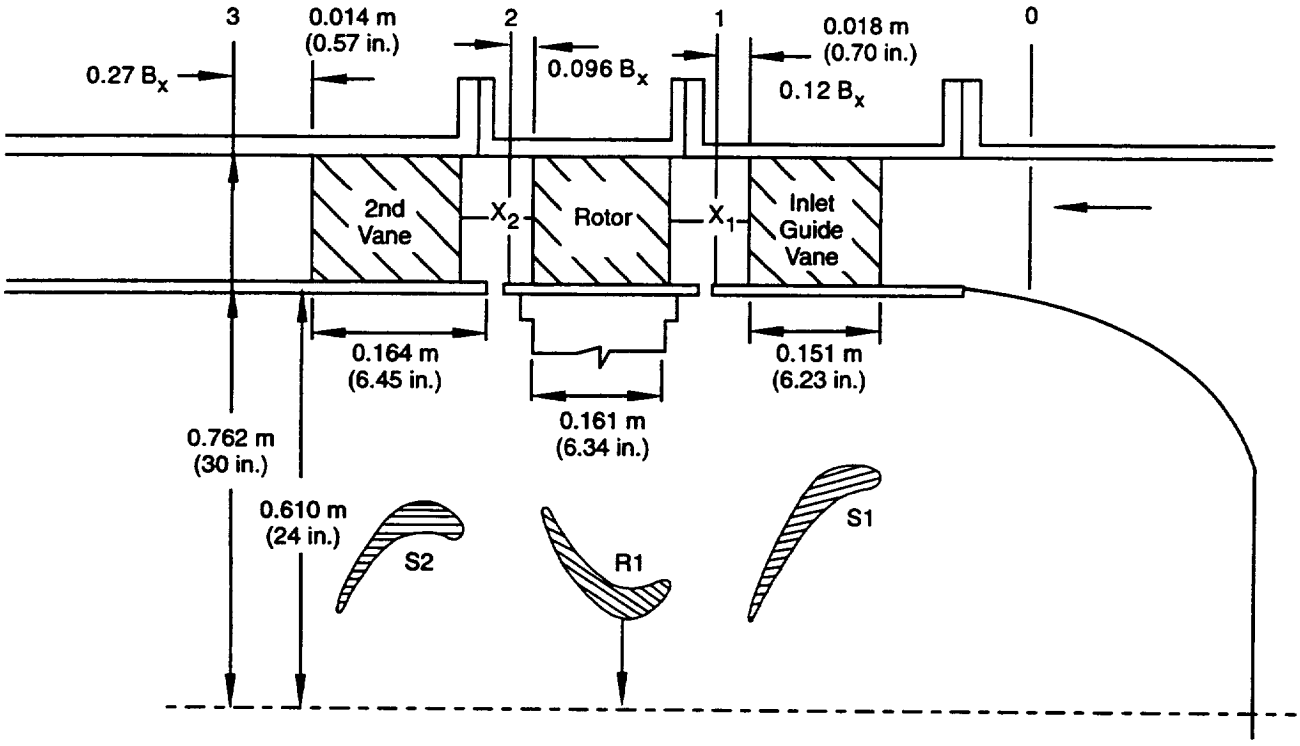

Gap (X_2/B_x-Rotor)	X_2 (in.)	X_1 (in.)
0.30	2.485	4.823
0.55	3.485	4.823
0.71	4.485	4.823

Axial Spacing Program
- Midspan Loss
- Steady Loadings
- Heat Transfer

Gap (X_2/B_x-Rotor)	X_2	X_1 (in.)
0.54 and/or 0.75	3.39	4.05
	4.73	2.71

Full Traverse Plane Program
- Full Span Angles/Pressures
- Full Span Loadings
- Unsteady Loadings (P&W Data)
- Heat Transfer Data

71992.cdr

Figure 114. Schematic of Large-Scale Rotating Rig Geometric Test Parameters

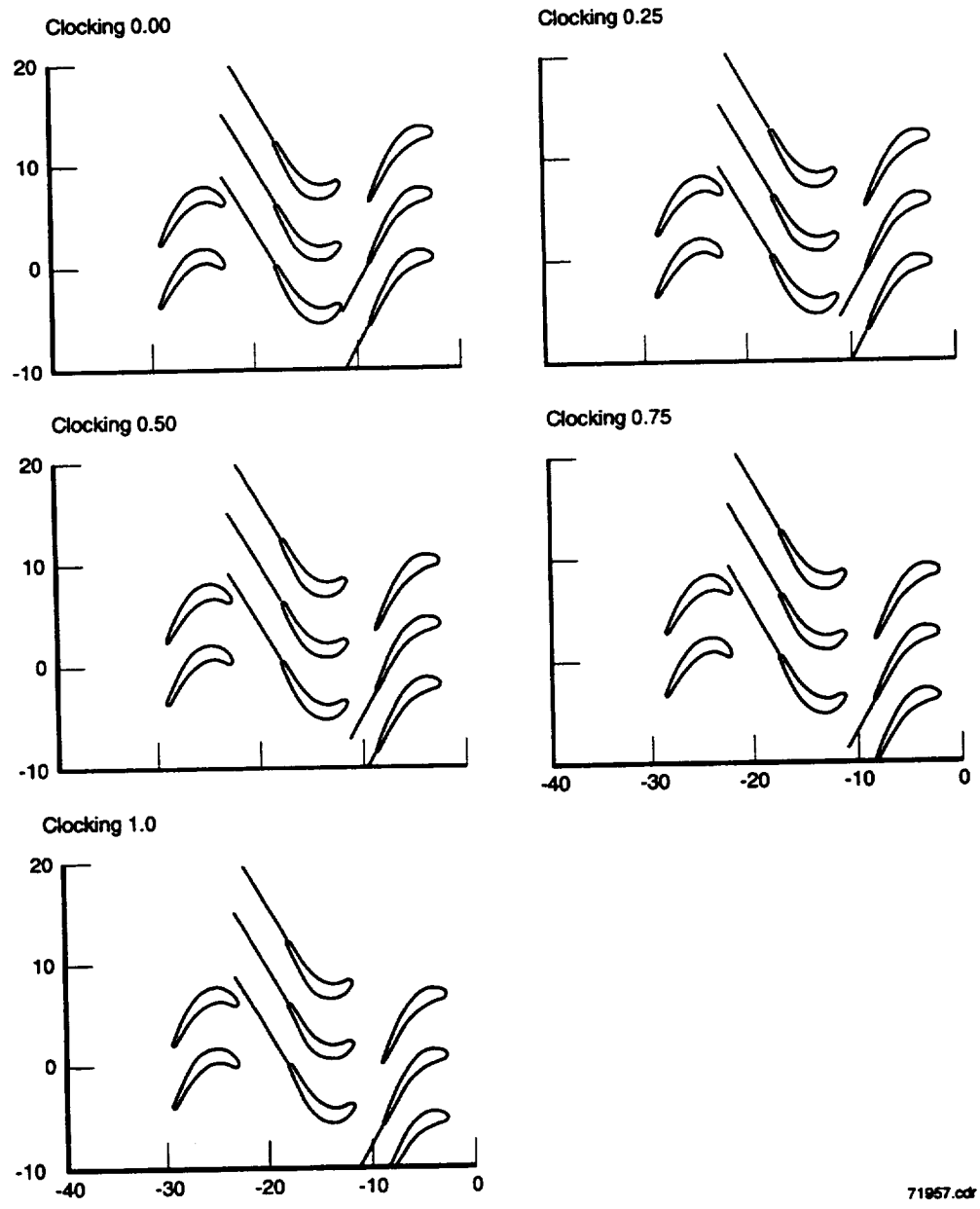

Figure 115. Schematic of First to Second Stator Clocking Positions

APPENDIX C — LARGE-SCALE ROTATING RIG 1 1/2-STAGE RIG BASELINE DATA

The objective of this appendix is to present data acquired in the large-scale rotating rig (LSRR) for the baseline rig configuration consisting of 28 first stators, 28 rotors, and 28 second stators at a first stator/rotor nominal spacing. The rig had been configured with 22 first stators, 28 rotors, and 28 second stators until recently; therefore, it was necessary to document the rig flowfield for this configuration (new baseline). The aerodynamic data documented acquired were airfoil, spanwise pressure distributions on all three rows of airfoils (shown in Sections 6 and 7), second stator midspan heat transfer data (shown in Sections 6 and 7), and full plane traverse data at the exit of each airfoil row (shown in Appendix C). The rig geometry at which these data were acquired is described in Appendix B.

The data to be presented have been divided into three sections: first stator, rotor, and second stator. By this means, each section can be extracted as a whole for any subsequent analysis or use of the data. Also, the plots should be of such a scale and gridded appropriately enough so that parameter values may be easily obtained from them, if necessary.

No attempt has been made to deduce or infer any particular point or conclusion in any of these sections, as these have been handled in the main body of the text. Nor is there any attempt to discuss in length any of the data presented other than to describe what is being shown, the conditions under which the data were acquired, and the rig geometry, as applicable. The principal objective is to present the data that were acquired during the course of the investigation from which the conclusions made in the main body were based. These three sections and the data contained in them are briefly described below.

Table 13 presents full span traverse results for the three airfoil exit planes. The data acquired at the first stator and second stator exit planes were acquired in the absolute frame of reference. The data acquired at the rotor exit plane were acquired in the relative frame of reference. The first stator exit plane is denoted as STA 1, the rotor exit plane is denoted as STA 2, and the second stator exit plane is denoted as STA 3. These locations are shown in Figure B-2. These data were acquired with a five-hole probe over two airfoil pitches. These data are compared with the data acquired in the original 22/28/28 rig configuration. Also shown in this appendix are contour plots of relative total pressure coefficient, absolute total pressure coefficient, rotary total pressure coefficient, static pressure coefficient, relative and absolute velocity ratio, and velocity vector plots.

Table 13. Nomenclature for Appendix C

Nomenclature	*Definition*
CP	Pressure coefficient $(P_0 - P)/Q_{UM}$
CPTABSM	Mass-averaged absolute total poressure coefficient $(P_0 - PTABS)/Q_{UM}$
CPSA	Area-averaged static pressure coefficient = $(P_0 - PSA)/Q_{UM}$
CPTRELM	Mass-averaged relative total pressure coefficient = $(P_0 - PTREL)/Q_{UM}$
CPROTM	Mass-averaged rotary total pressure coefficient = $(P_0 - PTROT)/Q_{UM}$
CTANM	Mass-averaged absolute tangential velocity ratio = $CTANM/U_m$
CTANA	Area-averaged absolute tangential velocity ratio = $CTANA/U_m$
CTOT	Total absolute velocity
CTOTM	Mass-averaged absolute total velocity ratio = $CTOT/U_m$
CTOTA	Area-averaged absolute total velocity ratio = $CTOT/U_m$
CRA	Area-averaged radial velocity ratio = CR/ U_m
CXA	Area-averaged axial velocity ratio = CX/ U_m
C_x	Rig inlet average midspan axial flow velocity, ft/sec
C_x/U_m	Rig flow coefficient
P	Static pressure, psia
P_0	Rig inlet total pressure, psia
PCSPAN	Percent of airfoil span = (R - Rhub)/(Rtip-Rhub)* 100
PHIABSA	Area-averaged absolute pitch angle, deg
PHIRELA	Area-averaged relative pitch angle, deg
PTREL	Relative total pressure = $(PTREL = P+Q_{local})$
PTROT	Rotary total pressure = $(PTROT=PREL-Q_{UM})$
Q_{local}	$1/2\ \rho_0 CTOT^2$
Q_{UM}	Dynamic pressure = $1/2\rho_0 Um^2$, psia
S	Airfoil span, inches
STA1	Station 1 - 1V exit plane
STA2	Station 2 - 1B exit plane
STA3	Station 3 - 2V exit plane

Table 13. Nomenclature for Appendix C (Continued)

Nomenclature	*Definition*
TNCTMCXA	Area averaged absolute yaw angle = $\tan^{-1}$(CTANM/CXA)
TNWTMCXA	Area averaged relative yaw angle = $\tan^{-1}$(WTANM/CXA)
U_m	Rotor midspan wheel speed, ft/sec
WTANA	Area-averaged relative tangential velocity ratio = WTANA/ U_m
WTANM	Mass-averaged relative tangential velocity ratio = WTANM/ U_m
WTOTA	Area-averaged relative total velocity ratio = WTOTA/ U_m
WTOTM	Mass-averaged relative total velocity ratio = WTOTM/ U_m
YAWABSA	Area-averaged absolute yaw angle, deg
YAWRELA	Area-averaged relative yaw angle, deg
X	Airfoil axial location from leading edge, inches
X_1	Axial distance from leading edge of rotor to trailing edge of first stator, inches
X_2	Axial distance from trailing edge of rotor to leading edge of second stator, inches
ρ_0	Rig inlet density, slugs/ft^3
r	Radius, inches

The data were acquired with a five-hole probe (oval-shaped head) that was calibrated using the non-nulling calibration technique. After the data were acquired, the probe was calibrated a second time, and some of the data was re-reduced. This was done to check the probe calibration, and the data as the non-nulling technique was done for the first time in the LSRR facility. Until this time, all five-hole traversing had been done using the probe nulling (yaw nulling) technique. The advantage of the non-nulling technique is that the time required to acquire a plane of data is considerably less than that for the yaw nulling technique.

The data are presented for the three airfoil exit planes, starting with the first stator exit plane denoted as STA1. The data for the rotor exit plane are denoted as STA2, and the second stator exit plane is denoted as STA3. The data are presented as various spanwise mass-averaged or area-averaged quantities, which are defined below, versus the nondimensional spanwise distance from hub to tip. The mass-average and the area-average of a quantity "F" are defined as follows:

$$\text{FMA} = \text{Mass-average of "F"} = \int rFCx\, d\theta \,/\, \int rCx\, d\theta$$

$$\text{FAA} = \text{Area-average of "F"} = \int F d\theta \,/\, \int d\theta$$

The choice of which average is important is based on through flow analysis considerations (Joslyn, et al. [1986]).

At the end of the traverse data for each airfoil row, contour and vector plots are presented for each plane. For the vector plots, the radial component of velocity has been removed so that the plots show the tangential component as it appears coming from the plane.

Finally, all parameters are nondimensional, except for the flow angles, which are presented in degrees. All velocities are normalized by the rotor mean midspan wheel speed, U_m, and the pressures are normalized by the dynamic pressure, Q_m.

Full span traverse results for the first stator, rotor, and second stator are shown in the figures that follow the text portion of this appendix (Figures 116 through 208).

References for Appendix C:

Joslyn, D. and Dring, R.P., *Three-Dimensional Flow in an Axial Turbine: Part 1 - Aerodynamic Mechanisms*, J. of Turbomachinery, Vol. 114, 1992, pp. 61-70.

First Stator Exit Flowfield Data (28 Airfoil Count) Acquired at X_2/B_x - rotor = 0.746, 0.54, Cx/U = 0.78

Compared to Data Acquired as Part of Air Force Office of Scientific Research Contract

(STA1)

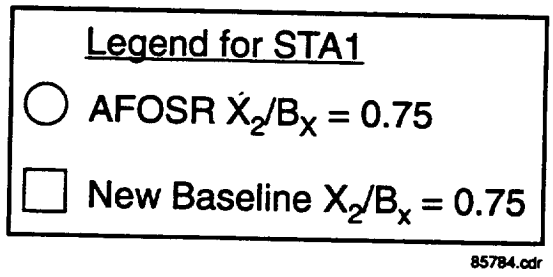

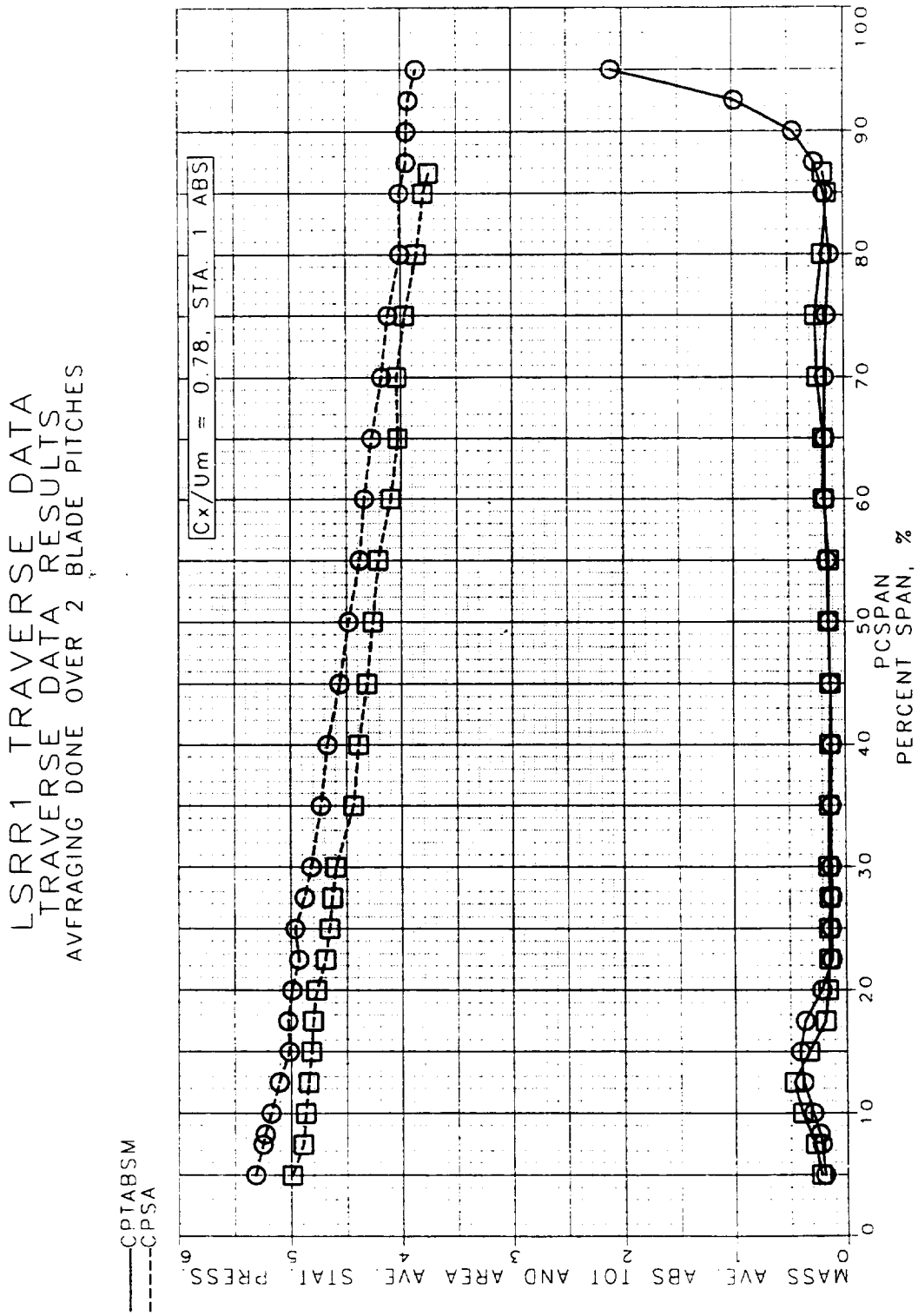

Figure 116. Mass Averaged Absolute and Static Pressure Coefficient at STA1

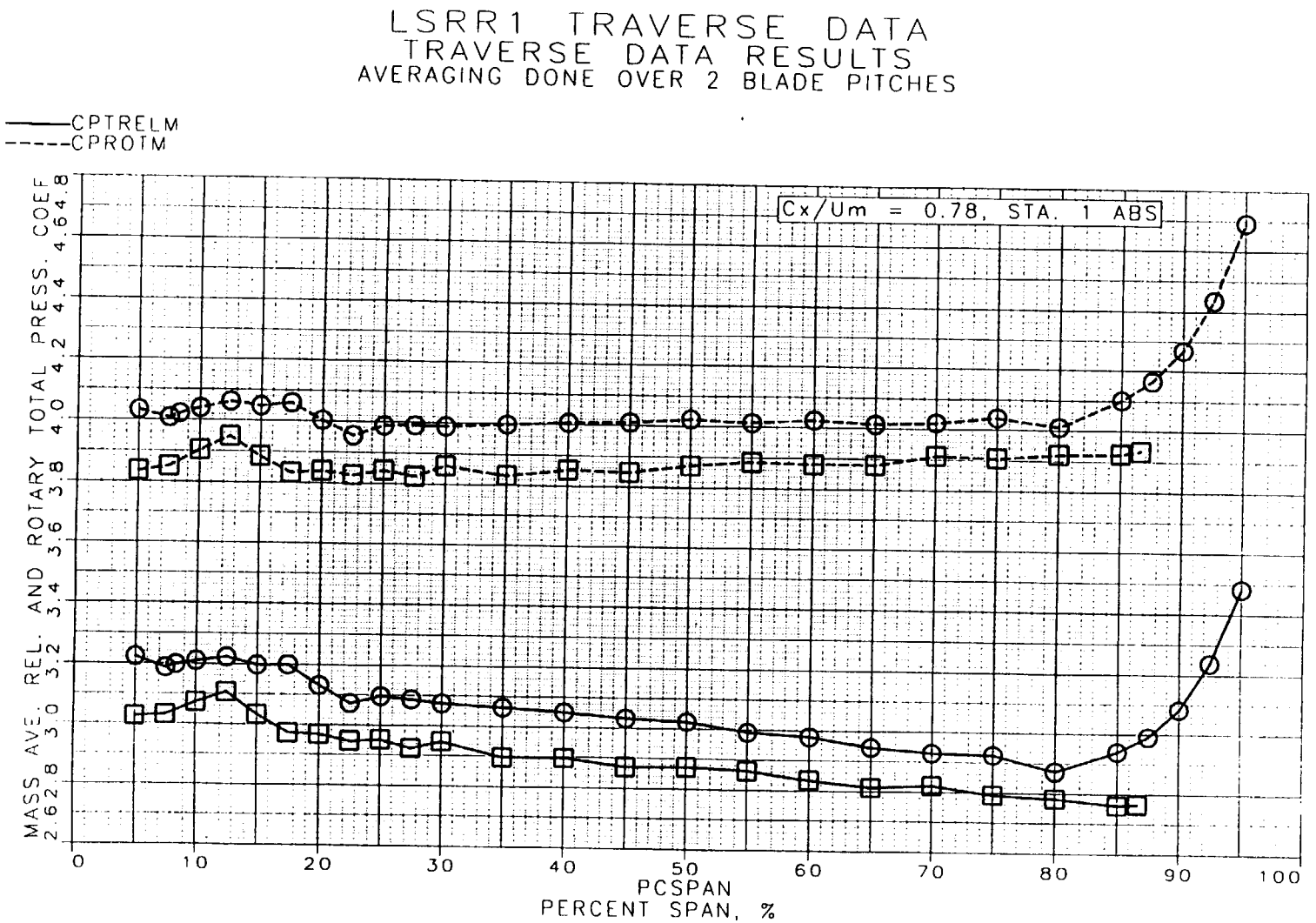

Figure 117. Mass Averaged Relative and Rotary Total Pressure Coefficient at STA1

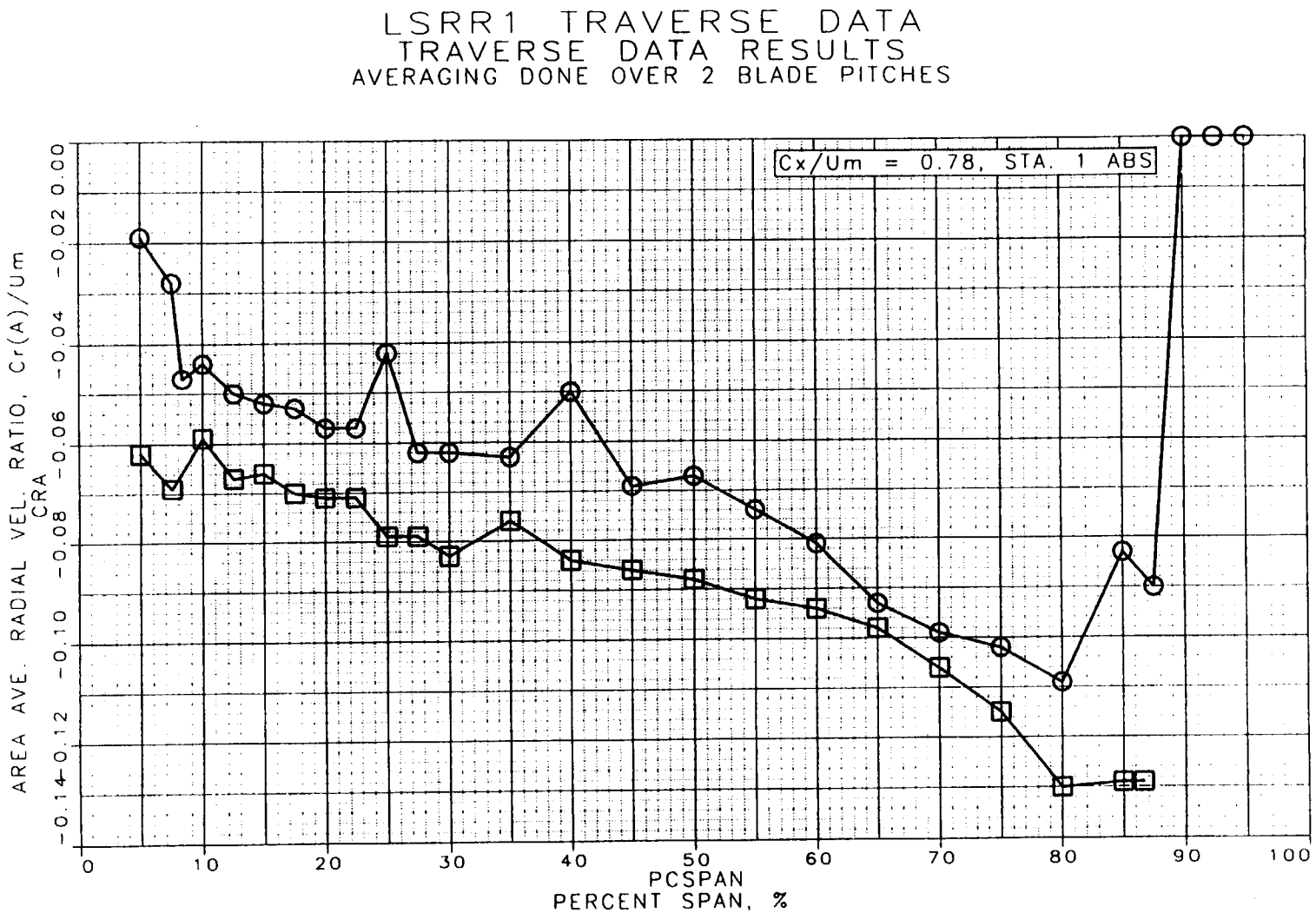

Figure 118. Area Averaged Radial Velocity Ratio at STA1

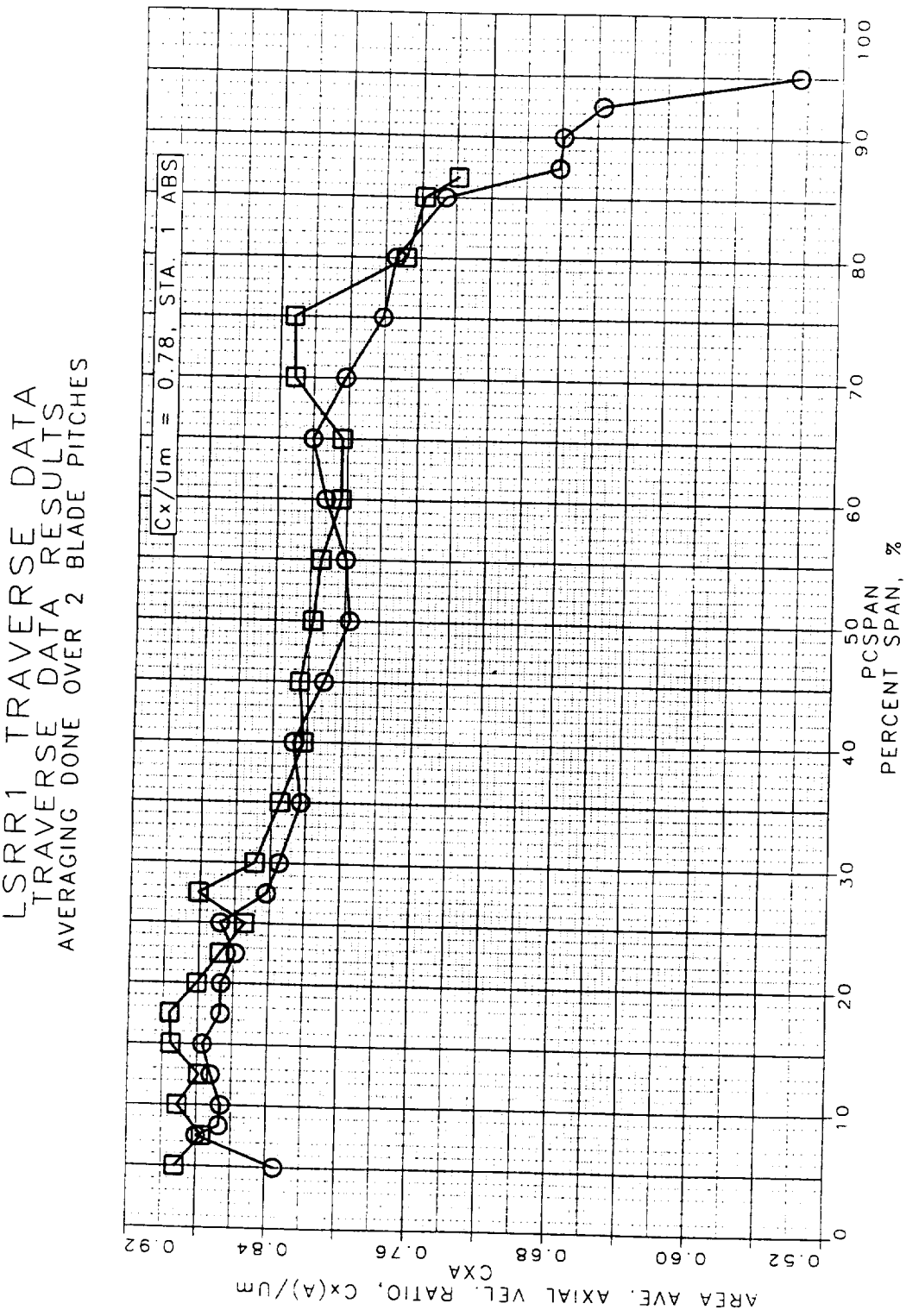

Figure 119. Area Averaged Axial Velocity Ratio at STA1

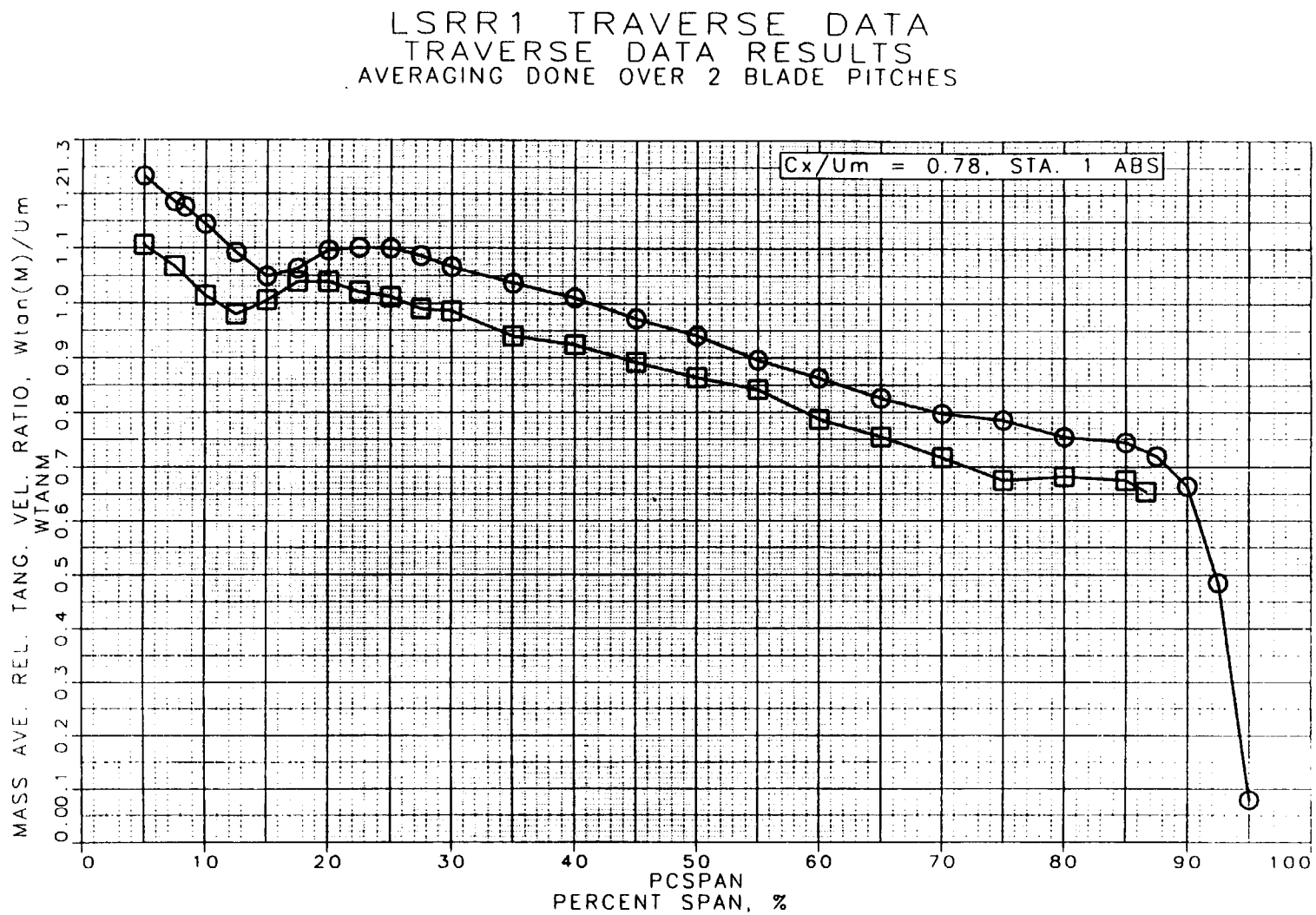

Figure 120. Mass Averaged Total Velocity Ratio at STA1

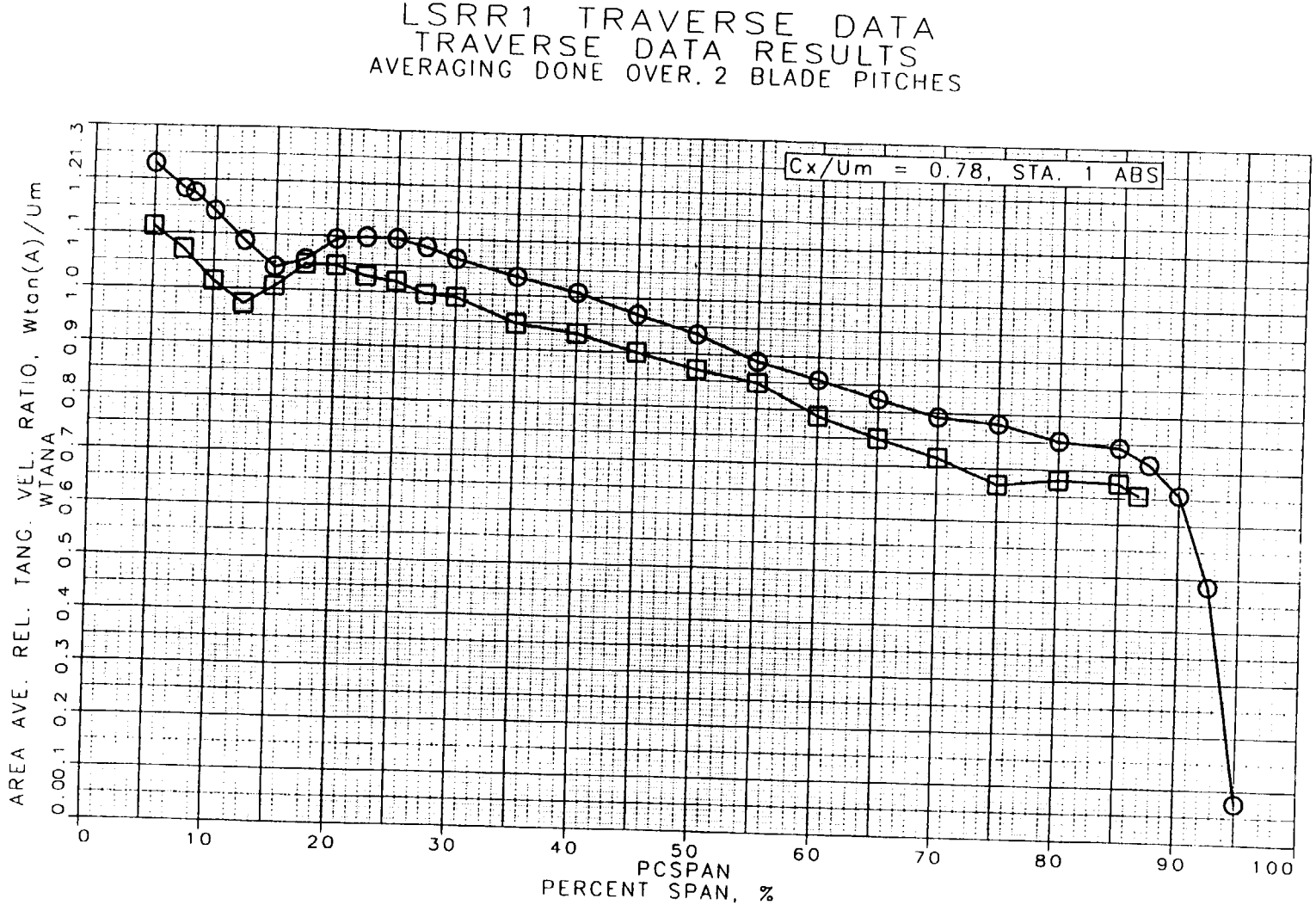

Figure 121. Area Averaged Total Velocity Ratio at STA1

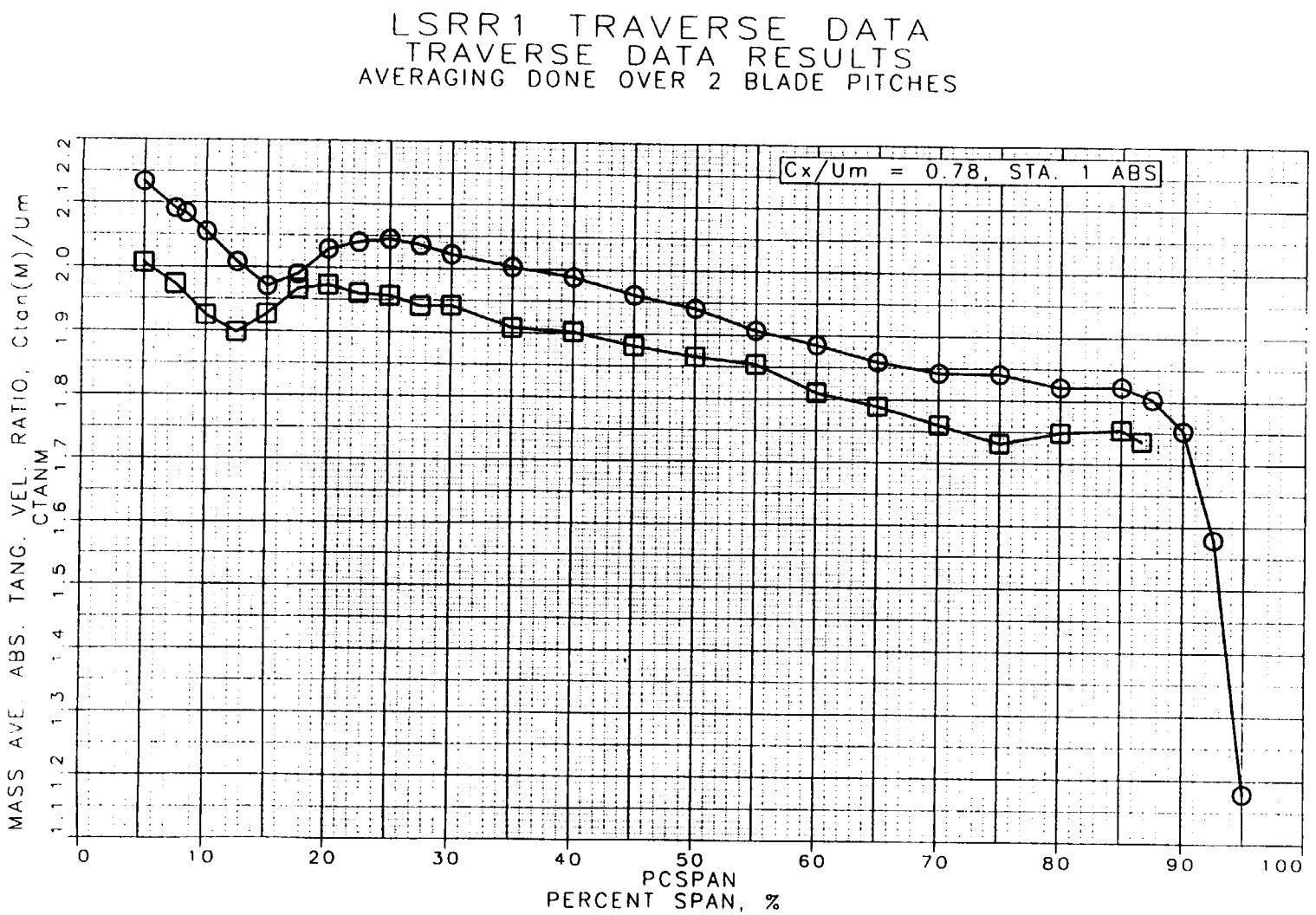

Figure 122. Mass Averaged Tangential Velocity Ratio at STA1

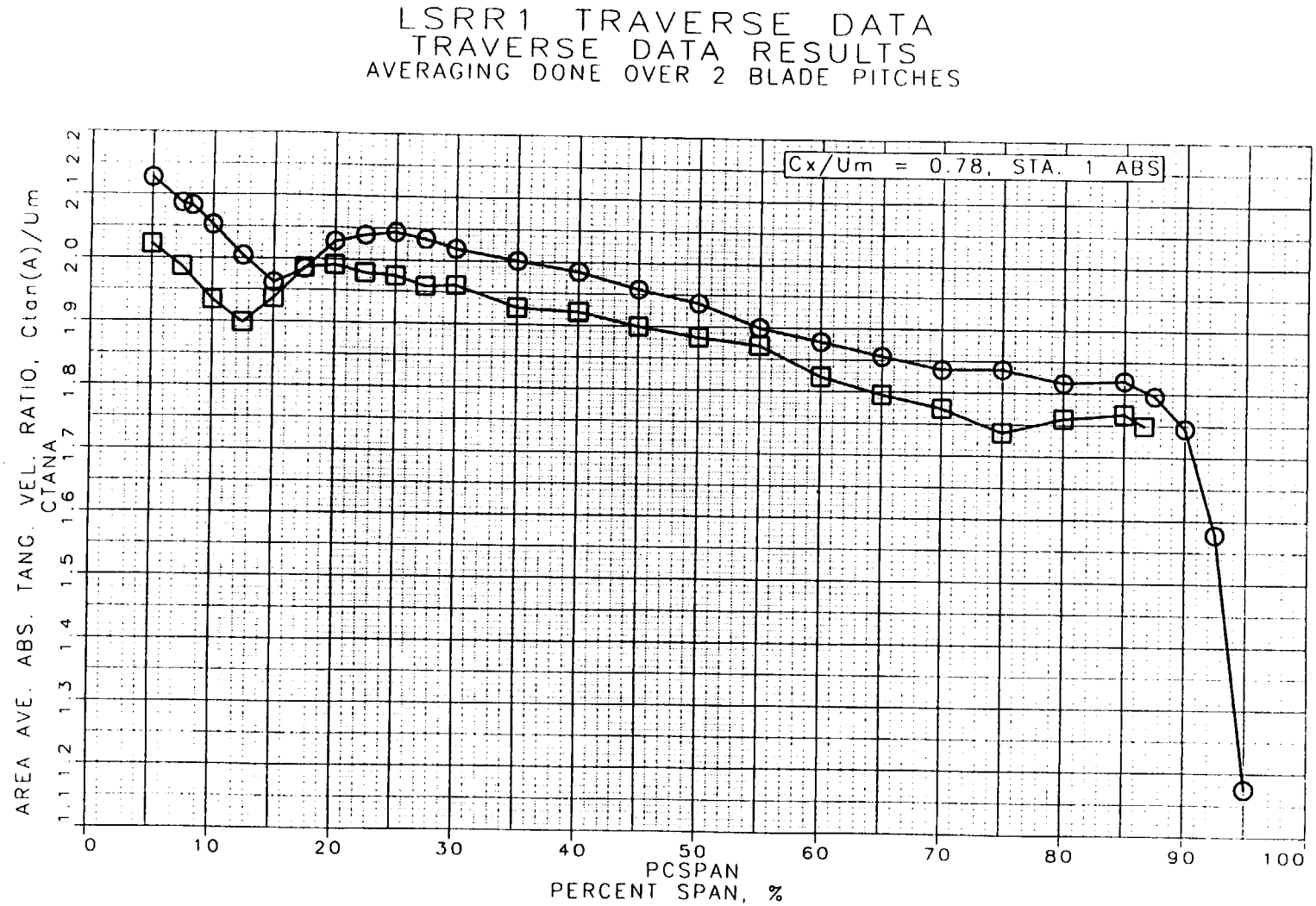

Figure 123. Area Averaged Tangential Velocity Ratio at STA1

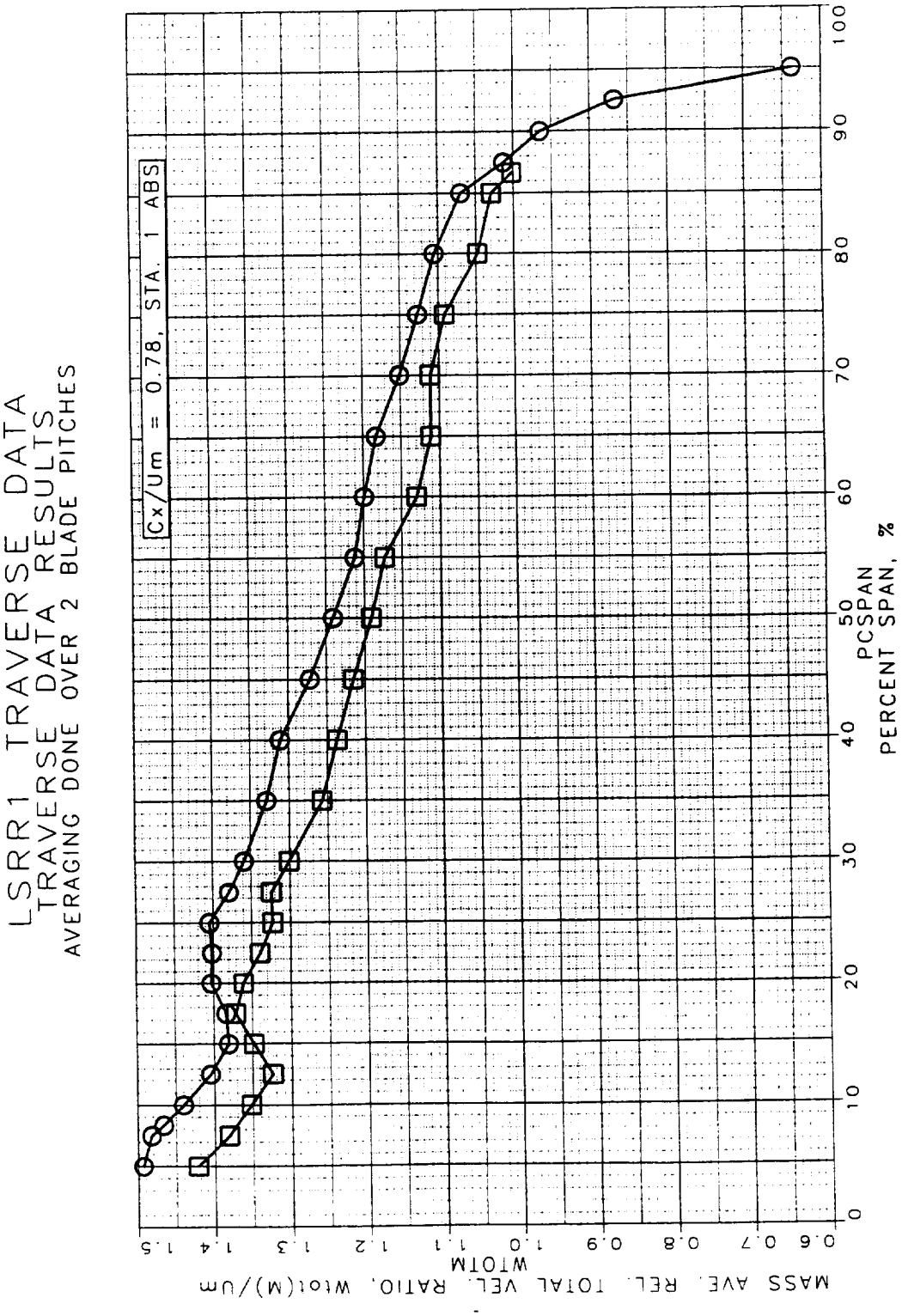

Figure 124. Mass Averaged Total Relative Velocity Ratio at STA1

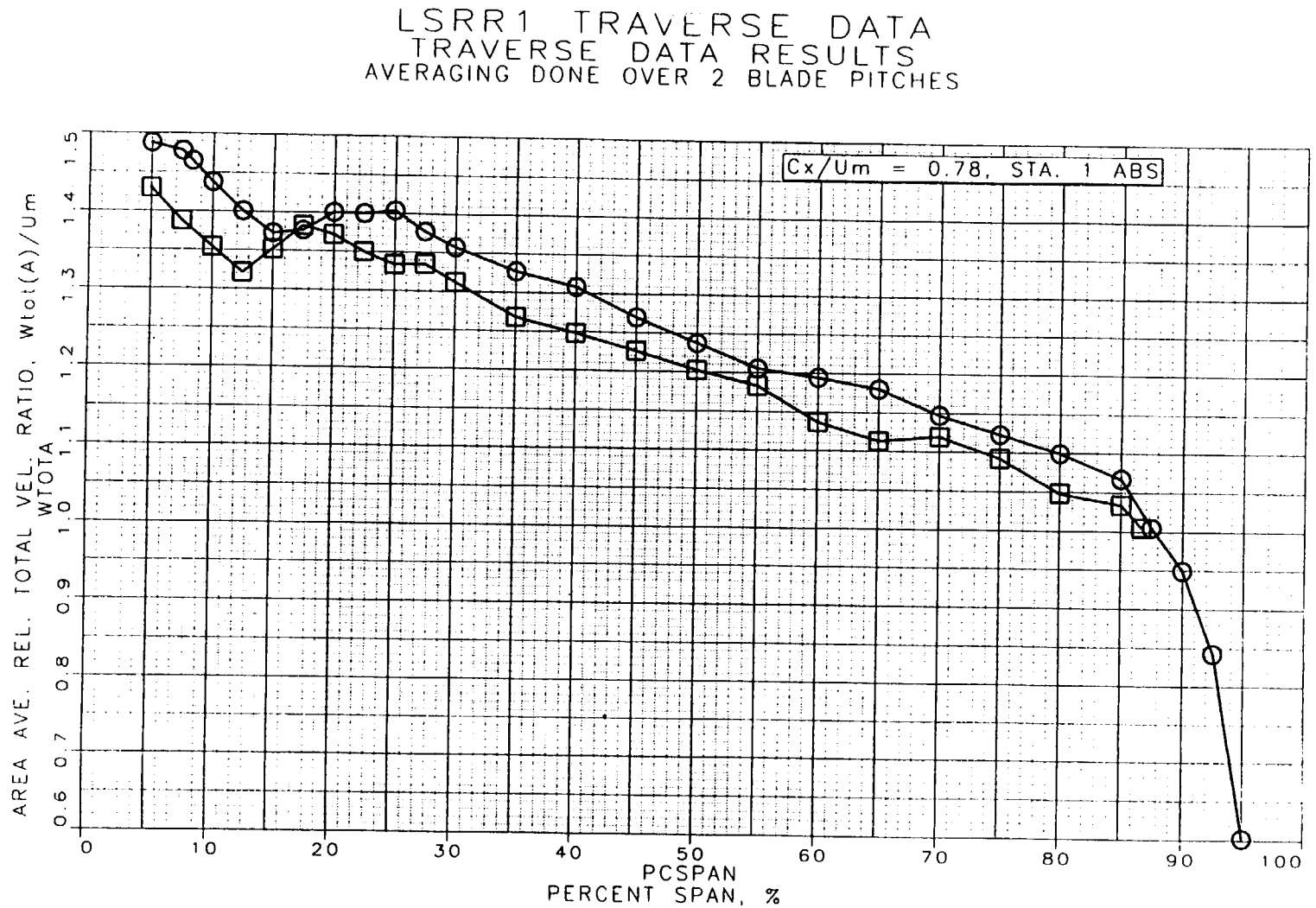

Figure 125. Area Averaged Total Relative Velocity Ratio at STA1

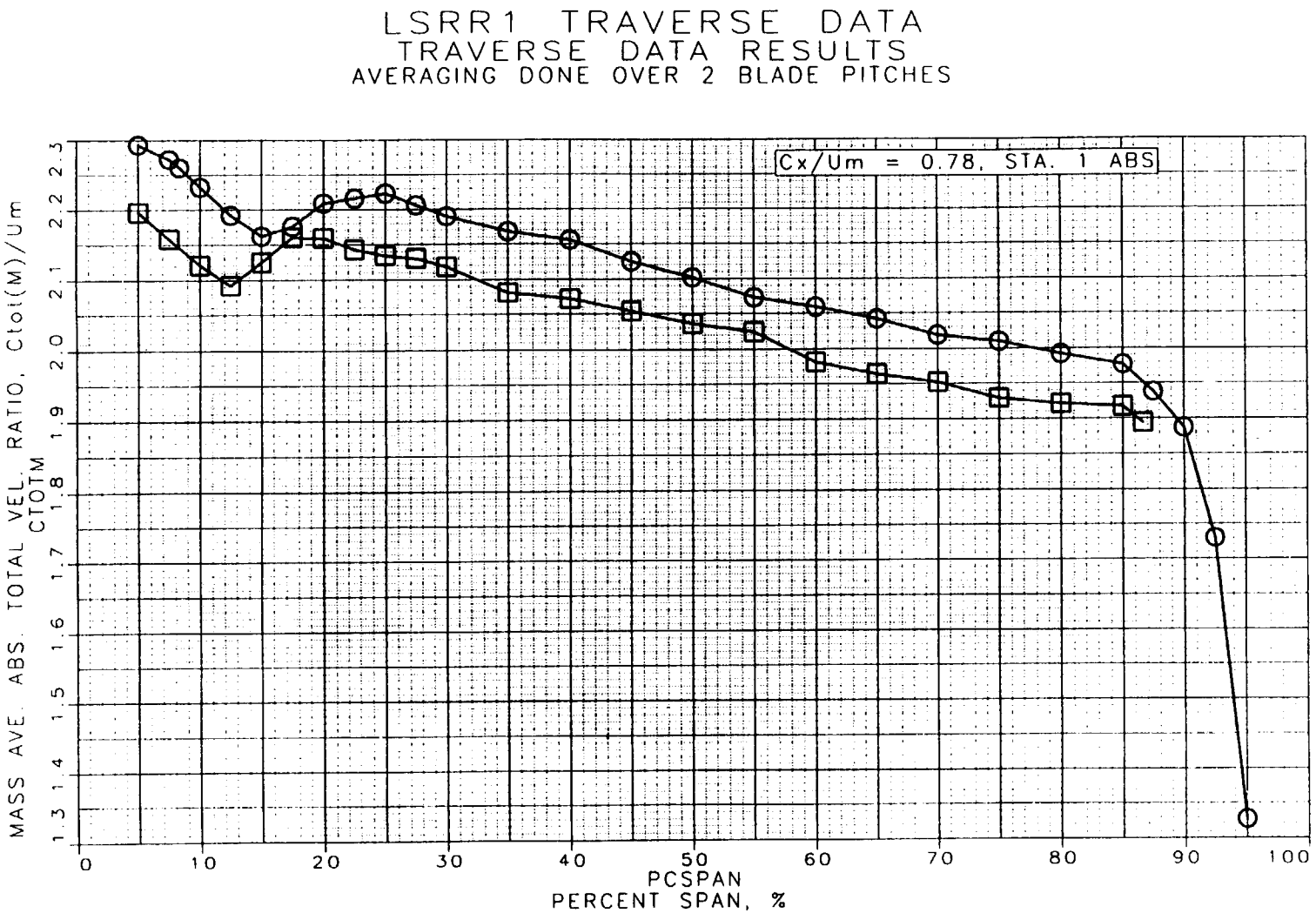

Figure 126. Mass Averaged Absolute Total Velocity Ratio at STA1

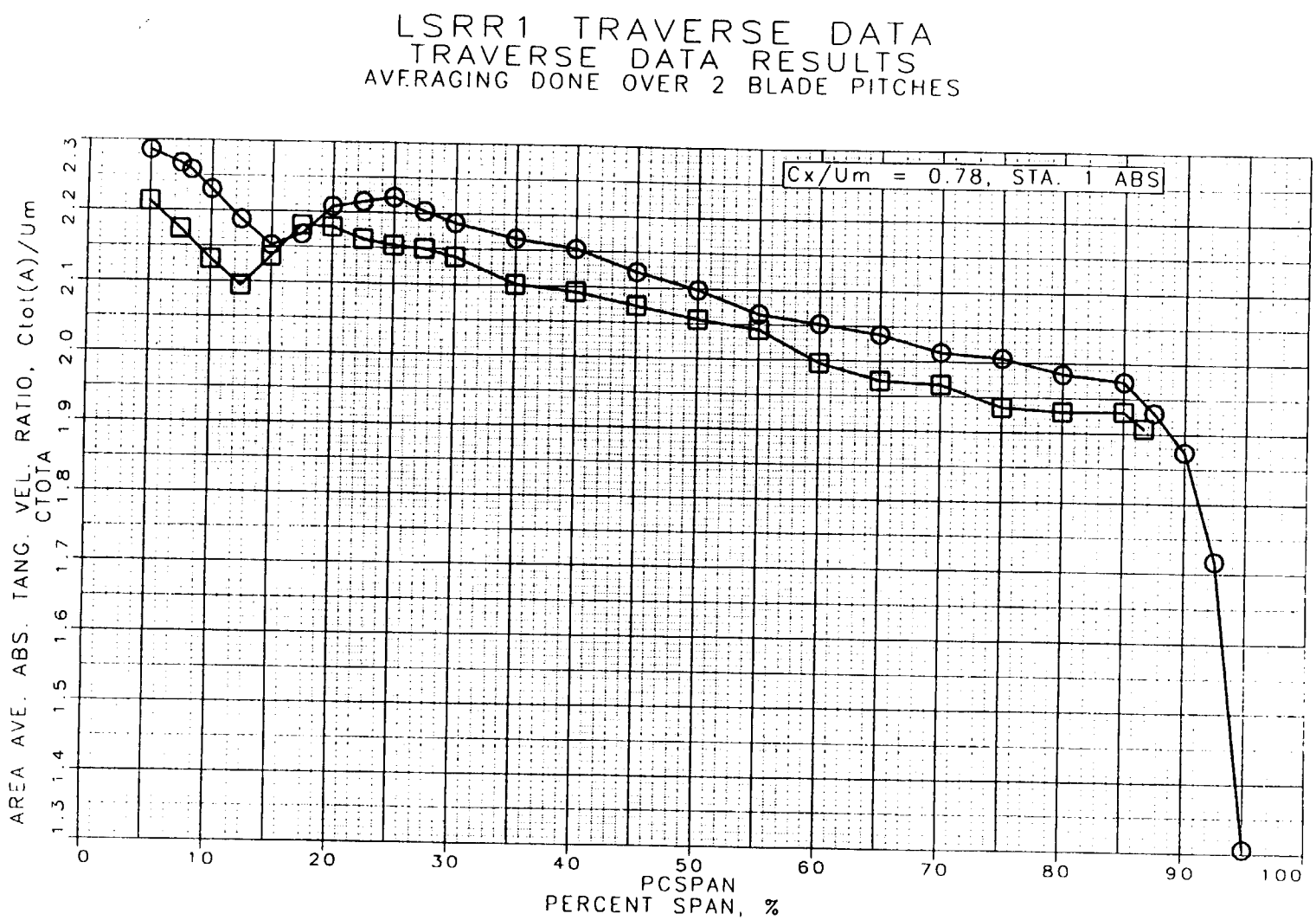

Figure 127. Area Averaged Relative Tangential Velocity Ratio at STA1

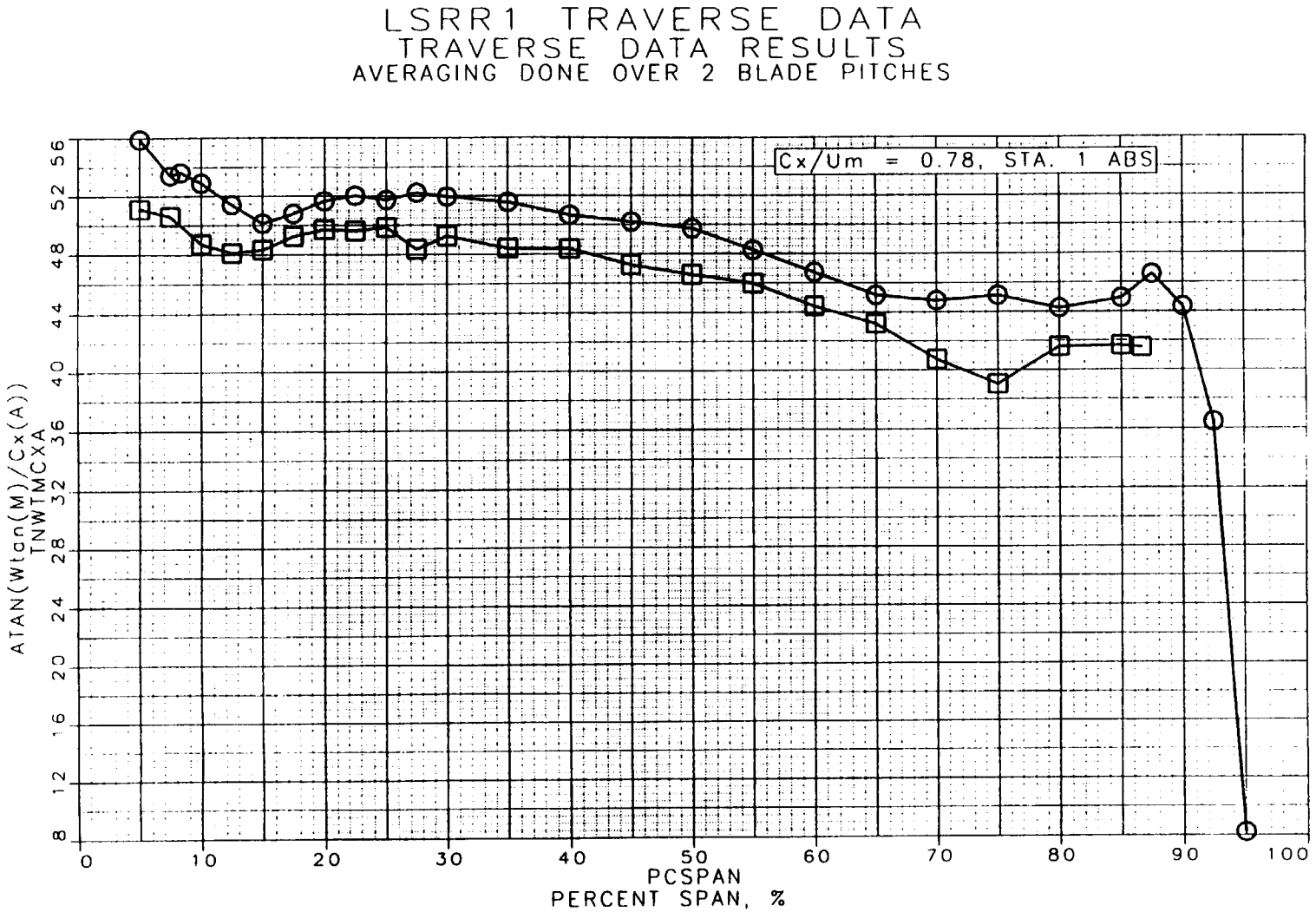

Figure 128. Area Averaged Absolute Yaw Angle at STA1

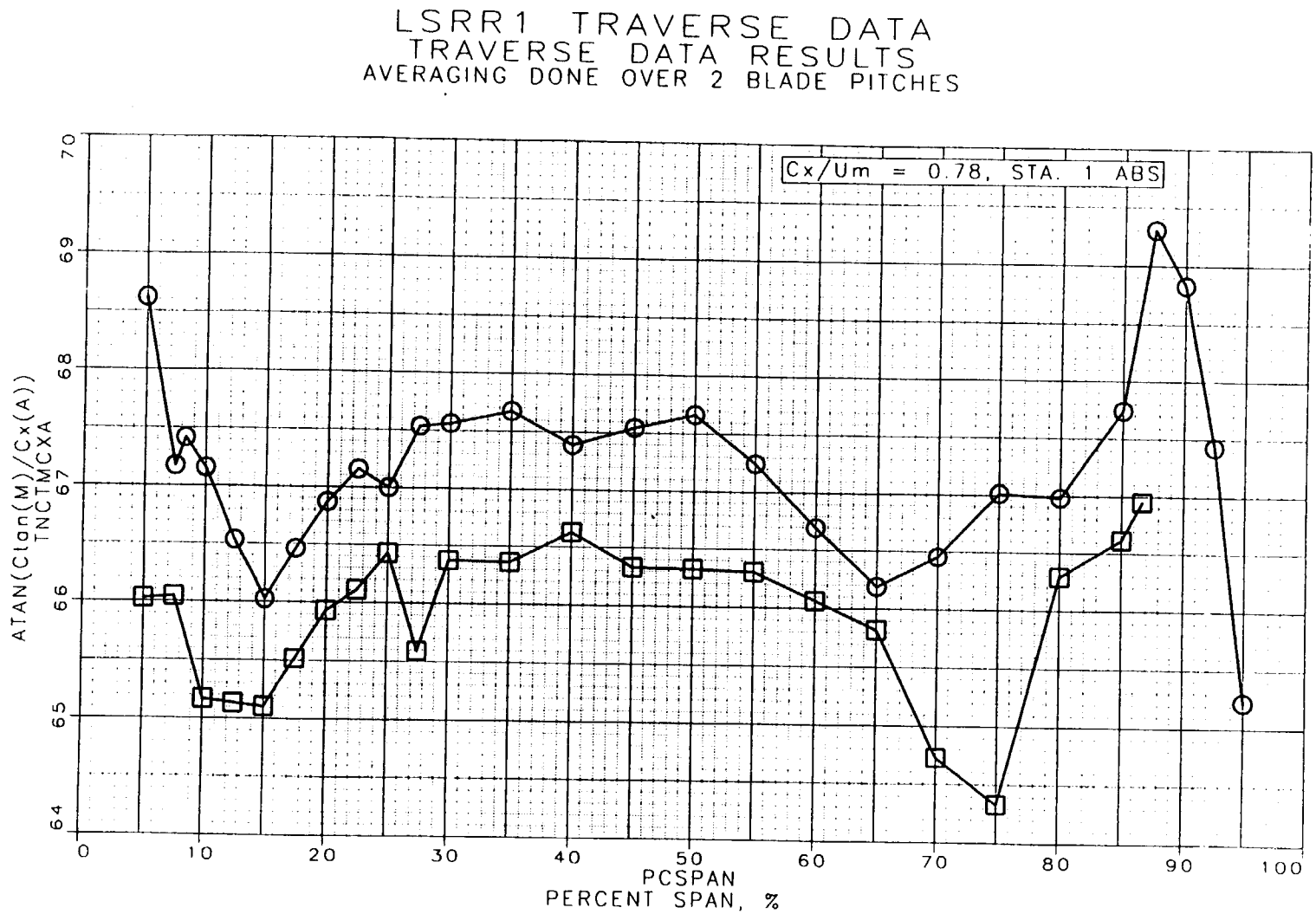

Figure 129. Area Averaged Relative Yaw Angle at STA1

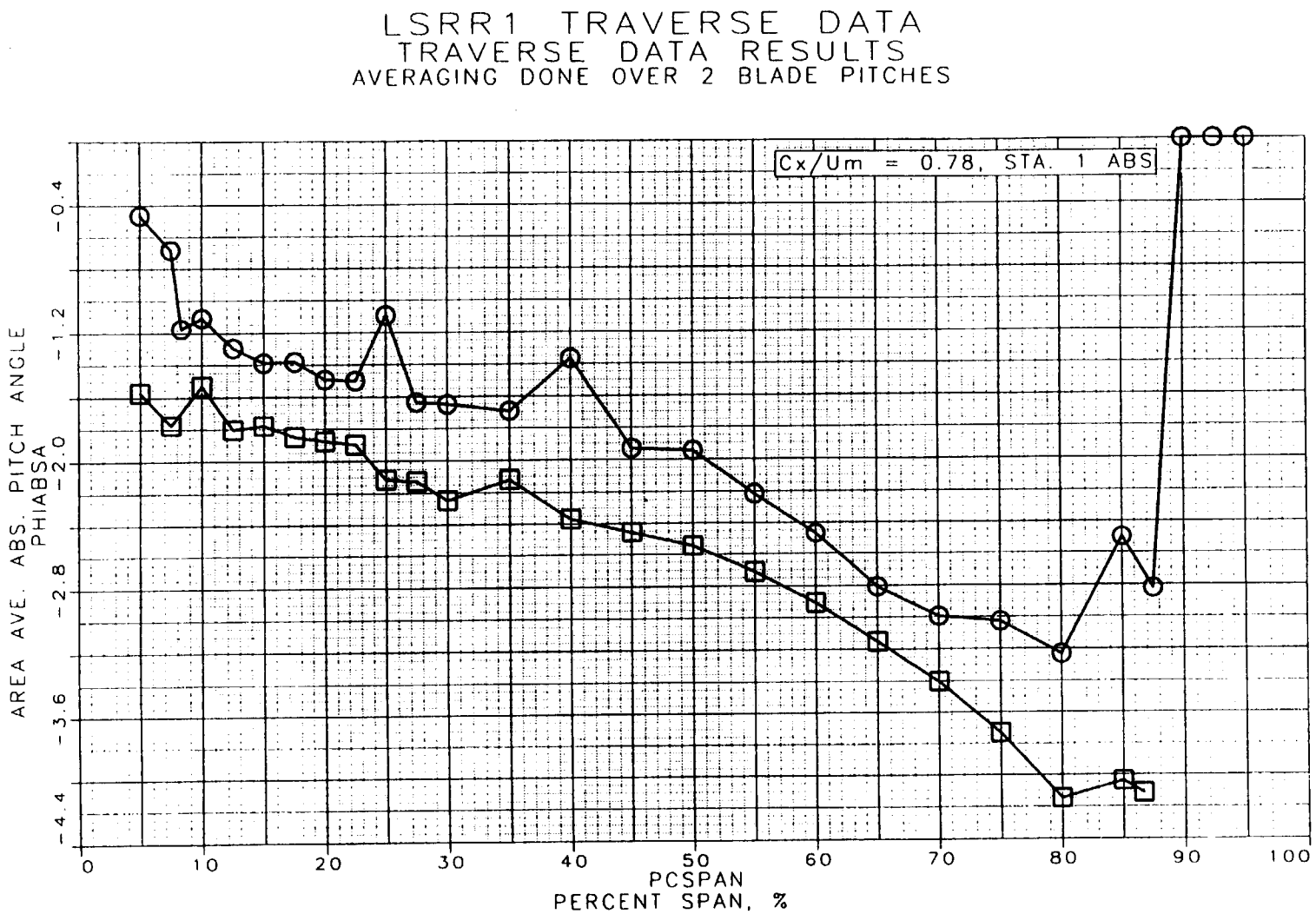

Figure 130. Area Averaged Absolute Pitch Angle at STA1

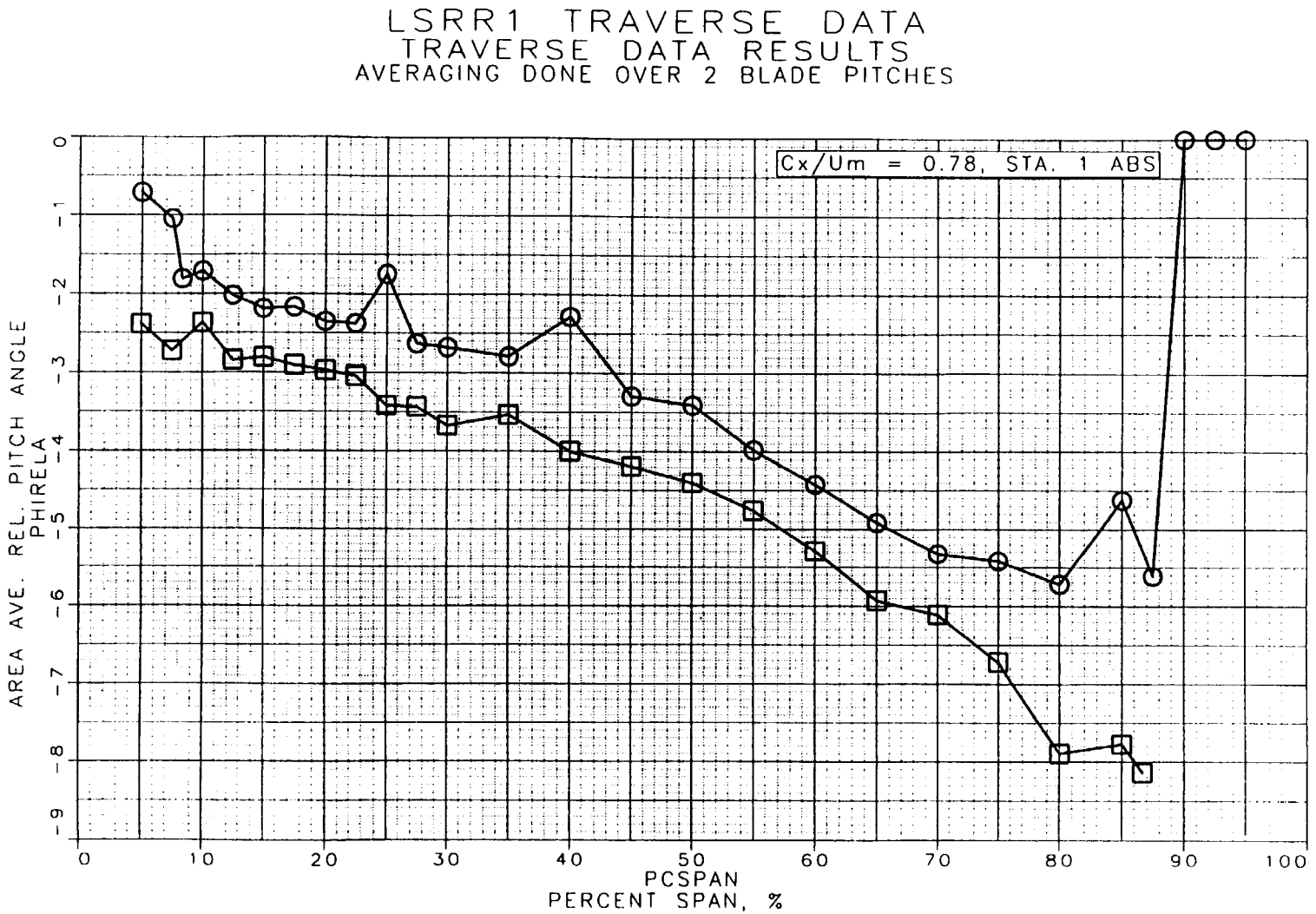

Figure 131. Area Averaged Relative Pitch Angle at STA1

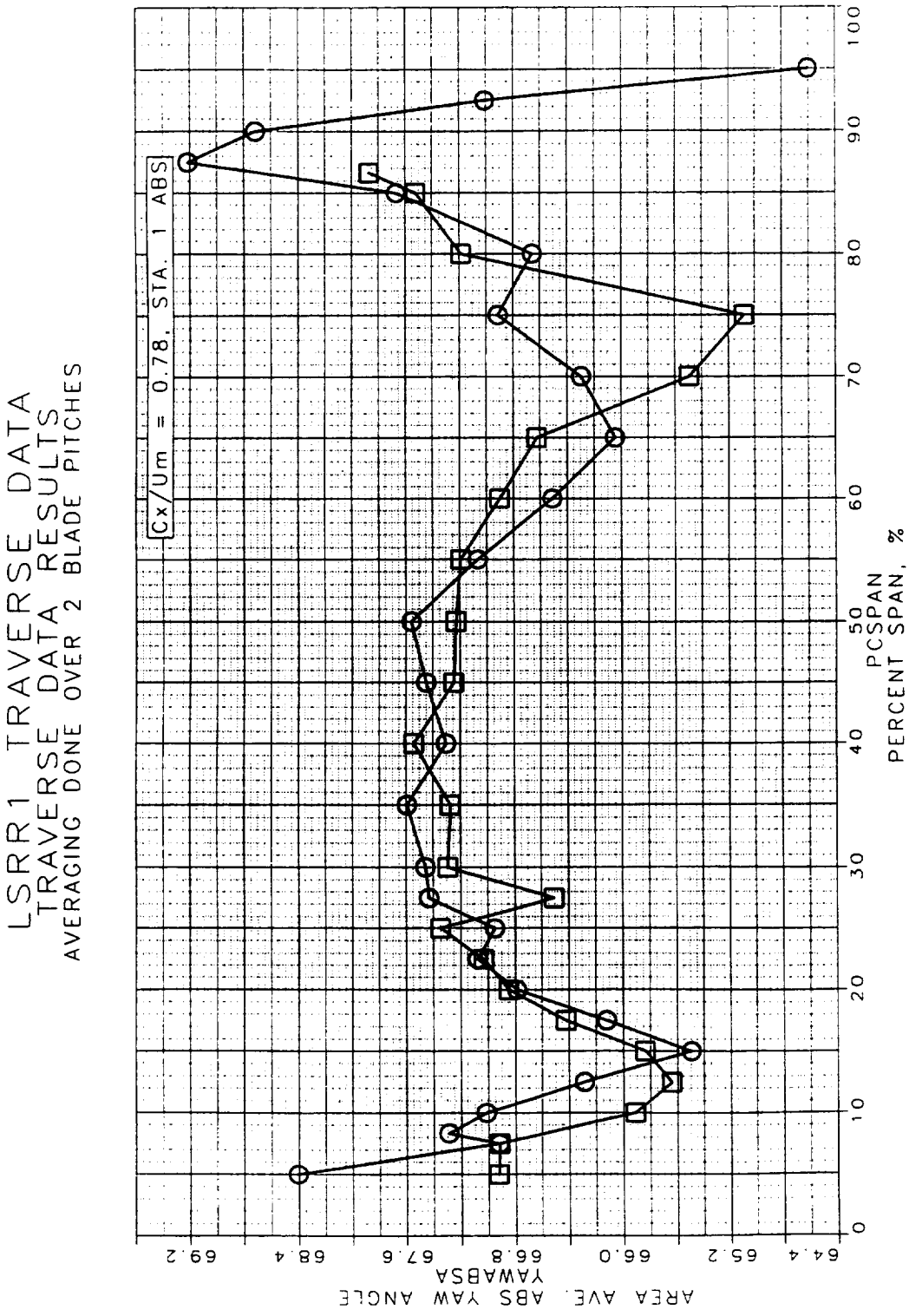

Figure 132. Area Averaged Absolute Yaw Angle at STA1

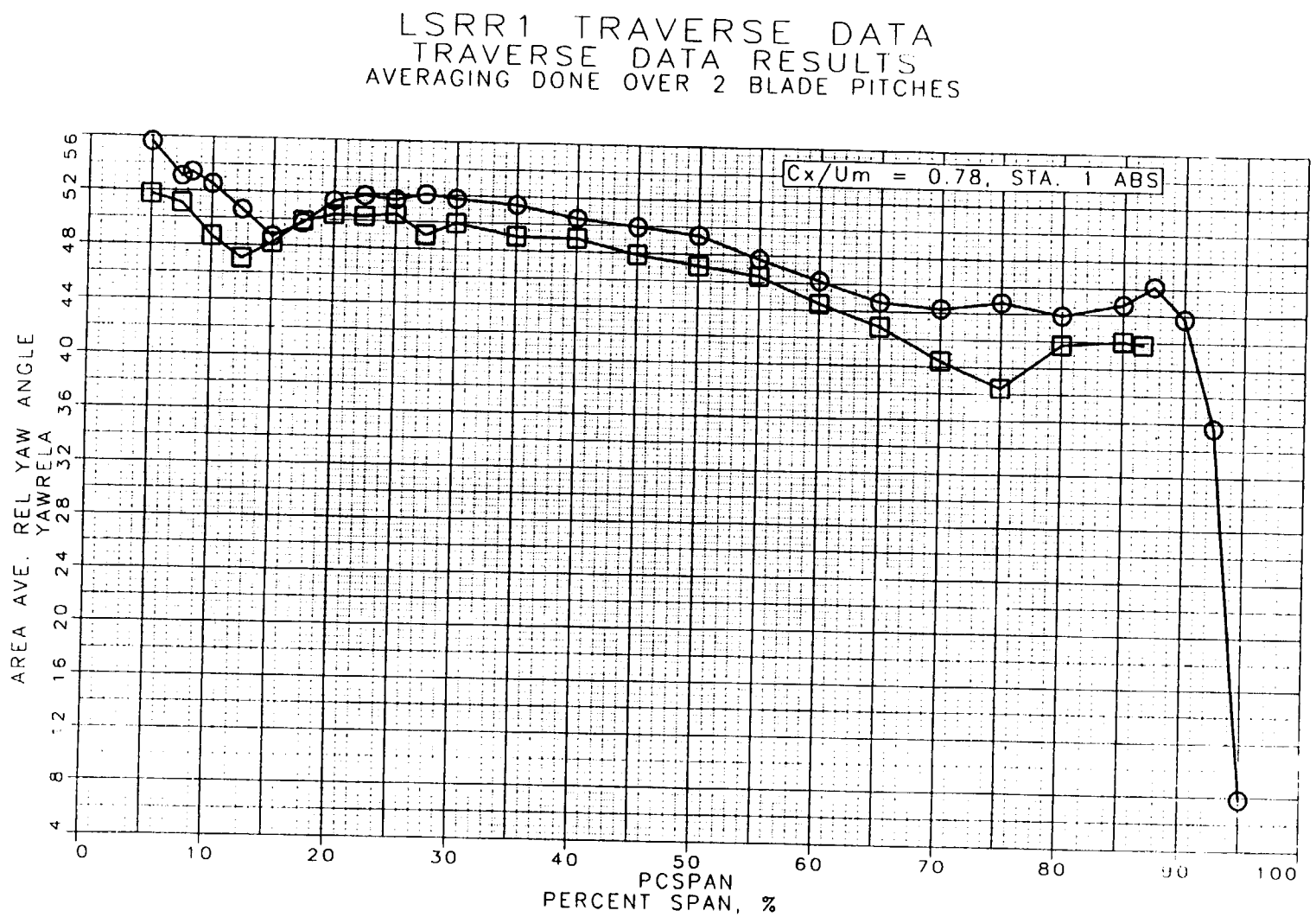

Figure 133. Area Averaged Relative Yaw Angle at STA1

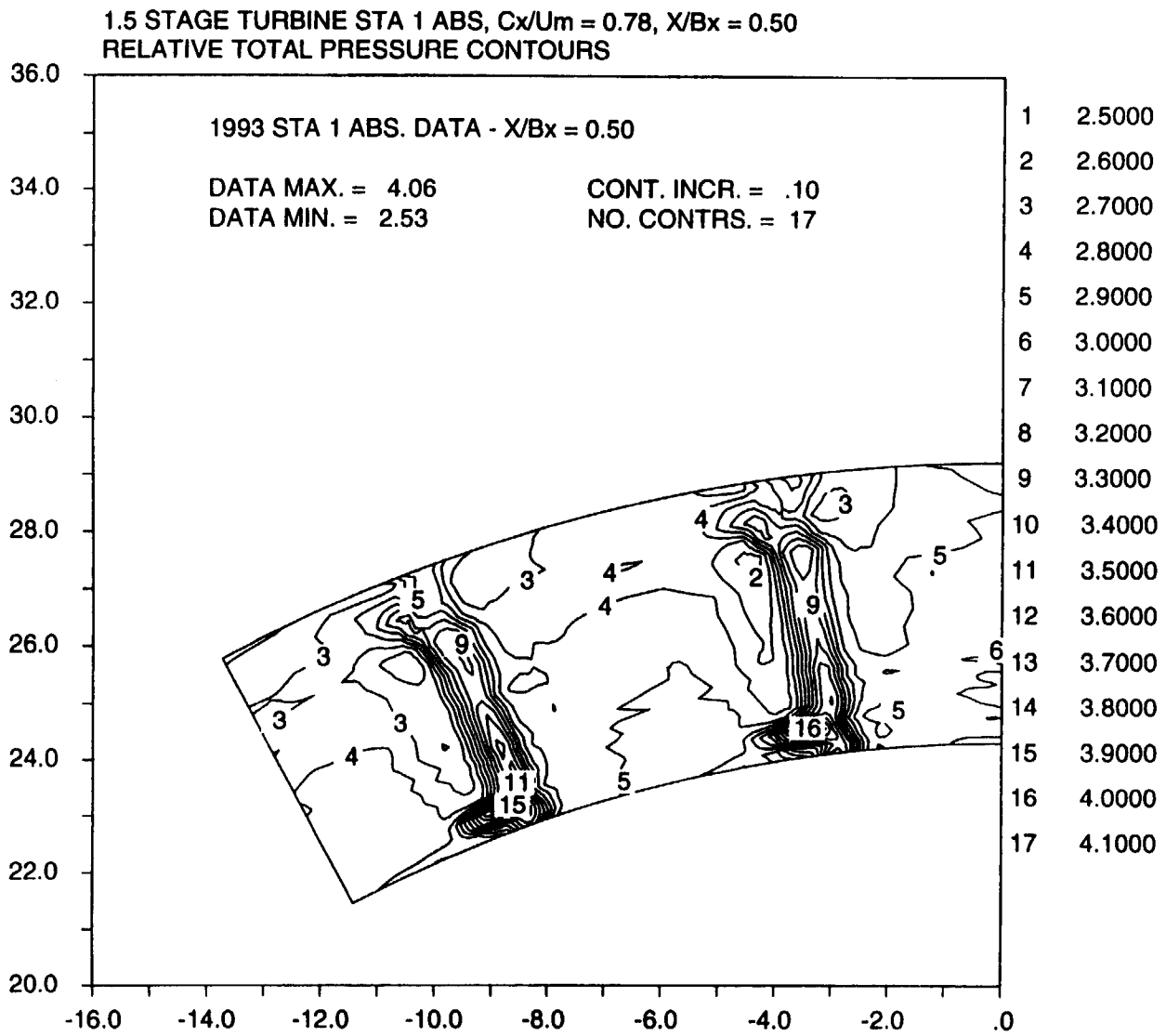

Figure 134. Relative Total Pressure Coefficient Contours at STA1

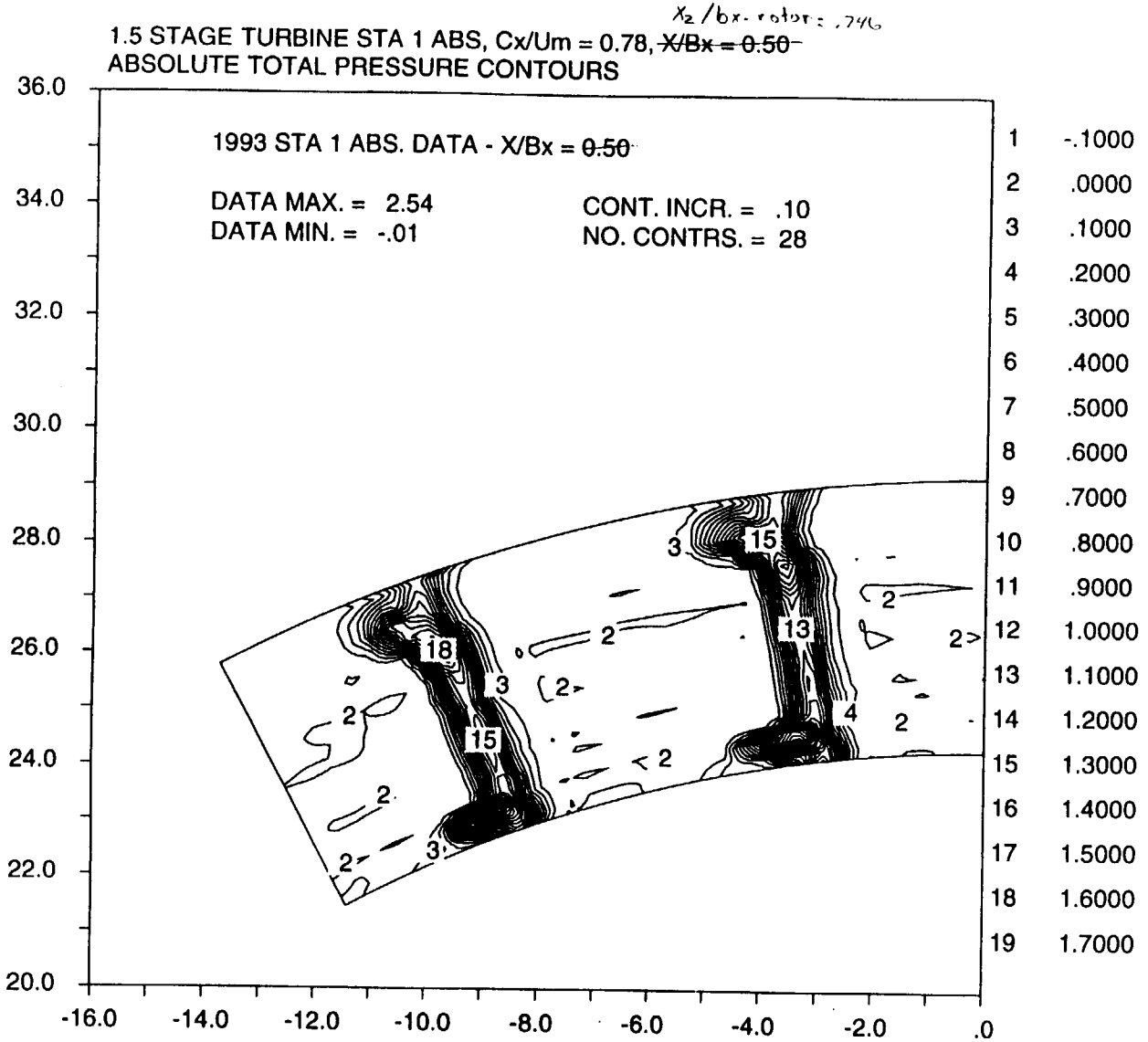

Figure 135. Absolute Total Pressure Coefficient Contours at STA1

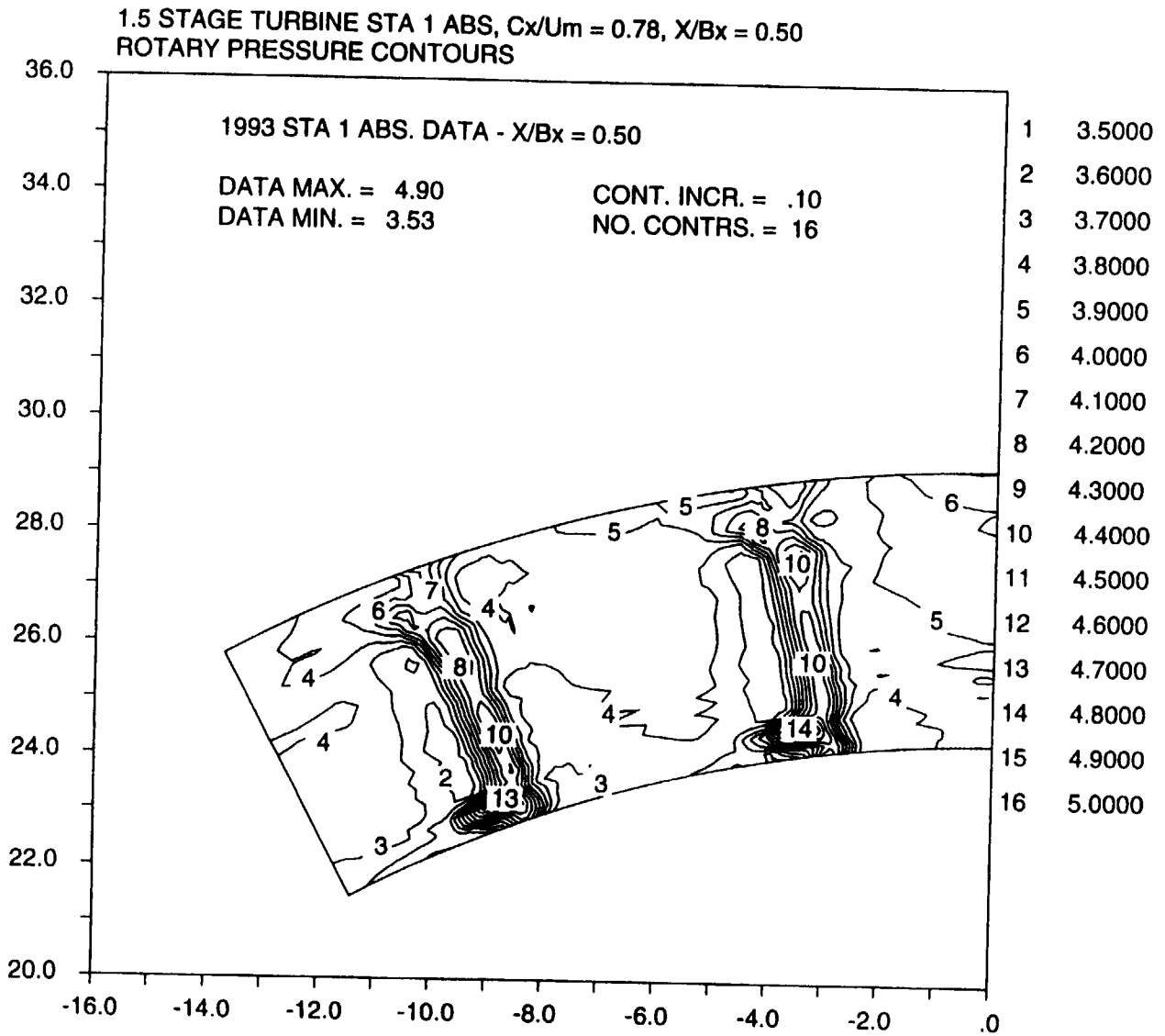

Figure 136. Rotary Total Pressure Coefficient Contours at STA1

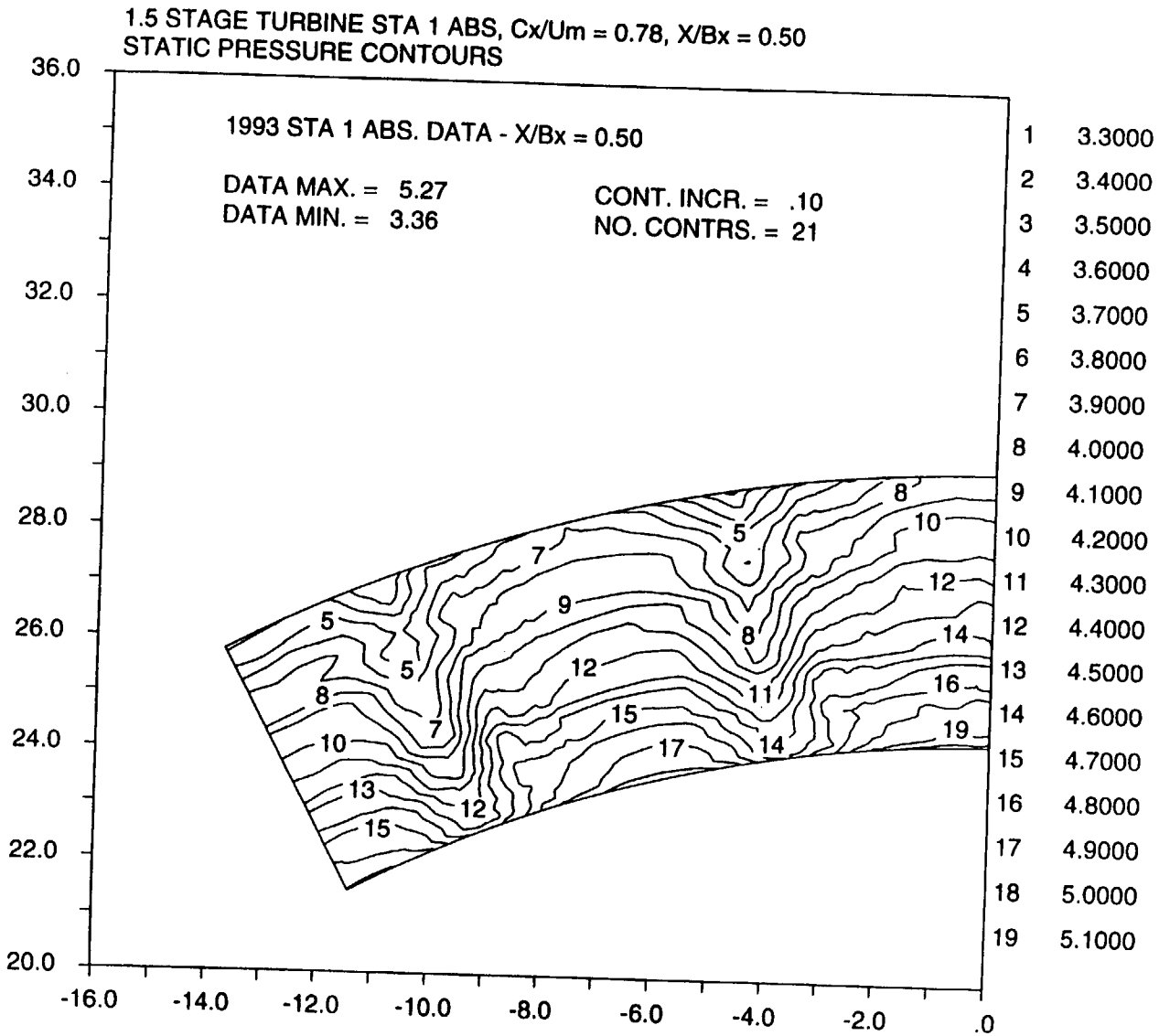

Figure 137. Static Pressure Coefficient Contours at STA1

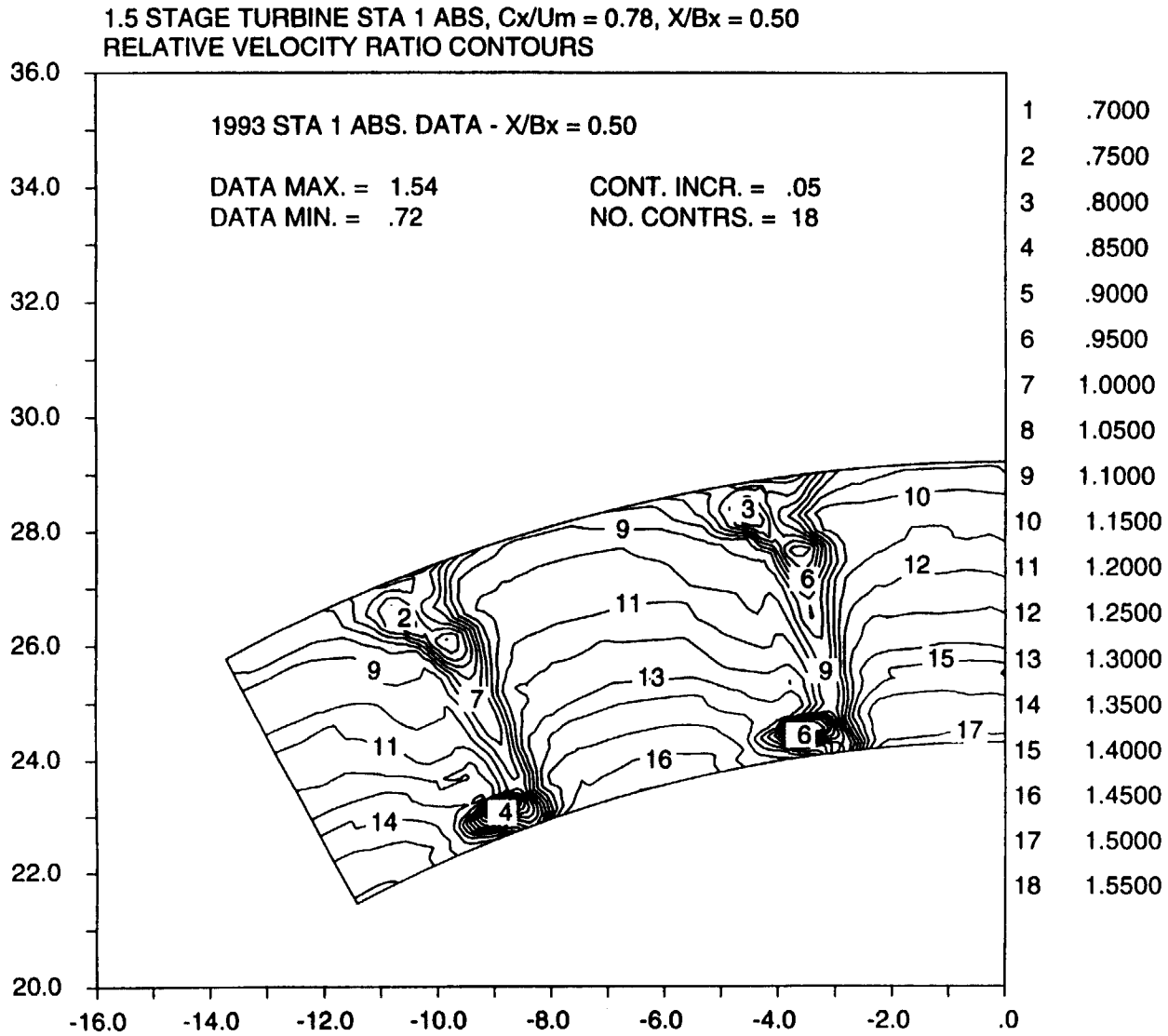

Figure 138. Relative Velocity Ratio Contours at STA1

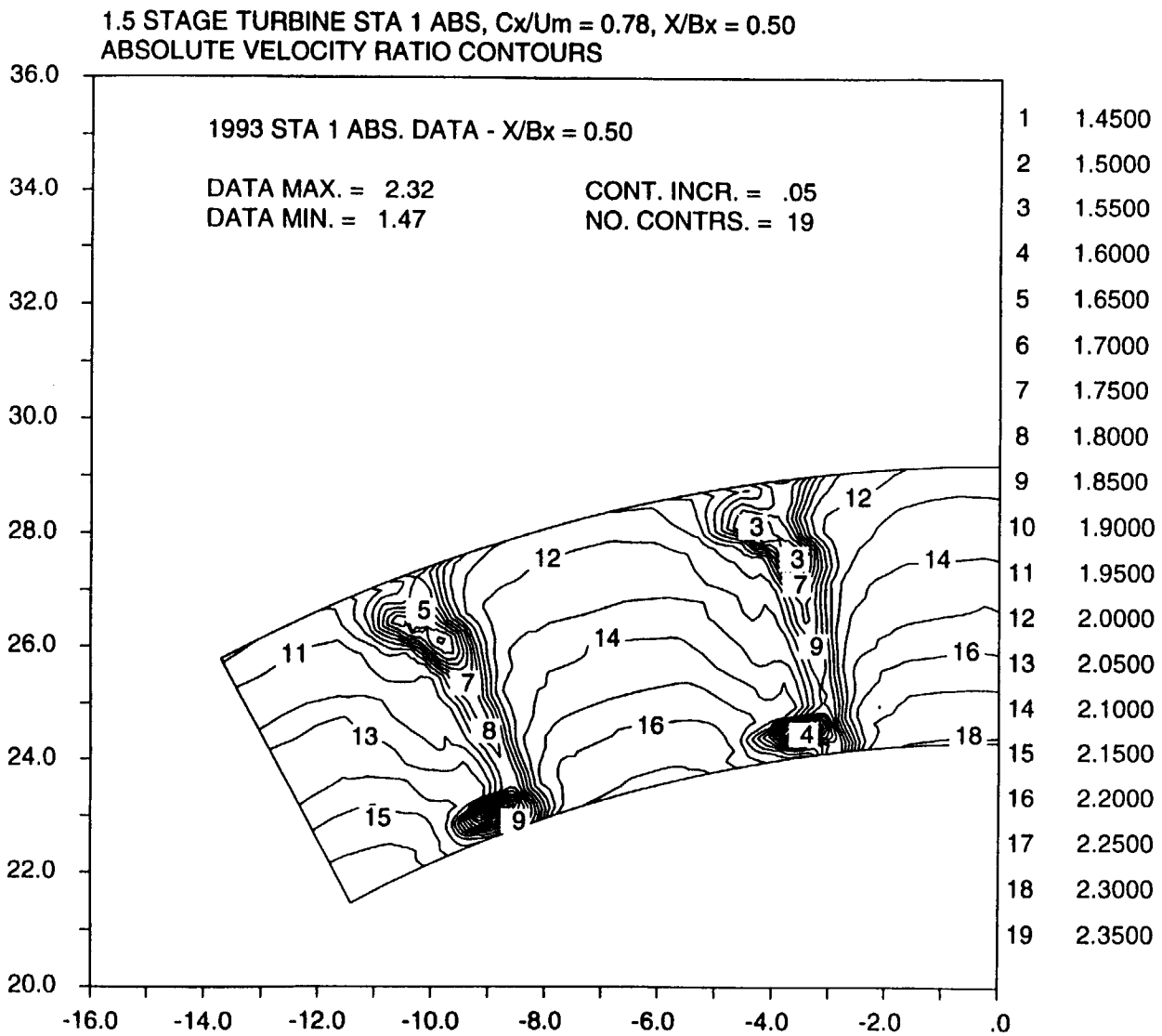

Figure 139. Absolute Velocity Ratio Contours at STA1

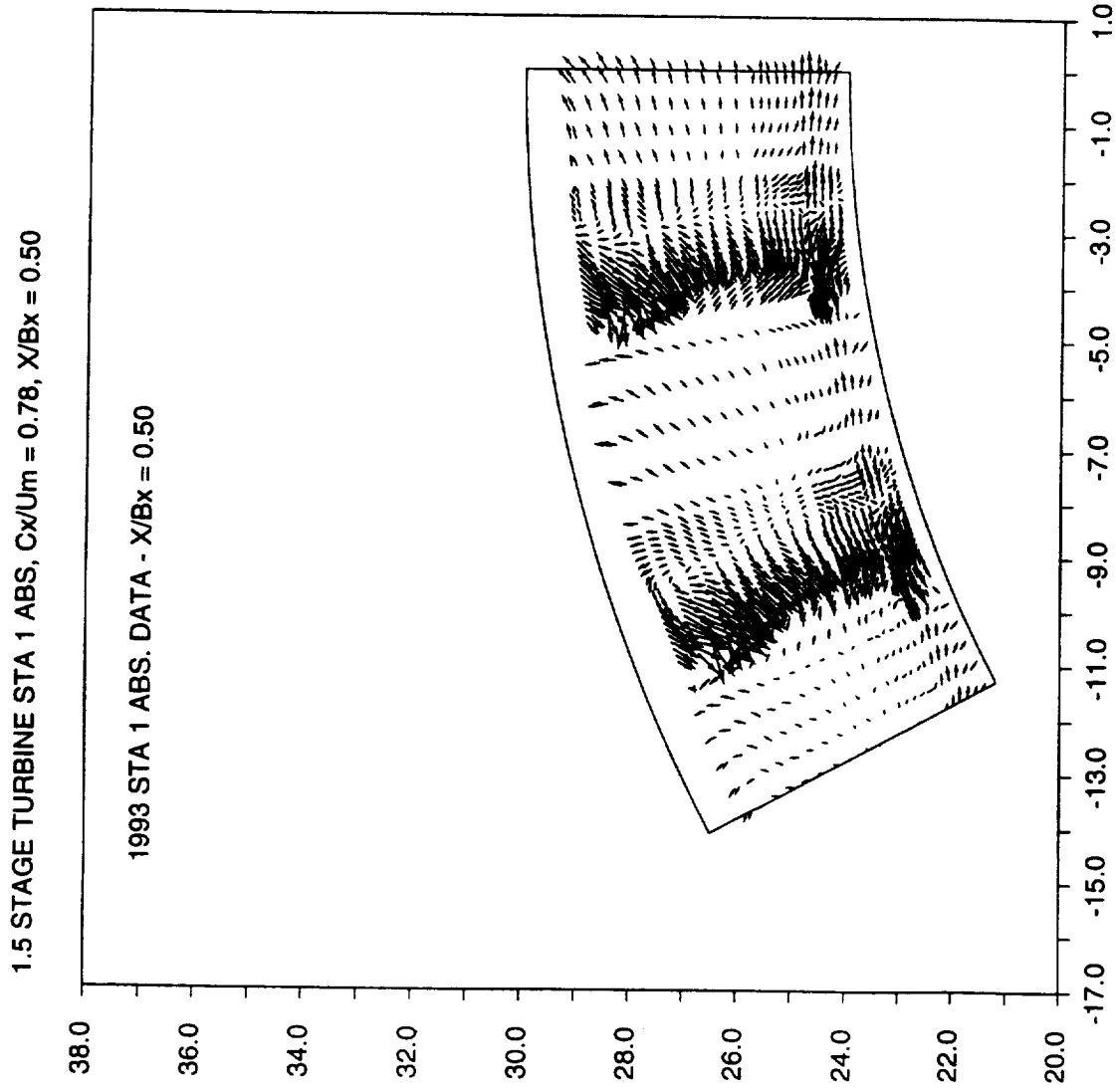

Figure 140. Velocity Vectors at STA1

Rotor Exit Flowfield Data (28 Airfoil Count) Acquired at X_2/B_x - rotor = 0.746, Cx/U = 0.78

Compared to Data Acquired as Part of Air Force Office of Scientific Research Contract

(STA2)

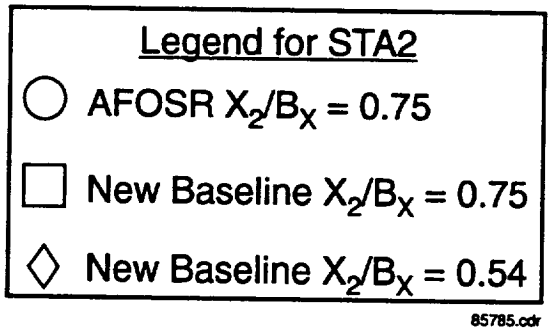

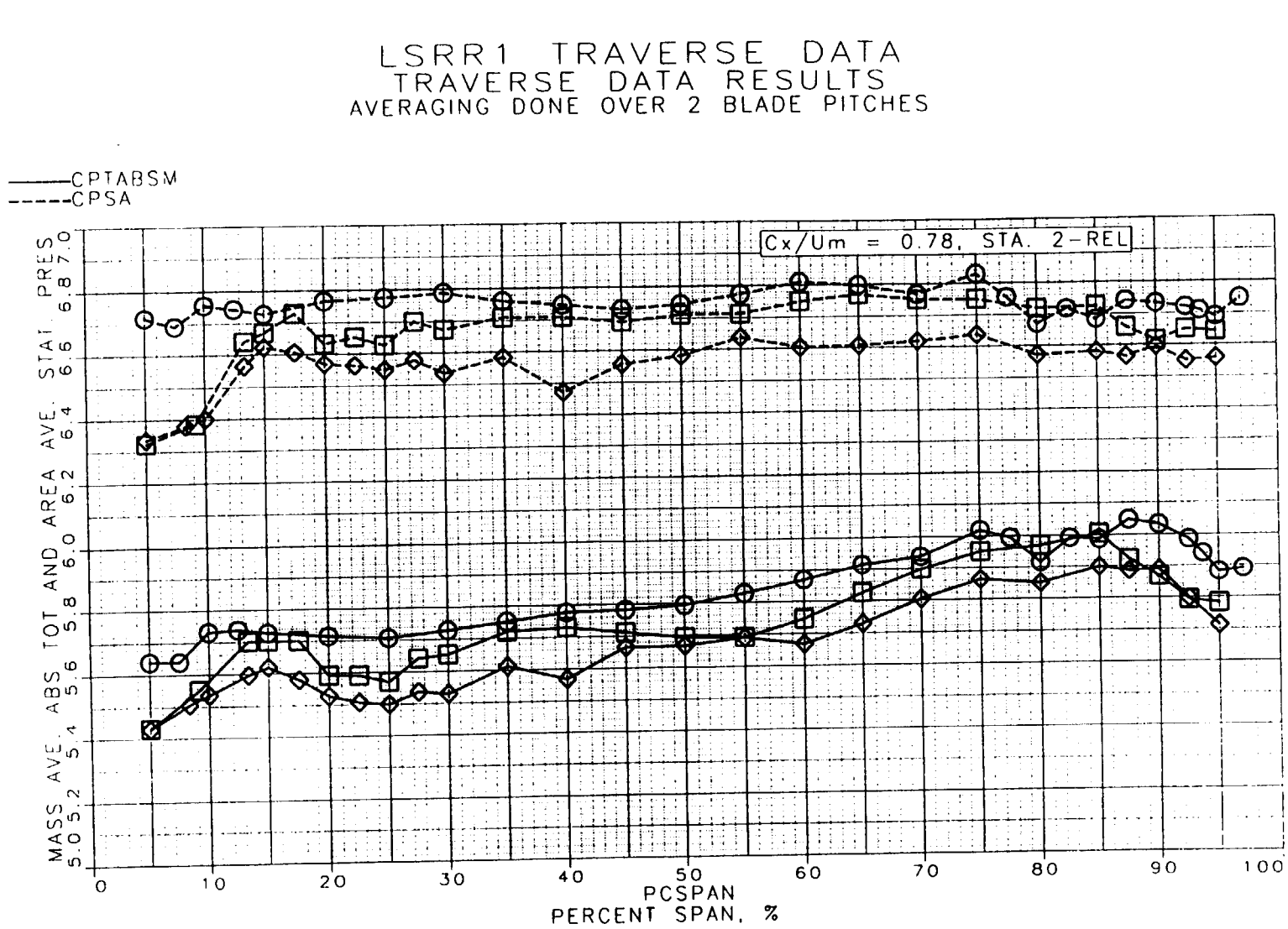

Figure 141. Mass Averaged Absolute and Static Pressure Coefficient at STA2

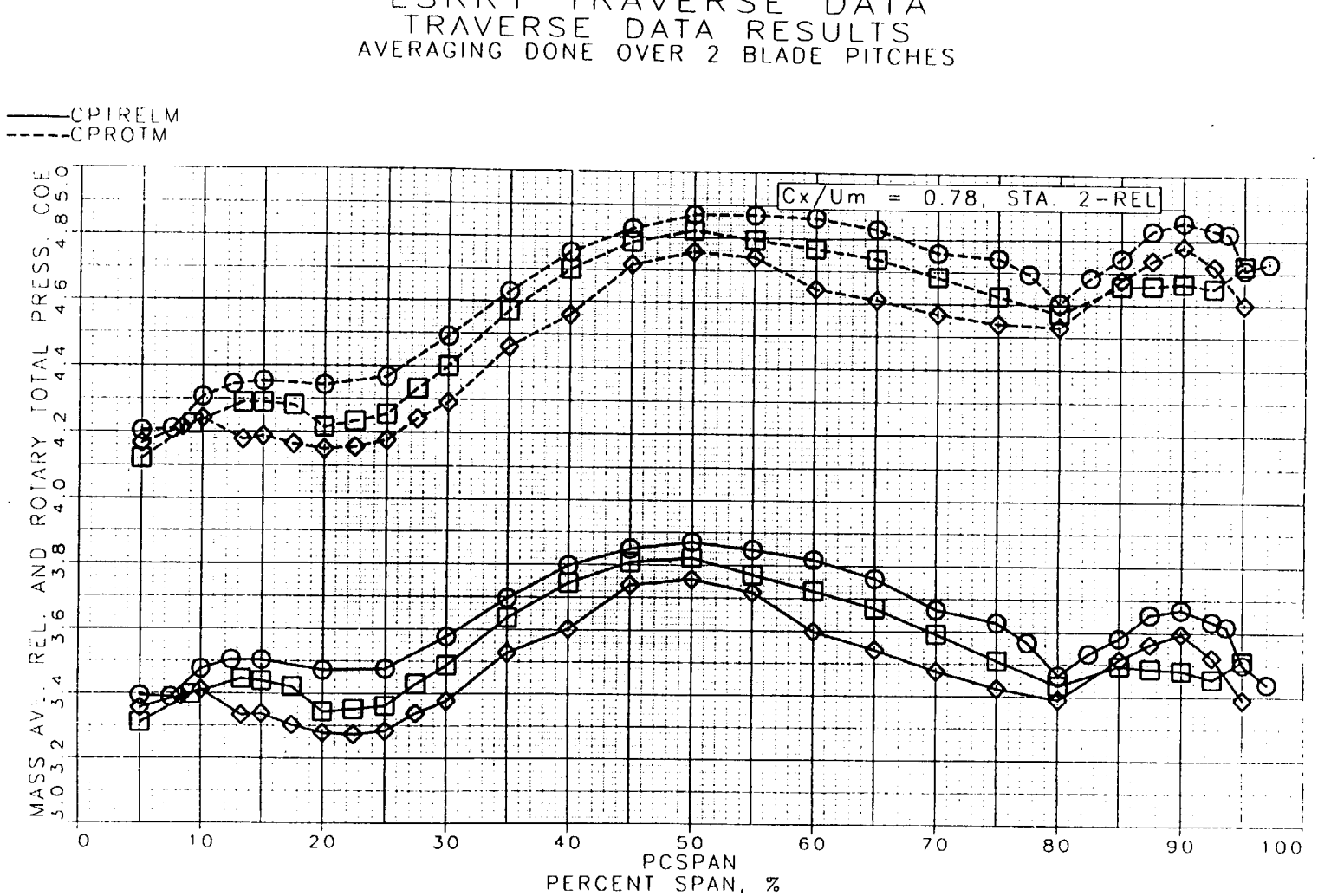

Figure 142. Mass Averaged Relative and Rotary Total Pressure Coefficient at STA2

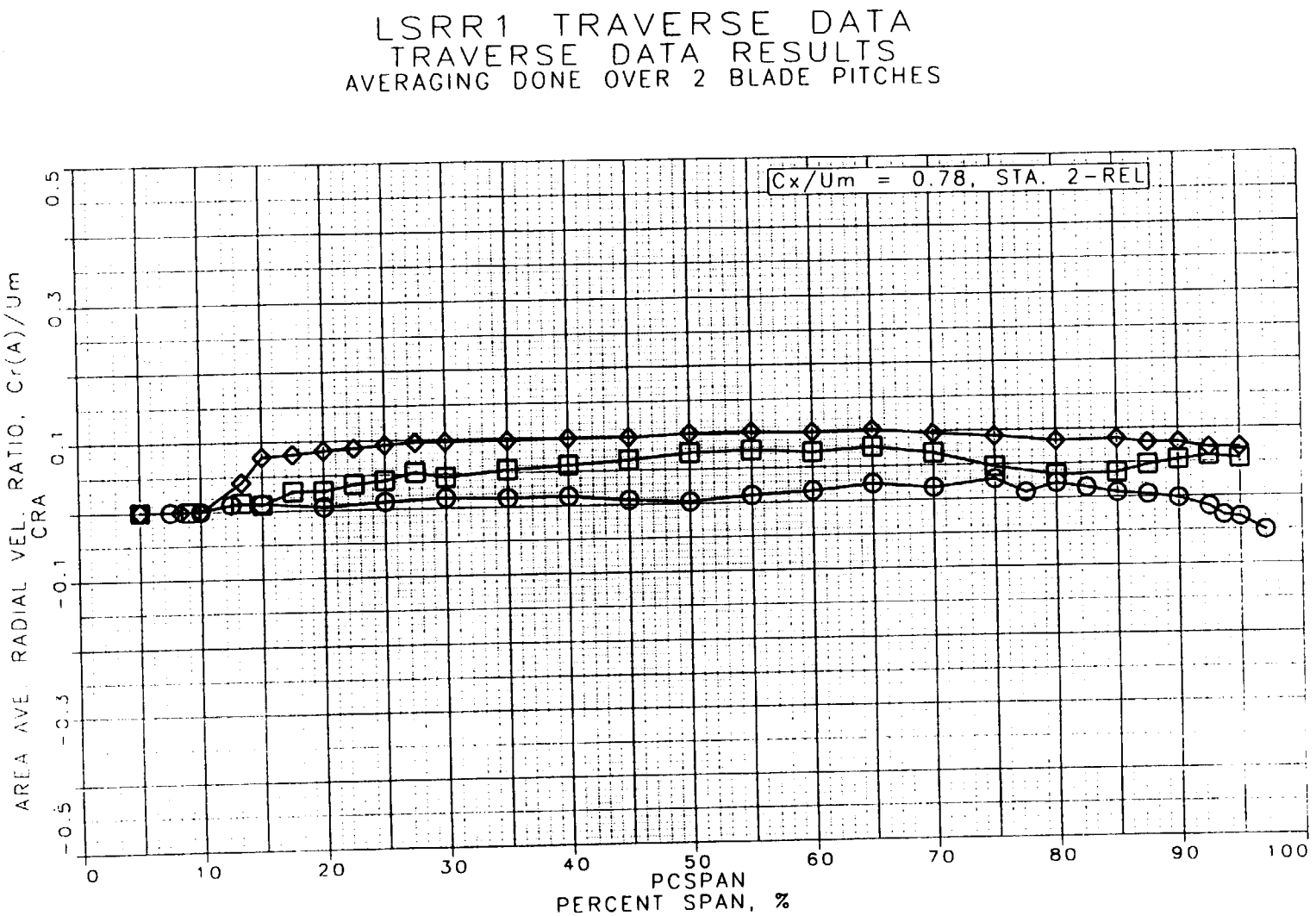

Figure 143. Area Averaged Radial Velocity Ratio at STA2

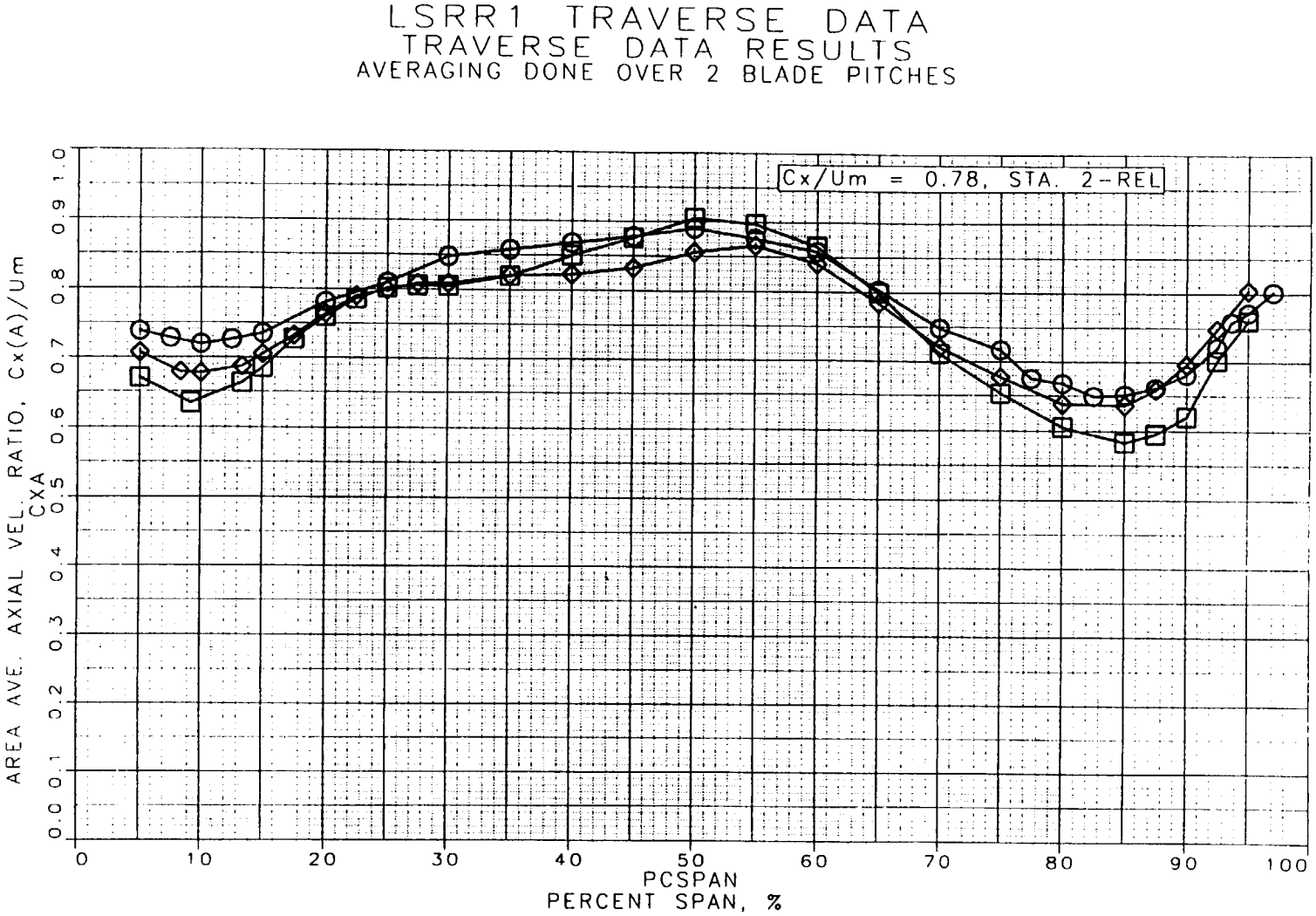

Figure 144. Area Averaged Axial Velocity Ratio at STA2

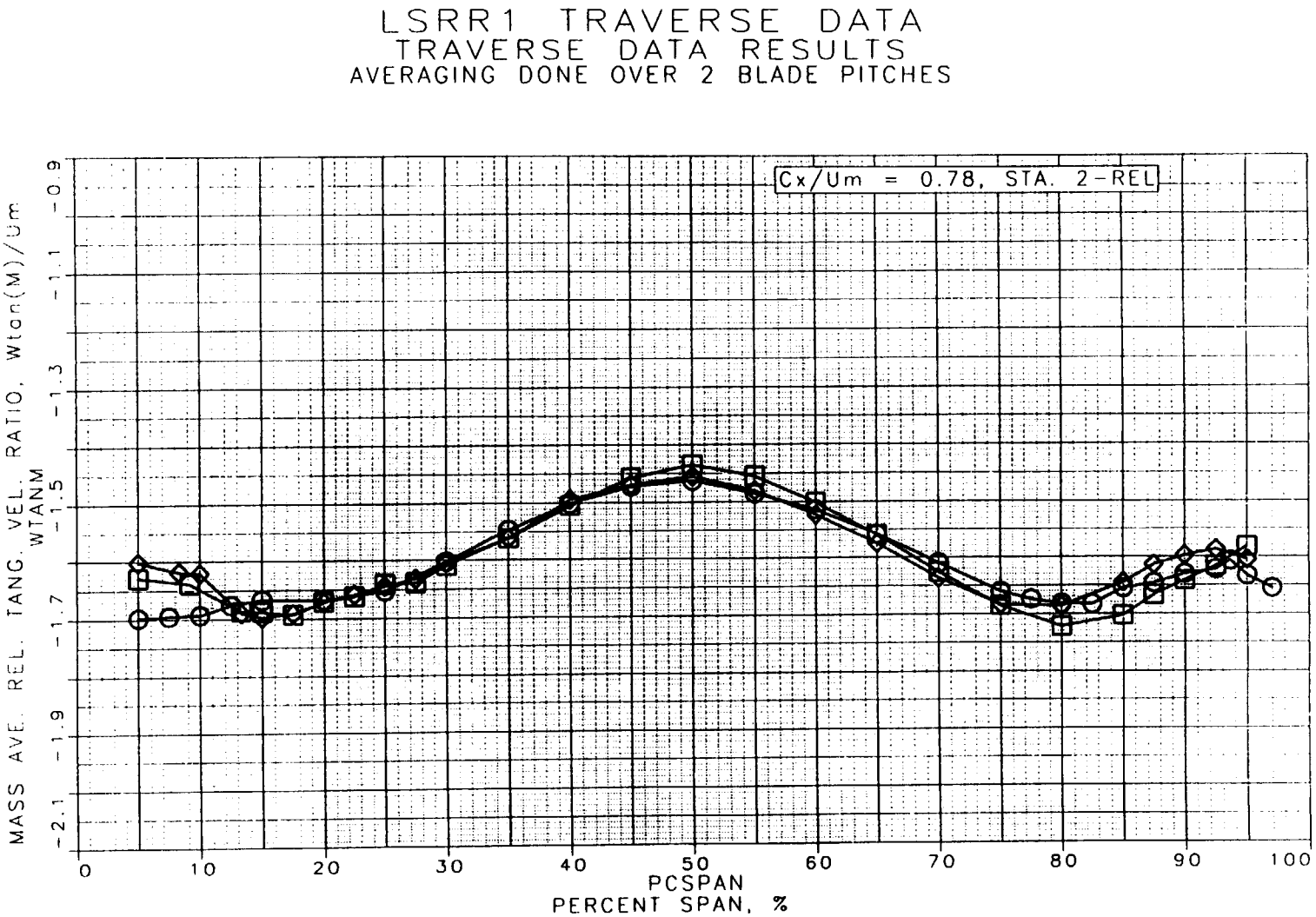

Figure 145. Mass Averaged Total Velocity Ratio at STA2

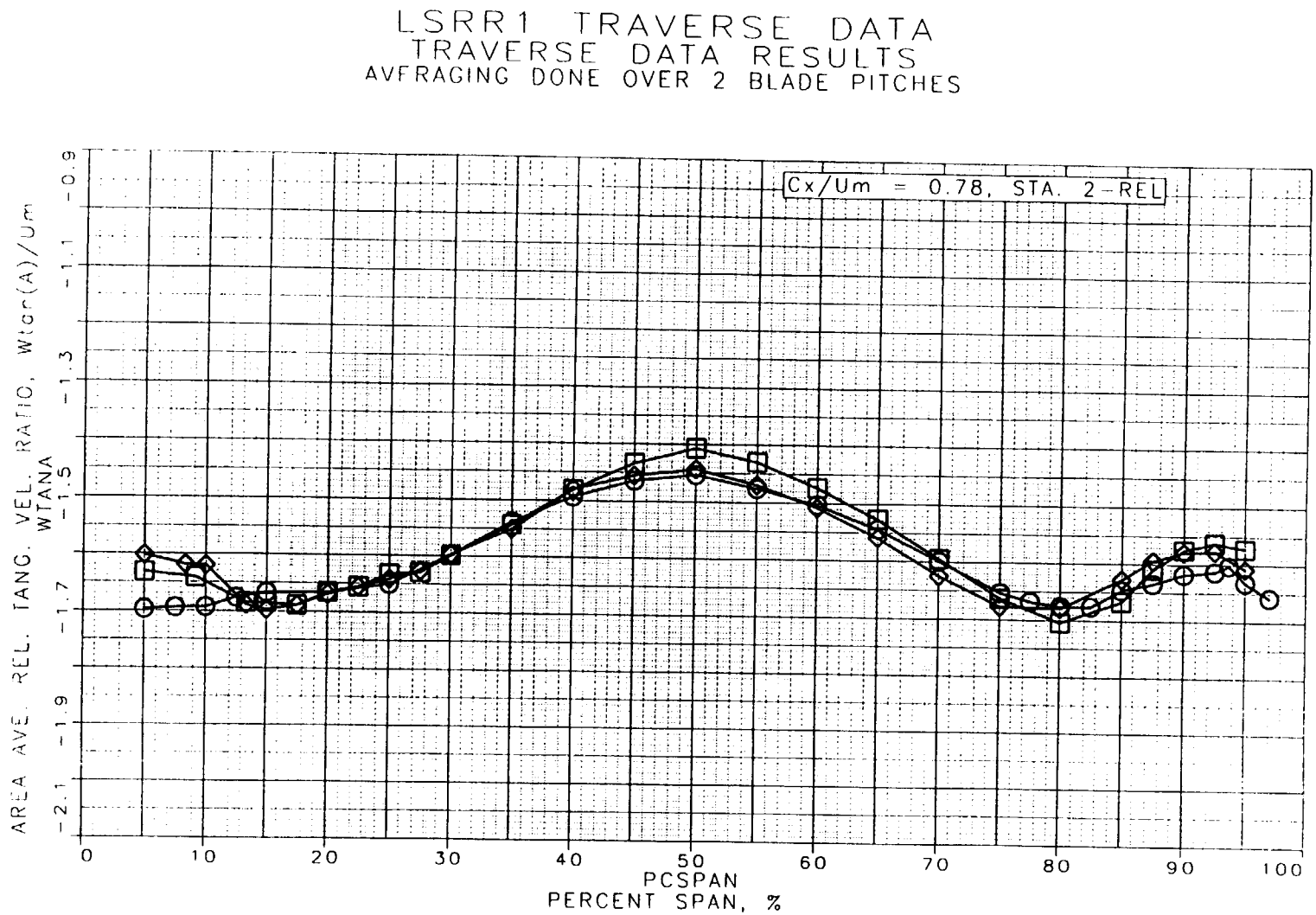

Figure 146. Area Averaged Total Velocity Ratio at STA2

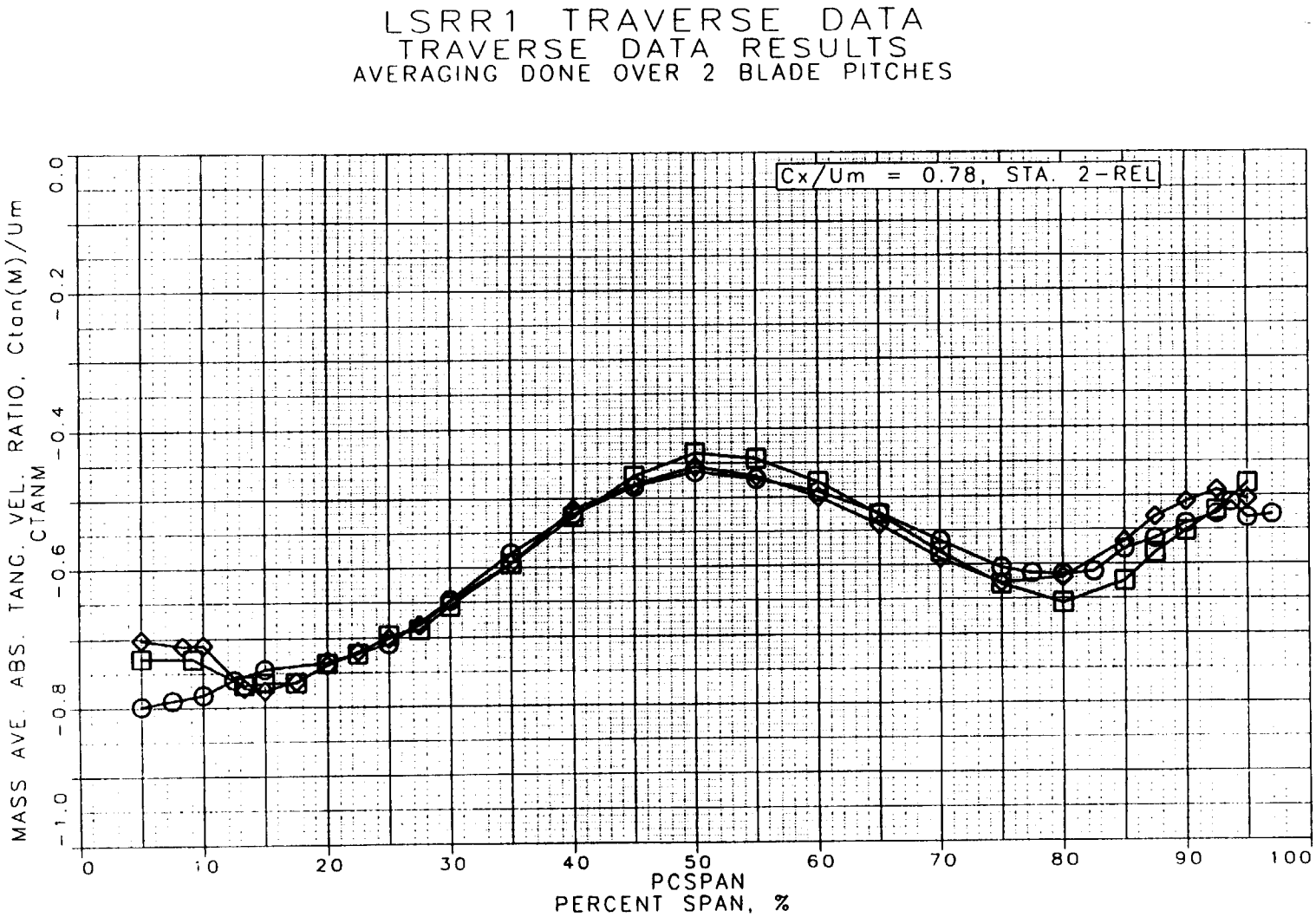

Figure 147. Mass Averaged Tangential Velocity Ratio at STA2

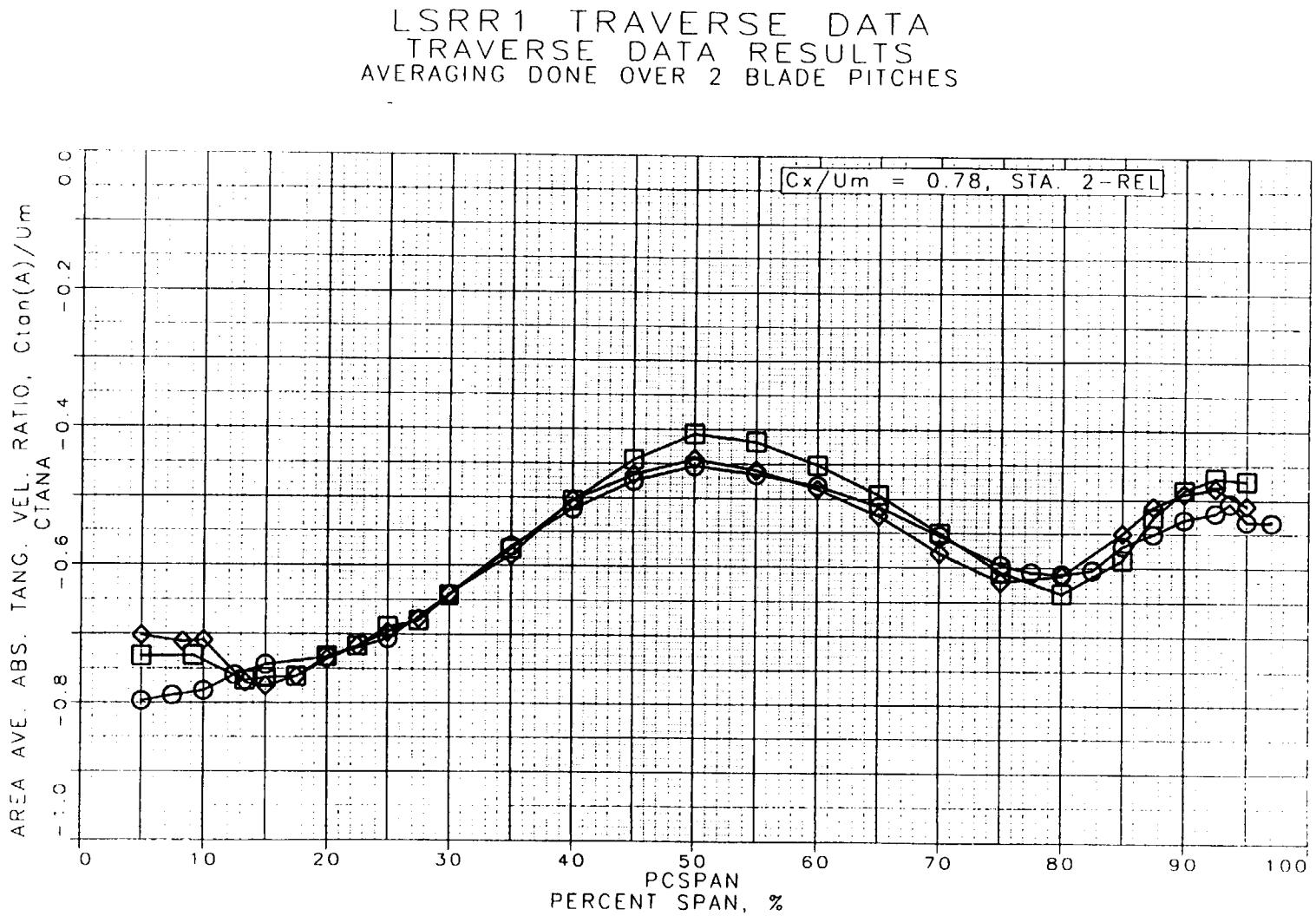

Figure 148. Area Averaged Tangential Velocity Ratio at STA2

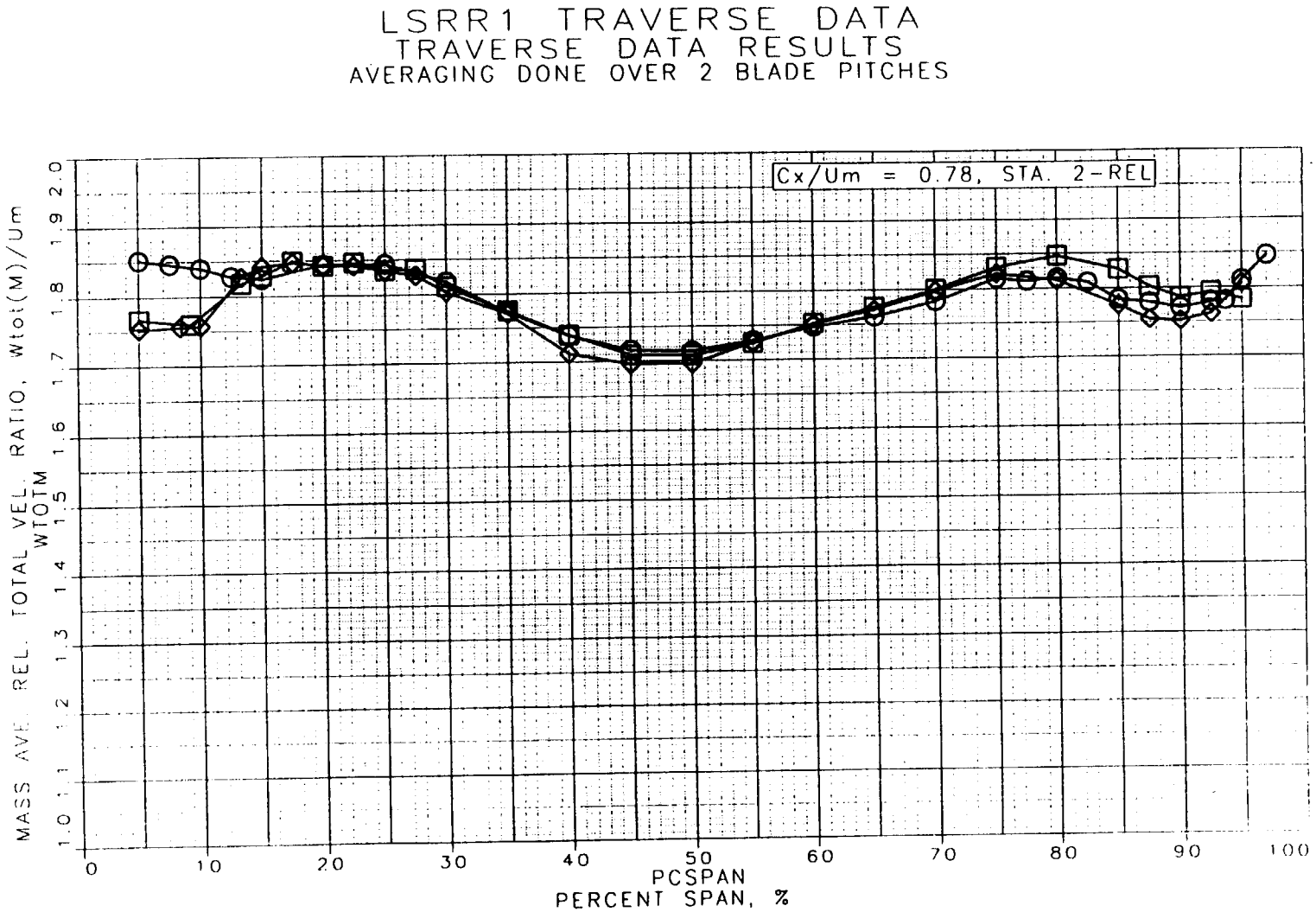

Figure 149. Mass Averaged Relative Total Velocity Ratio at STA2

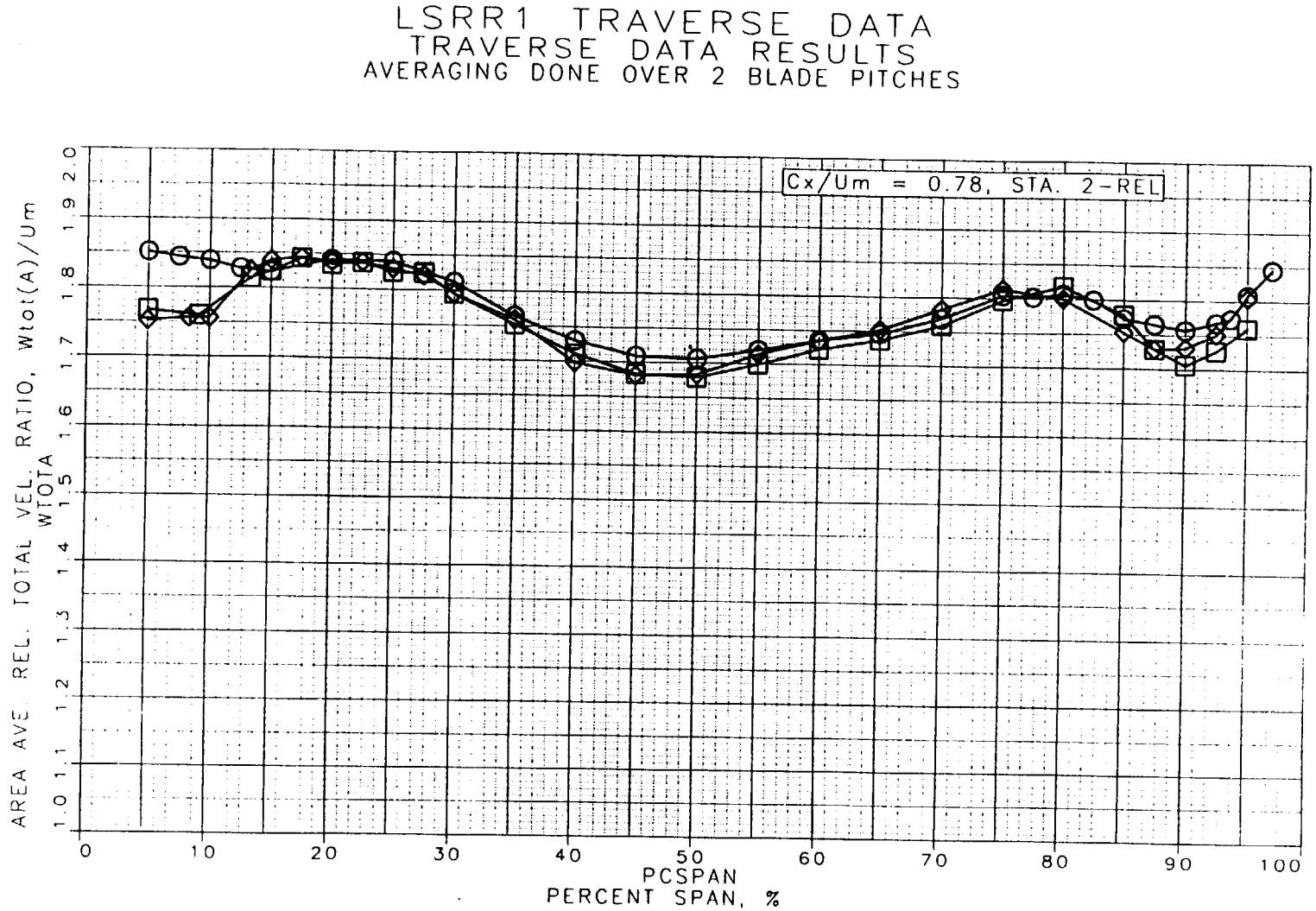

Figure 150. Area Averaged Relative Total Velocity Ratio at STA2

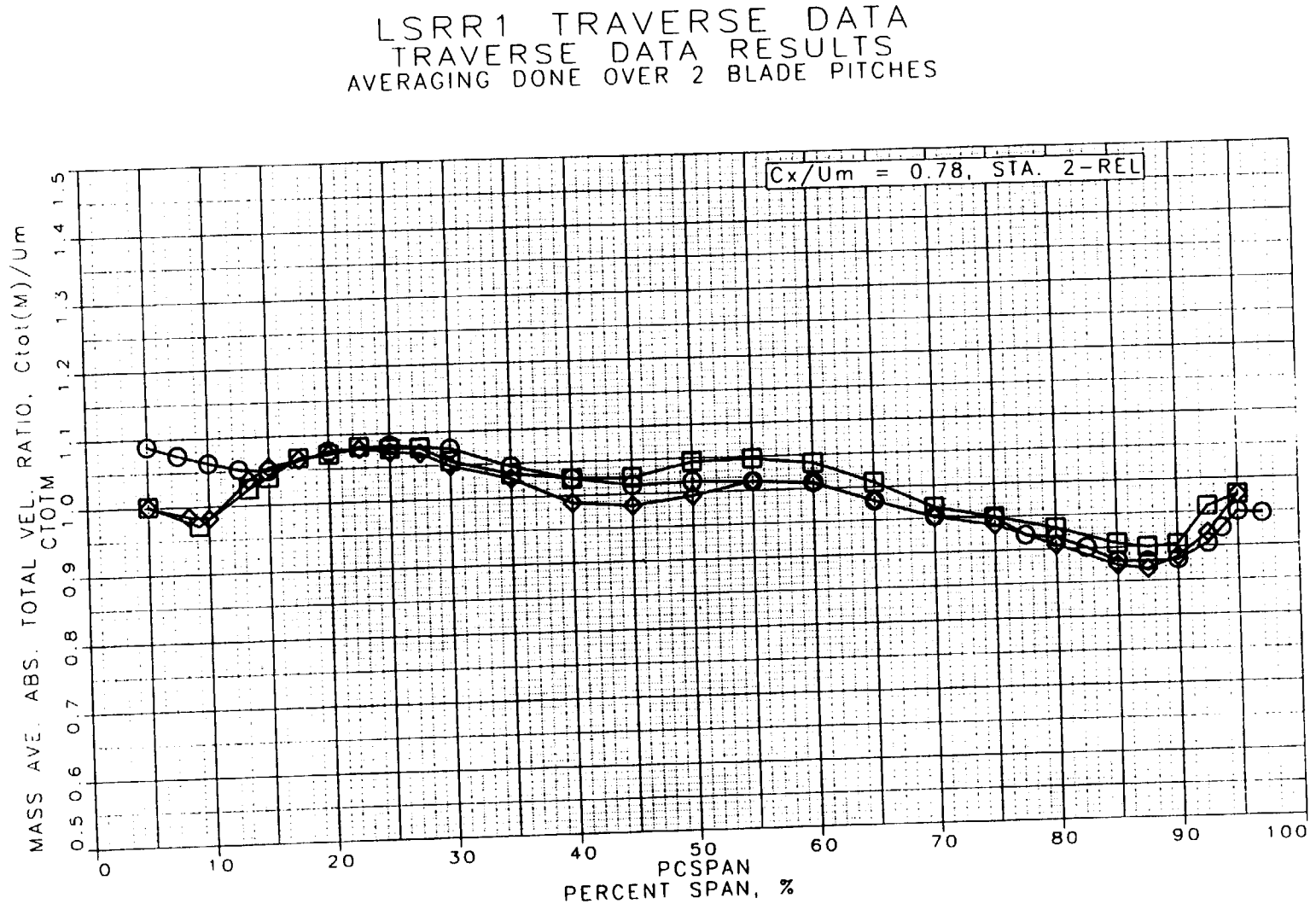

Figure 151. Mass Averaged Absolute Total Velocity Ratio at STA2

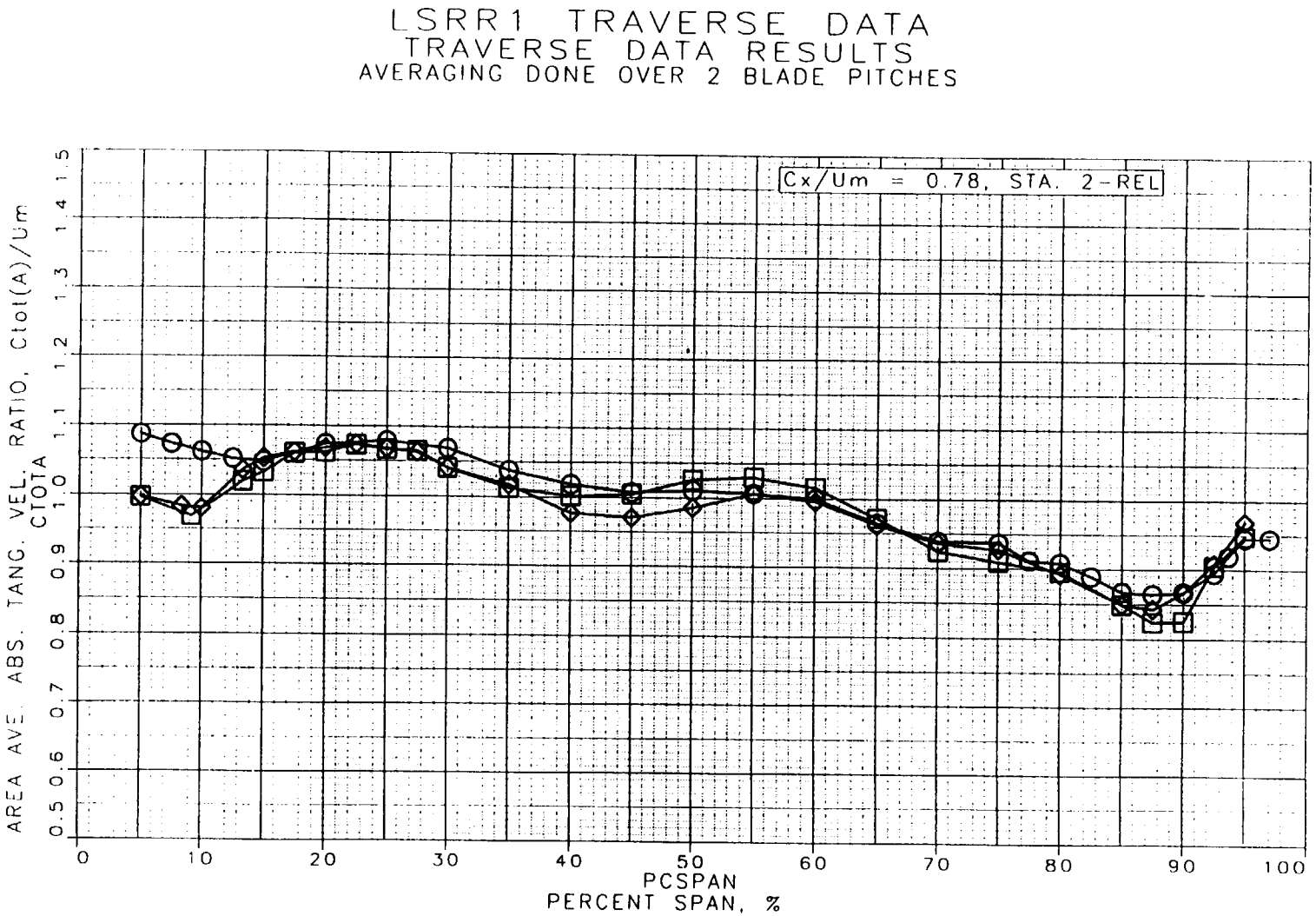

Figure 152. Area Averaged Absolute Tangential Velocity Ratio at STA2

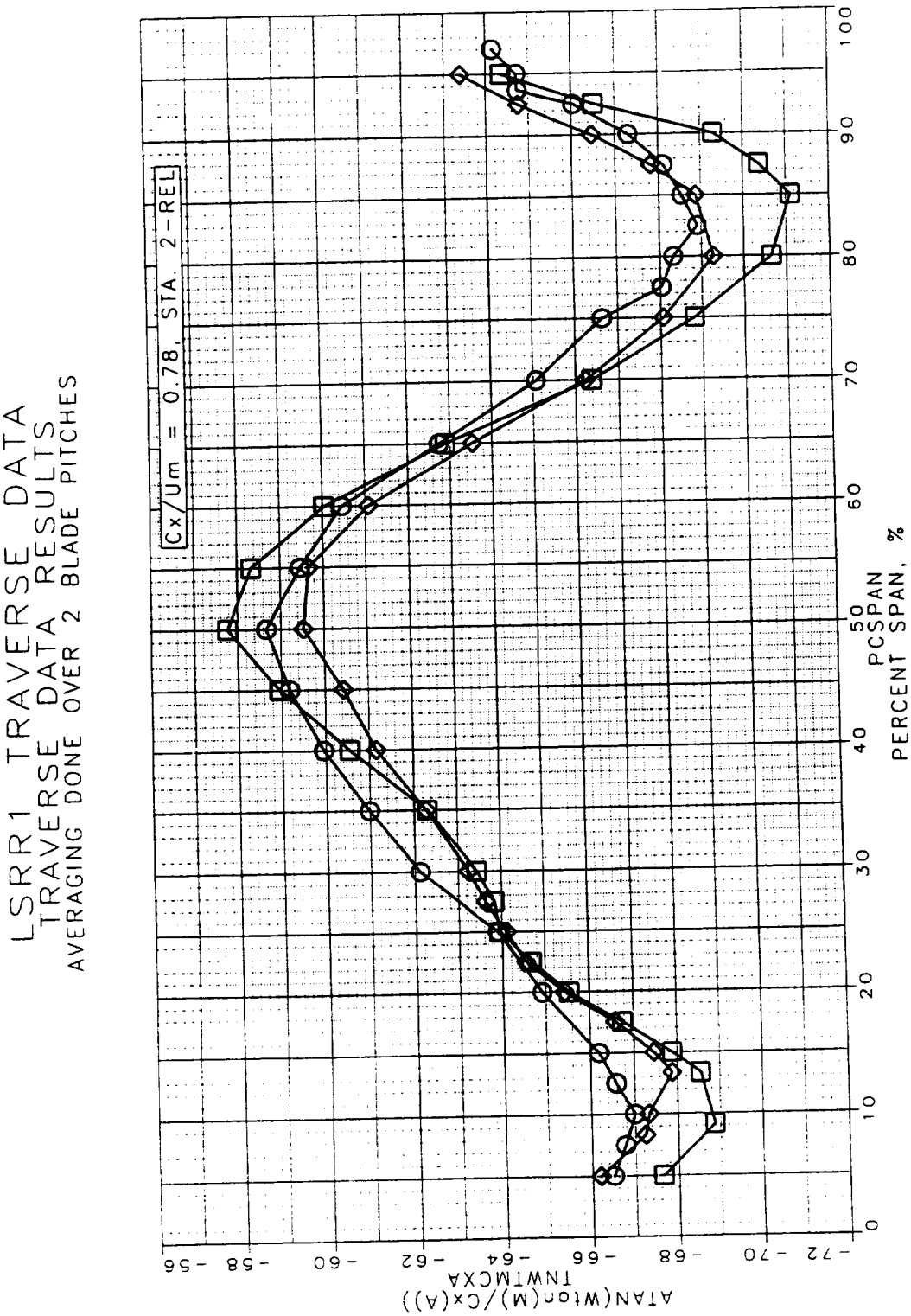

Figure 153. Area Averaged Absolute Yaw Angle at STA2

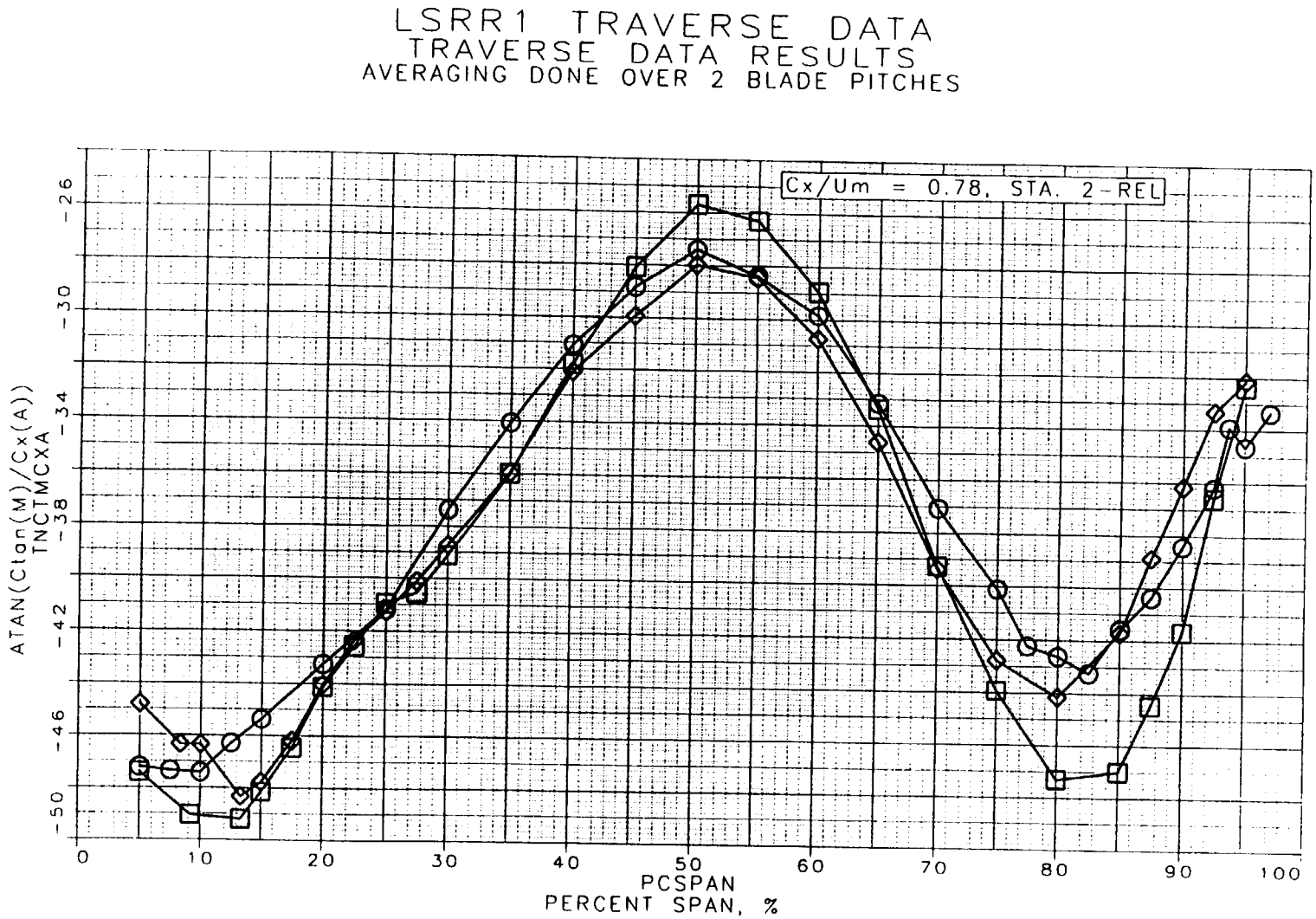

Figure 154. Area Averaged Relative Yaw Angle at STA2

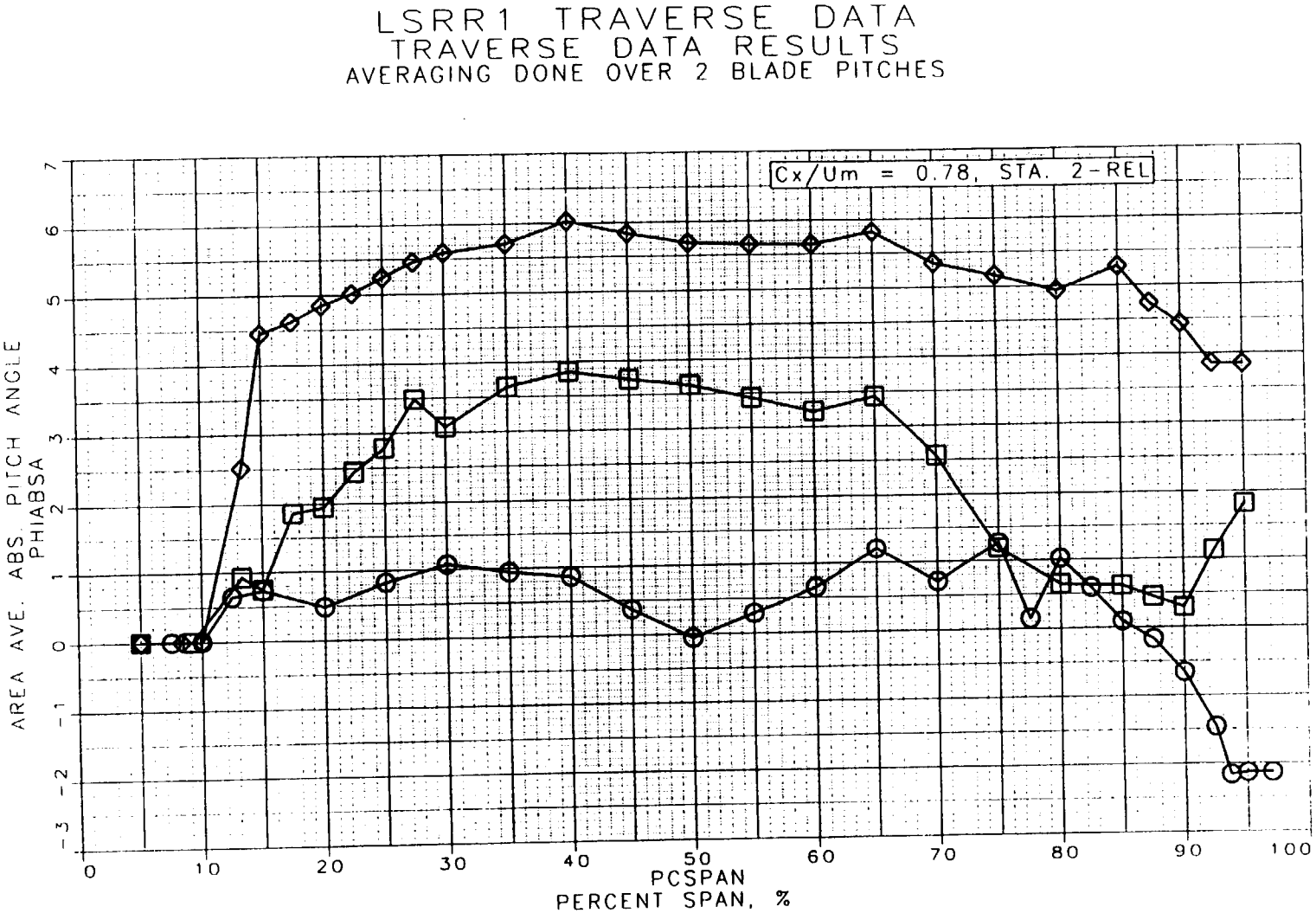

Figure 155. Area Averaged Absolute Pitch Angle at STA2

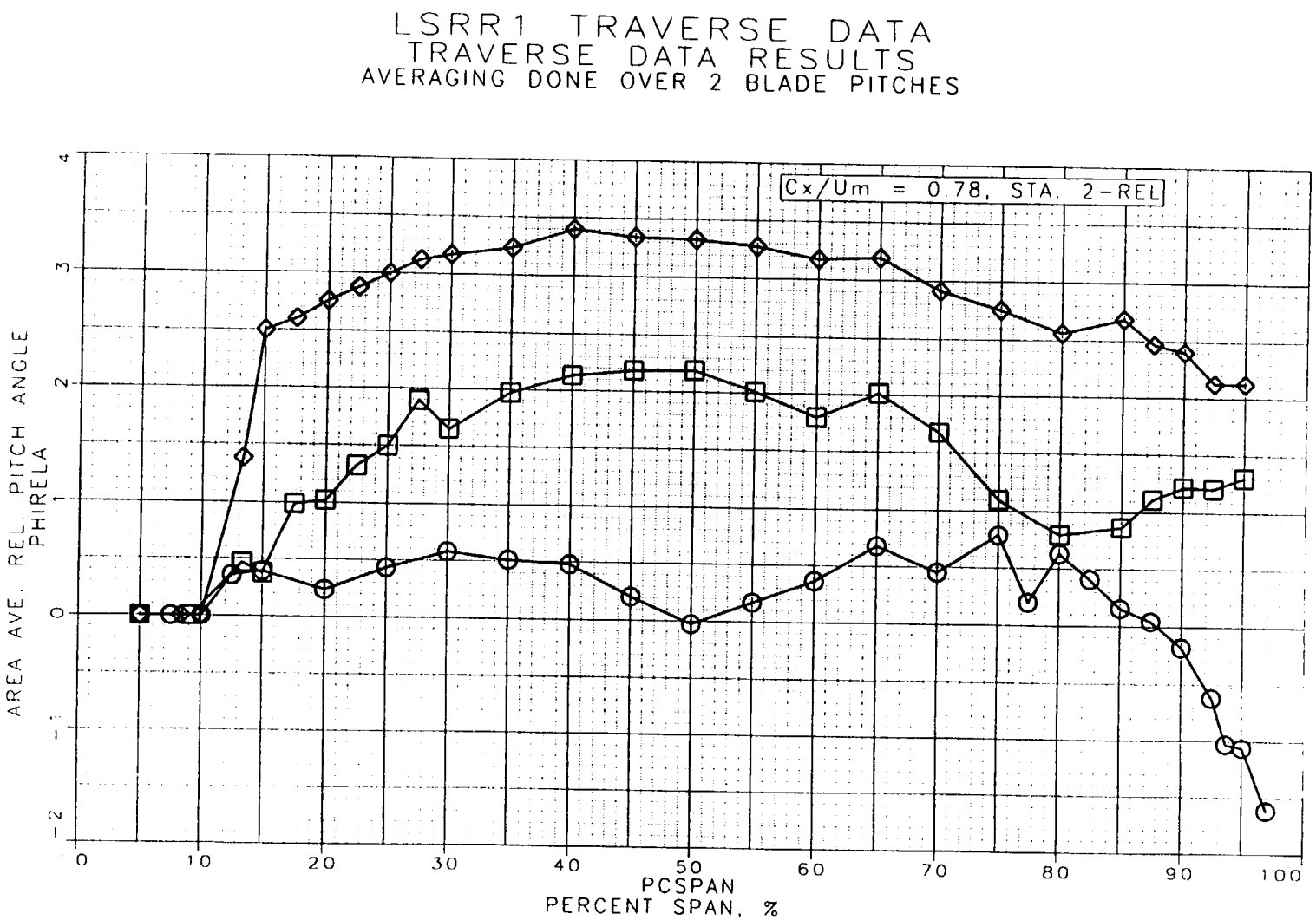

Figure 156. Area Averaged Relative Pitch Angle at STA2

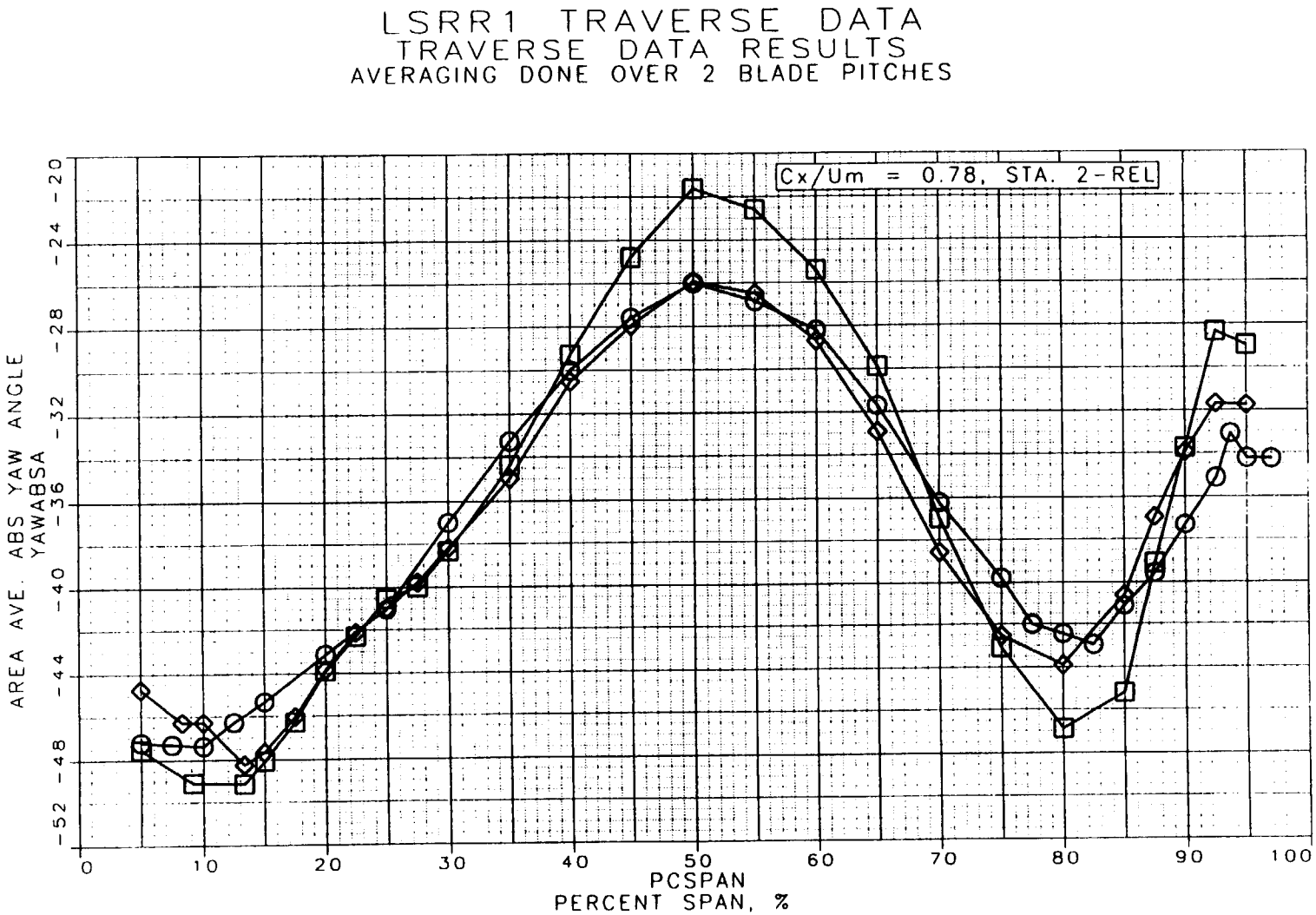

Figure 157. Area Averaged Absolute Yaw Angle at STA2

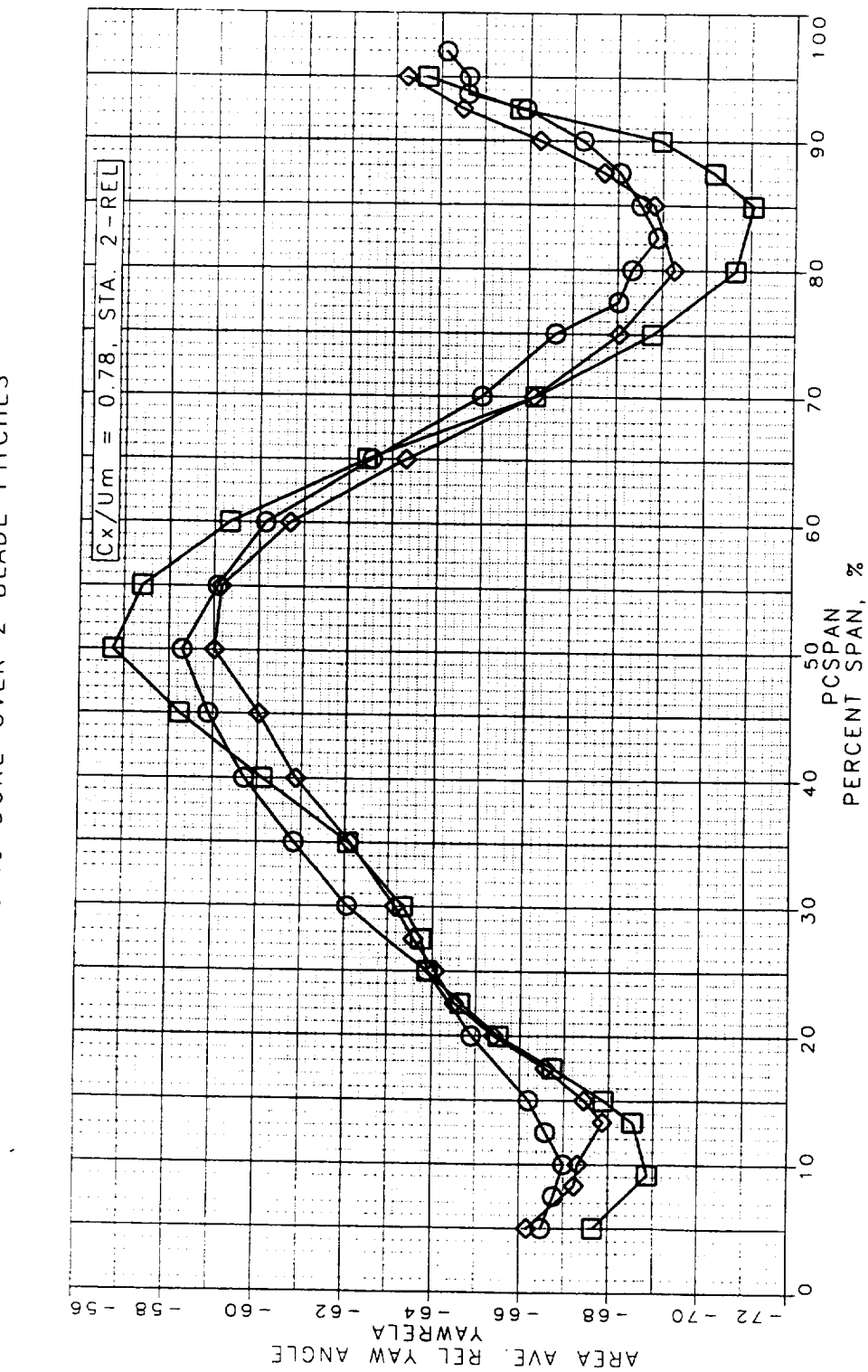

Figure 158. Area Averaged Relative Yaw Angle at STA2

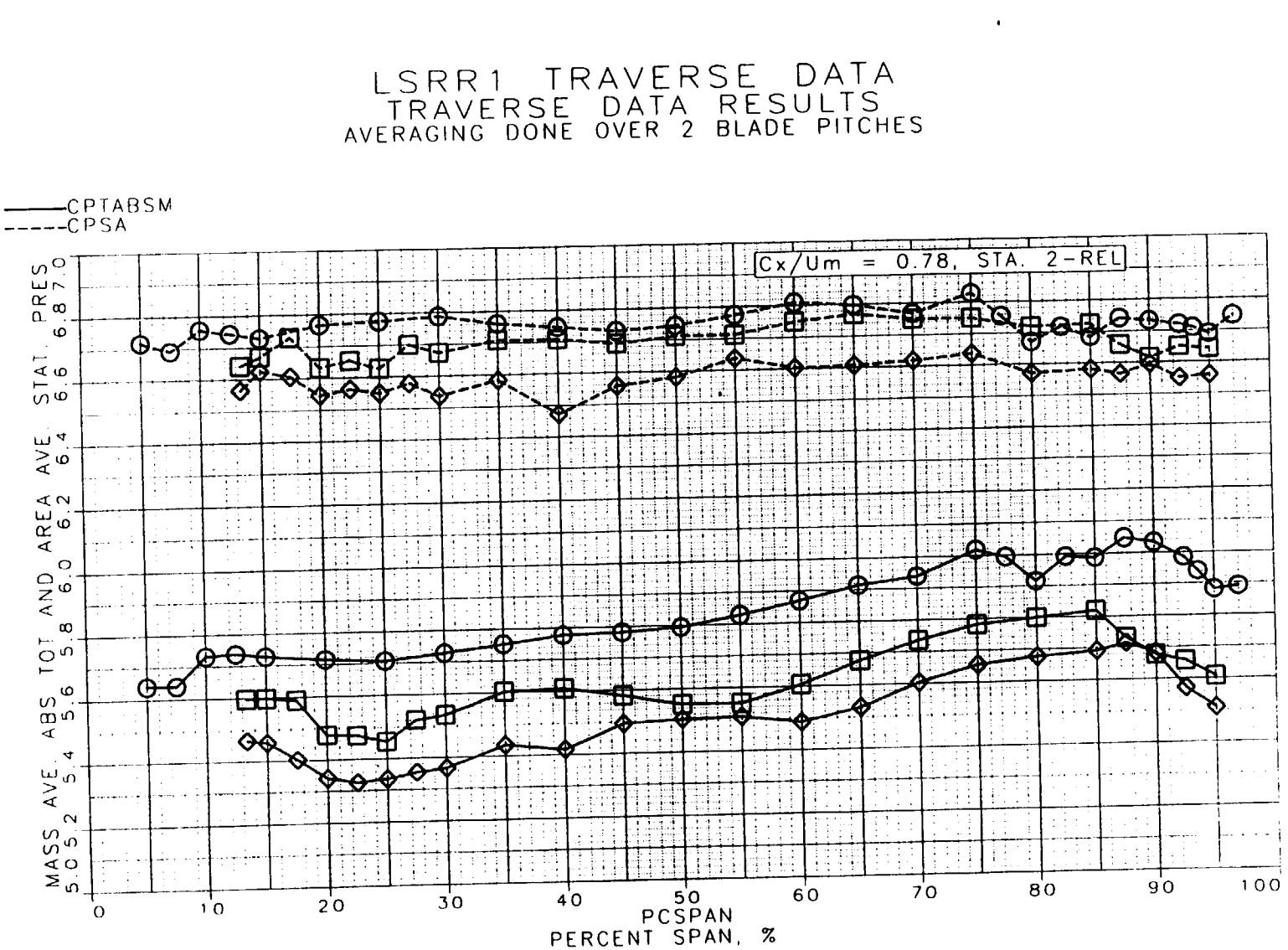

Figure 159. Mass Averaged Absolute and Area Averaged Static Pressure at STA2

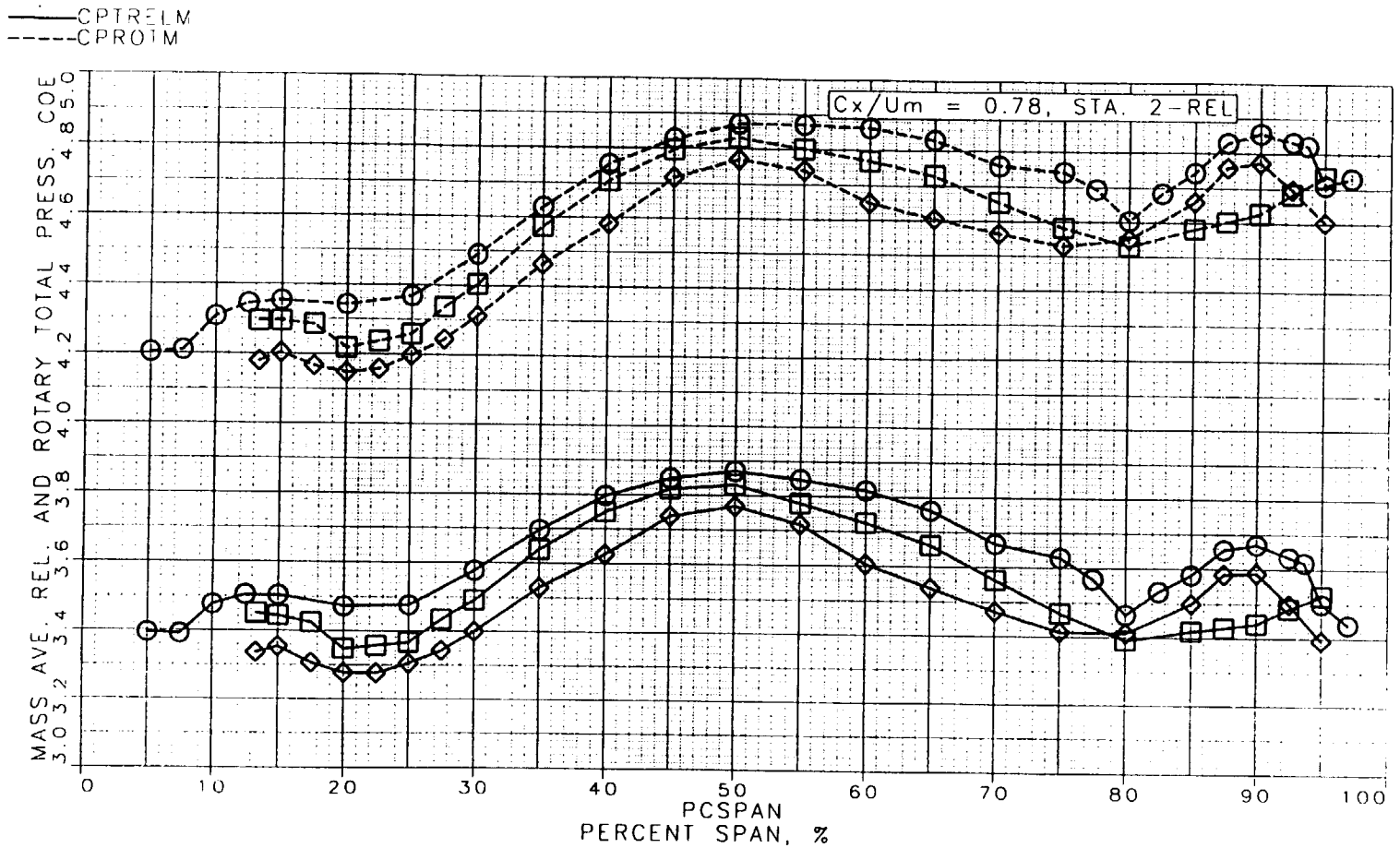

Figure 160. Mass Averaged Reliability and Rotary Total Pressure Coefficient at STA2

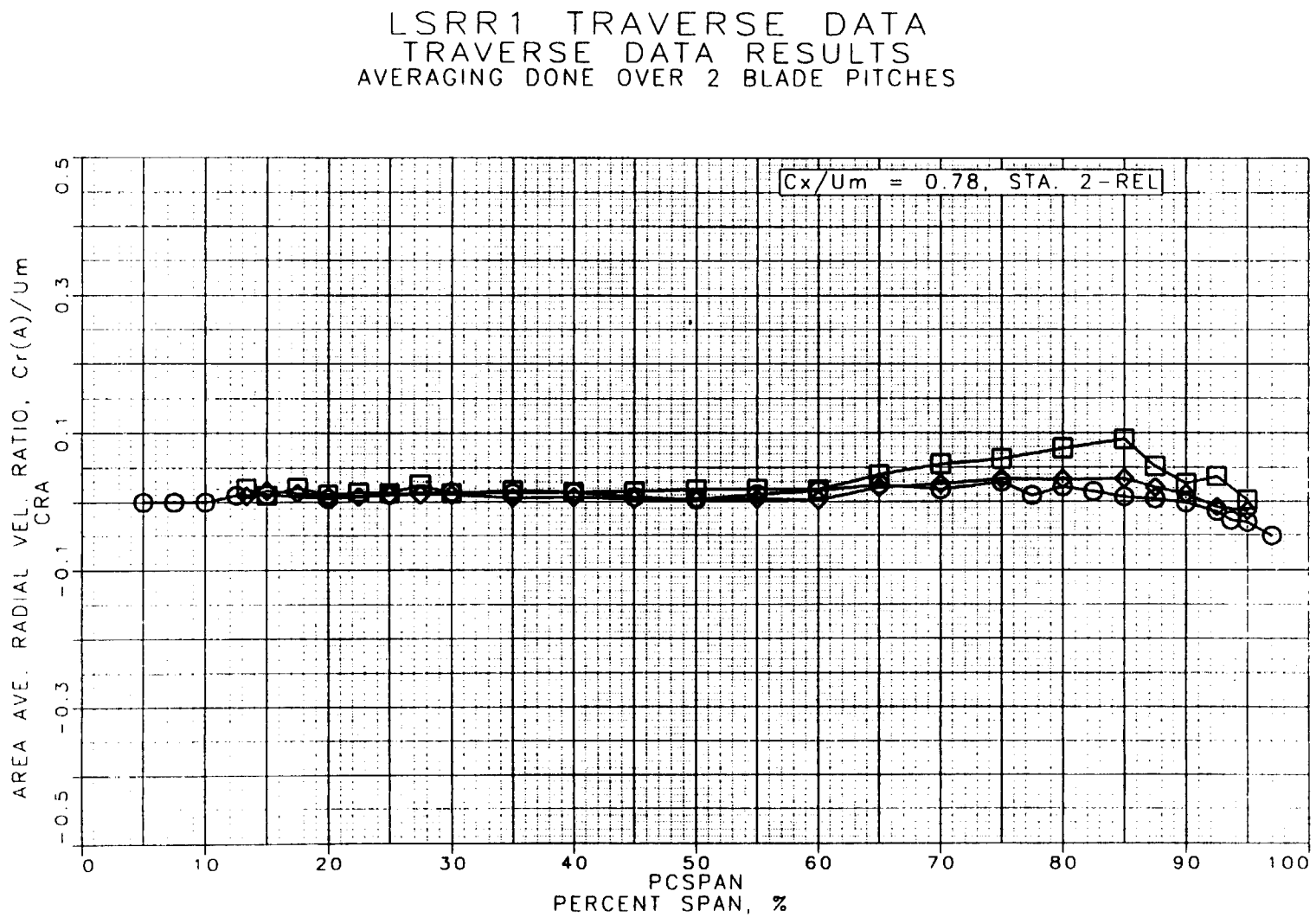

Figure 161. Area Averaged Radial Velocity Ratio at STA2

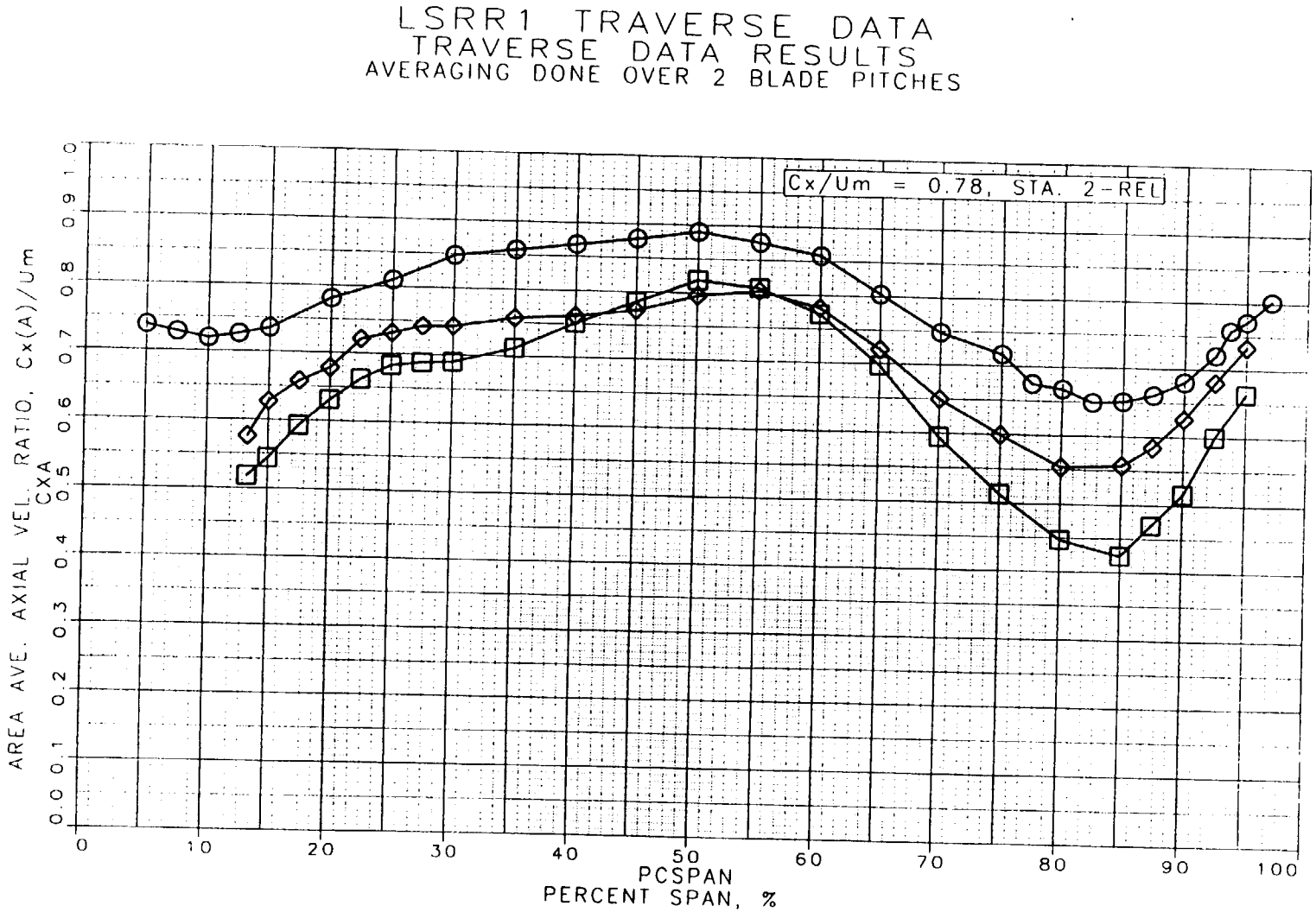

Figure 162. Area Averaged Axial Velocity Ratio at STA2

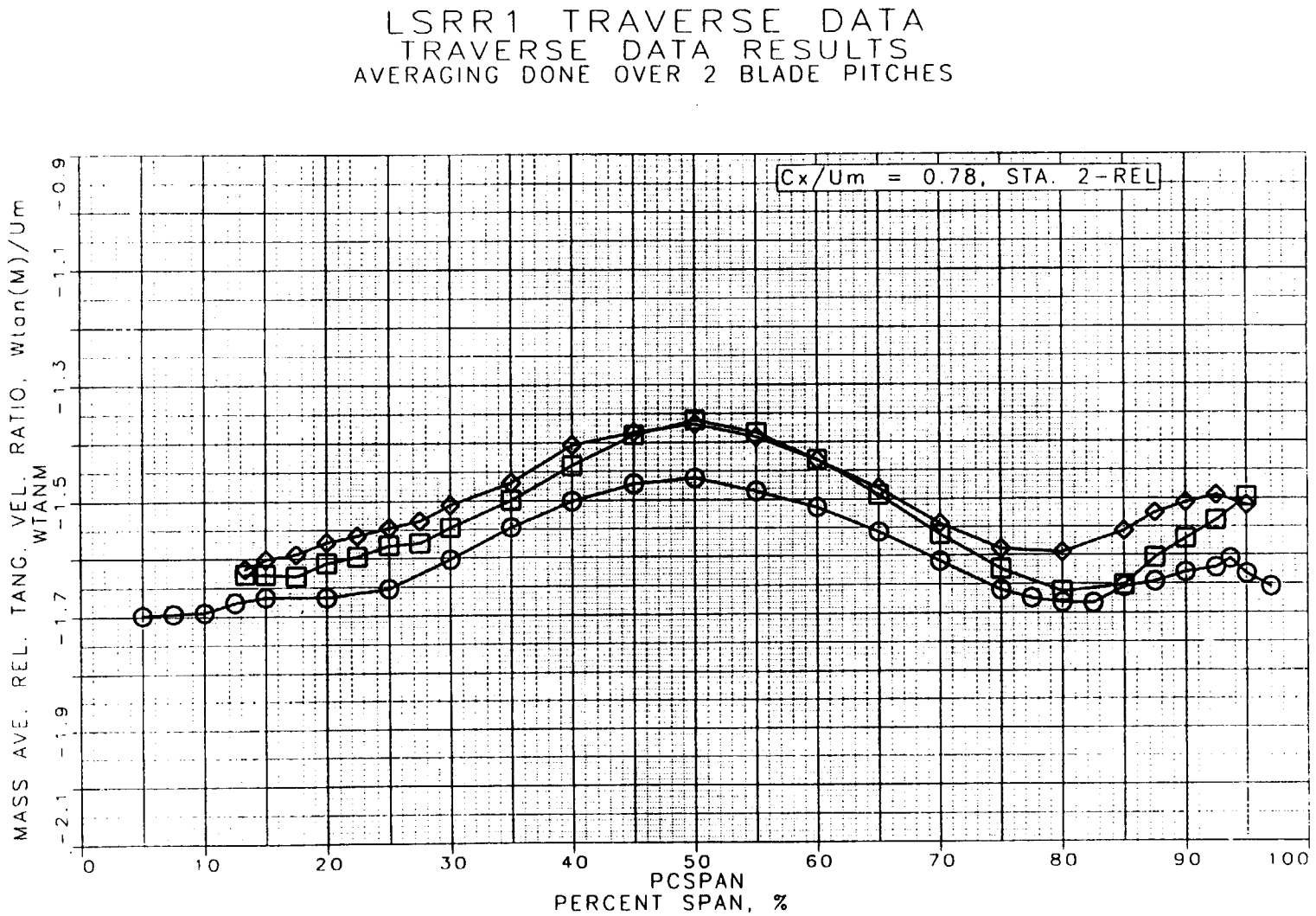

Figure 163. Mass Averaged Relative Tangential Velocity Ratio at STA2

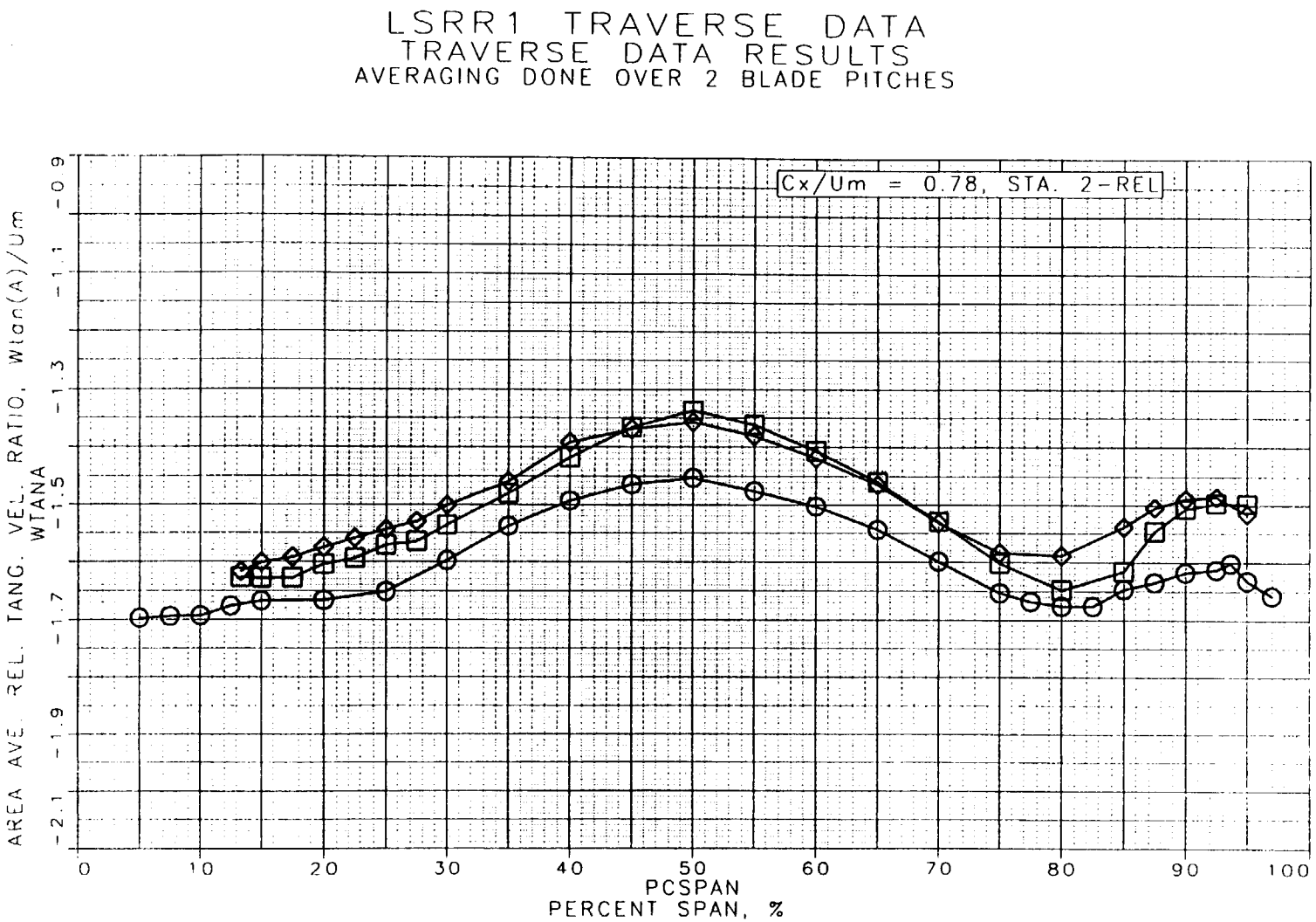

Figure 164. Area Averaged Relative Tangential Velocity Ratio at STA2

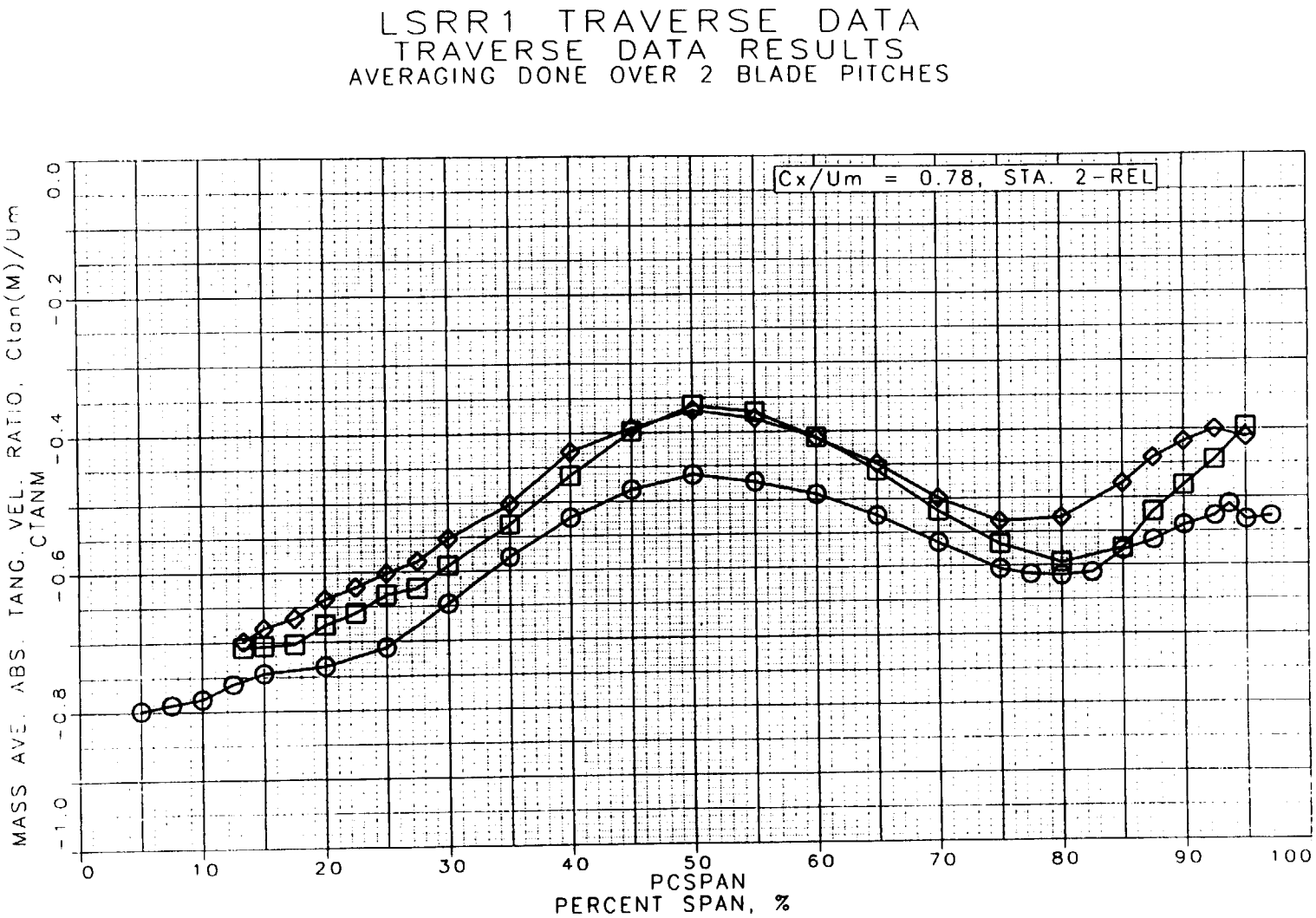

Figure 165. Mass Averaged Absolute Tangential Velocity Ratio at STA2

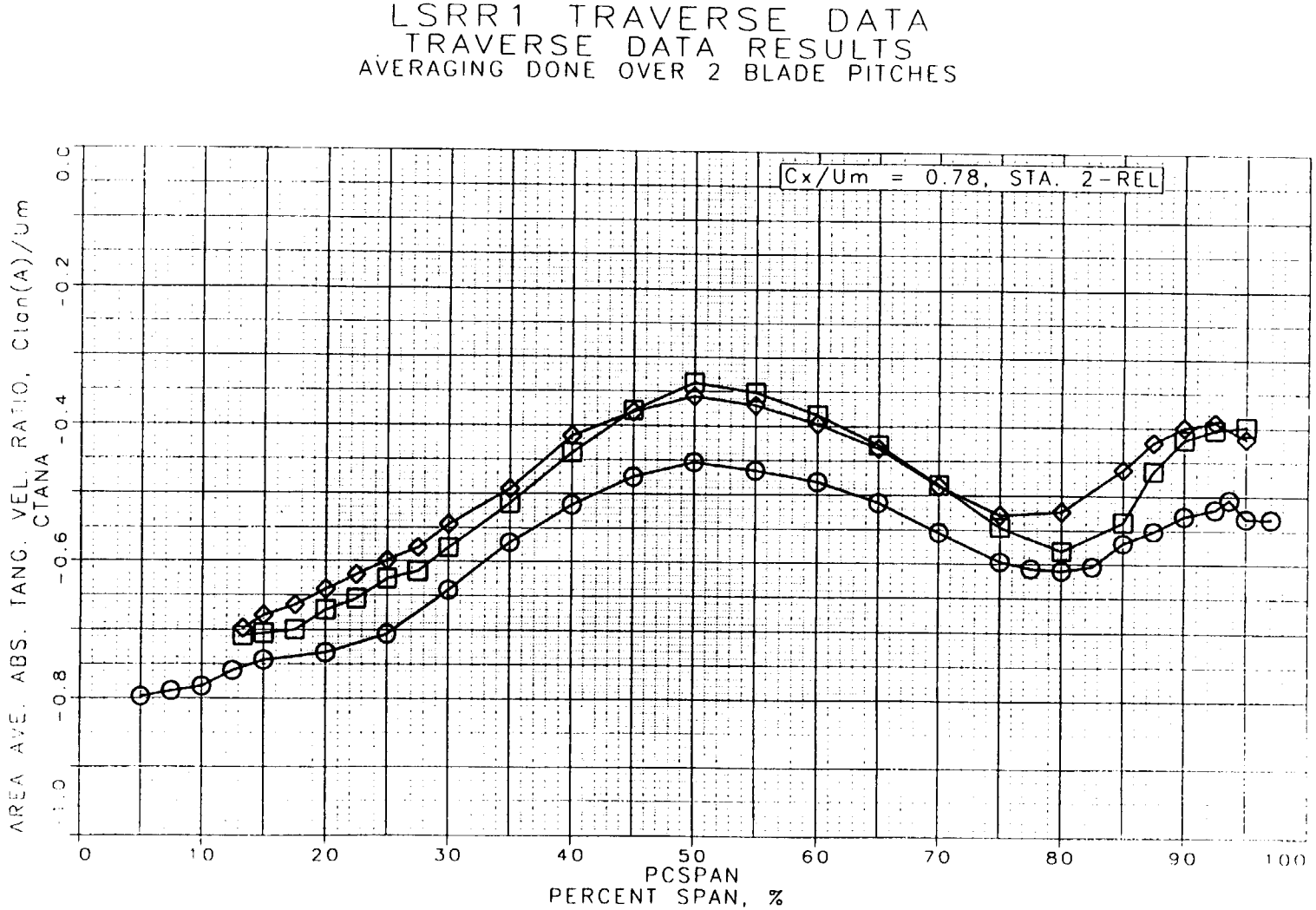

Figure 166. Area Averaged Absolute Tangential Velocity Ratio at STA2

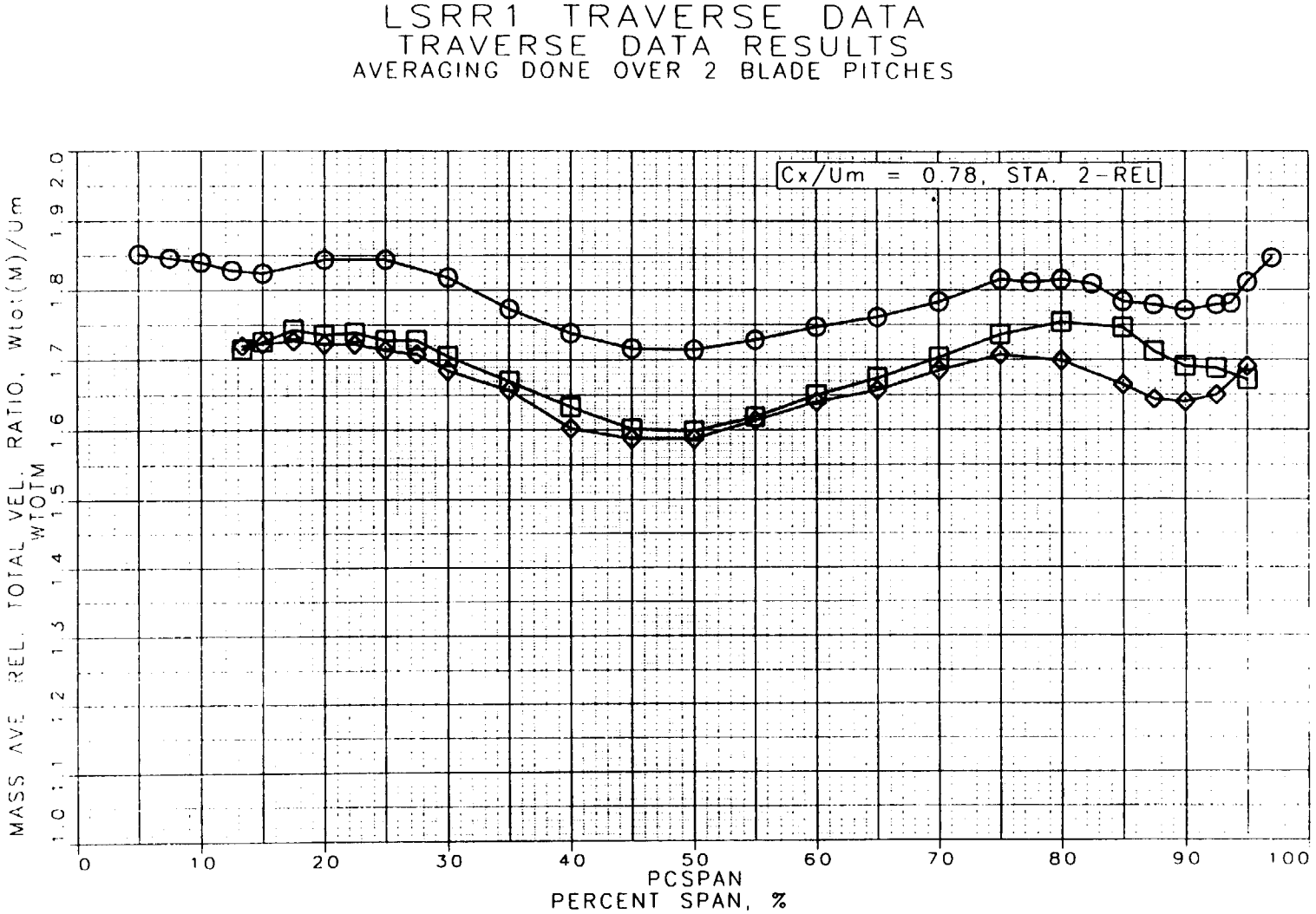

Figure 167. Mass Averaged Relative Total Velocity Ratio at STA2

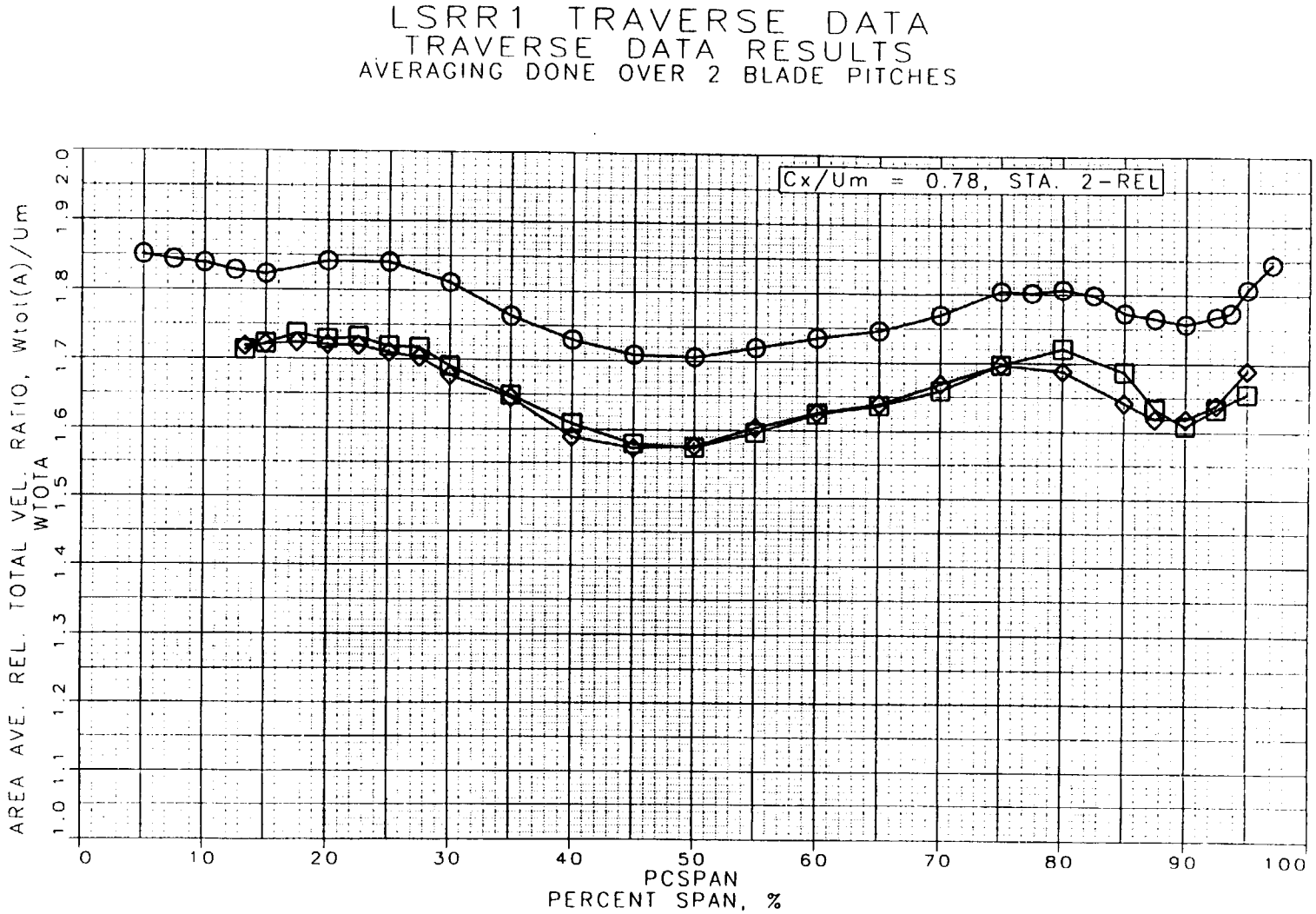

Figure 168. Area Averaged Reliability Total Velocity Ratio at STA2

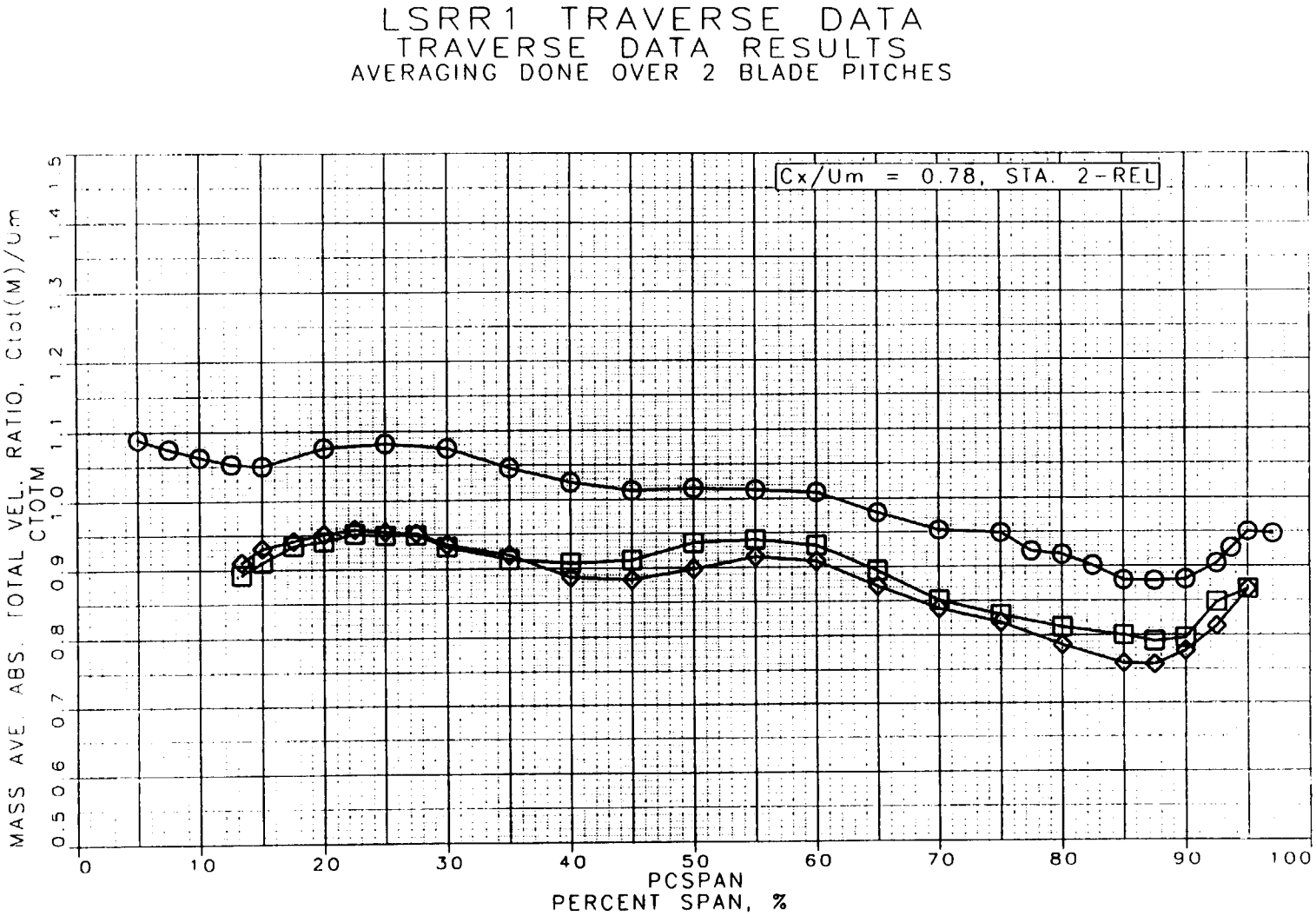

Figure 169. Mass Averaged Absolute Total Velocity Ratio at STA2

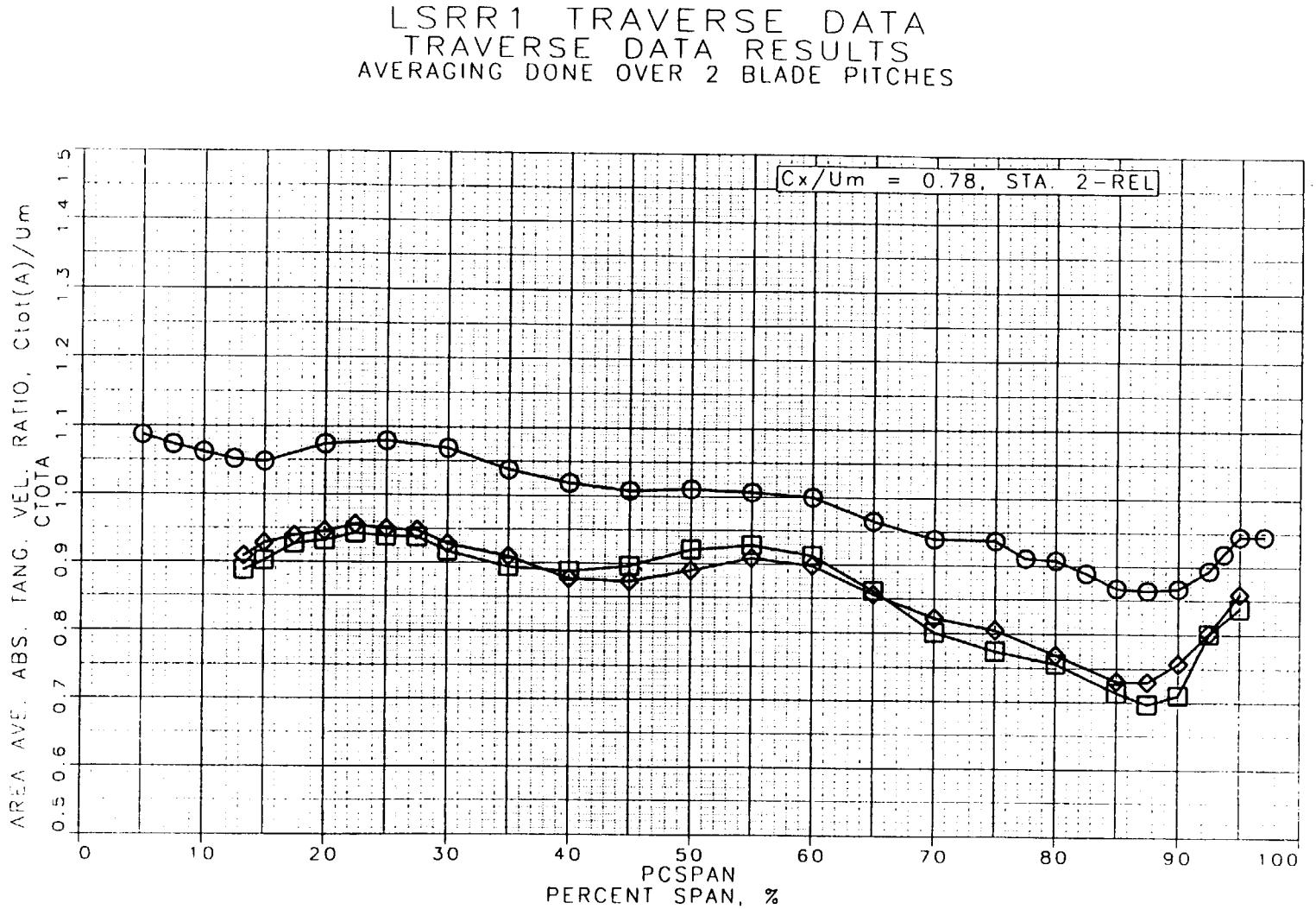

Figure 170. Area Averaged Absolute Tangential Velocity Ratio at STA2

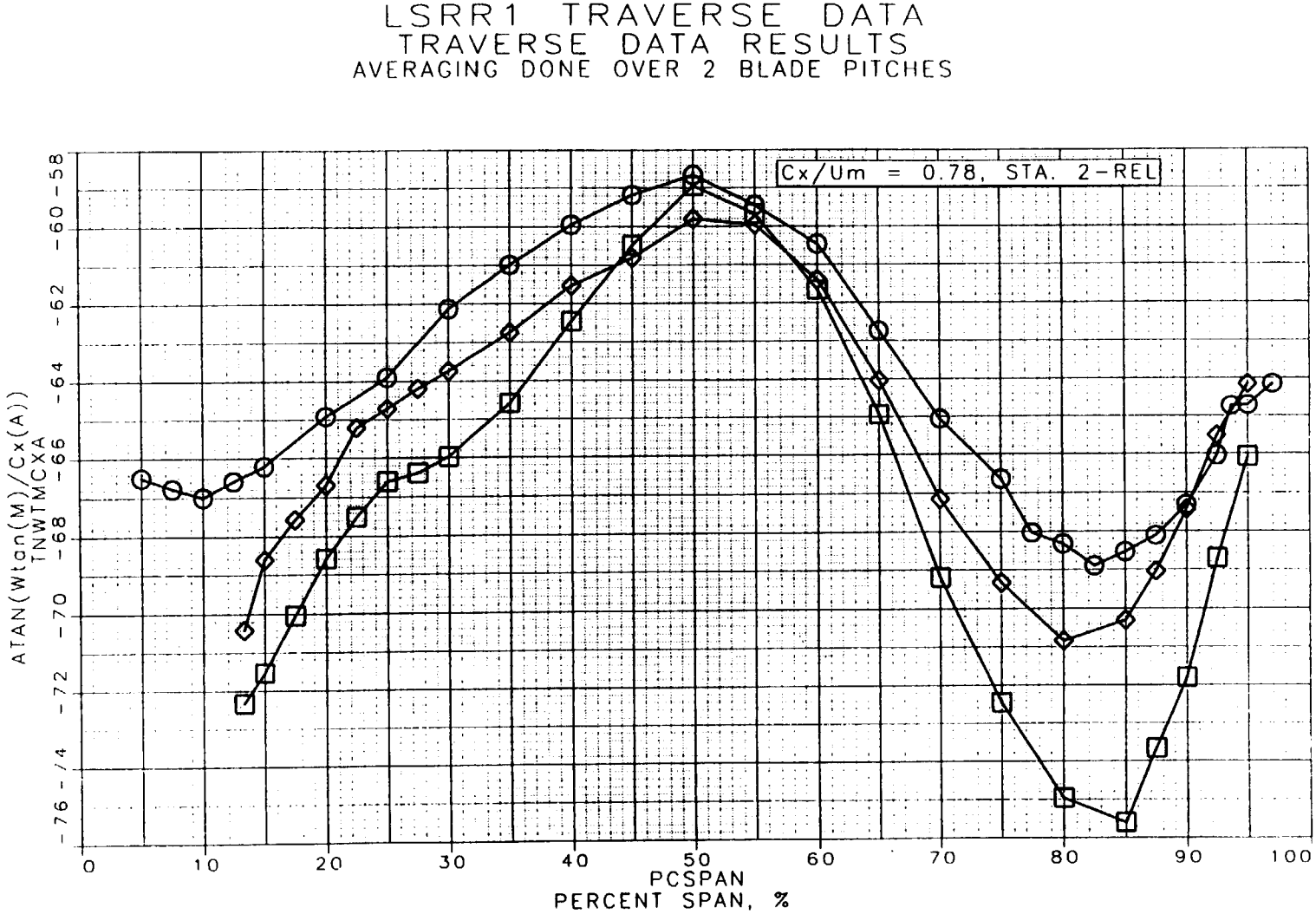

Figure 171. Area Averaged Absolute Yaw Angle at STA2

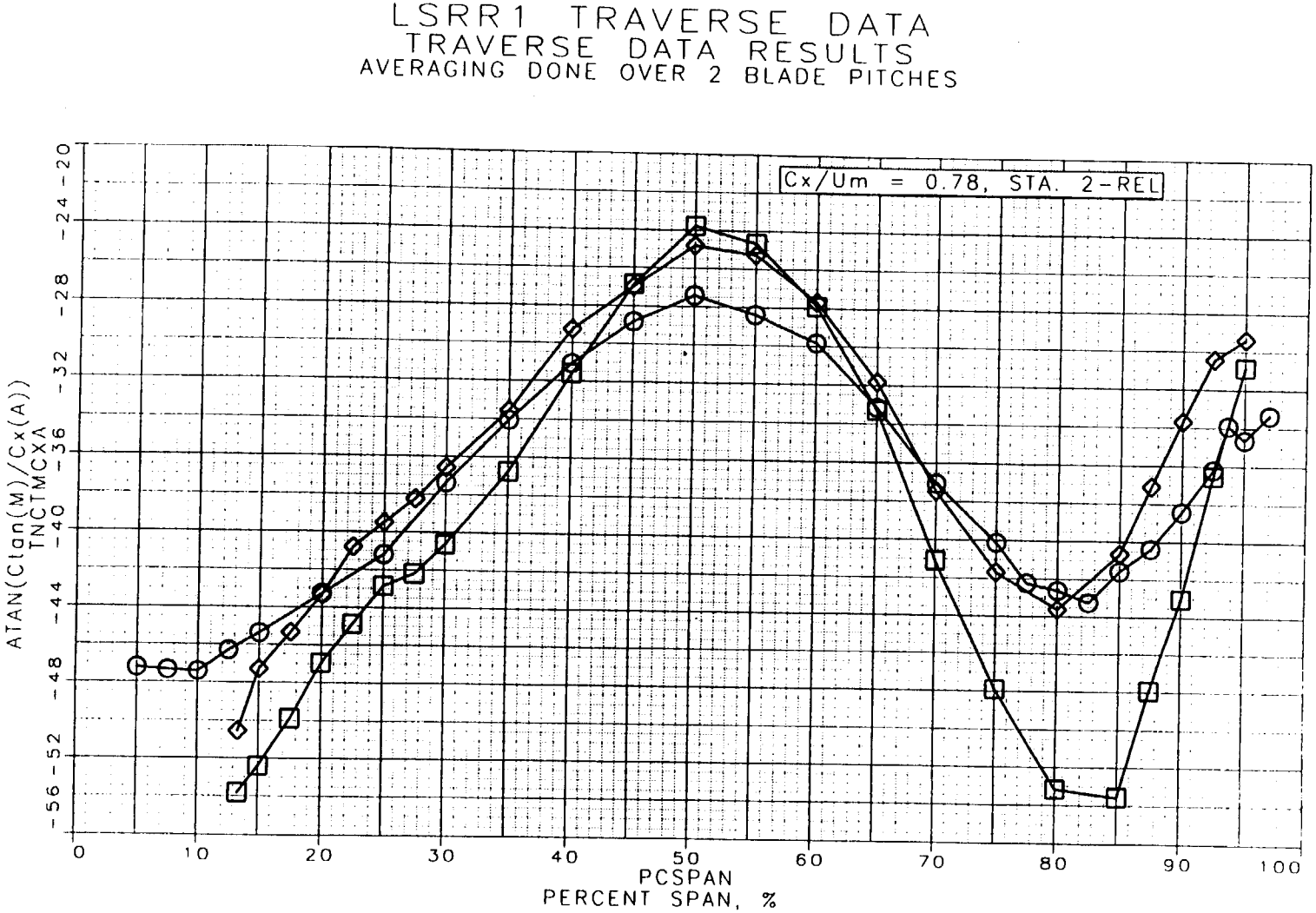

Figure 172. Area Averaged Relative Yaw Angle at STA2

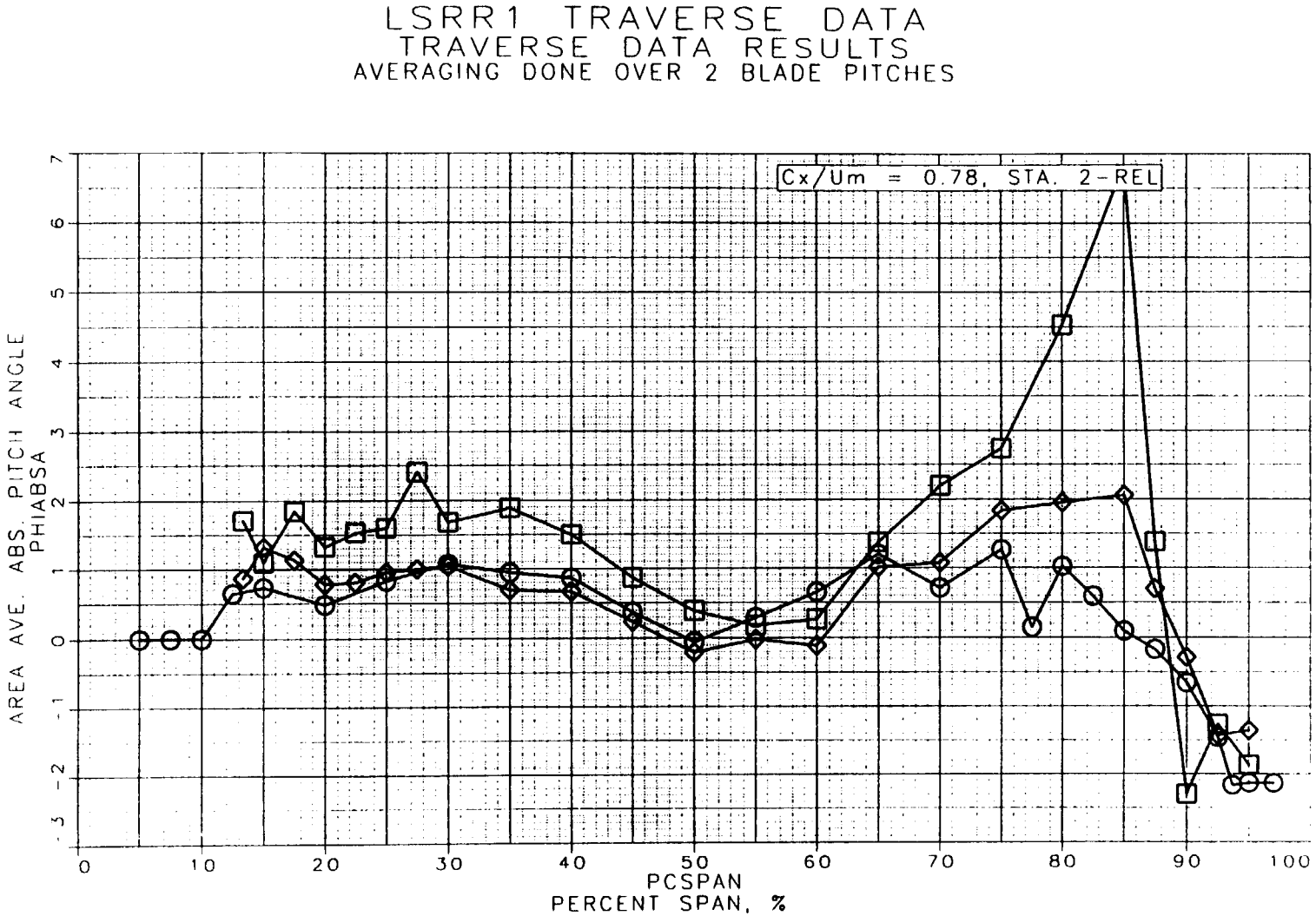

Figure 173. Area Averaged Absolute Pitch Angle at STA2

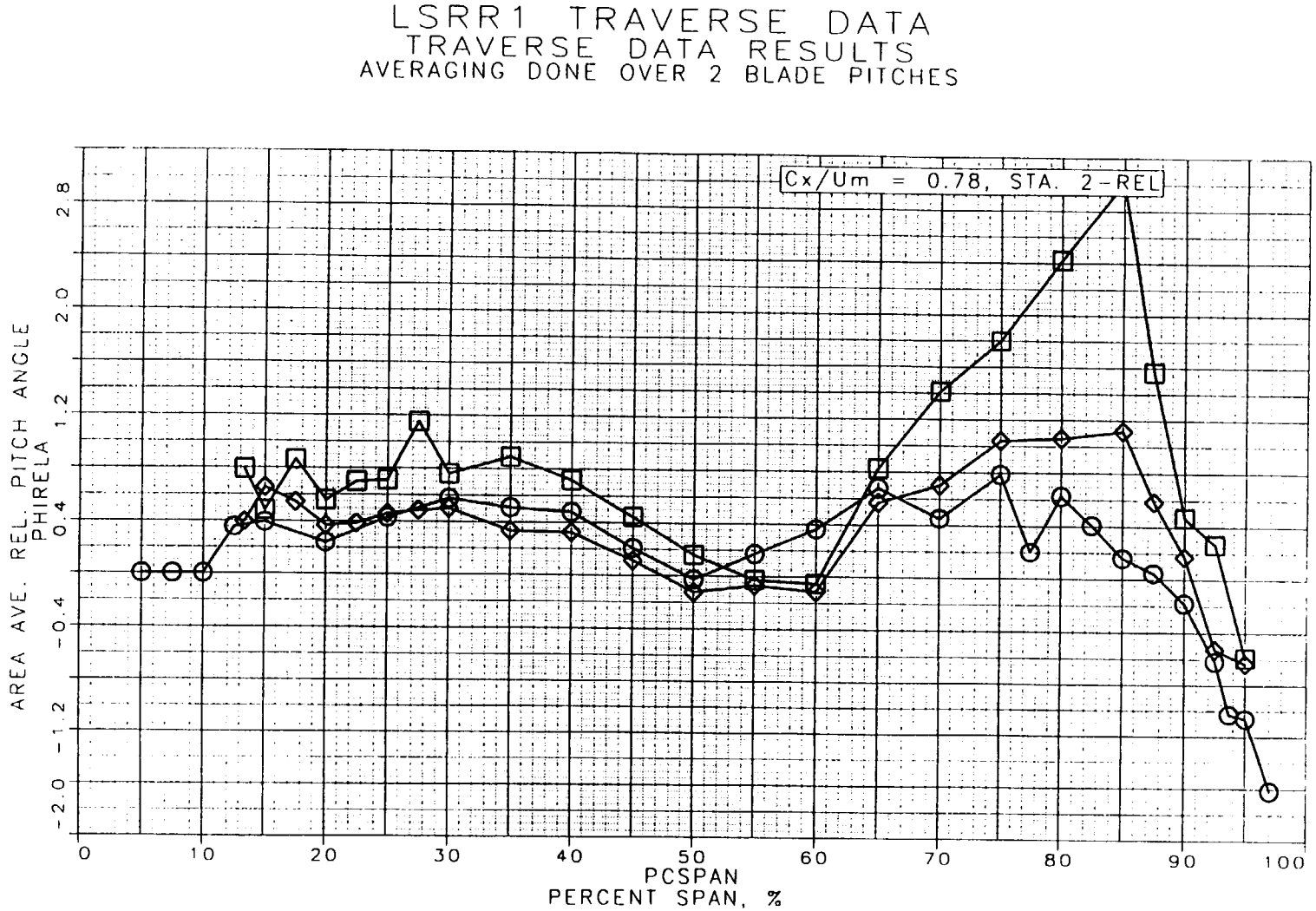

Figure 174. Area Averaged Relative Pitch Angle at STA2

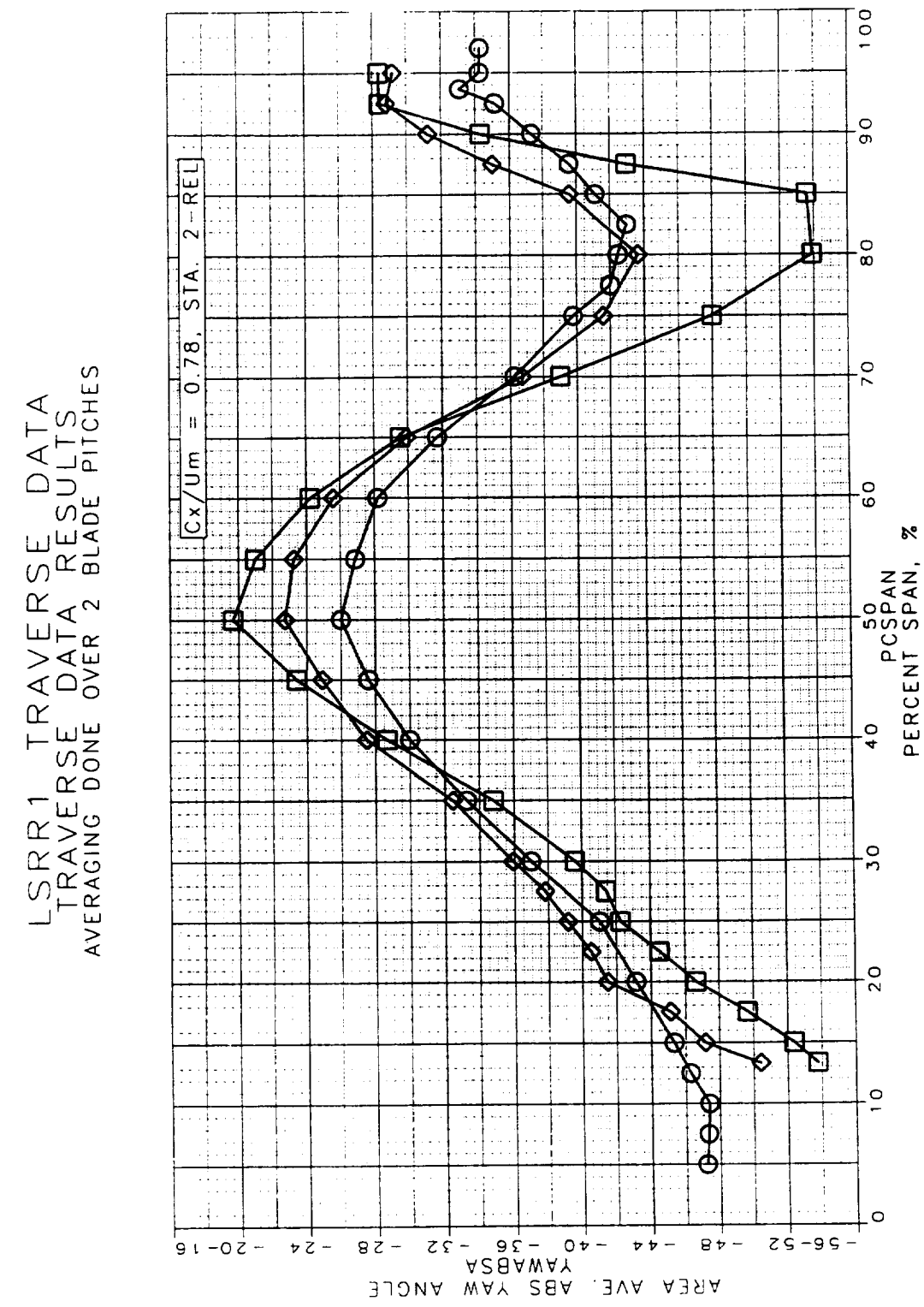

Figure 175. Area Averaged Absolute Yaw Angle at STA2

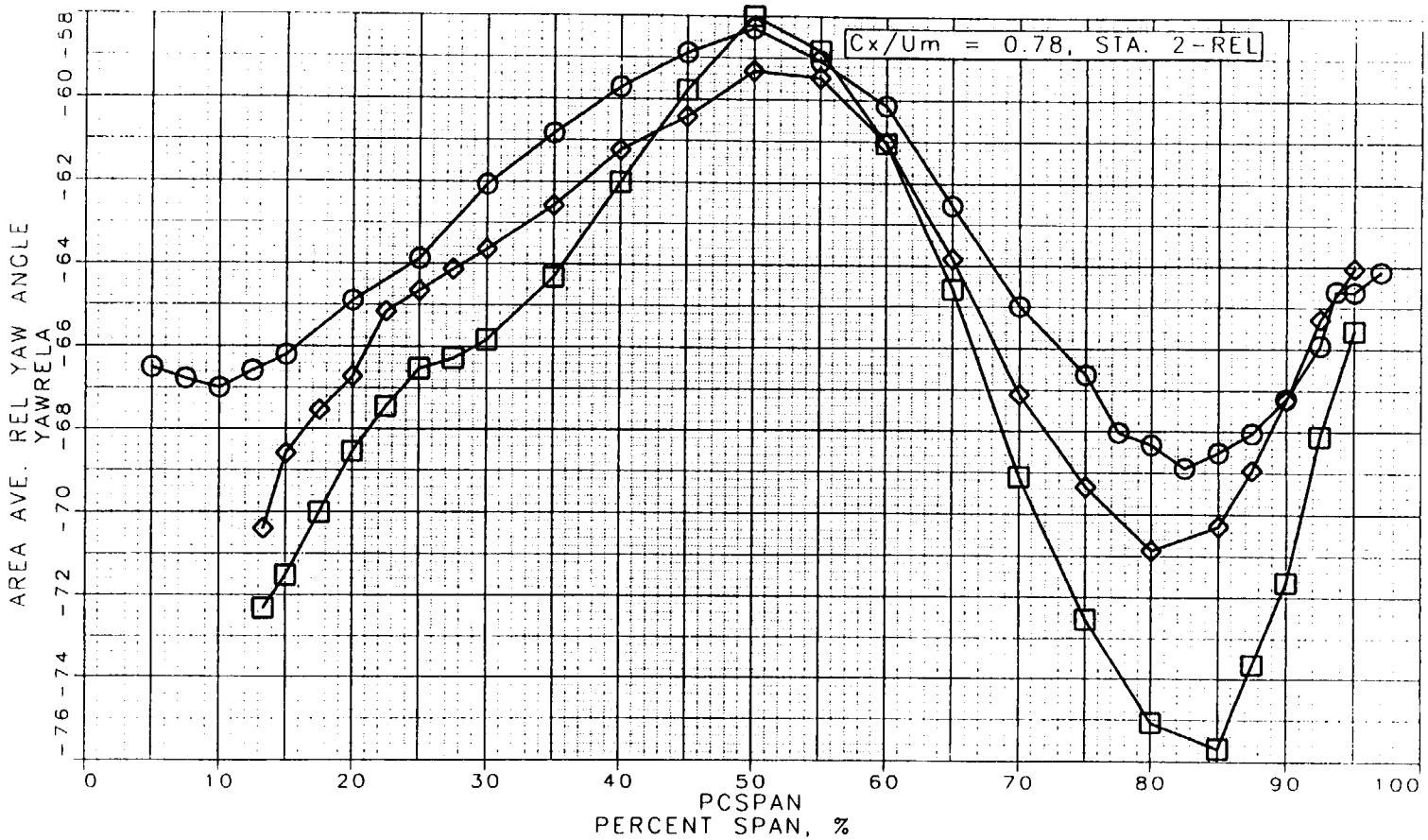

Figure 176. Area Averaged Relative Yaw Angle at STA2

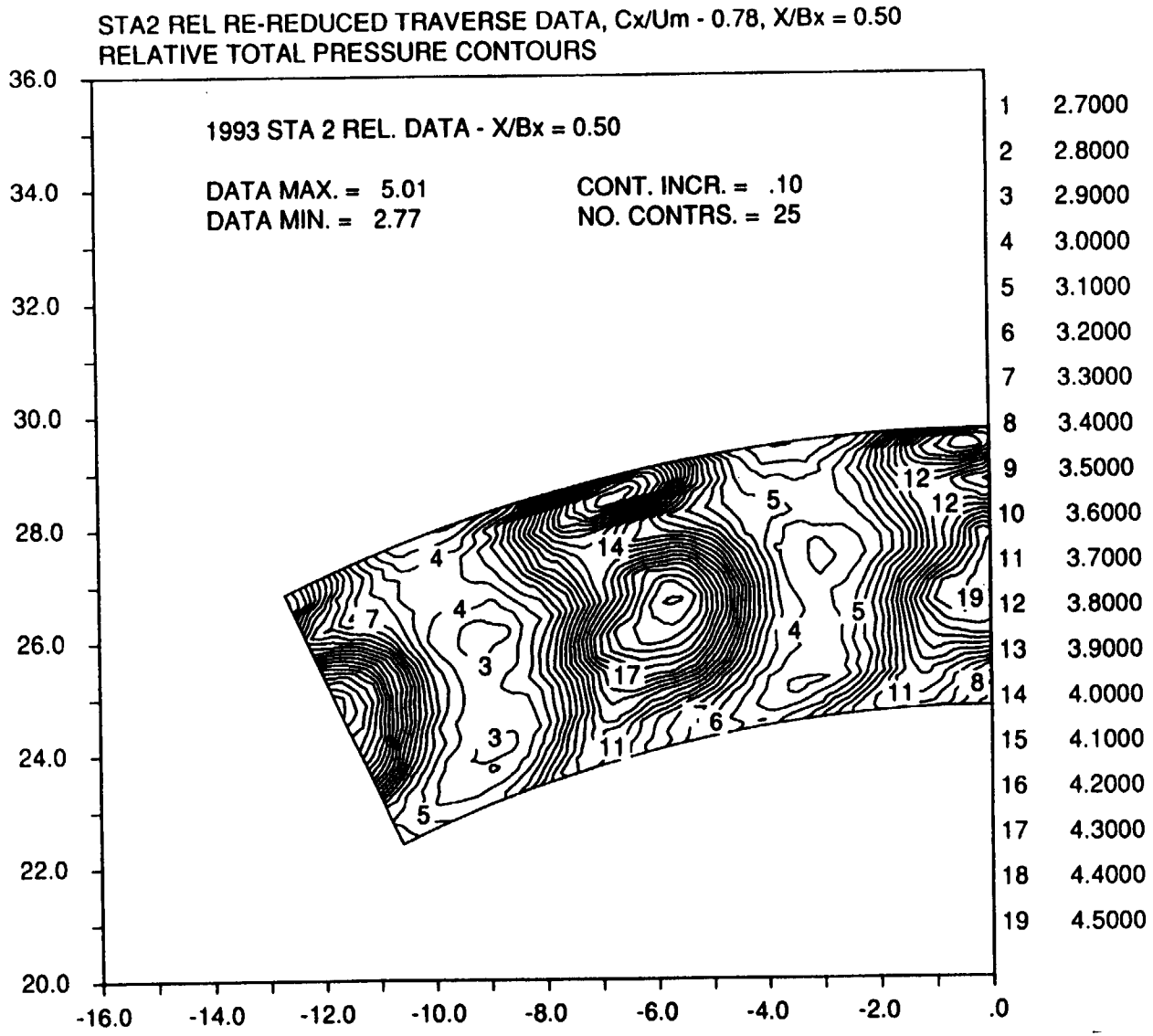

Figure 177. Relative Total Pressure Coefficient Contours at STA2

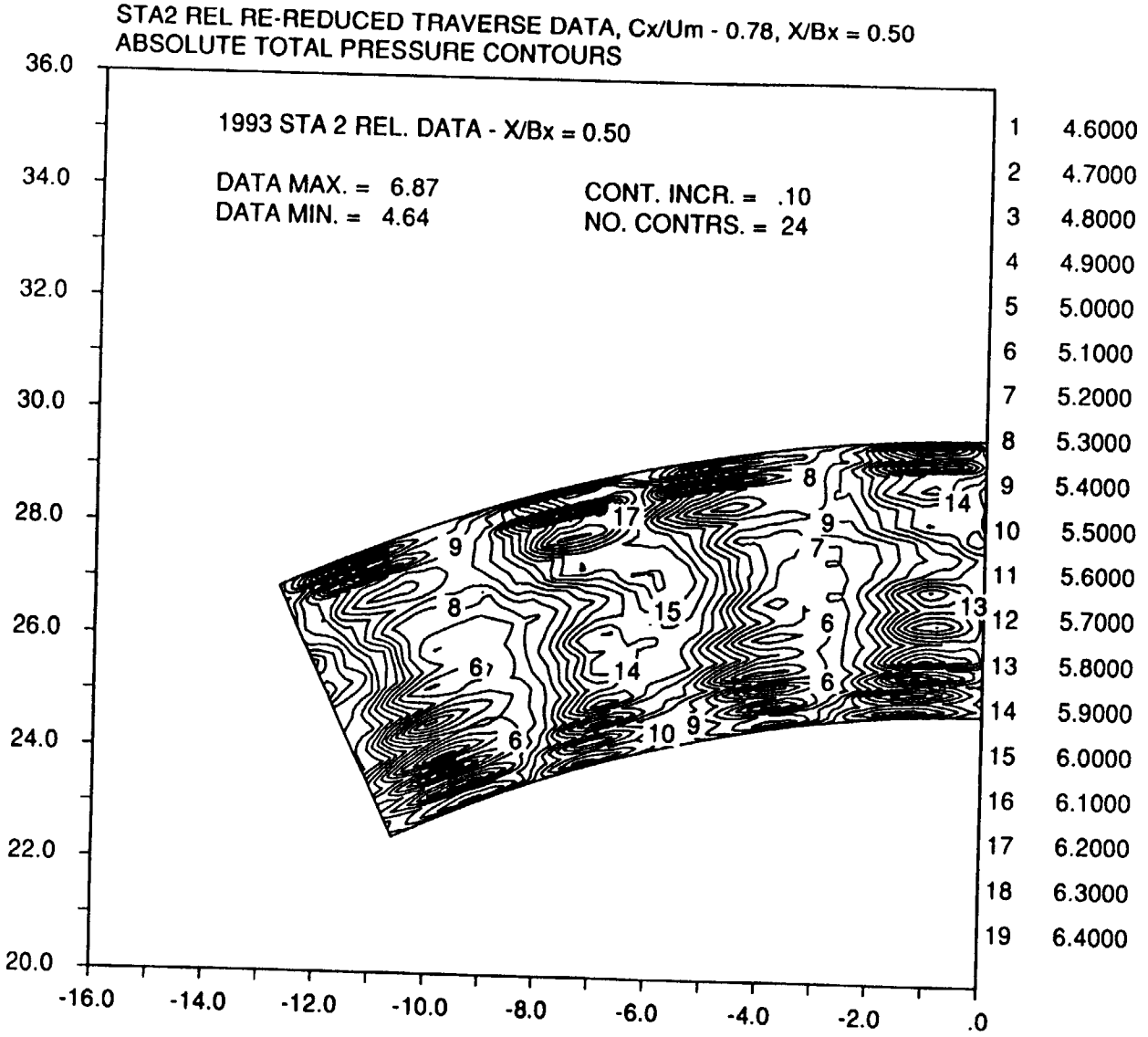

Figure 178. Absolute Total Pressure Coefficient Contours at STA2

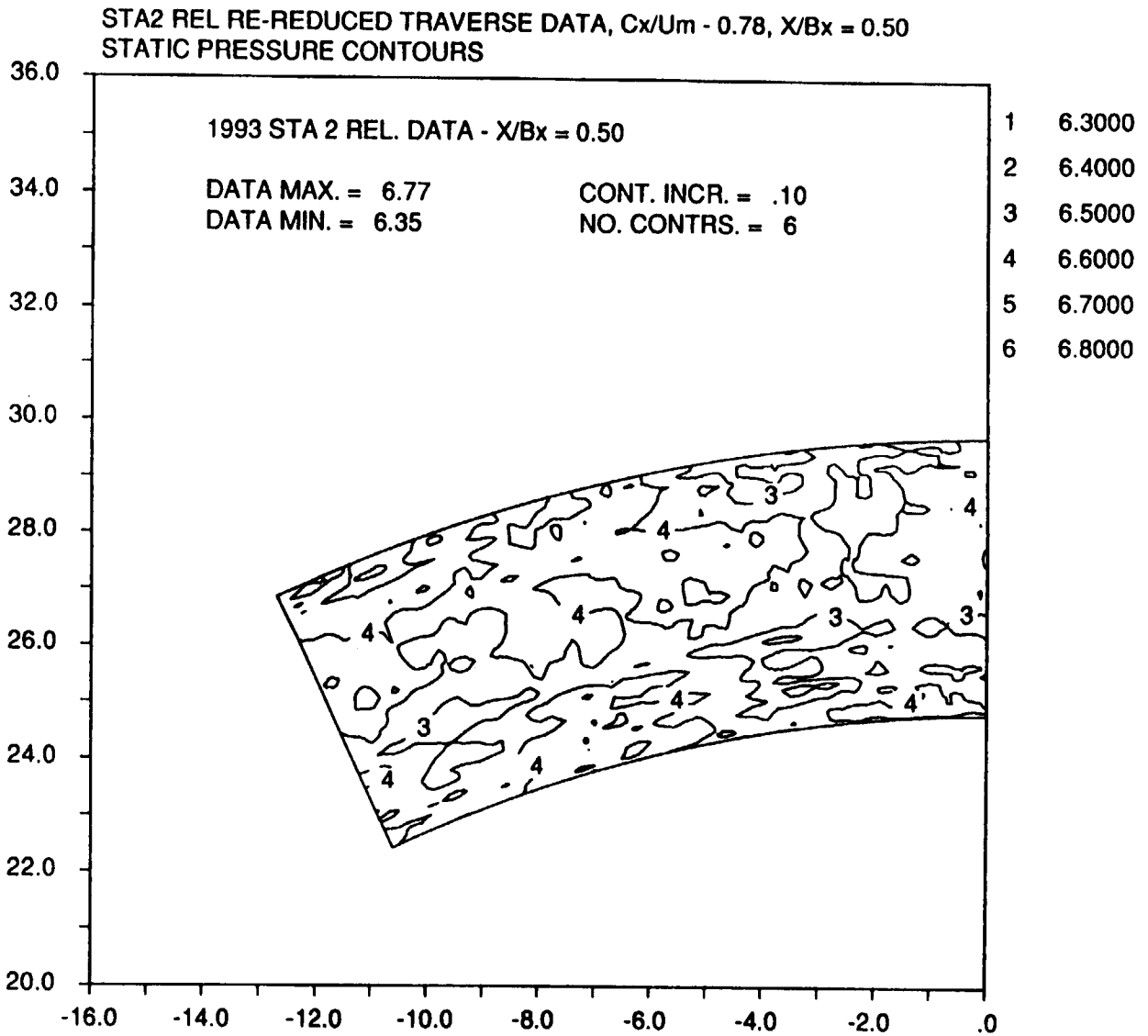

Figure 179. Rotary Total Pressure Coefficient Contours at STA2

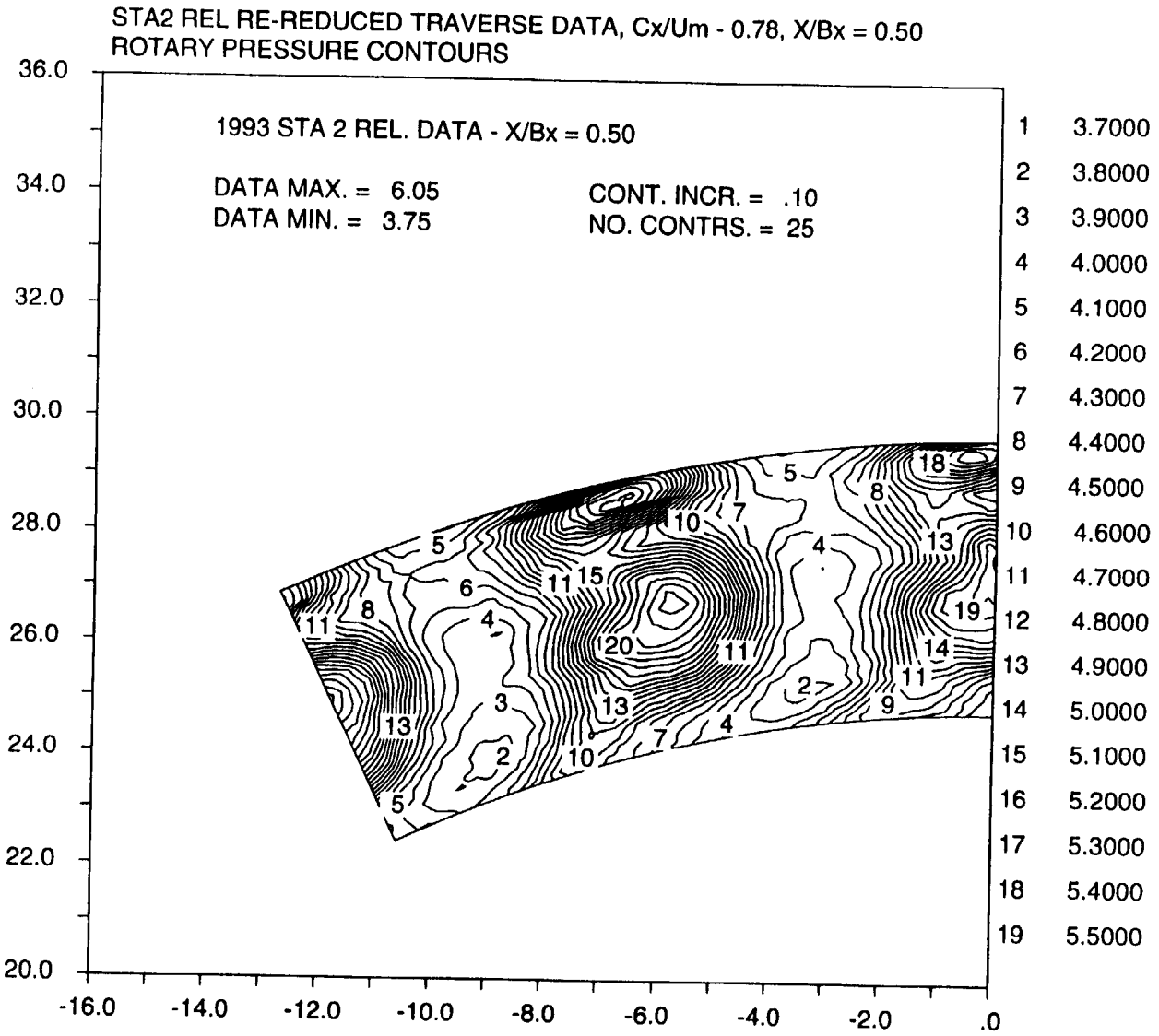

Figure 180. Static Pressure Coefficient Contours at STA2

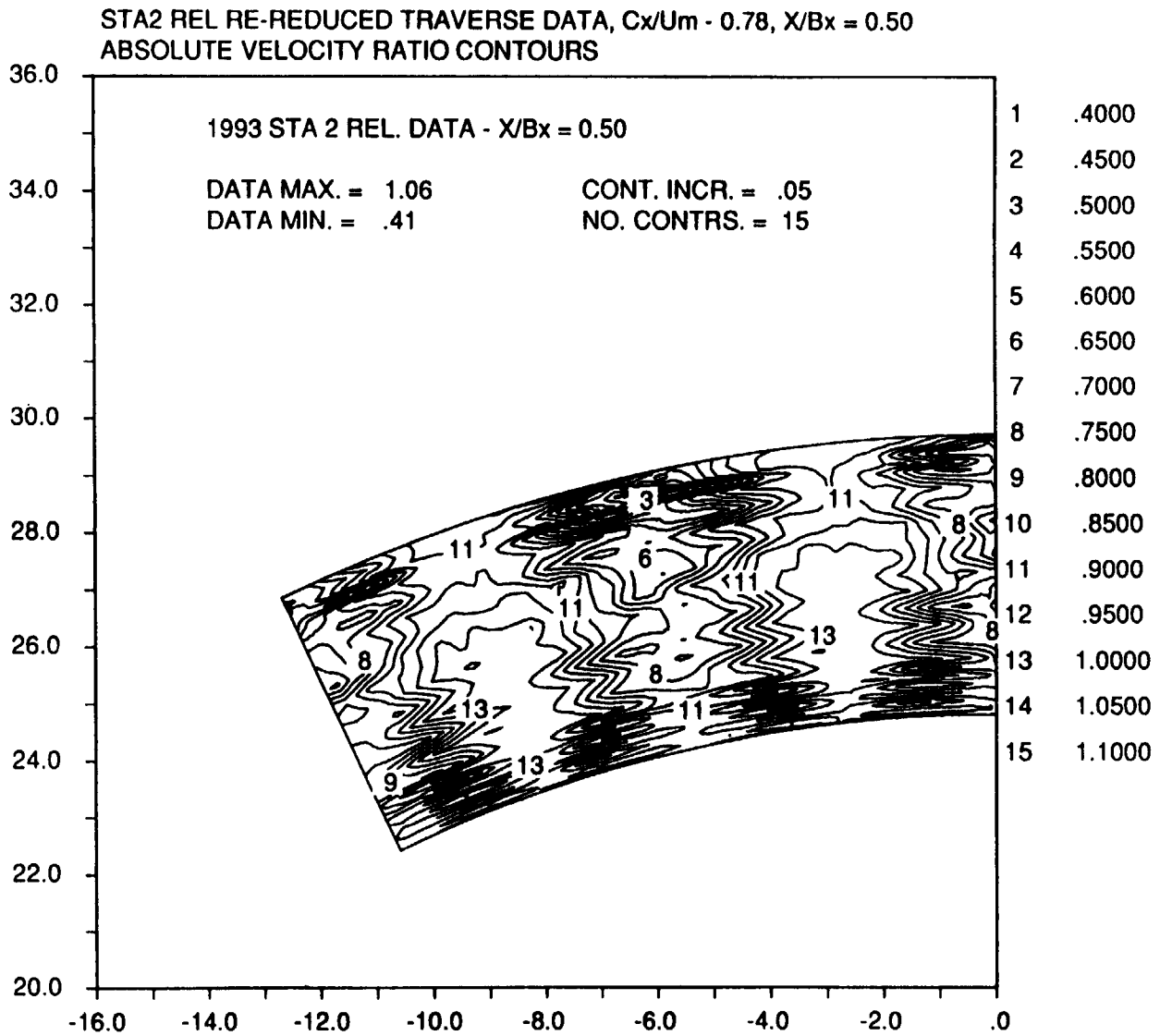

Figure 181. Relative Velocity Ratio Contours at STA2

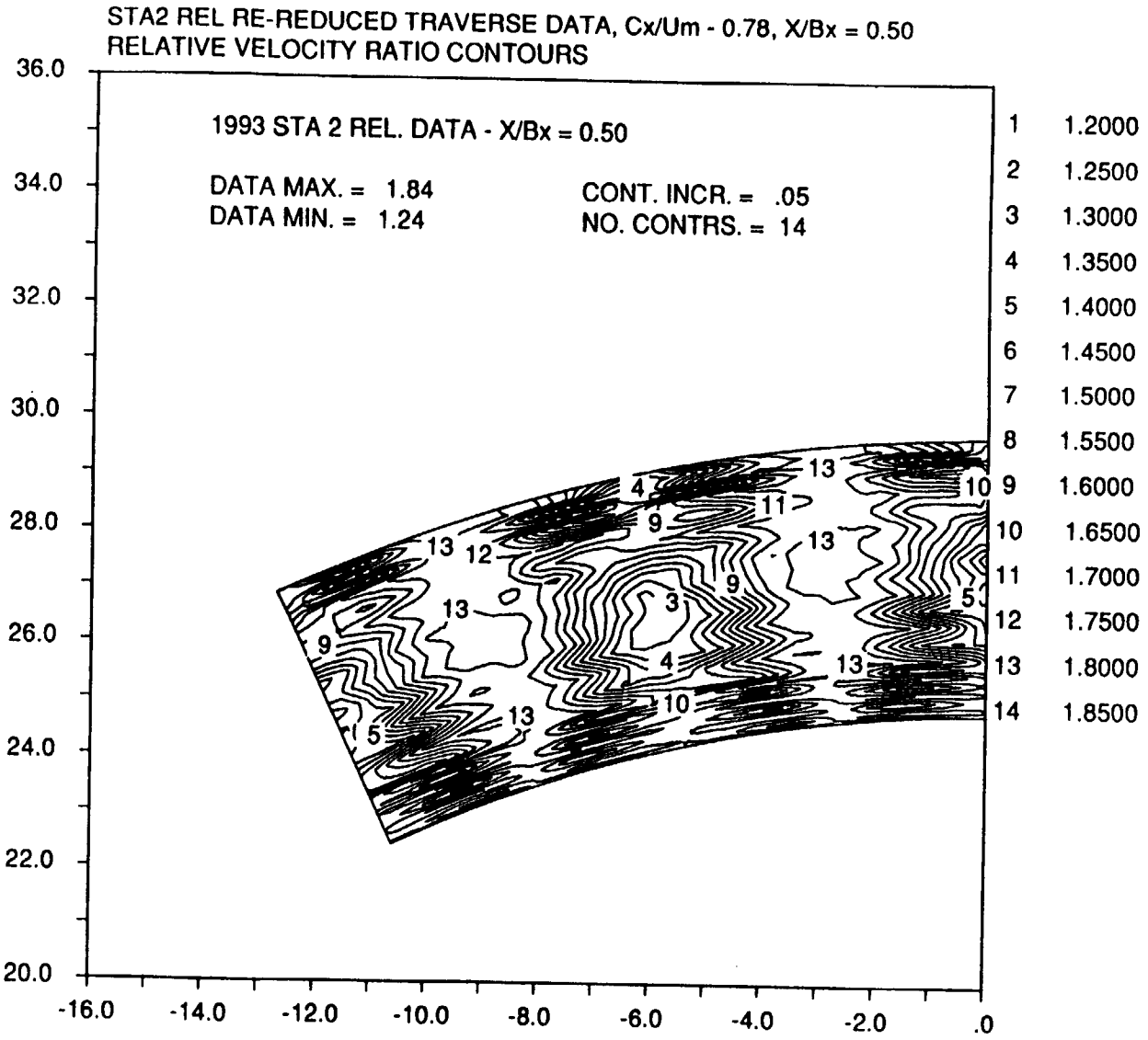

Figure 182. Absolute Velocity Ratio Contours at STA2

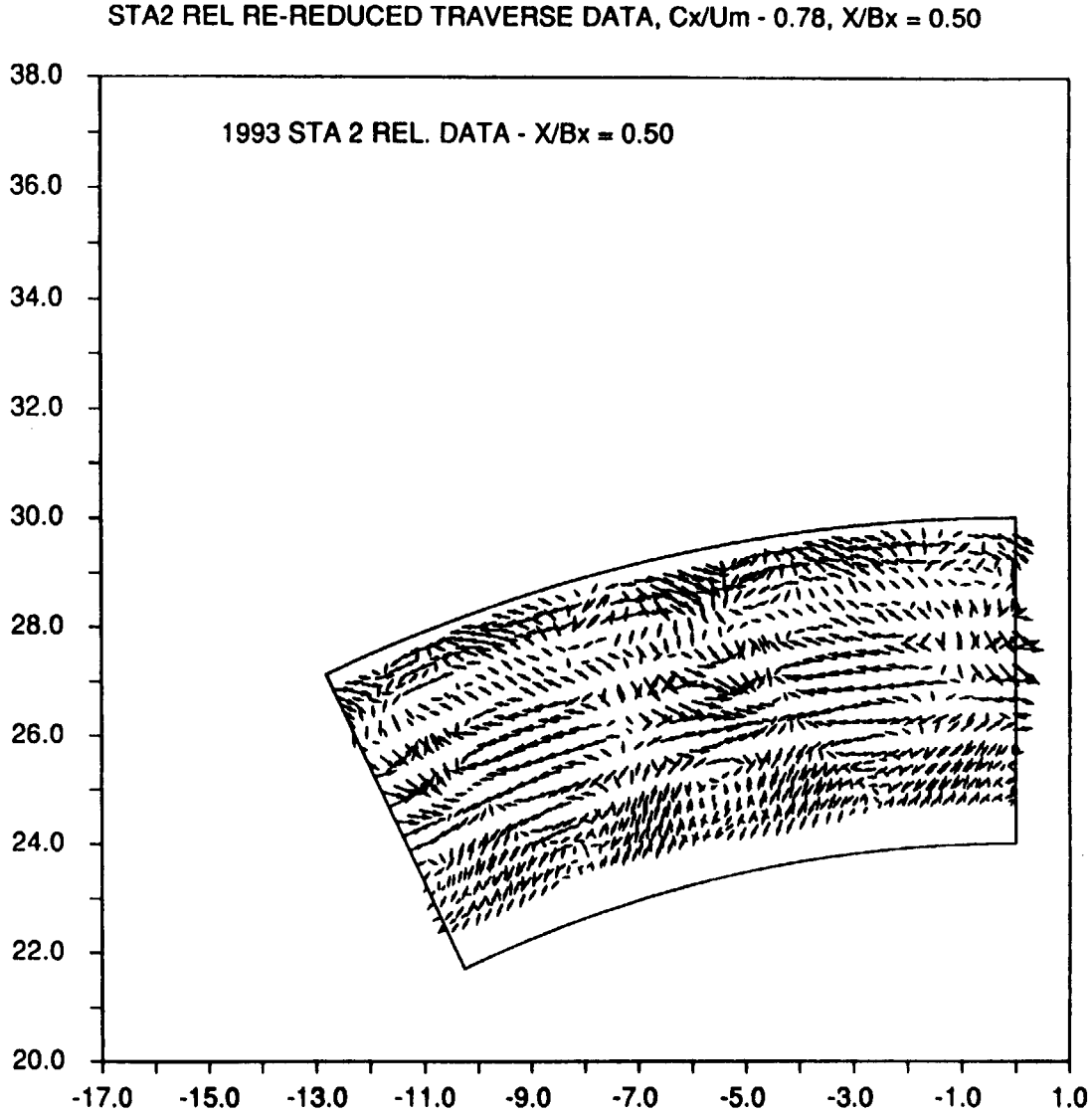

Figure 183. Velocity Vectors at STA2

Second Stator Exit Flowfield Data (28 Airfoil Count) Acquired at X_2/B_x - rotor = 0.746, 0.54, Cx/U = 0.78

in Relative Frame

Compared to Data Acquired as Part of Air Force Office of Scientific Research Contract

(STA3)

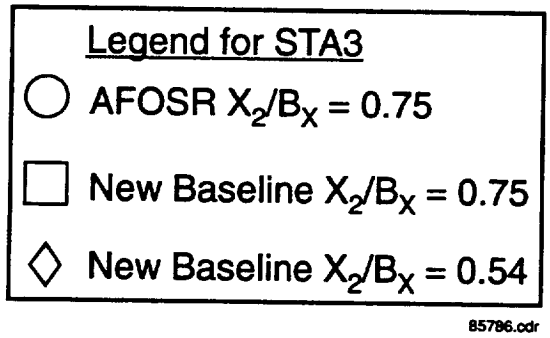

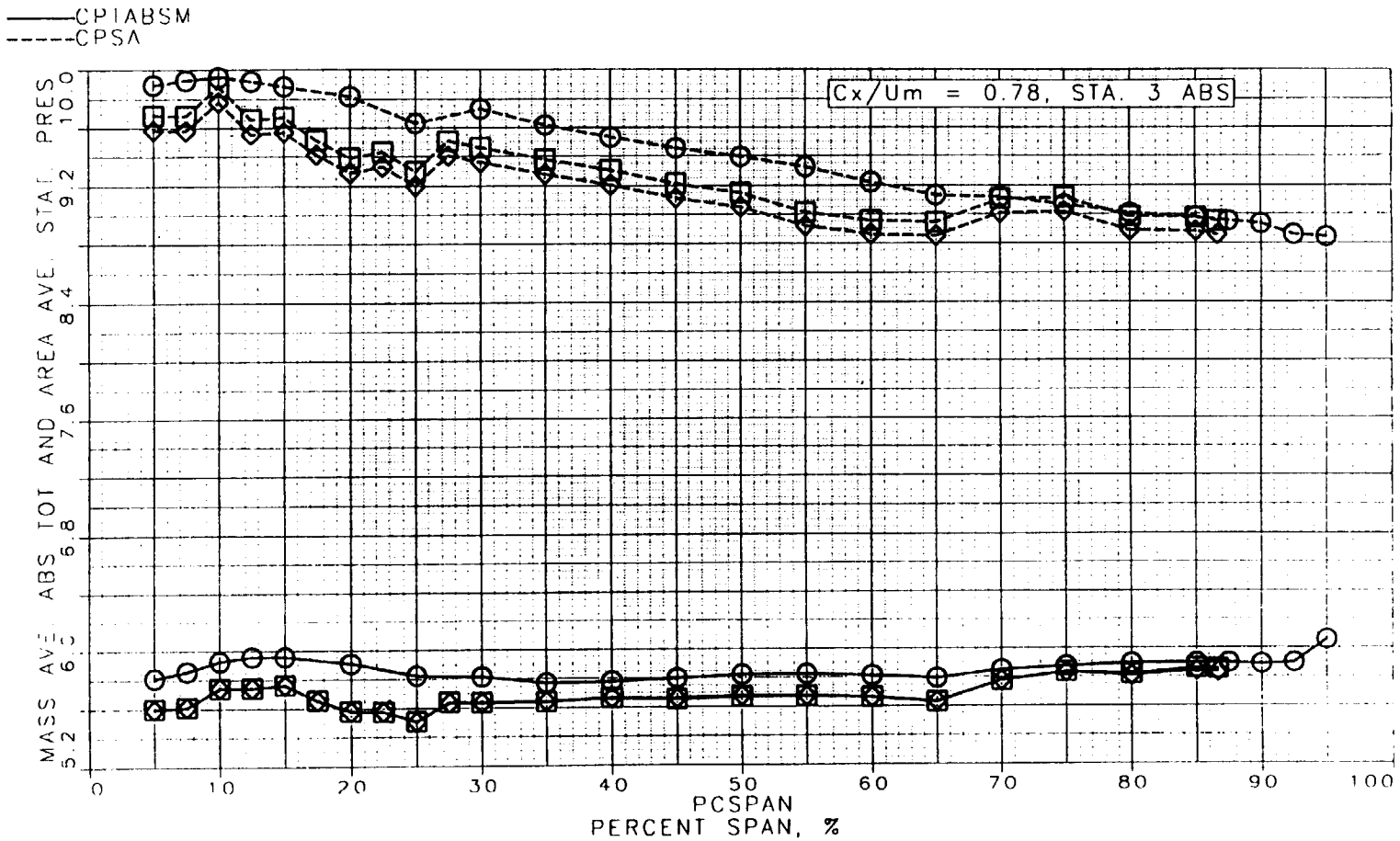

Figure 184. Mass Averaged Absolute and Static Pressure Coefficient at STA3

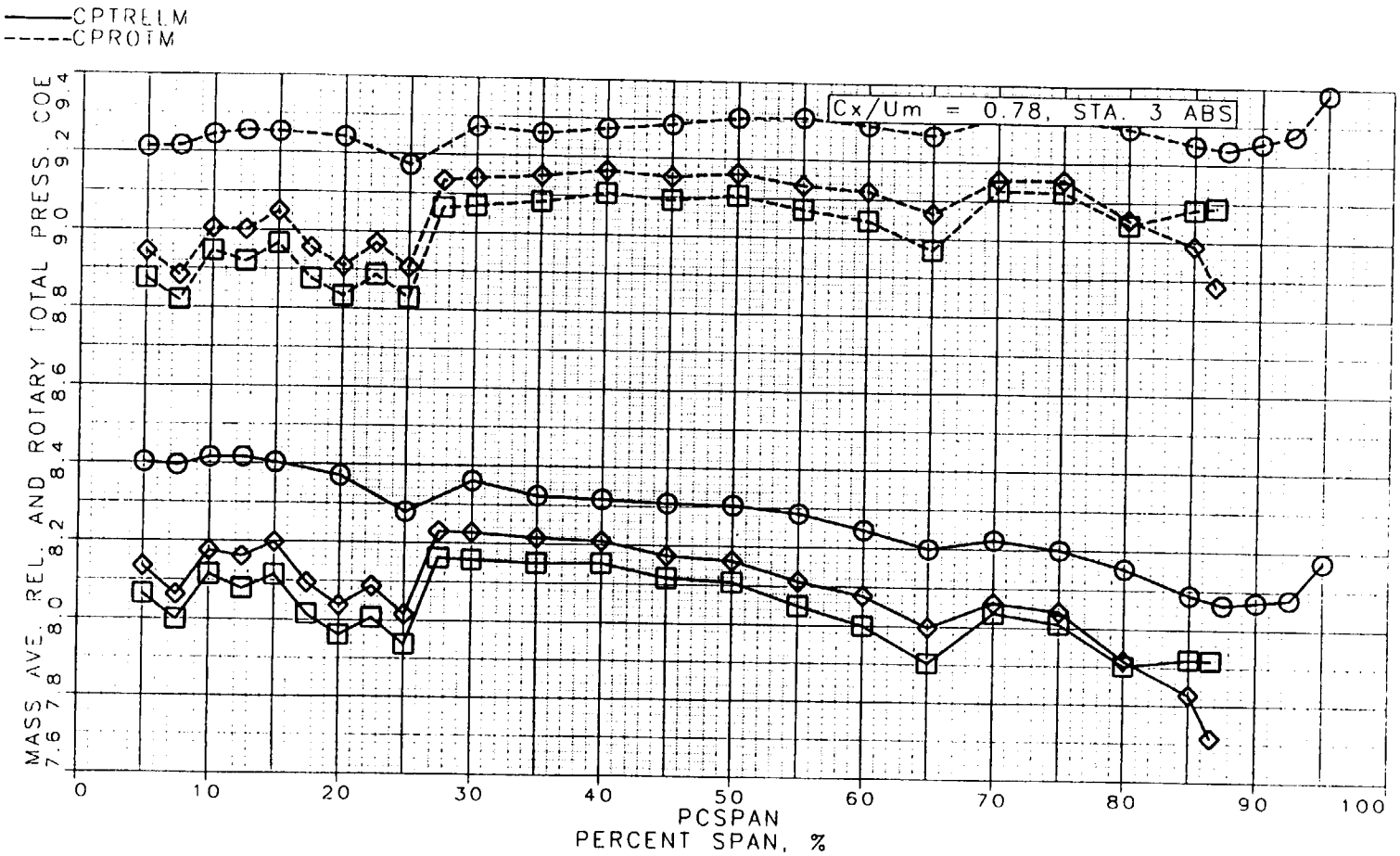

Figure 185. Mass Averaged Relative and Rotary Total Pressure Coefficient at STA3

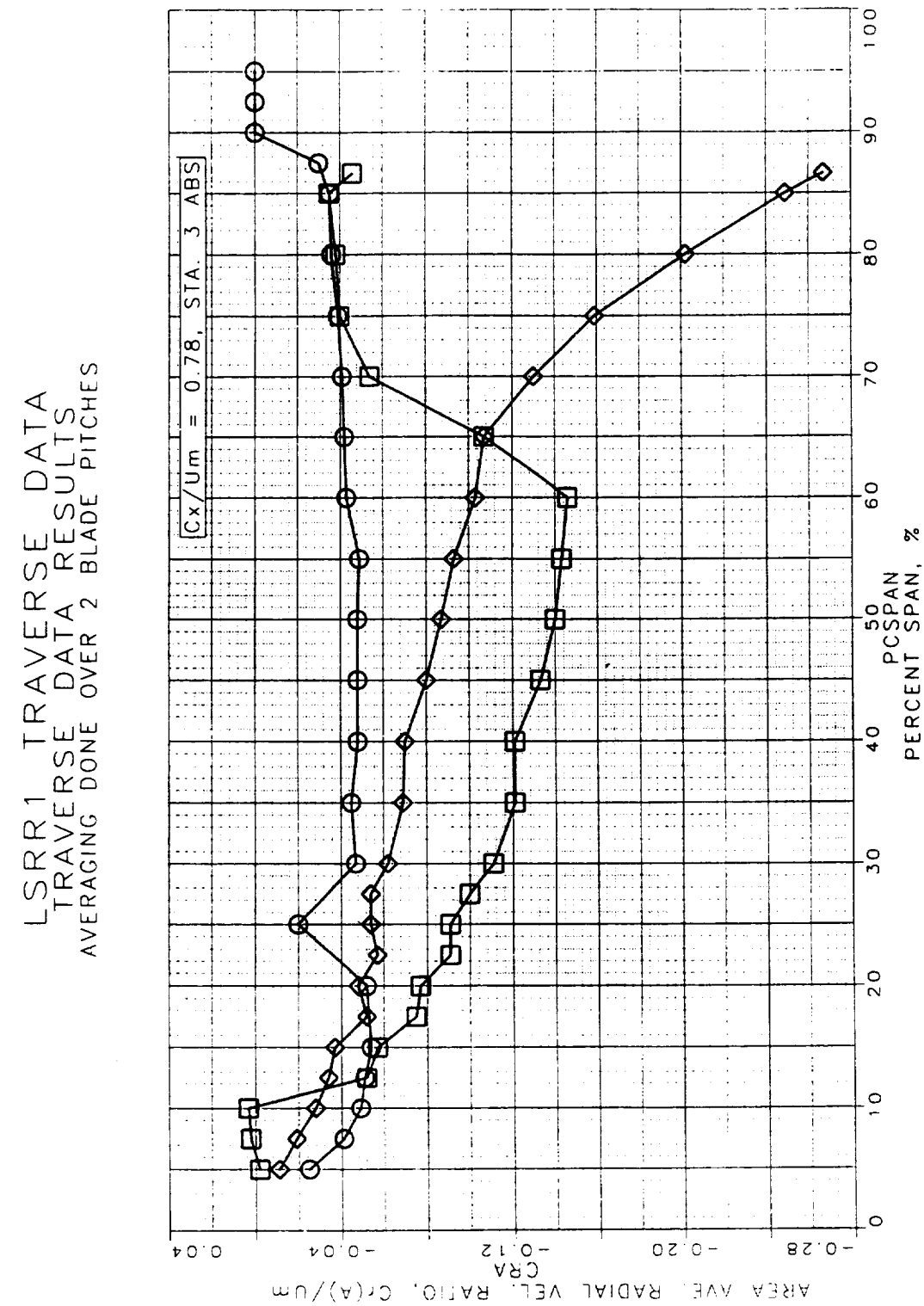

Figure 186. Area Averaged Radial Velocity Ratio at STA3

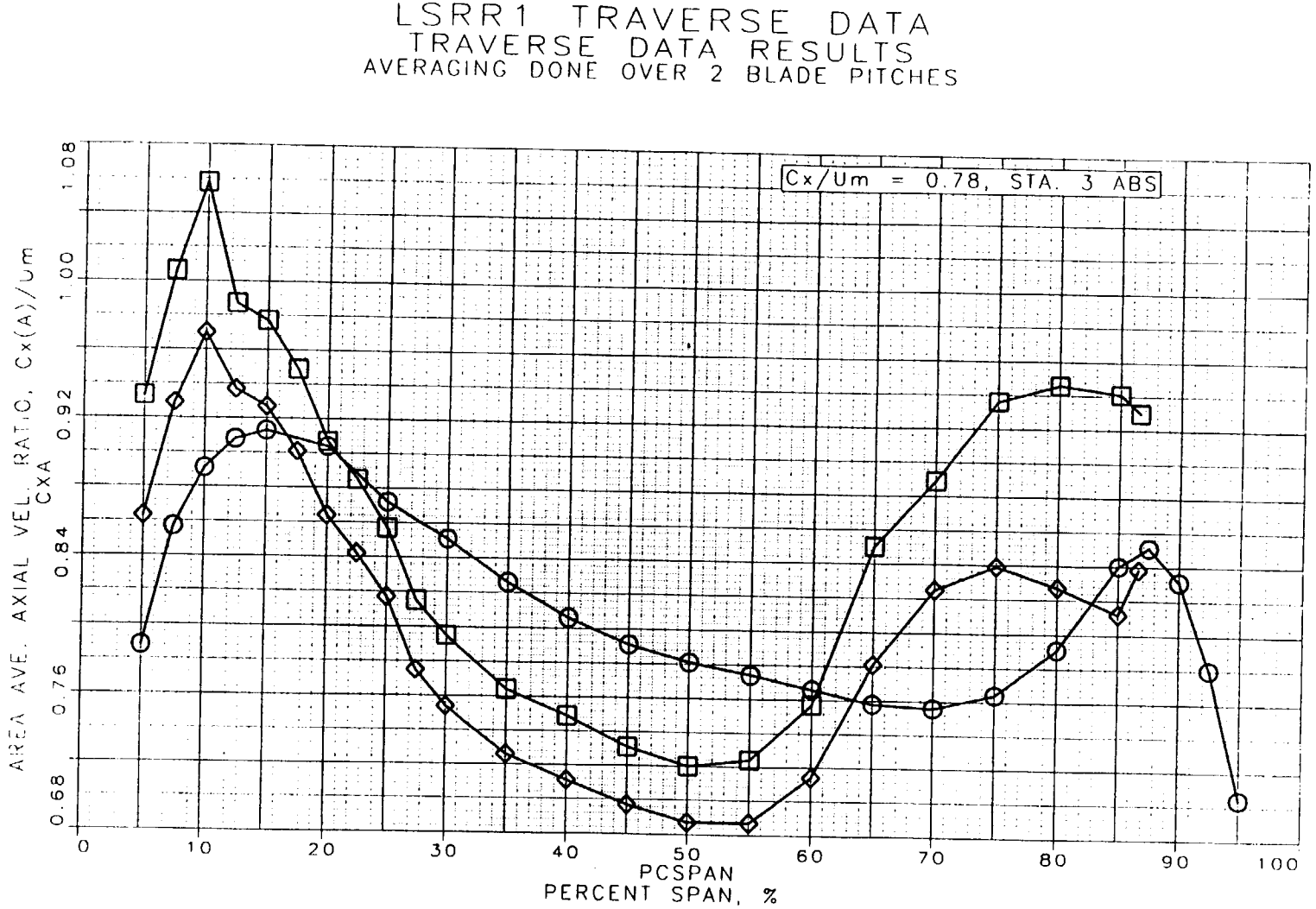

Figure 187. Area Averaged Axial Velocity Ratio at STA3

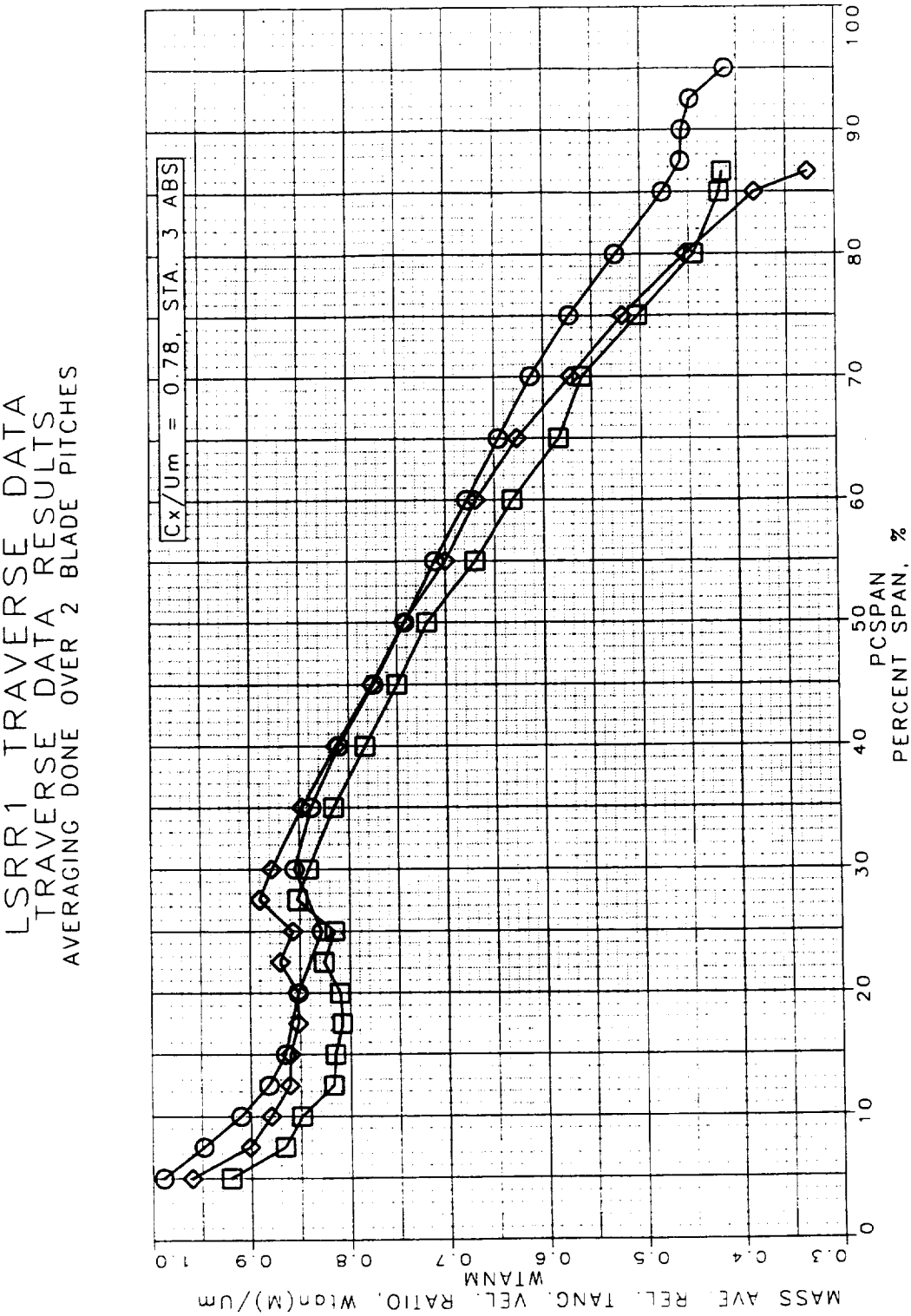

Figure 188. Mass Averaged Total Velocity Ratio at STA3

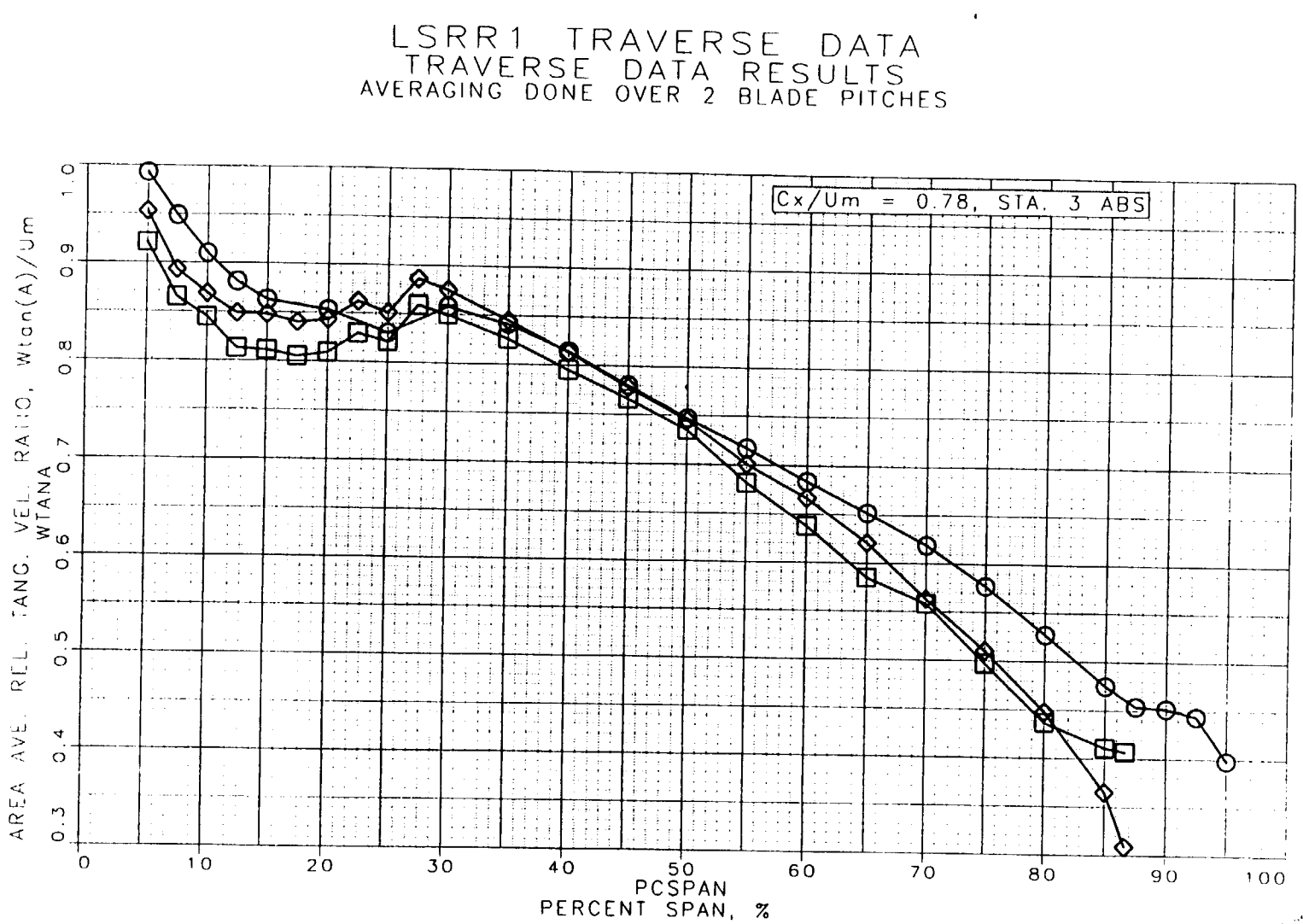

Figure 189. Area Averaged Total Velocity Ratio at STA3

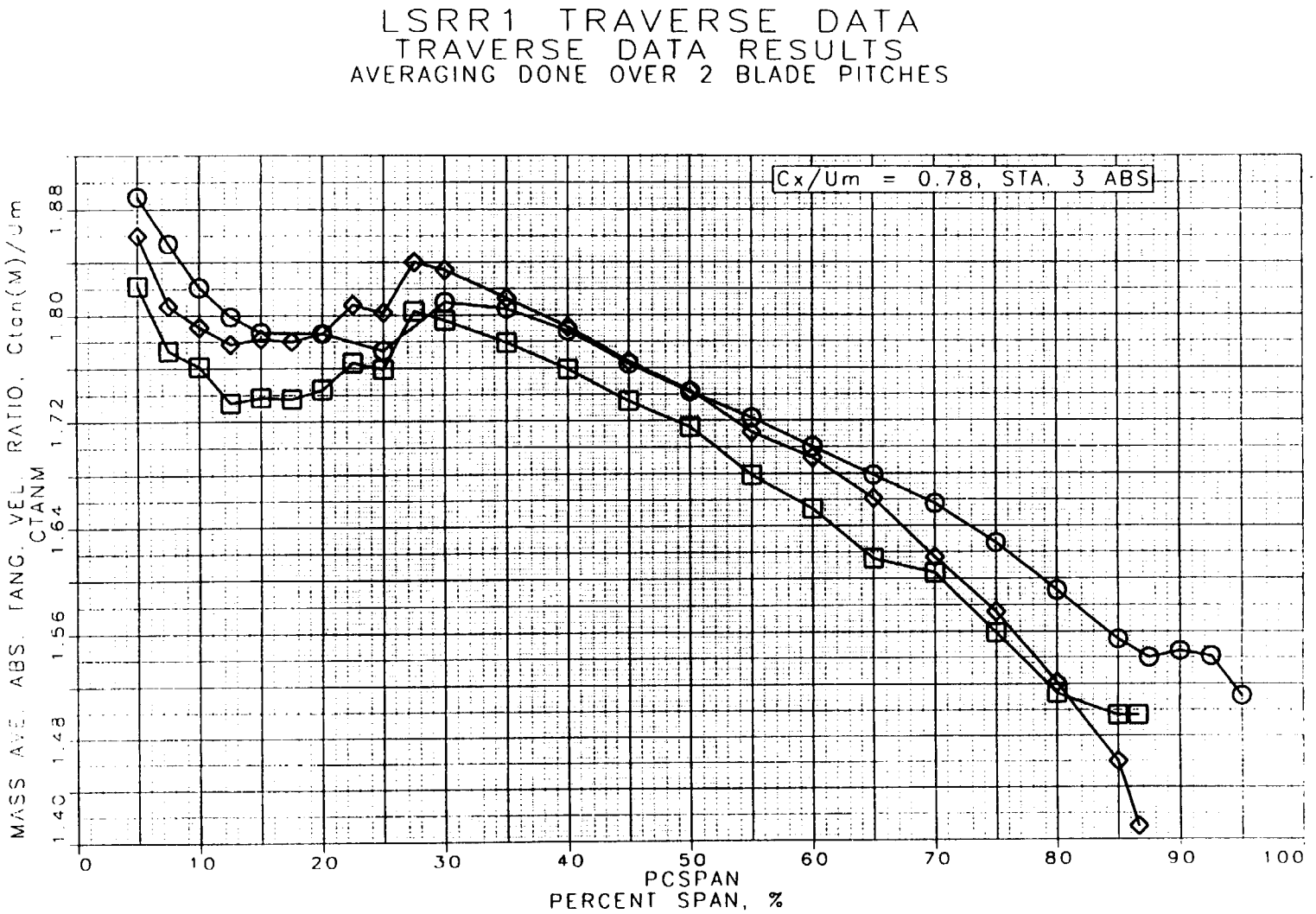

Figure 190. Mass Averaged Tangential Velocity Ratio at STA3

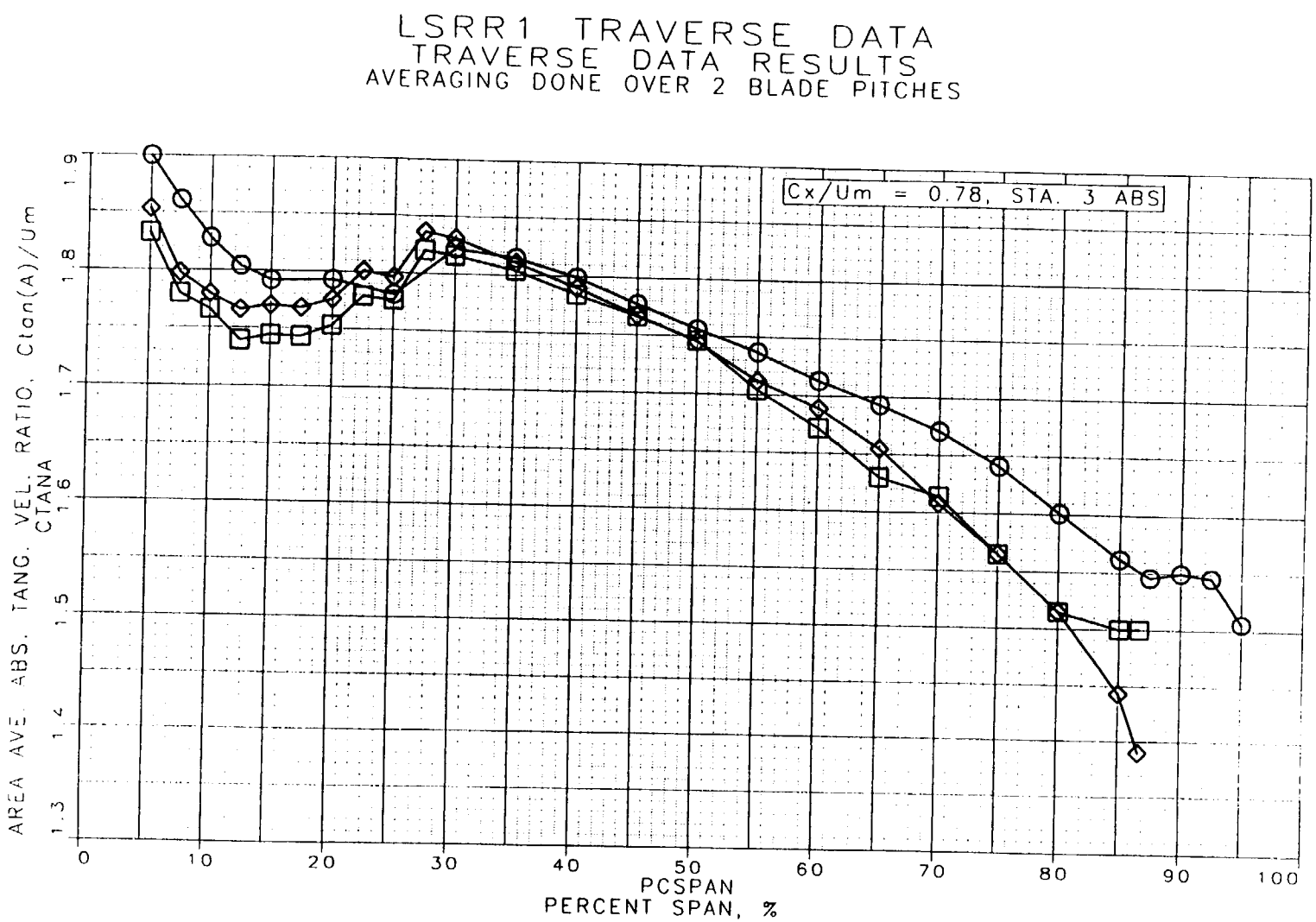

Figure 191. Area Averaged Tangential Velocity Ratio at STA3

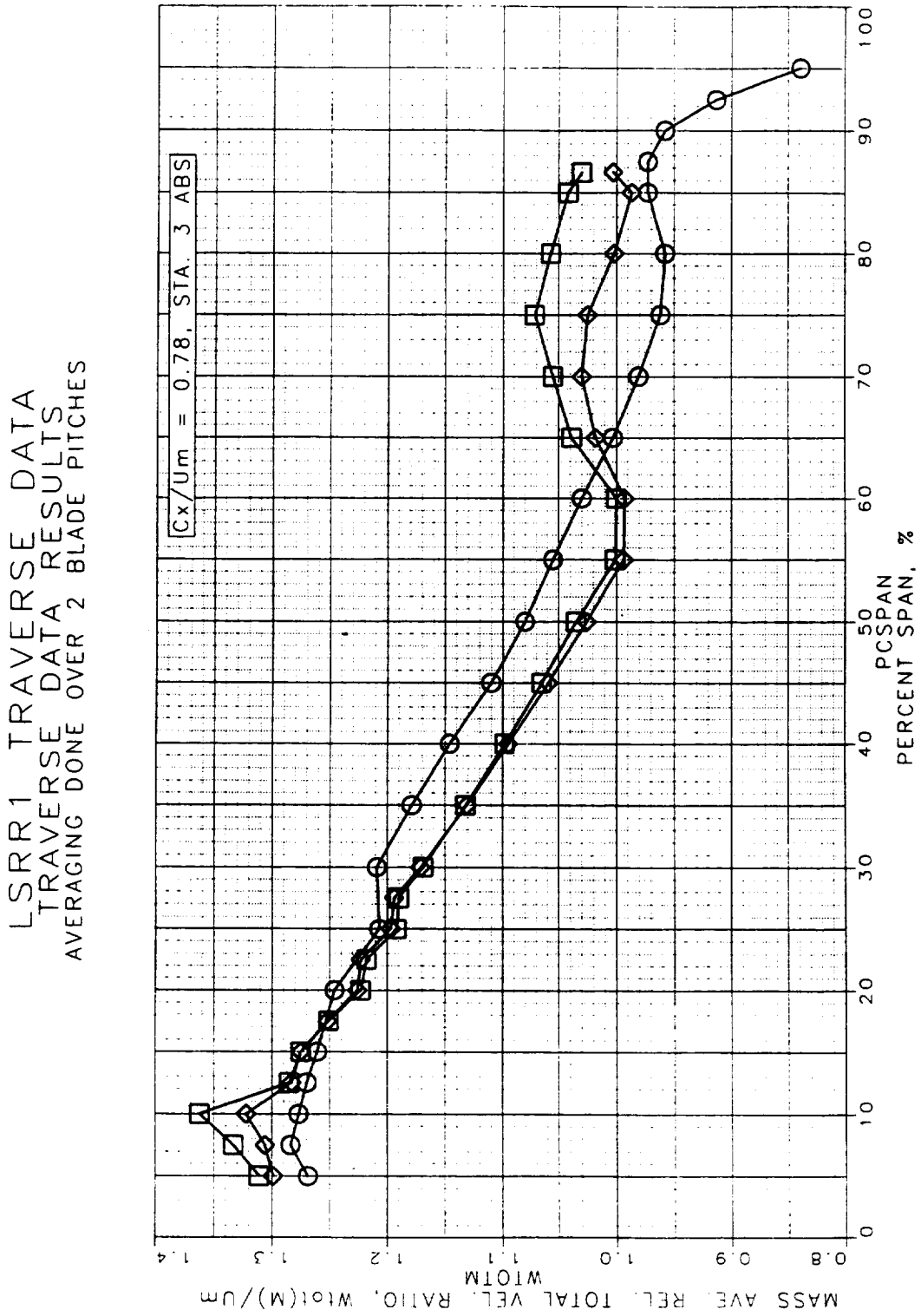

Figure 192. Mass Averaged Total Relative Velocity Ratio at STA3

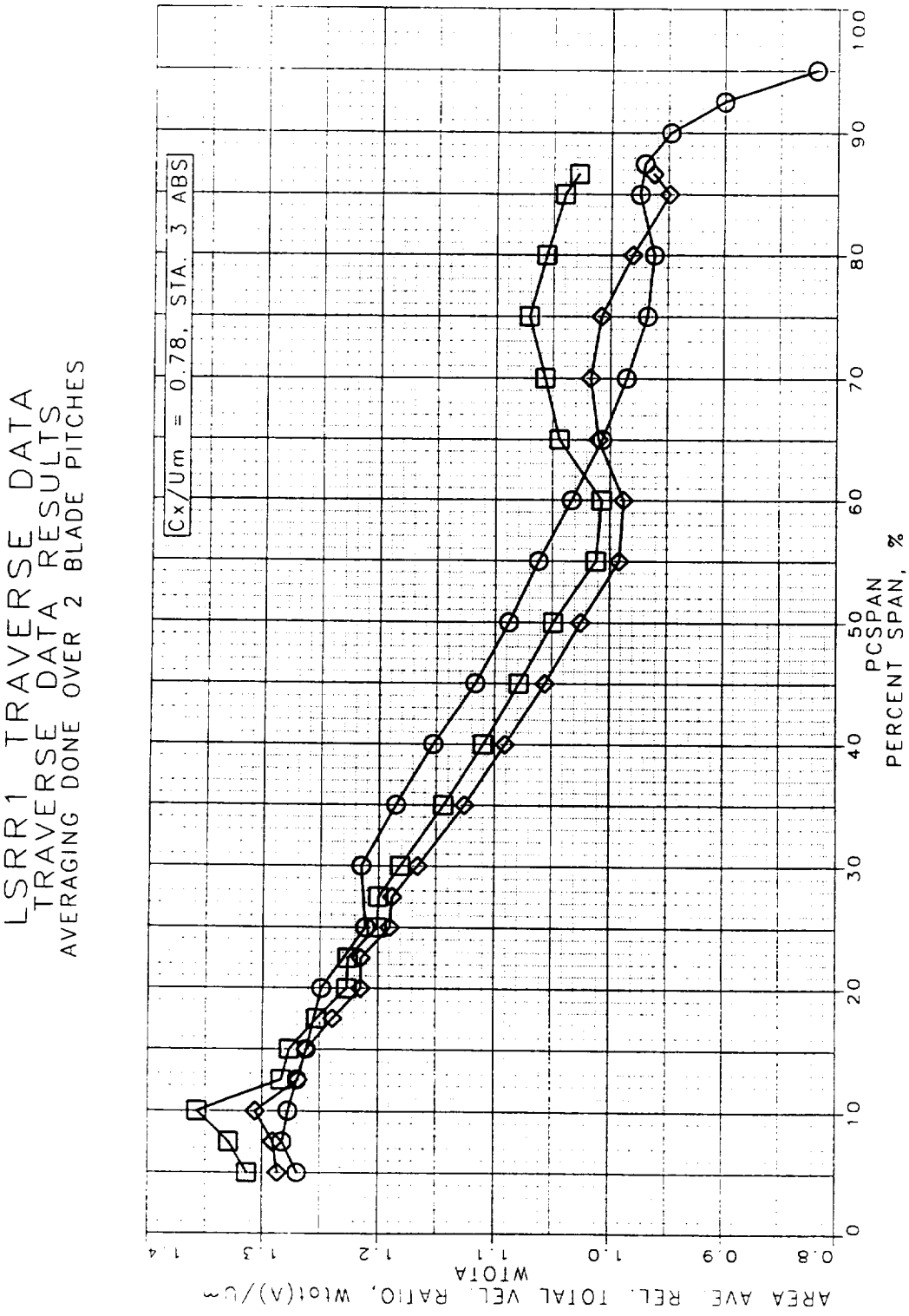

Figure 193. Area Averaged Total Relative Velocity Ratio at STA3

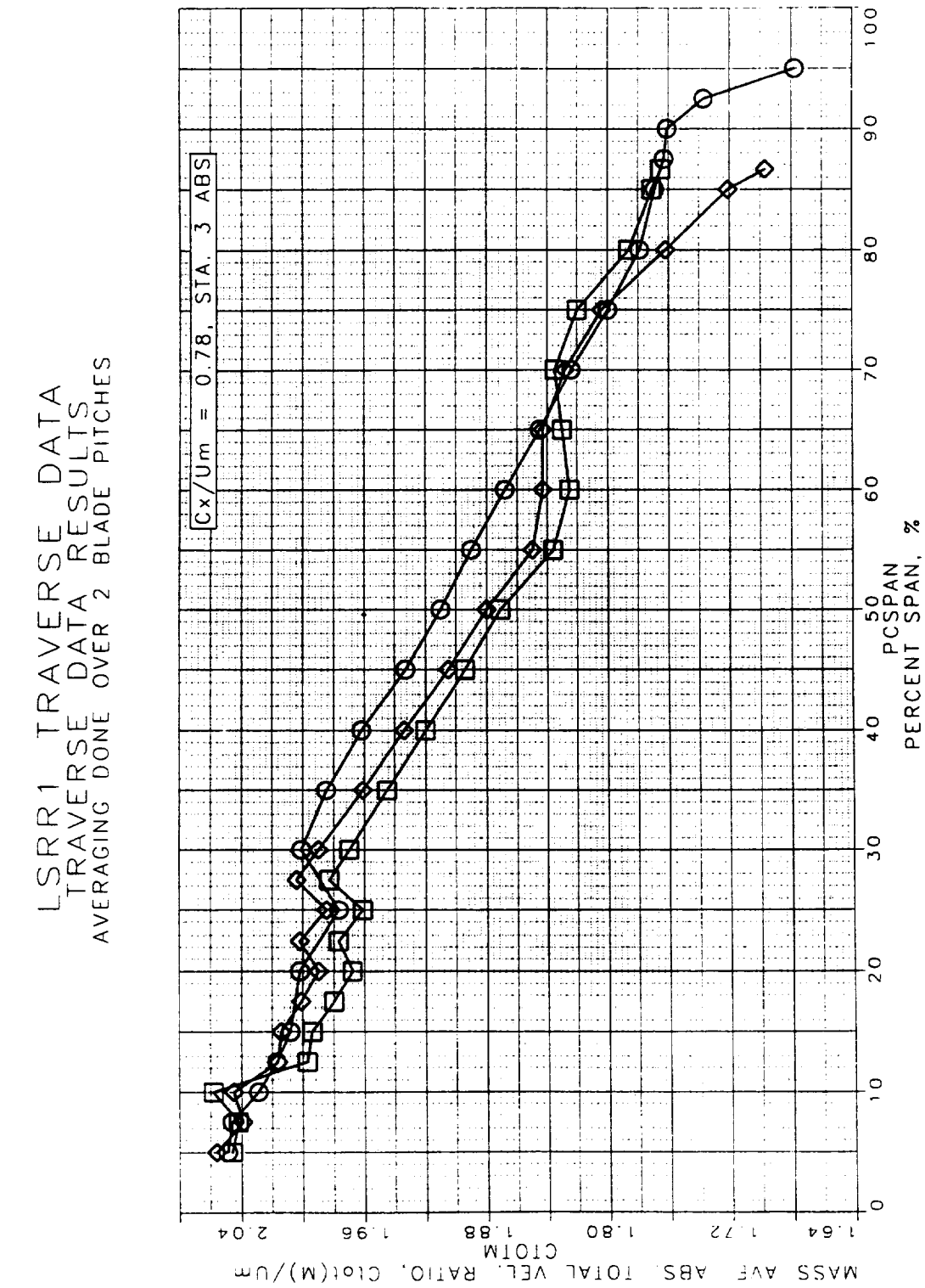

Figure 194. Mass Averaged Total Velocity Ratio at STA3

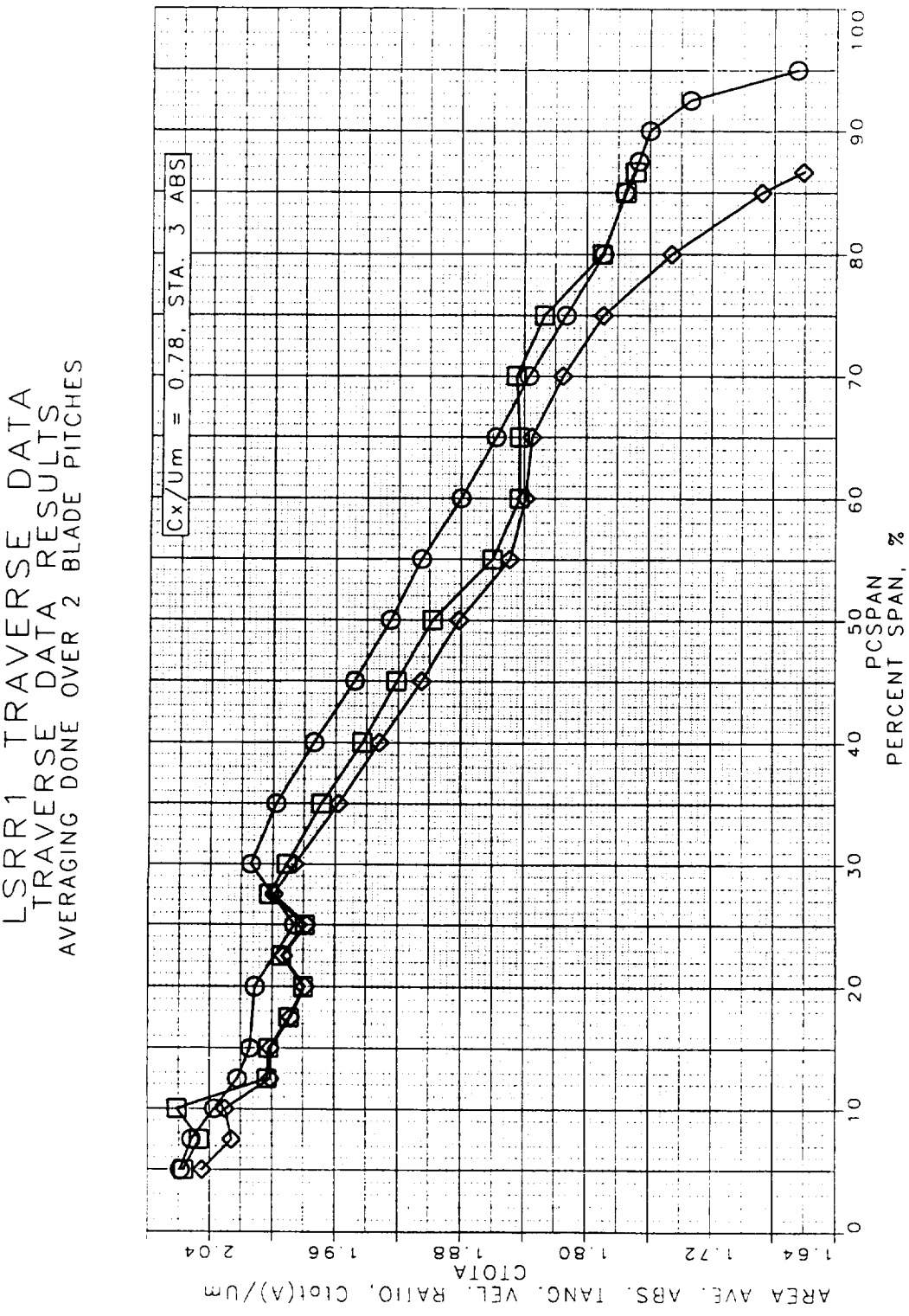

Figure 195. Area Averaged Absolute Tangential Velocity Ratio at STA3

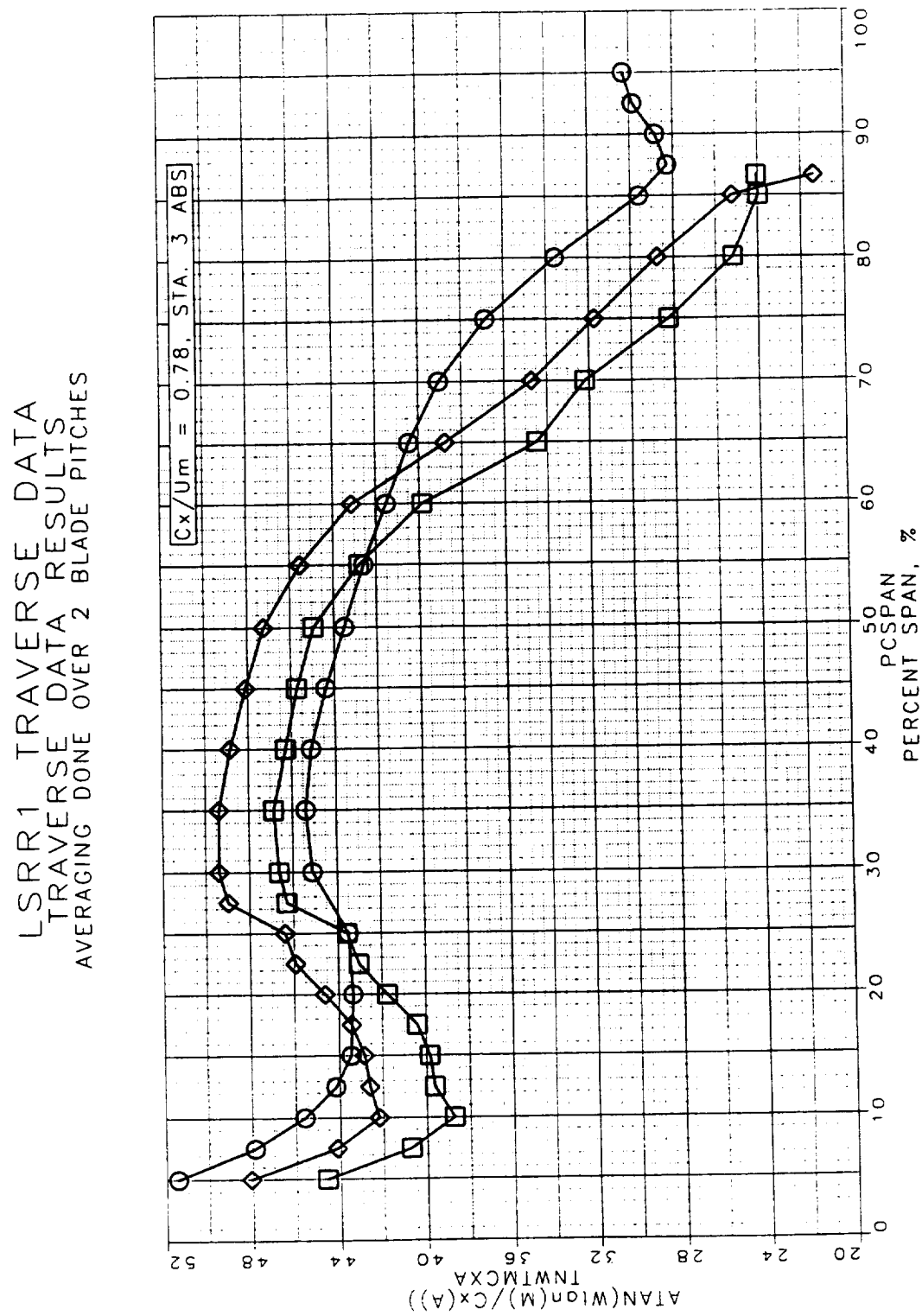

Figure 196. Area Averaged Absolute Yaw Angle at STA3

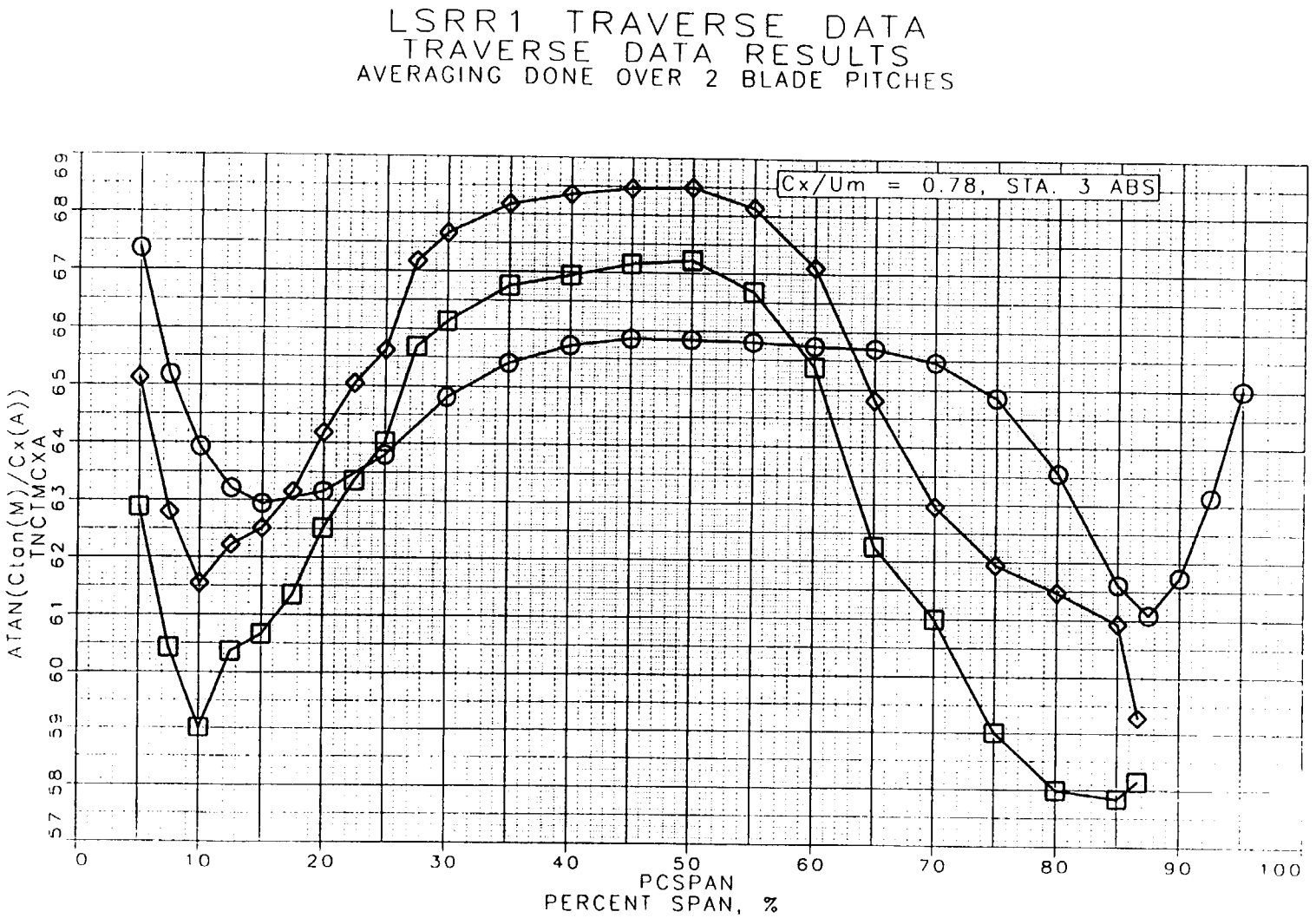

Figure 197. Area Averaged Relative Yaw Angle at STA3

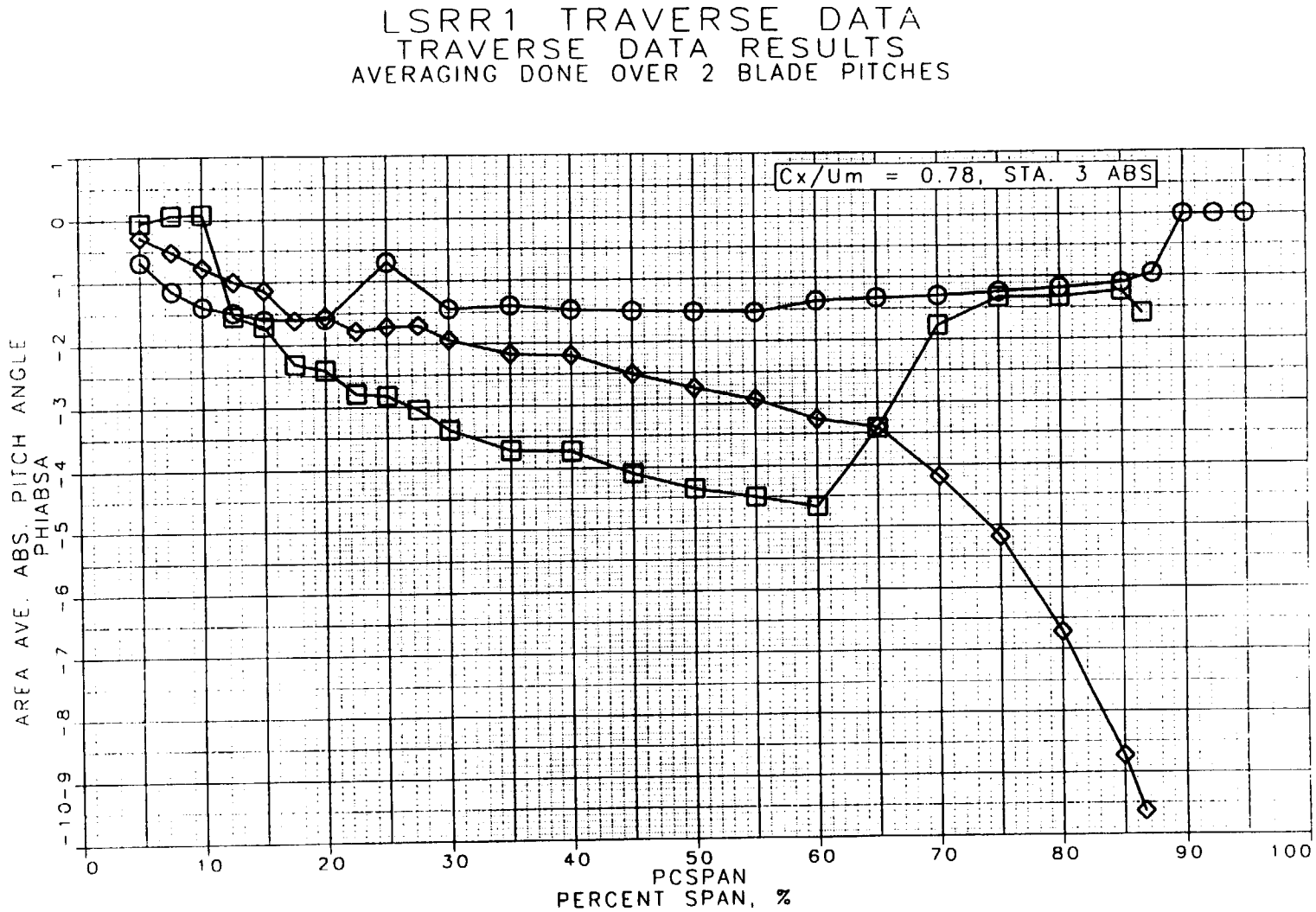

Figure 198. Area Averaged Absolute Pitch Angle at STA3

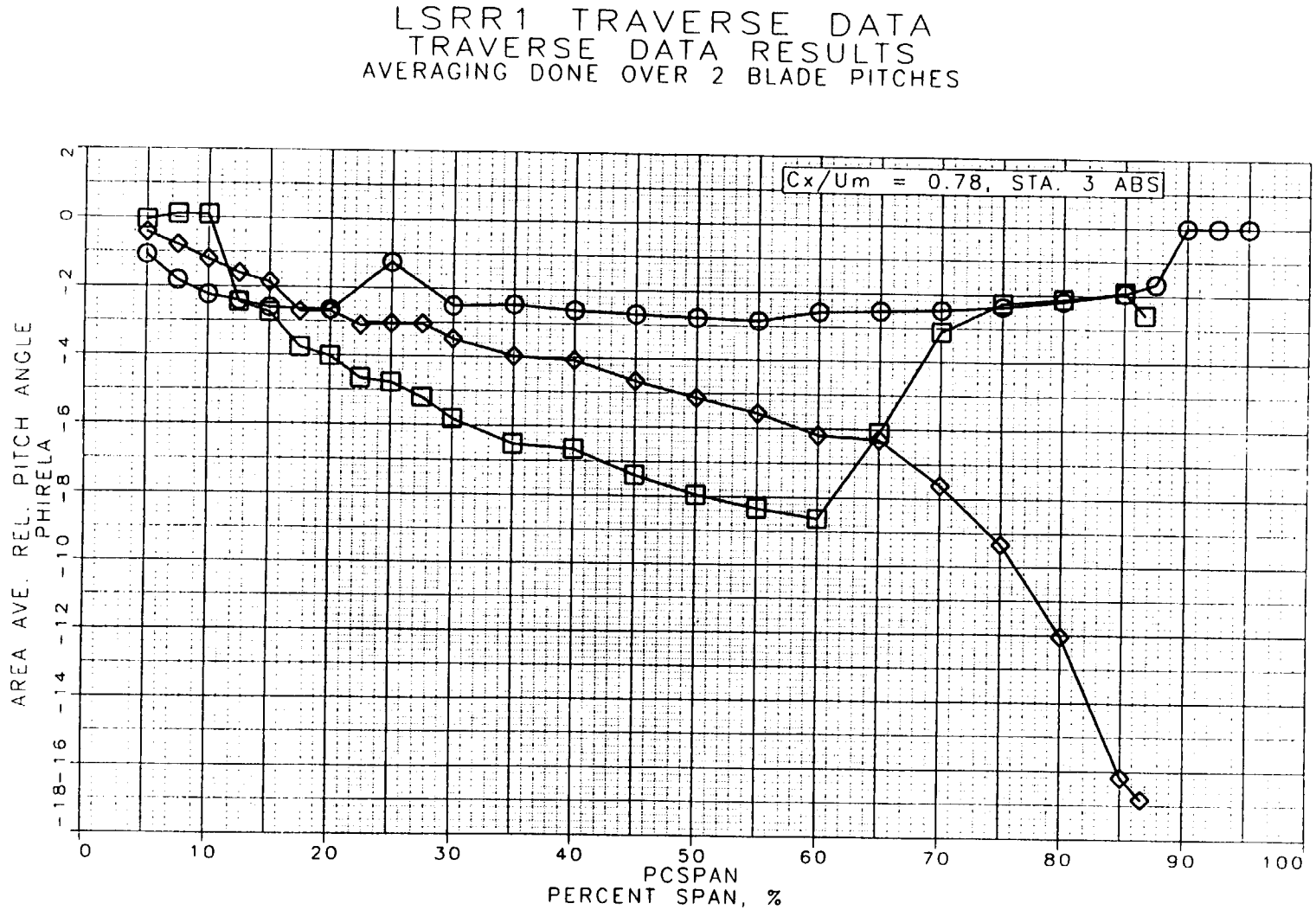

Figure 199. Area Averaged Relative Pitch Angle at STA3

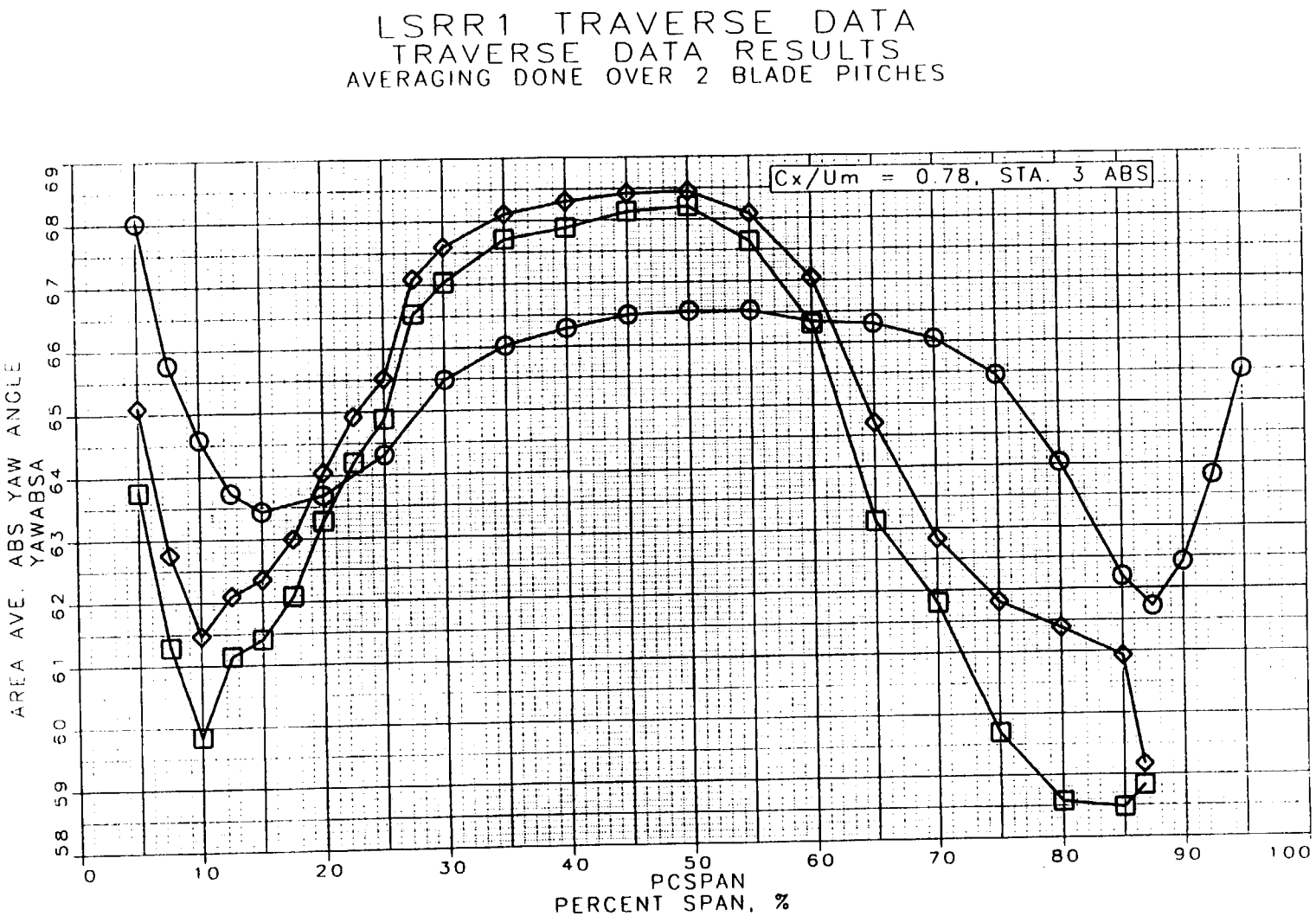

Figure 200. Area Averaged Absolute Yaw Angle at STA3

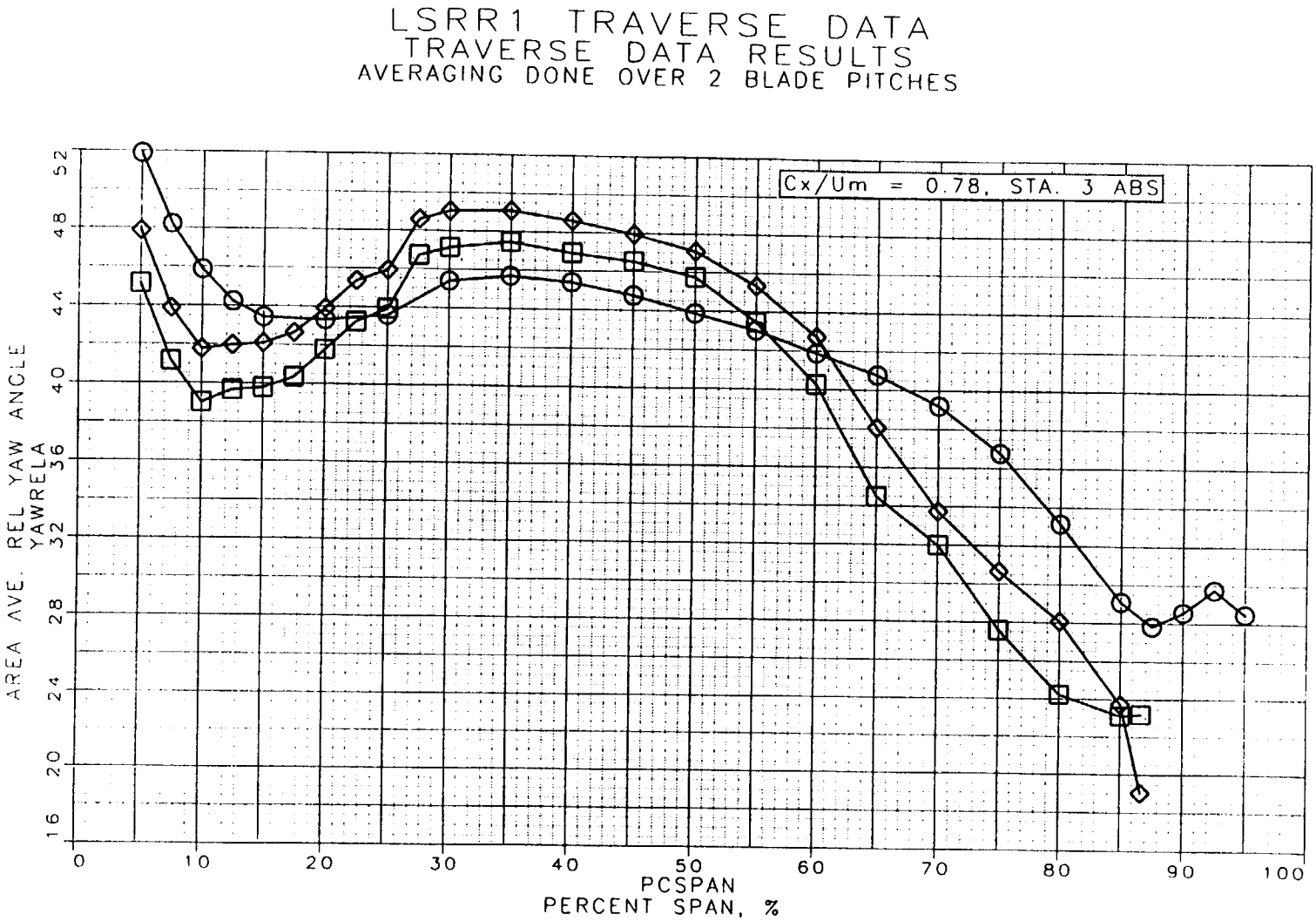

Figure 201. Area Averaged Relative Yaw Angle at STA3

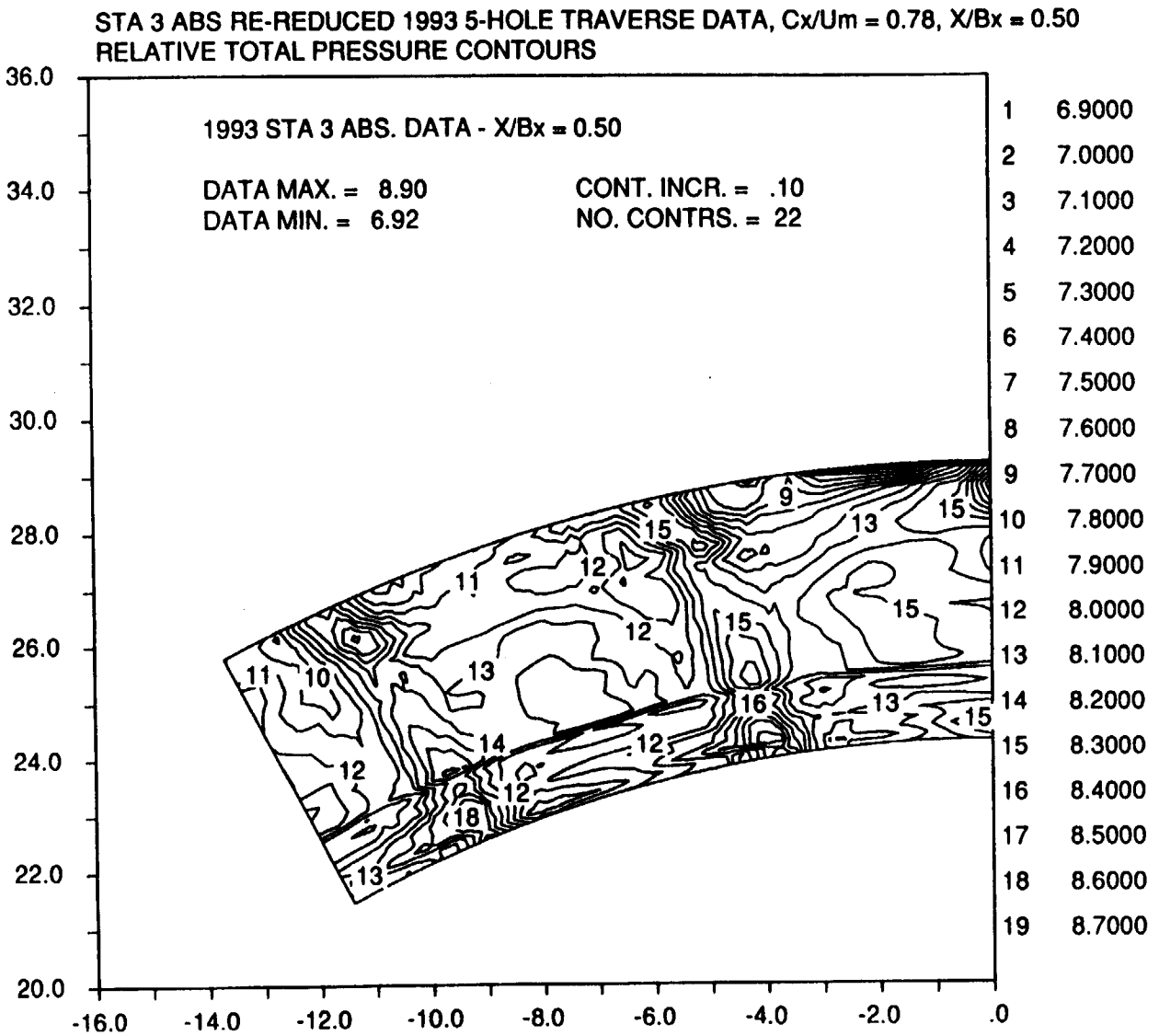

Figure 202. Relative Total Pressure Contours at STA3

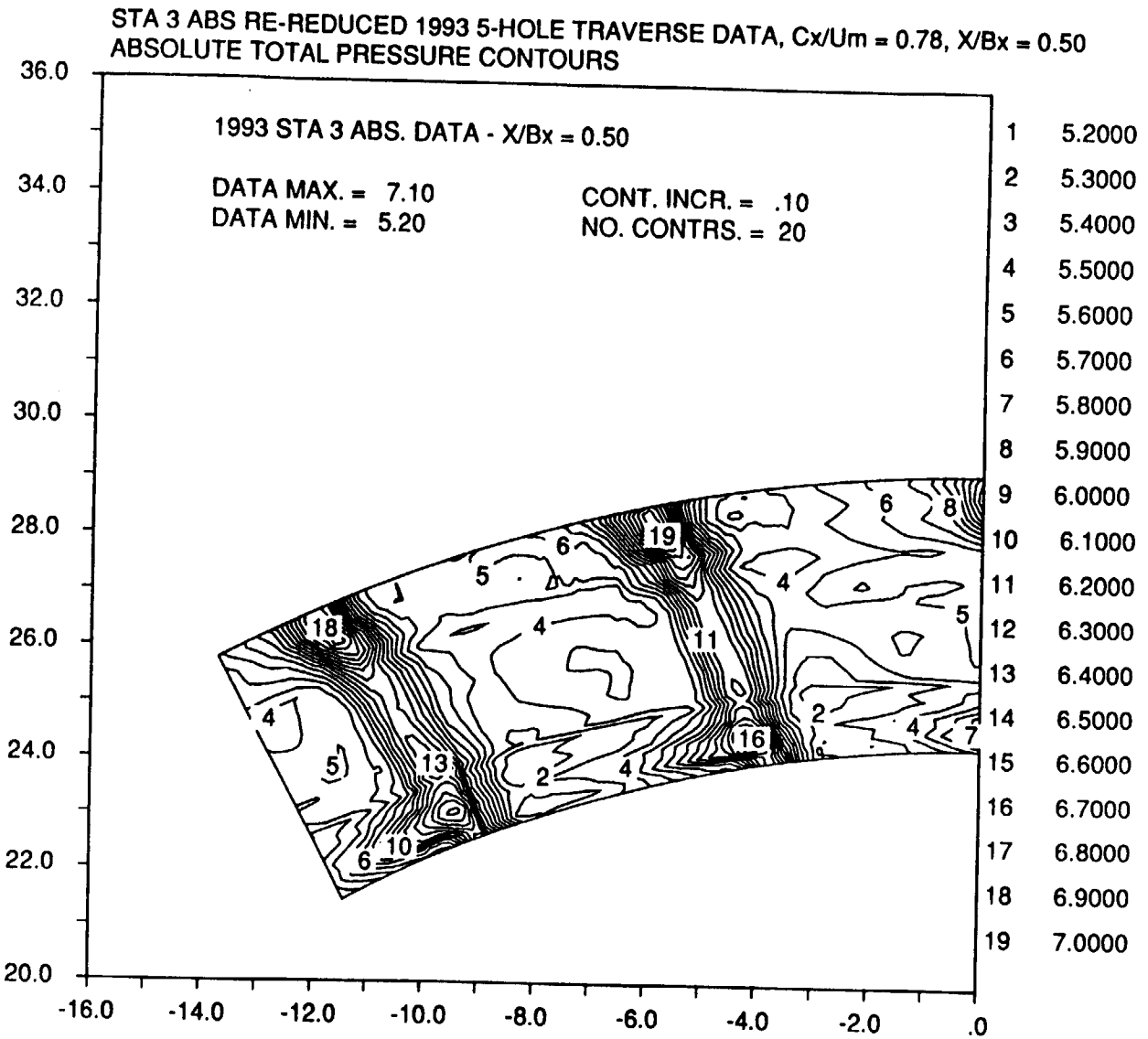

Figure 203. Absolute Total Pressure Contours at STA3

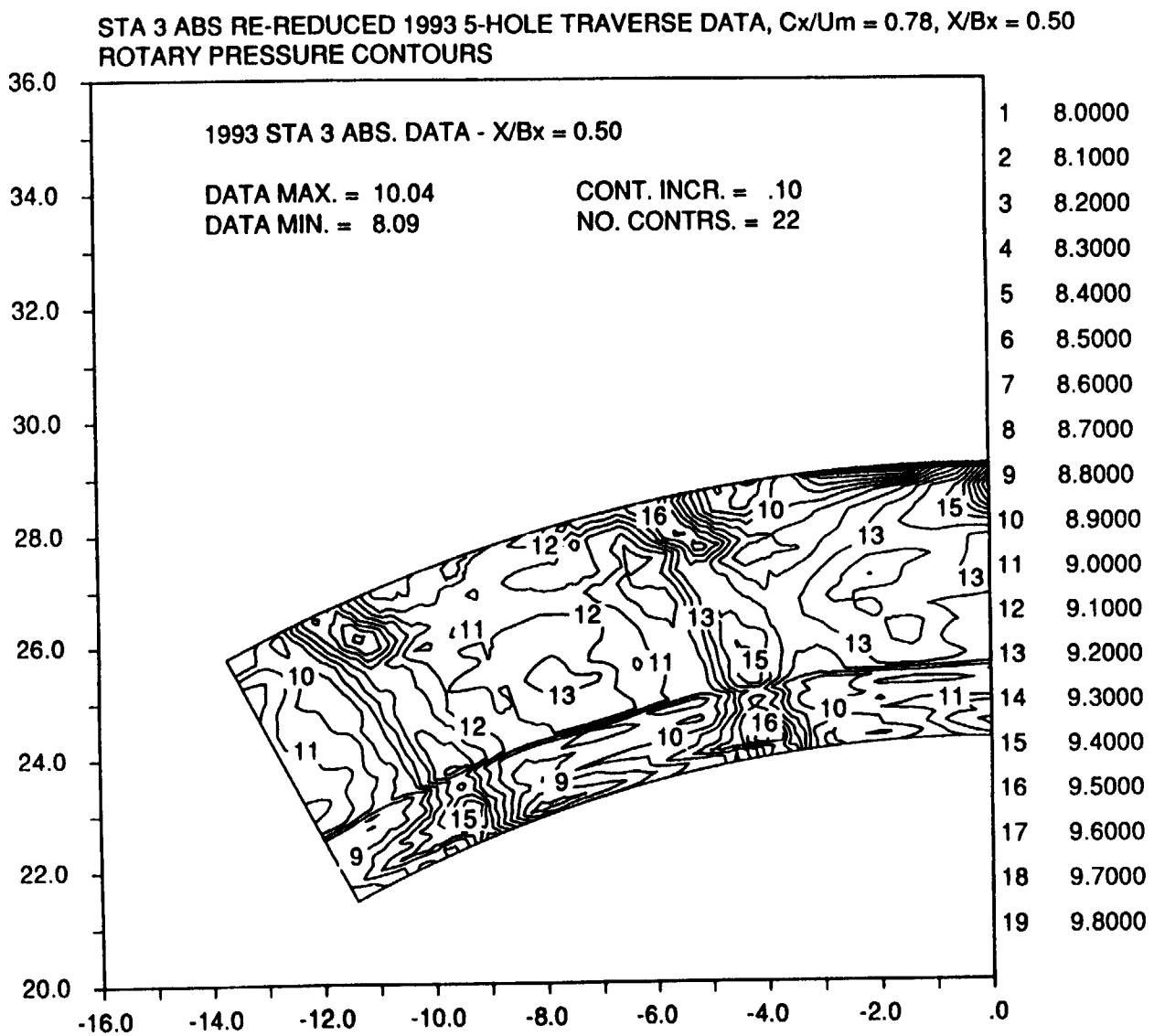

Figure 204. Static Pressure Contours at STA3

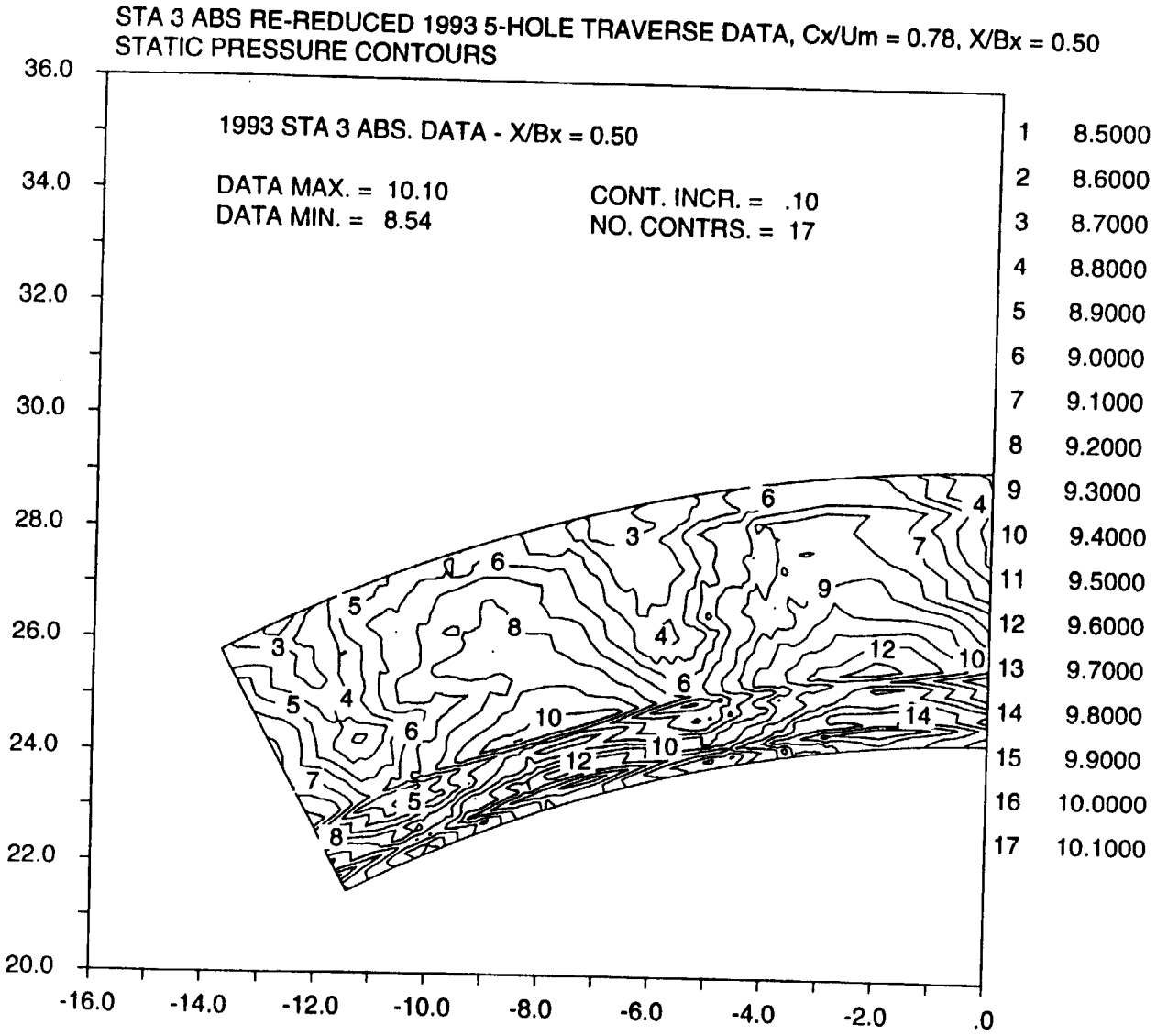

Figure 205. Rotary Pressure Contours at STA3

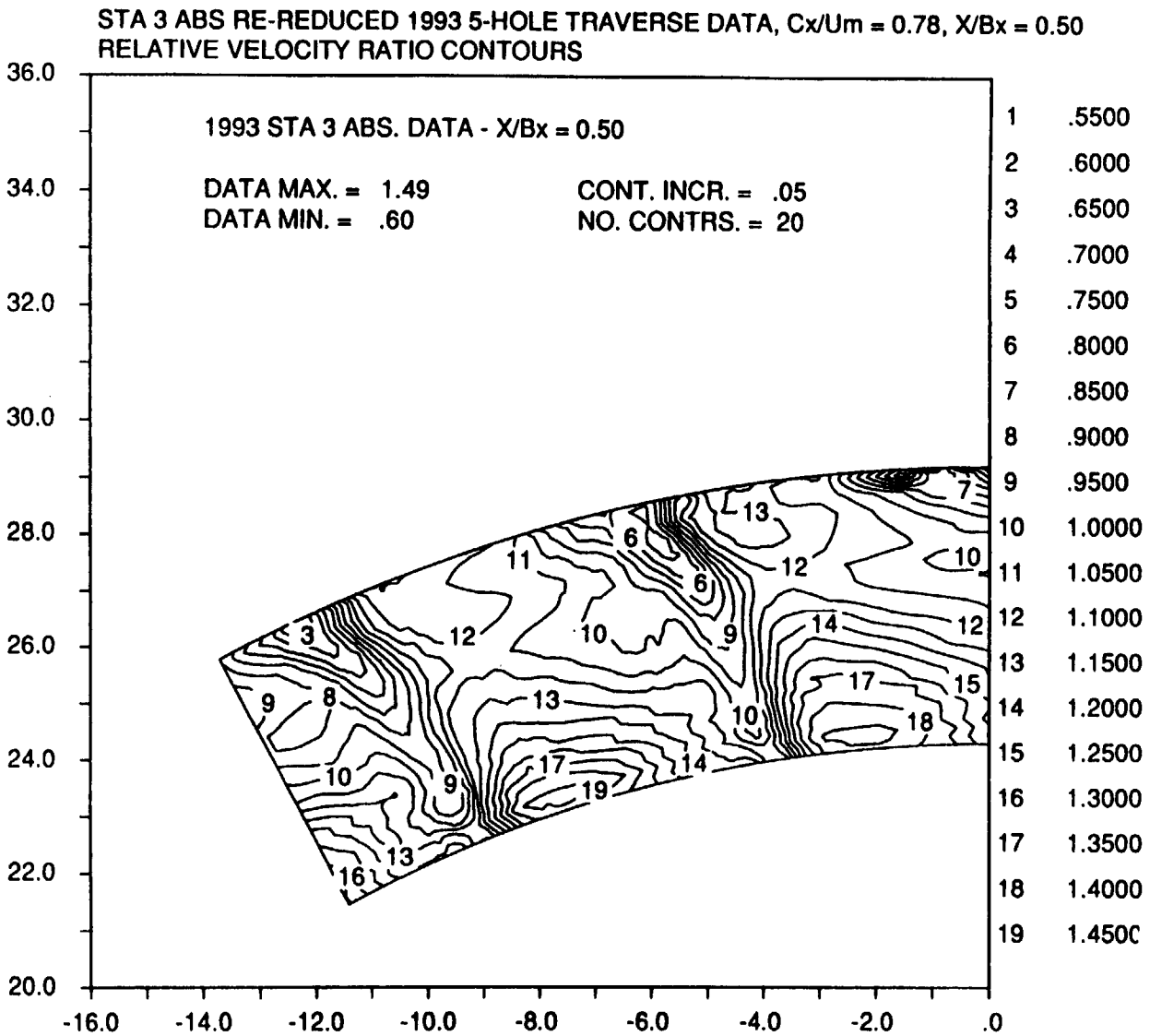

Figure 206. Absolute Velocity Ratio Contours at STA3

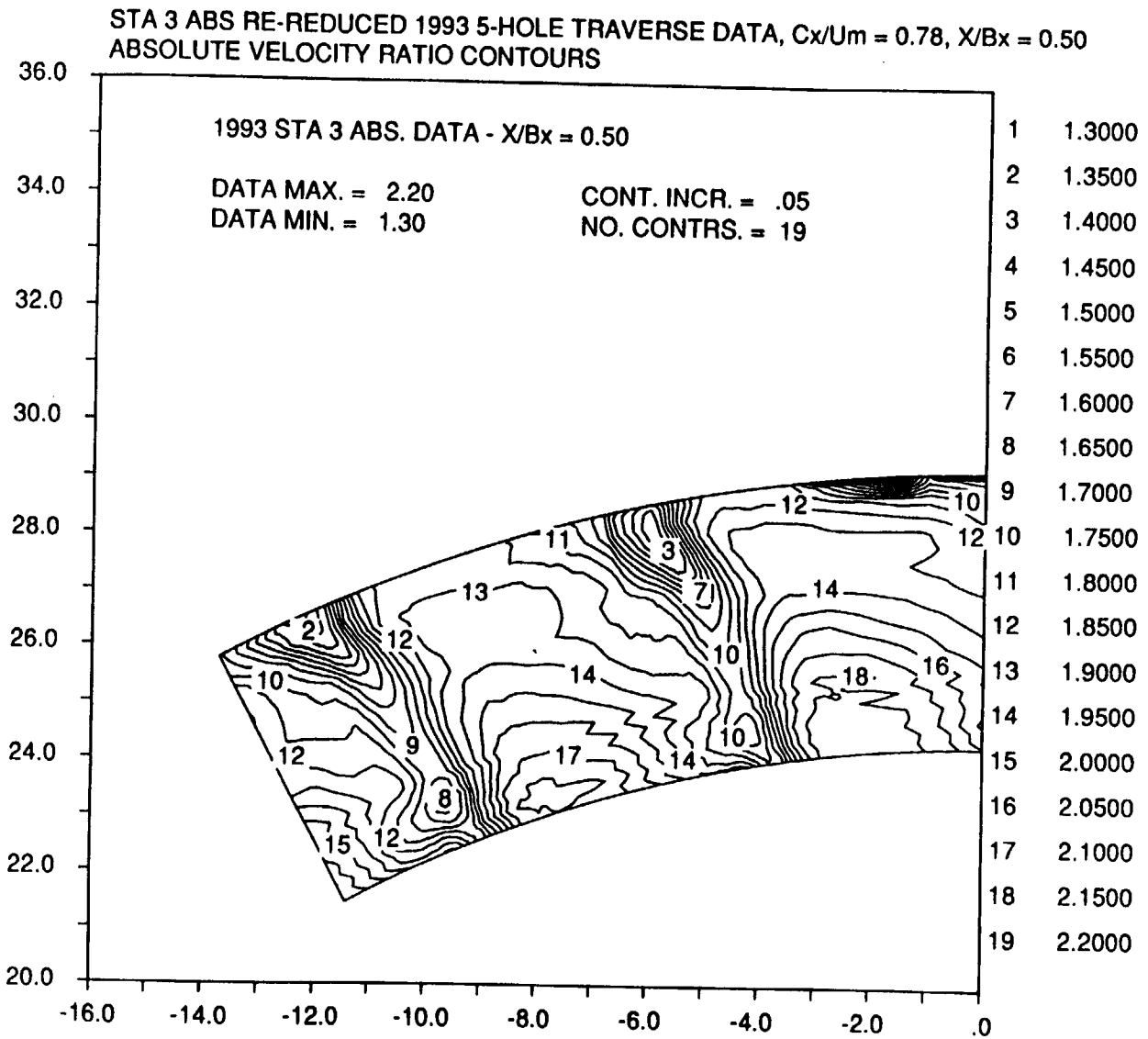

Figure 207. Relative Velocity Ratio Contours at STA3

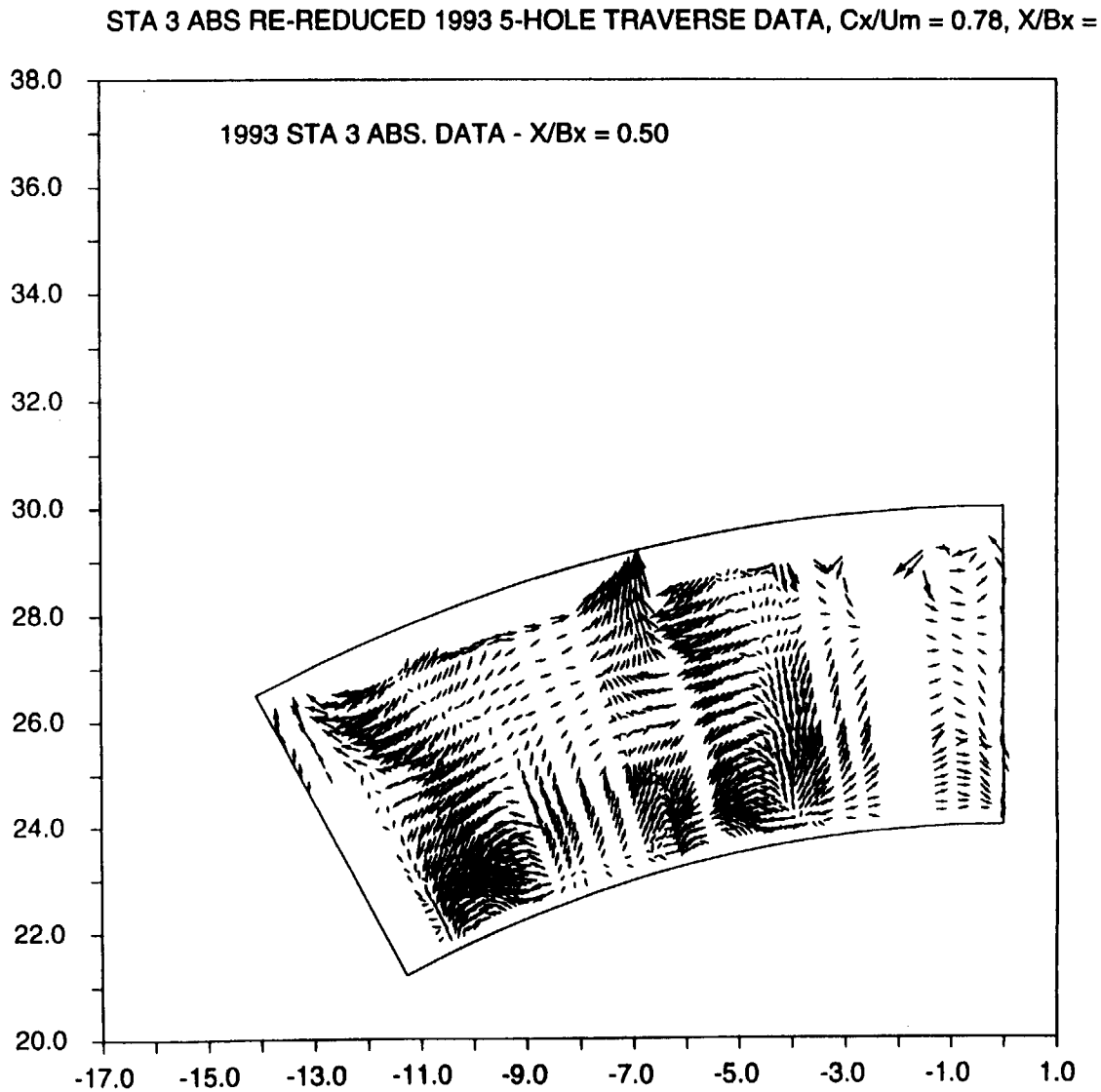

Figure 208. Velocity Vectors at STA3

APPENDIX D — SYNOPSIS OF PROPOSED PROGRAM

This appendix is a synopsis of the proposed program, *Performance and Heat Load Predictions for Multistage Turbines*, 11 August 1989 (Proposal Number 87-1223).

The understanding of unsteady flows in turbomachines prior to the start of the contract in 1990 is discussed in this appendix. The turbine design community recognized that the impact of unsteadiness was significant, and it needed to be accounted for in the design process. It was known that unsteadiness resulted in the following:

- Early transition of boundary layers
- Excessively high temperatures in turbine rotor blades
- Separation of boundary layers for airfoils operating at low Reynolds numbers
- Periodic breaking up of secondary flow vortices in turbines.

The impact of some of these effects will be reviewed in more detail to lay the groundwork for the current investigation.

Wakes from upstream airfoil rows have a significant effect on the performance and heat load characteristics of downstream airfoil rows. The time-averaged influence of upstream wakes on the boundary layer thickness and heat transfer coefficient on the suction side of two turbine rotor airfoils are shown in Figures 209 and 210. Also shown in Figure 209 is the data obtained for these airfoils in steady cascade configurations and calculated results from a boundary layer code. The steady cascade data show good agreement with two-dimensional (2-D) transitional boundary layer calculations. The time-averaged data, from the rotor affected by wakes from the upstream nozzle vane, lie between the transitional and fully turbulent calculations. These figures indicate that boundary layer transition is influenced by the wakes from the upstream airfoil. Steady cascade data with large levels of inlet turbulence can also produce a similar characteristics. Since wakes contain high levels of turbulence, the periodic high turbulence level could be considered responsible for this change in the boundary layer characteristics.

The upstream row distortions (wakes, secondary flow structures turbulence) not only affect the airfoil boundary layers of downstream rows, but also influence the secondary vortical flow structure in the downstream row passages. This phenomenon is graphically shown in Figure 211, where the rotor exit relative total pressure contours are shown at an instant in time for three different positions of the upstream stator. In this figure, the residence time of the fluid particles in the rotor passage is accounted for so that the exit flowfield corresponds to the given inlet flowfield. When the inlet flow is uniform, the exit flow exhibits the presence of three distinct vortices due to the hub and tip secondary flows and the tip leakage flows. When the upstream stator distortion is present in the rotor flowfield, the hub and tip secondary flow vortices exhibit a different structure, while the tip leakage vortex stays relatively constant.

Secondary flow vortices from upstream airfoils can significantly alter the flowfield in the downstream airfoil rows. Work performed by Pratt & Whitney (P&W) in the University of Connecticut water tunnel showed that when an upstream vortex passed through a downstream cascade passage, the secondary flow pattern in the passage was significantly affected. The upstream secondary flow was generated by a low turning airfoil suspended in the central part of the inlet duct generating inner and outer tip vortices, similar to the flow generated by a high turning upstream airfoil.

This flow then propagated downstream to a typical turbine airfoil, as shown schematically in Figure 212. Laser techniques were used to show the flow patterns at the low turning airfoil exit and across the throat of the high turning downstream airfoil. These flow patterns are shown in Figure 213, where Figure 213(a) shows the two inlet vortices entering the cascade. Figure 213(b) shows that when these inlet vortices enter near the cascade suction side, they propagate through the cascade and hug the suction side. Figure 213(c through e) shows three *snapshots* in time when these vortices entered near the pressure side indicating highly unstable flow in a *steady* flow condition.

Although a relatively simple experiment, it visually shows that a vortex from an upstream airfoil row can have a significant effect on the secondary flow generation for the downstream row.

This same effect is observed in the data obtained in the United Technologies Research Laboratory (UTRC) large-scale rotating rig (LSRR), as shown in Figure 214, as the spanwise distribution of circumferential averaged exit gas angles for the rotor and second stator. The geometries for these airfoil rows are almost identical, as shown in Figure 215, but the angle profiles exiting each of the airfoil rows is quite different, as shown in Figure 214. These angles indicate that there is large secondary flow in the rotor passage, but very little secondary flow in the second stator passage. The second stator angle is essentially inverted, relative to the rotor. This rig data and the data from the water tunnel indicated inlet secondary flow can significantly impact the flow in the downstream airfoil. The impact of this phenomenon on the airfoil performance is still not well understood.

In addition to the incoming wakes and secondary flow vortices, the flowfield in an airfoil row is also influenced by temperature distortions generated in the burner upstream of the turbine. This effect of temperature distortion was experimentally assessed in the UTRC LSRR. It was demonstrated that the first stator flowfield was unaffected by the inlet temperature profile. The rotor flowfield, however, appeared to be affected, as shown by the CO_2 concentration and redistribution in Figure 216 for two inlet temperature distortions. Numerical simulations conducted with a three-dimensional (3-D), unsteady Euler analysis showed that the hot streak convects through the vane and then impinges on the rotor pressure surface (Figure 217). Since the resonant time on the pressure surface was longer than the suction surface, the time-averaged temperature on the pressure side was greater than the average inlet temperature, as shown in Figure 218. To confirm that this hotter pressure side was a result of periodic interaction, the Euler analysis was run steady (with a mixing plane) and unsteady. The results show that the time-averaged unsteady agrees much better with the measured data, as shown in Figure 219. This again shows the significance of inlet flow distortion and the impact of unsteadiness on the time-averaged flowfield.

In summary, the influence of turbulence from upstream wakes on the boundary layer characteristics of downstream airfoil rows has been documented and first order models have been formulated to simulate these effects. The influence of periodic flow distortion, such as wakes and secondary flow, on downstream airfoil performance requires further investigation.

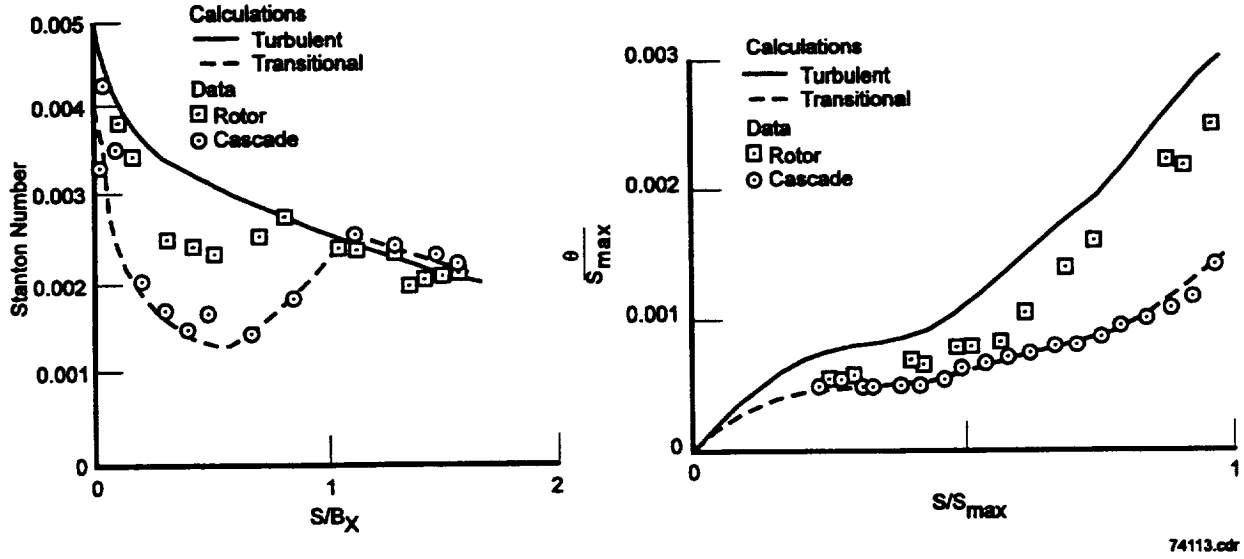

Figure 209. Measured Stanton No. Distribution on Rotor Falls Between Cascade Data and Turbulent Calculations

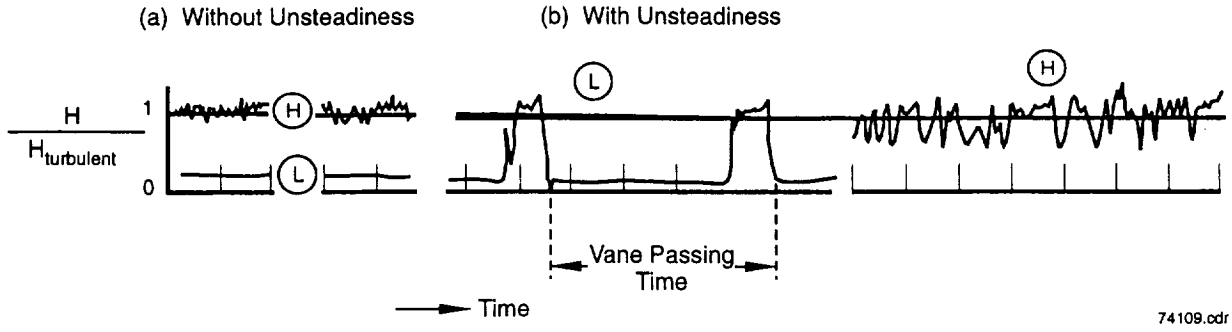

Figure 210. Heat Transfer Coefficient Data, Measured on Airfoil Suction Surface in Turbine Cascade, at Two Levels of Background Turbulence, With Unsteadiness Generated by Rotating Bar, Upstream of Cascade, Indicate That Upstream Wakes Have Significant Effects on Laminar Boundary Layers and Little Effect on Turbulent Boundary Layers

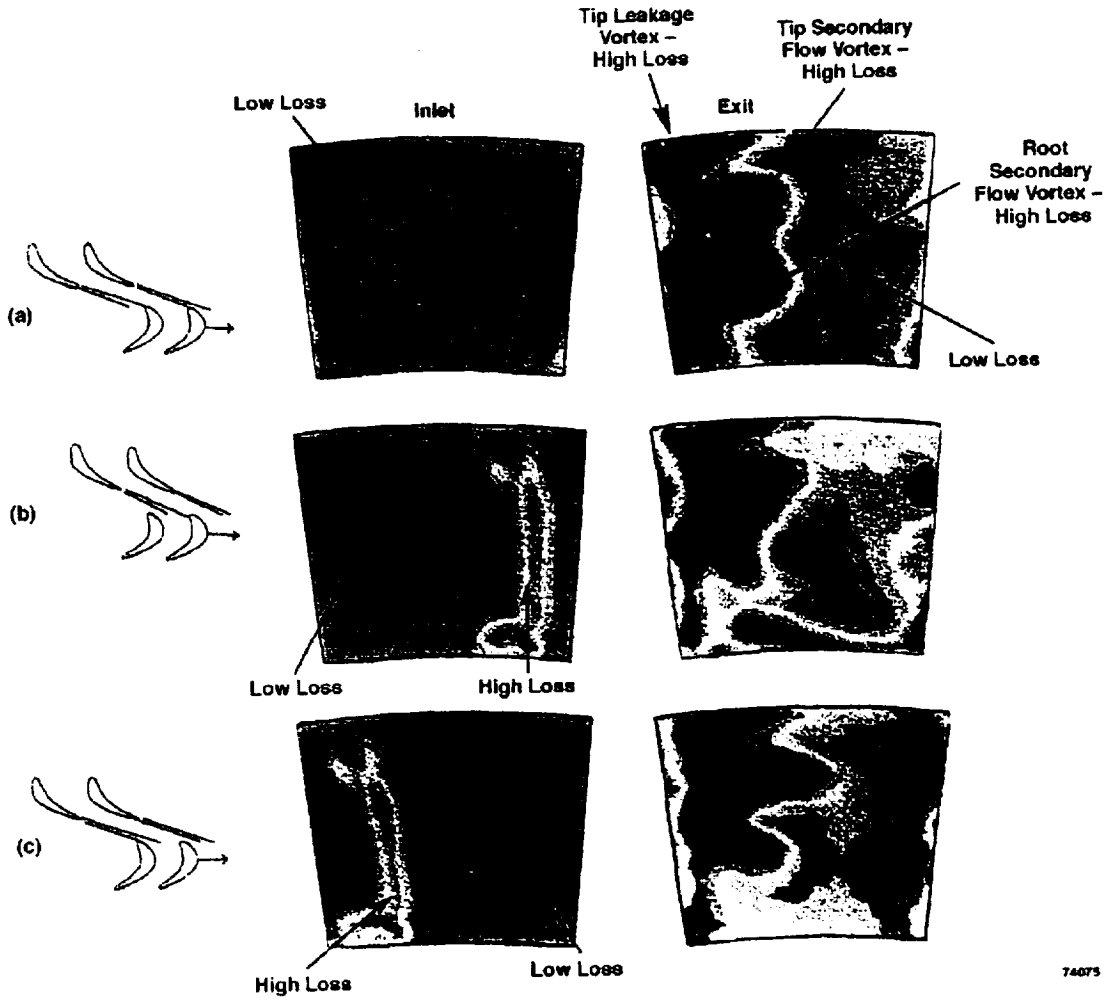

Figure 211. Relative Total Pressure Contours Upstream and Downstream of Rotor Indicating Change in Organized Flow Structures, as Affected by Upstream Circumferential Distortion

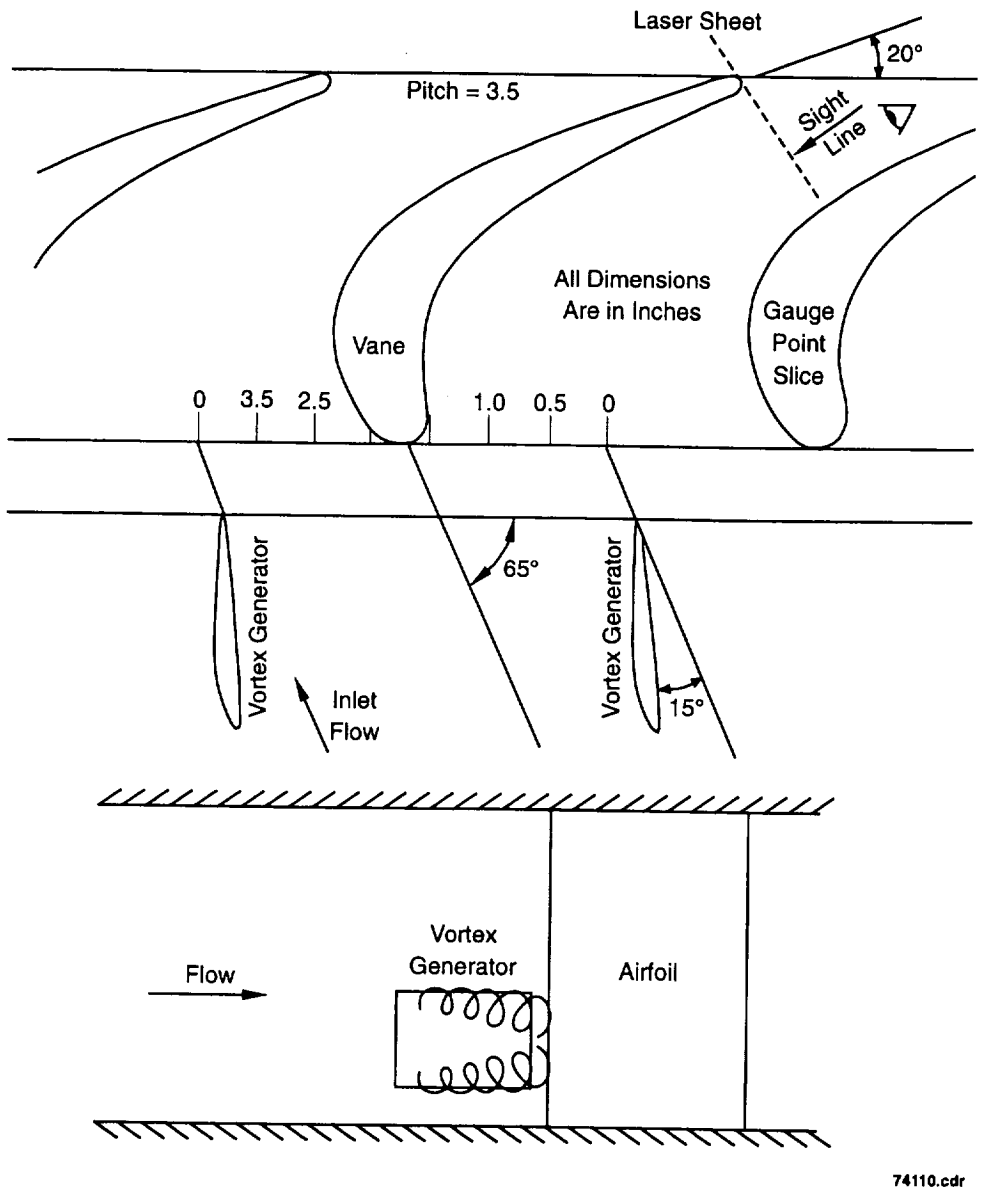

Figure 212. Water Tunnel Geometry of Turbine Airfoil Cascade and Vortex Generator

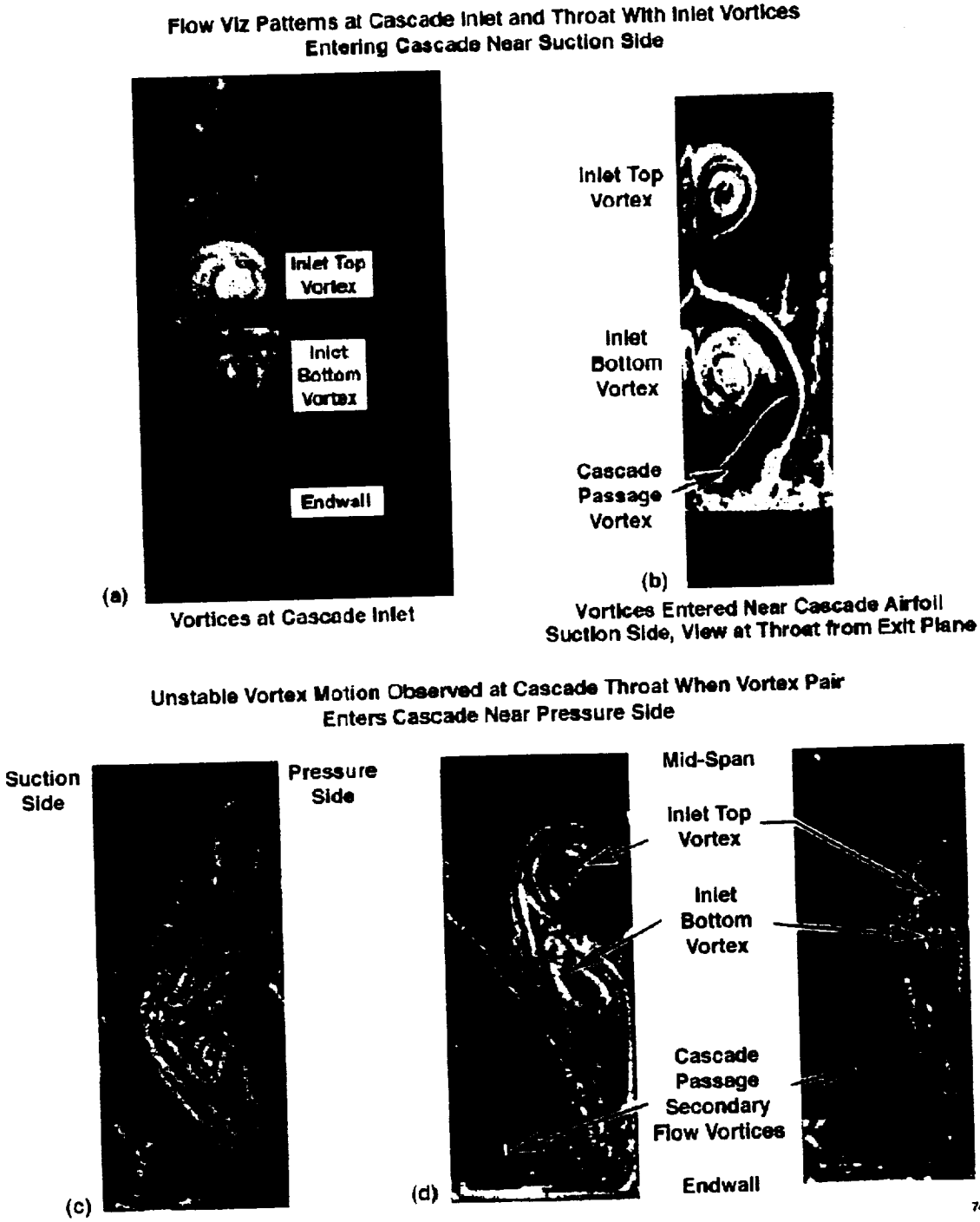

Figure 213. Flow Visualization Patterns at Cascade Inlet and Gage Plane When Inlet Vortices Entered Cascade Near Pressure and Suction Side of Cascade Airfoils

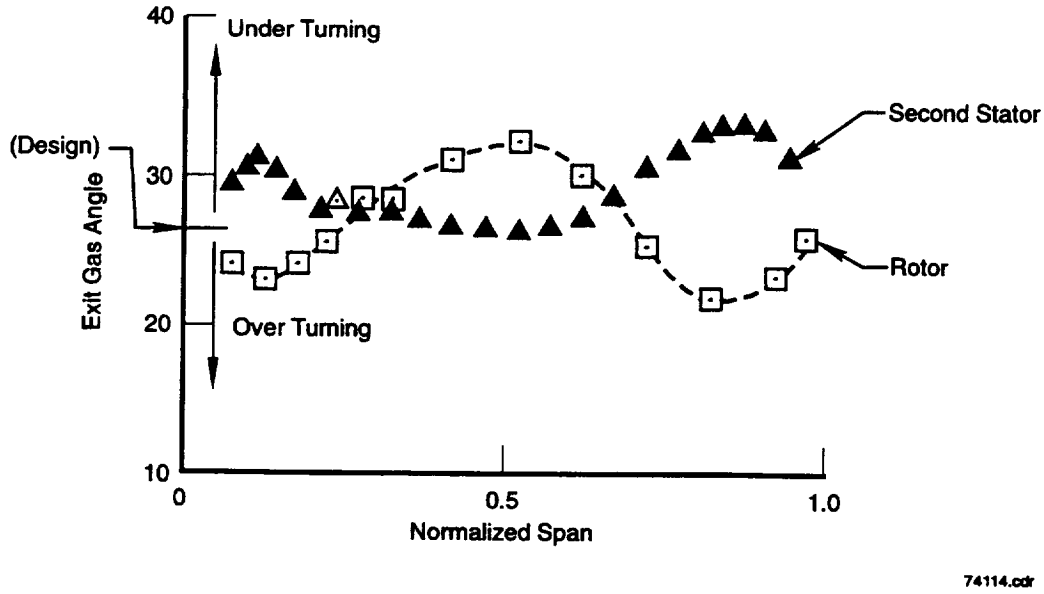

Figure 214. Spanwise Distribution of Measured Gas Angles of Second Stator Show Opposite Characteristics of Secondary Flow Compared to Rotor

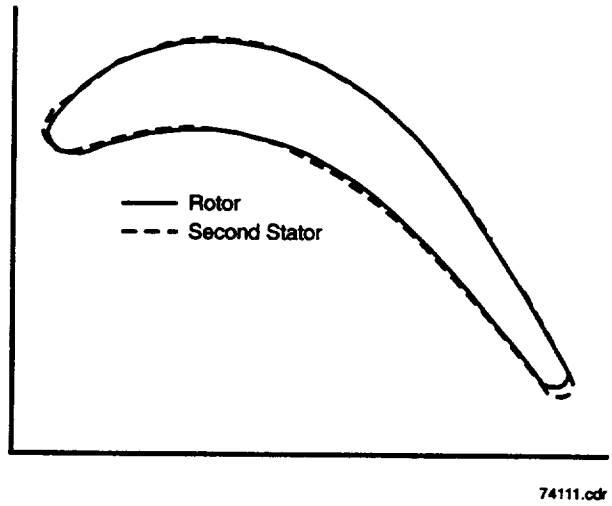

Figure 215. Rotor and Second Stator Mean Section Shows That Both Airfoils Have Almost Identical Cross-Section Geometry

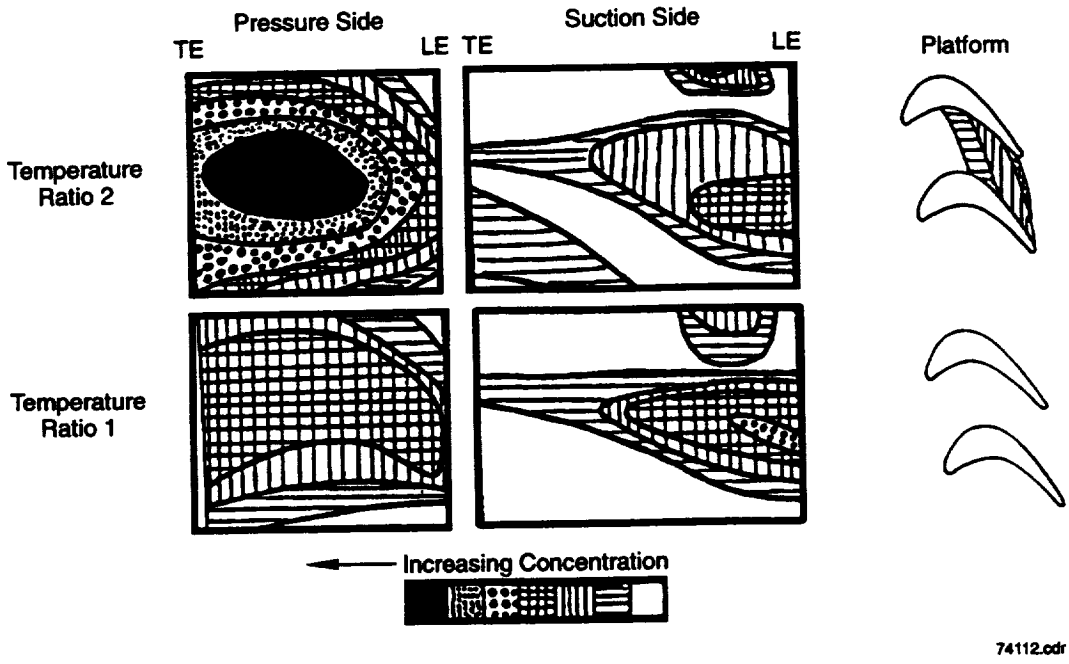

Figure 216. Inlet Total Temperature Distortion Results in Increased Magnitudes of Secondary Flows

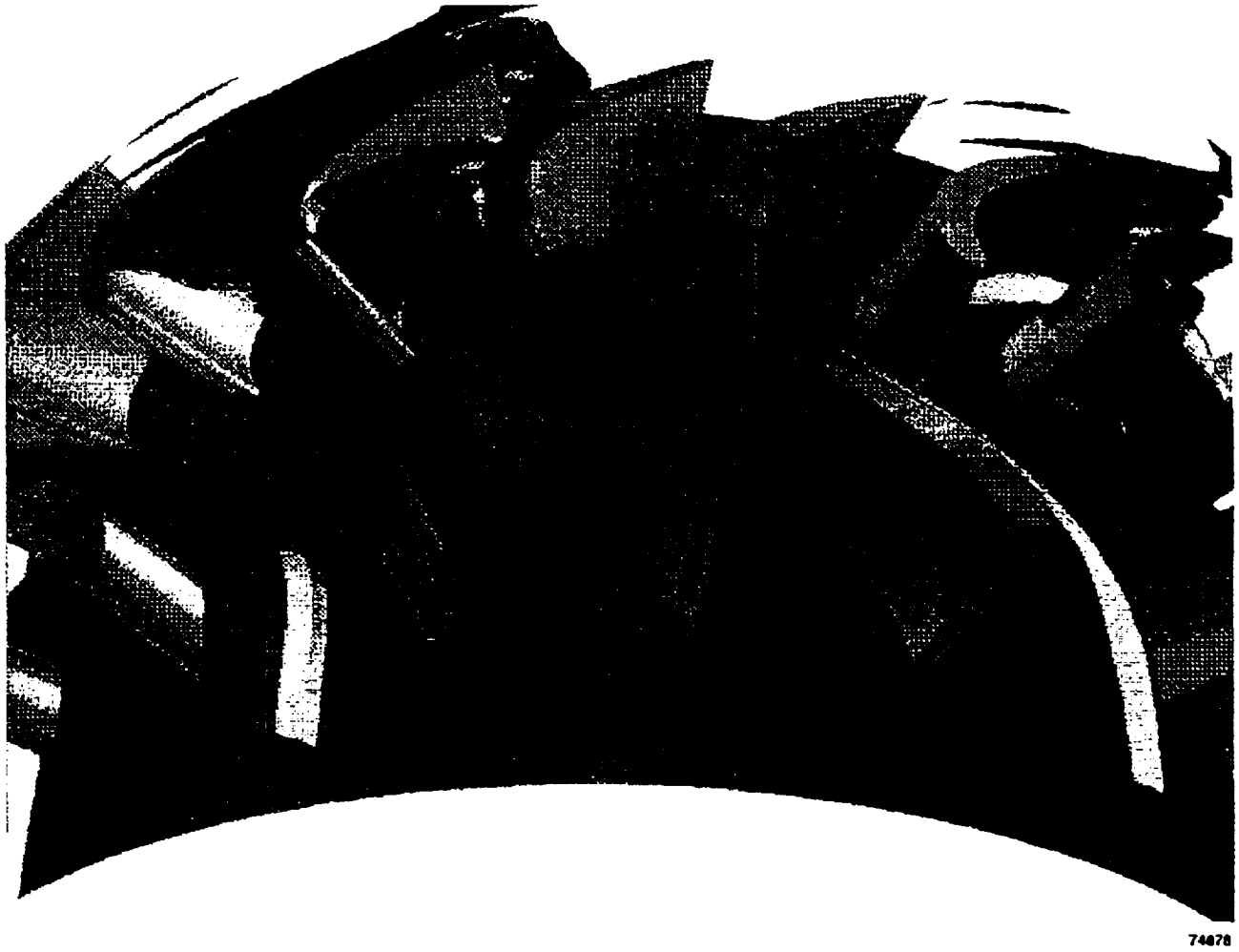

Figure 217. Snapshot in Time of 3-D Unsteady Euler Simulation of Hot Streak in LSRR Stage Turbine; Hot Streak Convects Through Stator Passage With No Distortion and Then Interacts With Passing Rotor

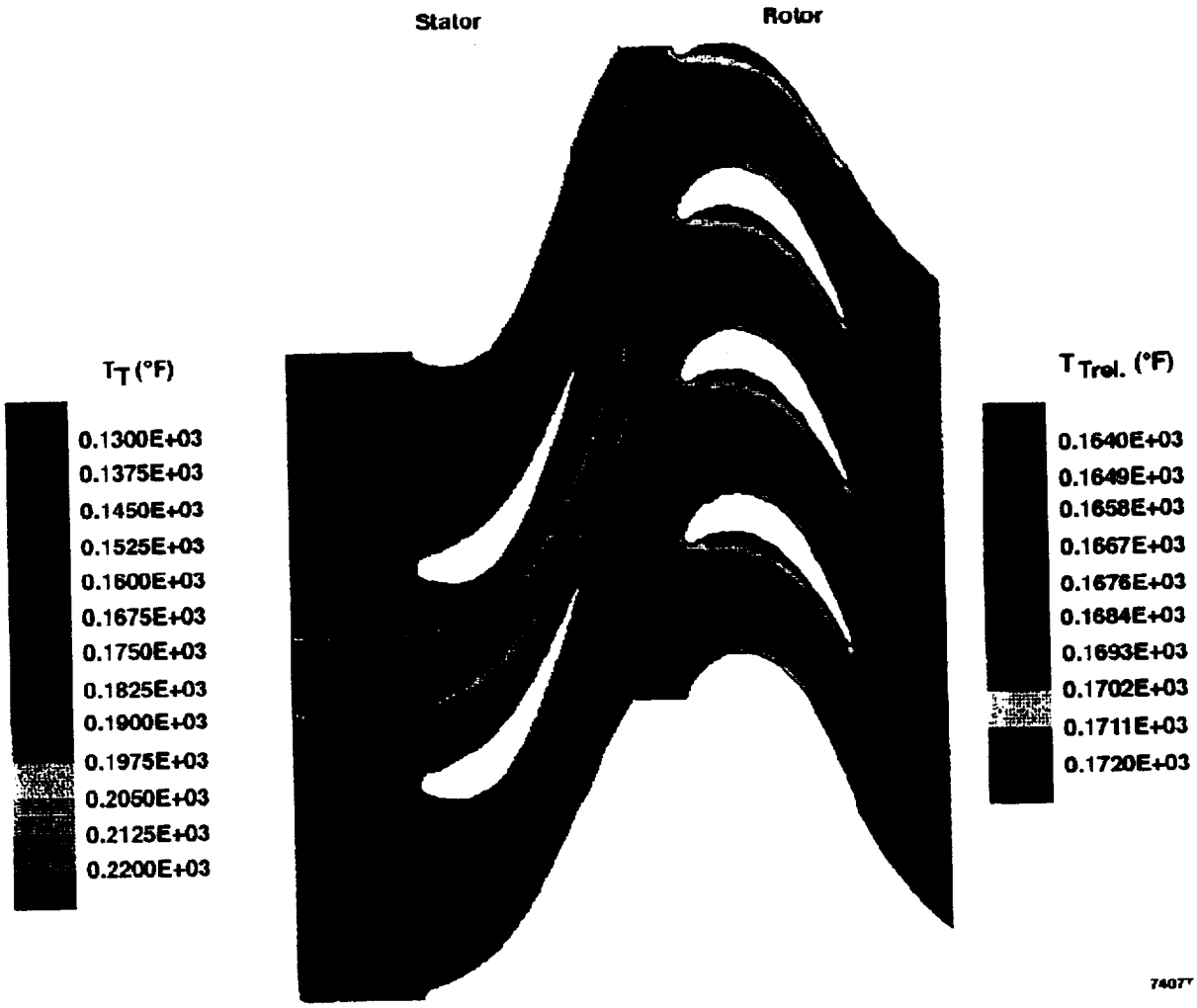

Figure 218. Time Average of Unsteady Flow Simulation Predicts Hotter Temperature on Rotor Airfoil Pressure Side; This Temperature Is Higher Than Average Temperature at Rotor Inlet and Is in AgreementWith Experimental Data

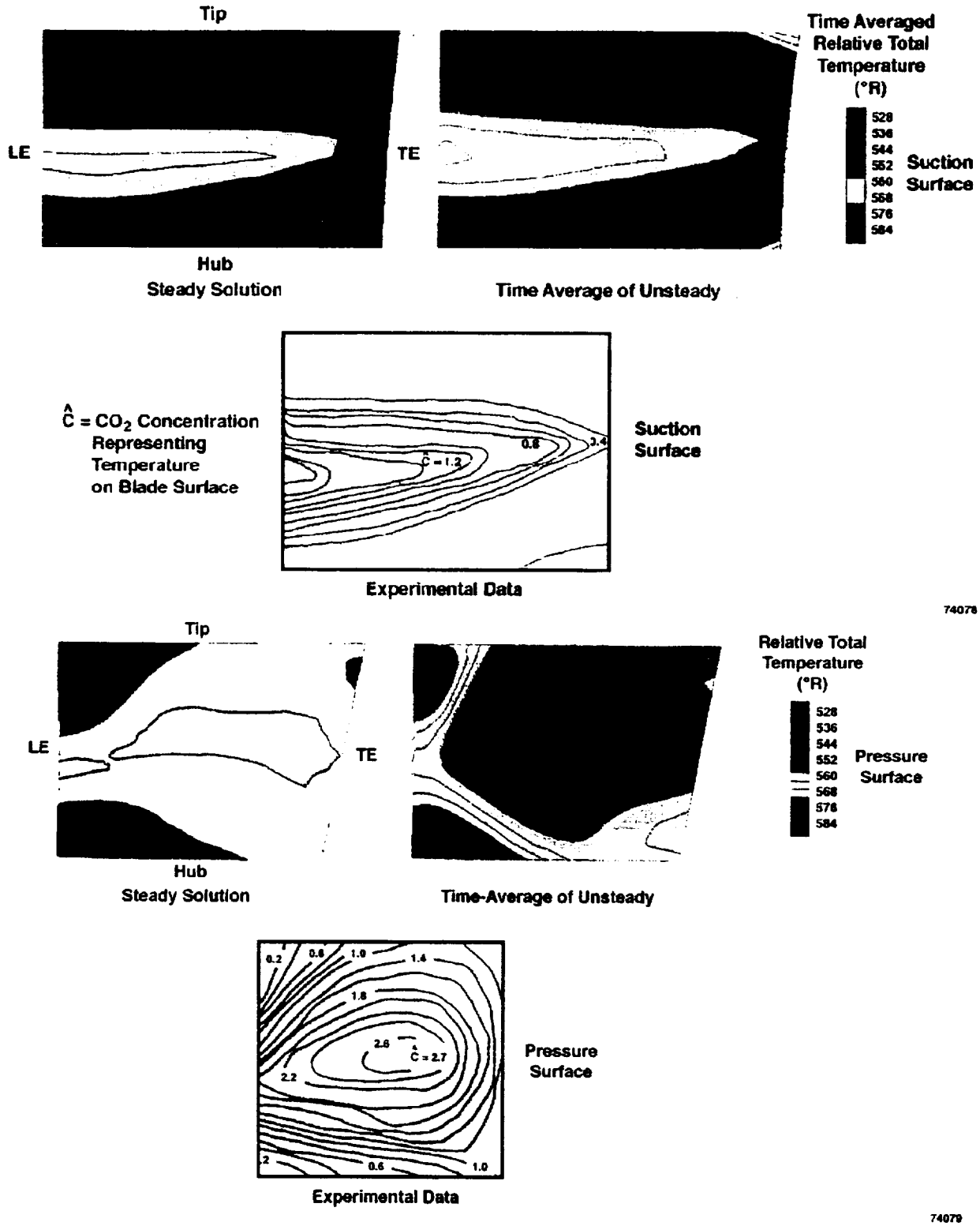

Figure 219. Comparison of Time-Averaged Unsteady and Steady Solutions for Rotor Suction and Rotor Pressure Surfaces With Experimental Data

REPORT DOCUMENTATION PAGE

Form Approved
OMB No. 0704-0188

Public reporting burden for this collection of information is estimated to average 1 hour per response, including the time for reviewing instructions, searching existing data sources, gathering and maintaining the data needed, and completing and reviewing the collection of information. Send comments regarding this burden estimate or any other aspect of this collection of information, including suggestions for reducing this burden, to Washington Headquarters Services, Directorate for Information Operations and Reports, 1215 Jefferson Davis Highway, Suite 1204, Arlington, VA 22202-4302, and to the Office of Management and Budget, Paperwork Reduction Project (0704-0188), Washington, DC 20503.

1. AGENCY USE ONLY (*Leave blank*)	2. REPORT DATE	3. REPORT TYPE AND DATES COVERED
	January 1997	Final Contractor Report

4. TITLE AND SUBTITLE

Impact of Periodic Unsteadiness on Performance and Heat Load in Axial Flow Turbomachines

5. FUNDING NUMBERS

WU–538–06–14
C–NAS3–25804

6. AUTHOR(S)

Om P. Sharma, Gary M. Stetson, William A. Daniels, Edward M. Greitzer, Michael F. Blair, and Robert P. Dring

7. PERFORMING ORGANIZATION NAME(S) AND ADDRESS(ES)

Pratt & Whitney
400 Main Street
East Hartford, Connecticut 06108

8. PERFORMING ORGANIZATION REPORT NUMBER

E–10624
FR–24232

9. SPONSORING/MONITORING AGENCY NAME(S) AND ADDRESS(ES)

National Aeronautics and Space Administration
Lewis Research Center
Cleveland, Ohio 44135–3191

10. SPONSORING/MONITORING AGENCY REPORT NUMBER

NASA CR–202319

11. SUPPLEMENTARY NOTES

Om P. Sharma and Gary M. Stetson, Pratt & Whitney; William A. Daniels, Michael F. Blair, and Robert P. Dring, United Technologies Research Center, East Hartford, Connecticut 06108; Edward M. Greitzer, Massachusetts Institute of Technology, Cambridge, Massachusetts 02139–4307. Technical Manager, John J. Adamczyk, Turbomachinery and Propulsion Systems Division, NASA Lewis Research Center, organization code 5800 (216) 433–5829. Project Manager, James W. Gauntner, Turbomachinery and Propulsion Systems Division, NASA Lewis Research Center, organization code 5880, (216) 433–7435.

12a. DISTRIBUTION/AVAILABILITY STATEMENT

Unclassified - Unlimited
Subject Category 07

This publication is available from the NASA Center for AeroSpace Information, (301) 621–0390.

12b. DISTRIBUTION CODE

13. ABSTRACT ***(Maximum 200 words)***

Results of an analytical and experimental investigation, directed at the understanding of the impact of periodic unsteadiness on the time-averaged flows in axial flow turbomachines, are presented. Analysis of available experimental data, from a large-scale rotating rig (LSRR) (low speed rig), shows that in the time-averaged axisymmetric equations the magnitude of the terms representing the effect of periodic unsteadiness (*deterministic stresses*) are as large or larger than those due to random unsteadiness (turbulence). Numerical experiments, conducted to highlight physical mechanisms associated with the migration of combustor generated hot-streaks in turbine rotors, indicated that the effect can be simulated by accounting for *deterministic stress* like terms in the time-averaged mass and energy conservation equations. The experimental portion of this program shows that the aerodynamic loss for the second stator in a 1–1/2 stage turbine are influenced by the axial spacing between the second stator leading edge and the rotor trailing edge. However, the axial spacing has little impact on the heat transfer coefficient. These performance changes are believed to be associated with the change in *deterministic stress* at the inlet to the second stator. Data were also acquired to quantify the impact of indexing the first stator relative to the second stator. For the range of parameters examined, this effect was found to be of the same order as the effect of axial spacing.

14. SUBJECT TERMS

Axial flow turbomachines; Airfoil interaction; Periodic unsteadiness; Random unsteadiness; Turbulence

15. NUMBER OF PAGES

301

16. PRICE CODE

A14

17. SECURITY CLASSIFICATION OF REPORT	18. SECURITY CLASSIFICATION OF THIS PAGE	19. SECURITY CLASSIFICATION OF ABSTRACT	20. LIMITATION OF ABSTRACT
Unclassified	Unclassified	Unclassified	